frontiers | Research Topics

Extreme climate events: Variability, mechanisms, and numerical simulations

Edited by
Bo Sun, Lu Zhang, Shangfeng Chen and Stephen Outten

Published in
Frontiers in Earth Science

ISSN 1664-8714
ISBN 978-2-83251-965-3
DOI 10.3389/978-2-83251-965-3

About Frontiers

Frontiers is more than just an open access publisher of scholarly articles: it is a pioneering approach to the world of academia, radically improving the way scholarly research is managed. The grand vision of Frontiers is a world where all people have an equal opportunity to seek, share and generate knowledge. Frontiers provides immediate and permanent online open access to all its publications, but this alone is not enough to realize our grand goals.

Frontiers journal series

The Frontiers journal series is a multi-tier and interdisciplinary set of open-access, online journals, promising a paradigm shift from the current review, selection and dissemination processes in academic publishing. All Frontiers journals are driven by researchers for researchers; therefore, they constitute a service to the scholarly community. At the same time, the *Frontiers journal series* operates on a revolutionary invention, the tiered publishing system, initially addressing specific communities of scholars, and gradually climbing up to broader public understanding, thus serving the interests of the lay society, too.

Dedication to quality

Each Frontiers article is a landmark of the highest quality, thanks to genuinely collaborative interactions between authors and review editors, who include some of the world's best academicians. Research must be certified by peers before entering a stream of knowledge that may eventually reach the public - and shape society; therefore, Frontiers only applies the most rigorous and unbiased reviews. Frontiers revolutionizes research publishing by freely delivering the most outstanding research, evaluated with no bias from both the academic and social point of view. By applying the most advanced information technologies, Frontiers is catapulting scholarly publishing into a new generation.

What are Frontiers Research Topics?

Frontiers Research Topics are very popular trademarks of the *Frontiers journals series*: they are collections of at least ten articles, all centered on a particular subject. With their unique mix of varied contributions from Original Research to Review Articles, Frontiers Research Topics unify the most influential researchers, the latest key findings and historical advances in a hot research area.

Find out more on how to host your own Frontiers Research Topic or contribute to one as an author by contacting the Frontiers editorial office: frontiersin.org/about/contact

Extreme climate events: Variability, mechanisms, and numerical simulations

Topic editors

Bo Sun — Nanjing University of Information Science and Technology, China
Lu Zhang — CSIRO Land and Water, Australia
Shangfeng Chen — Monsoon Systems Research Center, Institute of Atmospheric Physics, Chinese Academy of Sciences (CAS), China
Stephen Outten — Nansen Environmental and Remote Sensing Center (NERSC), Norway

Citation

Sun, B., Zhang, L., Chen, S., Outten, S., eds. (2023). *Extreme climate events: Variability, mechanisms, and numerical simulations*. Lausanne: Frontiers Media SA. doi: 10.3389/978-2-83251-965-3

Table of contents

frontiers | Frontiers in Earth Science

TYPE Editorial
PUBLISHED 06 March 2023
DOI 10.3389/feart.2023.1159605

OPEN ACCESS

EDITED AND REVIEWED BY
Yuqing Wang,
University of Hawaii at Manoa,
United States

*CORRESPONDENCE
Bo Sun,
sunb@nuist.edu.cn

SPECIALTY SECTION
This article was submitted to Atmospheric Science, a section of the journal Frontiers in Earth Science

RECEIVED 06 February 2023
ACCEPTED 27 February 2023
PUBLISHED 06 March 2023

CITATION
Sun B, Zhang L, Chen S and Outten S (2023), Editorial: Extreme climate events: Variability, mechanisms, and numerical simulations.
Front. Earth Sci. 11:1159605.
doi: 10.3389/feart.2023.1159605

Editorial: Extreme climate events: Variability, mechanisms, and numerical simulations

Bo Sun[1,2]*, Lu Zhang[3], Shangfeng Chen[4] and Stephen Outten[5]

[1]Key Laboratory of Meteorological Disasters Joint International Research Laboratory of Climate and Environment Change Collaborative Innovation Center on Forecast and Evaluation of Meteorological Disasters, Ministry of Education, Nanjing University of Information Science and Technology, Nanjing, China, [2]Southern Marine Science and Engineering Guangdong Laboratory, Zhuhai, China, [3]CSIRO Land and Water, Canberra, ACT, Australia, [4]Institute of Atmospheric Physics, Chinese Academy of Sciences, Beijing, China, [5]Nansen Environmental and Remote Sensing Center, Bergen, Norway

KEYWORDS

extreme climate events, climate change, variability, prediction, global warming

Editorial on the Research Topic
Extreme climate events: Variability, mechanisms, and numerical simulations

The IPCC AR6 reported that the frequency and intensity of extreme high temperature and heat wave events have increased significantly over most parts of the globe during the past few decades. The frequency and/or intensity of extreme precipitation have also increased over many land areas in central and South Asia, United States, northwest Australia, central and northern Europe, West and South Africa. In addition, some compound extreme events such as co-occurrent heatwaves and droughts are becoming more frequent. These extreme climate events are very likely to continue to increase as global warming intensifies in the future, thus increasing the threat the security of food and water for human communities.

Although scientists around the world have made great efforts to understand how and why the extreme climate events are changing, we are still facing several crucial challenges: What are the mechanisms for the change of regional extreme climate events under global warming? How to improve the predictability of extreme climate events at a regional scale? More importantly, what are the broad effects of extreme climate events on the ecosystem and environment? Answers to these questions would help society to know more clearly what actions should be taken to better predict the extreme climate events and to reduce the associated adverse impacts.

This Research Topic collects 16 papers focusing on the above scientific questions, and contributes to a better understanding of the variability, mechanisms, prediction, and impacts of extreme climate events. Below is a brief introduction of the 16 papers in this Research Topic.

Shin et al. investigated the synoptic features of a record-breaking heavy rainfall event during August 2018 in the Korean peninsula. They compared the synoptic environmental and frontal structures of the heavy rainfall events during August and the Changma period. The results indicate that these events have several common characteristics, including an expanded western Pacific subtropical high (WPSH) as well as strong low-level winds along the western or northwestern edge of the WPSH. Their study shows the importance of anomalous WPSH to the occurrence of heavy rainfall events in East Asia.

Wan et al. explored the impact of extreme weather events on the ground-level air pollution over eastern China and the association with the premature deaths. They suggest that the compound hot and dry extreme events could lead to a notable increase in the ground-level ozone concentration over eastern China. The extreme hot weather events may result in an increase in the ozone-related premature deaths. These results contribute to a better understanding of the influence of weather extremes on human health.

Wu et al. elucidated a strengthened relationship between summer rainfall over North China and Pacific Decadal Oscillation (PDO) since the mid-2000's. The results suggest that the negative phase of PDO brought more summer rainfall in North China *via* modulating the upper-level jet stream and the East Asia-Pacific teleconnection since the mid-2000's. Results of this study could help improve the understanding of the factors contributing to interdecadal variation of wet/dry condition over North China.

Yan et al. investigated the projected future change of the gross primary productivity (GPP) of the northern Asian ecosystem and the impact of extreme heat events. Their results suggest an overall increase of the GPP and extreme heat events over northern Asia in the future. The impact of extreme heat events on GPP exhibit spatiotemporal heterogeneity, indicating a complex relationship between the extreme events and the ecosystem GPP.

Huang et al. identified a decadal variation in the frequency of tropical cyclones (TCs) in the South China Sea. They found a seesaw interdecadal variation in the frequencies of two types of tropical cyclones around 1997, which are generated in the South China Sea and the western North Pacific. This seesaw variation of the two types of tropical cyclones is affected by the genesis positions of TCs and the large-scale environmental flow patterns. Their study contributes to a better understanding of the variability of tropical cyclones that influence East Asia.

Huang et al. analyzed two heavy rainfall events in northwestern China during the summer of 2012 and 2013. They suggest that the northwestward-moving plateau vortex plays an important role in the two heavy rainfall events, which affect the moist potential vorticity, moisture helicity, and convective clouds characteristics in association with heavy rainfall. This study indicates an important impact of plateau vortices originating from the Tibetan Plateau on the extreme weathers in East Asia.

Sun et al. explored the quasi-biweekly oscillation in the atmospheric circulation associated with the mei-yu onset period. They found that the quasi-biweekly oscillation in the geopotential height over the Ural Mountains and the Northwest Pacific has an important influence on the onset of mei-yu in the Yangtze-River valley. During recent years, extreme mei-yu events have occurred more frequently, causing flood and/or drought disasters. The results of this study may help to understand these extreme events.

Zhu et al. estimated the prediction skill of the CFSv2 for the extreme high temperature events (EHTE) in eastern China, which is relatively poor at present. They explored the influential factors of EHTE and constructed a physical-empirical model for predicting the EHTE in eastern China. The results indicate that this physical-empirical model may greatly improve the prediction of EHTE in eastern China. This study provides an approach for obtaining a better prediction of extreme high temperature events over China.

Lv et al. showed that during the past 35 years, there is no significant poleward migration of TC in the western North Pacific, but there is large interdecadal variation in the TC tracks over the western North Pacific. The interdecadal variation of TC tracks is mainly affected by the Interdecadal Pacific Oscillation.

Qianrong et al. investigated the atmospheric circulation anomalies associated with a heavy rainfall event in West China during August 2020. They found this event resulted from a combination of different factors, including westward extended and anomalously strong WPSH, eastward extended South Asian High, and an anomalous low over Mongolia. These results indicate that extreme rainfall in the interior region of Eurasia is associated with the interaction between low latitude factors and mid-to-high latitude factors.

Li et al. studied the characteristics of Madden-Julian Oscillation (MJO) activity under three super El Niño events. Anomalous propagation and intensity of the MJO are detected during the developing, maturation, and decaying stages of the super El Niño events, which are suggested to be related to the atmospheric circulation and moisture anomalies caused by these El Niño events. Their study contributes to a better understanding of the influence of extreme El Niño events.

Cheng et al. explored the atmospheric circulation anomalies associated with the record-breaking rainfall over South China during the "Dragon Boat Water" season in 2022. They found that this record-breaking rainfall was mainly caused by anomalous meridional atmospheric circulation, which accounts for about 86% of the actual rainfall anomaly. These results exhibit the importance of meridional water vapor transport to the extreme rainfall in East Asia.

Wolf et al. investigated the relationship among the extreme sea levels, extreme astronomical tide, and extreme storm surge along the Norwegian coast. They found the highest storm surges mostly coincided with moderate astronomical tides and *vice versa*. Their study shows the possibility to estimate extreme sea level return values based on a three-variable system.

Huo et al. studied the extreme mei-yu in the Yangtze-Huaihe River Valley during the summer of 2021. Their results suggest that the occurence of this extreme mei-yu event is due to the joint impacts of an anomalous quasi-stationary atmospheric wave train propagating northeastward from Hainan Island to northwestern Pacific, and an anomalous quasi-stationary atmospheric wave train propagating eastward in the mid-latitudes originating from the tropical Atlantic. This study contributes to a better understanding of the mechanisms of extreme mei-yu events.

Omondi and Lin. investigated the long-term trend and spatial-temporal variations of drought characteristics over equatorial East Africa in boreal spring during the last 120 years. The results exhibit a weak long-term drying trend and an increase in drought areal extent after the 1980s in equatorial East Africa, which suggest that the drought risks are increasing in equatorial East Africa under global warming.

Fan et al. explored the interdecadal variation of summer extreme high temperature days (EHTDs) in northern Eurasia and the underlying mechanisms. They found that the number of summer EHTDs in northern Eurasia notably increased after the mid-1990's, especially in the areas around Lake Baikal and the Caspian Sea. They suggest that anomalous Rossby wave activities induced by a warmer

state of North Atlantic plays an important role in this interdecadal increase of EHTDs. This study contributes to a better understanding of the interdecadal variation of heat waves in Northern Hemisphere.

Author contributions

All authors listed have made a substantial, direct, and intellectual contribution to the work and approved it for publication.

Acknowledgments

We thank all authors, reviewers, and editors that have contributed to this Research Topic.

Conflict of interest

Author LZ was employed by CSIRO.

The remaining authors declare that the research was conducted in the absence of any commercial or financial relationships that could be construed as a potential conflict of interest.

Publisher's note

frontiers | Frontiers in Earth Science

ORIGINAL RESEARCH
published: 27 June 2022
doi: 10.3389/feart.2022.940785

Synoptic Features of August Heavy Rainfall Episodes Accompanied By a Quasi-Stationary Front Over the Korean Peninsula and Its Relationship With the Western Pacific Subtropical High

Uju Shin[1], *Sang-Hun Park*[1]*, *Yong-Ro Yun*[1] *and Chimook Oh*[2]

[1]Department of Atmospheric Sciences and Global Environmental Laboratory, Yonsei University, Seoul, South Korea, [2]Republic of Korea Air Force, Cheongju-si, South Korea

OPEN ACCESS

Edited by:
Bo Sun,
Nanjing University of Information Science and Technology, China

Reviewed by:
Chujie Gao,
Hohai University, China
Kang Xu,
South China Sea Institute of Oceanology (CAS), China

***Correspondence:**
Sang-Hun Park
pshun@yonsei.ac.kr

Specialty section:
This article was submitted to Atmospheric Science, a section of the journal Frontiers in Earth Science

Received: 10 May 2022
Accepted: 01 June 2022
Published: 27 June 2022

Citation:
Shin U, Park S-H, Yun Y-R and Oh C (2022) Synoptic Features of August Heavy Rainfall Episodes Accompanied By a Quasi-Stationary Front Over the Korean Peninsula and Its Relationship With the Western Pacific Subtropical High. Front. Earth Sci. 10:940785. doi: 10.3389/feart.2022.940785

In this study, we investigated the synoptic features of the August 26–27, 2018 heavy rainfall episode, which was accompanied by a quasi-stationary front over the Korean peninsula, as well as its relationship with the climatological characteristics of the Western Pacific Subtropical High (WPSH), using reanalysis and observational data. Through a case study, we analyzed the synoptic environment and frontal structure of the heavy rainfall event by comparing it with a heavy rainfall event associated with a quasi-stationary front that occurred on June 26–27, 2018 (during the Changma period). The case study indicates that the environment and structure of the quasi-stationary fronts in both events exhibited common characteristic features: an extended WPSH and strong low-level winds along the western or northwestern edge of the WPSH and a northward tilted frontal structure. Although differences in the moisture transport path were observed (southwesterly for the Changma event and southerly for the August event), their contributions to maintaining the quasi-stationary fronts were comparable around the Korean peninsula. We further investigated the climatological characteristics of these two heavy rainfall episodes for a 30 year period (1990–2019). We identified heavy rainfall days similar to those of the case study using pattern correlations of the 850 hPa geopotential height anomaly. The occurrence frequencies for each period indicate that the environmental features of the Changma event can be regarded as the typical heavy rainfall environment during the Changma period, whereas the environmental features of the August event were not typical for heavy rainfall during August. The main difference between similar and different cases to the August event is the expansion of the WPSH. Analysis of the relationship between annual variations in the WPSH indices and the occurrence frequency of heavy rainfall days during each August period also indicates that heavy rainfall with a quasi-stationary front similar to the August event is closely related to WPSH expansion.

Keywords: heavy rainfall, August rainfall, changma, quasi-stationary front, west pacific subtropical high index

1 INTRODUCTION

A Changma front is a quasi-stationary front located over the Korean peninsula during the Changma period of the monsoon season, which typically occurs from the end of June to the middle of July. It has been well documented that a significant portion of the summertime precipitation over the Korean peninsula occurs during the Changma period (KMA, 2011). During this period, the Changma front develops along the boundary between the monsoon and continental or marine polar air masses, and its meridional location oscillates between southern Japan and the middle of the Korean peninsula. The front is elongated from China to Japan and is closely related to the Baiu (Japan) and Mei-Yu (China) fronts. Ninomiya and Akiyama, (1992) suggested that the structure of the front varies with longitude. The Baiu front (135–160°E) exhibits a typical polar front structure, with a deep baroclinic structure, while the Mei-Yu front (100–120°E) exhibits a shallow structure, in which the vertical vorticity is confined to the lower layer. The Changma front (120–135°E) is regarded as a transition zone between these two frontal structures.

The Changma front is characterized by a meridional moisture gradient instead of a temperature slope, as indicated by Ninomiya, (2000). The onset and withdrawal dates of the Changma period are determined by the meridional oscillations of the Changma front, which has been investigated by previous studies (e.g., Byun and Lee, 2002; Ha et al., 2005; Seo et al., 2011; Choi et al., 2012; Park et al., 2015). Seo et al. (2011) proposed criteria for determining the onset and withdrawal dates of the Changma period using factors such as the meridional gradient of equivalent potential temperature, 500 hPa geopotential height, and 200 hPa zonal wind. Based on these factors, the onset and withdrawal dates of the Changma period were defined as when the Changma front crosses 32.4°N in mid-June and 40°N in late July. Seo et al. (2011) also found that these favorable environmental factors retreat southward over the Korean peninsula during late August, even though such an occurrence is not considered as a part of the Changma period.

Compared to climatological research on the Changma period, few studies have been performed regarding heavy rainfall in August, despite late summer rainfall events being climatologically important over the Korean peninsula (e.g., Byun and Lee, 2002; Ha et al., 2007). Previous studies of heavy rainfall during August over the Korean peninsula have suggested that these episodes exhibit similar environmental conditions as those of heavy rainfall episodes during the Changma period (Lee and Cho, 2007). Both types of heavy rainfall episodes occur at the edge of the West Pacific Subtropical High (WPSH), and the warm moist air transported by the strong southwesterly winds plays a crucial role in the occurrence of heavy rainfall over the Korean peninsula. However, the detailed features of the synoptic pressure patterns that produce heavy rainfall during August differ slightly from those during the Changma period. Park et al. (2021) classified the synoptic weather patterns of the warm season's heavy rainfall events in South Korea. They found that heavy rainfall events associated with the quasi-stationary frontal boundary between low and high, which is the typical heavy rainfall environment during the Changma period, occurred mainly during the first rainy period (late June to July). In contrast, synoptic environments associated with the extratropical cyclone from eastern China and local disturbances at the edge of the WPSH were observed frequently during the second rainy period (mid-August to mid-September), which differed from the typical heavy rainfall during the Changma period.

Climatologically, different characteristics also exist between heavy rainfall episodes in August and in the Changma period. First, heavy rainfall caused by the Changma front tends to occur regularly every year, whereas the August heavy rainfall episodes caused by a quasi-stationary front do not occur regularly because synoptic systems such as typhoons can substantially influence them (e.g., Kim et al., 2006; Byun and Lee, 2012; Cheung et al., 2018; Lee et al., 2021). Suzuki, (1967) reported that the amount of August rainfall in Japan was composed mainly of rainfall caused by thunderstorms and typhoons. Second, the Changma front is closely related to the Mei-Yu (China) and Baiu (Japan) fronts. The average onset and withdrawal dates for the Mei-Yu/Baiu fronts are June and July, respectively (Tomita et al., 2011). Therefore, determining the relationship between the quasi-stationary front in August and the Mei-Yu/Baiu fronts is difficult using climatological analyses.

During August 26–September 1, 2018, a record-breaking heavy rainfall episode occurred over the Korean peninsula, accompanied by a quasi-stationary front. During this episode, heavy rainfall occurred in a long-lasting quasi-stationary frontal zone without the presence of the propagating extratropical cyclone from eastern China. According to the Korean Ministry of the Interior and Safety, this heavy rainfall event resulted in three casualties and approximately $50 million in property damage (Ministry of the Interior and Safety, R. of K, 2018). The second-highest precipitation amount was recorded on August 26, 2018 among the station-averaged daily precipitation during August over the past 10 years, excluding precipitation due to the direct effects of typhoons (Lee et al., 2020). Therefore, in order to prepare for damage caused by this type of heavy rainfall, it is essential to understand the synoptic environments and climatological characteristics that can cause heavy rainfall over the Korean peninsula during August. It is also necessary to determine the similarities and differences with heavy rainfall that occurs during the Changma period. Therefore, this study addressed the following questions by comparing heavy rainfall events in August and during the Changma period: 1) Is there a difference between the synoptic environments of heavy rainfall that occurs during August and the Changma period? and 2) What is the main driver of heavy rainfall on the Korean peninsula during August?

To address these questions, we investigated the synoptic characteristics of the August heavy rainfall episode that was accompanied by a quasi-stationary front over the Korean peninsula. We also investigated the relationship of this episode with key synoptic-scale features using reanalysis and observational data. **Section 2** documents the data and method used in this study. In **Section 3**, we examine the environment and frontal structure of heavy rainfall events during August 26–27, 2018 by comparing it with the Changma front that formed earlier

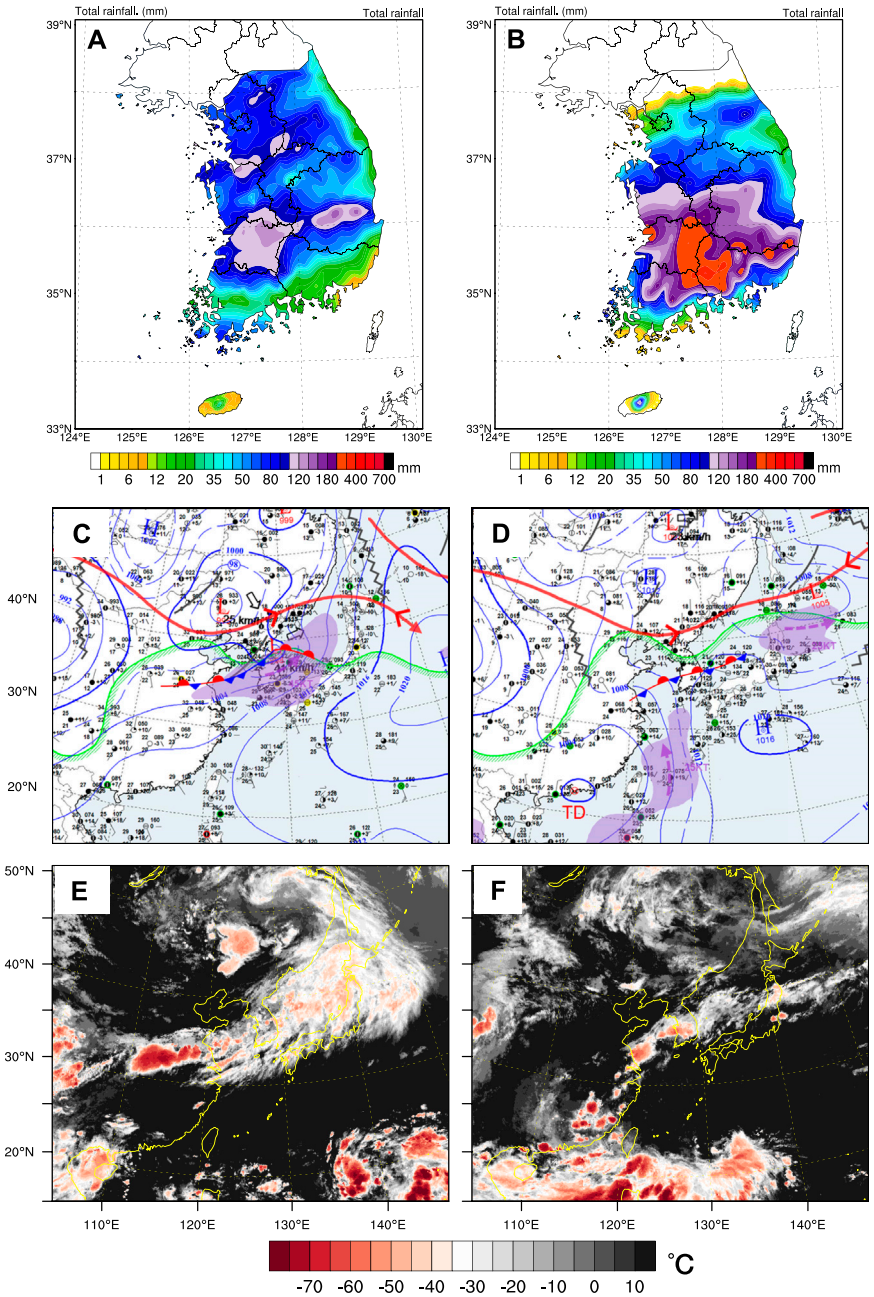

FIGURE 1 | The upper panels show the 36 h accumulated rainfall amounts (mm) from **(A)** 15:00 UTC on June 25 to 03:00 UTC on June 27, 2018 and from **(B)** 15:00 UTC on August 25 to 03:00 UTC on August 27, 2018. The middle panels show surface weather charts obtained from the KMA at **(C)** 12:00 UTC on June 26, 2018 and **(D)** 12:00 UTC on August 26, 2018. The solid blue lines indicate the sea-level pressure (hPa), and the violet shadings represent the area with wind speed >25 knots. The text "TD" in **(D)** represents the tropical depression. The bottom panels are satellite images obtained from the Communication, Ocean, and Meteorological Satellite (COMS) at **(E)** 12:00 UTC on June 26, 2018 and **(F)** 12:00 UTC on August 26, 2018.

in the year. The climatological characteristics of the August heavy rainfall are analyzed in **Section 4**. In addition, we examine the relationship between heavy rainfall episodes associated with the quasi-stationary front in August and the WPSH using three different WPSH indices. Finally, the summary and conclusions are provided in **Section 5**.

2 DATA AND METHODS

2.1 Data and Classification of Heavy Rainfall

We used the European Centre for Medium-Range Weather Forecasts (ECMWF) Re-Analysis Interim (ERA-Interim; Dee et al., 2011) dataset at 6 h intervals with a 0.75° × 0.75°

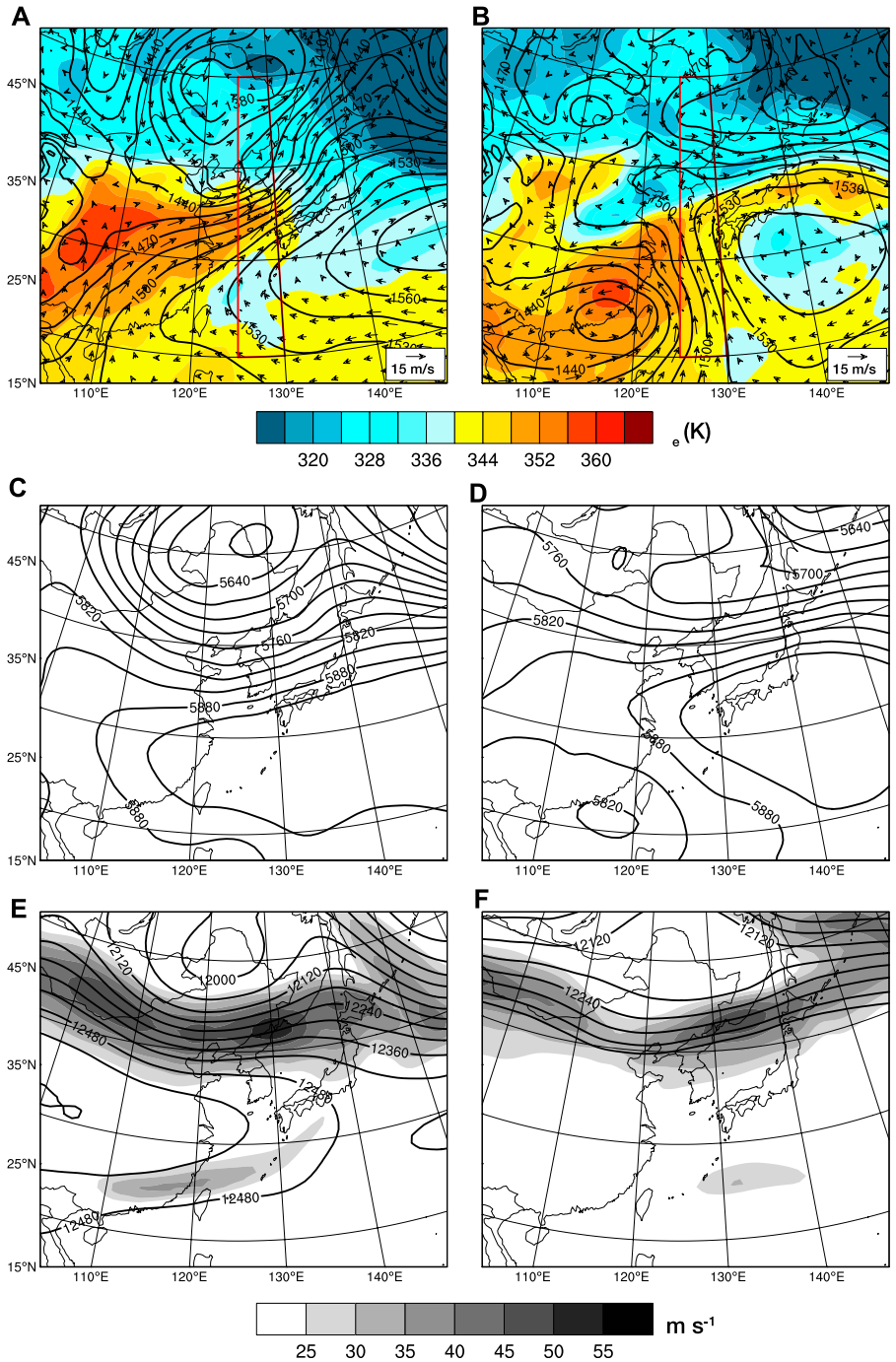

FIGURE 2 | Isobaric level analyses for June 26 (left) and August 26, 2018 (right). **(A,B)** Geopotential heights (gpm, solid lines), equivalent potential temperatures (K, shaded), and wind vectors (ms^{-1}, black arrows) at 850 hPa, **(C,D)** geopotential heights (gpm, solid lines) at 500 hPa, and **(E,F)** geopotential heights (gpm, solid lines) and isopachs (ms^{-1}, shaded) at 200 hPa.

horizontal resolution. Observational data were obtained from the Korean Meteorological Administration (KMA), including upper-air observations, satellite data, and hourly rainfall amounts from Automatic Weather Stations (AWS) to analyze the synoptic environment and the vertical structure of the front. In addition, we used Automated Surface Observing System (ASOS) data obtained from the KMA to classify the heavy rainfall events.

We also investigated the environmental conditions during the Changma and August periods over a 30 years duration (1990–2019). We defined the Changma and August periods as June 20–July 19 and August 6–September 4, respectively, and

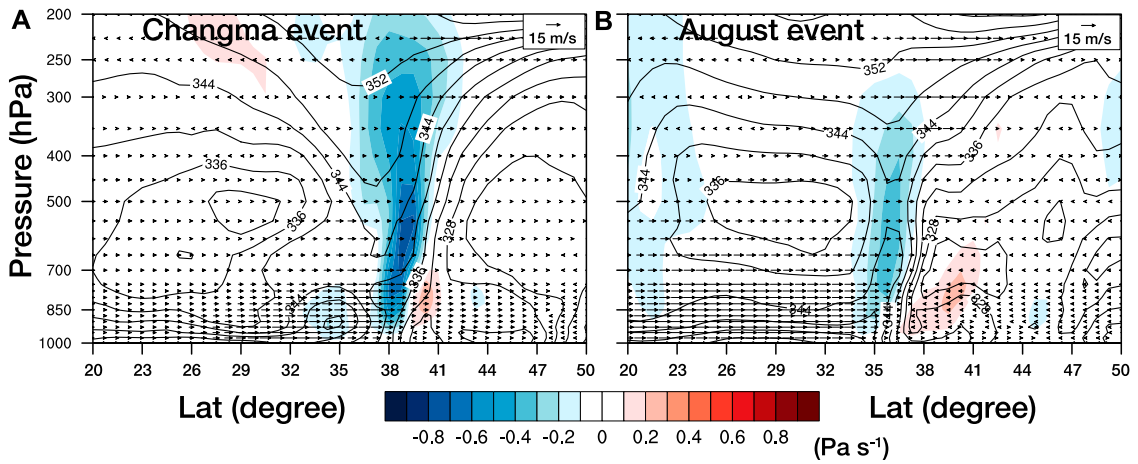

FIGURE 3 | Vertical cross sections along latitudes for events on **(A)** June 26 and **(B)** August 26, 2018. All values at each latitude were calculated by averaging between 125° and 130°E (red boxes). The solid lines, shading, and arrows represent the equivalent potential temperatures (K), vertical velocities (Pa s^{-1}), and horizontal wind vectors (ms^{-1}), respectively.

classified each period into heavy and non-heavy rainfall days. Both periods were defined by analyzing the rainfall climatology as in Seo et al. (2011)', which exhibited two rainfall peaks during the Changma and August periods. We observed the same two peaks (Changma and August) in the ASOS rainfall data, extending its period to the past 30 years (Supplementary Figure 1). In this study, a heavy rainfall event is defined by the KMA as an event with 24 h rainfall accumulations >80 mm at a minimum of two ASOS stations. In order to investigate their relationship with the expansion of WPSH, 190 and 189 cases were statistically analyzed for the Changma and August periods, respectively.

We identified heavy rainfall days similar to those in the case study by calculating the pattern correlation of the 850 hPa geopotential height anomaly with the selected events in each period (i.e., events on June 26 and August 26, 2018). The pattern correlation was calculated in the 15°–45°N, 110°–160°E area, which adequately represents the synoptic-scale pressure pattern in East Asia.

2.2 Western Pacific Subtropical High Index

In this study, we selected three WPSH indices to examine the relationship between the expansion of the WPSH and the heavy rainfall episode in August over the Korean peninsula. The WPSH indices were calculated based on the indices proposed by Liu and Wu, (2004; LW index), Choi and Kim, (2019; CK index), and Riyu, (2002; LU index). Each of these indices diagnoses different variables, but their physical meanings represent similar WPSH behavior over East Asia.

To calculate the LW index, the analysis domain was modified for the purposes of this study. We first set an analysis domain as the area within 10°–45°N and 92°–155°E, and established a WPSH ridgeline at 500 hPa. The WPSH ridgeline is defined as a line that connects grids where the zonal wind speeds are zero and the meridional gradient of the zonal wind is positive. We then found the easternmost 5880 gpm point on the WPSH ridgeline in the domain. The longitude determined using this process was used as the westward extension longitude of the WPSH. Note that if the geopotential height of the grid point located at the right end of the WPSH ridge line is less than 5880 gpm, the westward extension longitude of the WPSH is treated as a missing value. The other two indices were calculated based on geopotential height anomalies instead of horizontal wind shear. The CK (Choi and Kim, 2019) index is defined as the averaged geopotential height anomaly values at 500 hPa for the area within 9°–32°N and 105°–150°E, while the LU (Riyu, 2002) index is averaged over the area within 30°–40°N and 120°–150°E at 850 hPa. For both indices, a positive (negative) anomaly indicates the strengthening (weakening) of the WPSH over East Asia.

3 CASE STUDIES

In this study, we describe the characteristic features of two heavy rainfall events over the Korean peninsula that were accompanied by a quasi-stationary front. During the Changma event on June 26–27, 2018, the AWS rainfall amount over 36 h was over 100 mm in the southern part of the Korean peninsula, with the maximum rainfall exceeding 130 mm (**Figure 1A**). The surface weather chart from the KMA at 12:00 UTC on June 26, 2018 (**Figure 1C**) shows a typical pressure pattern during the Changma period (KMA, 2011), with the WPSH located southeast of the Korean peninsula and a migrating low-pressure system to the north of the peninsula. A strong pressure-gradient was located between the low-pressure system and the WPSH, and a quasi-stationary front extended from eastern China to the Korean peninsula. The satellite image obtained from the Communication, Ocean, and Meteorological Satellite (COMS) for 12:00 UTC on June 26 shows a wide cloud band that extended from eastern China to northern Japan along the quasi-stationary front, and convective clouds with cloud-top temperatures below −35°C (shaded in red) were located over the Korean peninsula (**Figure 1E**).

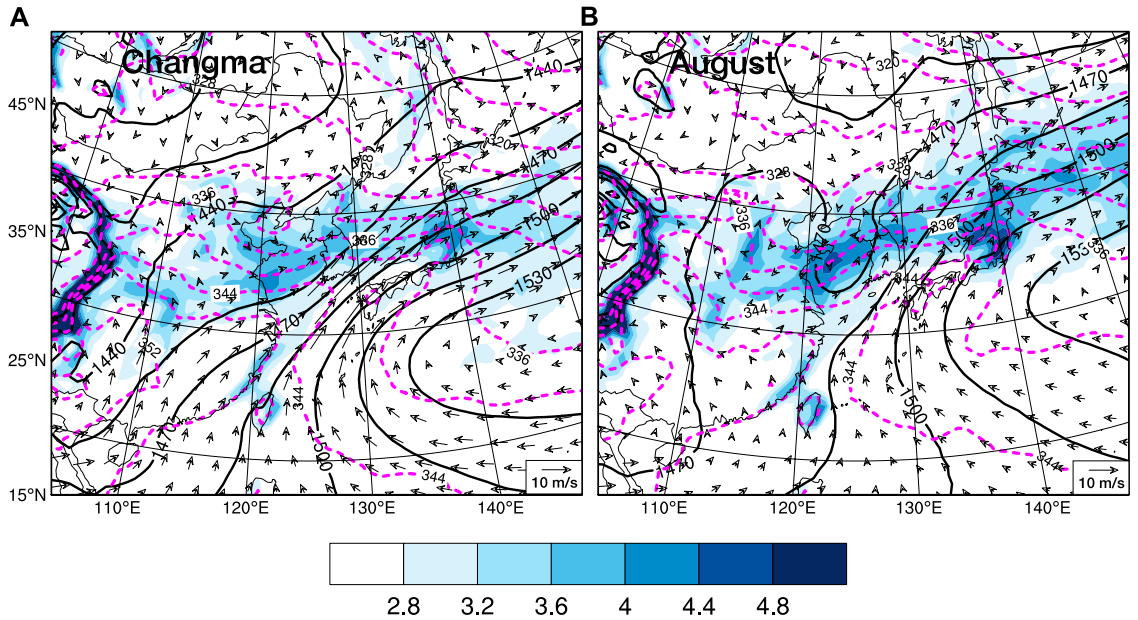

FIGURE 4 | Geopotential heights (gpm, solid black lines), equivalent potential temperatures (K, dashed magenta lines), equivalent potential temperature gradients (K/100 km, shaded), and wind vectors (ms^{-1}, black arrow) at 850 hPa for heavy rainfall days during the **(A)** Changma and **(B)** August periods.

The other heavy rainfall event occurred on August 26–27, 2018 over the southern part of the Korean peninsula. During this event, precipitation exceeding 300 mm was observed on the southern Korean peninsula, with a maximum rainfall amount of ~400 mm (**Figure 1B**). The surface weather chart at 12:00 UTC on August 26, 2018 (**Figure 1D**) shows that the WPSH was located southeast of the Korean peninsula, and a tropical depression (labeled TD) was located on the southern coast of China. A low-pressure system was located northeast of the Korean peninsula, and the trough extended from the center of the low-pressure system to the tropical depression. A strong pressure gradient was present east of Taiwan between the WPSH and the tropical depression. A quasi-stationary front extended east–west to the southern Korean peninsula at the northern end of this strong pressure gradient. In the satellite image (**Figure 1F**), the development of a narrow and intense cloud band is depicted along the quasi-stationary front over the southern Korean peninsula.

The considerable similarity between these two events is that heavy rainfall occurred in an environment in which the WPSH extended to the west, and that heavy rainfall occurred over the Korean peninsula due to convective systems that developed within a cloud band on a quasi-stationary front that extended from eastern China to the Korean peninsula. However, the low-pressure disturbances associated with the front exhibited different features during each event. In the Changma event, the quasi-stationary front developed in the vicinity of the strong pressure gradient between the WPSH and the synoptic-scale low to the north of the Korean peninsula. In contrast, in the August event, the strong pressure gradient occurred between the WPSH and a tropical depression to the south of Korea, and the quasi-stationary front developed at the northern end of the strong pressure gradient.

We further investigated the heavy rainfall environments using pressure level analyses from the ERA-Interim for the Changma (June 26, 2018) and August (August 26, 2018) events. The meteorological fields shown in **Figure 2** represent the averages between 00:00 UTC and 12:00 UTC. The 850 hPa pressure chart for the Changma event indicates that the WPSH and the synoptic-scale low were located to the southeast and north of the Korean peninsula, respectively. A region with a strong height gradient was located between the WPSH and the synoptic-scale low, while strong westerly–southwesterly currents in this region transported warm and moist air toward the Korean peninsula. As a result, an area of high-θ_e air extended from China to the Korean peninsula. The quasi-stationary front (**Figures 1C,E**) developed in the strong θ_e gradient region (**Figure 2A**). In the 850 hPa pressure chart for the August event, a strong southerly flow was observed over the ocean between the WPSH and the tropical depression. Warm and moist air was transported from the East China Sea by the strong southerly flow, and a strong θ_e gradient extending from the eastern part of China to Japan, was located along the northern edge of the strong southerly flow (**Figure 2B**). The Changma and August events exhibited different transport paths for the warm and moist air. Owing to the synoptic pattern differences, the warm and moist air was transported by strong southerly wind in August, whereas the prevailing winds during the Changma event were southwesterly. However, these moisture transports supported maintaining both quasi-stationary fronts, thereby presenting common environmental features between the two cases. The strong low-level flow was located in the strong geopotential height gradient region, and the warm and moist air

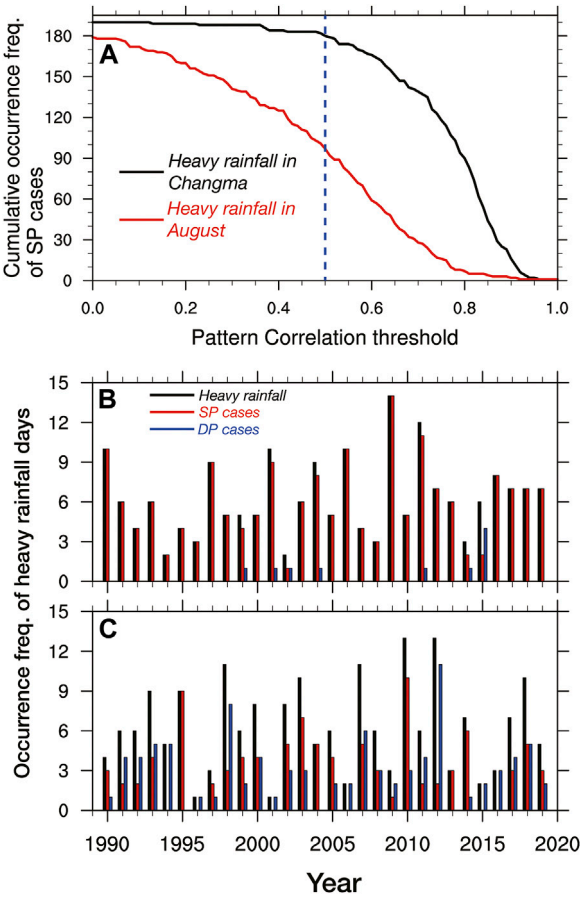

FIGURE 5 | (A) Cumulative occurrence frequency of cases with similar patterns (SP) during the Changma period (June 20–July 19, black line) and August (August 6–September 4, red line) depending on the pattern correlation threshold. The dashed blue line indicates a pattern correlation threshold of 0.5. **(B,C)** Time series of the frequency of heavy rainfall days (black bars), cases with similar patterns (SP, red bars), and cases with different patterns (DP, blue bars) during the **(B)** Changma period and **(C)** August.

was transported toward the Korean peninsula. As warm and humid air was supplied, an area with a robust θ_e gradient appeared over the Korean peninsula and the quasi-stationary front developed in this region.

Similarities at low-level pressure fields were also apparent in the upper-level analysis. During both events, the 500 hPa pressure chart indicates that the WPSH was located southeast of the Korean peninsula, with the west end of the 5880 gpm contour extending into China (**Figures 2C,D**). At the northern edge of the WPSH, a strong geopotential height gradient was located over the Korean peninsula. In the 200 hPa pressure chart, the upper-level jet axis was located to the north of the Korean peninsula, and the Korean peninsula was located on the right side of the jet entrance (**Figures 2E,F**).

The vertical structures of the quasi-stationary fronts are shown in **Figure 3**, showing latitude-pressure cross-sections between 20°N and 50°N for both events. The values at each latitude are represented by averaged values between 125° and 130°E (i.e., red box in **Figures 2A,B**). **Figure 3** shows vertical cross-sections of the θ_e, vertical velocity, and horizontal wind vectors during the Changma and August events. During both events, high-θ_e air below 700 hPa was located south of the Korean peninsula, while an area of low-θ_e air was located toward the northern Korean peninsula. This front, which is defined as the boundary between high- and low-θ_e air, was tilted steeply northward. A low-level strong southerly flow upstream of the front transported the high-θ_e air toward the Korean peninsula, which rose as it encountered the front. Previous studies of the Changma front (e.g., Sampe and Xie, 2010; Seo et al., 2011) have shown that its vertical structure is characterized by the northward tilt of the front from the lower to the upper troposphere. The typical structure of the Changma front was observed in both the Changma and August events.

Although the two case studies developed from different synoptic patterns, the environment and structure of the front for both events exhibited common characteristic features: an extended WPSH and strong low-level winds along the western or northwestern edge of the WPSH, and a northward tilting frontal structure. Differences were observed regarding the moisture transport path (southwesterly in the Changma event and southerly in the August event); however, their contributions to maintaining their respective quasi-stationary fronts around the Korean peninsula were comparable.

4 HEAVY RAINFALL EVENTS IN AUGUST AND CLIMATOLOGY

There are climatological issues related to the characteristics of the heavy rainfall in August. As we discussed above, heavy rainfall caused by the Changma front tends to occur regularly every year, and the Changma front is closely related to the Mei-Yu (China) and Baiu (Japan) fronts. These characteristics are important factors that define the Changma front. Thus, the long-term climatological characteristics of the quasi-stationary front during both the Changma and August events should be considered.

Figure 4 shows the mean geopotential height field and equivalent potential temperatures at 850 hPa during heavy rainfall episodes from 1990 to 2019. During the Changma period (190 cases), the northwestern edge of the WPSH extended from southwestern China to the Korean peninsula and northern Japan. A synoptic disturbance was located northwest of the Korean peninsula and a stationary trough extended from the disturbance to the downstream region of the Tibetan Plateau (**Figure 4A**). These characteristic features during the Changma period are in agreement with those of the Changma event, as shown in the case study revealed in **Figure 2A**.

The mean August synoptic field from 189 heavy rainfall events in **Figure 4B** indicates that the synoptic-scale ridge extended from the northwestern edge of the WPSH to eastern China. The western edge of the WPSH did not extend to southern China as in the Changma period, and a strong trough was located in the

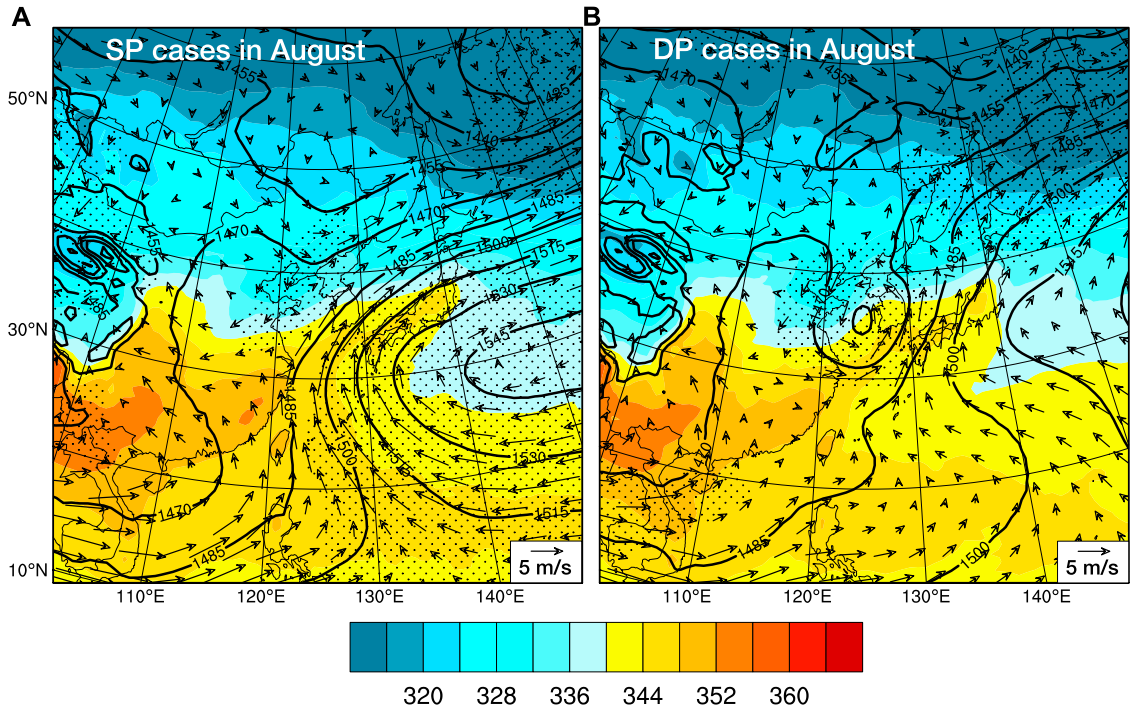

FIGURE 6 | Composite geopotential height (gpm, solid lines), equivalent potential temperature (K, shaded), and wind vector (ms^{-1}, arrows) fields at 850 hPa for **(A)** SP cases and **(B)** DP cases during August from 1990 to 2019. The dots indicate that the value is significant at the 95% confidence level.

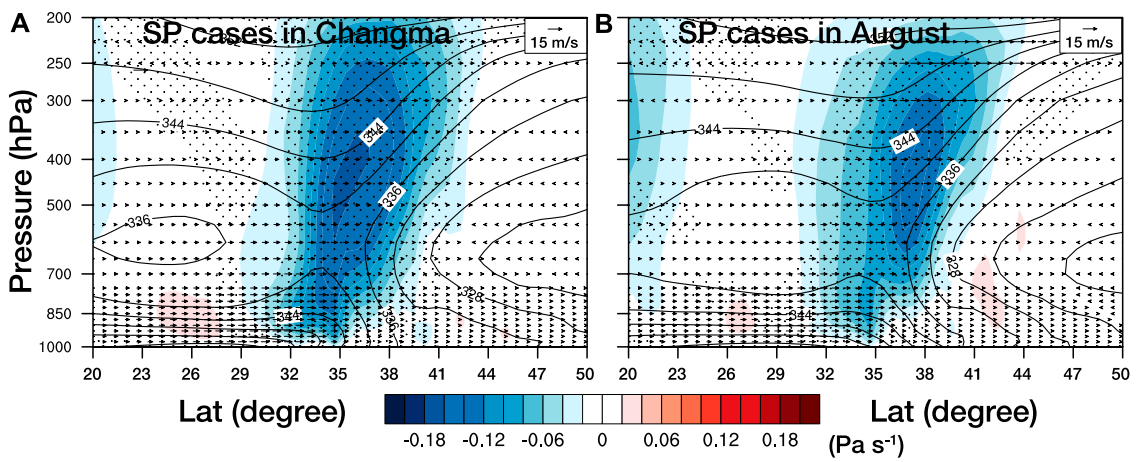

FIGURE 7 | Same as **Figure 3**, but for the similar pattern (SP) cases during the **(A)** Changma period and **(B)** August from 1990 to 2019. Note that the magnitude of vertical motion is different from that shown in **Figure 3**. The dots indicate that the value is significant at the 95% confidence level.

vicinity of Taiwan. The synoptic features of the mean August field differ from those of the mean Changma field, represented by the strong trough near Taiwan, the strong disturbance near the Korean peninsula, and the location of the synoptic cyclone northeast of the Korean peninsula. Note that the mean heavy rainfall environment during August (**Figure 4B**) does not match the August event in the case study precisely (**Figure 2B**). This may be due to the diversity of the synoptic environment that causes heavy rainfall during August, as documented by Park et al. (2021).

Considering the diversity of the heavy rainfall environment during August, we identified the heavy rainfall days in each period as similar pattern (SP) and different pattern (DP) cases by calculating the pattern correlation of the 850 hPa geopotential height anomaly with the selected August event (i.e., August 26, 2018). For comparison, the same analysis was performed on the

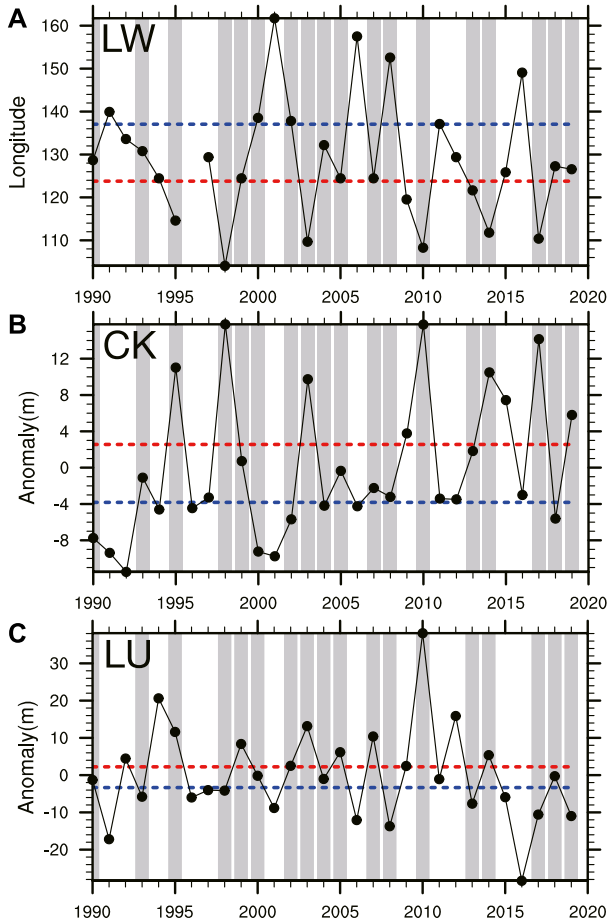

FIGURE 8 | Annual variations in the westward extension of the WPSH: **(A)** LW (Liu and Wu, 2004), **(B)** CK (Choi and Kim, 2019), and **(C)** LU (Riyu, 2002) Indices. All indices were calculated during August of each year from 1990 to 2019. Thick gray bars indicate years with three or more SP cases. Red (blue) dashed lines indicate the mean values of years with (without) three or more SP cases.

Changma period using the selected Changma event (i.e., June 26, 2018). **Figure 5A** shows the change in the cumulative occurrence frequency of the SP cases according to the change in the pattern correlation threshold. For the Changma period, the cumulative occurrence frequency of the SP cases remained above 180 (95%) up to a pattern correlation threshold of 0.5 and retained values of 90 (47%) even at a pattern correlation threshold of 0.8. Unlike the Changma period, the cumulative occurrence frequency of the SP cases during August decreased rapidly with an increasing pattern correlation threshold. The cumulative occurrence frequencies of the SP cases during August were approximately 97 (51%) and 7 (4%) cases when the pattern correlation thresholds were 0.5 and 0.8, respectively. Notably, the occurrence frequencies of the SP cases during the two periods were quite different. The occurrence frequencies of the SP cases during both periods implies that the environmental features of the Changma event can be regarded as the typical heavy rainfall environment during the Changma period, while the environmental features of the August event cannot be regarded as typical for heavy rainfall during August. For example, the occurrence frequencies of the heavy rainfall days, SP cases, and DP cases when the pattern correlation threshold was assumed to be 0.5 (**Figures 5B,C**) indicate that, during the Changma period, SP cases occurred on 95% of the heavy rainfall days. In contrast, during August, only 51% of the heavy rainfall days were similar to the August event described above.

Since the SP and DP cases both exhibited similar occurrence frequencies during August, we examined the environmental features of the SP cases during August by comparing them with the DP cases. Days with a pattern correlation value greater than 0.5 were classified as SP cases (97), whereas those with values less than 0.5 were classified as DP cases (92). **Figure 6** shows constant pressure charts for the SP and DP cases during August. The composite charts of the SP cases from **Figure 6A** exhibited environmental features that were consistent with those of the August event as shown in **Figure 2B**. In the 850 hPa pressure chart for the SP cases, the WPSH extended to China and the front (i.e., east–west line of the high θ_e gradient) was located at the northern end of the strong low-level southerly wind that flows toward the Korean peninsula along the western flank of the WPSH (**Figure 6A**). The expansion of the WPSH was also apparent in the 500 hPa pressure chart, and the upper-level jet axis was located north of the Korean peninsula (not shown). In the composite charts of the DP cases from **Figures 6A,B** low-pressure system was located over the Yellow Sea and the Korean peninsula that extended from the eastern part of China to the northern part of Japan, crossing the low-pressure system. Note that the synoptic trough and disturbances around Taiwan and the Korean peninsula revealed in **Figure 4B** were from DP cases during August, as shown in **Figure 6B**. The SP and DP cases exhibited considerable differences regarding the development of the front over the Korean peninsula. In the SP cases, the strong southerly or southwesterly wind along the western flank of the WPSH plays an important role in the front development, as in the heavy rainfall environment during the Changma period. In contrast, from DP cases (**Figure 6B**), the cyclonic circulation associated with the mesoscale low near the Korean peninsula was the main driver of heavy rainfall systems. By decomposing **Figure 4B** into **Figures 6A,B**, we found that these differences were strongly associated with the expansion of the WPSH. In the SP cases, the 1500 gpm and 1485 gpm contours extended further northwest than in the DP cases, while the northwestern edge of the WPSH extended to the southern part of the Korean peninsula.

The vertical structure of the SP cases during the Changma and August periods were similar to those of the case studies (**Figure 3**), although the fields were smoother than the case study events. **Figures 7A,B** show the vertical structure of the SP cases during the Changma and August periods, respectively. During both periods, high-θ_e air below 700 hPa was located south of the Korean peninsula, while an area of low-θ_e air was located north of the Korean peninsula in the layer between the surface and the upper troposphere (**Figures 7A,B**), as shown in the case studies (**Figures 3A,B**). Moreover, significant upward motion was observed over the region with a strong horizontal θ_e gradient.

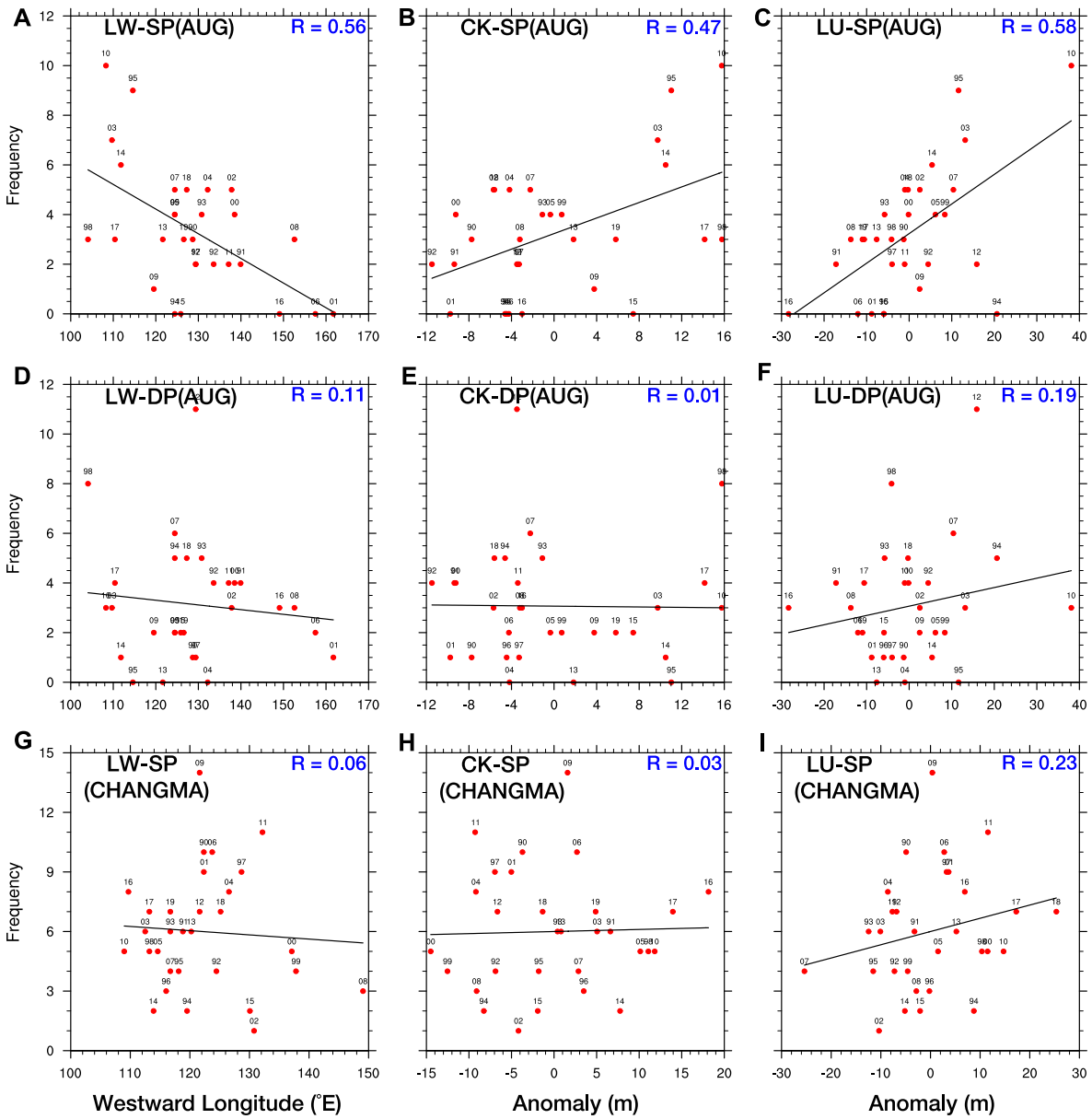

FIGURE 9 | Correlation coefficients between the WPSH indices (left, middle, and right panels represent the LW, CK, and LU indices, respectively) and annual frequencies of **(A–C)** SP cases in August, **(D–F)** DP cases in August, and **(G–I)** SP cases during the Changma period from 1990 to 2019. Note that the results of the DP cases during the Changma period are not shown, as the total frequency was only 10 days during 1990–2019.

Analyses of the SP cases during both the Changma and August periods demonstrate that they occurred in each period in an environment similar to those of the case study events. As mentioned above, this study was motivated to find favorable synoptic conditions for heavy rainfall events during August with a quasi-stationary front. Here, the environmental conditions of the SP cases in August suggest that similar heavy rainfall events can occur under certain synoptic conditions in which the WPSH extends northwestward. Therefore, based on the importance of the expansion of the WPSH for heavy rainfall development during August, we examined the relationship between the frequency of heavy rainfall days in August and the WPSH index for each year.

Figure 8 shows the annual variations in the WPSH indices for the August events. All of the indices were calculated during August of each year from 1990 to 2019. As shown in **Figure 8A**, the annual variations in the LW index indicate that the average longitude of the WPSH between 1990 and 2019 was ~128.8°E. The mean extension longitude of the WPSH during years with three or more SP cases (red dashed) was ~123.7°E, which is farther west than in other years (blue dashed line) at 137°E. For the other two WPSH indices, the mean

values during years with (without) three or more SP cases had positive (negative) anomalies, and the differences between the red and blue dashed lines were 6.4 and 5.5 m for the CK and LU indices, as shown in **Figures 8B,C**, respectively.

The relationship between the WPSH indices and the annual occurrence frequencies of heavy rainfall days during August was also examined using the correlation coefficient (**Figure 9**). The LW index exhibited a negative correlation with heavy rainfall occurrence for the SP cases (0.56) in August, while the CK and LU indices exhibited positive correlations (0.47 and 0.58, respectively), as shown in **Figures 9A–C**. In contrast to the SP cases, the relationship between the WPSH indices and the heavy rainfall occurrence frequency for the DP cases exhibited a nearly random pattern, with correlation coefficients of 0.11, 0.01, and 0.19 for the LW (**Figure 9D**), CK (**Figure 9E**), and LU indices (**Figure 9F**), respectively. The annual variations in the WPSH indices and the annual occurrence frequencies of heavy rainfall days during August indicate that a strengthening of the WPSH is closely related to the occurrence of heavy rainfall for the SP cases, while it was unrelated to the occurrence of heavy rainfall for the DP cases.

We also applied the above analysis to the Changma period. **Figures 9G–I** show the relationships between the WPSH indices and the occurrence frequency of the SP cases during the Changma period. The results for the DP cases during the Changma period have been excluded, as the total frequency of the DP cases was only 10 during 1990–2019, as shown in **Figure 5A**. For the SP cases during the Changma period, the correlation coefficients were 0.06, 0.03, and 0.23 for the LW (**Figure 9G**), CK (**Figure 9H**), and LU (**Figure 9I**) indices, respectively. These values were substantially smaller than the correlation coefficients for the SP cases in August (**Figures 9A–C**) and exhibited a nearly random pattern. During the Changma period, since the occurrence frequency of the SP cases occupied 95% of the heavy rainfall occurrences, we can conclude that the relationship between the annual variations in the WPSH and heavy rainfall occurrence is very weak, indicating that the expansion of WPSH is not a key feature of heavy rainfall over the Korean peninsula. Complicated development processes exist for the quasi-stationary front in the Changma period, such as the impact of the Tibetan Plateau (e.g., Hsu and Liu, 2003; Son et al., 2019; Seok and Seo, 2021) or large-scale diabatic heating effects (e.g., Yun et al., 2010; Jin et al., 2013). More detailed analysis of various aspects of heavy rainfall during the Changma period is beyond the scope of this study, and further research should be performed on this subject. In contrast, we found that heavy rainfall events that occurred in a similar synoptic environment as that of the August event were very closely related to WPSH expansion.

5 SUMMARY AND CONCLUSION

We investigated the relationships between heavy rainfall in August over the Korean peninsula and the climatological characteristics of the WPSH using reanalysis and observational data. Based on the two case studies, the synoptic environment and frontal structure during August 26–27, 2018 were compared with those of the heavy rainfall event during the Changma period. Furthermore, we investigated the climatological characteristics of heavy rainfall episodes during the Changma (190 cases) and August periods (189 cases) from 1990 to 2019.

The case studies indicate that the environment and structure of the quasi-stationary front for both events exhibited common characteristics: an expanded WPSH and strong low-level winds along the western or northwestern edge of the WPSH; and a northward tilting frontal structure. These characteristics are consistent with those of the Changma front, as defined by previous studies. However, the moisture transport path differed between the two events: moisture transport was mainly derived from the southwest in the Changma event, but was derived from the south in the August event. This difference is due to the synoptic pressure caused by the presence of the cyclonic system over the southern coast of China. However, the moisture transports supported maintaining both quasi-stationary fronts presenting common environmental features between the two cases.

We classified the heavy rainfall days during each period from 1990 to 2019 as SP and DP cases by calculating the pattern correlations with each period's selected events. The occurrence frequency of the SP cases was dependent on the pattern correlation threshold for both periods, thereby indicating that the environmental features of the Changma event can be regarded as the typical heavy rainfall environment during the Changma period. In contrast, environmental features of the August 2018 event could not be regarded as the typical heavy rainfall environment during August, but accounted for half of the heavy rainfall during August when the pattern correlation threshold was 0.5.

A major difference between the SP and DP cases during August was the expansion and intensity of the WPSH. In the SP cases, the strong southerly or southwesterly winds along the western flank of the WPSH played an important role in the development of the front, as in the heavy rainfall environment during the Changma period. However, the cyclonic circulation associated with a mesoscale low near the Korean peninsula was the main driver of heavy rainfall systems. The environmental conditions in the SP cases indicate that heavy rainfall events similar to the August event in the case studies can occur under certain synoptic conditions in which the WPSH extends northwestward.

To examine the influence of the WPSH expansion on heavy rainfall during August over the Korean peninsula, we analyzed the relationships between the annual variations in three WPSH indices and the annual occurrence frequency of heavy rainfall days during August and the Changma period. The results indicate that heavy rainfall during August accompanied by a quasi-stationary front was very closely related to WPSH expansion.

This study focused on investigating the relationship between the heavy rainfall environment during August and the expansion of the WPSH. To better understand the characteristics of heavy rainfall during August, further research regarding the heavy rainfall environment with WPSH modulation (e.g., Yang and Li, 2020) and the environment considered in this study should be conducted. In addition, the influence of tropical cyclone activity

on heavy rainfall during August should be addressed more clearly in future research.

DATA AVAILABILITY STATEMENT

The original contributions presented in the study are included in the article/**Supplementary Material**, further inquiries can be directed to the corresponding author.

AUTHOR CONTRIBUTIONS

US: Conceptualization, Analysis, Methodology, Software. S-HP: Conceptualization, Methodology, Writing–original draft, Supervision. Y-RY: Software, Data collection. CO: Software, Data collection, Analysis. All authors reviewed the final manuscript.

FUNDING

This research was supported by the Korea Meteorological Administration Research and Development Program (No. KMI 2020-01112).

SUPPLEMENTARY MATERIAL

The Supplementary Material for this article can be found online at: https://www.frontiersin.org/articles/10.3389/feart.2022.940785/full#supplementary-material

REFERENCES

Byun, H.-R., and Lee, D.-K. (2002). Defining Three Rainy Seasons and the Hydrological Summer Monsoon in Korea Using Available Water Resources Index. *J. Meteorological Soc. Jpn.* 80, 33–44. doi:10.2151/jmsj.80.33

Byun, K.-Y., and Lee, T.-Y. (2012). Remote Effects of Tropical Cyclones on Heavy Rainfall over the Korean Peninsula - Statistical and Composite Analysis. *Tellus A Dyn. Meteorology Oceanogr.* 64, 14983. doi:10.3402/tellusa.v64i0.14983

Cheung, H. M., Ho, C.-H., Jhun, J.-G., Park, D.-S. R., and Yang, S. (2018). Tropical Cyclone Signals on Rainfall Distribution during Strong vs. Weak Changma/Baiu Years. *Clim. Dyn.* 51, 2311–2320. doi:10.1007/s00382-017-4014-1

Choi, K.-S., Wang, B., and Kim, D.-W. (2012). Changma Onset Definition in Korea Using the Available Water Resources Index and its Relation to the Antarctic Oscillation. *Clim. Dyn.* 38, 547–562. doi:10.1007/s00382-010-0957-1

Choi, W., and Kim, K.-Y. (2019). Summertime Variability of the Western North Pacific Subtropical High and its Synoptic Influences on the East Asian Weather. *Sci. Rep.* 9, 7865. doi:10.1038/s41598-019-44414-w

Dee, D. P., Uppala, S. M., Simmons, A. J., Berrisford, P., Poli, P., Kobayashi, S., et al. (2011). The ERA-Interim Reanalysis: Configuration and Performance of the Data Assimilation System. *Q.J.R. Meteorol. Soc.* 137, 553–597. doi:10.1002/qj.828

Ha, K.-J., Jeon, E.-H., and Oh, H.-M. (2007). Spatial and Temporal Characteristics of Precipitation Using an Extensive Network of Ground Gauge in the Korean Peninsula. *Atmos. Res.* 86, 330–339. doi:10.1016/j.atmosres.2007.07.002

Ha, K.-J., Yun, K.-S., Jhun, J.-G., and Park, C.-K. (2005). Definition of Onset/Retreat and Intensity of Changma During the Boreal Summer Monsoon Season. *J. Korean Meteor. Soc.* 41, 927–942.

Hsu, H. H., and Liu, X. (2003). Relationship between the Tibetan Plateau Heating and East Asian Summer Monsoon Rainfall. *Geophys. Res. Lett.* 30, 30–33. doi:10.1029/2003GL017909

Jin, Q., Yang, X.-Q., Sun, X.-G., and Fang, J.-B. (2013). East Asian Summer Monsoon Circulation Structure Controlled by Feedback of Condensational Heating. *Clim. Dyn.* 41, 1885–1897. doi:10.1007/s00382-012-1620-9

Kim, J.-H., Ho, C.-H., Lee, M.-H., Jeong, J.-H., and Chen, D. (2006). Large Increase in Heavy Rainfall Associated with Tropical Cyclone Landfalls in Korea after the Late 1970s. *Geophys. Res. Lett.* 33, a–n. doi:10.1029/2006GL027430

KMA (2011). *Changma White Paper*. Seoul, Korea: Korean Meteorological Administration.

Lee, J., Paz, I., Schertzer, D., Lee, D. I., and Tchiguirinskaia, I. (2020). Multifractal Analysis of Rainfall-Rate Datasets Obtained by Radar and Numerical Model: The Case Study of Typhoon Bolaven (2012). *J. Appl. Meteorol. Climatol.* 59, 819–840. doi:10.1175/JAMC-D-18-0209.1

Lee, T.-Y., and Cho, N.-S. (2007). "Variation and Characteristics of Heavy Rainfall in August over the Korean Peninsula," in Autumn Metting KMS 8–10, 488–489.

Lee, T.-Y., Shin, U., and Park, S.-H. (2021). Atmospheric Structure for Convective Development in the Events of Cloud Clusters over the Korean Peninsula. *Asia-Pacific J. Atmos. Sci.* 57, 511–531. doi:10.1007/s13143-020-00211-4

Liu, Y., and Wu, G. (2004). Progress in the Study on the Formation of the Sumertime Subtropical Anticyclone. *Adv. Atmos. Sci.* 21, 322–342. doi:10.1007/BF02915562

Ministry of the Interior and Safety, R. of K (2018). *Statistical Yearbook of Natural Disaster 2018*. Sejong, Korea: Korean Ministry of the Interior and Safety.

Ninomiya, K., and Akiyama, T. (1992). Multi-scale Features of Baiu, the Summer Monsoon over Japan and the East Asia. *J. Meteorological Soc. Jpn.* 70, 467–495. doi:10.2151/jmsj1965.70.1B_467

Ninomiya, K. (2000). Large- and Meso-α-Scale Characteristics of Meiyu/Baiu Front Associated with Intense Rainfalls in 1-10 July 1991. *J. Meteorological Soc. Jpn.* 78, 141–157. doi:10.2151/jmsj1965.78.2_141

Park, C., Son, S.-W., Kim, J., Chang, E.-C., Kim, J.-H., Jo, E., et al. (2021). Diverse Synoptic Weather Patterns of Warm-Season Heavy Rainfall Events in South Korea. *Mon. Weather Rev.* 149, 3875–3893. doi:10.1175/MWR-D-20-0388.1

Park, H.-l., Seo, K.-H., and Son, J.-H. (2015). Development of a Dynamics-Based Statistical Prediction Model for the Changma Onset. *J. Clim.* 28, 6647–6666. doi:10.1175/JCLI-D-14-00502.1

Riyu, L. (2002). Indices of the Summertime Western North Pacific Subtropical High. *Adv. Atmos. Sci.* 19, 1004–1028. doi:10.1007/s00376-002-0061-5

Sampe, T., and Xie, S.-P. (2010). Large-Scale Dynamics of the Meiyu-Baiu Rainband: Environmental Forcing by the Westerly Jet. *J. Clim.* 23, 113–134. doi:10.1175/2009JCLI3128.1

Seo, K.-H., Son, J.-H., and Lee, J.-Y. (2011). A New Look at Changma. *Atmos. (Basel)* 21, 109–121.

Seok, S.-H., and Seo, K.-H. (2021). Sensitivity of East Asian Summer Monsoon Precipitation to the Location of the Tibetan Plateau. *J. Clim.* 34, 8829–8840. doi:10.1175/jcli-d-21-0154.1

Son, J. H., Seo, K. H., and Wang, B. (2019). Dynamical Control of the Tibetan Plateau on the East Asian Summer Monsoon. *Geophys. Res. Lett.* 46, 7672–7679. doi:10.1029/2019GL083104

Suzuki, E. (1967). A Statistical and Climatological Study on the Rainfall in Japan. *Pap. Met. Geophy.* 18, 103–181. doi:10.2467/mripapers1950.18.3_103

Tomita, T., Yamaura, T., and Hashimoto, T. (2011). Interannual Variability of the Baiu Season Near Japan Evaluated from the Equivalent Potential Temperature. *J. Meteorological Soc. Jpn.* 89, 517–537. doi:10.2151/jmsj.2011-507

Yang, S., and Li, T. (2020). Cause for Quasi-Biweekly Oscillation of Zonal Location of Western Pacific Subtropical High during Boreal Summer. *Atmos. Res.* 245, 105079. doi:10.1016/j.atmosres.2020.105079

Yun, K.-S., Ha, K.-J., Wang, B., and Ding, R. (2010). Decadal Cooling in the Indian Summer Monsoon after 1997/1998 El Niño and its Impact on the East Asian Summer Monsoon. *Geophys. Res. Lett.* 37, a–n. doi:10.1029/2009GL041539

Conflict of Interest: The authors declare that the research was conducted in the absence of any commercial or financial relationships that could be construed as a potential conflict of interest.

Publisher's Note: All claims expressed in this article are solely those of the authors and do not necessarily represent those of their affiliated organizations, or those of the publisher, the editors and the reviewers. Any product that may be evaluated in this article, or claim that may be made by its manufacturer, is not guaranteed or endorsed by the publisher.

frontiers | Frontiers in Earth Science

TYPE Original Research
PUBLISHED 22 July 2022
DOI 10.3389/feart.2022.970296

OPEN ACCESS

EDITED BY
Shangfeng Chen,
Institute of Atmospheric Physics (CAS), China

REVIEWED BY
Anning Huang,
Nanjing University, China
Huopo Chen,
Institute of Atmospheric Physics (CAS), China

*CORRESPONDENCE
Botao Zhou,
zhoubt@nuist.edu.cn

SPECIALTY SECTION
This article was submitted to Atmospheric Science, a section of the journal Frontiers in Earth Science

RECEIVED 15 June 2022
ACCEPTED 04 July 2022
PUBLISHED 22 July 2022

CITATION
Yan M, Yue X, Zhou B, Sun X and Xin N (2022), Projected changes of ecosystem productivity and their responses to extreme heat events in northern asia. *Front. Earth Sci.* 10:970296. doi: 10.3389/feart.2022.970296

Projected changes of ecosystem productivity and their responses to extreme heat events in northern asia

Minchu Yan[1,2], Xu Yue[3], Botao Zhou[1,2]*, Xiaoling Sun[1,2] and Ning Xin[1,2]

[1]Collaborative Innovation Center on Forecast and Evaluation of Meteorological Disasters/Key Laboratory of Meteorological Disaster, Ministry of Education/Joint International Research Laboratory of Climate and Environment Change, Nanjing University of Information Science and Technology, Nanjing, China, [2]School of Atmospheric Sciences, Nanjing University of Information Science and Technology, Nanjing, China, [3]School of Environmental Science and Engineering, Nanjing University of Information Science and Technology, Nanjing, China

Change of ecosystem productivity and its response to climate extremes in the context of global warming are of great interest and particular concern for ecosystem management and adaptation. Using the simulations with and without the CO_2 fertilization effect from the Yale Interactive Biosphere (YIBs) model driven by seven CMIP5 climate models, this article investigates the future change in the gross primary productivity (GPP) of the Northern Asian ecosystem as well as the impacts from extreme heat events under the RCP2.6 and RCP8.5 scenarios, respectively. The results show an overall increase of GPP in Northern Asia during the growing season (May-September) under both scenarios, in which the CO_2 fertilization effect plays a dominant role. The increases in GPP under RCP8.5 are larger than that under RCP2.6, and the greatest projected increases occur in western Siberia and Northeast China. The extreme heat events are also projected to increase generally and their influences on the Northern Asian ecosystem GPP exhibit spatiotemporal heterogeneity. Under the RCP2.6 scenario, the positive and adverse effects from the extreme heat events coexist in Northern Asia during the middle of the 21st century. During the end of the 21st century, the areas dominated by positive effects are expected to expand particularly in Northeast China and central-western Siberia. For the RCP8.5 scenario, the facilitation effects of the extreme heat events are widely distributed in Northern Asia during the middle of the 21st century, which tends to decline in both intensity and extent during the end of the 21st century. The case is similar after the CO_2 fertilization effect is excluded.

KEYWORDS

extreme heat events, YIBs model, ecosystem GPP, northern asia, projection

Introduction

Terrestrial ecosystem is an important component of global carbon cycle. It can absorb and fix a large amount of CO_2 through photosynthesis, thus reducing atmospheric CO_2 concentration and playing an important role in climate change (IPCC, 2013). On the other hand, the terrestrial ecosystem is also highly sensitive to climate change (Walther et al., 2002; Ni, 2011; Piao et al., 2013; Wang et al., 2014). As revealed by observational evidence and modeling findings, global climate warming has exerted profound impacts on the terrestrial ecosystem (IPCC, 2014). In response to future warming caused by continued emissions of greenhouse gases, an increasing tendency toward the end of the 21st century in the gross primary productivity (GPP), a critical indicator of the terrestrial carbon cycle, is projected (Yu et al., 2014; Zhu et al., 2018; Schlund et al., 2020).

Appropriate warming of the temperature can better satisfy the thermal demand of vegetation, thereby improving the leaf photosynthetic efficiency and consequently increasing the ecosystem productivity. However, high temperatures beyond the plant tolerance threshold can increase plant respiration and inhibit photosynthesis (Salvucci and Crafts-Brandner, 2004). Some studies have shown that temperature extremes may decrease the plant productivity and change the carbon cycle of the ecosystem through affecting plant physiological processes (Meehl et al., 2000; Smith et al., 2009; Frank et al., 2015; Piao et al., 2019; Peng et al., 2022). For example, the heat wave event occurring in western Russia in 2010 led to a significant decrease in local ecosystem productivity (Bastos et al., 2014). The extreme heat events promoting plant growth at middle and high latitudes has also been reported. Based on the data from the European Carbon Flux Observatory network, Delpierre et al. (2010) indicated that the extreme warm spring in 2007 caused an increase in ecosystem photosynthesis and respiration, with the increase in photosynthesis larger than that in respiration. As a consequence, the carbon uptake was enhanced. These studies suggest that the effects of extreme heat events on the ecosystem may promote or inhibit productivity, depending on the location, duration and intensity of extreme events, and vegetation type, etc.

Northern Asia, especially Siberia, is a region with rich vegetation and diverse ecosystem. It is famous particularly for a widespread of taiga. The GPP change in this region is crucial to the Asian and even global carbon cycle. Meanwhile, Northern Asia is also one of the regions that are most sensitive to climate extremes (Xu et al., 2017; Zhou et al., 2020; IPCC, 2021). Accompanied with future warming, significant changes in frequency, intensity and duration of temperature extremes are anticipated in this region (IPCC, 2021). However, the impact of future changes in temperature extremes on the ecosystem remains an open issue. Exploring this issue can deepen our understanding of terrestrial carbon sequestration and ecological risks to climate extremes. It is also demanded for ecosystem management and adaptation.

In this study, we use the simulations of the Yale Interactive Biosphere (YIBs) model which are driven by multiple CMIP5 models under the low and high emission scenarios, i.e, RCP2.6 and RCP8.5 (Taylor et al., 2012), to project the GPP change in Northern Asia. The impacts of extreme heat events on the Northern Asian GPP during the middle and end of the 21st century under the two scenarios are also quantified, with the aim to provide scientific support for ecosystem management and adaptation.

TABLE 1 CIMP5 models used to drive the YIBs model.

Model name	Country	Atm. Resolution (lon×lat)
BCC-CSM-1.1	China	128 × 64
BCC-CSM-1.1(M)	China	320 × 160
CNRM-CM5	France	256 × 128
GFDL-ESM2G	U.S.	144 × 90
GFDL-ESM2M	U.S.	144 × 90
MIROC5	Japan	256 × 128
MRI-CGCM3	Japan	320 × 160

Model, data, and methods

Data, model, and simulations

The YIBs model (Yue et al., 2020) with a spatial resolution of 1° × 1° is applied for the simulations of ecosystem productivity. This model dynamically produces the leaf area index and tree height in terms of carbon assimilation and allocation. The hourly leaf photosynthesis is calculated by the scheme of Farquhar et al. (1980), and different responses of sunlit and shading leaves to diffuse and direct light (Spitters, 1986) are taken into account. Carbon absorbed by plants is firstly used to maintain life activities and then distributed among leaves, stems, and roots to support plant growth (Clark et al., 2011). Soil respiration is calculated by the carbon transition among 12 soil carbon pools (Schaefer et al., 2008). There are nine plant functional types (PFTs) considered in the model, including evergreen broadleaf forest (EBF), evergreen needleleaf forest (ENF), deciduous broadleaf forest (DBF), tundra, shrubland, C3/C4 grass, and C3/C4 crop.

The simulations of the YIBs are driven by the daily meteorological fields under the historical simulation (1986–2005) as well as the RCP2.6 and RCP8.5 scenarios (2006–2100) of seven CMIP5 climate models (Table 1). The meteorological variables include surface temperature, precipitation, specific humidity, surface downward shortwave radiation, surface pressure and surface wind speed. The domain

for the YIBs simulations focuses on the Northern Asian region (60°-140°E, 40°-60°N). The RCP2.6 (RCP8.5) scenario is a low (high) emission pathway with the radiative forcing peaking at 2.6 (8.5) W m^{-2} by 2,100 (Taylor et al., 2012). The seven models chosen not only provide all available daily meteorological data that are needed to drive the YIBs, but also yield a warming of temperature close to 1.5°C (relative to the pre-industrial era) under the RCP2.6 scenario, which meets the long-term warming target pursued by the Paris Agreement.

To exclude the effect of CO_2 fertilization, two groups of experiments are conducted, i.e., total factor simulation (ALL) and meteorological element simulation (MET). The sole difference between the two groups of experiments is that the ALL simulation allows the year-to-year variation of CO_2 concentrations in line with the CMIP5 simulations, while the CO_2 concentration in the MET simulation after 2000 is fixed at the level of 2000. More information about the YIBs model and experiments can refer to the study of Yue et al. (2020).

The satellite retrieval NIRv-based GPP data at a resolution of 0.05° × 0.05° (Wang et al., 2021) are used as the observation to assess the YIBs performance. To facilitate the comparison, the data are interpolated to the same 1° × 1° resolution as the YIBs model.

Methods

In this study, the period 1986–2005 is taken as the reference period and the periods 2041–2060 and 2081–2100 are referred to as the middle of the 21st century (the mid-century) and the end of the 21st century (the end-century), respectively. The ensemble is calculated as the arithmetic mean with the same weight.

As the growing season for plants in the Northern Hemisphere is confined to the period from May to September, the present and future extreme heat events at each grid of Northern Asia are identified during these 5 months by the 95% percentile threshold method (Zhai and Pan, 2003) on the daily scale. Specifically, the threshold of extreme heat events at one grid for a certain calendar day is calculated as the 95th percentile of daily temperature from May to September of the reference period, with the given day centered on a 31-days slide window. When the daily temperature exceeds the corresponding threshold for three consecutive days, one extreme heat event is considered to occur.

The anomalies of GPP associated with extreme heat events (abbreviated as EHE-GPP) relative to the climate mean state are composited to represent the impact of extreme heat events on the ecosystem. The GPP anomalies are calculated separately on each date of the growing season to exclude the influence of seasonal variations of GPP. The statistical significance is assessed by the Student's t-test.

Performance of the YIBs model

The performance of the YIBs model in the simulation of GPP over Northern Asia is evaluated through the comparison with the observation. Figures 1A–C show the spatial distributions of the ensemble simulated and the observed GPP as well as their difference in Northern Asia over the course of 1986–2005, respectively. In general, the ensemble simulated climatological distribution of GPP bears a resemblance to the counterpart shown in the observation, although the GPP values are somewhat overestimated in parts of Siberia and Northeast China and underestimated in the remaining regions. For the region west of 110°E, large GPP values are mainly located in the north flank of 50°N, particularly in the vast area of Siberia. Due to the widespread distribution of Gobi and desert south of 50°N, only the Altai Mountains and the Tianshan Mountains show large GPP values. To the east of 110°E, large values of GPP are more widely distributed with the largest values situated in Northeast China. The spatial correlation coefficient between the ensemble simulation and the observation is 0.75, higher above the 99.9% significance level. In addition, the observed GPP shows an upward trend, which can be generally captured by the ensemble simulation (Figure 1D). The temporal correlation coefficient between the ensemble simulation and the observation is 0.53, also higher above the 99.9% significance level. Overall, the evaluation suggests that the YIBs model performs well in capturing the climatological distribution and trend of GPP in Northern Asia.

Result

Projected changes in GPP

The spatial distributions of the ensemble projected changes in GPP during the mid-century and the end-century under the RCP2.6 and RCP8.5 scenarios in the ALL simulations are displayed in Figure 2. Under the low emission scenario (RCP2.6), relative to the reference period, an increase in GPP is projected for both the mid-century and the end-century, and the increasing amplitudes show little change from the mid-century to the end century (Figures 2A,B). In comparison, the GPP is projected to increase continuously from the mid-century to the end century under the high emission scenario (RCP8.5) (Figures 2C,D). The projected greatest increases under the two scenarios both occur in western Siberia and Northeast China, with the increasing magnitudes much larger under the RCP8.5 scenario than under the RCP2.6 scenario. Regionally averaged in Northern Asia, compared to the reference period, the GPP during the mid-century and the end-century under the RCP2.6 scenario is projected to increase by 0.49 $gCm^{-2}d^{-1}$ and 0.56 $gCm^{-2}d^{-1}$, respectively. The projected increases under the

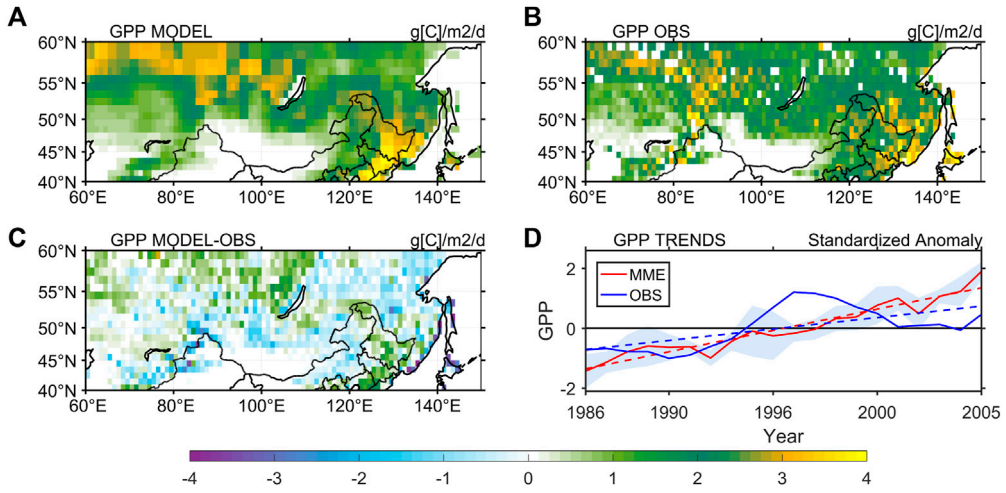

FIGURE 1
Spatial distributions of **(A)** ensemble simulated and **(B)** observed GPP ($gCm^{-2}d^{-1}$) as well as **(C)** their difference (simulation-observation) in Northern Asia during the period of 1986–2005. **(D)** Time series of the normalized GPP (smoothed with a 5-years window) from the ensemble simulation (red line) and observation (blue line). The time series are smoothed with a 5-years running mean filter. The shading indicates the spread of the individual CMIP5 simulations.

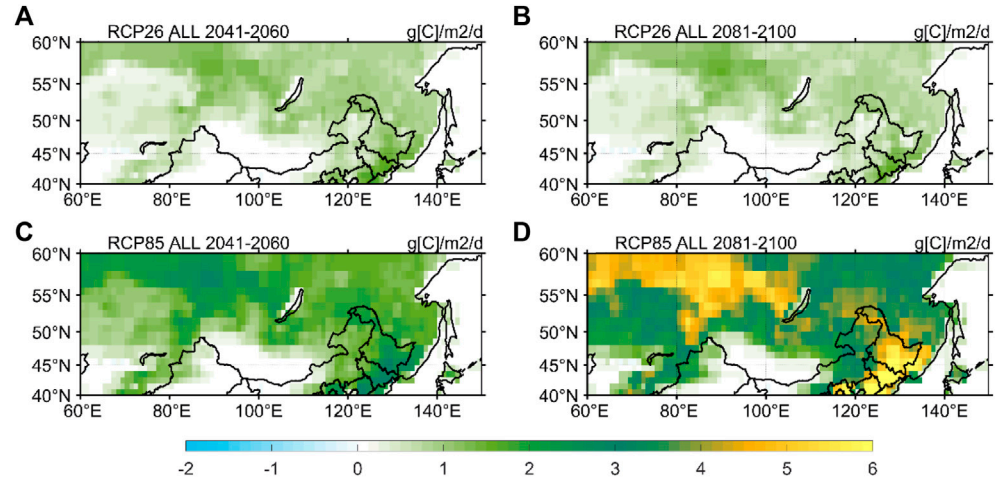

FIGURE 2
Ensemble projected anomalies in GPP ($gCm^{-2}d^{-1}$) during **(A,C)** the mid-century and **(B,D)** the end-century relative to the reference period 1986–2005 under **(A,B)** RCP2.6 and **(C,D)** RCP8.5 in the ALL simulations.

RCP8.5 scenario are 1.16 $gCm^{-2}d^{-1}$ in the mid-century and further to 2.57 $gCm^{-2}d^{-1}$ in the end-century, much higher than the counterpart under the low emission scenario. Figure 3 presents the ensemble projected GPP changes from the MET simulations, in which the influence of CO_2 change on the ecosystem is eliminated; only the meteorological elements vary with time following the RCP path. It is found that the projections in the MET simulations differ from that shown in the ALL simulations. Although the increases of GPP still appear in most of Northern Asia in warmer scenarios, the magnitudes of increases are much weaker than that of the ALL simulation in which the effect of CO_2 is taken into consideration. Moreover, slight decreases in GPP are even projected in some areas of the upper reaches of the Ob River and Northeast China. On the regional average, the projected GPP in the mid-century and the end-century increases around 0.11 $gCm^{-2}d^{-1}$ under the RCP2.6 scenario, and that under the RCP8.5 scenario increases by 0.15 $gCm^{-2}d^{-1}$ and 0.26 $gCm^{-2}d^{-1}$, respectively.

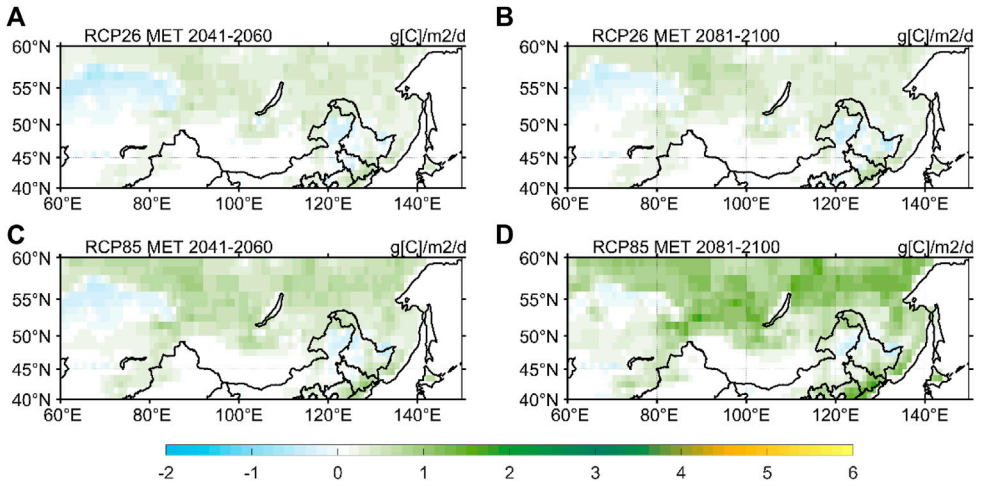

FIGURE 3
Ensemble projected anomalies in GPP ($gCm^{-2}d^{-1}$) during **(A,C)** the mid-century and **(B,D)** the end-century relative to the reference period 1986–2005 under **(A,B)** RCP2.6 and **(C,D)** RCP8.5 in the MET simulations.

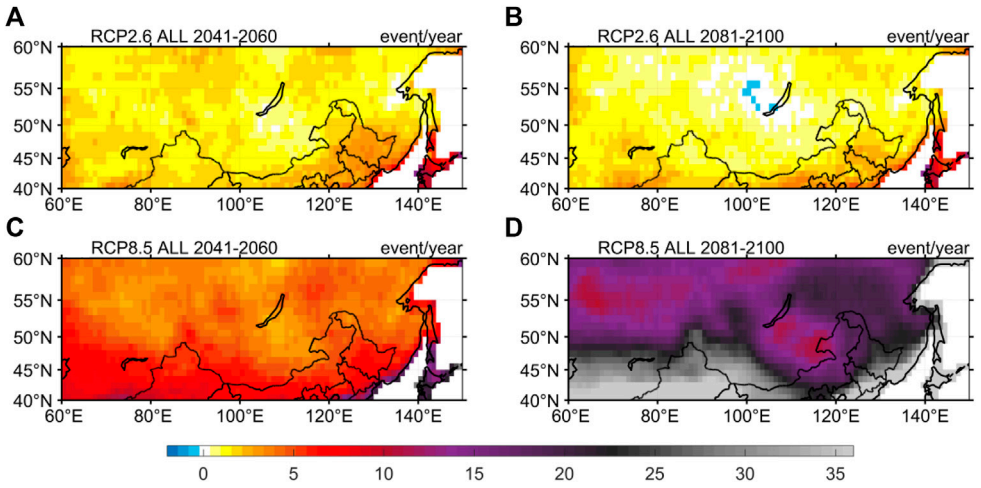

FIGURE 4
Ensemble projected anomalies in extreme heat events (times/year) during **(A,C)** the mid-century and **(B,D)** the end-century relative to the reference period 1986–2005 under **(A,B)** RCP2.6 and **(C,D)** RCP8.5 in the ALL simulations.

In summary, the above findings illustrate that the Northern Asian ecosystem GPP positively responds to the future warmer scenarios, with larger increases under the high emission scenario (RCP8.5) than that under the low emission scenario (RCP2.6). The enhancement of CO_2 fertilization effect in the future plays a dominant role in the projected increase in GPP. When excluding the CO_2 fertilization effect, the future climate warming also shows a positive contribution, likely due to that the increase of ambient temperature can better meet the thermal demand of plant growth and improve the photosynthetic efficiency of vegetation.

Projected impacts of extreme heat events on GPP

Figure 4 shows the spatial distributions of the ensemble projected changes in extreme heat events during the mid-

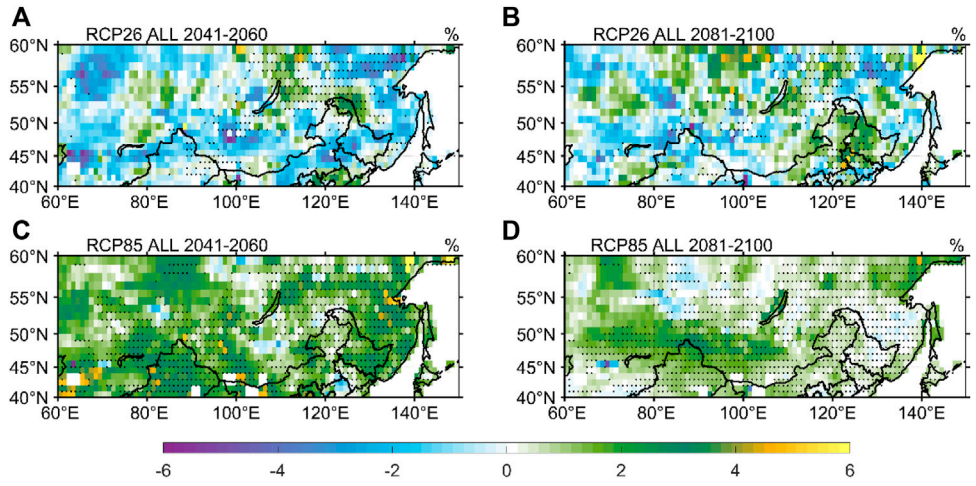

FIGURE 5
Ensemble projected percentage anomalies (%) of EHE-GPP relative to the climatological state during **(A,C)** the mid-century and **(B,D)** the end-century under **(A,B)** RCP2.6 and RCP8.5 **(C,D)** from the ALL simulations. Regions with six out of seven models exceeding the 95% significance level are dotted.

century and the end-century relative to the reference period under the RCP2.6 and RCP8.5 scenarios from the ALL simulations. As global climate continues to warm in the future, an increase in the frequency of extreme heat events is anticipated in Northern Asia, with larger increase under the high emission scenario than under the low emission scenario, which is consistent with the previous studies (IPCC, 2013; 2021). For the RCP2.6 scenario (Figures 4A,B), the projected increases are comparable between the mid-century and the end-century. A slight decrease in the frequency of extreme heat events is seen around Lake Baikal. For the RCP8.5 scenario (Figures 4C,D), the increases of extreme heat events are projected to strengthen from the mid-century to the end-century. During the mid-century, the magnitudes of increases are in general 3–9 times per year with the exceedance of 12 times per year in some coastal areas. During the end-century, the projected extreme heat events increase more significantly in the south than in the north. The north region show an increase of more than 12 times per year, while the increase in the south region is above 30 times per year.

Future increases in extreme heat events are expected to exert effects on the GPP in Northern Asia. Figure 5 shows the percentage anomalies of EHE-GPP relative to the climatological state in the mid-century and the end-century as projected from the ALL simulation. Under the RCP2.6 scenario, in the mid-century (Figure 5A), negative anomalies can be noticed in a majority of Northern Asia, indicating a general adverse effect on the local GPP from the extreme heat events. In contrast, the northwest-southeast oriented belt region from around Lake Baikal to Heilongjiang Province of Northeast China shows an increase of above 3% in GPP as a response to the occurrence of extreme heat events, indicating a significant facilitation effect from the extreme heat events. In the end-century (Figure 5B), the areas dominated by negative EHE-GPP anomalies tend to shrink. Instead, the regions covered by positive EHE-GPP anomalies expand particularly in Northeast China and central-western Siberia. This result hints at a relatively strengthening (weakening) of the facilitation (inhibition) effect on the ecosystem productivity from the extreme heat events in the end-century compared to the mid-century under the low emission scenario. For the RCP8.5 scenario, the extreme heat events contribute to the increase of GPP in most regions (Figures 5C,D). Contrary to the case under the RCP2.6 scenario, the percentage increases in EHE-GPP during the mid-century are much more salient than that during the end-century in both intensity and extent. It suggests that the facilitation effect from the extreme heat events on the ecosystem productivity tends to decline from the mid-century to the end-century under the high emission scenario. During the end-century, the large positive anomalies of EHE-GPP are concentrated in the belt region near 50°N and the coastal zone of Russian Far East.

The spatial characteristics of the effect of extreme heat events on the GPP in Northern Asia from the MET simulations are similar to that of the ALL simulations, but with a reduction in intensity particularly under the RCP8.5 scenario (Figure 6). For instance, the magnitudes of increases in EHE-GPP forced by the MET simulations are about half (one fifth) of that in the ALL simulations during the mid-century (the end-century) under the RCP8.5 scenario. Therefore, although the presence of CO_2 can promote the ecosystem productivity and improve the GPP level on the whole, it will not change the impact of extreme heat events on the ecosystem.

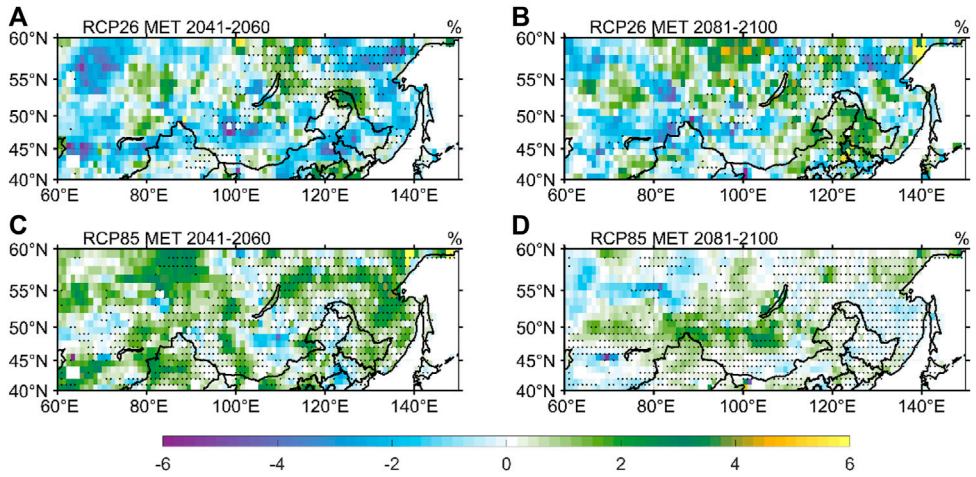

FIGURE 6
Ensemble projected percentage anomalies (%) of EHE-GPP relative to the climatological state during **(A,C)** the mid-century and **(B,D)** the end-century under **(A,B)** RCP2.6 and RCP8.5 **(C,D)** from the MET simulations. Regions with six out of seven models exceeding the 95% significance level are dotted.

TABLE 2 Spatial correlation coefficients of the total ecosystem GPP anomalies with the ENF/tundra GPP anomalies under the influence of extreme heat events.

	Vegetation type	RCP2.6		RCP8.5	
		2041–2060	2081–2100	2041–2060	2081–2100
ALL Simulations	ENF	0.67	0.66	0.63	0.77
	tundra	0.56	0.54	0.50	0.63
MET Simulations	ENF	0.68	0.67	0.66	0.74
	tundra	0.57	0.54	0.56	0.60

It should be worth noting that the effects of extreme heat events on the ecosystem are spatially heterogeneous around the world, since the needs of temperature for the growth of ecosystem are not the same in different regions. For example, the projected increases of temperature tend to promote the vegetation growth in the high latitudes of the Northern Hemisphere (Yu et al., 2014; Jeong, 2020). However, in the tropics, future temperature increases will inhabit the vegetation growth and hence weaken the GPP (Park et al., 2015).

Given that the ENF and tundra are widely distributed in Northern Asia (Zhang et al., 2015), we also calculate the GPP anomalies of these two vegetation types under the influence of extreme heat events. It is found that the spatial patterns under the RCP2.6 and RCP8.5 scenarios in the All and MET simulations are similar to Figures 5, 6, respectively, and the relative changes of the tundra GPP affected by the extreme heat events are generally larger than that for the ENF (Figure not shown). The spatial correlations of the EHE-GPP anomalies in ENF and tundra with that of the whole vegetation from the ALL and MET simulations exceed 0.50 (significant at the 99.9% level) for both the mid-century and the end-century under each scenario (Table 2), indicating that the GPP changes of the ENF and tundra influenced by the extreme heat events are consistent with that for the whole vegetation. As the ENF is the dominant vegetation type and the most important GPP provider in Northern Asia (Pan et al., 2011), its GPP change affected by the extreme heat events will largely determine the influence of extreme heat events on the whole ecosystem productivity in Northern Asia. Although the tundra is also extensive in Northern Asia, its GPP change shows less contribution to the change of total GPP, due to small proportion of tundra GPP to the whole Northern Asian ecosystem GPP.

Conclusion

Based on the YIBs model simulations driven by 7 CMIP5 models under the low-emission (RCP2.6) and high-emission (RCP8.5) scenarios respectively with the CO_2 effect included and excluded, this study projects the changes of GPP in Northern Asia during the middle and the end of the 21st century. The impacts of future changes in extreme heat events on the Northern Asian ecosystem productivity are further examined. The main findings are summarized as follows:

1) The GPP during the growing season is projected to increase in Northern Asia, accompanied with larger increases under RCP8.5 than under RCP2.6. The greatest increases are projected in western Siberia and Northeast China. In addition, the projected increases are enhanced from the mid-century to the end-century under the RCP8.5 scenario, whereas under the RCP2.6 scenario they are comparable between the middle and the end of the 21st century. The enhancement of CO_2 fertilization effect plays a dominant role in the projected increase of GPP. After removing the influence of CO_2 effect, the projected increase of GPP in Northern Asia becomes weaker.
2) The impacts of future increases in the extreme heat events on the Northern Asian GPP show spatiotemporal heterogeneity. Under the RCP2.6 scenario, during the mid-century, the adverse effect of extreme heat events exists in most of the region except the northwest-southeast oriented belt region from around Lake Baikal to Heilongjiang Province where the positive effect from the extreme heat events is projected. The positive effect tends to expand in the end-century particularly in Northeast China and central-western Siberia. Under the RCP8.5 scenario, the positive effect from the extreme heat events is projected to dominate most regions in the mid-century and to shrink in the end-century. Although the CO_2 fertilization effect can amplify the facilitation effect from the warming, it will not alter the spatial regime of the impact of extreme heat events on the GPP.
3) The spatial distributions of the impacts on the evergreen needleleaf forest and tundra from the extreme heat events under each scenario with and without the effect of CO_2 fertilization approximate that for the whole ecosystem in Northern Asia. In addition, larger relative changes are projected for the tundra GPP than for the evergreen needleleaf forest GPP that are affected by the extreme heat events.

Note that this study aims at the projected impacts of extreme heat events on the GPP in Northern Asia. The physical processes for their impacts on the GPP are not addressed. Naturally, the processes of extreme heat events affecting the ecosystem are complicated, which includes a variety of physicochemical processes and a number of elements that are mutually positively and negatively interacted (Allen and Breshears, 1998; Peng et al., 2009; Allen et al., 2010). Further in-depth investigations are needed in the future work to explore detailed physical processes for different behaviors of the impacts of extreme heat events on the Northern Asian ecosystem GPP under different scenarios.

Data availability statement

The original contributions presented in the study are included in the article, further inquiries can be directed to the corresponding author.

Author contributions

BZ and XY designed and supervised the research; MY performed data analysis and drafted the manuscript; BZ prepared the final manuscript with the contribution from all co-authors.

Funding

This research was jointly supported by the National Natural Science Foundation of China (41991285) and the National Key Research and Development Program of China (2017YFA0605004).

Conflict of interest

The authors declare that the research was conducted in the absence of any commercial or financial relationships that could be construed as a potential conflict of interest.

Publisher's note

Acknowledgments

We acknowledge the World Climate Research Program's Working Group on Coupled Modeling and thank the climate modeling groups for producing and sharing their model outputs.

References

Allen, C. D., and Breshears, D. D. (1998). Drought-induced shift of a forest-woodland ecotone: Rapid landscape response to climate variation. *Proc. Natl. Acad. Sci. U. S. A.* 95, 14839–14842. doi:10.1073/pnas.95.25.14839

Allen, C. D., Macalady, A. K., Chenchouni, H., Bachelet, D., Mcdowell, N., Vennetier, M., et al. (2010). A global overview of drought and heat-induced tree mortality reveals emerging climate change risks for forests. *For. Ecol. Manag.* 259, 660–684. doi:10.1016/j.foreco.2009.09.001

Bastos, A., Gouveia, C. M., Trigo, R. M., and Running, S. W. (2014). Analysing the spatio-temporal impacts of the 2003 and 2010 extreme heatwaves on plant productivity in europe. *Biogeosciences* 11, 3421–3435. doi:10.5194/bg-11-3421-2014

Clark, D. B., Mercado, L. M., Sitch, S., Jones, C. D., Gedney, N., Best, M. J., et al. (2011). The joint UK land environment simulator (JULES), model description–Part 2: Carbon fluxes and vegetation dynamics. *Geosci. Model Dev.* 4, 701–722. doi:10.5194/gmd-4-701-2011

Delpierre, N., Soudani, K., François, C., Köstner, B., DufrÊne, E., Nikinmaa, E., et al. (2010). Exceptional carbon uptake in European forests during the warm spring of 2007: A data–model analysis. *Glob. Chang. Biol.* 15 (6), 1455–1474. doi:10.1111/j.1365-2486.2008.01835.x

Farquhar, G. D., Caemmerer, S. V., and Berry, J. A. (1980). A biochemical model of photosynthetic CO_2 assimilation in leaves of C3 species. *Planta* 149, 78–90. doi:10.1007/BF00386231

Frank, D., Reichstein, M., Bahn, M., Thonicke, K., Frank, D., Mahecha, M., et al. (2015). Effects of climate extremes on the terrestrial carbon cycle: Concepts, processes and potential future impacts. *Glob. Chang. Biol.* 21, 2861–2880. doi:10.1111/gcb.12916

IPCC (2013). *Climate change 2013: The physical science basis. Contribution of working group I to the fifth assessment report of the intergovernmental panel on climate change*. Cambridge, UK and New York: Cambridge University Press.

IPCC (2014). *Climate change 2014: Synthesis report*. Cambridge, UK and New York: Cambridge University Press.

IPCC (2021). *Climate change 2021: The physical science basis. Contribution of working group I to the sixth assessment report of the intergovernmental panel on climate change*. Cambridge, UK and New York: Cambridge University Press.

Jeong, S. (2020). Autumn greening in A warming climate. *Nat. Clim. Chang.* 10, 712–713. doi:10.1038/s41558-020-0852-7

Meehl, G. A., Karl, T., Easterling, D. R., Changnon, S., Pielke, R., Changnon, D., et al. (2000). An introduction to trends in extreme weather and climate events: Observations, socioeconomic impacts, terrestrial ecological impacts, and model projections. *Bull. Amer. Meteor. Soc.* 108, 46–51.

Ni, J. (2011). Impacts of climate change on Chinese ecosystems: Key vulnerable regions and potential thresholds. *Reg. Environ. Change* 11, 49–64. doi:10.1007/s10113-010-0170-0

Pan, Y., Birdsey, R. A., Fang, J., Houghton, R., Kauppi, P. E., Kurz, W. A., et al. (2011). A large and persistent carbon sink in the world's forests. *Science* 333, 988–993. doi:10.1126/science.1201609

Park, H., Jeong, S., Ho, C., Kim, J., Brown, M. E., Schaepman, M. E., et al. (2015). Nonlinear response of vegetation green-up to local temperature variations in temperate and boreal forests in the northern Hemisphere. *Remote Sens. Environ.* 165, 100–108. doi:10.1016/j.rse.2015.04.030

Peng, C., Zhou, X., Zhao, S., Wang, X., Zhu, B., Piao, S., et al. (2009). Quantifying the response of forest carbon balance to future climate change in northeastern China: Model validation and prediction. *Glob. Planet. Change* 66, 179–194. doi:10.1016/j.gloplacha.2008.12.001

Peng, X. B., Yu, M., and Chen, H. S. (2022). Projected changes in terrestrial vegetation and carbon fluxes under 1.5°C and 2.0°C global warming. *Atmos. (Basel).* 13, 42. doi:10.3390/atmos13010042

Piao, S., Sitch, S., Ciais, P., Friedlingstein, P., Peylin, P., Wang, X., et al. (2013). Evaluation of terrestrial carbon cycle models for their response to climate variability and to CO_2 trends. *Glob. Chang. Biol.* 19, 2117–2132. doi:10.1111/gcb.12187

Piao, S., Zhang, X., Chen, A., Liu, Q., Wu, X., Wang, X., et al. (2019). The impacts of climate extremes on the terrestrial carbon cycle: A review. *Sci. China Earth Sci.* 49, 1551–1563. doi:10.1007/s11430-018-9363-5

Salvucci, M. E., and Crafts-Brandner, S. J. (2004). Inhibition of photosynthesis by heat stress: The activation state of rubisco as A limiting factor in photosynthesis. *Physiol. Plant.* 120, 179–186. doi:10.1111/j.0031-9317.2004.0173.x

Schaefer, K., Collatz, G. J., Tans, P., Denning, A. S., Baker, I., Berry, J., et al. (2008). Combined simple biosphere/carnegie-ames-stanford approach terrestrial carbon cycle model. *J. Geophys. Res.* 113, G03034. doi:10.1029/2007JG000603

Schlund, M., Eyring, V., Camps-Valls, G., Friedlingstein, P., Gentine, P., Reichstein, M., et al. (2020). Constraining uncertainty in projected gross primary production with machine learning. *J. Geophys. Res. Biogeosci.* 125, e2019JG005619. doi:10.1029/2019JG005619

Smith, M., Knapp, A. K., and Collins, S. L. (2009). A framework for assessing ecosystem dynamics in response to chronic resource alterations induced by global change. *Ecology* 90, 3279–3289. doi:10.1890/08-1815.1

Spitters, C. (1986). Separating the diffuse and direct component of global radiation and its implications for modeling canopy photosynthesis Part II. Calculation of canopy photosynthesis. *Agric. For. Meteorol.* 38, 231–242. doi:10.1016/0168-1923(86)90061-4

Taylor, K. E., Stouffer, B. J., and Meehl, G. A. (2012). An overview of CMIP5 and the experiment design. *Bull. Am. Meteorol. Soc.* 93, 485–498. doi:10.1175/BAMS-D-11-00094.1

Walther, G. R., Post, E., Convey, P., Menzel, A., Parmesan, C., Beebee, T., et al. (2002). Ecological responses to recent climate change. *Nature* 416, 389–395. doi:10.1038/416389a

Wang, S., Zhang, Y., Ju, W., Qiu, B., and Zhang, Z. (2021). Tracking the seasonal and inter-annual variations of global gross primary production during last four decades using satellite near-infrared reflectance data. *Sci. Total Environ.* 755, 142569. doi:10.1016/j.scitotenv.2020.142569

Wang, X., Piao, S., Ciais, P., Friedlingstein, P., Myneni, R. B., Cox, P., et al. (2014). A two-fold increase of carbon cycle sensitivity to tropical temperature variations. *Nature* 506, 212–215. doi:10.1038/nature12915

Xu, Y., Zhou, B., Wu, J., Han, Z., Zhang, Y., Wu, J., et al. (2017). Asian climate change under 1.5-4°C warming targets. *Adv. Clim. Change Res.* 8, 99–107. doi:10.1016/j.accre.2017.05.004

Yu, M., Wang, G. L., Parr, D., and Ahmed, K. F. (2014). Future changes of the terrestrial ecosystem based on A dynamic vegetation model driven with RCP8.5 climate projections from 19 GCMs. *Clim. Change* 127, 257–271. doi:10.1007/s10584-014-1249-2

Yue, X., Liao, H., Wang, H., Zhang, T., Unger, N., Sitch, S., et al. (2020). Pathway dependence of ecosystem responses in China to 1.5°C global warming. *Atmos. Chem. Phys.* 20, 2353–2366. doi:10.5194/ACP-20-2353-2020

Zhai, P., and Pan, X. (2003). Change in extreme temperature and precipitation over northern China during the second half of the 20th century. *Acta Geogr. Sin.* 58, 1–10. doi:10.11821/xb20037s001

Zhang, Y., Chen, J., Chen, L., Li, R., Zhang, W., Lu, N., et al. (2015). Characteristics of land cover change in siberia based on globe land 30, 2000-2010. *Prog. Geogr.* 34 (10), 1324–1333. doi:10.18306/dlkxjz.2015.10.013

Zhou, B., Xu, Y., Han, Z., Shi, Y., Wu, J., and Li, R. (2020). CMIP5 projected changes in mean and extreme climate in the belt and road region. *Trans. Atmos. Sci.* 43 (1), 255–264. doi:10.13878/j.cnki.dqkxxb.20191125009

Zhu, Z., Liu, Y., Liu, Z., and Piao, S. (2018). Projection of changes in terrestrial ecosystem net primary productivity under future global warming scenarios based on CMIP5 models. *Clim. Chang. Res.* 14, 31–39. doi:10.12006/j.issn.1673-1719.2017.042

frontiers | Frontiers in Earth Science

TYPE Original Research
PUBLISHED 26 July 2022
DOI 10.3389/feart.2022.965005

OPEN ACCESS

EDITED BY
Stephen Outten,
Nansen Environmental and Remote Sensing Center (NERSC), Norway

REVIEWED BY
Zhiqiang Lin,
Chengdu University of Information Technology, China
Haiyun Shi,
Southern University of Science and Technology, China

*CORRESPONDENCE
Xulin Ma,
xulinma@nuist.edu.cn
Yue Ma,
mayue630@126.com

SPECIALTY SECTION
This article was submitted to Atmospheric Science, a section of the journal Frontiers in Earth Science

RECEIVED 09 June 2022
ACCEPTED 07 July 2022
PUBLISHED 26 July 2022

CITATION
Huang Y, Ma X, Ma Y and Qing Y (2022), Heavy precipitation events in northwestern China induced by northeastward plateau vortex: Two cases comparison.
Front. Earth Sci. 10:965005.
doi: 10.3389/feart.2022.965005

Heavy precipitation events in northwestern China induced by northeastward plateau vortex: Two cases comparison

Yujing Huang[1], Xulin Ma[1]*, Yue Ma[2]* and Yiyu Qing[1]

[1]Key Laboratory of Meteorological Disaster, Ministry of Education (KLME)/Collaborative Innovation Center on Forecast and Evaluation of Meteorological Disasters (CIC-FEMD)/Joint International Research Laboratory of Climate and Environment Change (ILCEC)/Joint Center for Data Assimilation Research and Applications, School of Atmospheric Sciences, Nanjing University of Information Science & Technology, Nanjing, China, [2]Shanghai Jiading District Meteorological Bureau, Shanghai, China

The plateau vortex is one of the dominant weather systems that modulate summer rainfall in northwestern China, a typical arid/semi-arid area worldwide. Two heavy rainfall cases in the summer of 2012 and 2013, accompanying the northeastward movement of plateau vortexes, are selected here. The role of plateau vortexes in these two cases is explored by diagnosing their moist potential vorticity, helicity, and convective clouds characteristics, using numerous data (ERA-Interim reanalysis, multi-sourced precipitation data, FY-2E satellite images). The plateau vortexes enhanced convective instability in the rainfall area by entraining upper-level dry and cold air, manifested as salient vertical gradients of moist potential vorticity and steep pseudo-equivalent potential temperature isolines. The rainfall occurred eastward relative to the vortex movement track and intensified on the left of cloud black body temperature (TBB) with larger gradients at the middle to late stages of the vortex life span. The generation of moisture helicity is dictated by the water vapor transportation, with the negative value concentrated in the water vapor-rich areas. Notably, the two cases differ in tracks, life spans, water vapor sources, and precipitation amounts, which may be attributed to large-scale circulation background, vertical vortex structure, and moisture condition.

KEYWORDS

plateau vortex moving northeastward, heavy precipitation, diagnostic analysis, moist potential vorticity, helicity

Introduction

Northwestern China is one of the world's typical arid/semi-arid climate regions. Climatologically (54-year) annual precipitation is 299 mm, of which summer rainfall accounts for the majority of this (Huang et al., 2016; Shang et al., 2018). In arid and mountainous northwestern China, heavy rainfall has a double-edged effect here, benefiting agriculture against drought, reservoir storage, and power generation while it is also a potential reason to lead to secondary disasters such as floods and mudslides.

Rainstorms in northwestern China are less frequent and less intense than those in eastern China. Due to poor rainproof facilities in arid regions, even less intense rainfall can sometimes cause severe damage, not to mention heavy rainfall. For instance, in the summer of 2012, Subei County in Gansu Province was hit by an extreme precipitation event, where torrential flooding annihilated the road and farmland (Xinhua News Agency, 2012). In July 2013, Shaanxi province suffered a record-breaking extreme rainstorm, affecting 460,000 people in 387 townships and causing economic losses of 542 million CNY (China News Service, 2013). These two heavy precipitation events, which attracted much attention and caused severe disasters, were both related to the plateau vortex.

Plateau vortex is an α mesoscale cyclone generated on the Tibetan Plateau (the plateau for short) in summer-half years. Evident at the 500-hPa isobaric surface, the plateau vortex is one of the dominant precipitation-related weather systems in the summertime on the plateau. The plateau vortex is active at its genesis source and mainly regulates precipitation in the central and western plateau. Under favorable synoptic conditions, some plateau vortexes can move out of the plateau and cause widespread heavy rainfall (Li, 2013; Curio et al., 2019) downstream. According to the moving tracks (Wang, 1987; Lin, 2015), plateau vortexes can be separated into three categories: eastward plateau vortex (EPV), northeastward plateau vortex (NEPV), and southeastward plateau vortex (SEPV), which affect different areas downstream of the plateau (Yu et al., 2014; Li et al., 2020b; Sun et al., 2022).

Several previous studies have documented that the plateau vortex is crucial in the formation of heavy rainfall, especially in eastern China. The upper-level divergences in westerly and lower-level convergences in vortex have been argued to favor the development of EPV, with the former acting as a vital role in the genesis of vortex-induced precipitation (Liu and Fu, 1986; Li et al., 2019; Li et al., 2020b). Yang et al. (2017) reported that the positive vorticity advection in front of the EPV was one of the triggering mechanisms of rainstorms. Water vapor conditions are also essential for EPV. Yu (2002) pointed out that the water vapor vortex in the middle-to-upper troposphere is indicative of EPV, for their development and movement are in line with that of EPV. The role of EPV in precipitation has been widely investigated (Huang and Li, 2007; Huang and Li, 2009; Huang et al., 2010). After diagnosing the circulation of three EPVs moving processes, they found that the variations of physical quantities such as helicity, moist potential vortex, and non-geotropic Q vector are consistent with the variation of EPV precipitation, which may provide the predictable source for precipitation.

The previous studies deepen our understanding of the role of the eastward-moving plateau vortex, i.e., EPV in the precipitation of eastern China. For rainfall occurring in northwestern China, the role of the northeastward-moving plateau vortex, i.e., NEPV may be more critical. A NEPV event can cause > 100 mm of precipitation in one single day over Northwestern China, making a great contribution to the inherently low annual total precipitation amount in this arid region (Shang et al., 2018). However, the research on the effect of NEPV on precipitation in Northwestern China remains notably absent. Compared to EPV, NEPV has a more northerly moving track and a shorter life span. Even constrained by the limited water vapor supplements, the NEPV can also cause heavy precipitation. Furthermore, NEPV is observed to weaken when it moves off the Plateau (Sun et al., 2022). So how does the NEPV affect precipitation in its weakening period? The mechanism of its influence on precipitation deserves further study.

Therefore, two typical cases of heavy summer precipitation associated with NEPV in 2012 and 2013 are selected here to explore the physical mechanisms of NEPV-induced precipitation, by diagnosing the quantities including moist potential vorticity, helicity, and mesoscale cloud cluster characteristics in the two cases, based on multi-source datasets. This work aims to deepen the cognition of the NEPV to provide information for the plateau vortex-induced precipitation forecast, and highlight the role of the Tibetan Plateau in the weather and climate of China. This paper is organized as follows. Section 2 presents the data and methods used in this work. Section 3 describes the precipitation profile and the movement of NEPV, and then the precipitation intensity caused by the NEPV was statistically analyzed. Section 4 investigates the heavy precipitation feature of NEPV, including precipitation conditions and physical quantities. A summary and discussion are provided in Section 5.

Data and methods

Data

The Yearbook of Low Vortex Shear Lines over the Tibetan Plateau compiled by the Institute of Plateau Meteorology, China meteorological administration, 2012 (CMA), Chengdu (Li et al., 2013), is consulted here for NEPV case selection. These are the four standards that we use to pick up typical cases: 1. NEPV that moving off plateau, 2.24-h accumulate precipitation more than 50 mm, 3. Life span longer than 48 h, 4. Having close source area. Therefore, we selected the two cases with heavy precipitation induced by NEPV under different sensible heating over the plateau, one on June 3–5 in 2012 (referred to as Case 2012) and the other on July 19–22 in 2013 (referred to as Case 2013) among all the recorded NEPVs. ERA-Interim reanalysis dataset (6-h time interval, 2.5° × 2.5° latitude-longitude grid) is used to depict environmental circulations and calculate physical quantities (e.g., moist potential vorticity, helicity), for its better performance in vortex tracks identification than other reanalysis datasets according to Lin et al. (2020). The rainfall area

during the NEPV movement is captured using CMORPH integrated hourly precipitation amount data with a 0.1° × 0.1° latitude-longitude grid (Joyce et al., 2004), while the specific precipitation amount generated is determined by the daily and hourly precipitation amount observed in automatic weather stations provided by the National Meteorological Information Center of CMA. Hourly Black Body Temperature (TBB) data retrieved from the FY-2E geostationary satellite (Yang et al., 2015) is used to further analyze the cloud top brightness temperature associated with precipitation intensity.

Methods

Moist potential vorticity (MPV) and helicity, are useful physical quantities in diagnosing rainfall cases, especially those related to severe convective weather such as mid-latitude torrential rain (Gao et al., 2007; Onderlinde and Nolan, 2014; Luhunga and Djolov, 2017). The studies on plateau vortex-induced precipitation have mainly focused on EPV (Huang and Li, 2007; Huang and Li, 2009; Huang et al., 2010). Reflecting the combined characteristic of air-water vapor, thermal and dynamic simultaneously (Bennetts and Hoskins, 1979; Marquet, 2014), MPV in the p-coordinate system is expressed as (Wu et al., 1995):

$$MPV = -g(\zeta + f)\frac{\partial \theta_{se}}{\partial p} + g\left(\frac{\partial v}{\partial p}\frac{\partial \theta_{se}}{\partial x} - \frac{\partial u}{\partial p}\frac{\partial \theta_{se}}{\partial y}\right) \quad (1)$$

Where g is the gravitational acceleration, ζ is the vertical vorticity, f is the Coriolis parameter, θ_{se} is the potential pseudo-equivalent temperature, p is the pressure, and u, v is the horizontal wind. The first term on the right is the barotropy moist potential vortex (MPV_1), which is the vertical component of the wet potential vortex, reflecting the effect of convective stability $-g\partial\theta_{se}/\partial p$. The second term is the baroclinic moist potential vortex (MPV_2), which is the horizontal component of the moist potential vortex and can be used as a tracer of warm and wet air. The moist potential vortex unit is PVU, 1 PVU = 10^{-6} m^2 K·s^{-1} kg^{-1}.

Helicity is commonly applied to describe the degree of rotation along the direction of motion for rotating fluids, and the rotational properties of weather systems are comprehensively depicted (Moffat, 1969; Lilly, 1986; Wu and Tan, 1989). Given a large number of definitions of helicity and the fact that the effect of water vapor on helicity is discussed in this study, the formula of moisture helicity is adopted (Lei et al., 2006):

$$H_q = w\zeta\nabla\cdot(qV) = \frac{\omega}{\rho g}\left(\frac{\partial v}{\partial x} - \frac{\partial u}{\partial y}\right)\left(\frac{\partial uq}{\partial x} + \frac{\partial vq}{\partial y}\right) \quad (2)$$

Where q is the specific humidity, ρ is the density. When there is upward motion ($w > 0$) and positive vertical vorticity ($\zeta > 0$), H_q is negative (positive) under water vapor flux convergence $\nabla\cdot(qV) < 0$ (>0 for divergence). The moist helicity reflects the relationship between the development and maintenance of weather systems and the intensity of synoptic phenomena. Generally, the smaller the H_q the more favorable the precipitation production.

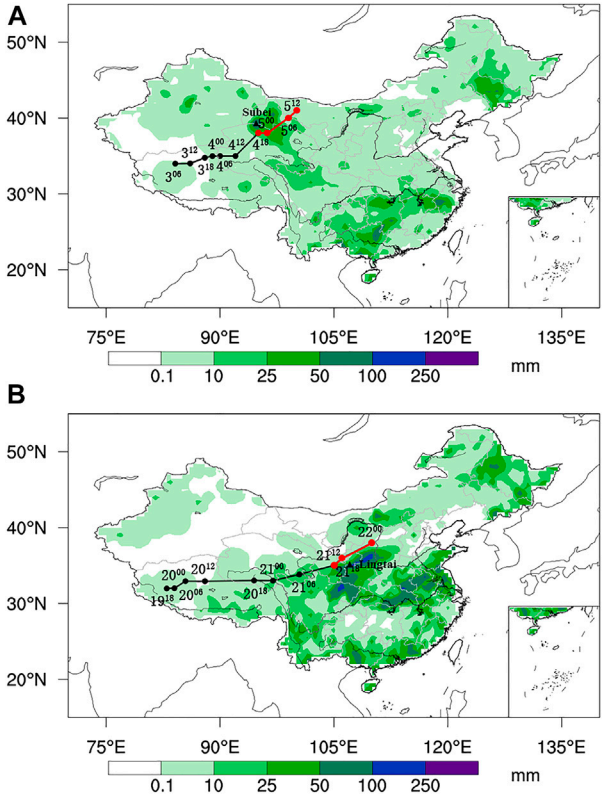

FIGURE 1
Moving tracks (black dots, moving-out in red dots) and accumulated daily precipitation (shaded) in 3–5 June 2012 **(A)** and 19–21 July 2013 **(B)** (marked as vortex position corresponding to date in the superscript and time in the subscript, ▲: precipitation maximum station) based on ERA-Interim reanalysis datasets and CMORPH.

The precipitation profile and the movement of northeastward plateau vortex

The characteristics of heavy precipitation events associated with northeastward plateau vortex

Figure 1 shows the NEPV moving tracks (black dotted curves) and total precipitation amount (shaded) in the two cases. In Case 2012, the plateau vortex bred in Ali, Tibet, then

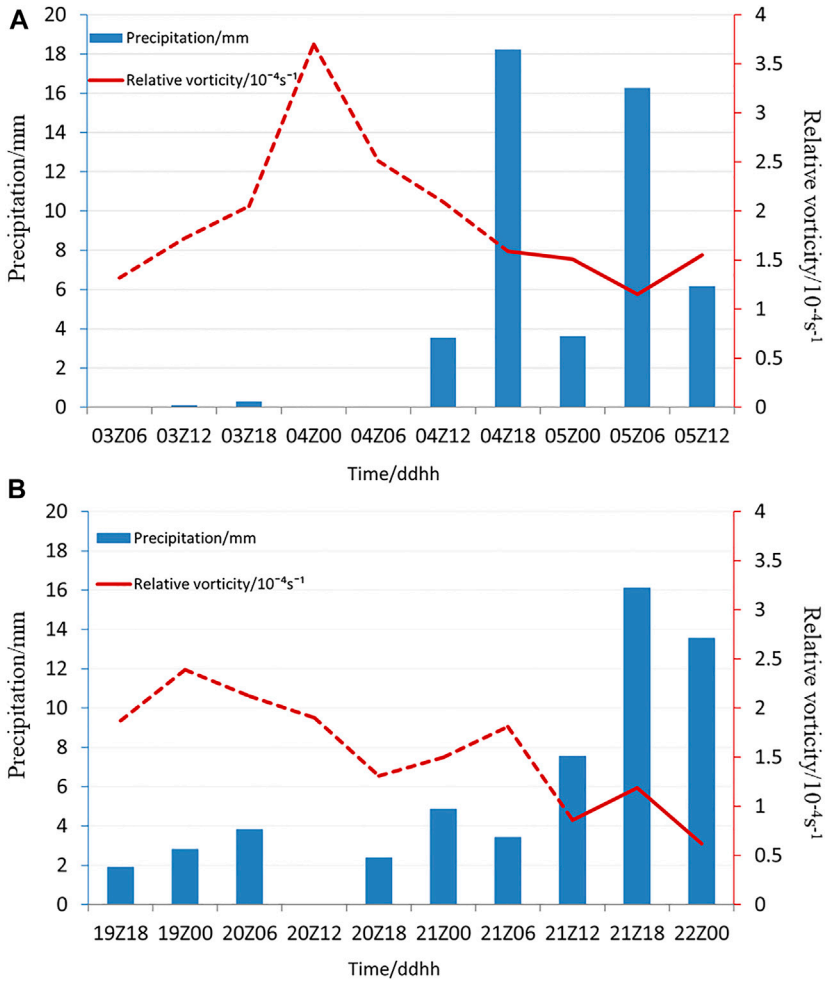

FIGURE 2
The relative vorticity of vortex center (curves, plateau stages in dashed lines and moving-out plateau stages in solid lines, unit: 10−4·s-1) and the variation of 6-h accumulated precipitation (bars, unit: mm) at 6-h intervals in the range of 2° × 2°centered at the vortex center in Case 2012 **(A)** and Case 2013 **(B)**

moved northeastward and died out in western Inner Mongolia (Figure 1A). During its movement, precipitation mainly occurred on 5 June 2012, with the rainfall center in Hexi Corridor. The vortex of Case2013 was also generated in Ali, Tibet, but disappeared in the northeast of Loess Plateau (Figure 1B). As the two vortexes moved out of the plateau, the Loess Plateau region experienced heavy precipitation, with the rainfall area to the southeast of the vortex tracks.

To better distinguish the effects of different phases in NEPV movements on precipitation, the vortex movements are subdivided into plateau stages and moving-out plateau stages according to their tracks and influences on precipitation. Figure 2 shows the variations of relative vorticity (curves) and 6-h accumulative precipitation (bars), averaged over a 2° × 2° range centered at the vortex center at 6-h intervals. Prominent relative vorticity was observed at the plateau stage in the two cases under the heating in the Ali. Constrained by water vapors supplement, less precipitation was generated in both the cases. However, as the vortex moved off the plateau, vortex-induced precipitation at the northeastern edge of the plateau as well as downstream areas were detectable. Heavy rainfall at the moving-out plateau stage began at 18:00 on the 4th, and ended at 12:00 on the 5th in Case 2012 (Figure 2A), while it was 12:00 on the 21st to 00:00 on 22nd in Case 2013 (Figure 2B), suggesting a substantial influence of NEPV on precipitation in the middle-to-late life span.

The intensity of NEPV-induced precipitation in Northwestern China was graded into four levels following the CMA's criteria (2012). The numbers of stations at each level in two cases are listed in Table 1. The precipitation amount at most stations in Case2012 was at moderate to heavy

TABLE 1 Overview of precipitation (graded into four levels following the CMA's criteria) and moving tracks of plateau vortex in Case2012 and Case2013.

	Moving tracks	Life span (h)	Number of observation stations				The heaviest precipitation
			Moderate rain	Heavy rain	Rainstorm	Heavy rainstorm	
Case2012	Northeastward (northerly)	60	26	5	2	-	Subei Station (39.52°N, 94.87°E, 93.8 mm)
Case2013	Northeastward (easterly)	54	47	50	17	6	Lingtai Station (35.07°N, 107.62°E, 184.6 mm)

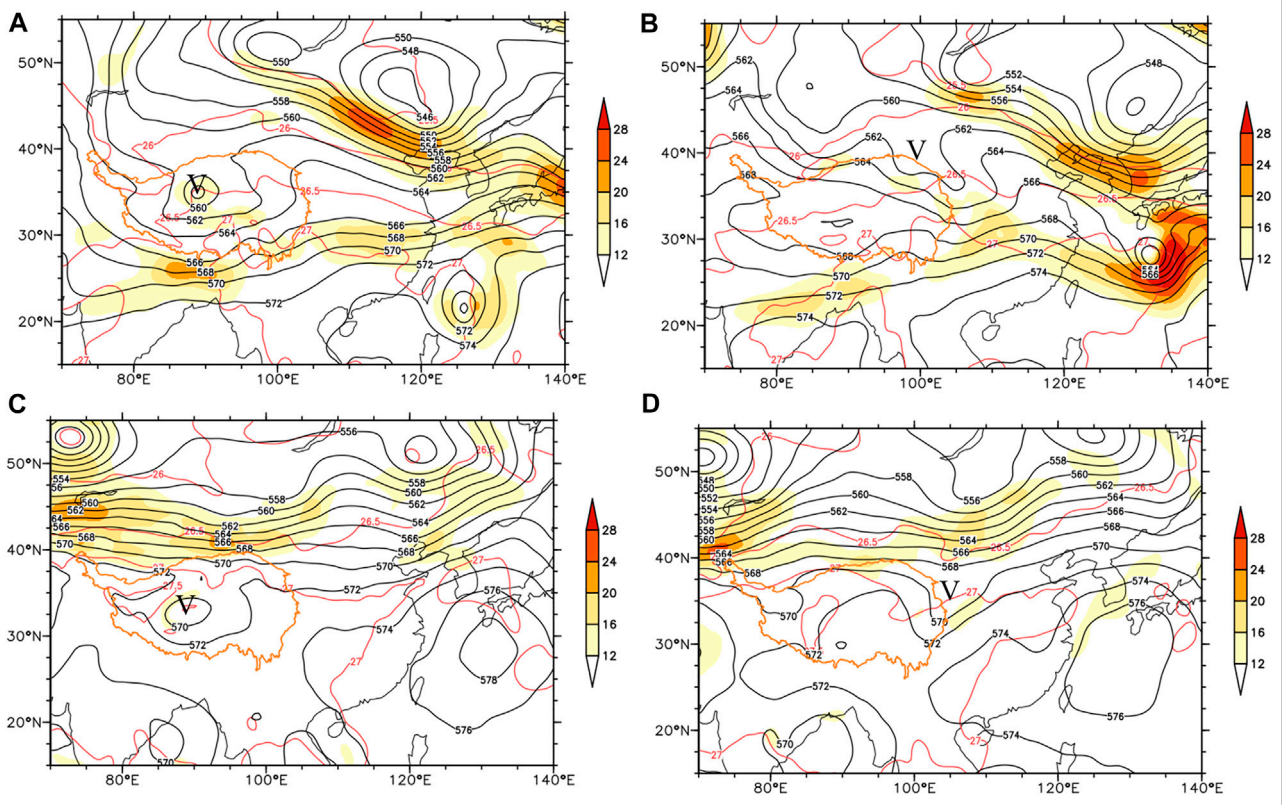

FIGURE 3
Geopotential height (black isolines; Unit: dagpm), temperature (red isolines; Unit: °C) and strong wind area (shaded, wind speed ≥12 m/s) on 500 hPa at intermediate moments of plateau stage **(A,C)** and moving-out plateau stage **(B,D)** **(A)** 00:00 4 June 2012, **(B)** 06:00 5 June 2012, **(C)** 12:00 20 July 2013, **(D)** 18:00 21 July 2013, V denotes the position of the vortex at the corresponding time) in Case 2012 **(A,B)** and Case 2013 **(C,D)** (The brown solid line is Tibetan plateau boundary).

levels, while only two stations (Subei and Yumenzhen) were at rainstorm level. On 21 July 2013, the daily rainfall of Lingtai station reached 184.6 mm, exceeding its historical extreme. In Case 2013, the vortex moved eastward, producing a narrower and longer rainfall area than Case 2012. The rainstorm located at the southeast quadrant relative to the NEPV center. In the following, the synoptic-scale circulation environments are examined to further detail the case differences.

Synoptic-scale circulation environments

Sun et al. (2022) figured that the plateau vortex movement is mainly influenced by the westerly wind at 200 hPa and the ridge in the east of plateau at 500 hPa. The former mainly affect the plateau vortex movement at plateau stage, and the latter at moving-out plateau stage. Typically, the cyclonic circulation of NEPV is found to be most pronounced in the

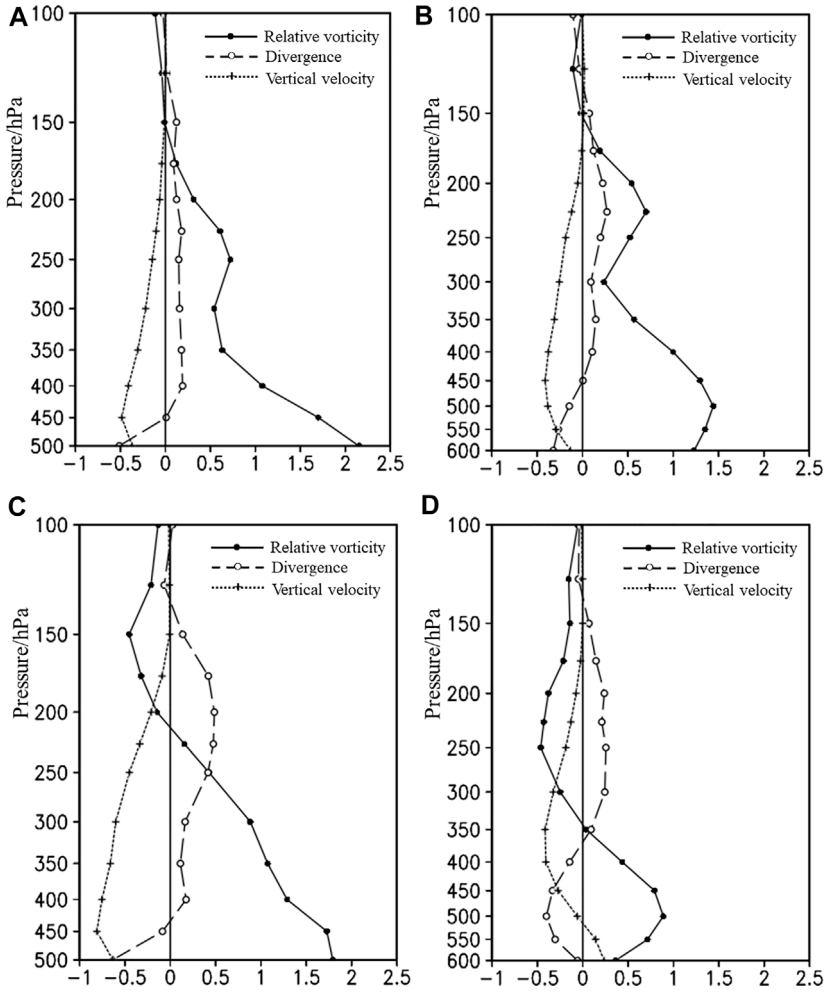

FIGURE 4
The vertical distribution of relative vorticity (solid, Unit: 10^{-4} s^{-1}), divergence (hollow, Unit: 10^{-4} s^{-1}) of vortex center and vertical velocity (cross, Unit: Pa·s^{-1}) at plateau stage and moving-out plateau stage in Case 2012 **(A,B)** and Case 2013 **(C,D)**.

middle troposphere (500 hPa) (Sun et al., 2022). As for our study, the NEPV movement in plateau stage was mainly easterly in both cases, the northeasterly movement was mainly occurred when moving out plateau. Therefore, in this section, we investigated the impacts of 500 hPa-ridge on the NEPV movement. Figure 3 illustrated the 500-hPa large-scale environmental circulation at intermediate moments during the different stages in the two cases. Specifically, at the plateau stage in Case 2012 (06:00 on 3rd --18:00 on 4th, Figure 3A), a meridional structure of "two troughs and one ridge" was observed in middle-high latitudes of Eurasia, with a closed depression center in the central part of the Tibetan Plateau, and a deep cold trough stable along the northeast of Lake Baikal to the east coast China. Suppressed by the strong cold air from the north, the plateau vortex mainly moved eastward at the plateau stage. Subsequently, the large northern vortex weakened and moved eastward by about 10° longitudes at the moving-out plateau stage (18:00 on 4th -- noon on 5th, Figure 3B). Guided by the southwesterly on the east edge of the plateau, the vortex moved towards the northeast. On the contrary, the environmental circulation in Case2013 is more zonal, causing the vortex to move eastward easily in response to the guiding airflow. Particularly, the stronger southerly in front of the trough at the moving-out stage (noon on 21st -- 00:00 on 22nd, Figure 3C) than that at the plateau stage (18:00 on 19th -- noon on 21st, Figure 3D) made an apparent northward movement of the vortex. The result regarding the effects of 500 hPa trough on NEPV is consistent with the statistical analysis by Sun et al. (2022). The horizontal distribution of the environmental fields for the two cases is discussed in this section. The following section will focus on the changes in the vertical structure of NEPV.

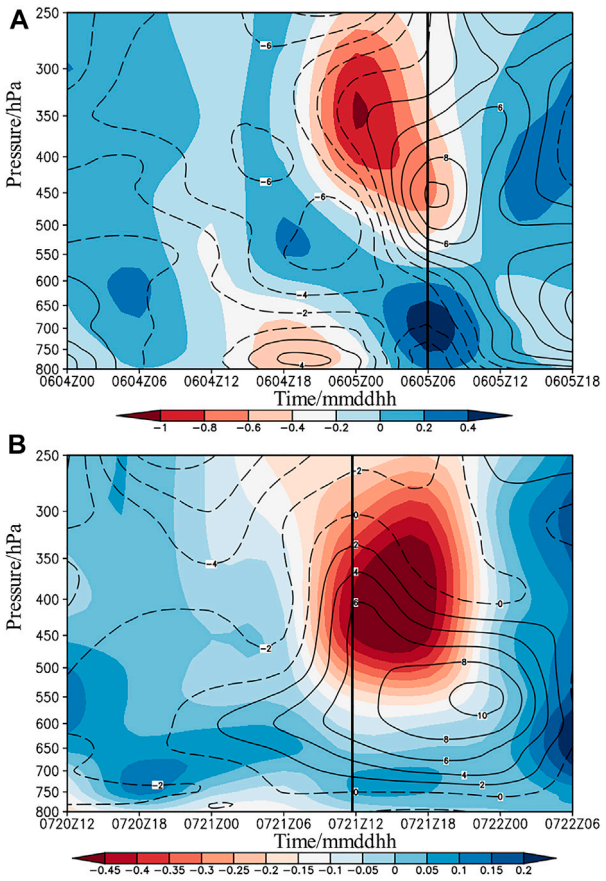

FIGURE 5
Time-height profile of relative vorticity (positive vorticity: solid contours; negative vorticity: dashed contours, Unit: 10^{-5} s^{-1}) and vertical velocity (shaded, Unit: Pa·s^{-1}) of the rainstorm center **(A)** (100°E, 40°N) in Case 2012; **(B)** (106°E, 35°N) in Case 2013) (the vertical line is the time when vortex passes through rainstorm center).

Vertical structure of northeastward plateau vortex

To obtain the vertical structure of NEPV during its movement, a composited analysis of the vertical profile of relative vorticity, divergence, and vertical velocity in the middle and upper troposphere at the two stages was performed (Figure 4). We found that the early-stage plateau vortex moved slowly and intensified in its birth-source area, reaching its strongest intensity over its life span (not shown) in the two cases. Notably, the two NEPVs have commonalities in the strongest centered relative vorticity maintained at 500 hPa (solid), convergent flow below 450 hPa (hollow), and upward motion from 500 hPa to the top troposphere (cross). As the vortex moved to the northeast, the vorticity maximum decreased with the weakened convergence in the middle troposphere. Subsequently, abundant water vapor led to widespread heavy precipitation downstream as showed in Figure 1.

Also, the two NEPVs diverge in their triggering of rainfall. In Case 2012, a deeper cyclonic circulation with two positive vorticity maxima was found in the vertical stratification (Figures 4A,B), which favors vortex maintenance, in line with the observed NEPV lifetime (Figure 1). In Case 2013, the positive (negative) vorticity was accompanied by convergence (divergence) in the lower (upper) level (Figure 4C), resulting in a robust upper-level pumping and lower-level water vapor accumulation at the moving-off plateau stage (Figure 4D). Therefore, more severe precipitation occurred in Case2013 than in Case2012 in Figure 2. In addition, a salient upper-level divergence appeared at the plateau stage in Case2013 that rapidly allowed vortex intensity and vertical extension height to reach their maximum within 6 h (not shown), which may be attributed to the plateau heating effect (Zhou et al., 2022). It can be concluded that the consistent circulation from middle to upper levels is favorable for the vortex to live longer. The coupling structure of low-level convergence with positive vorticity and upper-level divergence with negative vorticity, combined with a robust pumping effect, enhanced the convergence of middle-to-lower water vapor in the rainstorm area. As a result, the precipitation continues to accumulate in the vortex-weakening period.

Heavy precipitation feature of northeastward plateau vortex

Dynamic conditions

To confirm the dynamical effects of NEPV on heavy precipitation, the time-height evolution of relative vorticity and vertical velocity above 800 hPa at the rainstorm center in the two cases is given in Figure 5. Before the onset of heavy precipitation, the entire troposphere at the rainstorm center was controlled by the negative vorticity (dashed contours). The downdraft in the middle-to-lower troposphere inhibited the moisture convergence in the rainfall area. With the northeastward movement of the vortex, positive vorticity (solid contours) appeared in the mid-troposphere and was accompanied by upward motion (shaded in red). The strongest updraft at the rainstorm center appeared about 6-h earlier than the relative vorticity reaching its maximum in both cases, indicating that the wind modification precedes the vorticity. The vertical motion signal in Case2012 is a better predictor of precipitation (Figure 5A). With the appearance of the maximum updraft, the mid-level vorticity began to transform from negative to positive. Influenced by the descent plateau topography, the favorable precipitation conditions (positive

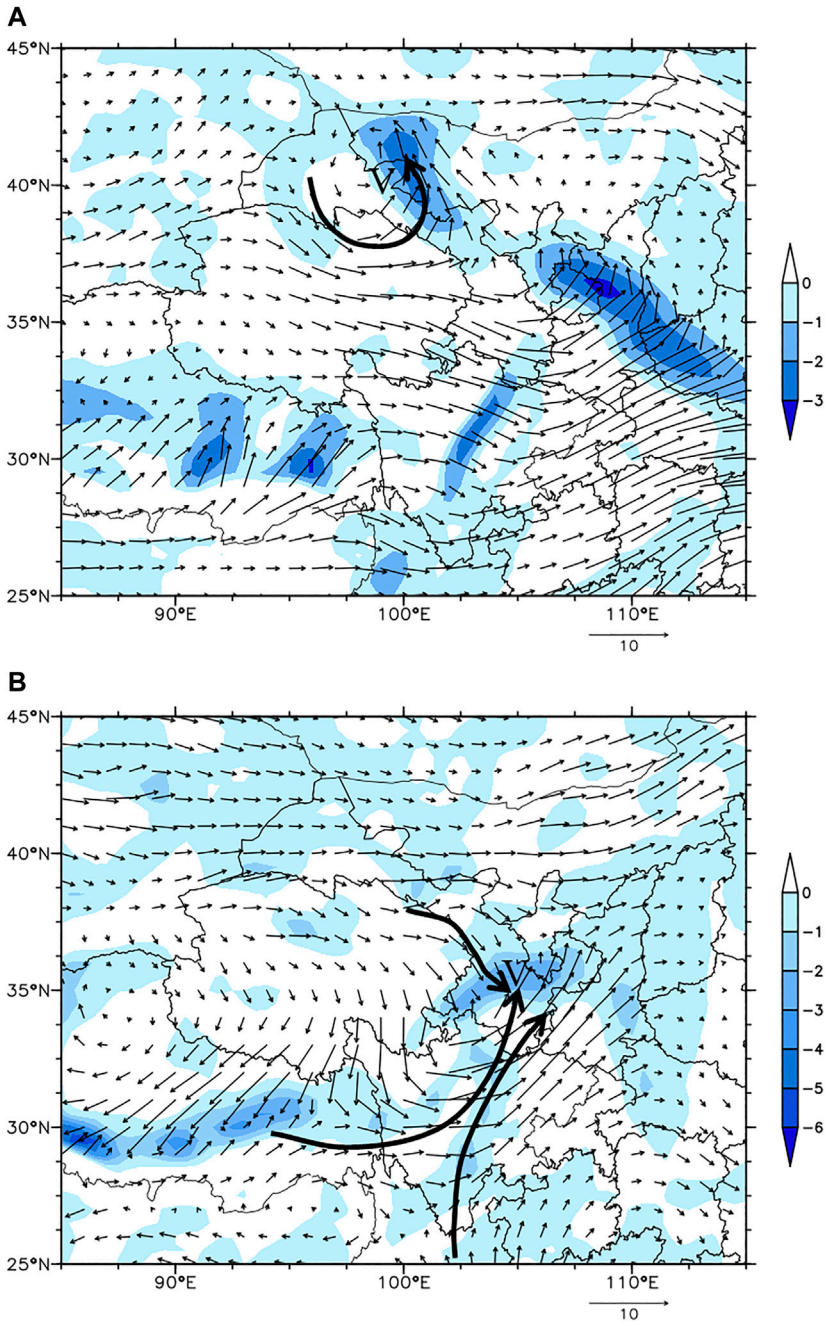

FIGURE 6
The water vapor flux divergence (shaded; Unit: 10^{-6} g cm^{-2}·hPa^{-1} s^{-1}) and water vapor flux (vectors; Unit: g·cm^{-1} hPa^{-1} s^{-1}) on 500 hPa at 06: 00 5 June 2012 **(A)** and at 12: 00 21 July 2013 **(B)** (the thick arrows denote water vapor transport path, V denotes the position of the vortex at the corresponding time).

vorticity and upward motion) tended to shift downward with time. In Case 2013 (Figure 5B), the positive vorticity (solid contours) signal of the vortex appeared 12-h earlier than the time vortex passes through the rainstorm center (black vertical line). When the vortex approached the rainstorm center, the updraft (shaded in red) was rapidly enhanced. In a word, the plateau vortex provides a favorable dynamic environment for a rainstorm.

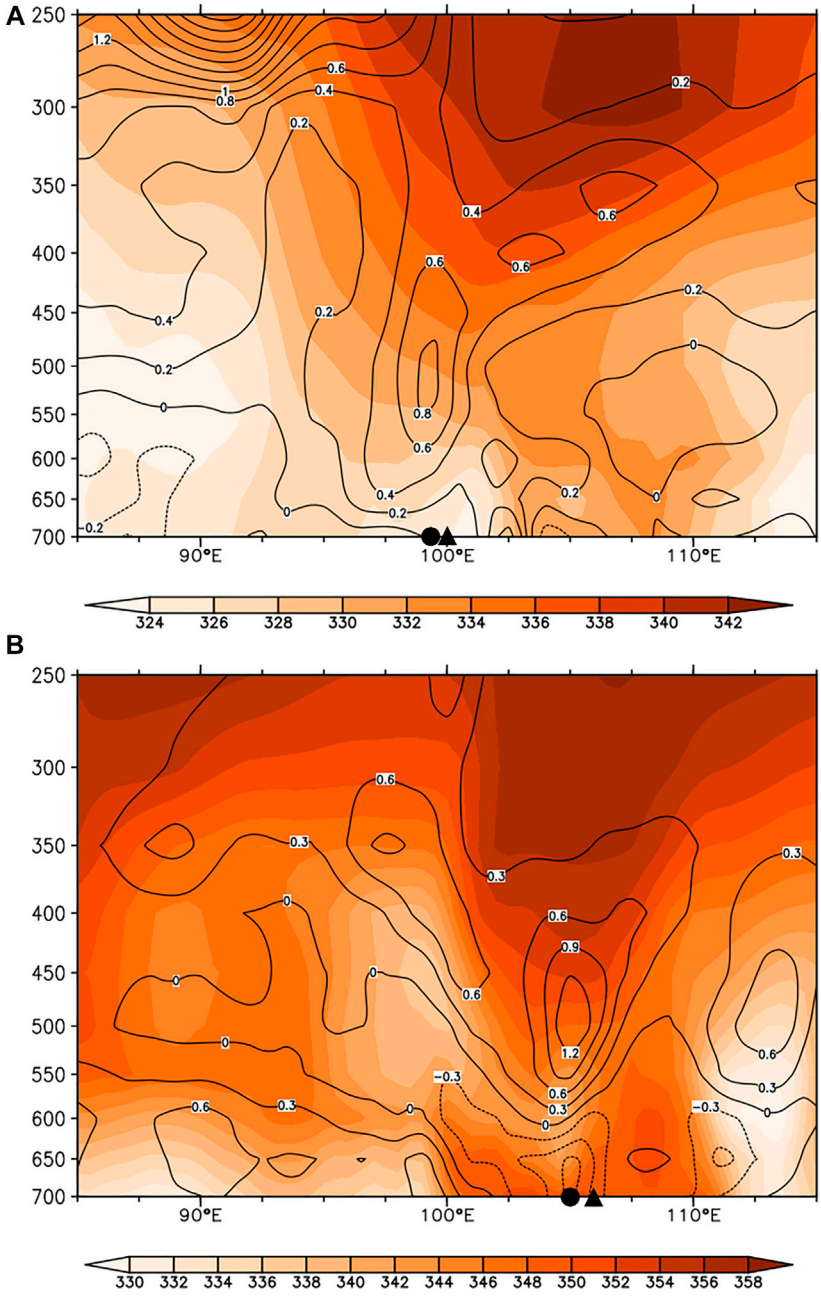

FIGURE 7
The longitude - height profile of MPV_1 (positive value: solid isoline; negative value: dashed isoline, Unit: PVU) and θ_{se} (shaded, Unit: K) along 40°N at 06: 00 5 June 2012 **(A)** and 35°N at 12: 00 21 July 2013 **(B)** (●: vortex center, ▲: storm center).

Water vapor conditions

Knowing that the weakened cyclonic circulation as the NEPV moved out of the plateau, we hypothesize that the water vapor condition plays a crucial role in heavy precipitation. Flows associated with the Indian monsoon and the South China Sea monsoon create the main water vapor transport channel to northwestern China in summer (Wang et al., 2018). As the vortex circulation on the plateau is strongest at 500 hPa, we use the water vapor flux at 500 hPa when the vortex moves through to depict the convergence of the water vapor transports (Figure 6).

The maximum values of water vapor flux divergence in the two rainstorm areas were both 2.5×10^{-6} g cm^{-2}·hPa^{-1}·s^{-1}. The

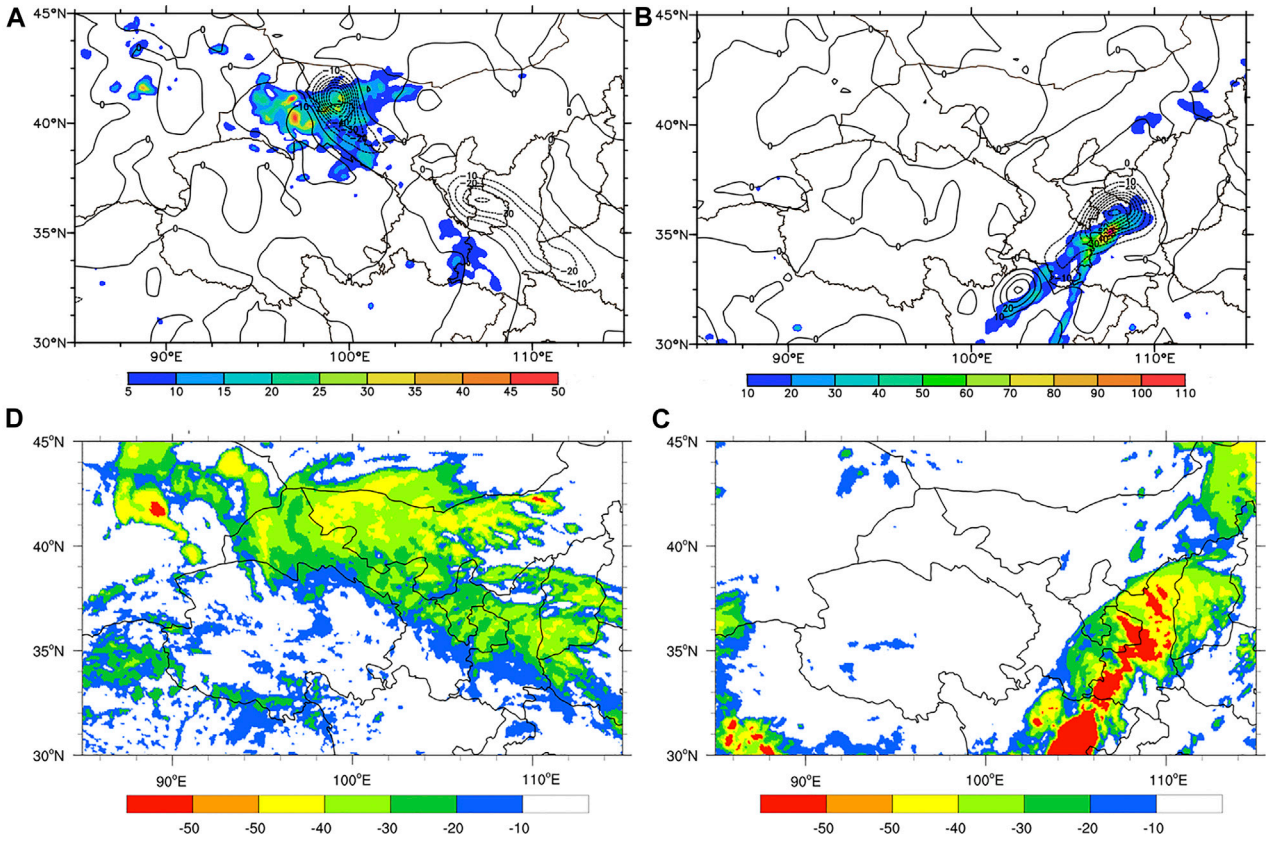

FIGURE 8
The moisture helicity (Unit: 10^{-11} m s^{-3}) on 500 hPa and 6-h accumulated precipitation (Unit: mm) **(A,B)**, black-body temperature (TBB) by FY-2E satellite **(C,D)** at 06: 00 5 June 2012 in Case 2012 **(A,C)** and at 12: 00 21 July 2013 in Case 2013 **(B,D)**.

TABLE 2 Comparisons of two heavy precipitation cases (Case2012 and Case 2013) induced by northeastward plateau vortices (NEPV).

		Case2012	Case2013
Characteristics	Life span	60 h: plateau stage 42 h, moving-out stage 18 h	54 h: plateau stage 42 h, moving-out stage 12 h
	Moving tracks	Northeastward (northerly)	Northeastward (easterly)
	Circulation	Meridional	Flat
	Main fall area	Hexi Corridor Area (more concentrated)	Loess Plateau (narrower)
	Precipitation intensity	Mainly moderate to heavy rain, few rainstorm	Large-scale rainstorm
	The vorticity maximum	3.7×10^{-4}·s^{-1}	2.4×10^{-4}·s^{-1}
	Primary water vapor source	Local	Subtropical high
	Vertical structure	Two vorticity maxima	Vorticity and divergence are coupled
Commonalities	Precipitation period	Moving-out stage (the middle and late period of life span)	
	Relative position of fall area	Moved eastward compared to the vortex	
	MPV_1	Large vertical gradient (invasion of dry and cold air caused convection instability)	
	Moist helicity	The negative area is affected by the water vapor transport path	
	TBB	The precipitation always occurred in large gradient area on the left of TBB	

water vapor convergence center in Case2012 was located on the northeast side of the vortex (Figure 6A, shaded). In Figure 3A, the ridgeline of West Pacific Subtropical High (WPSH) was positioned south of 20°N in Case 2012. Blocked by the terrain of the Loess Plateau in the way, it is difficult for water vapor to be transported from the Bay of Bengal to northwestern China. Therefore, in the absence of strong external supplements of water vapor for the rainfall area, the vortex convergence can only lead to local water vapor accumulation with a shorter duration and less amount of precipitation. Nevertheless, the ridgeline of WPSH was northward in Case 2013 (Figure 3B). The vortex caused a large amount of water vapor to gather around the rainfall area (Figure 6B, shaded). One of them was the water vapor from the Bay of Bengal, which flowed around the southern boundary of the plateau and crossed the Hengduan Mountains. These external water vapors joined the water vapor conveyor belt around the WPSH, climbed along the south side of the Loess Plateau, and converged near the vortex. Therefore, the rainfall area in Case2013 was southward shifted to the convergence area and presented a banded distribution along the plateau. In addition, it can also be found that water vapor convergence appears in the southeast of the vortex in Case2012 and the southwest of the vortex in Case 2013, and the convergence even was stronger than that of the NEPV falling area. However, in the absence of the dynamic lifting conditions of the vortex, there was no significant precipitation in these regions. In fact, not only the water vapor supply, the other factors which cause heavier rainstorm in Case2013 will be discussed later.

Distribution of moist potential vorticity

To investigate the convective stability in the rainstorm center brought by the NEPV, the longitude-height profile of MPV_1 and θ_{se} (potential pseudo-equivalent temperature) is depicted in Figure 7. The rainstorm center in Figure 1 was located near the vortex center and slightly eastward. The plateau vortex led the upper-level positive MPV_1 and θ_{se} maxima to extend downward and invade the rainfall area, leaving the MPV_1 maxima center at 500 hPa. The θ_{se} line near the vortex was steep, which induce the dry and cold air to diffuse downward and suppress the warm and wet air in the lower atmosphere. Therefore, both cases show great changes in vertical convective stability. Particularly in Case 2013 (Figure 7B), there was a significant negative MPV_1 in the middle-to-lower troposphere over the rainstorm area, leading to a large vertical gradient of MPV_1. The layer where the MPV_1 sign changed from positive to negative was exactly corresponding to the low θ_{se}. It is indicated that the cold air invaded from the middle troposphere and met the warm air at 600 hPa below the vortex. This convergence of warm and cold air led to significantly enhanced convective instability. The rainstorm center was located downstream with dense θ_{se} lines.

The NEPV led to the entrain of dry and cold air from the upper layer to the rainfall area, manifesting as a salient vertical gradient of MPV and a steep iso-θ_{se} line in the rainstorm center. The configuration of middle-level dry and clod air invasion and low-level instability is conducive to the storage and release of convective instability energy, creating conditions for the outbreak of rainstorms, similar to the previous analyzes of convective rainstorms induced by Meiyu-front (Zheng et al., 2019).

Distribution of moisture helicity and black body temperature characteristics

Moisture helicity measures both the vortex energy and the water vapor conditions. The area with negative moisture helicity is reported to correspond well to the rainfall area in EPV cases (Huang et al., 2011). For our NEPV cases, the negative moisture helicity in Case2012 was mainly in the junction of Gansu Province and Inner Mongolia, along the plateau edge, covering the rainfall area (Figure 8A). Strong updraft driven by low-level convergence and abundant water vapor encouraged the occurrence and development of heavy precipitation. Although the Loess Plateau also has covered by negative moisture helicity, there was no significant precipitation in the lack of vortex dynamic effect. For Case 2013, the negative moisture helicity in southern Gansu to the central Shaanxi presented a northwest-southwest distribution (Figure 8B). The less energy transportation outward and abundant moisture in this region benefited the precipitation generation. The negative moisture helicity center was slightly northward than the rainstorm center.

The TBB on cloud top obtained by the FY-2E satellite is depicted to investigate convective cloud cluster characteristics around the vortex. The mesoscale convective cloud cluster mainly appeared over the area including northern Gansu, western Inner Mongolia, Ningxia, central Shaanxi, and southern Shanxi Provinces at 06: 00 on 5 June 2012, covering an area of 800–1,000 km (Figure 8C). The convection associated with the vortex is to the north of 37°N. The region with TBB below—30°C presented an inverted triangle shape. The convective cloud belt was generally near the vortex trough at 500 hPa, with its outline highly aligned with the 562 dagpm isoline in Figure 3B and its shape similar to the 6-h accumulated rainfall area. The heavy precipitation clouds and rainfall areas with TBB below -40°C were to the northwest of the inverted triangle. At the same time, a convective cloud also appeared on the southeast of the vortex cloud cluster, which was far away from the vortex circulation and did not produce effective precipitation. A northeast-southwest oriented convective cloud cluster in Case2013 appeared from the north of Sichuan to the south of Shanxi, presenting a northeast-southwest oriented distribution (Figure 8D). It is necessary to pointed out that the largest cloud cluster in central Shaanxi was mainly affected by vortex, while the strongest cloud cluster in Sichuan was mainly affected by topography uplift of Hengduan Mountains, which was hardly affected by the vortex. The lower TBB indicated the higher cloud

top height and deeper vertical movement. The TBB is significantly lower than that of Case 2012, which can be as low as below −50°C in Case 2013. Thus, a more favorable dynamic condition with lower TBB in Case2013 generated a larger rainstorm area with stronger rainfall intensity than Case 2012.

The distribution of moisture helicity reflects the concentration of energy and water vapor in NEPV. Consistent with the evolution of rainfall area, the evolution of the negative moisture helicity region is affected by water vapor transportation. In both cases, the rainfall areas of the NEPV were to the left of TBB with a large gradient. The lower the TBB reflected by the satellite images, the better the dynamic conditions that trigger precipitation. Therefore, the strong rainfall always appeared near the large gradient area on the left of TBB.

Conclusion

Two typical cases of heavy precipitation induced by NEPV are selected here to analyze their moving track, precipitation characteristics and physical mechanism in detail, using multi-source data (automatic station observation, ERA-interim reanalysis and satellite images). A comparative analysis of heavy precipitation by using physical quantities such as MPV and helicity is conducted (Table 2). The main conclusions are as follows:

1) In terms of precipitation conditions, the plateau vortex led to the invasion of dry and cold air from the upper layer to the rainfall area, which resulted in a strong vertical gradient of MPV and steep iso-θ_{se} line in the rainstorm center and strengthened the convective instability in the rainfall area. The heavy precipitation always appeared near the large gradient area on the left of TBB, and the rainfall area moved eastward compared to the vortex. The vortex cyclonic circulation and updraft from middle to upper levels may be useful signals for precipitation forecast.
2) In terms of water vapor sources, the water vapor transportation was blocked by plateau topography in Case 2012, leading to less precipitation. In Case 2013, the low-level water vapor climbed up to the plateau and converged in the vortex center. The interaction of lower-level water vapor and the upper-level dry and cold air produced heavier precipitation. Affected by the water vapor transport path, the negative moisture helicity appeared in water vapor-rich regions, such as the edge of the plateau and outside of the subtropical high. The NEPV-induced precipitation occurred after the vortex moved out of the plateau.
3) In terms of vortex structure, there were two positive vorticity maxima in the vertical structure of the vortex in Case 2012, and the consistent circulation from middle to upper levels is conducive to the vortex maintenance. The coupling structure of vorticity and divergence in lower and upper levels, combined with the strong pumping effect enhanced the convergence of middle and low-level water vapor in the rainstorm area.

Discussion

This work conducted a study on NEPV and precipitation it causes in two cases. It is found that the precipitation induced by NEPV is crucial to northwestern China, and the water vapor supply and vortex structure play important roles in the precipitation process. However, the cause analysis of the difference between the two NEPVs is not addressed, including the thermal factors in the development of the two vortexes and precipitation. At the same time, the data completeness on Tibetan plateau remains inadequate, although there are several kinds of reanalysis data, it is unknown whether other data can reproduce the results of this paper, and it is necessary for further analysis using additional research methods, such as radar data analysis and numerical model. In addition, the total amount of such NEPV is relatively small, and some results may lack of representativeness. Moreover, some vortex develop strongly but do not move out of the plateau, whether these plateau vortices can induce precipitation in the downstream through wave propagation mechanism is also a topic worthy of future study. Therefore, the conclusions of this study deserve further confirmation by more cases and more diagnostic analysis.

Data availability statement

Publicly available datasets were analyzed in this study. This data can be found here: https://apps.ecmwf.int/datasets/data/interim-full-daily/levtype=sfc/ https://satellite.nsmc.org.cn/portalsite/default.aspx http://data.cma.cn/data/detail/dataCode/SEVP_CLI_CHN_MERGE_CMP_PRE_HOUR_GRID_0.10.html.

Author contributions

YH conducted the work, analyzed the result data, and drafted the manuscript. XM and YM made contributions to the design of the work and revised the manuscript. XM made contributions in guidance and discussion of the work and helped in editing the content. YQ helped in analyzing the data and revised the manuscript.

Funding

This research was sponsored by the National Natural Science Foundation of China (Grant No. 42030611 and 42165005) and

National Key R&D Program of China (Grant No. 2018YFC1505705).

Conflict of interest

The authors declare that the research was conducted in the absence of any commercial or financial relationships that could be construed as a potential conflict of interest.

Publisher's note

All claims expressed in this article are solely those of the authors and do not necessarily represent those of their affiliated organizations, or those of the publisher, the editors and the reviewers. Any product that may be evaluated in this article, or claim that may be made by its manufacturer, is not guaranteed or endorsed by the publisher.

References

Bennetts, D. A., and Hoskins, B. J. (1979). Conditional symmetric instability - a possible explanation for frontal rainbands. *Q. J. R. Meteorol. Soc.* 105, 945–962. doi:10.1002/qj.49710544615

China meteorological administration (2012). *Grade of precipitation GB/T28592-2012*. Beijing: Standards Press of china.

China News Service (2013). *Heavy rains and floods in Shaanxi have affected more than 450,000 people and killed nine*. Available at: https://www.chinanews.com.cn/gn/2013/07-23/5073171.shtml (Accessed July 23, 2013).

Curio, J., Schiemann, R., Hodges, K. I., and Turner, A. G. (2019). Climatology of Tibetan Plateau vortices in reanalysis data and a high-resolution global climate model. *J. Clim.* 32 (6), 1933–1950. doi:10.1175/JCLI-D-18-0021.1

Gao, S., Li, X., Tao, W., Shie, C., and Lang, S. (2007). Convective and moist vorticity vectors associated with tropical oceanic convection: A three-dimensional cloud-resolving model simulation. *J. Geophys. Res.* 112 (D1), D01105. doi:10.1029/2006JD007179

Huang, C., and Li, G. (2007). Synoptic and dynamic diagnostic analysis for a case of plateau vortex moving east. *J. Meteorol. Res.* 27 (12), 36–43. doi:10.3969/j.issn.1009-0827.2007.z1.006

Huang, C., and Li, G. (2009). A case study of plateau vortex moving east ward with heavy rainfalls based on helicity and non-geostrophic wet Q-vector. *Plateau Meteor* 28 (02), 319–326. doi:10.1016/j.snb.2013.12.103

Huang, C., Gu, Q., and Li, G. (2010). Mechanism analysis of plateau vortex moving east trigger rainstorm in Sichuan basin. *Plateau Meteor* 29 (04), 832–839.

Huang, C., Li, G., Niu, J., Luo, L., and Zhang, W. (2011). Moist helicity analysis of a heavy rainstorm in Sichuan basin induced by plateau vortex moving eastward. *Plateau Meteor* 30 (6), 1427–1434.

Huang, J., Ji, M., Xie, Y., Wang, S., He, Y., Ran, J., et al. (2016). Global semi-arid climate change over last 60 years. *Clim. Dyn.* 46 (3-4), 1131–1150. doi:10.1007/s00382-015-2636-8

Joyce, R. J., Janowiak, J. E., Arkin, P. A., and Xie, P. P. (2004). CMORPH: A method that produces global precipitation estimates from passive microwave and infrared data at high spatial and temporal resolution. *J. Hydrometeorol.* 5 (3), 487–503. doi:10.1175/1525-7541(2004)005<0487:CAMTPG>2.0.CO;2

Lei, Z., Ren, J., Ma, J., and Zhou, H. (2006). A case analysis of vortex-merging process in a jianghuai river valley Meiyu rainstorm. *Trans. Atmos. Sci.* 29 (03), 358–363. doi:10.1016/S1003-6326(06)60040-X

Li, Y., Yu, S., and Peng, J. (2013). *Yearbook of low vortex shear lines over the Tibetan Plateau*. Sichuan Province, Chengdu: Institute of Plateau Meteorology, CMA.

Li, L., Zhang, R., Wen, M., and Duan, J. (2019). Development and eastward movement mechanisms of the Tibetan Plateau vortices moving off the Tibetan Plateau. *Clim. Dyn.* 52 (7-8), 4849–4859. doi:10.1007/s00382-018-4420-z

Li, L., Zhang, R., Wu, P., Wen, M., and Duan, J. (2020b). Roles of Tibetan Plateau vortices in the heavy rainfall over southwestern China in early July 2018. *Atmos. Res.* 245, 105059. doi:10.1016/j.atmosres.2020.105059

Li, G. (2013). Advances in Tibetan plateau vortex and southwest vortex research and related scientific problems. *Desert Oasis Meteor* 7 (03), 1–6. doi:10.3969/j.issn.1002-0799.2013.03.001

Lilly, D. K. (1986). The structure, energetics and propagation of rotating convective storms. Part II: Helicity and storm stabilization. *J. Atmos. Sci.* 43 (2), 126–140. doi:10.1175/1520-0469(1986)043<0126:tseapo>2.0.co;2

Lin, Z., Guo, W., Jia, L., Yao, X., and Zhou, Z. (2020). Climatology of Tibetan Plateau vortices derived from multiple reanalysis datasets. *Clim. Dyn.* 55 (7), 2237–2252. doi:10.1007/s00382-020-05380-6

Lin, Z. (2015). Analysis of Tibetan Plateau vortex activities using ERA-Interim data for the period 1979–2013. *J. Meteorol. Res.* 29, 720–734. doi:10.1007/s13351-015-4273-x

Liu, F., and Fu, M. (1986). Research of eastward Tibetan plateau vortex. *Plateau Meteorol.* (02), 125–134.

Luhunga, P. M., and Djolov, G. (2017). Evaluation of the use of moist potential vorticity and moist potential vorticity vector in describing annual cycles of rainfall over different regions in Tanzania. *Front. Earth Sci.* 5, 7. doi:10.3389/feart.2017.00007

Marquet, P. (2014). On the definition of a moist-air potential vorticity. *Q. J. R. Meteorol. Soc.* 140, 917–929. doi:10.1002/qj.2182

Moffat, H. K. (1969). The degree of knottedness of tangled vortex lines. *J. Fluid Mech.* 35, 117–129. doi:10.1017/S0022112069000991

Onderlinde, M. J., and Nolan, D. S. (2014). Environmental helicity and its effects on development and intensification of tropical cyclones. *J. Atmos. Sci.* 71 (11), 4308–4320. doi:10.1175/JAS-D-14-0085.1

Shang, S., Lian, L., Ma, T., Zhuang, K., and Han, T. (2018). Spatiotemporal variation of temperature and precipitation in northwest China in recent 54 years. *Arid Zone Res.* 35 (01), 68–76. doi:10.13866/j.azr.2018.01.09

Sun, F., Zhou, S., Wang, M., Ma, S., Zhou, S., and Huang, Y. (2022). Activity characteristics of the northeast-moving Tibetan plateau vortices in early summer. *Meteor Mon.* 48 (3), 324–333. doi:10.7519/j.issn.1000-0526.2021.112501

Wang, K., Sun, M., and Gong, N. (2018). Spatial and temporal distribution and transportation of the water vapor in northwestern China. *Arid. Land Geogr.* 41 (02), 290–297. doi:10.13826/j.cnki.cn65-1103/x.2018.02.009

Wang, B. (1987). The development mechanism for Tibetan Plateau warm vortices. *J. Atmos. Sci.* 44 (20), 2978–2994. doi:10.1175/1520-0469(1987)044<2978:TDMFTP>2.0.CO;2

Wu, R., and Tan, Z. (1989). Conservative laws on generalized vorticity and potential vorticity and its applications. *Acta Meteor Sin.* (04), 436–442. doi:10.11676/qxxb1989.058

Wu, G., Cai, Y., and Tang, X. (1995). Moist potential vorticity and slantwise vorticity development. *Acta Meteor Sin.* 053 (004), 387–405. doi:10.11676/qxxb1995.04

Xinhua News Agency (2012). *Heavy rain hit Subei, Gansu province*. Available at: http://www.gov.cn/govweb/jrzg/2012-06/05/content_2153837.htm (Accessed June 5, 2012).

Yang, X., Fei, J., Huang, X., Cheng, X., Carvalho, L. M. V., He, H., et al. (2015). Characteristics of mesoscale convective systems over China and its vicinity using geostationary satellite FY2. *J. Clim.* 28 (12), 4890–4907. doi:10.1175/JCLI-D-14-00491.1

Yang, K., Lu, P., and Zhuang, L. (2017). Analyses of heavy rainstorm in warm sector under the influence of the low- pressure system of Qinghai-Xizang plateau. *J. Trop. Meteor.* 33 (03), 415–425. doi:10.16032/j.issn.1004-4965.2017.03.012

Yu, S., Gao, W., Peng, J., and Xiao, Y. (2014). Observational facts of sustained departure Plateau Vortexes. *J. Meteorol. Res.* 28 (2), 296–307. doi:10.1007/s13351-014-3023-9

Yu, S. (2002). Water vapor images during the eastward movement of the plateau vortex. *Plateau Meteor* (02), 199–204. doi:10.3321/j.issn:1000-0534.2002.02.013

Zheng, C., Liu, X., Fang, T., and Zhou, M. (2019). An analysis of trigger and enhance mechanisms of two typical Meiyu-front heavy rains in mid-west Zhejiang province. *Meteor. Sci. Technol.* 47 (03), 469–475. doi:10.19517/j.1671-6345.20180330

Zhou, S., Sun, F., Wang, M., Zhou, S., and Qing, Y. (2022). Effects of atmospheric heat source on the Tibetan plateau vortex in different stages: A case study in June 2016. *Atmosphere* 13, 689. doi:10.3390/atmos13050689

frontiers | Frontiers in Earth Science

ORIGINAL RESEARCH
published: 05 August 2022
doi: 10.3389/feart.2022.947001

Weather Extremes Led to Large Variability in O_3 Pollution and Associated Premature Deaths in East of China

Yu Wan[1,2], *Zhicong Yin*[1,3,4]*, *Qianyi Huo*[1], *Botao Zhou*[1] and *Huijun Wang*[1,3,4]

[1]Key Laboratory of Meteorological Disaster, Ministry of Education/Joint International Research Laboratory of Climate and Environment Change (ILCEC)/Collaborative Innovation Center on Forecast and Evaluation of Meteorological Disasters (CIC-FEMD), Nanjing University of Information Science and Technology, Nanjing, China, [2]Wuhan Central Meteorological Observatory, Wuhan, China, [3]Southern Marine Science and Engineering Guangdong Laboratory (Zhuhai), Zhuhai, China, [4]Nansen-Zhu International Research Centre, Institute of Atmospheric Physics, Chinese Academy of Sciences, Beijing, China

As global warming intensifies, hot extremes and heavy precipitation frequently happen in East of China. Meanwhile, severe surface ozone (O_3) pollution resulting from the interactions of anthropogenic emissions and meteorological conditions also occur more frequently. In this study, we quantified the impact of weather extremes on ground-level O_3 concentration during the summers of 2015–2021 and associated premature deaths in East of China. The O_3 pollution influenced by hot extremes [maximum 8-h average O_3 concentration (MDA8 O_3) = 152.7 μg m^{-3}] was 64.2% more severe than that associated with heavy rain (MDA8 O_3 = 93 μg m^{-3}) on the daily time scale. The compound hot and dry air extremes had a larger impact, and the associated MDA8 O_3 could be up to 165.5 μg m^{-3}. Thus, weather extremes could drastically perturb the O_3 level in the air to exhibit large variability. Based on GEOS-Chem simulations with fixed anthropogenic emissions, forcing of weather extremes could successfully reproduce the large daily variability of O_3 concentration because the weather extremes significantly influenced the physicochemical processes in the atmosphere. Furthermore, hot extremes magnified the single-day O_3-related premature death to 153% of that under other-condition events, while heavy rain events decreased it to 70% in East of China. The findings of the present study have the potential to promote daily to weekly O_3 forecasts and further improve our comprehensive understanding of the health effects of weather extremes and air pollution.

Keywords: weather extreme, high temperature, heavy rain, O_3 pollution, premature mortality

OPEN ACCESS

Edited by:
Stephen Outten, Nansen Environmental and Remote Sensing Center (NERSC), Norway

Reviewed by:
Yongli He, Lanzhou University, China
Shaobo Qiao, Sun Yat-Sen University, China

***Correspondence:**
Zhicong Yin
yinzhc@nuist.edu.cn

Specialty section:
This article was submitted to Atmospheric Science, a section of the journal Frontiers in Earth Science

Received: *18 May 2022*
Accepted: *23 June 2022*
Published: *05 August 2022*

Citation:
Wan Y, Yin Z, Huo Q, Zhou B and Wang H (2022) Weather Extremes Led to Large Variability in O_3 Pollution and Associated Premature Deaths in East of China. Front. Earth Sci. 10:947001. doi: 10.3389/feart.2022.947001

INTRODUCTION

Weather extremes have been occurring more frequently and are posing huge threats to human society, infrastructure, and the natural environment (Zhang Q. et al., 2017; Chen and Sun, 2021; Wang et al., 2022). The sequential flood-heatwave disasters in Japan during 2018 caused thousands of deaths in a single week (Kim et al., 2019). In 2021, an extreme precipitation event hit the Henan Province in China and resulted in more than 300 deaths and an economic loss of 17.7 billion dollars (World Meteorological Organization, 2021). In addition, the heatwave in the summer of 2003 led to

about 70,000 deaths in Europe (Robine et al., 2008). Furthermore, largest warming (particularly increases in maximum air temperature) and enhanced heavy precipitation were projected to occur in East of China in most of the coming decades (Zhou et al., 2014; Li et al., 2021; Qiao et al., 2021; Yang et al., 2021).

In recent years, ground-level ozone (O_3) has exceeded fine particulate matters to become a primary air pollutant that affects East of China (Wang et al., 2017; Fu et al., 2019). Meanwhile, the O_3 pollution in the summer was the most serious and would have caused a greater impact on human health. Because anthropogenic emissions remain approximately invariant on the daily time scale, the daily variability of O_3 concentration was mainly dominated by weather conditions (Han et al., 2020; Yin and Ma, 2020; Tang G. et al., 2021). Large concentrations of surface O_3 were observed to occur frequently with high air temperature, strong solar radiation, and low air humidity (Pu et al., 2017; Li et al., 2022). The relationships between high ozone days and weather extremes in the eastern U.S. have been analyzed, and Zhang H. et al. (2017) found that high ozone extremes were most sensitive to daily maximum air temperature and minimum relative humidity. Based on simulations of the Weather Research and Forecasting model coupled with Chemistry (WRF-Chem), the O_3 concentration in the U.S. associated with heat waves and atmospheric stagnation proved to be much larger than that under non-extreme weather conditions in the present and also in the future. Moreover, compound weather events had a larger impact than a single event because the temperature was noticeably higher and the wind speed was abnormally weaker (Zhang et al., 2018). However, quantitative studies on the impacts of weather extremes on O_3 pollution in East of China are far less than sufficient to the best of our knowledge.

Short-term exposure to peak levels of ozone can largely affect the lungs, the respiratory tract, and the eyes, and increase susceptibility to inhaled allergens. In the worst situation, it can even lead to premature mortalities (Chen et al., 2017; Orellano et al., 2020). Even when O_3 concentration was lower than the level influencing pulmonary function, the blood pressure of healthy adults could still increase and possibly affect their cardiovascular health (Day et al., 2017). Fenech et al. (2019) examined the meteorological drivers associated with two five-day episodes of air pollution in 2006 and found about 70 daily premature deaths because of short-term O_3 exposure across the UK. In China, the number of premature deaths attributed to short-term O_3 exposure increased by 9,100 from 2013 to 2018 in 74 key cities, and the national premature mortalities in 2018 were 6.32×10^4 (Wang et al., 2021). With every 10 $\mu g/m^3$ increase in ozone, the rates of respiratory deaths and non-accidental deaths respectively increased by 2.22 and 0.05% in highly O_3-polluted areas of China (Lei et al., 2019). As shown clearly from site observations, large daily variabilities of O_3 concentration existed (**Supplementary Figure S1**), and must have resulted in evident day-to-day differences in premature mortalities.

At present, few studies have been conducted to quantify to what extent weather extremes (e.g., hot, hot-dry, and heavy rain events) influence O_3 concentration and their associated health effects in East of China. Accurate quantification of large O_3 variability and premature deaths associated with different weather extremes could not only provide scientific support for O_3 pollution forecasts but also contribute to a comprehensive understanding of the health effects of weather extremes and air pollution.

DATA AND METHODS

Observations

The daily meteorological data with a horizontal resolution of 0.5° latitude by 0.625° longitude from 1981 to 2021 were derived from the Modern-Era Retrospective analysis for Research and Applications version 2 (MERRA2) dataset (Gelaro et al., 2017). The data included daily maximum temperature (Tmax), surface relative humidity, precipitation, planetary boundary layer (PBL) height, and downward solar radiation. In addition, the Tmax and precipitation data from the gridded daily observation dataset over China region (CN05.1) were downloaded to verify the impact of weather extremes on O_3. Surface O_3 concentrations have been observed and widely implemented since 2015 in China. The impact of weather extremes on O_3 during 2015–2021 were studied. Ground-level O_3 concentrations from 2015–2021 were downloaded from https://quotsoft.net/air/. The daily maximum 8-h average O_3 concentration (MDA8 O_3) was used to represent ozone pollution condition.

Weather Extremes

Following Lu et al. (2016) and Zhang et al. (2011), we used percentile-based indices to describe three types of weather extremes as follows:

(1) Warm temperature events indicated weather conditions with Tmax higher than the 90th percentile threshold during 1981–2010 (hereafter called TX90).
(2) Compound hot and dry air events indicated weather conditions with Tmax higher than the 90th percentile threshold and relative humidity smaller than 10th percentile during 1981–2010 (hereafter called TX90H10).
(3) Heavy precipitation events indicated weather conditions with daily precipitation higher than the 95th percentile threshold during 1981–2010 (hereafter called R95).

All other weather conditions, except for the aforementioned three weather extremes in the summer, were defined as other-condition events (hereafter called OCE).

GEOS-Chem Simulation

A global 3-D chemical transport model (GEOS-Chem) was implemented to simulate surface ozone concentration in East of China. The GEOS-Chem model includes fully coupled O_3-NOx-hydrocarbon and aerosol chemistry with more than 80 species and 300 reactions (Bey et al., 2001). The major physical-chemical processes used for the budget diagnostics included chemical reaction, transport, PBL mixing, convection, and their summary within the PBL (Liao et al., 2006).

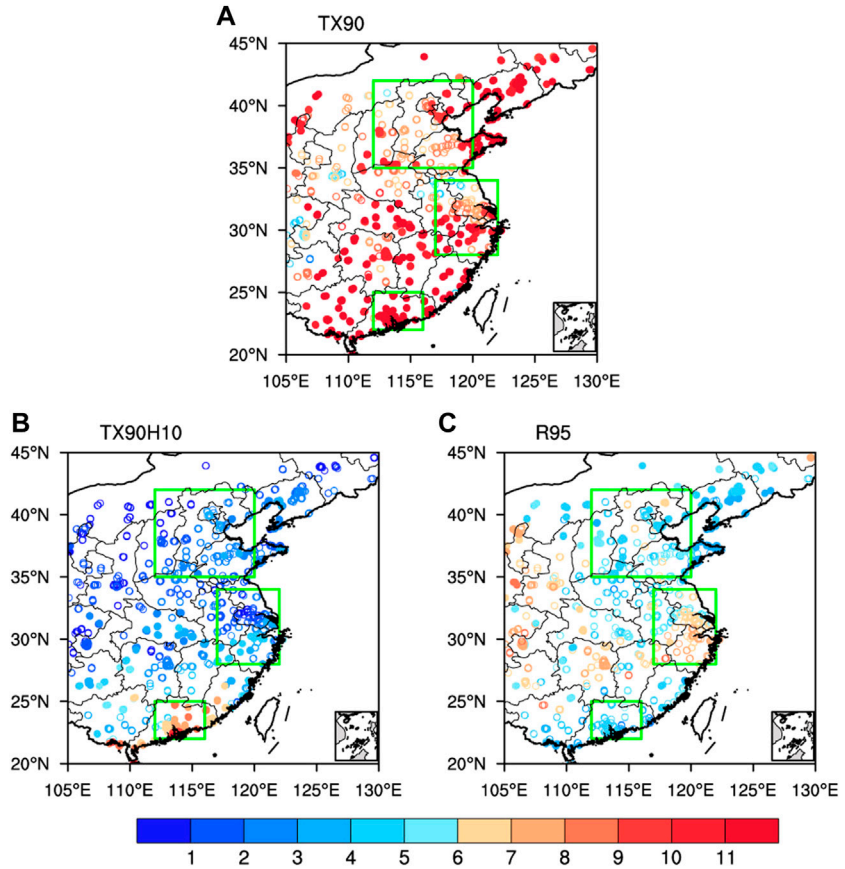

FIGURE 1 | Observed numbers of **(A)** warm temperature events (TX90), **(B)** compound hot and dry air events (TX90H10), and **(C)** heavy precipitation events (R95) in the summers of 2015–2021. The solid circles indicate that the mean extreme weather days during 2015–2021 were higher than that during 1981–2014. The green boxes represent the location of North China, Yangtze River Delta, and Pearl River Delta.

The GEOS-Chem model could well reproduce the daily-interannual variation and spatial distribution of surface ozone concentration (Yin and Ma, 2020; Ma and Yin, 2021). In this study, we also evaluated the performance of the GEOS-Chem model. Observations and model results during the summer of 2020 and extreme weather events during 2015–2021 were shown in **Supplementary Figure S1**. Statistical metrics such as correlation coefficient (Cor), normalized mean bias (NMB), and normal mean error (NME) were calculated. The spatial correlation coefficient between observations and the model simulation, respectively, is 0.87 and 0.82 during the summer of 2020 and extreme weather events, indicating that the simulated MDA8 O_3 agreed well with the observed distribution. Moreover, NMB was 0.49% (4.9%) and NME was 10.2% (11.2%) during the summer of 2020 (extreme weather events), indicating a good capability of the GEOS-Chem model for the simulation of MDA8 O_3 concentration both on a daily time scale and weather extremes. However, the GEOS-Chem model was short of reproduction when the MDA8 O_3 > 150 μg m^{-3}, i.e., underestimating the severest surface O_3 caused by weather extremes (**Supplementary Figure S1b**).

Premature Mortality

The Environmental Benefits Mapping and Analysis Program-Community Edition (BenMAP-CE) has been used to calculate the premature mortality due to short-term exposure to ozone pollution (Fenech et al., 2019). The formulas are as follows:

$$M = Y_0 P\left[\frac{(R-1)}{R}\right], \quad (1)$$

$$R = exp^{\beta(C-C_f)}, \quad (2)$$

where M is the all-cause premature mortality attributed to ambient ozone, Y_0 is the baseline mortality rate due to a specific disease category, and P is the population. The value of Y_0 from 2015 to 2019 could be obtained from the China Public Health and Family Planning Statistical Yearbook, and Y_0 for 2020–2021 was set to be the same as that in 2019. The gridded population data were downloaded from the Socioeconomic Data and Applications Center. R is the relative risk for a specific disease, which can be calculated by utilizing the integrated exposure response (IER) model. β is the estimated slope of the log-linear relationship between ozone concentration and all-cause mortality. Ye et al. (2020) conducted a meta-analysis of

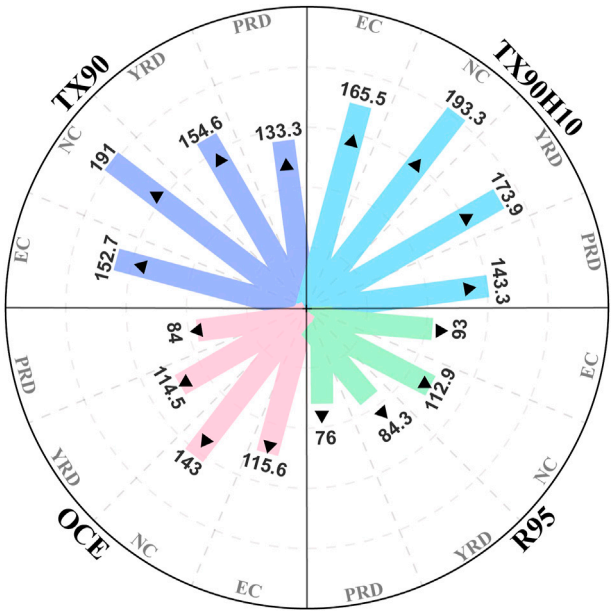

FIGURE 2 | Area-averaged MDA8 O_3 concentrations (unit: μg m^{-3}) corresponding to TX90, TX90H10, R95, and OCE during the summers of 2015–2021 in East of China (EC), North China (NC), the Yangtze River Delta (YRD), and the Pearl River Delta (PRD). The numbers represent ozone concentrations. The results from GEOS-Chem simulations were denoted by solid triangles on the bars.

the associations between short-term ozone exposure and human mortality in China. Their result (β = 0.0003992) was used in the present study. C is the observed ozone concentration (unit: μg m^{-3}), and C_f is the theoretical minimum concentration is set to 70 μg m^{-3} (Wang et al., 2021).

LARGE O_3 VARIABILITIES DUE TO WEATHER EXTREMES

During the summers of 2015–2021, the occurrence frequencies of hot extreme and heavy rain (i.e., TX90 and R95) were higher than those during 1981–2014 in most of the stations in East of China (**Figures 1A,C**). There were 10.2 TX90 days per summer in East of China (8.3 in NC, 8.4 in YRD, and 15 days in PRD) during 2015–2021, while the number of R95 days was 5.1 per summer (5, 6.1, and 4 days in NC, YRD, and PRD, respectively). The mean of Tmax values accompanied with the occurrences of TX90 and R95 events were 37.3 and 28.9°C, respectively. The intensities of precipitation during TX90 and R95 were 0.4 and 34 mm/d, respectively. This result indicated significant differences in meteorological conditions (above 95% confidence level). Furthermore, the mean PBL heights on the days of TX90 and R95 were 585.7 m (12.7% higher than OCE) and 442.6 m (14.8% lower than OCE) and the surface incoming shortwave fluxes were 9.7×10^5 J m^{-2} (26% stronger than OCE) and 4.8×10^5 J m^{-2} (37.7% weaker than OCE), respectively (**Supplementary Figure S2**). As a compound extreme weather, TX90H10 represented the meteorological conditions with both hot temperature (mean Tmax = 37.5°C) and dry air (mean relative humidity = 29.4%). There were 2.8 TX90H10 days per summer in East of China (2.1, 2.2, and 7 days in NC, YRD, and PRD, respectively, as shown in **Figure 1B**). Hot temperature contributed to efficient photochemical reactions and natural precursor emissions (Pu et al., 2017). Dry air and strong solar radiation also helped to enhance photochemical reactions in the air (Zhang and Wang, 2016; Lu et al., 2019). Detected by tethered balloons, higher PBL height with stronger free convection condition were found to be beneficial for the aggravation of ozone pollution in China (Tang R. et al., 2021). The impacts of precipitation on surface O_3 were relatively complex. In addition to temperature reduction and cloud shading accompanied with precipitation process, heavy rain itself could remove the stock of O_3 in the air (Meleux et al., 2007). Therefore, large daily differences in weather conditions potentially resulted in large variabilities of surface O_3 concentration.

To quantify the impacts of weather extremes, O_3 concentrations under TX90, TX90H10, and OCE during the summers of 2015–2021 were composited. The values were 152.7 μg m^{-3}, 165.5 μg m^{-3}, and 115.6 μg m^{-3}, respectively, in East of China (**Figure 2**). That is, the hot extremes could increase O_3 concentration by 32.1% in East of China with respect to O_3 concentration under OCE conditions. When dry air was coexistent with hot temperature (i.e., compound extreme TX90H10), the anomalous percentage of O_3 concentration was raised to 43.2%. However, the mean O_3 concentration in R95 days was only 93 μg m^{-3}, indicating that the meteorological condition of heavy rain could reduce O_3 concentration by 19.6% (**Figure 2**). In general, the O_3-polluted condition corresponding to TX90 (TX90H10) was 51.7% (62.8%) worse than that corresponding to R95. In other words, weather extremes resulted in quite large variabilities of ground-level O_3 concentration. In addition to the aforementioned observational analysis, the GEOS-Chem model was also driven by weather extremes but with fixed anthropogenic emissions to simulate O_3 concentration. Many previous studies pointed out that numerical models had limited capability for the simulation of weather extremes and air pollution in response to the extremes (Zhang and Wang, 2016; Zhang et al., 2018; Zhang et al., 2020).

Underestimation of high concentrations of O_3, as shown in **Supplementary Figure S1B**, is one of the possible reasons that the GEOS-Chem model failed to simulate the large percentage change of MDA8 O_3 induced by weather extremes in East of China. Results of the present study indicate that, although the quantitative values simulated by the GEOS-Chem model were smaller, the significant influences of TX90, TX90H10, and R95 on O_3 concentration were well verified (**Figure 2**; **Supplementary Figure S3**). Similar analysis was also conducted for each individual year. The abnormal percentages of O_3 concentration remain steadily at around 30% under TX90, 40% under TX90H10, and −20% under R95 during the years of 2015–2021 (**Supplementary Figure S3**). These quasi-steady percentage changes would be helpful in forecasting O_3 pollution on daily to weekly time scales.

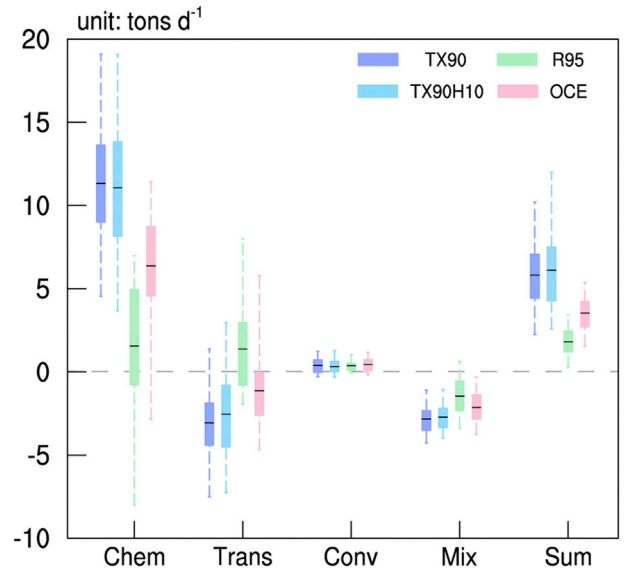

FIGURE 3 | Mass fluxes of ozone (units: tons d^{-1}) simulated by the GEOS-Chem corresponding to TX90, TX90H10, R95, and OCE during the summers of 2015–2021 in East of China. The boxplots showed the 25th percentile and 75th percentile and medians. The *x*-axis indicates the physicochemical processes: chemistry, transport, convection, mixing and their sum within the planetary boundary layer.

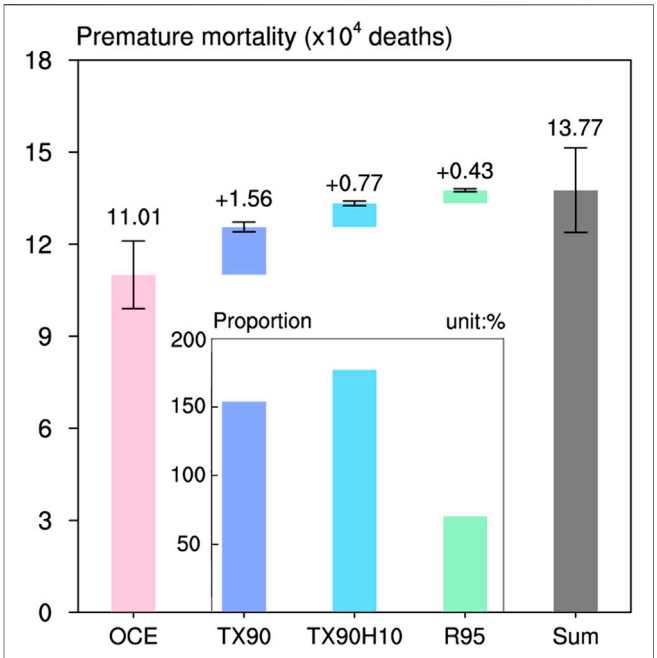

FIGURE 4 | Numbers of premature deaths in East of China corresponding to TX90, TX90H10, R95, OCE, and their accumulated total in the summers of 2015–2021. Vertical black bars represent the ±10% intervals. The proportions of area-averaged premature death during TX90, TX90H10, and R95 with respect to those during OCE were also displayed in the inner panel.

To explore the spatial heterogeneity of O_3 concentration, the impact of weather extremes in three severely O_3-polluted areas were analyzed. The summer-mean O_3 pollution was the severest in NC (145.7 μg m^{-3}), followed by that in YRD (115.9 μg m^{-3}) and PRD (91.2 μg m^{-3}). O_3 concentrations in all the three areas significantly exceeded the peak-season threshold of O_3 concentration (i.e., 60 μg m^{-3}) recommended by the World Health Organization (Zhu et al., 2022). Closely related to the regional O_3-polluted level, the O_3 concentrations under TX90 (TX90H10) were 191 (193.3), 154.6 (173.9), and 133.3 (143.3) μg m^{-3} in NC, YRD, and PRD during the summers of 2015–2021 (**Figure 2**). Under the meteorological condition of heavy rain, however, the O_3 concentrations were only 112.9, 84.3, and 76.0 μg m^{-3} in NC, YRD, and PRD, respectively (**Figure 2**). Unlike absolute O_3 concentration, the anomalous percentage of O_3 concentration under TX90 compared to that under OCE was about 34% both in NC and YRD, but it increased to 60% in PRD (**Supplementary Figure S4**). This result indicated that hot extremes could induce a larger percentage increase of O_3 concentration compared to that in normal conditions in PRD than in the other two regions. The O_3 anomalous percentage under R95 was −20.9, −25.8, and −6.1% in NC, YRD, and PRD, respectively, during the summers of 2015–2021. These regional differences were also evident in the GEOS-Chem simulations (**Supplementary Figure S4**), and they probably had close relationships with local climate conditions and anthropogenic emissions.

Associated physical-chemical processes in East of China were analyzed based on the GEOS-Chem simulations (**Figure 3**). During OCE days, the mass fluxes of chemistry, transport, convection, and PBL mixing were 6.36, −1.14, 0.44, and −2.14 Tons d^{-1}. In regard to chemical processes, high temperature could induce larger natural emissions of $BVOC_S$ and soil NO_X, accelerate photochemical reaction (Lu et al., 2019), and enhance thermal decomposition of peroxyacetyl nitrate (PAN) to provide additional NO_X (Doherty et al., 2013). Conversely, heavy rain with more cloud cover could reduce the photolysis rate of NO_2 (Lien and Hung, 2021). Meanwhile, the reduced solar radiation led to decreases in ozone production rate and natural emission (Jiang et al., 2021). Consequently, hot extremes led to almost double mass flux of chemistry (11.32 Tons d^{-1}). In contrast, the chemical flux was largely suppressed by heavy rainfall in East of China (1.55 Tons d^{-1}, **Figure 3**). The fluxes of transport and mixing processes heavily depended on wind anomalies, free convection conditions, ozone level and its concentration gradient (Jiang et al., 2021; Tang G. et al., 2021). During TX90 days, the atmospheric circulation could transport more O_3 pollutants under TX90 condition (−3.07 Tons d^{-1}). However, the mass flux of transport turned out to be positive (1.37 Tons d^{-1}) during heavy rainfall events, indicating that more O_3 pollutants remained in the air (**Figure 3**). Compared to that in the OCE days, the anomaly of PBL mixing flux was negative (−0.69 Tons d^{-1}) due to hot temperature, while that under the influence of heavy rain was positive (0.68 Tons d^{-1}). As shown in **Figure 3**, the quantity value of convection and its response to weather extremes were both tiny. In summary, when the weather was hot (hot-dry), 64.6% (72.5%) more O_3 pollutants were produced. However, the O_3 production was reduced by half during heavy precipitation events (**Figure 3**).

IMPACTS ON PREMATURE DEATHS

Weather extremes not only affected human health by basic meteorological factors (i.e., hot environment and rainfall intensity), but also modulated premature deaths associated with surface O_3 pollution. Short-term O_3 exposure could increase human premature deaths by elevating the risks of respiratory and cardiovascular diseases (Dong et al., 2016; Lei et al., 2019). To comprehensively understand the causes and consequences related to large variabilities of ozone pollution, the all-cause premature mortalities due to short-term O_3 exposure were calculated using the BenMAP-CE approach. The number of accumulated premature mortalities in the summers of 2015–2021 was 13.8×10^4 (90% CI: 12.4–15.1 $\times 10^4$) in East of China (**Figure 4**). Furthermore, the premature mortalities were greatly different between NC (5.6×10^4, 90% CI: 5.0–6.1 $\times 10^4$), YRD (2.7×10^4, 90% CI: 2.4–3.0 $\times 10^4$), and PRD (0.3×10^4, 90% CI: 0.29–0.35 $\times 10^4$). These obvious regional differences were mainly a result of local levels of O_3 pollution and resident population. For example, C_f was set to 70 $\mu g\, m^{-3}$, which did not frequently occur in PRD, and the premature mortalities were obviously lesser than in the other two regions (**Supplementary Figure S5**).

In addition to the spatial disparity, the aforementioned premature mortalities also varied greatly on a daily time scale. Hot temperature enlarged the daily death toll owing to short-term O_3 exposure to 153% of that under OCE conditions. Dry air would pile up another 23% increase in danger. However, heavy rain would decrease the O_3 concentration and thus cause fewer daily premature deaths, which was 70% under the OCE conditions. As shown in **Figure 4**, the premature mortalities due to O_3 exposure associated with TX90 (excluding TX90H10), TX90H10, and R95 in East of China were 1.56×10^4 (90% CI: 1.40–1.71 $\times 10^4$), 0.77×10^4 (90% CI: 0.69–0.84 $\times 10^4$), and 0.43×10^4 (90% CI: 0.38–0.47 $\times 10^4$) persons, respectively. Although the impacts of weather extremes on short-term O_3 exposure were significant, 79.7% of premature mortalities occurred without weather extremes because of a much larger OCE frequency (**Figure 4**). It is noted that while TX90 and R95 were not independent, there was only 1 day in seven summers in East of China when these two weather extremes happened simultaneously, which had little impact on total premature mortalities. The percentages were 82.3, 82.1, and 11.9% in NC, YRD, and PRD (**Supplementary Figure S5**), respectively. The small percentage in PRD was closely related to the relatively good air quality there, and indicated most remarkable impacts of weather extremes on premature mortalities due to short-term O_3 exposure.

CONCLUSION AND DISCUSSION

In this study, we quantified the impacts of weather extremes on surface O_3 pollution in East of China and their modulation of premature deaths caused by short-term O_3 exposure. Hot extremes (i.e., TX90 with Tmax = 37.3°C) could greatly enhance the mass fluxes of chemistry, which was favorable for production of more O_3 pollutants (**Figure 3**). Although more O_3 could be removed by transport and PBL mixing processes, the summary mass fluxes were still 64.6% higher than those under other-condition events (i.e., OCE). Conversely, heavy precipitation (i.e., R95 with rain intensity = 34 mm/d) and associated meteorological conditions could obviously reduce the production of O_3 pollutants (−48.7% lower than that in OCE days). Consequently, the MDA8 O_3 were 152.7 and 93 $\mu g\, m^{-3}$ in East of China under TX90 and R95 conditions, respectively, which were 32.1% higher and 19.6% lower than their mean values in OCE days. The compound hot-dry extreme could result in a larger O_3 concentration that is 43.2% higher than that under the OCE conditions (**Figure 2**). Furthermore, the impacts of weather extremes on O_3 variability were geographically inhomogeneous. That is, a hot environment could lead to a larger deviation of O_3 concentration in PRD than in the other two regions, while the influence of heavy rainfall on O_3 concentration was the weakest in PRD. In addition to observational analysis, GEOS-Chem simulations were also conducted to verify the large variability in O_3 pollution driven by weather extremes. To enhance the reliability of the conclusion, the CN05.1 dataset was also employed to explore the impact of weather extremes on O_3 concentration. As shown in **Supplementary Figure S6**, identical results were obtained.

The health benefits of short-term O_3 exposure were also evaluated under different weather conditions. It is found that hot extremes increased the daily death toll to 153% of that under other-condition events. In contrast, the daily death toll decreased to 70% of that under other-condition events by heavy precipitation. The premature mortalities due to short-term O_3 exposure respectively associated with TX90 (excluding TX90H10), TX90H10, and R95 were 1.56×10^4 (90% CI: 1.40–1.71 $\times 10^4$), 0.77×10^4 (90% CI: 0.69–0.84 $\times 10^4$), and 0.43×10^4 (90% CI: 0.38–0.47 $\times 10^4$) persons in East of China (**Figure 4**). However, these results about premature mortality were preliminarily estimated by an idealized tool named BenMAP-CE, and they did not exactly correspond to the actual mortalities. It is imperative to check the relationships based on clinical cases and analyze the associated mechanisms. Furthermore, the weather extremes could also affect human health and lead to premature mortality by the meteorological conditions without O_3 pollution. Therefore, it is emergent to distinguish the health effects between weather extremes themselves and the associated O_3 extremes. More importantly, the new findings of the present study provides a more comprehensive understanding of health effects of weather extremes and air pollution.

Nowadays, daily to weekly forecasts of weather and air quality to a great extent depends on numerical models. It is widely known that weather models still have limited capability for forecasting weather extremes; that is, obvious biases exist in the numerical prediction (Huang and Ding, 2021). In this study, we find that the atmospheric chemical model failed to simulate the large percentage change of MDA8 O_3 induced by weather extremes in East of China, which implies the

imperative necessity to improve model performance for the simulation of extreme events by both numerical weather models and atmospheric chemical models. In addition, the mechanisms of how a specific meteorological element influenced the atmospheric physical-chemical processes (particularly fluxes of transport and PBL mixing) were still unclear and needed further studies. The observed quasi-steady changes of MDA8 O_3 concentration influenced by weather extremes had the potential to promote daily to weekly forecasts and further support short-term control measures, such as limitations on industrial and traffic emissions.

DATA AVAILABILITY STATEMENT

The original contributions presented in the study are included in the article/**Supplementary Material**; further inquiries can be directed to the corresponding author.

AUTHOR CONTRIBUTIONS

HW and BZ designed and supported this research. ZY and YW performed statistical and numerical studies. QH participated in analysis of health benefits. ZY prepared the manuscript with contributions from all co-authors.

FUNDING

This research is supported by the National Natural Science Foundation of China (No. 42088101).

SUPPLEMENTARY MATERIAL

The Supplementary Material for this article can be found online at: https://www.frontiersin.org/articles/10.3389/feart.2022.947001/full#supplementary-material

REFERENCES

Bey, I., Jacob, D. J., Yantosca, R. M., Logan, J. A., Field, B. D., Fiore, A. M., et al. (2001). Global Modeling of Tropospheric Chemistry with Assimilated Meteorology: Model Description and Evaluation. *J. Geophys. Res.* 106, 23073–23095. doi:10.1029/2001jd000807

Chen, H., and Sun, J. (2021). Anthropogenic Influence Has Increased Climate Extreme Occurrence over China. *Sci. Bull.* 66, 749–752. doi:10.1016/j.scib.2020.12.001

Chen, K., Zhou, L., Chen, X., Bi, J., and Kinney, P. L. (2017). Acute Effect of Ozone Exposure on Daily Mortality in Seven Cities of Jiangsu Province, China: No Clear Evidence for Threshold. *Environ. Res.* 155, 235–241. doi:10.1016/j.envres.2017.02.009

Day, D. B., Xiang, J., Mo, J., Li, F., Chung, M., Gong, J., et al. (2017). Association of Ozone Exposure with Cardiorespiratory Pathophysiologic Mechanisms in Healthy Adults. *JAMA Intern Med.* 177, 1344–1353. doi:10.1001/jamainternmed.2017.2842

Doherty, R. M., Wild, O., Shindell, D. T., Zeng, G., MacKenzie, I. A., Collins, W. J., et al. (2013). Impacts of Climate Change on Surface Ozone and Intercontinental Ozone Pollution: A Multi-Model Study. *J. Geophys. Res. Atmos.* 118, 3744–3763. doi:10.1002/jgrd.50266

Dong, J. Y., Liu, X. R., Zhang, B. Z., Wang, J. Y., and Shang, K. Z. (2016). Meta-analysis of Association between Short-Term Ozone Exposure and Population Mortality in China. *Acta Sci. Circums* 36, 1477–1485. doi:10.13671/j.hjkxxb.2015.0555

Fenech, S., Doherty, R. M., Heaviside, C., Macintyre, H. L., O'Connor, F. M., Vardoulakis, S., et al. (2019). Meteorological Drivers and Mortality Associated with O3 and PM2.5 Air Pollution Episodes in the UK in 2006. *Atmos. Environ.* 213, 699–710. doi:10.1016/j.atmosenv.2019.06.030

Fu, Y., Liao, H., and Yang, Y. (2019). Interannual and Decadal Changes in Tropospheric Ozone in China and the Associated Chemistry-Climate Interactions: A Review. *Adv. Atmos. Sci.* 36, 975–993. doi:10.1007/s00376-019-8216-9

Gelaro, R., McCarty, W., Suárez, M. J., Todling, R., Molod, A., Takacs, L., et al. (2017). The Modern-Era Retrospective Analysis for Research and Applications, Version 2 (MERRA-2). *J. Clim.* 30, 5419–5454. doi:10.1175/jcli-d-16-0758.1

Han, H., Liu, J., Shu, L., Wang, T., and Yuan, H. (2020). Local and Synoptic Meteorological Influences on Daily Variability in Summertime Surface Ozone in Eastern China. *Atmos. Chem. Phys.* 20, 203–222. doi:10.5194/acp-20-203-2020

Huang, X., and Ding, A. (2021). Aerosol as a Critical Factor Causing Forecast Biases of Air Temperature in Global Numerical Weather Prediction Models. *Sci. Bull.* 66, 1917–1924. doi:10.1016/j.scib.2021.05.009

Jiang, Z., Li, J., Lu, X., Gong, C., Zhang, L., and Liao, H. (2021). Impact of Western Pacific Subtropical High on Ozone Pollution over Eastern China. *Atmos. Chem. Phys.* 21, 2601–2613. doi:10.5194/acp-21-2601-2021

Kim, H., Madakumbura, G. D., Wang, S. Y., Shiogama, H., Fischer, E. M., Utsumi, N., et al. (2019). Flood and Heatwave in Japan 2018 and Future Increase of Consecutive Compound Risk in a Warmer World. *AGU Fall Meet. Abstr.* GC53C–07. . Available at: https://agu.confex.com/agu/fm19/meetingapp.cgi/Paper/630667.

Lei, R., Zhu, F., Cheng, H., Liu, J., Shen, C., Zhang, C., et al. (2019). Short-term Effect of PM2.5/O3 on Non-accidental and Respiratory Deaths in Highly Polluted Area of China. *Atmos. Pollut. Res.* 10, 1412–1419. doi:10.1016/j.apr.2019.03.013

Li, C., Zwiers, F., Zhang, X., Li, G., Sun, Y., and Wehner, M. (2021). Changes in Annual Extremes of Daily Temperature and Precipitation in CMIP6 Models. *J. Clim.* 34, 3441–3460. doi:10.1175/jcli-d-19-1013.1

Li, M., Yang, Y., Wang, P., Ji, D., and Liao, H. (2022). Impacts of Strong El Niño on Summertime Near-Surface Ozone over China. *Atmos. Ocean. Sci. Lett.* 15, 100193. doi:10.1016/j.aosl.2022.100193

Liao, H., Chen, W.-T., and Seinfeld, J. H. (2006). Role of Climate Change in Global Predictions of Future Tropospheric Ozone and Aerosols. *J. Geophys. Res.* 111, D12304. doi:10.1029/2005jd006852

Lien, J., and Hung, H.-M. (2021). The Contribution of Transport and Chemical Processes on Coastal Ozone and Emission Control Strategies to Reduce Ozone. *Heliyon* 7, e08210. doi:10.1016/j.heliyon.2021.e08210

Lu, C., Sun, Y., Wan, H., Zhang, X., and Yin, H. (2016). Anthropogenic Influence on the Frequency of Extreme Temperatures in China. *Geophys. Res. Lett.* 43, 6511–6518. doi:10.1002/2016gl069296

Lu, X., Zhang, L., Chen, Y., Zhou, M., Zheng, B., Li, K., et al. (2019). Exploring 2016-2017 Surface Ozone Pollution over China: Source Contributions and Meteorological Influences. *Atmos. Chem. Phys.* 19, 8339–8361. doi:10.5194/acp-19-8339-2019

Ma, X., and Yin, Z. (2021). Dipole Pattern of Summer Ozone Pollution in the East of China and its Connection with Climate Variability. *Atmos. Chem. Phys.* 21, 16349–16361. doi:10.5194/acp-21-16349-2021

Meleux, F., Solmon, F., and Giorgi, F. (2007). Increase in Summer European Ozone Amounts Due to Climate Change. *Atmos. Environ.* 41, 7577–7587. doi:10.1016/j.atmosenv.2007.05.048

Orellano, P., Reynoso, J., Quaranta, N., Bardach, A., and Ciapponi, A. (2020). Short-term Exposure to Particulate Matter (PM10 and PM2.5), Nitrogen Dioxide (NO2), and Ozone (O3) and All-Cause and Cause-specific Mortality: Systematic Review and Meta-Analysis. *Environ. Int.* 142, 105876. doi:10.1016/j.envint.2020.105876

Pu, X., Wang, T. J., Huang, X., Melas, D., Zanis, P., Papanastasiou, D. K., et al. (2017). Enhanced Surface Ozone during the Heat Wave of 2013 in Yangtze River Delta Region, China. *Sci. Total Environ.* 603-604, 807–816. doi:10.1016/j.scitotenv.2017.03.056

Qiao, S. B., Chen, D., Wang, B., Cheung, H. N., Liu, F., Cheng, J. B., et al. (2021). The Longest 2020 Meiyu Season over the Past 60 Years: Subseasonal Perspective and its Predictions. *Geophys Res. Lett.* 48, e2021GL093596. doi:10.1029/2021gl093596

Robine, J.-M., Cheung, S. L. K., Le Roy, S., Van Oyen, H., Griffiths, C., Michel, J.-P., et al. (2008). Death Toll Exceeded 70,000 in Europe during the Summer of 2003. *Comptes Rendus Biol.* 331, 171–178. doi:10.1016/j.crvi.2007.12.001

Tang, G., Liu, Y., Huang, X., Wang, Y., Hu, B., Zhang, Y., et al. (2021). Aggravated Ozone Pollution in the Strong Free Convection Boundary Layer. *Sci. Total Environ.* 788, 147740. doi:10.1016/j.scitotenv.2021.147740

Tang, R., Huang, X., Zhou, D., Wang, H., Xu, J., and Ding, A. (2021). Global Air Quality Change during the COVID-19 Pandemic: Regionally Different Ozone Pollution Responses COVID-19. *Atmos. Ocean. Sci. Lett.* 14, 100015. doi:10.1016/j.aosl.2020.100015

Wang, F., Qiu, X., Cao, J., Peng, L., Zhang, N., Yan, Y., et al. (2021). Policy-driven Changes in the Health Risk of PM2.5 and O3 Exposure in China during 2013-2018. *Sci. Total Environ.* 757, 143775. doi:10.1016/j.scitotenv.2020.143775

Wang, H., Dai, Y., Yang, S., Li, T., Luo, J., Sun, B., et al. (2022). Predicting Climate Anomalies: A Real Challenge. *Atmos. Ocean. Sci. Lett.* 15, 100115. doi:10.1016/j.aosl.2021.100115

Wang, T., Xue, L., Brimblecombe, P., Lam, Y. F., Li, L., and Zhang, L. (2017). Ozone Pollution in China: A Review of Concentrations, Meteorological Influences, Chemical Precursors, and Effects. *Sci. Total Environ.* 575, 1582–1596. doi:10.1016/j.scitotenv.2016.10.081

World Meteorological Organization (WMO) (2021). State of the Climate in 2021: Extreme Events and Major Impacts. Available at: https://public.wmo.int/en/media/press-release/state-of-climate-2021-extreme-events-and-major-impacts.

Yang, J., Zhou, M., Ren, Z., Li, M., Wang, B., Liu, D. L., et al. (2021). Projecting Heat-Related Excess Mortality under Climate Change Scenarios in China. *Nat. Commun.* 12, 1039. doi:10.1038/s41467-021-21305-1

Ye, W. P., Liu, M. M., and Bi, J. (2020). Meta-analysis of the Associations between Short-Term Ozone Exposure and Human Mortality in China. *Acta Sci. Circumst. (in Chin.* 40, 2644–2651.

Yin, Z., and Ma, X. (2020). Meteorological Conditions Contributed to Changes in Dominant Patterns of Summer Ozone Pollution in Eastern China. *Environ. Res. Lett.* 15, 124062. doi:10.1088/1748-9326/abc915

Zhang, H., Wang, Y., Park, T.-W., and Deng, Y. (2017). Quantifying the Relationship between Extreme Air Pollution Events and Extreme Weather Events. *Atmos. Res.* 188, 64–79. doi:10.1016/j.atmosres.2016.11.010

Zhang, J., Gao, Y., Luo, K., Leung, L. R., Zhang, Y., Wang, K., et al. (2018). Impacts of Compound Extreme Weather Events on Ozone in the Present and Future. *Atmos. Chem. Phys.* 18, 9861–9877. doi:10.5194/acp-18-9861-2018

Zhang, Q., Zheng, Y., Singh, V. P., Luo, M., and Xie, Z. (2017). Summer Extreme Precipitation in Eastern China: Mechanisms and Impacts. *J. Geophys. Res. Atmos.* 122, 2766–2778. doi:10.1002/2016jd025913

Zhang, X., Alexander, L., Hegerl, G. C., Jones, P., Tank, A. K., Peterson, T. C., et al. (2011). Indices for Monitoring Changes in Extremes Based on Daily Temperature and Precipitation Data. *WIREs Clim. Change* 2, 851–870. doi:10.1002/wcc.147

Zhang, Y., and Wang, Y. (2016). Climate-driven Ground-Level Ozone Extreme in the Fall over the Southeast United States. *Proc. Natl. Acad. Sci. U.S.A.* 113, 10025–10030. doi:10.1073/pnas.1602563113

Zhang, Y., Yang, P., Gao, Y., Leung, R. L., and Bell, M. L. (2020). Health and Economic Impacts of Air Pollution Induced by Weather Extremes over the Continental U.S. *Environ. Int.* 143, 105921. doi:10.1016/j.envint.2020.105921

Zhou, B. T., Wen, Q. H., Xu, Y., Song, L. C., and Zhang, X. B. (2014). Projected Changes in Temperature and Precipitation Extremes in China by the CMIP5 Multimodel Ensembles. *J. Clim.* 27, 591–6611. doi:10.1175/jcli-d-13-00761.1

Zhu, T., Wan, W., Liu, J., Xue, T., Gong, J., and Zhang, S. (2022). Insights into the New WHO <italic>Global Air Quality Guidelines</italic>. *Chin. Sci. Bull.* 67, 697–706. doi:10.1360/tb-2021-1128

Conflict of Interest: The authors declare that the research was conducted in the absence of any commercial or financial relationships that could be construed as a potential conflict of interest.

Publisher's Note: All claims expressed in this article are solely those of the authors and do not necessarily represent those of their affiliated organizations, or those of the publisher, the editors, and the reviewers. Any product that may be evaluated in this article, or claim that may be made by its manufacturer, is not guaranteed or endorsed by the publisher.

frontiers | Frontiers in Earth Science

TYPE Original Research
PUBLISHED 30 August 2022
DOI 10.3389/feart.2022.980220

OPEN ACCESS

EDITED BY
Stephen Outten,
Nansen Environmental and Remote Sensing Center (NERSC), Norway

REVIEWED BY
Qingyuan Liu,
Chinese Academy of Meteorological Sciences, China
Nannan Qin,
Fudan University, China
Zhiqiang Lin,
Chengdu University of Information Technology, China

*CORRESPONDENCE
Jianjun Xu,
jxu@gdou.edu.cn
Mei Liang,
liangmei@gdou.edu.cn

SPECIALTY SECTION
This article was submitted to Atmospheric Science, a section of the journal Frontiers in Earth Science

RECEIVED 28 June 2022
ACCEPTED 05 August 2022
PUBLISHED 30 August 2022

CITATION
Huang P, Xu J and Liang M (2022), Decadal variation in the frequency of tropical cyclones originating in the South China Sea and migrating from the western North Pacific.
Front. Earth Sci. 10:980220.
doi: 10.3389/feart.2022.980220

Decadal variation in the frequency of tropical cyclones originating in the South China Sea and migrating from the western North Pacific

Peilan Huang[1,2,3,4], Jianjun Xu[1,5,4]* and Mei Liang[1,2,3,4]*

[1]South China Sea Institute of Marine Meteorology, Guangdong Ocean University, Zhanjiang, China, [2]College of Ocean and Meteorology, Guangdong Ocean University, Zhanjiang, China, [3]CMA-GDOU Joint Laboratory for Marine Meteorology, Zhanjiang, China, [4]Key Laboratory of Climate, Resources and Environment in Continental Shelf and Deep Sea of Department of Education of Guangdong Province, Guangdong Ocean University, Zhanjiang, China, [5]Shenzhen Institute of Guangdong Ocean University, Shenzhen, China

A decadal variation in the frequency of tropical cyclones (TCs) that reached their lifetime maximum intensity (LMI) in the South China Sea (SCS; 5°N-25°N, 107°E-121°E) from 1978 to 2020 was identified. TCs that generated and reached LMI in the SCS were named "local TCs," while those that generated in the western North Pacific (WNP) and reached LMI in the SCS were named "migratory TCs." A seesaw phenomenon in the frequencies of these two types of TCs was found before and after 1997. From 1978 to 1996, TC frequency was generally lower in local TCs but higher in migratory TCs. The opposite was true from 1997 to 2020. The main factors responsible for this "seesaw" phenomenon include changes in the genesis positions of TCs and the interdecadal variation of large-scale environmental flow patterns. From 1997 to 2020, during which the large-scale steering flow was favorable for local TCs, the monsoon trough over the WNP withdrew westward along with the warm pool and the subtropical high strengthened westward. Meanwhile, the sea surface temperature (SST) gradient between the equator and mid-latitudes decreased and the north wind weakened near 120°E. Easterly winds were strengthened in the equatorial region, which led to an abnormal anticyclone and the divergence of water vapor in the WNP. In contrast, the SST of the SCS, an internal sea, increased significantly. Under local atmosphere-ocean interaction, abnormal cyclonic circulation appeared in the SCS, which led to intensified convergence and intensified wet convection. Changes in the environmental fields in the WNP and SCS are the main reasons for the seesaw phenomenon observed in these two types of TCs.

KEYWORDS

tropical cyclones, lifetime maximum intensity, interdecadal variation, seesaw, South China Sea

1 Introduction

The South China Sea (SCS), located south of mainland China, lies in the western part of the Pacific Ocean. It is one of the locations where tropical cyclones (TCs) form (Chen, 1990) and is influenced by westward-shifting TCs generated in the western North Pacific (WNP). Approximately 67% of rapid intensification of TCs occurred in the SCS, which is much higher than that in the East China Sea (23%) and Yellow Sea (10%) (Liu and Rong, 1995; Yan, 1996; Lin et al., 2006). TCs in the SCS have caused severe damage to South China and Vietnam owing to their rapid intensification, variable paths, and complex rainstorm patterns (Chen et al., 2004; Zhang et al., 2009; Duan et al., 2014; Wen et al., 2019; Tran-Quang et al., 2020). There are obvious differences in climate characteristics of the SCS and WNP basins (Zhang, 2003). The WNP basin is vast and less influenced by the surrounding land and the upper ocean warm water is deeper than the SCS (Lin et al., 2008), leading to a higher upper ocean heat content (Goni and Trinanes, 2003; Lin et al., 2009). As a powerful large-scale circulation background factor for TCs genesis, the spatial scale and intensity of the monsoon troughs are often stronger in the WNP than in the SCS (Harr and Elsberry, 1995; Mao and Wu, 2010). A large difference exists between TCs over the SCS and the WNP. Approximately 76% of TCs over the WNP develop into typhoons or super typhoons, while TCs over the SCS which annual average number of typhoons or super typhoons accounted for 28.6% of the total number of TCs are much weaker (Yuan et al., 2007; Feng et al., 2013; Hao and Mao, 2015). Therefore, it is important to study the different characteristics of TCs between the SCS and WNP in a changing climate.

Previous studies on TC activity in the SCS and WNP have mainly focused on decadal timescales. Three suppressed TC frequency periods (1951–1960, 1973–1985, and 1995–2018) and two enhanced TC frequency periods (1961–1972 and 1986–1994) were found in the WNP (Yumoto and Matsuura, 2001; Liu and Chan, 2013). However, two inactive periods (1979–1993 and 2003–2010) and two active periods (1965–74 and 1995–2004) were identified in the SCS. These activities in the SCS might be due to changes in the surface sea temperature (SST) gradient between the Indian Ocean and the WNP and the intensity of the East Asian jet stream (Wang et al., 2012; Li and Zhou, 2014). Another study showed that the birthplace of TCs and vertical moisture advection dominated the interdecadal variation in TCs intensity over the SCS (Zheng and Wang, 2022). Previous studies have also found that the TC frequency across oceans appeared to show "seesaw" variability, which means the inverse phase change. Wang et al. (2022) identified a decadal variation in TCs genesis between the WNP and North Atlantic (NA) with a seesaw variability, which is proposed to be related to the contact teleconnection of the subtropical east-west triggered by the Atlantic Decadal Oscillation and causes the opposite changes of the environmental fields in the WNP and NA. A seesaw phenomenon was also observed in TC activities in North America and the Northeast Pacific (Elsner et al., 1999), caused by opposite changes in the large-scale conditions of these basins shaped by the El Nino-Southern Oscillation (ENSO), Atlantic Multidecadal Oscillation (AMO), and Atlantic Meridional Modes (Frank and Young, 2007; Wang and Lee, 2009; Patricola et al., 2017). Wang et al. (2020) proposed that opposite large-scale conditions in the NA and North Pacific are associated with reverse standing wave activity (tropical upper tropospheric trough) in both oceans. However, few studies have focused on the interdecadal comparison of TCs between the SCS and WNP. It is also unknown whether the frequencies of TCs in the WNP and SCS show a seesaw phenomenon.

Many studies have investigated the activities of TCs lifetime maximum intensity (LMI). The annual average LMI latitude of TCs above the tropical storm intensity increased significantly from 1960 to 2016 (Liu and Chan, 2019). They also found that a significant interdecadal variation was observed in strong TCs (category 4–5), that is, TCs LMI latitudes were higher in 1960–1969 and 1991–2011, but lower in 1970–1990 and 2012–2016. Song et al. (2018) studied standard deviation of LMI and found that the occurrence frequency of the strongest and weakest TCs around the world during 1999–2016 was greater than that during 1981–1998. Lu and Tang (2021) used a machine learning method to study the distribution of the LMI, which revealed that the circulation of high LMI is that lower latitude is embedded in the continuous band with high vorticity in the lower troposphere, and the circulation in the upper and lower troposphere is more dense. Recent studies have mainly focused on the characteristics of LMI in global regions or oceans, but few studies have focused on local small continental seas, such as the SCS.

The remainder of the paper is structured as follows: Section 2 presents the data and methods. Section 3 studies the decadal variation of the two types of TCs is studied and discusses the possible factors causing these changes. Finally, Section 4 presents the discussion and conclusions.

2 Data and methods

2.1 Data

Monthly average atmospheric circulation reanalysis data were provided by the US Center for Environmental Prediction (Kalnay et al., 1996), covering the period 1978–2020 with a horizontal resolution of 2.5° latitude × 2.5° longitude and nine layers from 1000 to 200 hPa in the vertical direction, including vertical velocity, potential height, specific humidity, and wind. Because of our TCs research range in the WNP and SCS, we used the International Best Track Archive for Climate Stewardship (IBTrACS) Version 04 data (Knapp et al., 2010), including the

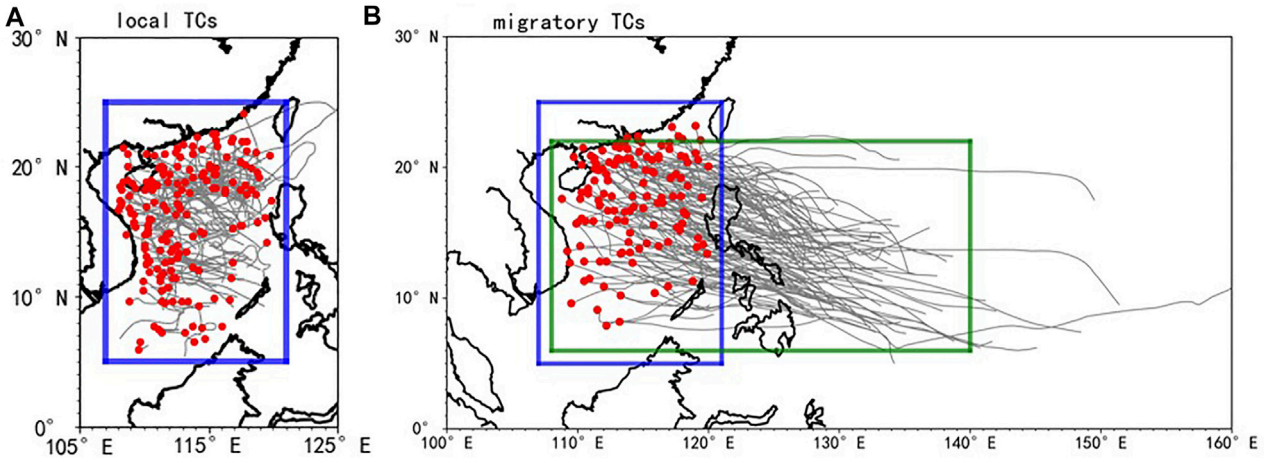

FIGURE 1
TCs Locations that reached their LMI (red dots) and the tracks from TCs genesis positions to their LMI location (gray lines) during 1978–2020 for **(A)** local TCs that generated and reached LMI in the SCS and **(B)** migratory TCs that generated in the WNP and reached LMI in the SCS. The blue boxes indicate the SCS region. Green box indicates the SCS and the WNP region. TCs data is from best-track dataset of JTWC during 1978–2020.

TC records from Joint Typhoon Warning Center (JTWC), Shanghai Typhoon Institute of China Meteorological Administration (CMA), and Hong Kong Observatory (HKO), etc. Monthly mean SST data covering 1978–2020 were obtained from the Hadley Center (Rayner et al., 2006), with a horizontal resolution of 1.0° latitude × 1.0° longitude.

2.2 Methods

One of the previous research metrics for TC is LMI, and LMI of TCs has been recommended as a steady indicator to study TCs, because its geographical location is comparatively insensitive to data uncertainties (Kossin et al., 2014, 2016; Moon et al., 2015, Moon et al., 2016; Zhan and Wang 2017; Song et al., 2018; Wang and Wu 2019; Zhao et al., 2022). This study follows the previous definition of LMI, in which TCs.

Reach maximum wind speed in their lifetime (Kossin et al., 2014, 2016; Song et al., 2018; Zhao et al., 2022). To better study the characteristics of TC LMI in the SCS (5°N-25°N, 107°E-121°E), we selected TCs that passed over the SCS and reached the maximum wind speeds in their lifetime.

The first point at which the intensity was ≥25 knots was defined as the TC genesis position. Two types of TCs enter the SCS: one is generated locally and the other is generated from the WNP and moves into the SCS. However, the intensity and genesis frequency of these two types of TCs differ (Chen, 1990; Yuan et al., 2007). To better reveal the decadal variations of these two types TCs, TCs that reach LMI in the SCS were divided into two groups: those that generated and reached LMI in the SCS were “local TCs” and those that generated in the WNP and reached LMI in the SCS were “migratory TCs.” The large-scale circulation fields, thermal and dynamic characteristics (Emanuel and Nolan, 2004) that reveal the causes of TC frequency seesaw, were respectively composited by the two types of TCs. The statistical test method used in this study was student’s t-test.

3 Results

3.1 A seesaw relationship

A total of 303 TCs reached the LMI in the SCS from 1978 to 2020, of which 173 were local TCs (accounting for 57.1% of total TCs reached the LMI in the SCS) and 130 were migratory TCs (accounting for 42.9% of total TCs reached the LMI in the SCS). As with all typhoons, the generation of local and migratory TCs is influenced by Coriolis forces (Gray, 1979), resulting in the location of TC generation being mainly concentrated north of 5°N. The local TCs generation positions were evenly distributed in the interior of the SCS. Note that most of the migratory TCs generated west of 140°E of the WNP (Figure 1). However, because TCs generation positions was not the focus of this study, no further investigation will be conducted. As shown in Figure 1, the prevailing tracks of local TCs prevailing tracks were variable, mainly consisting of northwest and northeast, while the majority of migratory TCs were westward into the SCS. Local TCs reached LMI mainly on the western and northern of the SCS while the locations where migratory TCs reached LMI were more evenly distributed. The reason why migratory TCs reached LMI were more evenly distributed was not the focus of this study.

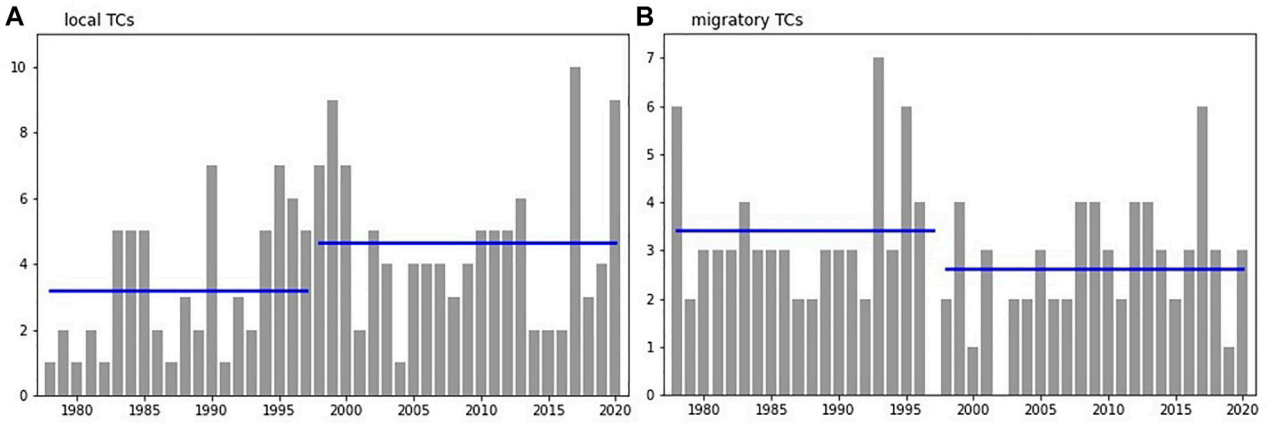

FIGURE 2
Annual frequency of **(A)** local TCs and **(B)** migratory TCs reaching LMI in the SCS region. The blue lines denote 1978–1996 and 1997–2020 average of the TCs frequency. TCs data is from best-track dataset of JTWC during 1978–2020.

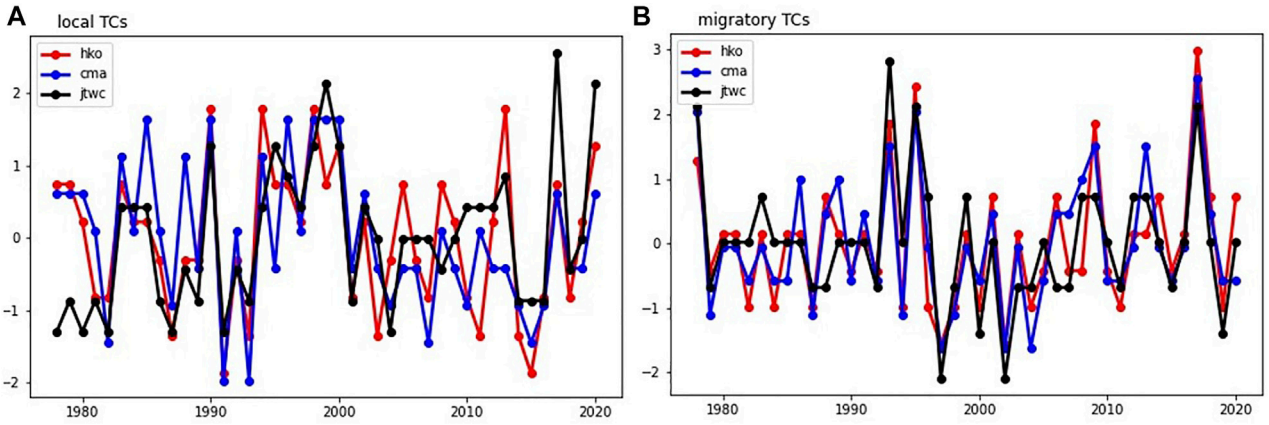

FIGURE 3
Annual standardized frequency of **(A)** local TCs and **(B)** migratory TCs that reaching LMI using different best-track dataset from the HKO, CMA, JTWC during 1978–2020.

From 1978 to 2020, the average frequency of local TCs (4.02 per year) was greater than that of migratory TCs (3.02 per year). The interdecadal variation of these two TC groups showed a seesaw phenomenon around 1997 (Figure 2). That is, the average frequency of local TCs increased significantly from 3.21 from 1978 to 1996 to 4.67 from 1997 to 2020 ($p<0.05$). In contrast, the average frequency of migratory TCs was 3.47 from 1978 to 1996 and decreased to 2.67 ($p<0.1$) from 1997 to 2020. Several datasets were used for verification to ensure the reliability of these observed seesaw phenomena. Standardized TC frequencies of the CMA, JTWC, and HKO that reached the LMI in the SCS were compared (Figure 3). The interannual variations and linear trends of different institutions were the similar from 1978 to 2020. To facilitate the analysis, JTWC data were adopted for further analysis.

Wang (2013) showed the seasonal variation characteristics of TCs genesis in the SCS using the genesis potential index (GPI) (Emanuel and Nolan, 2004), finding that the number of TCs in the SCS increases after May and peaks in August and September. Wang et al. (2007) found that, from 1948 to 2003, 157 TCs generated north of 12°N from May–September (southwest monsoon period), while 65 TCs generated south of 18°N from October–December (northeast monsoon period). According to our statistics, 303 TCs reached LMI in the SCS from 1978 to

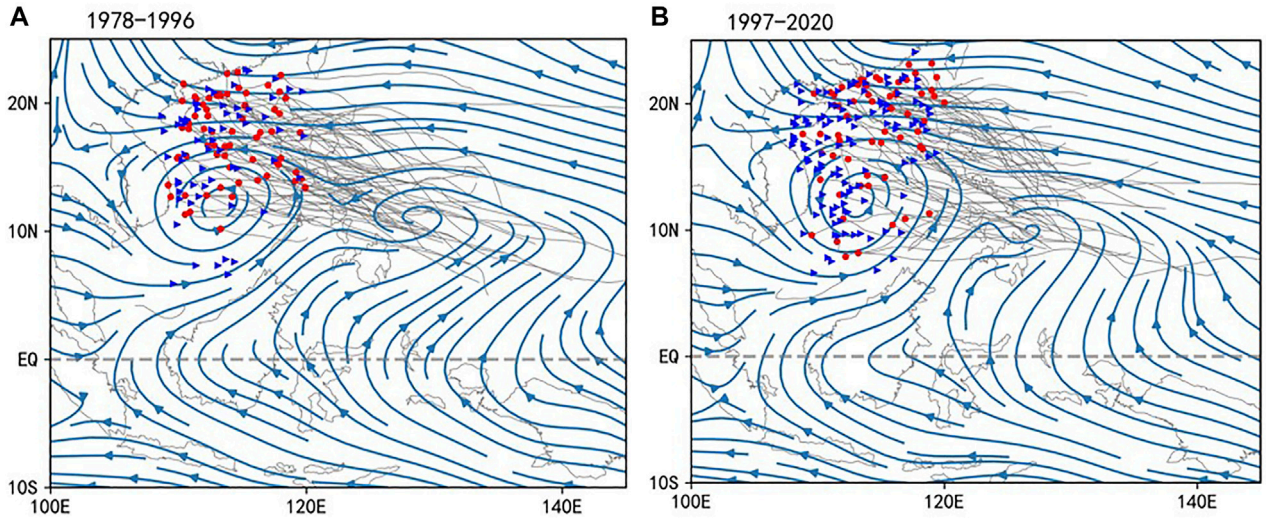

FIGURE 4
The streamline at 850-hPa and location of the LMI of local TCs (red dots) and migratory TCs (blue dots) for June–November during **(A)** 1978–1996 and **(B)** 1997–2020. The gray lines are TCs track from the genesis position to their LMI location.

2020, with 265 reaching LMI from June–November, accounting for 87.5% of the total. In addition, TC genesis was mainly concentrated from June–November, which is consistent with the conclusions of previous studies that TCs generally form in boreal summer and autumn in the SCS (Zhang et al., 2009; Wang, 2013).

Since TCs that reached the LMI in the SCS generally originated from June–November, the TC genesis circulation characteristics from June–November can represent most TCs. Therefore, to discuss the possible reasons for the seesaw relationship between these two groups of TCs frequencies around 1997, the changes in atmospheric circulation and the ocean environment in the SCS and WNP from June–November were analyzed synthetically.

3.2 Large-scale circulation variations responsible for TC frequency changes

TC activity in the WNP is closely related to the location of the monsoon trough (Wu et al., 2012). When the monsoon trough retreated westward, fewer TCs were formed in the southeastern part of the WNP; that is, TCs were more likely to occur in the northwest. To analyze the changes in the monsoon trough in June–November from 1978 to 1996 and 1997–2020, the average streamline distributions at 850 hPa during these two periods are shown in Figure 4. From 1978 to 1996, the SCS was dominated by cyclonic circulation and the WNP was occupied by a monsoon trough extending from the SCS to the east of 140°E with a northwest-southeast trend (Figure 4A). At the same time, the positions where local TCs and migratory TCs reached LMI were mainly located in the west of the SCS. At the same time, these locations were relatively concentrated in the north of 10°N and the locations of migratory TCs were generally westward into the SCS. From 1997 to 2020, the cyclonic circulation over the SCS was strengthened and the monsoon trough in the WNP was weakened and retreated westward to the west of 140°E (Figure 4B). Under the evolution of these large-scale circulation variations, more local TCs appeared in the SCS and the LMI locations were more scattered. Note also that the genesis and LMI locations of migratory TCs were more westward with a more dispersed track.

From 1978 to 1996, the monsoon trough lied east-south over the WNP, local TCs reached LMI in the west of the SCS, and migratory TCs reached LMI east. Migratory TCs had a basically northwest path and were more concentrated north of 10°N (Figure 4A). From 1997 to 2020, the monsoon trough in the SCS was strengthened and the monsoon trough in the WNP was weakened. In other words, the monsoon trough retracted, which led to the westward TCs generation point, increasing the TCs generated in the SCS and decreasing the TCs generated in the WNP (Figure 4B). The SCS was favorable for the formation and strengthening of TCs while the WNP was unfavorable for the early development of TCs. The paths of migratory TCs were also northwestern but were relatively scattered and located north of 7°N. There was little difference between the two types of TCs in terms of the location where they reached LMI.

The western Pacific subtropical high (WPSH) is one of the main factors affecting TC genesis position and path (Wang et al., 2017). Since the easterly wave located between the WPSH and

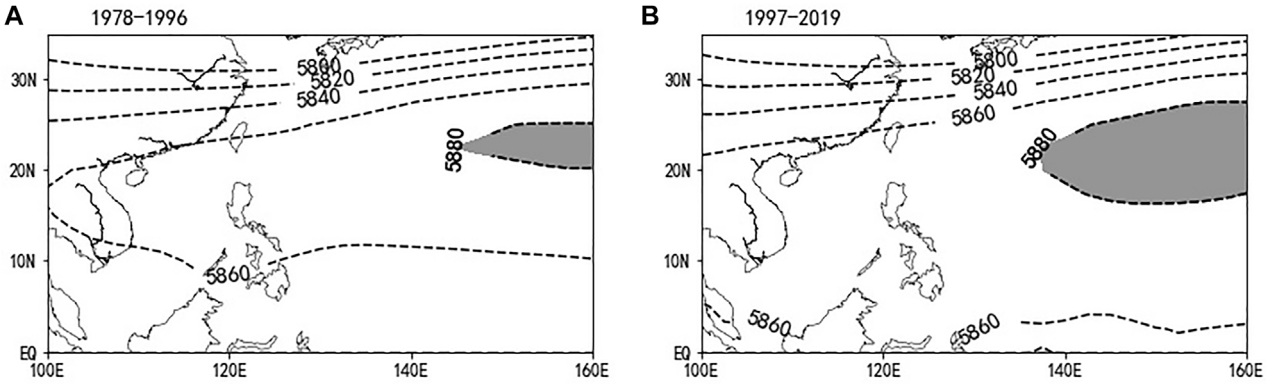

FIGURE 5
The 500-hPa geopotential height (unit: m) averaged for June–November during **(A)** 1978–1996 and **(B)** 1997–2020. The gray areas indicate the Western Pacific subtropical high region.

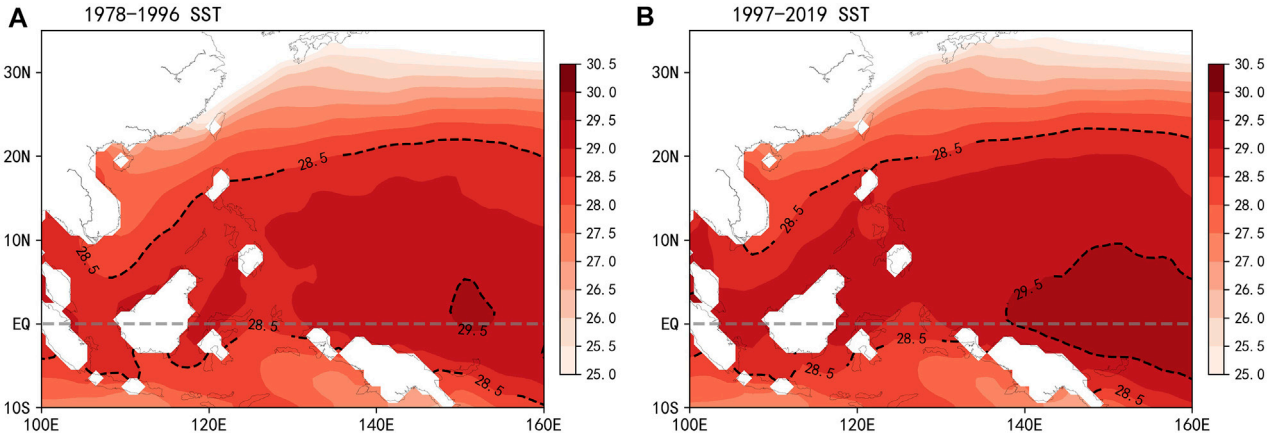

FIGURE 6
The sea surface temperature (shading, units: °C) and the 28.5°C and 29.5°C isothermal lines (black dashed lines) of the warm pool SST averaged for the June–November during **(A)** 1978–1996 and **(B)** 1997–2020.

equator is one of the main flow patterns affecting TC genesis, the intensity and north-south position of the WPSH may influence TCs genesis. The average geopotential heights at 500 hPa from June–November from 1978 to 1996 and 1997–2020 are shown in Figures 5A,B, respectively. From 1978 to 1996, the WPSH was located at approximately 20°N-25°N and 145°N-165°N with a rather small range, while it expanded westward and southward from 1997 to 2020. This may be one of the reasons that TCs genesis was more westward from 1997 to 2020. As a result, more TCs were likely to originate in the SCS and less in the WNP from 1997 to 2020 (Figure 4).

Chen and Huang (2006) studied the influence of the western Pacific warm pool thermal state on TCs over the WNP and indicated that there were fewer TCs in WNP and more TCs in SCS in warm years. Figures 6A,B show the distributions of the average SST from June–November from 1978 to 1996 and 1997–2020, respectively. Region of SST exceeding 28.5°C are conducive to TC genesis and development. From 1978 to 1996, the 28.5°C line was basically to the south of 10°N in the SCS and 18°N in the WNP (Figure 6A). From 1997 to 2020, the SST increased significantly, with the Region of 28.5°C SST expanding to 15°N in the SCS and the range of 29.5°C significantly from 5°N expanding to 10°N in the WNP (Figure 6B). As a result, it is expected that fewer TCs would be generated in the southeast quadrant of the WNP from 1997 to 2020, which is consistent with the results of Chen and Huang (2006).

The Walker circulation, a vast zonal overturning atmospheric circulation across the tropical Pacific Ocean, is

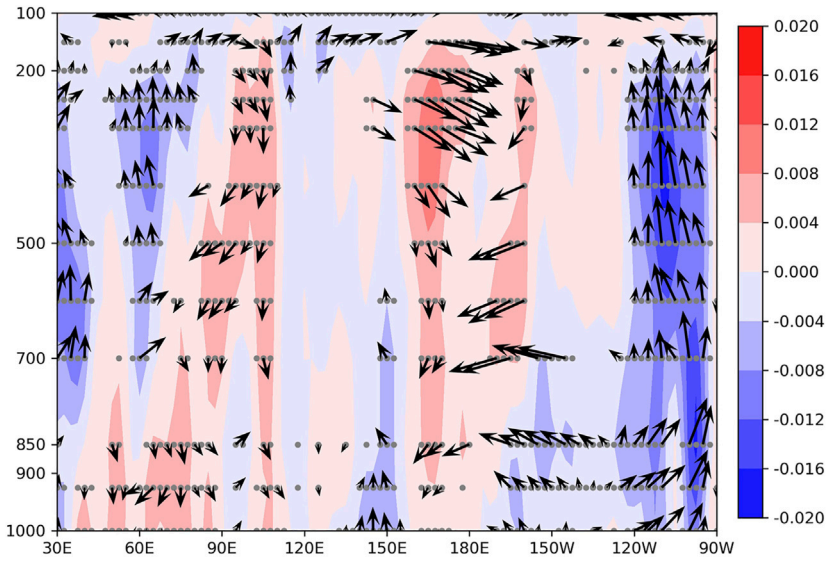

FIGURE 7
Composite anomalies of mean vertical velocities (shading, units: Pascal s^{-1}) profile between 10°N and 25°N for the June–November over the Indo-Pacific Ocean. Arrows indicate zonal velocities (units: m s^{-1}) and vertical velocities (units: 100 Pascal s^{-1}). Indian Ocean region [60°E-100°E], Northwest Pacific Ocean region [121°E-160°E], South China Sea region [107°E-121°E]. The stippled areas indicate the values are statistically significant at the 90% confidence level.

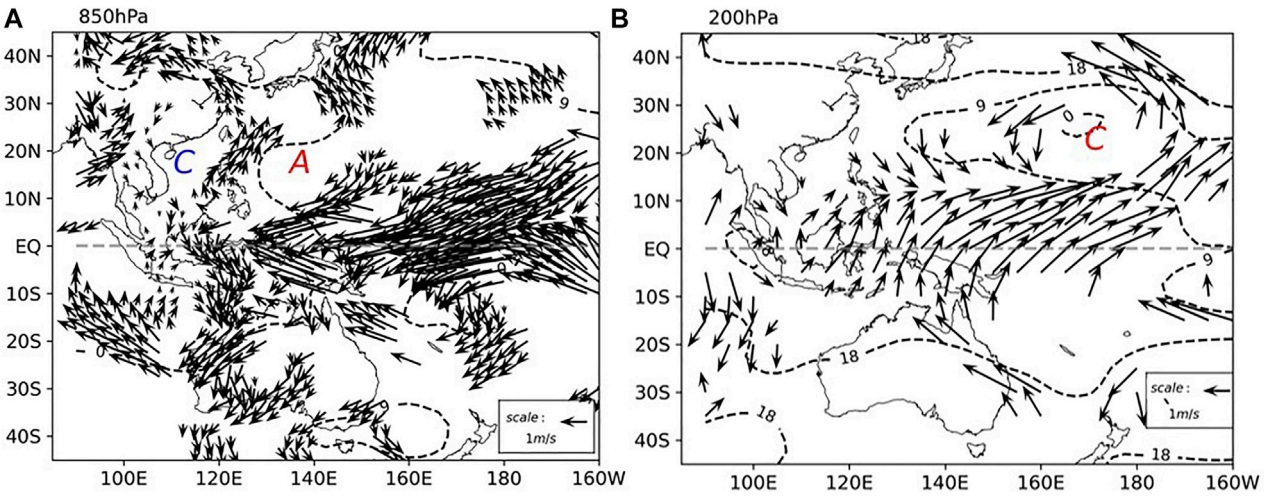

FIGURE 8
Composite anomalies of wind (vectors, units: m s^{-1}) and geopotential height (black dotted line, unit: m) at **(A)** 850-hPa and **(B)** 200-hPa. The arrow areas indicate the values are statistically significant at the 90% confidence level. The letter A and C indicates for anticyclonic and cyclonic circulation, respectively.

named after Sir Gilbert Walker and is one of the most important components of the global climate system. The rising branch of the Walker circulation over the WNP affects TC genesis and intensification (Chan, 1985). Because the TC genesis positions and moving tracks were mainly concentrated between 10 and 25°N, to observe the changes in Walker circulation in these two periods, the zonal mean vertical velocity difference in the 10°N-25°N region between the two periods was determined (Figure 7).

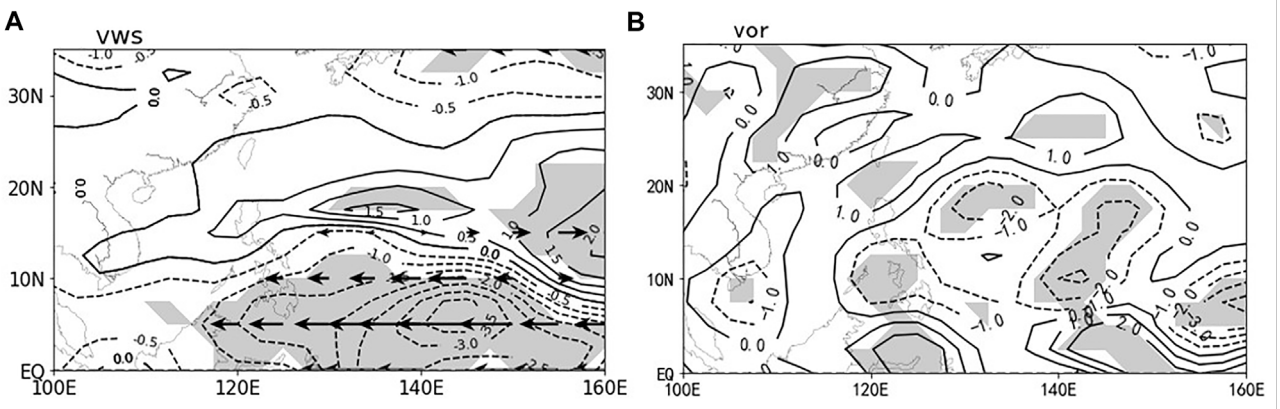

FIGURE 9
Composite anomalies of **(A)** vertical wind shear (vector, 200-hPa minus 850-hPa, unit: m s^{-1}) and **(B)** relative vorticity (contour, unit: 10^6 m s^{-1}) at 850-hPa. The vectors and shaded areas only indicate the values are statistically significant at the 90% confidence level.

The walker circulation was found to be weaker from 1997 to 2020 and the Indian Ocean and WNP basins showed abnormal sinking at 100°E and between 150°E and 180°E, respectively. Meanwhile, the rising branch of the Walker circulation over the SCS and WNP was enhanced (110°E-150°E) because the two abnormal sinking branches forced the production of abnormal updrafts, which were conducive to TCs genesis over the SCS and western WNP. As a result, the genesis position of migratory TCs was mainly located to the west of 140°E, and few were found to the east of 140°E (Figure 4).

3.3 Dynamic features

Previous studies have shown that, in contrast to TCs generation in the Atlantic Ocean, dynamic conditions play a much larger role than thermal conditions in influencing TC generation in the WNP (Fu et al., 2012). Figure 8 shows the difference between the wind field and contour field from 1978 to 1996 and 1997–2020. In the lower 850 hPa, the SCS was a low-pressure anomaly and the WNP was a high-pressure anomaly. There was abnormal easterly convergence at the equator and a southerly wind anomaly appeared near 120°E. From 1997 to 2020, the SST gradient of the equatorial region and TC-generating region of the Philippines decreased significantly, which may be the main reason for the south wind anomaly. There was a southwest wind anomaly and a cyclonic circulation anomaly in the lower troposphere in the SCS, which were favorable for convergence. The anticyclonic anomaly over the WNP was not conducive to the formation and development of TCs. At 200 hPa, there was abnormally high pressure over the SCS and a southwest anomaly of the equatorial flow over the SCS. At the same time, there was a convergence of the westerly winds over the WNP, a low-pressure anomaly over the central Pacific, and a cyclonic circulation anomaly. In terms of the wind field, the low-level cyclonic circulation anomaly in the SCS was favorable for the generation of TCs. The lower troposphere layer in the WNP had abnormal anticyclonic circulation, and the convergence of the high troposphere layer was not conducive to the formation of TCs, indicating that the formation of TCs was favorable to the west. The variation in the wind field during the two periods may explain the increasing frequency of local TCs and decreasing frequency of migratory TCs.

From the perspective of dynamics, strong vertical wind shear is usually not conducive to the enhancement of TCs. Wei et al. (2018) found that westerly wind shear has a more significant impact on TCs than easterly wind shear. Figure 9A shows the difference in vertical wind shear between the two periods and a positive anomaly of significant vertical wind shear and westerly zonal wind shear in the generating area of TCs in the WNP, which was not conducive to the generation and development of TCs. However, the vertical wind shear of SCS region remains unchanged compared with the SCS, the WNP was more unfavorable to the generation and development of TCs, which led to a westward shift in the generation point of TCs, leading to an increase in the frequency of TCs generated in the SCS, while the frequency of TCs generated in the WNP decreased.

Previous studies have shown that environmental vorticity distribution can affect the intensification of TCs (Rappin et al., 2011; Wu et al., 2020). The relative vorticity difference between the two periods was plotted to analyze the relative vorticity distribution of the environmental field (Figure 9B). Figure 9B shows insignificant positive vorticity anomalies in the SCS, while the relative vorticity in the WNP decreased and was partially significant; that is, the SCS was conducive to the generation and

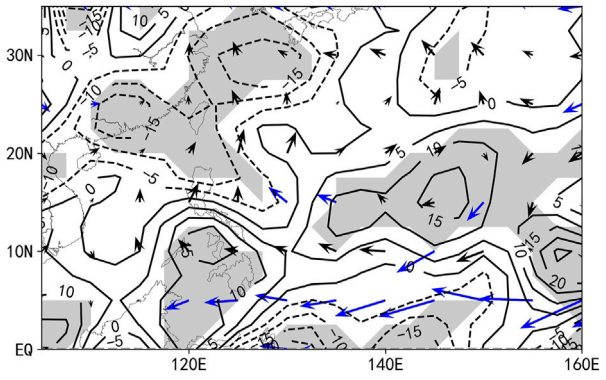

FIGURE 10
Composite anomalies of water vapor flux divergence (contour, unit: 10^{-5} kg m^{-2} s^{-1}) and water vapor flux (vectors, unit: 10^{2} kg m^{-1} s^{-1}). The shaded areas and blue vectors indicate the values are statistically significant at the 90% confidence level.

strengthening of TCs, whereas the WNP was unfavorable to the early development of TCs.

3.4 Thermodynamic features

From the perspective of thermodynamics, changes in SST, heat content of air-sea flux, and exchange coefficients significantly impact the intensification rate of TCs (Shen and Ginis, 2003; Gao and Chiu, 2010). According to Figure 6, SST increased from 1997 to 2020, increasing by 0.29°C in the WNP region, 0.32°C in the Indian Ocean region, and 0.41°C in the SCS region.

Ge et al. (2013) found that decreases in environmental humidity may inhibit the enhancement of TCs. From 1997 to 2020, the specific humidity increased in the SCS and WNP. The specific humidity increased more in the WNP (0.441) than in the SCS (0.316), indicating that specific humidity is not an important condition affecting TC generation.

Water vapor flux is a physical quantity that reflects water vapor transport and its value and direction can represent the size and source of water vapor transport in a region (Li et al., 2015; Li et al., 2018). Figure 10 shows the average divergence and difference in water vapor flux between 1000 and 500 hPa from June-November from 1978 to 1996 and 1997–2020. The TC generation area north of 10°N in the SCS region shows mid-low level moisture convergence and some areas pass the significance test, while the area east of 130°E in the WNP has mid-low level moisture divergence. The water vapor flux enters the SCS region from the WNP.

3.5 Complex connections between various processes

Figure 11 combines the changes in large-scale circulation fields and dynamic and thermal conditions from 1978 to 1996 and 1997–2020. From 1997 to 2020, owing to the SST gradient between the equatorial regions and TCs, the area reduced and the near 120°E north wind was weakened. At the same time, the equator east wind was strengthened, warm water accumulation and SST of the WNP and SCS increased, and the western Pacific warm pool expanded. The monsoon trough trended westward and enhanced the monsoon trough in the SCS area, whereas the WNP monsoon trough was abated. The WPSH extended westward to the south and the overall area expanded. Because the SCS is an inland sea near the mainland, its SST rose more than those of the northwestern Pacific and Indian oceans. Through local air-sea interaction, the SCS forms low-level anomalous cyclonic circulation and low-level convergence. At the

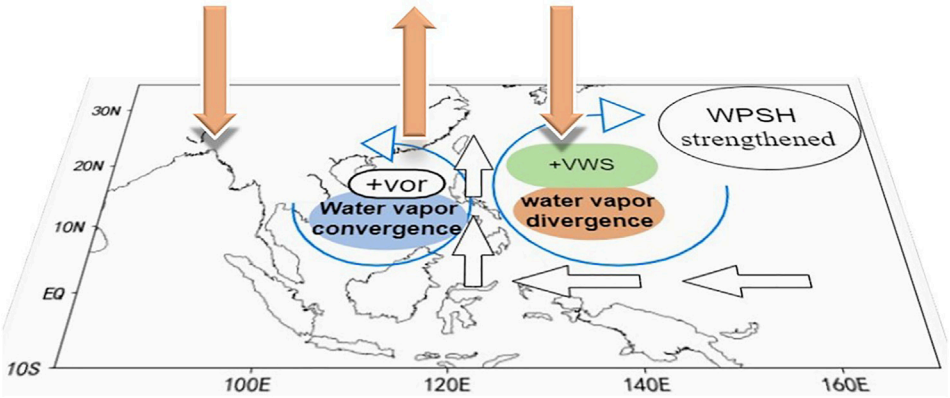

FIGURE 11
Physical mechanism diagram of interannual variation of TC frequency reaching LMI in the SCS. White arrows indicate wind, blue arrows circles indicate cyclonic circulation (or anticyclonic circulation), green area indicate positive vertical wind shear anomalies, and orange arrows indicate zonal circulation anomalies from 10°N to 25°N. The blue and orange areas indicate water vapor convergence and divergence areas. The white area indicates positive relative vorticity.

same time, the WNP region and Indian Ocean region Walker circulations were anomalous, forcing local updrafts in the maritime continent and SCS area and the SCS vorticity increased. The convergence of water vapor in the middle and lower layers, namely the increase in wet convection, formed an environment conducive to the generation of TCs. Because the equatorial east wind enhanced and the north wind weakened near 120°E, in the WNP region, anomalous anticyclonic circulation formed, local sinking airflow appeared, vertical wind shear increased, and atmospheric stability increased. The SST of the WNP increased and the specific humidity increased, but lower water vapor divergence and dynamic and thermal conditions were formed against the TCs generated by the environment.

4 Conclusion and discussion

4.1 Conclusion

Previous studies on LMI were limited to the latitude and intensity of TCs reaching LMI in large regional oceans (Wang and Lee, 2009; Patricola et al., 2017; Wang et al., 2020). This study divided the frequency of TCs reaching the LMI in the SCS into local and migratory TCs according to the source of generation. There was a seesaw phenomenon in the frequency variation of the two types of TCs before and after 1997. That is, local TCs showed an increase in mutations after 1997, while migratory TCs showed a decrease.

From 1997 to 2020, the monsoon trough retreated westward, the warm pool strengthened, and the WPSH strengthened westward. Owing to the decrease in the SST gradient at the equator and mid-latitudes, the north wind weakened in the region near 120°E, while the east wind strengthened in the equatorial region, which led to an abnormal anticyclone in the WNP region. In the WNP, the abnormal anticyclone enhanced divergence, which led to the abnormal subsidence of zonal circulation, increased vertical wind shear, increased atmospheric stability, and water vapor divergence. However, the SCS is an internal sea adjacent to the mainland and experienced a more significant increase in SST than the WNP. Under the action of local sea and air, abnormal cyclonic circulation and convergence were enhanced, zonal circulation showed a weak abnormal rise, vorticity increased, and wet convection was enhanced. The change in the environmental field in the WNP and SCS was the main reason for the seesaw phenomenon in the two types of TCs.

4.2 Discussion

Different from previous studies on the seesaw of TCs in the two oceans, for example, Wang et al. (2022) study on the seesaw of TCs between the Atlantic Ocean and the WNP, which found that it was related to the Atlantic Decadal Oscillation while the seesaw of TCs activities in North America and the Northeast Pacific Ocean were caused by the ENSO, AMO, and Atlantic Meridional Modes (Frank and Young, 2007; Wang and Lee, 2009; Patricola et al., 2017), this paper only analyzed the reasons for the seesaw phenomenon in the variation trend of the frequency of the two types of TC around 1997 considering the influencing system and dynamic and water vapor conditions. Such an air-sea interaction may shed light on the projected suppressed TC genesis in the WNP but enhanced TC genesis in the SCS in global warming. In addition, whether the intensity of the two types of TC also showed a seesaw phenomenon from 1978 to 2020 and the reasons for this need to be further discussed.

Data availability statement

Publicly available datasets were analyzed in this study. This data can be found here: https://www.ncei.noaa.gov/products/international-best-track-archive?name=ib-v4-access; https://psl.noaa.gov/data/gridded/data.ncep.reanalysis.pressure.html; https://www.metoffice.gov.uk/hadobs/hadsst4/data/download.html.

Author contributions

PH was responsible for the conception, writing and drawing of the article. JX is responsible for the discussion, guidance, modification and project support of the article. ML is responsible for the discussion, guidance and revision of the article.

Funding

This study was jointly supported by State Key Program of National Natural Science of China (Grant No. 42130605) and Program for Scientific Research Start-up Funds of Guangdong Ocean University (Grant No. 060302032108).

Conflict of interest

The authors declare that the research was conducted in the absence of any commercial or financial relationships that could be construed as a potential conflict of interest.

Publisher's note

References

Chan, J.-C. (1985). Tropical cyclone activity in the northwest Pacific in relation to the El Niño/Southern Oscillation phenomenon. *Mon. Weather Rev.* 113 (4), 599–606. doi:10.1175/1520-0493(1985)113<0599:TCAITN>2.0.CO;2

Chen, G.-H., and Huang, R.-H. (2006). The effect of warm pool thermal states on tropical cyclone in West Northwest Pacific. *J. Trop. Meteor* 22 (6), 527–532. doi:10.1016/S1872-2032(06)60022-X

Chen, L. S., Luo, Z. X., and Li, Y. (2004). Research advances on tropical cyclone landfall process. *J. Acta Meteorol. Sin.* 62 (5), 541–549. doi:10.11676/qxxb2004.055

Chen, S.-R. (1990). Source regions of tropical storms over northwest Pacific Ocean. *J. Meteorol. Mon. (in Chin.* 16 (2), 23–26. doi:10.7519/j.issn.1000-0526.1990.2.004

Duan, Y.-H., Chen, L.-S., Liang, J.-Y., Wang, Y., Wu, L.-G., Cui, X.-P., et al. (2014). Research progress in the unusual variations of typhoons before and after landfalling. *J. Acta Meteorol. Sin.* 72 (5), 969–986. doi:10.11676/qxxb2014.085

Elsner, J. B., Elsner, G. J. B., and Kara, A. B. (1999). *Hurricanes of the north atlantic: Climate and society*. M. Oxford University Press on Demand.

Emanuel, K., and Nolan, D. S. (2004). Tropical cyclone activity and the global climate system. C. In 26th Conference on Hurricanes and Tropical Meteorolgy.

Feng, T., Huang, R.-H., andChen, G.-H., Wu, L., Huang, P., and Wang, L. (2013). Progress in recent climatological research on tropical cyclone activity over the western North Pacific. *J. Chin. J. Atmos. Sci.* 37 (2), 364–382. doi:10.3878/j.issn.1006-9895.2012.12307

Frank, W.-M., and Young, G.-S. (2007). The interannual variability of tropical cyclones. *Mon. Weather Rev.* 135, 3587–3598. doi:10.1175/mwr3435.1

Fu, B., Peng, M.-S., Li, T., and Stevens, D. E. (2012). Developing versus nondeveloping disturbances for tropical cyclone formation. Part II: Western North Pacific. *Mon. Weather Rev.* 140 (4), 1067–1080. doi:10.1175/2011MWR3618.1

Gao, S., and Chiu, L. S. (2010). Surface latent heat flux and rainfall associated with rapidly intensifying tropical cyclones over the western North Pacific. *Int. J. Remote Sens.* 31 (17-18), 4699–4710. doi:10.1080/01431161.2010.485149

Ge, X., Li, T., and Peng, M. (2013). Effects of vertical shears and midlevel dry air on tropical cyclone developments. *J. Atmos. Sci.* 70 (12), 3859–3875. doi:10.1175/JAS-D-13-066.1

Goni, G. J., and Trinanes, J. A. (2003). Ocean thermal structure monitoring could aid in the intensity forecast of tropical cyclones. *Eos Trans. AGU.* 84 (51), 573–578. doi:10.1029/2003EO510001

Gray, W. M. (1979). Hurricanes: Their formation, structure and likely role in the tropical circulation. *J. Meteorology over Trop. oceans* 155, 218.

Hao, S., and Mao, J.-Y. (2015). Differences of the seasonal variations of tropical cyclone activities over the South China Sea and the western North Pacific and the possible causes. *J. Clim. Environ. Res. (in Chinese)* 20 (4), 380–392. doi:10.3878/j.issn.1006—9585.2014.14063

Harr, P. A., and Elsberry, R. L. (1995). Large-scale circulation variability over the tropical western North Pacific. Part I: Spatial patterns and tropical cyclone characteristics. *Mon. Weather Rev.* 123 (5), 1225–1246. doi:10.1175/1520-0493(1995)123<1225:LSCVOT>2.0.CO;2

Kalnay, E., Kanamitsu, M., Kistler, R., Collins, W., Deaven, D., Gandin, L., et al. (1996). The NCEP/NCAR 40-year reanalysis project. *Bull. Am. Meteorol. Soc.* 77 (3), 437–471. doi:10.1175/1520-0477(1996)077<0437:TNYRP>2.0.CO;2

Knapp, K. R., Kruk, M. C., Levinson, D. H., Diamond, H. J., and Neumann, C. J. (2010). The international best track archive for climate stewardship (IBTrACS) unifying tropical cyclone data. *Bull. Am. Meteorol. Soc.* 91 (3), 363–376. doi:10.1175/2009BAMS2755.1

Li, B.-S., Fan, L.-L., Zou, T., and Song, Z.-Q. (2015). Analysis on water vapor transport of the "5.11" heavy rainfall process in shenzhen. *J. Journal of Guangdong Ocean University* 35 (3), 100–108. doi:10.3969/j.issn.1673-9159.2015.03.015

Li, Q.-H., Lu, H.-C., Zhong, W., Wang, W.-C., Guo, X.-L., and Yuan, M. (2018). Meso-scale transport characteristics and budget diagnoses of water vapor in binary typhoons. *Acta Phys. Sin.* 67 (3), 039201–039214. doi:10.7498/aps.67.20170455

Li, Richard.- C.-Y., and Zhou, W. (2014). Interdecadal change in South China Sea tropical cyclone frequency in association with zonal sea surface temperature gradient. *J. Clim.* 27 (14), 5468–5480. doi:10.1175/JCLI-D-13-00744.1

Lin, I.-I., Pun, I.-F., and Wu, C.-C. (2009). Upper-ocean thermal structure and the western North Pacific category 5 typhoons. Part II: Dependence on translation speed. *Mon. Weather Rev.* 137 (11), 3744–3757. doi:10.1175/2009MWR2713.1

Lin, I.-I., Wu, C.-C., Pun, I.-F., and Ko, D.-S. (2008). Upper-ocean thermal structure and the western North Pacific category 5 typhoons. Part I: Ocean features and the category 5 typhoons' intensification. *Mon. Weather Rev.* 136 (9), 3288–3306. doi:10.1175/2008MWR2277.1

Lin, L.-X., Liang, Q.-Q., and Huang, Z. (2006). Analysis of circulation pattern of rapidly intensified offshore tropical cyclones of South China. *J. Meteorological.* doi:10.7519/j.issn.1000-0526.2006.2.003

Liu, C.-X., and Rong, G.-X. (1995). The climatic analysis of the relationship between the explosive development of typhoon and its environment flow field. *J. Journal of Tropical Meteorology*. CNKI:SUN:RDQX.0.1995-01-006.

Liu, K.-S., and Chan, J.-C.-L. (2013). Inactive period of Western North Pacific tropical cyclone activity in 1998-2011. *J. Clim.* 26, 2614–2630. doi:10.1175/JCLI-D-12-00053.1

Liu, K.-S., and Chan, J.-C. -L. (2019). Inter-decadal variability of the location of maximum intensity of category 4–5 typhoons and its implication on landfall intensity in East Asia. *Int. J. Climatol.* 39 (4), 1839–1852. doi:10.1002/joc.5919

Lu, R., and Tang, X. (2021). Relationship between early-stage features and lifetime maximum intensity of tropical cyclones over the western North Pacific. *Atmosphere (Basel).* 12 (7), 815. doi:10.3390/atmos12070815

Mao, J.-Y., and Wu, G.-X. (2010). Intraseasonal modulation of tropical cyclogenesis in the western North pacific: A case study. *Theor. Appl. Climatol.* 100 (3), 397–411. doi:10.1007/s00704-009-0195-9

Moon, I. J., Kim, S. H., Klotzbach, P., and Chan, J.-C.-L. (2016). Reply to Comment on 'Roles of interbasin frequency changes in the poleward shifts of maximum intensity location of tropical cyclones. *Environ. Res. Lett.* 11 (6), 068002. doi:10.1088/1748-9326/11/6/068002

Moon, I. J., Kim, S. H., Klotzbach, P., and Chan, J.-C. (2015). Roles of interbasin frequency changes in the poleward shifts of the maximum intensity location of tropical cyclones. *Environ. Res. Lett.* 10 (10), 104004. doi:10.1088/1748-9326/10/10/104004

Patricola, C. M., Saravanan, R., and Chang, P. (2017). A teleconnection between Atlantic sea surface temperature and eastern and central North Pacific tropical cyclones. *Geophys. Res. Lett.* 44 (2), 1167–1174. doi:10.1002/2016GL071965

Rappin, E.-D., Morgan, M.-C., and Tripoli, G.-J. (2011). The impact of outflow environment on tropical cyclone intensification and structure. *J. Atmos. Sci.* 68 (2), 177–194. doi:10.1175/2009JAS2970.1

Rayner, N. A., Brohan, P., Parker, D. E., Folland, C. K., Kennedy, J. J., Vanicek, M., et al. (2006). Improved analyses of changes and uncertainties in sea surface temperature measured *in situ* since the mid-nineteenth century: The HadSST2 dataset. *J. Clim.* 19 (3), 446–469. doi:10.1175/JCLI3637.1

Shen, W., and Ginis, I. (2003). Effects of surface heat flux-induced sea surface temperature changes on tropical cyclone intensity. *Geophys. Res. Lett.* 30 (18). doi:10.1029/2003GL017878

Song, J., Klotzbach, P. J., Tang, J., and Wang, Y. (2018). The increasing variability of tropical cyclone lifetime maximum intensity. *Sci. Rep.* 8 (1), 16641–16647. doi:10.1038/s41598-018-35131-x

Tran-Quang, D., Pham-Thanh, H., Vu, T.-A., Kieu, C., and Tan, P.-V. (2020). Climatic shift of the tropical cyclone activity affecting Vietnam's coastal region. *J. Appl. Meteorol. Climatol.* 59 (10), 1755–1768. doi:10.1175/JAMC-D-20-0021.1

Wang, C., and Lee, S. K. (2009). Co-variability of tropical cyclones in the North Atlantic and the eastern North Pacific. *Geophys. Res. Lett.* 36 (24), L24702. doi:10.1029/2009GL041469

Wang, C., Wang, B., Wu, L., and Luo, J.- J. (2022). A seesaw variability in tropical cyclone genesis between the western North Pacific and the North Atlantic shaped by Atlantic Multidecadal variability. *J. Clim.* 35 (8), 2479–2489. doi:10.1175/JCLI-D-21-0529.1

Wang, G., Su, J., Ding, Y., and Chen, D. (2007). Tropical cyclone genesis over the south China sea. *J. Mar. Syst.* 68 (3-4), 318–326. doi:10.1016/j.jmarsys.2006.12.002

Wang, L. (2013). Climatology of tropical cyclone genesis over the South China Sea. C. The 17th Pacific Asian marginal Sea (PAMS) Meeting.

Wang, R., and Wu, L. (2019). Influence of track changes on the poleward shift of LMI location of western North Pacific tropical cyclones. *J. Clim.* 32 (23), 8437–8445. doi:10.1175/JCLI-D-18-0855.1

Wang, X., Zhou, W., Li, C.-Y., and Wang, D.-X. (2012). Effects of the East Asian summer monsoon on tropical cyclone genesis over the South China Sea on an interdecadal time scale. *Adv. Atmos. Sci.* 29 (2), 249–262. doi:10.1007/s00376-011-1080-x

Wang, Y.-X., Sun, Y., Liao, Q.-F., Zhong, Z., Hu, Y.-J., and Liu, K.-F. (2017). Impact of initial storm intensity and size on the simulation of tropical cyclone track and western Pacific subtropical high extent. *J. Meteorol. Res.* 31 (5), 946–954. doi:10.1007/s13351-017-7024-3

Wang, Z., Zhang, G., Dunkerton, T. J., and Jin, F.-F. (2020). Summertime stationary waves integrate tropical and extratropical impacts on tropical cyclone activity. *Proc. Natl. Acad. Sci. U. S. A.* 117 (37), 22720–22726. doi:10.1073/pnas.2010547117

Wei, N., Zhang, X.- H., Chen, L.- S., and Hu, H. (2018). Comparison of the effect of easterly and westerly vertical wind shear on tropical cyclone intensity change over the western North Pacific. *Environ. Res. Lett.* 13 (3), 034020. doi:10.1088/1748-9326/aaa496

Wen, G.-H., Huang, G., Huang, H.-J., Liu, C.-X., and Bi, X.-Y. (2019). Observed rainfall asymmetry of tropical cyclone in the process of making landfall in Guangdong, south China. *Int. J. Climatol.* 39 (7), 3379–3395. doi:10.1002/joc.6027

Wu, L., Wen, Z., Huang, R., and Wu, R. (2012). Possible linkage between the monsoon trough variability and the tropical cyclone activity over the western North Pacific. *Mon. Weather Rev.* 140 (1), 140–150. doi:10.1175/MWR-D-11-00078.1

Wu, Y., Chen, S., Li, W., Fang, R., and Liu, H. (2020). Relative vorticity is the major environmental factor controlling tropical cyclone intensification over the western North Pacific. *Atmos. Res.* 237, 104874. doi:10.1016/j.atmosres.2020.104874

Yan, J.-Y. (1996). Climatological characteristics of rapidly intensifying tropical cyclones over the offshore of China. *J. Quarterly Journal of Applied Meteorology*. CNKI:SUN:YYQX.0.1996-01-003.

Yuan, J.-N., Wang, D.-X., Liu, C.-X., Huang, J., and Huang, H.-J. (2007). The characteristic differences of tropical cyclones forming over the western North Pacific and the South China Sea. *J. Acta Oceanologica Sinica* (4), 29–43.

Yumoto, M., and Matsuura, T. (2001). Interdecadalvariability of tropical cyclone activity in the western North Pacific. *Journal of the Meteorological Society of Japan.* 79, 23–35. doi:10.2151/jmsj.79.23

Zhan, R., and Wang, Y. (2017). Weak tropical cyclones dominate the poleward migration of the annual mean location of lifetime maximum intensity of northwest Pacific tropical cyclones since 1980. *J. Climate* 30, 6873–6882. doi:10.1175/JCLI-D-17-0019.1

Zhang, Q., Wu, L.-G., and Liu, Q.-F. (2009). Tropical cyclone damages in China 1983–2006. *Bull. Am. Meteorol. Soc.* 90 (4), 489–496. doi:10.1175/2008BAMS2631.1

Zhang, Z. (2003). *Study of south China sea typhoons between 1999 and 2002*. Hong Kong: University of Science and Technology.

Zhao, H.-K., Zhao, K., Klotzbach, P. J., Wu, L.-G., and Wang, C.-Z. (2022). Interannual and interdecadal drivers of meridional migration of western North Pacific tropical cyclone lifetime maximum intensity location. *J. Clim.* 35 (9), 2709–2722. doi:10.1175/JCLI-D-21-0797.1

Zheng, M.-L., and Wang, C.-Z. (2022). Interdecadal changes of tropical cyclone intensity in the South China Sea. *Clim. Dyn.* doi:10.1007/s00382-022-06305-1

frontiers | Frontiers in Earth Science

TYPE Original Research
PUBLISHED 31 August 2022
DOI 10.3389/feart.2022.957940

OPEN ACCESS

EDITED BY
Lu Zhang,
CSIRO Land and Water, Australia

REVIEWED BY
Yaocun Zhang,
Nanjing University, China
Manish K. Joshi,
Genesis Ray Energy India Pvt. Ltd., India

*CORRESPONDENCE
Haiwen Liu,
hwliu@cauc.edu.cn

SPECIALTY SECTION
This article was submitted to Atmospheric Science, a section of the journal Frontiers in Earth Science

RECEIVED 31 May 2022
ACCEPTED 22 July 2022
PUBLISHED 31 August 2022

CITATION
Wu K, Liu H, Zhao L, Lin Y and Yang Z (2022), The strengthening relationship between summer rainfall over North China and PDO since the mid-2000s. *Front. Earth Sci.* 10:957940. doi: 10.3389/feart.2022.957940

The strengthening relationship between summer rainfall over North China and PDO since the mid-2000s

Kaijun Wu[1], Haiwen Liu[1]*, Liang Zhao[2], Yihua Lin[2,3] and Zhaohong Yang[1]

[1]Department of Aviation Meteorology, Civil Aviation University of China, Tianjin, China, [2]College of Earth and Planetary Sciences, University of Chinese Academy of Sciences, Beijing, China, [3]State Key Laboratory of Numerical Modeling for Atmosphere Sciences and Geophysical Fluid Dynamics, Institute of Atmospheric Physics, Chinese Academy of Sciences, Beijing, China

The interdecadal change of the summer (July–August) rainfall over North China (SRNC) is of great concern to the climate research community. Based on the sliding correlation and interdecadal difference analysis, the interdecadal change of SRNC was studied. Results show a significantly wetter period of SRNC since the mid-2000s, which was associated with strengthening negative relationship between SRNC and PDO. PDO affected the SRNC through the jet stream in the upper-level and the East Asia–Pacific (EAP) teleconnection pattern. In the negative phase of the PDO since the mid-2000s, the contractive upper-level jet stream in the west of North China resulted in the abnormal updraft over the southern region of North China. Meanwhile, the positive phase of the EAP teleconnection pattern brought warm and wet southeast flow entering North China from its eastern boundary, both bringing more rainfall in North China. The abnormal water vapor transport from the western Pacific was very different from that accompanying the East Asian summer monsoon.

KEYWORDS

North China, summer rainfall, interdecadal change, PDO, EAP, jet stream

Introduction

North China lies south of Yanshan mountains, east of Hetao Plain, north of Qinling Mountains and Huaihe River, and east of the Bohai Sea and Yellow Sea (Figure 1), where the capital of Beijing is located. The summer precipitation (July–August) accounts for 80% of the annual precipitation in North China (Tao, 1980). The shortage of summer precipitation in North China has seriously hindered the further development of industrial and agricultural production and the daily life of urban and rural residents there (Huang et al., 1999). North China experienced frequent and severe droughts in the past, which resulted in significant economic and environmental impacts and worsened the local hydrographic environment (Ma and Fu, 2006; Pei et al., 2015).

Numerous studies have investigated the causes of the decreasing summer (July–August) precipitation over North China (SRNC) since the mid-1960s and after

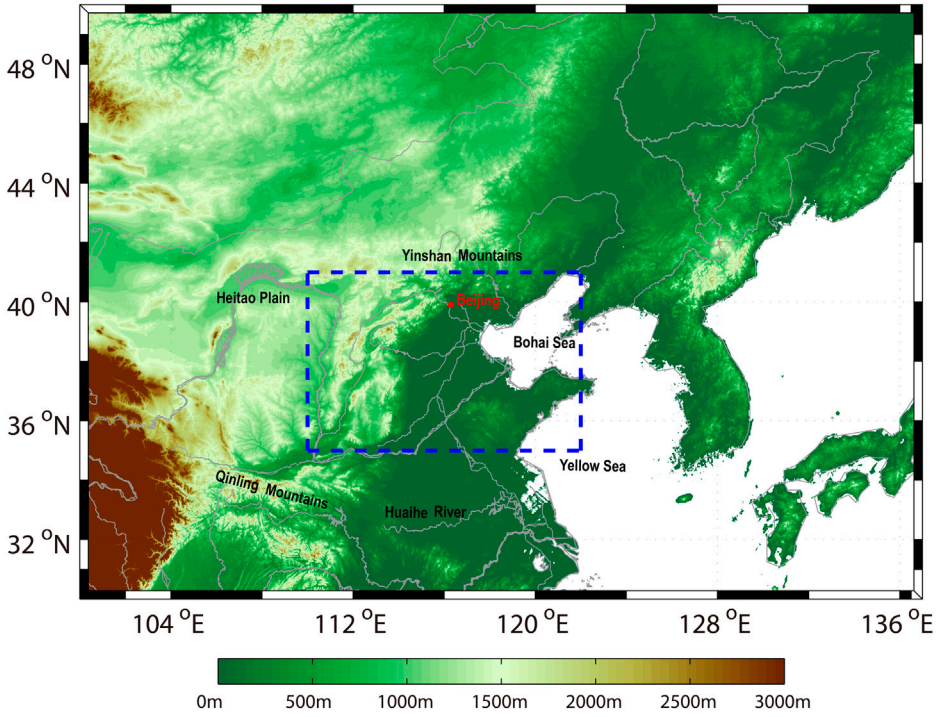

FIGURE 1
The topography around North China; the altitude (unit: m) is shaded. The box (35°N–41°N, 110°N–122°E) shows the region of North China.

the mid-1970s (Yan et al., 1990; Yatagai and Yasunari, 1994; Huang et al., 1999; Lu, 1999; Dai et al., 2003; Liu and Ding, 2010; Zhu et al., 2011). The main possible causes include the large-scale temperature changes due to the weakening thermal difference between land and ocean (Yan et al., 1990; Yan et al., 1991), the winter Arctic sea-ice variations (Wu et al., 1999), the teleconnection pattern including the North Pacific Oscillation (NPO) variation and the North Atlantic Oscillation (NAO) (Li and Li, 1999), the Pacific Decadal Oscillation (PDO or NPDO) and the South Pacific Decadal Oscillation (SPDO) pattern (Zhang et al., 1997; Chang et al., 2000; Yang and Lau, 2004; Li et al., 2020), the sea surface temperature (SST) of the central and eastern Pacific in the equatorial region (Huang et al., 1999), the interaction of the air-sea in the middle latitudes (Li and Liao, 1996), the circumglobal teleconnection (CGT) (Ding and Wang, 2005), the interdecadal weakening of East Asia Summer Monsoon (EASM) (Wang, 2001), the interdecadal changes of the western Pacific subtropical high (WPSH) over the eastern China regions (Nitta and Hu, 1996), the interdecadal cooling in the upper troposphere and lower stratosphere over East Asia (Yu and Zhou, 2007), and the thermal effect of aerosols over Asia such as the black carbon (Menon et al., 2002).

The natural variability at interdecadal timescales in the Pacific Ocean is termed the Pacific decadal variability, which is referred to as the Interdecadal Pacific Oscillation (IPO; Power et al., 1998, Power et al., 1999; Allan, 2000) for the basin-wide pattern or PDO (Mantua et al., 1997) for the North Pacific pattern (Joshi et al., 2022). Both IPO/PDO is defined as a long-lived El Niño-like pattern of Pacific climate variability that not only modulates the rainfall over India (Joshi and Pandey, 2011; Joshi and Rai, 2015; Joshi and Kucharski, 2017; Joshi et al., 2021), Sahel (Mohino et al., 2011; Villamayor and Mohino, 2015), and United States (Dai, 2013) but also over North China. There were two positive phases of PDO (1922–45 and 1977–2002) and one negative phase of PDO (1946–76) in the period of 1900–2010 (Qian and Zhou, 2014). Meanwhile, Ma (2007) found that the spring PDO index had a climate shift occurring in 1978/1979. In interdecadal timescale, PDO not only has a climate shift but also has a close relationship with SRNC. Qian and Zhou (2014) suggested that the dry conditions of North China in summer were influenced by the PJ/EAP meridional teleconnection pattern generated by one negative PDO phase (1946–76) using the Palmer Drought Severity Index data. Li et al. (2020) suggested that after removing the correlation between SPDO and NPDO, there was a significant positive (negative) correlation between SPDO (NPDO) and PRNC.

Numerous studies investigated the unstable relationships between the two time series and suggested that the

relationship between El Nino-Southern Oscillation (ENSO) and the Indian summer monsoon had broken down in recent decades (Kumar et al., 1999; Kulkarni et al., 2021). Liu et al. (2004) found that the interannual correlation between the winter sea ice over the Davis Strait and July rainfall over North China had weakened after 1994.

Previous studies indicated that PRNC had experienced an interdecadal decrease since the mid-1970s (Huang et al., 1999). However, the year after which PRNC entered an interdecadal wetter period was still of great concern to the climate research community. Has a new interdecadal change of PDO occurred? How did the interdecadal change of the PDO influence the interdecadal change of the SRNC? With these questions in mind, we firstly investigated the interdecadal variations of the PDO and SRNC and then verified the stability of the relationship between PDO and SRNC from decades to decades. This study was organized as follows. The data and analysis methods were introduced in the *Data and analysis methods* section. The *Results* section shows the interdecadal change of the relationship between PDO and SRNC, and the possible mechanism of PDO influencing the SRNC. The final section is *Conclusions and discussions*.

Data and analysis methods

The Climate Prediction Center (CPC) Unified Gauge-Based Analysis of Global Daily Precipitation dataset with a horizontal resolution of 0.5° × 0.5° (Xie et al., 2007) and the precipitation data of 17 gauge-based stations from 1979 to 2021 in North China (Liu et al., 2020) were used to investigate the interdecadal change of the SRNC. The SRNC is the regional averaged summer (July–August) precipitation over North China in the box of [35°N–41°N, 110°N–122°E] (Liu et al., 2020). Two precipitation datasets were consistent in indicating the interdecadal change of SRNC. For brevity, we only showed the SRNC index from the CPC dataset.

The monthly NCEP-DOE AMIP-II Reanalysis (R-2) (Kanamitsu et al., 2002) dataset and ERA5 dataset were used to reveal the interdecadal variations of atmospheric circulation. Two reanalyzed datasets have subtle differences in characterizing the interdecadal variations of atmospheric circulation. For brevity, we only showed the NCEP-DOE AMIP-II results in the following. Besides, the SST data from the NOAA Extended Reconstructed Sea Surface Temperature (SST) V5 dataset (Huang et al., 2017) and the monthly Pacific Decadal Oscillation (PDO) index derived from https://www.ncdc.noaa.gov/teleconnections/pdo/ were also used.

The vertically integrated water vapor flux from the ground to 300 hPa was calculated to further measure the interdecadal difference of the water vapor transportation. The vertically integrated water vapor flux is computed using the following formula as discussed by Ding (1989):

$$Q_x = \frac{1}{g}\int_{300}^{P_s}(uq)dp$$
$$Q_y = \frac{1}{g}\int_{300}^{P_s}(vq)dp \quad (1)$$

where Q_x and Q_y are the vertical integral of water vapor flux in the zonal and the meridional directions, respectively. g is gravitational acceleration, and u and v indicate the zonal and the meridional wind, respectively. q is specific humidity, and p is atmospheric pressure. P_s is the atmospheric pressure on the surface. 300 is the 300 hPa level.

We intend to discuss the interdecadal change of the summer precipitation over North China and its causes, which was about the difference between the adjacent 10 years. Therefore, we chose a 20-year running t-test to calculate the precipitation difference between the later and former 10-year periods. The 20-year running t-test has also been used earlier to verify the abrupt point of interdecadal change in the summer precipitation over North China (Liu et al., 2012). On the contrary, we used the 11-year sliding correlation to test the relationship variation between the summer rainfall over North China and PDO (Kumar et al., 1999; Liu H. W. et al., 2004).

Results

The characteristics of interdecadal change of the SRNC and PDO in the recent forty years

Figure 2A shows the time series of SRNC during 1979–2021. A 20-year moving t-test was performed to quantify the interdecadal change of SRNC, as shown in Figure 2B. The year 2006 is the first point with a significant precipitation difference between the later and earlier 10-year periods, reaching a 95% confidence level. It was apparent that SRNC had an interdecadal abrupt change point in 2006 during 1979–2021. Therefore, there were two interdecadal periods obviously. In the first period of 1979–2005, the SRNC showed an interdecadal negative anomaly with a mean value below the climate mean. Liu et al. (2020) discovered that SRNC had a weak, increasing trend since 1979 and then halted in the mid-1990s. However, this halted period did not last long (Hu, 1997–2005); then, SRNC entered a wetter period in 2006 (Figure 2A). It is worth noting that, since 2006, the SRNC was not only observed with an increasing trend but also showed an interdecadal positive anomaly with the mean value above the climate mean value. Moreover, the linear trend of SRNC during 2008–2021 was also significant, reaching the 95% confidence level. Thereby, the SRNC entered an interdecadal wetter period in the mid-2000s.

In order to further investigate the interdecadal change of the SRNC, the difference in the SRNC between 2006–2021 and 1979–2005 is shown in Figure 3. A significant positive

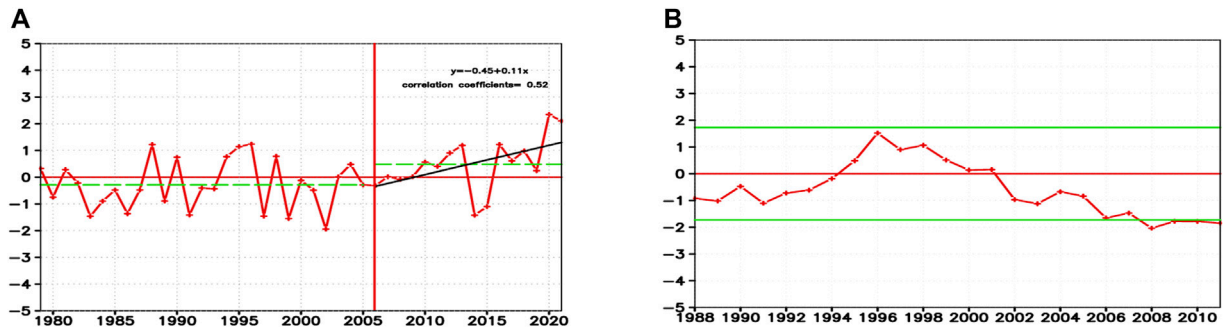

FIGURE 2
(A) Normalized time series of SRNC index during 1979–2021. The horizontal dash lines indicate the mean during two periods, the solid black line during 2006–2021 indicates the linear trend, and the vertical line indicates the interdecadal abrupt change year. **(B)** A 20-year running *t*-test of SRNC index, with two green lines showing a 95% confidence level.

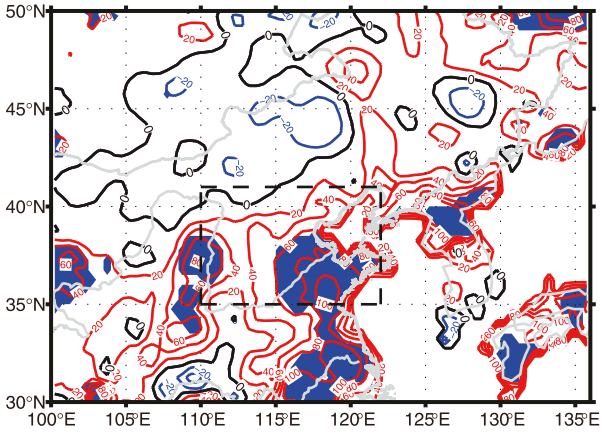

FIGURE 3
Climatological mean difference of summer precipitation during periods 2006–2021 and 1979–2005 using CPC dataset (unit: mm). The shading area indicates a difference reaching the 95% confidence level based on Student's *t*-test. The black box shows the region of North China.

anomaly is clearly observed in North China with blue shading areas. During 2006–2021, North China entered an interdecadal wetter period, which was consistent with the interdecadal change of the SRNC index (Figure 2).

Previous studies indicated a negative relationship between the PDO index and the SRNC (Ma, 2007; Qian and Zhou, 2014; Li et al., 2020). Since the SRNC experienced an interdecadal abrupt change in 2006, has the PDO experienced a similar interdecadal change? In order to investigate the interdecadal variation of PDO, the normalized time series of PDO index in July–August during 1979–2021 and the result of the 20-year moving t-test are shown in Figure 4. The PDO index revealed the characteristics of interannual and interdecadal variation in Figure 4A. PDO was almost in the positive phase before 2004 and then turned to the negative phase. The SRNC and the PDO index had a significantly negative relationship with a correlation coefficient of −0.361, reaching a 99% confidence level, which is consistent with numerous previous studies (Ma, 2007; Qian and Zhou, 2014; Li et al., 2020). The 20-year running t-test was performed to find the abrupt change point of the PDO index (Figure 4B). We found that the PDO index had a significant abrupt change during 2002–2004.

The difference in Pacific SST between the periods 2004–2021 and 1979–2003 is also shown in Figure 5. There were warm anomalies in North Pacific and the Warm Pool region, whereas cold anomalies existed in the eastern equatorial Pacific, which is similar to the previous results (Qian and Zhou, 2014). Thus, PDO changed from the negative phase to the positive phase in 2004, and the phase transition year of 2004 is roughly consistent with the interdecadal abrupt year of the SRNC. This reminds us that the interdecadal change of the SRNC is related to the phase transition of the PDO.

The interdecadal change in the interannual relationship between SRNC and PDO

As mentioned above, the PDO and SRNC both had similar interdecadal variations with close abrupt change or transition years. To further explore whether the interannual relationship between SRNC and the PDO index is stable, Figure 6 shows the sliding correlations between SRNC and the PDO index with an 11-year moving window. The negative correlations between SRNC and the PDO index had obvious interdecadal change. Based on the analysis result using data in the recent 40 years, the the correlations between SRNC and PDO have become stronger and more significant since 2007. Before 2007, the negative

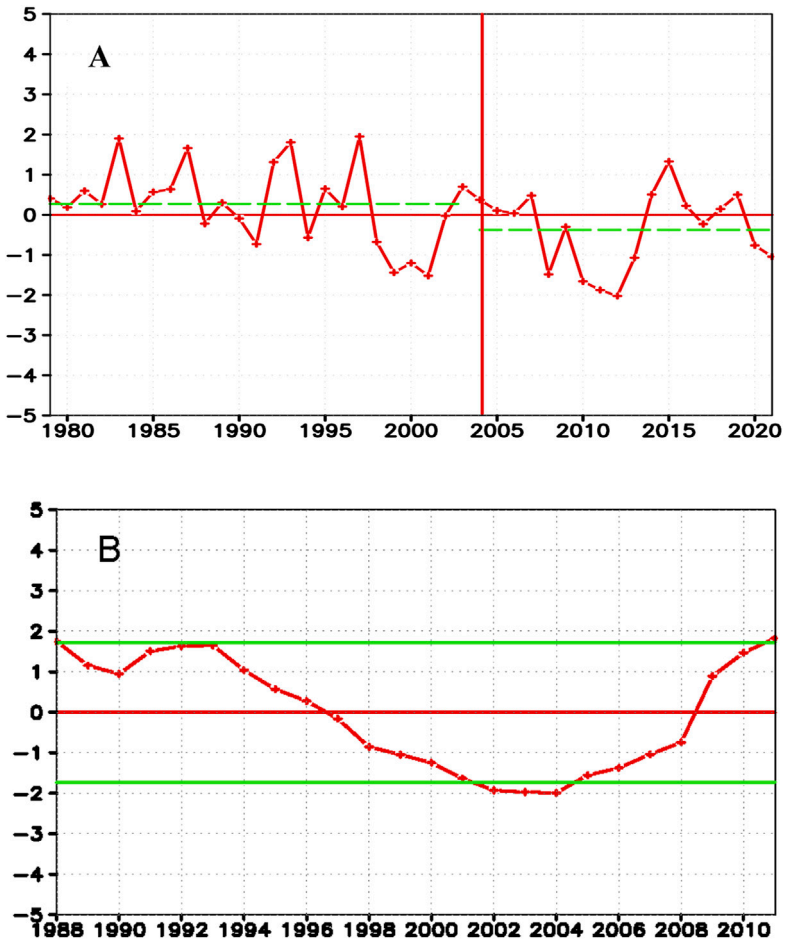

FIGURE 4
The same as Figure 2, but for normalized time series of PDO index in July–August during 1979–2021. The horizontal dash lines in **(A)** indicate the mean during two periods, and the vertical line indicates the interdecadal abrupt change year. Two green lines showing a 95% confidence level in the 20-year running t-test in **(B)**.

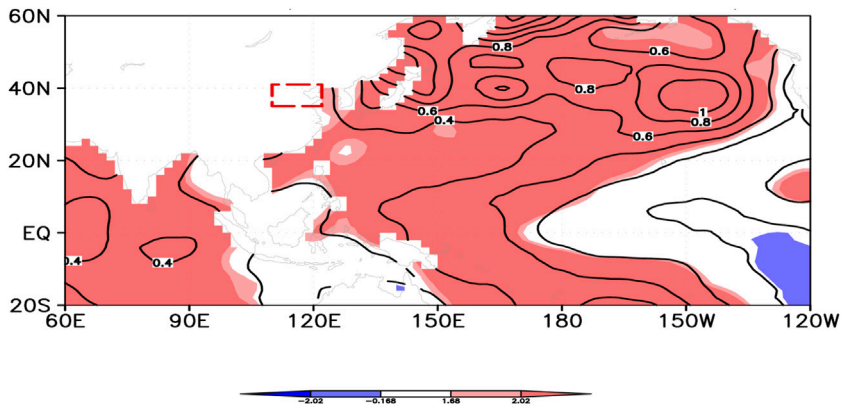

FIGURE 5
The same as Figure 3, but for the difference of SST during the periods 2004–2021 and 1979–2003 in the Pacific (unit: °C). Shaded areas show differences reaching 90% and 95% confidence levels according to Student's *t*-test. The box shows the region of North China.

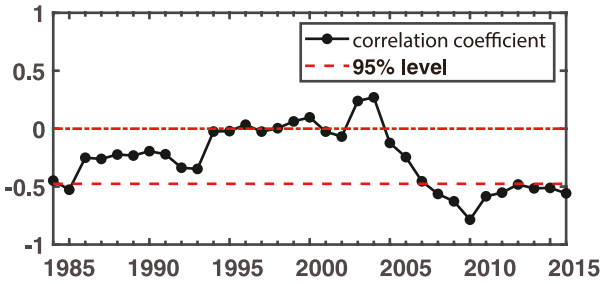

FIGURE 6
11-year sliding correlations between SRNC and the PDO index during 1979–2021. The red line of −0.476 indicates a critical value of a one-tailed 95% confidence level with n = 11.

correlations between SRNC and the PDO index were almost weak. Accompanying the enhanced interannual relationship between SRNC and the PDO index, the SRNC became wetter since the mid-2000s (Figure 2). This suggests that the interdecadal variations of the SRNC were closely related to the interdecadal variations of the negative relationship between SRNC and the PDO index.

To further demonstrate the interdecadal change in the relationship between the PDO index and SRNC, the wind vector at 850 hPa is regressed onto the normalized PDO index during two periods in Figure 7. During 1979–2005 (Figure 7A), the PDO index was almost positive, and the regression of the wind vector shows anomalous northwest wind over North China, reaching a 95% confidence level. An anomalous cyclone was found in Northeast China. On the contrary, during 2006–2021 (Figure 7B), the PDO index was almost negative, and the regression of the wind vector shows anomalous northeast wind to the southeast of North China. Therefore, while the PDO index was negative, there was anomalous southwest wind to the southeast of North China accompanied by an anomalous anticyclone around southern Japan. Obviously, more water vapor entered North China during 2006–2011, especially from the Pacific.

The possible causes of interdecadal wetter North China since 2006

The upper-level jet stream and its secondary circulation played an important role in the SRNC (Quan and Liuzhucheng, 2013). The correlation distributions between PDO index and zonal wind at 200 hPa were calculated during 1979–2005 and 2006–2021, respectively, to measure the interdecadal variations of the relationship between the upper-level jet stream and PDO during two periods, as shown in Figure 8. We firstly figured out how the PDO influenced the SRNC through the upper-level jet stream.

There were significant positive correlation coefficients to the west of North China in Figure 8A. During 1979–2005, the PDO was almost in the positive phase, so the upper-level jet stream was a positive anomaly to the west of North China. Uccellini and Johnson (1979) indicated a downdraft in the right hand of the exited region of the jet stream. North China is just below the exit region of the upper-level jet stream. Therefore, during 1979–2005, with an outstretched jet stream to the west of North China, there should be an abnormal downdraft over North China. Figure 9A further demonstrates an abnormal downdraft over southern North China during the period of 1979–2005, although the vertical velocity anomaly had not passed 95% confidence levels. This feature went against more rainfall in North China.

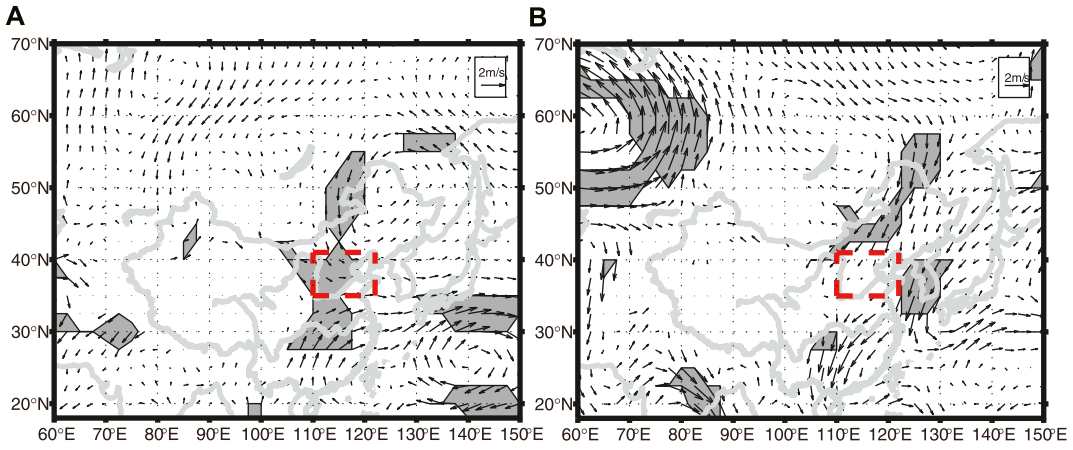

FIGURE 7
Regression results of wind vector at 850 hPa using the normalized PDO index during **(A)** 1979–2005 and **(B)** 2006–2021. Shaded areas indicate regression reaching 95% confidence levels according to Student's t-test. The box shows the region of North China.

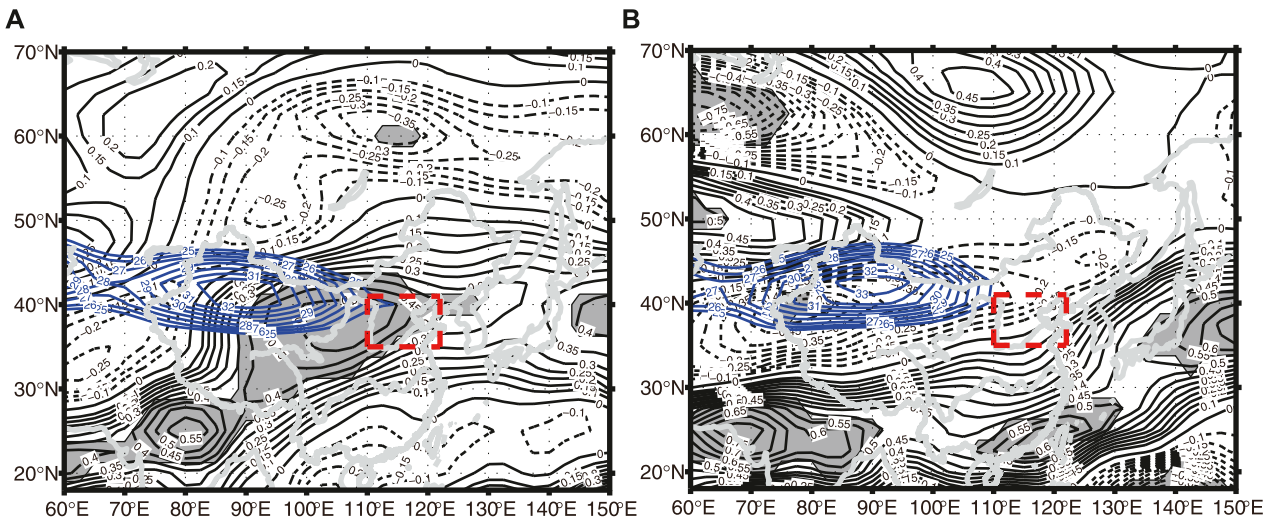

FIGURE 8
Correlation distributions between PDO and zonal wind at 200 hPa during **(A)** 1979–2005 and **(B)** 2006–2021. Shaded areas indicate correlation reaching 95% confidence levels according to Student's *t*-test. The box shows the region of North China. The blue isolines indicate the zonal wind greater than 25 m/s.

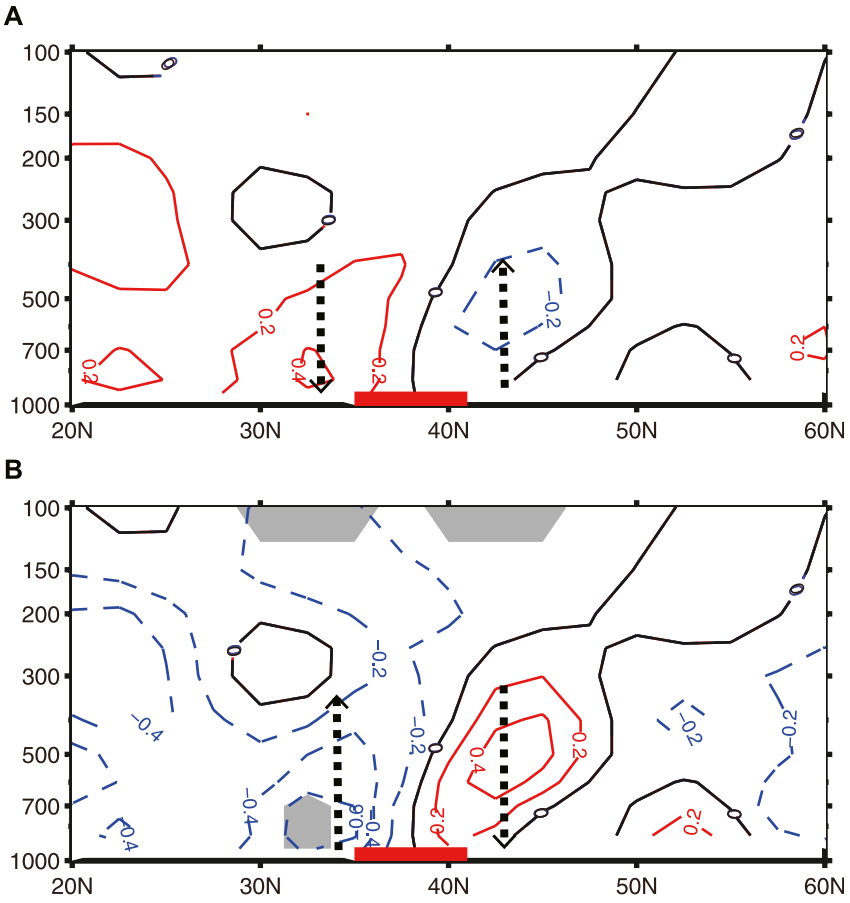

FIGURE 9
Latitude-height cross section of vertical velocity anomaly along 117.5°E in JA by **(A)** 1979–2005 mean minus 1979–2021 mean (unit: 10^{-2} Pa/s) and **(B)** 2006–2021 mean minus 1979–2021 mean. Shaded areas are statistically significant at the 95% confidence level according to Student's *t*-test. The red line shows the latitude range of North China. The black arrow line shows the abnormal vertical movement.

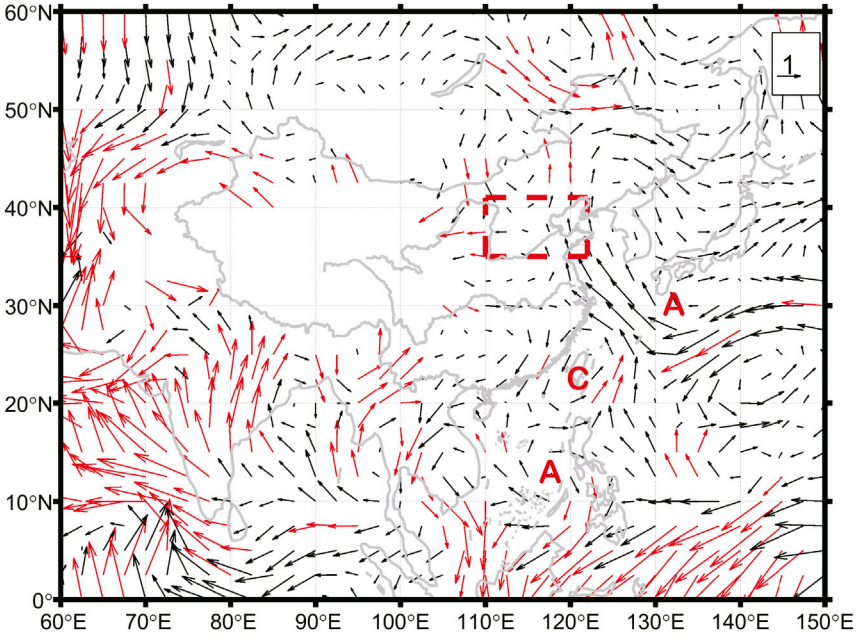

FIGURE 10
The same as Figure 3 but for 850 hPa wind vector (unit: m/s). Red arrows show the difference reaching 90% confidence levels according to Student's *t*-test. The box shows the region of North China.

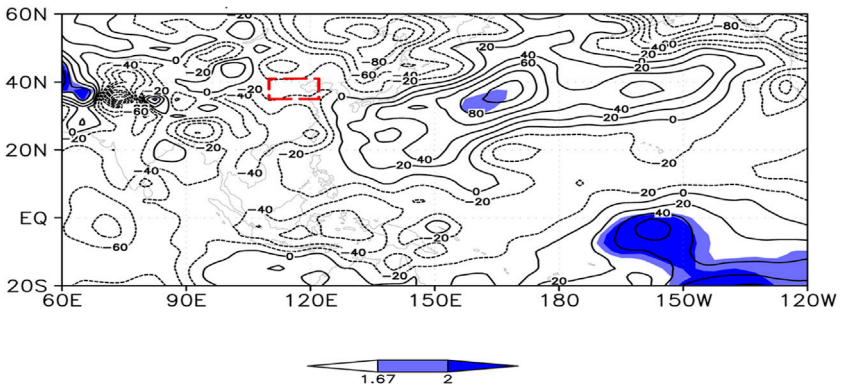

FIGURE 11
The same as Figure 3 but for sea level pressure (unit: hPa). Shaded areas show the difference reaching 90% and 95% confidence levels according to Student's *t*-test. The box shows the region of North China.

On the contrary, during 2006–2021, there were weak negative correlation coefficients to the west of North China in Figure 8B. During 2006–2021, the PDO was almost in the negative phase, so the upper-level jet stream was a weak positive anomaly to the west of North China. However, we found that the upper-level jet stream was contractive to the west of North China during 2006–2021 with respect to that during 1979–2005. There should be an abnormal updraft over North China. Figure 9B further demonstrates an abnormal updraft over southern North China during the period of 2006–2021, whereas the vertical velocity anomaly had passed 95% confidence levels. This feature made more rainfall in North China.

Numerous studies indicated that PDO influenced the SRNC mainly through the East Asia–Pacific (EAP)

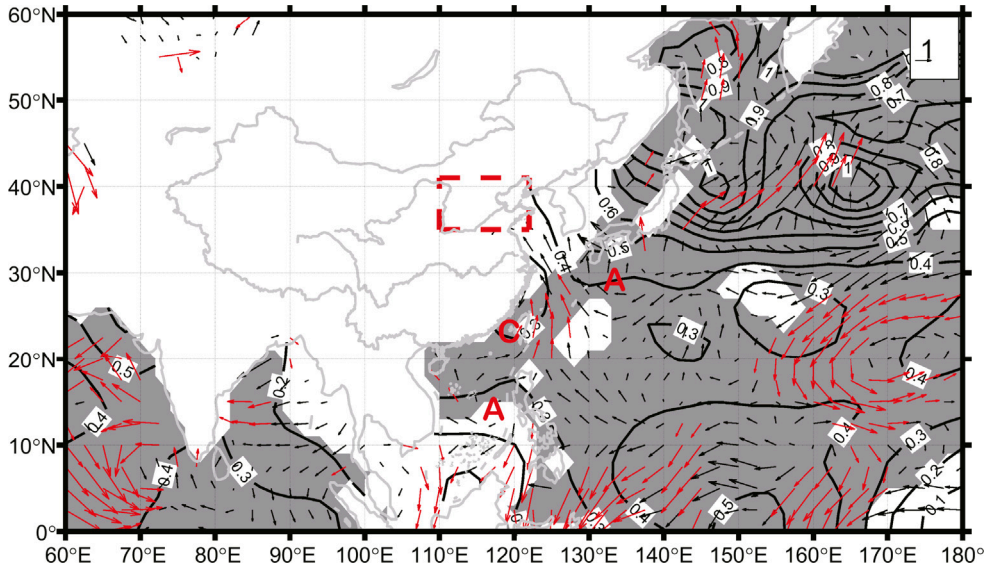

FIGURE 12
The same as Figure 3 but for wind vector at 1,000 hPa (unit: m/s) and SST in the Pacific (unit: °C). The isolines show the difference in SST. Shaded areas and red arrows indicate a difference reaching 95% confidence levels according to Student's *t*-test. The box shows the region of North China.

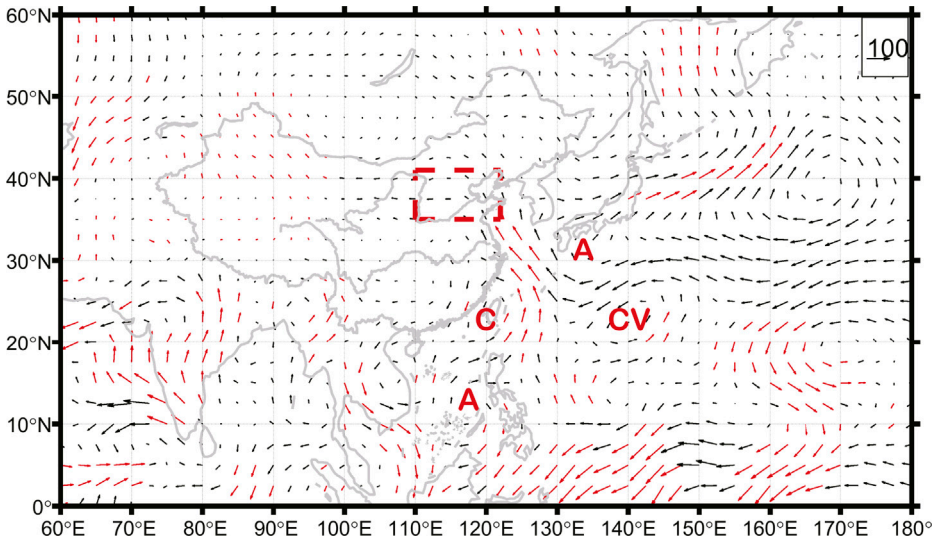

FIGURE 13
The same as Figure 10, but for the vertically integrated water vapor flux (unit: kg/m/s).

teleconnection pattern (Nitta, 1987; Huang and Sun, 1992; Qian and Zhou, 2014). Figure 10 shows the difference in wind vector by 2006–2021 minus 1979–2005. An anomalous anticyclone was found to the east of the Philippines island. In contrast, an anomalous cyclone was observed near Taiwan island and an anomalous anticyclone to the east of Japan island. The "+-+" pattern was very similar to the positive phase of the EAP teleconnection pattern (Nitta, 1987; Huang and Sun, 1992). North China is dominated by an anomalous southeast flow from the Pacific and an anomalous northwest

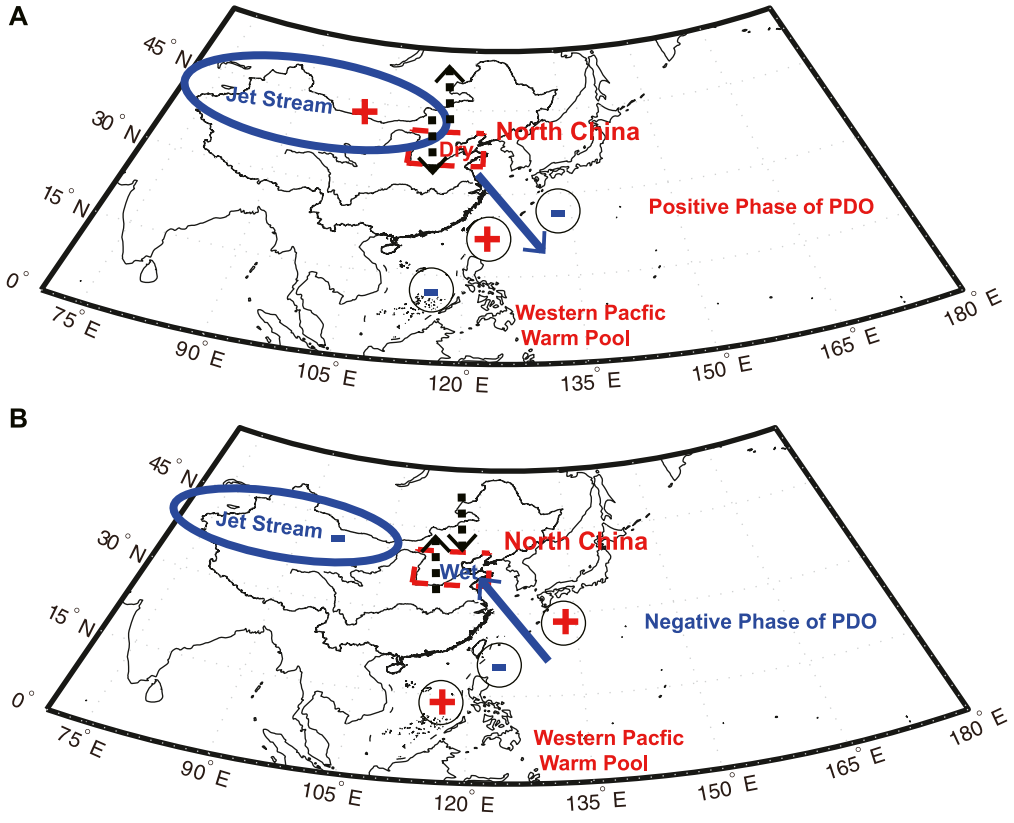

FIGURE 14
Schematic diagram of a mechanism for the abnormal summer rainfall over North China due to **(A)** positive phase of PDO during 1979–2005 and **(B)** negative phase of PDO during 2006–2021.

flow from Lake Baikal, resulting in the convergence over North China in the mid-lower troposphere. Thus, more precipitation has been observed in North China since the mid-2000s.

Although the difference in sea level pressure (SLP) by 2006–2021 minus 1979–2005 in Figure 11 does not show the typical positive phase of the EAP teleconnection pattern, it shows a distribution of low over the land and high over the Pacific along 40°N. This pattern benefited anomalous east wind, leading to more precipitation in north China (Liang et al., 2006).

The difference of wind vector at 1,000 hPa and SST in the Pacific by 2006–2021 minus 1979–2005 shows a positive phase of the EAP teleconnection pattern (Nitta, 1987; Huang and Sun, 1992) in Figure 12. The positive phase of the EAP would lead to more precipitation in North China, with the anomalous southeast wind bringing warm-moist air into North China. At the same time, the positive phase of the EAP strengthened the Kuroshio current in the east of the Japan island to keep the warmer SST in North Pacific. The warmer SST in North Pacific was beneficial to maintaining the negative phase of PDO. In general, PDO was conducive to the form of the EAP teleconnection pattern (Nitta, 1987; Huang and Sun, 1992), whereas the EAP teleconnection pattern contributed to maintaining the PDO in turn. Thus, a positive feedback mechanism was formed between the PDO and the EAP pattern. Furthermore, the negative phase of the PDO and the positive phase of the EAP pattern both led to abundant precipitation over North China (Wang and He, 2015).

In addition, when the PDO was in a negative phase, the SST in the Indian Ocean and the Maritime Continent was anomalously warm, which was significantly different from previous studies (Ma, 2007; Qian and Zhou, 2014). Meanwhile, the warmer SST in the Indian Ocean, around the Maritime Continent, and in the mid-high latitude of the western Pacific resulted in weaker East Asian summer monsoon (EASM) with weaker land-sea thermal contrast.

Figure 13 shows the difference in the water vapor transportation by 2006–2021 minus 1979–2005, which also reflected the characteristics of the positive phase of the EAP with the "+-+" pattern. Anomalous anticyclone of water vapor flux was found

near the Philippines island, and the anomalous cyclone of water vapor flux was observed over Taiwan island, while the anomalous anticyclone water vapor fluxed to the east of the Japan island. The anomalous water vapor entering North China between the anomalous cyclone over Taiwan island and the anomalous anticyclone to the east of Japan was significant, reaching a 95% confidence level. Another cyclone marked as "CV" also provided abundant water vapor and brought more precipitation to North China.

Conclusion and discussions

Previous studies (Yan et al., 1990; Yatagai and Yasunari, 1994; Huang et al., 1999; Lu, 1999; Dai et al., 2003; Liu and Ding, 2010; Zhu et al., 2011) proved that North China had undergone interdecadal drought since the mid-1960s and mid-1970s. However, we discovered the SRNC was interdecadal wetter since the mid-2000s. The enhanced negative relationship between SRNC and PDO has occurred since 2006. Accompanied by an enhanced negative relationship between SRNC and PDO, the negative phase of PDO since 2006 resulted in a significantly wetter anomaly of SRNC, which is different from previous results that the SRNC has become drier since the mid-1960s and mid-1970s. The possible major mechanisms are summarized in Figure 14.

In Figure 14A, during 1979–2005, with PDO in the positive phase, the upper-level jet stream extended to North China, resulting in anomalous downdraft over southern North China and the anomalous northwest wind to the southeast of North China, both leading to less rainfall over North China. However, in Figure 14B, during the enhanced relationship period (2006–2021) between the PDO and SRNC with PDO in the negative phase, the upper-level jet stream was contractive to the west of North China, resulting in an anomalous updraft over southern North China, and the anomalous southwest wind was found to the southeast of North China, both leading to more rainfall over North China.

Except for the upper-level jet stream, the PDO influenced the SRNC mainly through the East Asia–Pacific (EAP) teleconnection pattern (Nitta, 1987; Huang & Sun, 1992; Qian & Zhou, 2014). During 2006–2021 in the positive phase of the EAP teleconnection pattern and negative phase of the PDO, the water vapor transport into North China was mainly from the eastern boundary. The water vapor transport was very different from that provided by the traditional southwest summer monsoon. However, this also suggested that the wetter anomaly of SRNC would not be stable because the recent water vapor budget would be easily changed by the summer monsoon variations in the future, which is worthy of constant attention and research.

Except for two known interdecadal decrease phenomena of SRNC since the mid-1960s and mid-1970s (Yan et al., 1990; Yatagai and Yasunari, 1994; Huang et al., 1999; Lu, 1999; Dai et al., 2003; Liu and Ding, 2010; Zhu et al., 2011), we firstly discover another interdecadal increase phenomenon of the SRNC in this study and the unstable relationship between SRNC and PDO. It is worth noting that the SST in the Indian Ocean and the Maritime Continent are a warm anomaly, which is very different from previous studies when PDO was in a negative phase (Ma, 2007; Qian and Zhou, 2014). In this study, we just used PDO to explain the wetter anomaly of SRNC. However, the other factors, such as the Arctic sea-ice (Wu et al., 1999; Liu H. et al., 2004) and CGT (Ding and Wang, 2005), also need to be further studied.

Data availability statement

The original contributions presented in the study are included in the article/supplementary material. Further inquiries can be directed to the corresponding author.

Author contributions

KW and HL conducted the analyses. HL supervised the study. KW, HL, LZ, YL, and ZY wrote the manuscript. KW, HL, LZ, YL, and ZY contributed to the discussion of the results.

Funding

This work was supported by the State Key Program of the Joint Fund of the National Natural Science Foundation of China and the Civil Aviation Administration of China (U2033207), the Civil Aviation Security Capacity Building Fund project (2146903), and Fundamental Research Funds for the Central Universities (Civil Aviation University of China, 3122019134).

Conflict of interest

The authors declare that the research was conducted in the absence of any commercial or financial relationships that could be construed as a potential conflict of interest.

Publisher's note

References

Allan, R. J. (2000). "ENSO and climatic variability in the last 150 years," in *El Niño and the southern oscillation: Multiscale variability, global and regional impacts*. *3–56*. Editors H. F. Diaz and V. Markgraf (Cambridge, UK: Cambridge University Press).

Chang, C.-P., Zhang, Y., and Li, T. (2000). Interannual and interdecadal variations of the east asian summer monsoon and tropical pacific SSTs. Part I: Roles of the subtropical ridge. *J. Clim.* 13 (24), 4310–4325. doi:10.1175/1520-0442(2000)013<4310:IAIVOT>2.0.CO;2

Dai, A. (2013). The influence of the inter-decadal Pacific oscillation on US precipitation during 1923–2010. *Clim. Dyn.* 41, 633–646. doi:10.1007/s00382-012-1446-5

Dai, X., Wang, P., and Chou, J. (2003). Multiscale characteristics of the rainy season rainfall and interdecadal decaying of summer monsoon in North China. *Chin. Sci. Bull.* 48 (24), 2730–2734. doi:10.1007/BF02901765

Ding, Q., and Wang, B. (2005). Circumglobal teleconnection in the northern hemisphere summer. *J. Clim.* 18 (17), 3483–3505. doi:10.1175/JCLI3473.1

Ding, Y. (1989). *The diagnostic and analysis method in synoptic dynamics*. Beijing: Science Press, 293. [in Chinese].

Hu, Z.-Z. (1997). Interdecadal variability of summer climate over East Asia and its association with 500 hpa height and global sea surface temperature. *J. Geophys. Res.* 102, 19403–19412. doi:10.1029/97JD01052

Huang, B., Thorne, P. W., Banzon, V. F., Boyer, T., Chepurin, G., Lawrimore, J. H., et al. (2017). Extended Reconstructed Sea surface temperature, version 5 (ERSSTv5), upgrades, validations, and intercomparisons. *J. Clim.* 30 (20), 8179–8205. doi:10.1175/JCLI-D-16-0836.1

Huang, R., and Sun, F. (1992). Impacts of the tropical western pacific on the east asian summer monsoon. *J. Meteorological Soc. Jpn.* 70, 243–256. doi:10.2151/jmsj1965.70.1B_243

Huang, R., Xu, Y., and Zhou, L. (1999). The interdecadal variation of summer precipitations in China and the drought trend in north China. *Plateau. Meteor* 18, 465–476. [in Chinese]. doi:10.3321/j.issn:1000-0534.1999.04.001

Joshi, M. K., and Kucharski, F. (2017). Impact of interdecadal pacific oscillation on Indian summer monsoon rainfall: An assessment from CMIP5 climate models. *Clim. Dyn.* 48, 2375–2391. doi:10.1007/s00382-016-3210-8

Joshi, M. K., Kucharski, F., Rai, A., and Kulkarni, A. (2021). "Indian summer monsoon and its teleconnection with Pacific decadal variability," in *Indian summer monsoon variability: El niño-teleconnections and beyond*. Editors J. Chowdary, A. Parekh, and C. Gnanaseelan (Elsevier), 375–390.

Joshi, M. K., and Pandey, A. C. (2011). Trend and spectral analysis of rainfall over India during 1901–2000. *J. Geophys. Res.* 116, D06104. doi:10.1029/2010JD014966

Joshi, M. K., and Rai, A. (2015). Combined interplay of the Atlantic multidecadal oscillation and the interdecadal Pacific oscillation on rainfall and its extremes over Indian subcontinent. *Clim. Dyn.* 44, 3339–3359. doi:10.1007/s00382-014-2333-z

Joshi, M. K., Rai, A., and Kulkarni, A. (2022). Global-scale interdecadal variability a skillful predictor at decadal-to-multidecadal timescales for Sahelian and Indian Monsoon Rainfall. *Npj Clim. Atmos. Sci.* 5, 2. doi:10.1038/s41612-021-00227-1

Kanamitsu, M., Ebisuzaki, W., Woollen, J., Yang, S.-P., Hnilo, J. J., Fiorino, M., et al. (2002). NCEP–DOE AMIP-II Reanalysis (R-2). *Bull. Am. Meteorol. Soc.* 83 (11), 1631–1644. doi:10.1175/BAMS-83-11-1631

Kulkarni, A., Rao, K. K., Joshi, M. K., Rai, A., and Darshana, P. (2021). in *ENSO-Indian summer monsoon teleconnections in Indian summer monsoon variability: El niño-teleconnections and beyond*. Editors J. S. Chowdary, A. Parekh, and C. Gnanaseelan (Elsevier), 51–68. ISBN 9780128224021. doi:10.1016/B978-0-12-822402-1.00024-7

Kumar, K. K., Rajagopalan, B., and Cane, M. A. (1999). On the weakening relationship between the Indian monsoon and ENSO. *Science* 284 (5423), 2156–2159. doi:10.1126/science.284.5423.2156

Li, C., and Li, G. (1999). Variation of the NAO and NPO associated with climate jump in the 1960s. *Chin. Sci. Bull.* 44, 1983–1987. doi:10.1007/BF02887124

Li, C., and Liao, Q. (1996). Quasi-decadal oscillation of climate in east asia/northwestern pacific region and possible mechanism. *Clim. Environ. Res.* 1, 124–133. [in Chinese]. doi:10.3878/j.issn.1006-9585.1996.02.03

Li, G., Li, C., Yan, H., Jiang, X., and Ju, Y. (2020). The relationships of mid-summer rainfall over North China with north Pacific decadal oscillation and south Pacific decadal oscillation and their possible physical machenism. *Chin. J. Geophys.* 63 (11), 3952–3966. [in Chinese]. doi:10.6038/cjg2020N0417

Liang, P., Duan, L., Zhou, M., and Zhou, L. (2006). Circulation patterns for mid-summer drought/flood in north China and their early summer precursors. *Acta. Meteor. Sin.* 64, 385–391. [in Chinese]. doi:10.11676/qxxb2006.037

Liu, H., and Ding, Y. (2010). Analysis of daily precipitation characteristics over North China during summer seasons. *Chin. J. Atmos. Sci.* 34 (1), 12–22. [in Chinese]. doi:10.3724/SP.J.1037.2010.00186

Liu, H., Guo, P., and Zhang, J. (2004b). The interannual relationship between Davis Strait sea-ice and rainfall of North China and its decadal variability. *J. Nanjing. Inst. Meteor.* 27, 253–257. [in Chinese]. doi:10.13878/j.cnki.dqkxxb.2004.02.015

Liu, H., Miao, J., Wu, K., Du, M., Zhu, Y., and Hou, S. (2020). Why the increasing trend of summer rainfall over North China has halted since the mid-1990s. *Adv. Meteorology* 2020, 1–10. doi:10.1155/2020/9031796

Liu, H. W., Guo, P. W., and Zhang, J. (2004a). The interannual relationship between Davis Strait sea-ice and rainfall of North China and its decadal variability. *J. Nanjing Inst. meteor* 27 (2), 253–257. [in Chinese]. doi:10.3969/j.issn.1674-7097.2004.02.015

Liu, H. W., Zhou, T. J., Zhu, Y. X., and Lin, Y. H. (2012). The strengthening East Asia summer monsoon since the early 1990s. *Chin. Sci. Bull.* 57, 1553–1558. doi:10.1007/s11434-012-4991-8

Lu, R. (1999). Interdecadal variations of precipitations in various months of summer in north China. *Plateau. Meteor* 18, 510–519. [in Chinese]. doi:10.3321/j.issn:1000-0534.1999.04.005

Ma, Z., and Fu, C. (2006). Some evidence of drying trend over northern China from 1951 to 2004. *Chin. Sci. Bull.* 51, 2913–2925. doi:10.1007/s11434-006-2159-0

Ma, Z. (2007). The interdecadal trend and shift of dry/wet over the central part of North China and their relationship to the pacific decadal oscillation (PDO). *Chin. Sci. Bull.* 52, 2130–2139. doi:10.1007/s11434-007-0284-z

Mantua, N. J., Hare, S. R., Zhang, Y., Wallace, J. M., and Francis, R. C. (1997). A Pacific interdecadal climate oscillation with impacts on salmon production. *Bull. Am. Meteorol. Soc.* 78, 1069–1079. doi:10.1175/1520-0477(1997)078<1069:APICOW>2.0.CO;2

Menon, S., Hansen, J., Nazarenko, L., and Luo, Y. (2002). Climate effects of black carbon aerosols in China and India. *Science* 297, 2250–2253. doi:10.1126/science.1075159

Mohino, E., Janicot, S., and Bader, J. (2011). Sahel rainfall and decadal to multi-decadal sea surface temperature variability. *Clim. Dyn.* 37, 419–440. doi:10.1007/s00382-010-0867-2

Nitta, T. (1987). Convective activities in the tropical western pacific and their impact on the northern hemisphere summer circulation. *J. Meteorological Soc. Jpn.* 65, 373–390. doi:10.2151/jmsj1965.65.3_373

Nitta, T., and Hu, Z. Z. (1996). Summer climate variability in China and its association with 500 hPa height and tropical convection. *J. Meteorological Soc. Jpn.* 74, 425–445. doi:10.2151/jmsj1965.74.4_425

Pei, L., Yan, Z., and Yang, H. (2015). Multidecadal variability of dry/wet patterns in eastern China and their relationship with the pacific decadal oscillation in the last 413 years. *Chin. Sci. Bull.* 60, 97–108. [in Chinese]. doi:10.1007/s00382-014-2141-5

Power, S., Casey, T., Folland, C., Colman, A., and Mehta, V. (1999). Inter-decadal modulation of the impact of ENSO on Australia. *Clim. Dyn.* 15, 319–324. doi:10.1007/s003820050284

Power, S., Tseitkin, F., Torok, S., Lavery, B., Dahni, R., and McAvaney, B. (1998). Australian temperature, Australian rainfall and the southern oscillation, 1910-1992: Coherent variability and recent changes. *Aust. Meteorol. Mag.* 47, 85–101. doi:10.1016/S1352-2310(97)00414-7

Qian, C., and Zhou, T. (2014). Multidecadal variability of North China aridity and its relationship to PDO during 1900-2010. *J. Clim.* 27, 1210–1222. doi:10.1175/JCLI-D-13-00235.1

Quan, M., Liu, H. W., Zhu, Y. X., and Cheng, L. (2013). Study of the dynamic effects of upper-level jet stream on the Beijing rainstorm of 21 July 2021. *Acta Meteor Sin.* 71, 1012–1019. *[in Chinese]*. doi:10.11676/qxxb2013.092

Tao, S. (1980). *Heavy rainstorm in China*. Beijing: Science Press, 115. [in Chinese].

Villamayor, J., and Mohino, E. (2015). Robust Sahel drought due to the interdecadal pacific oscillation in CMIP5 simulations. *Geophys. Res. Lett.* 42, 1214–1222. doi:10.1002/2014GL062473

Wang, H., and He, S. (2015). the North China/northeastern Asia severe summer drought in 2014. *J. Clim.* 28, 6667–6681. doi:10.1175/JCLI-D-15-0202.1

Wang, H. (2001). The weakening of the asian monsoon circulation after the end of 1970's. *Adv. Atmos. Sci.* 18, 376–386. doi:10.1007/BF02919316

Wu, B., Huang, R., and Gao, D. (1999). Impacts of long-range variations of winter sea-ice extents in arctic on rainfall in north China. *Plateau. Meteor* 18, 590–594. [in Chinese]. doi:10.3321/j.issn:1000-0534.1999.04.014

Xie, P., Yatagai, A., Chen, M., Hayasaka, T., Fukushima, Y., Liu, C., et al. (2007). A gauge-based analysis of daily precipitation over East Asia. *J. Hydrometeorol.* 8, 607–626. doi:10.1175/JHM583.1

Yan, Z., Ji, J., and Ye, D. (1991). Northern hemispheric summer climatic jump in the 1960's (II)—sea Level pressure and 500 hPa height. *Sci. China Ser. B* 34, 87–96.

Yan, Z., Ji, J., and Ye, D. (1990). Northern hemispheric summer climatic jump in the 1960's (I)—rainfall and temperature. *Sci. China Ser. B* 33, 1092–1101.

Yang, F., and Lau, K. (2004). Trend and variability of China precipitation in spring and summer: Linkage to sea-surface temperatures. *Int. J. Climatol.* 24, 1625–1644. doi:10.1002/joc.1094

Yatagai, A., and Yasunari, T. (1994). Trends and decadal-scale fluctuations of surface air temperature and precipitation over China and Mongolia during the recent 40 Year period (1951-1990). *J. Meteorological Soc. Jpn.* 72 (6), 937–957. doi:10.2151/jmsj1965.72.6_937

Yu, R., and Zhou, T. (2007). Seasonality and three-dimensional structure of interdecadal change in the east asian monsoon. *J. Clim.* 20, 5344–5355. doi:10.1175/2007JCLI1559.1

Zhang, Y., Wallace, J. M., and Battisti, D. S. (1997). ENSO-Like interdecadal variability: 1900–93. *J. Clim.* 10, 1004–1020. doi:10.1175/1520-0442(1997)010<1004:ELIV>2.0.CO;2

Zhu, Y., Wang, H., Zhou, W., and Ma, J. (2011). Recent changes in the summer precipitation pattern in east China and the background circulation. *Clim. Dyn.* 36, 1463–1473. doi:10.1007/s00382-010-0852-9

frontiers | Frontiers in Earth Science

TYPE Original Research
PUBLISHED 01 September 2022
DOI 10.3389/feart.2022.994876

OPEN ACCESS

EDITED BY
Shangfeng Chen,
Institute of Atmospheric Physics (CAS), China

REVIEWED BY
Chujie Gao,
Hohai University, China
Yongli He,
Lanzhou University, China
Yaocun Zhang,
Nanjing University, China

*CORRESPONDENCE
Yuan Sun,
sunyuan1214@126.com

SPECIALTY SECTION
This article was submitted to Atmospheric Science, a section of the journal Frontiers in Earth Science

RECEIVED 15 July 2022
ACCEPTED 08 August 2022
PUBLISHED 01 September 2022

CITATION
Lv S, Sun Y, Zhong Z and Shen Y (2022), Possible reasons for the migration of tropical cyclone track over the western north pacific: Interdecadal pacific oscillation modulation.
Front. Earth Sci. 10:994876.
doi: 10.3389/feart.2022.994876

Possible reasons for the migration of tropical cyclone track over the western north pacific: Interdecadal pacific oscillation modulation

Shuo Lv[1], Yuan Sun[1]*, Zhong Zhong[1] and Yixuan Shen[2]

[1]College of Meteorology and Oceanography, National University of Defense Technology, Changsha, Hunan, China, [2]PLA Troop 32033, Haikou, Hainan, China

Recent studies have proposed a relatively reliable metric, i.e., the annual-mean latitude of tropical cyclone (TC) lifetime maximum intensity, to evaluate the observed trend of poleward migration of TC. The documented trend in the existing records of the metric suggests that anthropogenic factors might make considerable contributions to the poleward migration of TC. However, here we show that there is no significant TC migration trend in the western North Pacific (WNP). Instead, large interdecadal variation is found in the WNP TC track over the past 35 years. Rather than the anthropogenic factors, it is the natural variability, especially the Interdecadal Pacific Oscillation (IPO), that plays a key role in modulating the migration of WNP TC track. The IPO-related TC migration is assumed to cause systematic changes (i.e., increases and decreases) in regional hazard exposure and risk. The impact of IPO on the WNP TC migration is attributed to its influences on the large-scale circulation, TC genesis potential index, and the potential intensity in the TC prevailing region of the WNP.

KEYWORDS

tropical cyclones, poleward migration, anthropogenic, natural variability, IPO

1 Introduction

In the context of global warming and considering the economic damages and catastrophes resulting from tropical cyclones (TCs) in various ocean basins, it is of great interest and societal importance to understand whether some changes of the TC activity may occur outside of natural variability and thus can be attributed to anthropogenic forcing (Knutson et al., 2010; Wang et al., 2011; Lee et al., 2012; Kossin et al., 2014; Kossin et al., 2016; Lee et al., 2020). While great progress has been made in evaluating the impact of global warming on TC intensity and TC-induced rainfall (Knutson et al., 2010), by far relatively little is known about the anthropogenically forced changes in the current climate (Wang et al., 2011; Kossin et al., 2014).

Over the past 30 years, the annual-mean latitude where tropical cyclones (TCs) reach their lifetime maximum intensity (LMI) has significantly migrated poleward in the northern and southern hemispheres, which potentially would have profound impacts on life and property safety (Kossin et al., 2014). Increasing mortality risks and hazard exposures from TCs (Peduzzi et al., 2012) may be compounded in coastal cities at higher latitudes, while they might possibly be offset at lower latitudes (Cardon et al., 2012; Kossin et al., 2016). TCs from the western North Pacific (WNP), which is also the most active basin hosting the largest TC genesis numbers on earth, make the largest contribution to the trend of TC poleward migration in the northern hemisphere (Kossin et al., 2014; Kossin et al., 2016).

Recent studies suggested that the observed trend of WNP TC poleward migration can be attributed to a conflation of anthropogenic and natural factors (Shen et al., 2018). With a substantial portion occurring outside the dominant known modes of variability in the region [i.e., El Niño–Southern Oscillation (ENSO) and Pacific Decadal Oscillation (PDO)] (Ho et al., 2004; Camargo et al., 2007a; Liu & Chan, 2008; Kossin et al., 2010; Zhang et al., 2012; Liu & Chan, 2013; Wang & Wang, 2013; Mei et al., 2015), it is argued that the TC migration may be related to other forms of slow decadal forcing (possibly anthropogenic forcing) (Kossin et al., 2014; Kossin et al., 2016). ENSO and PDO are known to affect the large-scale environment and thus the genesis and trajectories of the WNP TCs, which eventually contribute to the WNP TC migration (Kossin et al., 2016; Camargo et al., 2007a). However, other variabilities (except for ENSO and PDO) may also contribute to the WNP TC migration, which, if anything, will raise the uncertainty in the contribution of anthropogenic forcing. The Interdecadal Pacific Oscillation (IPO), which is similar to the PDO but occurs over a wider area of the Pacific (Power et al., 1999; Folland et al., 2002; Henley et al., 2015), is expected to considerably contribute to the WNP TC migration. Nevertheless, no studies on the contribution of IPO to the WNP TC migration have been conducted yet. Moreover, despite some studies on recent changes of TC track and exposure under global warming conditions (Knutson et al., 2010; Wang et al., 2011; Lee et al., 2012; Kossin et al., 2014; Kossin et al., 2016), how the natural variability and anthropogenic forcing affect the WNP TC migration still remain unclear.

Here we try to address these issues by analyzing the observations during the 41-year period of 1980–2020, when the best-track data are considered to be most complete and with the highest quality in terms of both TC position and TC intensity due to the monitoring of geostationary satellites (Kalnay et al., 1996; Knapp & Kruk, 2010; Dee et al., 2011; Kossin et al., 2014). We focus on the contribution of IPO to the observed TC migration in the WNP, which has been proved to be an important issue but is underestimated and even ignored in the previous studies.

2 Data and methods

2.1 Climate index

The index "Niño 3.4" (5°N–5°S, 140°E–145°W) defined over this region is widely used to represent the ENSO index, which is available at http://www.esrl.noaa.gov/psd/gcos_wgsp/Timeseries/Nino34/. The "Pacific Decadal Oscillation" (PDO) is a long-lived El Niño-like pattern of Pacific climate variability (Mantua et al., 1997; Christensen, 2013). The PDO index is defined as the projections of monthly mean SST anomalies onto their first EOF vectors in the North Pacific (north of 20oN) (Mantua et al., 1997). The EOF vectors are derived for the period from 1900 to 1993, and climatological value is defined as monthly mean for the same period. Globally averaged monthly mean SST anomaly is subtracted from monthly mean SST anomaly of the Pacific Ocean north of 20°N before calculation of the first EOF vector for the purpose to remove the effect of global warming. The PDO index is available at https://www.esrl.noaa.gov/psd/gcos_wgsp/Timeseries/PDO/. The Interdecadal Pacific Oscillation (IPO) and the PDO are closely related modes of decadal to interdecadal climate variability in the Pacific Ocean (Mantua et al., 1997; Power et al., 1999; Folland et al., 2002; Christensen, 2013; Henley et al., 2015). The PDO can be considered as the North Pacific node of the Pacific-wide IPO (Power et al., 1999; Folland et al., 2002). The IPO is associated with a distinct "tripole" pattern of SST anomalies, and the IPO Tripole Index (TPI) is calculated as follows based on monthly global SST data (Henley et al., 2015): Firstly, subtract the monthly climatological value from SST in each grid cell to eliminate the seasonal cycle and calculate monthly mean SST anomalies ($SSTA_i$) in the three TPI regions using a chosen base period (1971–2000 used here). TPI regions are defined as follows: region 1 (25°N–45°N, 140°E–145°W); region 2 (10°S–10°N, 170°E–90°W); region 3 (50°S–15°S, 150°E–160°W). Secondly, the TPI is calculated as follows:

$$TPI = SSTA_2 - \frac{SSTA_1 + SSTA_3}{2}$$

The TPI is also available at https://www.esrl.noaa.gov/psd/data/timeseries/IPOTPI/.

SST data are taken from the US National Oceanic and Atmospheric Administration Extended Reconstruction of SST (NOAA-ERSST; Smith & Reynolds, 2003), which is a global gridded dataset reconstructed based on historical observations of SST data using statistical methods. This dataset has spatial

resolution of 2°×2° and temporal resolution of monthly, and the scope of this paper is global (0°–360°, 90°N-90°S).

2.2 Genesis potential index , potential intensity , and large-scale environmental flow

GPI has important indicative significance for the generation of TCs and has been widely used in the study of TCs. Its definition is as follows:

$$\mathrm{GPI} = \left|10^5 \eta_{850}\right|^{3/2} \times (1 + 0.1 \times V_{shear})^{-2} \times \left(H_{600}/50\right)^3 \times \left(PI/70\right)^3$$

Where η_{850} represents the vorticity of 850 h Pa, V_{shear} represents the vertical wind shear between 850 h Pa and 200 h Pa, H_{600} represents the relative humidity of 600 h Pa, and PI is the potential intensity. PI describes the thermodynamically-based maximum TC intensity that the environment will support and thus is closely associated with TC genesis and intensification. In conjunction with the work of Emanuel (1999), it is defined as follows:

$$PI^2 = \frac{C_k}{C_D} \times \frac{T_s}{T_0} \times \left(CAPE^* - CAPE^b\right)$$

where C_k and C_D represent exchange coefficient for enthalpy and drag coefficient respectively, T_s and T_0 represent sea surface temperature and average outflow temperature respectively. CAPE is the convective available potential energy, and $CAPE^*$ represents the CAPE value when an air mass within the radius of the maximum wind speed reaches saturation for the first time under the current SST and barometric conditions. $CAPE^b$ represents the value of CAPE of the air parcel in the surrounding boundary layer atmosphere reduced along the isotherm to the radius of the maximum wind speed. In our study, large-scale environmental flow is mainly represented by 500 hPa geopotential height and 850–300 hPa vertical-mean wind.

Note that the GPI, PI and large-scale environmental flow are all calculated from the National Centers for Environmental Prediction–National Center for Atmospheric Research Global Reanalysis (NCEP–NCAR) (Kalnay et al., 1996) data. This reanalysis dataset is using a state-of-the-art system to perform data assimilation with spatial resolution of 2.5×2.5 and temporal resolution of monthly. In this paper, these data are selected from 1980 to 2015, and the spatial range is the Western North Pacific region (100°E-180°, 0°-60°N).

2.3 TC data

Best-track data are obtained from the International Best Track Archive for Climate Stewardship (IBTrACS) v04r00 (Knapp et al., 2010; Knapp et al., 2018), which is available at http://www.ncdc.noaa.gov/ibtracs/. There are four best-track data provided by four different agencies in the WNP: the Joint Typhoon Warming Center (JTWC), Japan Meteorological Agency (JMA), China Meteorological Administration (CMA), and Hong Kong Observatory (HKO). Note that only TCs with LMI ≥35 kt and ≤1,000 hPa are used in our analysis.

2.4 CMIP5 data

To further examine the impact of anthropogenic forcing on meridional migration of WNP TCs in future, we use an ensemble of TCs generated by 14 CMIP5 models, which includes the twenty-first-century RCP4.5 and RCP8.5 projection simulations (Camargo, 2013). RCP4.5 (RCP8.5) is a scenario that stabilizes radiative forcing at 4.5 (8.5) W m^{-2} at the end of the century. CMIP5 models used in this paper include CanESM2, CCSM4, CSIRO Mk3.6.0, Fgoals-G2, GFDL CM3, GFDL-ESM2M, HADGEM2-ES, and INM-CM4.0. Ipsl-cm5a-lr, MIROC-ESM, MIROC5, MPI-ESM-LR, MRI-CGCM3, and NORESM1-M. RCP4.5 is a stabilization scenario and assumes that climate policies are invoked to achieve the goal of limiting emissions, while RCP8.5 corresponds to the pathway with the highest greenhouse gas emissions and is based on a presumption of no to little change from the present trajectories of greenhouse gas concentrations. RCP4.5 and RCP8.5 scenarios have better model coverage compared to the other scenarios, which is available at https://esgf-node.llnl.gov/search/cmip5/.

2.5 Residual analysis

The significance of residual analysis is to check whether the trend of TC poleward movement is still significant after removing the trend of natural variability from the trend of TC poleward migration. ENSO (PDO, IPO) variability is excluded from the annual-mean TC latitude at the time of LMI (φ_{LMI}) time series by regressing each individual φ_{LMI} series from the various best-track data onto the index of the Niño-3.4 (PDO, TPI) and analyzing the residuals named $\varepsilon_{\text{Niño-3.4}}$ ($\varepsilon_{\mathrm{PDO}}$, $\varepsilon_{\mathrm{TPI}}$). ENSO, PDO, and IPO variabilities are removed from the φ_{LMI} series by regressing the φ_{LMI} series onto the indices of Niño-3.4, PDO and TPI, and analyzing the residuals ($\varepsilon_{\mathrm{ALL3}}$).

3 Result

3.1 Insignificant trends of WNP TC poleward migration

The measurement of φ_{LMI} is much less uncertain, since the absolute LMI can be easily determined based on when the TC has reached its maximum intensity during its lifetime (Kossin et al., 2014). Because of the relatively short period of observation after

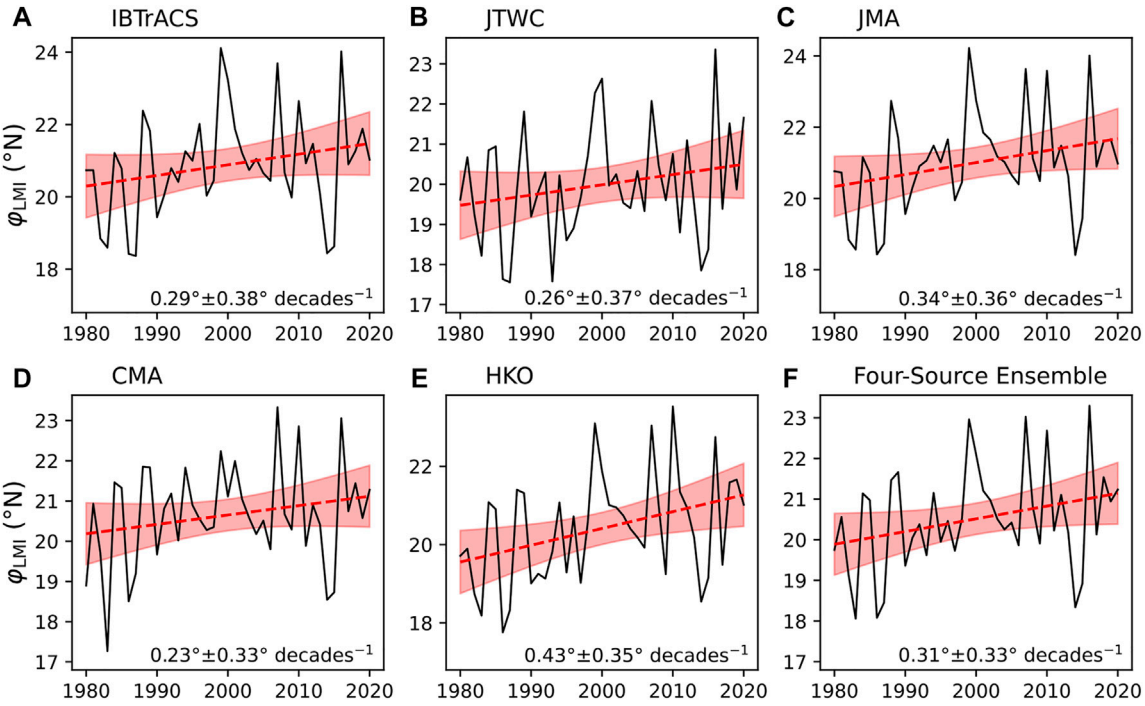

FIGURE 1
Migration of the location of LMI. Time series of annual-mean φ_{LMI} calculated from various best-track historical data over the WNP. **(A–F)** shows data from different sources, where **(A)** is IBTrACS, **(B)** is JTWC, **(C)** is JMA, **(D)** is CMA, **(E)** is HKO and **(F)** is the ensemble mean of JTWC, JMA, CMA and HKO. Linear trend lines (dashed) are shown with their 95% two-sided confidence intervals (shaded), which are also given by the annotated values.

TABLE 1 Linear trends of annual-mean latitude of LMI and its regression residuals for best-track data from various sources. The WNP TC track migration rates and 95% confidence intervals (latitude decade^{-1}) of annual-mean φ_{LMI}, the residuals of the regression of φ_{LMI} onto the JASON-mean Niño-3.4, PDO, and TPI indices (i.e., $\varepsilon_{Niño\text{-}3.4}$, ε_{PDO}, and ε_{TPI}) respectively and the residuals of the trivariate regression of φ_{LMI} onto the three indices (i.e., ε_{ALL3}) for the various best-track data sources. For the single-variate and trivariate regressions, the variance explained R^2 and the p value are also shown.

	IBTrACS	JTWC	JMA	CMA	HKO	Ensemble
φ_{LMI}	0.29 ± 0.38	0.26 ± 0.37	0.34 ± 0.36	0.23 ± 0.33	0.43 ± 0.35	0.31 ± 0.33
$\varepsilon_{Niño\text{-}3.4}$	0.30 ± 0.30	0.26 ± 0.33	0.34 ± 0.29	0.24 ± 0.29	0.44 ± 0.27	0.32 ± 0.27
R^2, p value	0.35, <0.001	0.19, 0.001–0.01	0.31, <0.001	0.21, 0.001–0.01	0.32, <0.001	0.29, <0.001
ε_{PDO}	0.11 ± 0.34	0.08 ± 0.33	0.15 ± 0.33	0.08 ± 0.30	0.21 ± 0.29	0.13 ± 0.28
R^2, p value	0.24, 0.001–0.01	0.22, 0.001–0.01	0.23, 0.001–0.01	0.20, 0.001–0.01	0.26, <0.001	0.29, <0.001
ε_{TPI}	0.03 ± 0.29	0.04 ± 0.31	0.08 ± 0.29	0.04 ± 0.28	0.15 ± 0.25	0.08 ± 0.25
R^2, p value	0.45, <0.001	0.30, <0.001	0.43, <0.001	0.32, <0.001	0.53, <0.001	0.45, <0.001
ε_{ALL3}	0.02 ± 0.29	−0.03 ± 0.31	0.04 ± 0.29	−0.03 ± 0.28	0.02 ± 0.25	−0.00 ± 0.25
R^2, p value	0.45, <0.001	0.32, 0.001–0.01	0.43, <0.001	0.33, 0.001–0.01	0.56, <0.001	0.47, <0.001

1980, the estimated trend of φ_{LMI} is highly sensitive to the sample size. For example, looking at the TCs in the IBTrACS best-track data during 1980–2013, the annual-mean φ_{LMI} (TC intensity is measured by maximum wind speed) in the western North Pacific shows a poleward migration trend (0.48 ± 0.46 latitude decade^{-1}), which is basically consistent with results of the previous studies (Kossin et al., 2014; Kossin et al., 2016). However, if the sample length is extended to 2020, the poleward migration trend decreases significantly (0.29 ± 0.38 latitude decade^{-1}) due to the low φ_{LMI} in 2014 and 2015 (Figure 1A; Table 1). Results based on other TC best-track data (i.e., JTWC, JMA, and CMA) also indicate that the poleward migration trend is no longer significant at the 95% confidence level when observations in 2014 and 2015 are considered (Table 1; Figures 1B–F) except

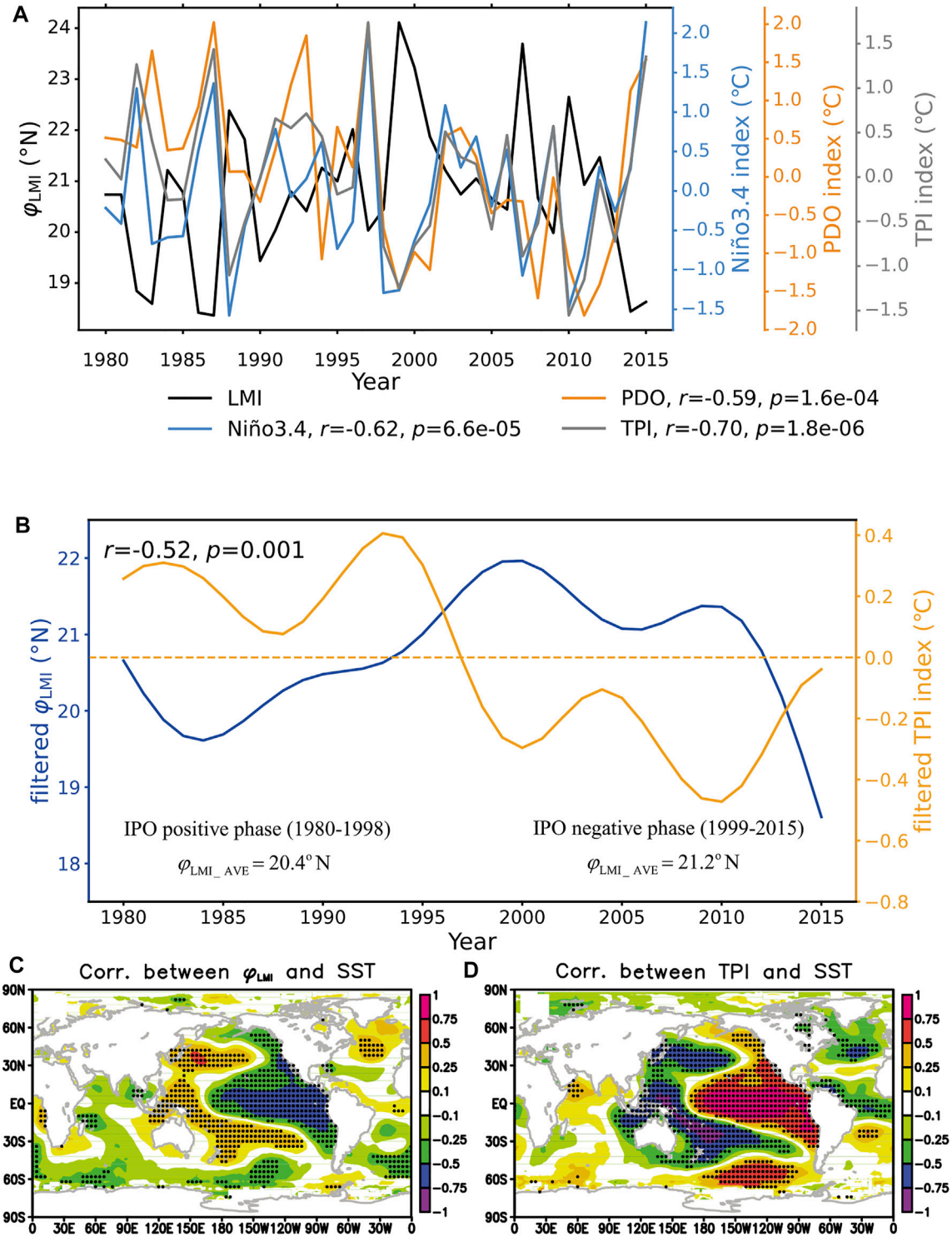

FIGURE 2
Relationship between the location of LMI over the WNP and the IPO. **(A)** Time series of annual-mean φ_{LMI} from the IBTrACS best-track data (black line) and JASON-mean TPI (grey line), Niño3.4 index (blue line), PDO (orange line); **(B)** Low pass filtered time series of TPI (orange line) and φ_{LMI} (blue line); **(C)** map of correlation coefficient between the annual-mean φ_{LMI} and JASON SST; and **(D)** map of correlation coefficient between the JASON TPI and JASON SST. The correlation coefficients (i.e., *r*) between φ_{LMI} and TPI or filtered TPI, and the *p*-value (i.e., *p*) for testing the hypothesis of no correlation are also shown in Figures 2A,B (annotated values). A 13-years Chebyshev low-pass filter is applied to obtain the filtered version of the two indices. The positive IPO phase corresponds to the period when the filtered TPI is no less than 0 °C (i.e., 1980–1998), while the IPO negative phase corresponds to the period when the filtered TPI is less than 0 °C (i.e., 1999–2015). The time-averaged φ_{LMI} in the two IPO phases are presented in Figure 2B (annotated values). Dotted areas in Figures 2C,D denote that the differences are significant at/above the 95% confidence level by the Student's *t* test.

HKO. More importantly, further analysis suggests that, rather than anthropogenic forcing, it is the natural variability that plays a critical role in modulating the migration of WNP TC track during the past 41 years.

3.2 Relationship between IPO and WNP TC migration

The variability of the WNP TC activity has received a large amount of attention during the past 2 decades, and many studies have linked TC track variability to ENSO (Camargo et al., 2007a; Liu & Chan, 2008) on interannual timescale. In recent years, the PDO has been found to have important influences on large-scale flow patterns and thus the TC track variability over the WNP (Liu & Chan, 2008; Mei et al., 2015). Here, averages of the ENSO (Niño-3.4), PDO, IPO (IPO tripole index, TPI) (Henley et al., 2015) indices are taken over July-November (JASON), which is considered as the peak TC season (about 80% of annual WNP TCs occur in these months) (Kossin et al., 2016). As expected, there is an inverse relationship between φ_{LMI} and the two indices (i.e., Niño-3.4 and PDO) with the correlation coefficients of −0.62 and −0.59 respectively, which indicate ENSO and PDO both have strong impacts on TC migration (Figure 2A). Moreover, compared with the ENSO and PDO, the IPO plays an even more important role in determining the WNP TC migration with a correlation coefficient of −0.70 between φ_{LMI} and TPI. Almost all the peaks of IPO negative (positive) values correspond to high (low) values of φ_{LMI} and φ_{LMI} increased dramatically during the transition of the IPO from positive to negative phase in the late 1990s (Meehl et al., 2013; Henley et al., 2015) (Figure 2A). Note that the low φ_{LMI} in 2014 and 2015 correspond to positive values of the TPI, which makes the poleward migration trend of φ_{LMI} insignificant when the study period is changed from 1980–2013 to 1980–2015. On the other hand, as the low frequency component of the IPO signal can be obtained by applying a 13-years Chebyshev low-pass filter to TPI (Henley et al., 2015), we calculated the filtered φ_{LMI} using the same filter, and found that the correlation coefficient between the filtered TPI and the filtered φ_{LMI} is −0.52, which is significant at the 99% confidence level (Figure 2B). This result strongly suggests that there is a significant inverse correlation between IPO and the WNP TC migration on interdecadal timescale. In addition, the map of correlation coefficient between φ_{LMI} and SST presents a pattern highly similar to the map of correlation coefficient between TPI and SST (Figures 2C,D). The latter displays a typical IPO pattern (see Figure 1 in the Henley et al., 2015) and thus provides robust evidence supporting the strong relationship between the WNP TC migration and IPO.

To further compare the contributions of various natural variabilities to the WNP TC migration, we calculate the residuals of annual-mean φ_{LMI} regressed onto the JASON-mean Niño-3.4, PDO, and TPI indices (i.e., $\varepsilon_{Niño\text{-}3.4}$, ε_{PDO}, and ε_{TPI}), respectively. The residuals of the trivariate regression of φ_{LMI} onto the three indices (i.e., ε_{ALL3}) are also calculated. For instance, ENSO is removed from the φ_{LMI} time series by regressing the φ_{LMI} series onto the Niño-3.4 index averaged over the peak TC season (July-November), and the residuals are analyzed. When the PDO and IPO variabilities are removed respectively, the residual TC migration rates (i.e., ε_{PDO}, and ε_{TPI}) are found to decrease substantially for various best-track data (Table 1; Figure 3). This suggests that the PDO and IPO considerably contribute to the TC migration rate. Moreover, as expected, the regression coefficients (i.e., R^2) are statistically significant, and the JASON-mean ENSO, PDO, IPO, and all these three indices together respectively explain 34.5%, 24.0%, 44.7%, and 44.7% of the φ_{LMI} variance in the IBTrACS best-track data (Table 1). These results further suggest that natural variability, especially IPO (Wang et al., 2013; Henley et al., 2015), whose contribution to the change of φ_{LMI} is similar to the total contribution of the three indices, is playing a critical role in the observed TC migration. Furthermore, when the IPO variability (i.e., time series of the TPI) is removed, the residual TC migration rate decreases significantly from 0.29 ± 0.38 latitude decade^{-1} (i.e., φ_{LMI} trend which is significant at 76% confidence level) to 0.03 ± 0.29 latitude decade^{-1} (see φ_{LMI} and ε_{TPI} in Table 1). This indicates that the poleward migration trend of the WNP TC track does not occur outside the IPO variability based on the observational records (1980–2020), and thus provides evidence against the proposed conclusions of previous studies on the contribution of anthropogenic factors to the TC poleward migration ((Kossin et al., 2014; Kossin et al., 2016). In this study, rather than studying the φ_{LMI} trend, we put emphasis on the close relationship between TC migration and IPO, especially the modulation of IPO on the WNP TC migration.

Despite the strong agreement between the two indices of PDO and IPO ($r = 0.75$), the IPO index (i.e., TPI) is based on the difference between SST averaged over the central equatorial Pacific and that over the northwestern and southwestern Pacific, and thus is substantially different from the PDO index which is mainly determined by SST in the North Pacific (north of 20oN) (Mantua et al., 1997). Thus, compared with the PDO index, the IPO index is more related to meridional and zonal gradients of SST over the WNP. The interdecadal changes of the SST gradients and related spatial SST distribution pattern make large contributions to the WNP TC migration, which will be discussed in detail in the next section.

3.3 Possible trend of WNP TC migration in future under global warming

As mentioned above, our observational results imply that the anthropogenic forcing does not contribute significantly to the observed WNP TC migration as expected. This also does not necessarily mean that the anthropogenic factors (e.g., global warming induced by greenhouse gases) will not significantly contribute to the poleward shift of the WNP TC in the future, since it is difficult to distinguish the contributions of anthropogenic

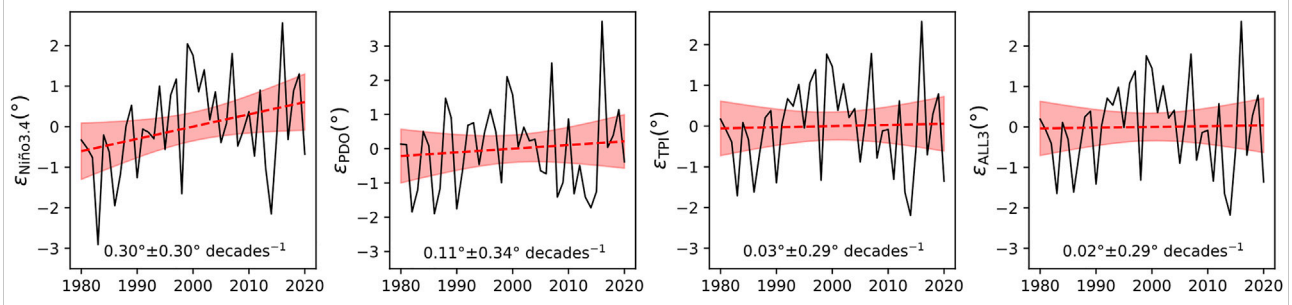

FIGURE 3
Possible effects of the three modes of variability on the migration of the latitude of LMI. Time series of **(A)** residuals of the single-variate of annual-mean φ_{LMI} onto JASON-mean Niño-3.4 index, **(B)** residuals of the single-variate of annual-mean φ_{LMI} onto JASON-mean PDO index, **(C)** residuals of the single-variate of annual-mean φ_{LMI} onto JASON-mean TPI index, and **(D)** residuals of the trivariate of annual-mean φ_{LMI} onto JASON-mean Niño-3.4, PDO, and TPI indices. Linear trend lines (dashed) are shown with their 95% two-sided confidence intervals (shaded), which are also shown by annotated values.

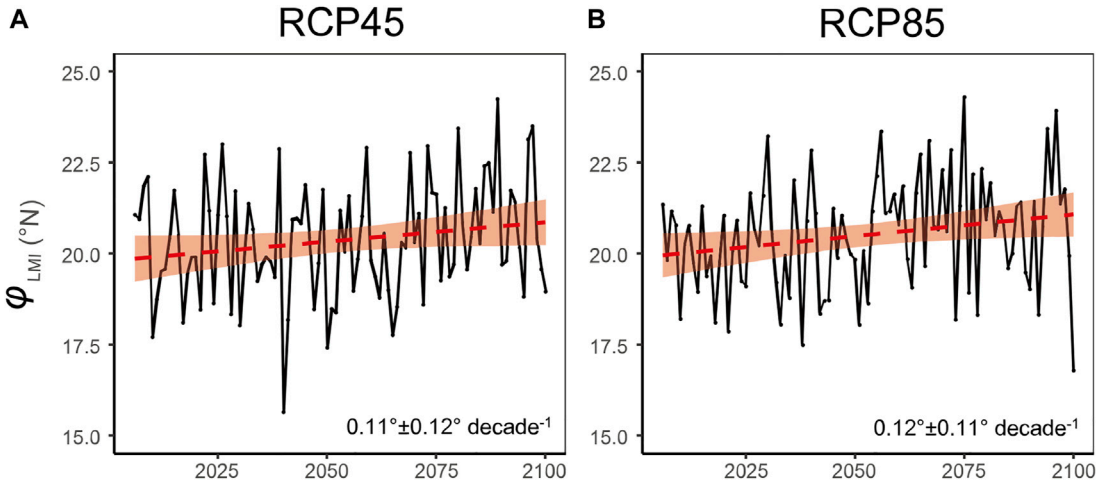

FIGURE 4
Projected migrations of the WNP TC in future under the two representative emission scenarios. Time series of annual-mean φ_{LMI} from WNP TCs explicitly generated in the 14 CMIP5 twenty-first-century **(A)** RCP4.5 and **(B)** RCP8.5 projection simulations.

forcing and natural variability based on the short time-period records (Allen et al., 2014; Lucas et al., 2014; Boo et al., 2015).

Thanks to the relatively long period (2006–2100) of RCP4.5 and RCP8.5 scenarios which is much longer than the period during which the known modes of natural variability are derived, it is relatively robust and reliable to draw the conclusions on the influence of anthropogenic forcing by using the results of these 14 CMIP5 models under the RCP4.5 and RCP8.5 scenarios. In the RCP4.5 projection simulations, the projected rate of migration of φ_{LMI} (0.11°±0.12° decade^{-1}) is insignificant just under the 95% confidence level (Figure 4). The difference in φ_{LMI} between RCP8.5 and RCP4.5 scenarios is hardly distinguishable, although the φ_{LMI} in RCP8.5 scenario (0.12°±0.11° decade^{-1}) is just at the 95% confidence level (Figure 4). Thereby, the projected rates of WNP TC migration are closely related to the carbon emission intensity, as the migration rates, in terms of φ_{LMI} trends, increase with the carbon emission intensity (Figure 4). In RCP4.5 scenario, the global warming remains unable to produce significant trend, indicating that the observed insignificant trend is confirmed in the model.

3.4 Possible mechanisms for the impact of IPO on WNP TC migration on interdecadal timescales

The φ_{LMI} of a TC is determined by TC genesis positon, TC intensity evolution and TC track pattern. The first determines the starting position of a TC during its lifetime, the second evolves before LMI is reached and controls when the LMI would occur during the TC lifetime, and the third determines the path of the

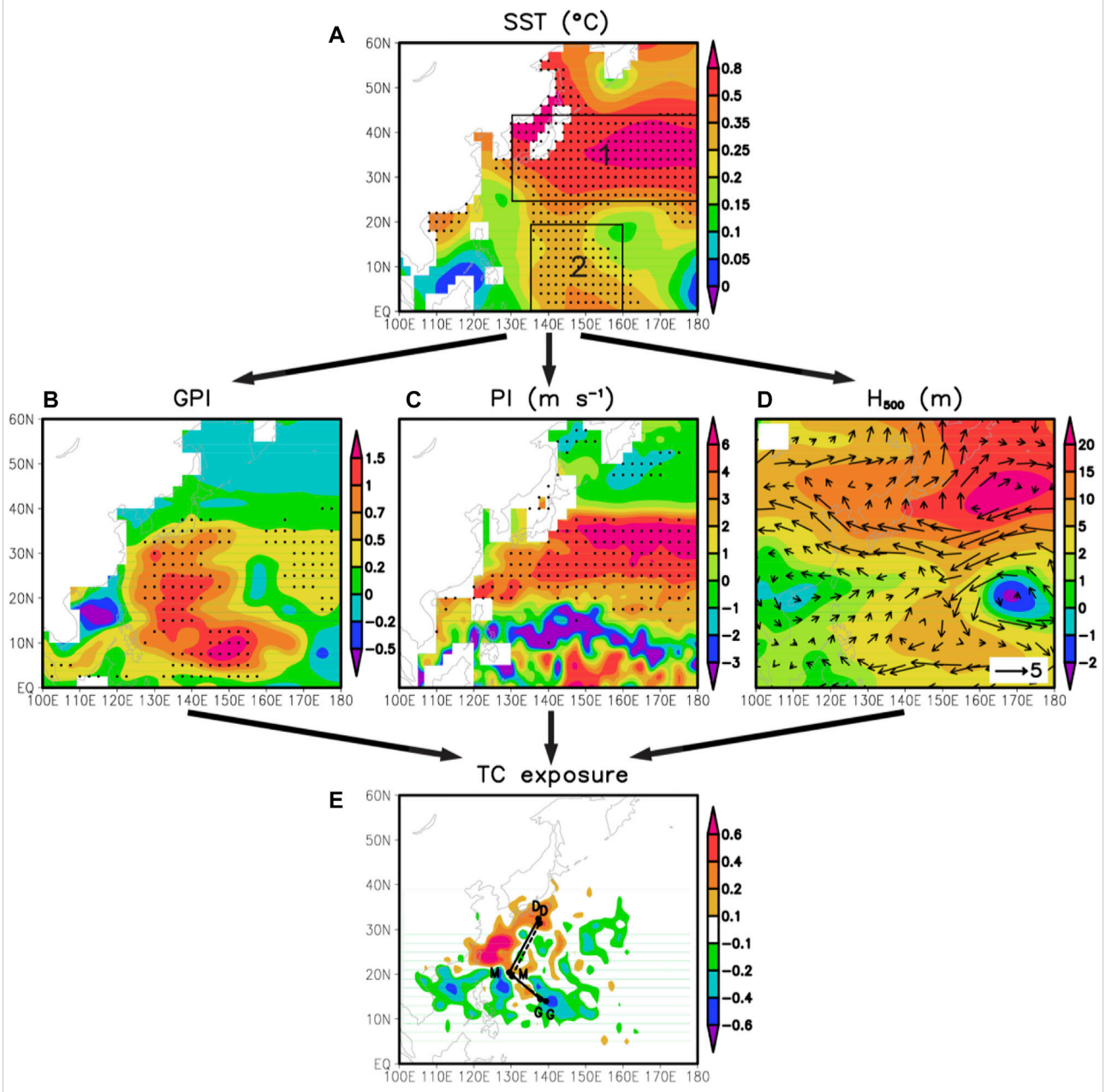

FIGURE 5
Differences in annual-mean JASON SST, GPI, PI, large-scale circulation, and TC exposure between negative IPO phase and positive IPO phase. **(A)** SST (°C), **(B)** GPI, **(C)** PI (m s^{-1}), **(D)** 500-hPa geopotential height (shaded; m) and 850–300 hPa vertical-mean wind (vectors; m s^{-1}), and **(E)** TC exposure (number of days of exposure per year per 2°×2° latitude–longitude grid box) and the positions of TC genesis (G), lifetime maximum intensity (M), and disappearance (D), which are depicted in dotted line in the positive IPO phase and in solid line in the negative IPO phase. The IPO negative phase refers to the period of 1980-1998, and the IPO positive phase refers to the period of 1999–2015. Dotted areas denote that the differences are significant at/above the 99% confidence level by the Student's *t* test. Black boxes indicate the two main regions where SST differences are significant at/above the 99% confidence (Region 1: 25°N-45°N, 130°E-180°E; Region 2: 0°N-20°N, 135°E-160°E).

TC and thus controls where the LMI would possibly occur during the TC lifetime. In this study, these three factors can be analyzed from the aspects of GPI, PI, and large-scale environmental flow respectively (Sun et al., 2020). Firstly, the GPI is widely used to analyze spatial distribution of TC genesis potential and the influence of environmental factors on tropical cyclogenesis (Camargo et al., 2007b). Secondly, PI is a known major factor modulating the TC intensity evolution (Emanuel, 1999). Thirdly,

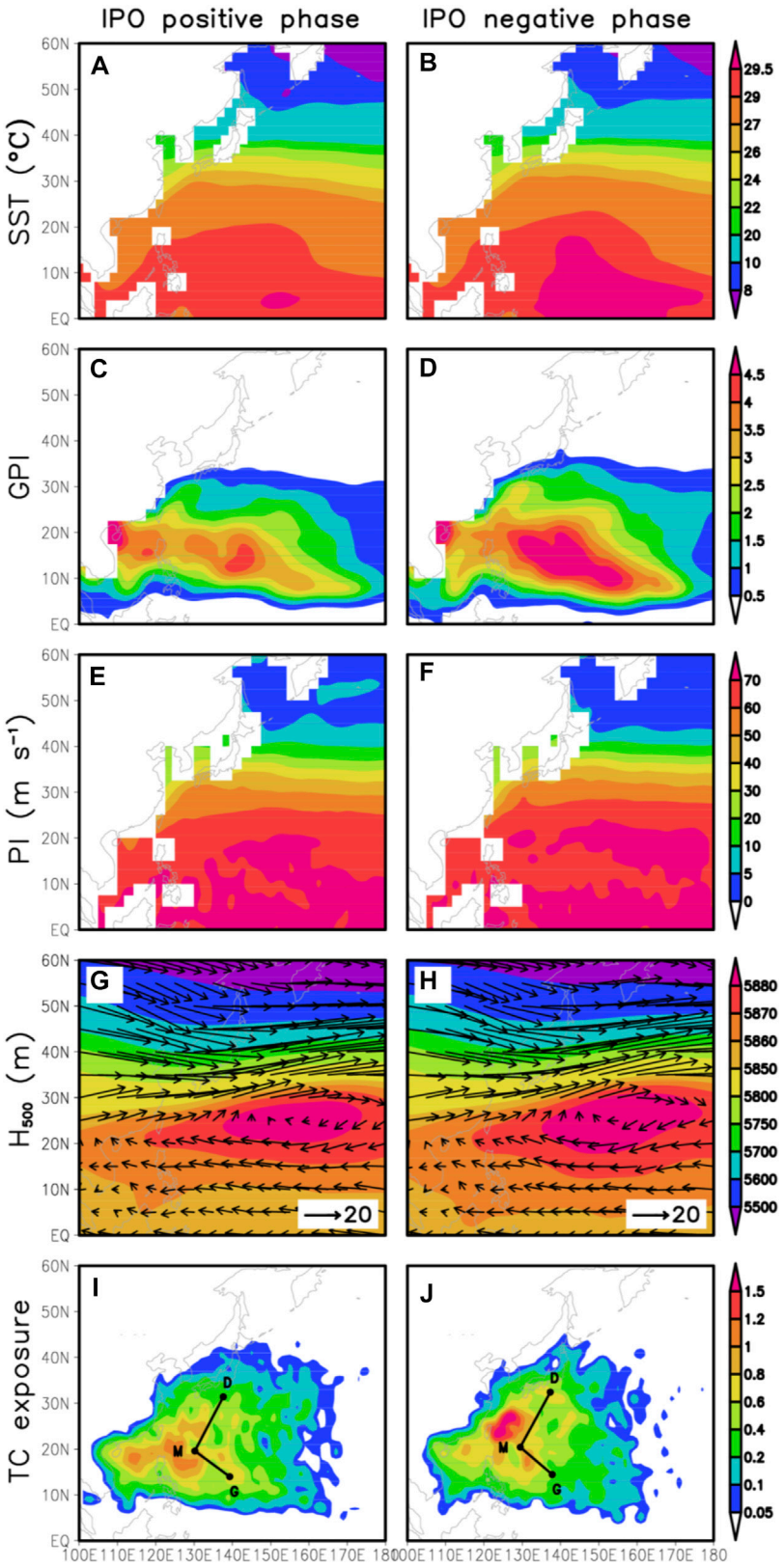

FIGURE 6
Annual-mean JASON SST, GPI, PI, large-scale circulation, and TC exposure during the positive IPO phase **(A,C,E and G)** and negative IPO phase **(B,D,F and H)**. **(A,B)** SST (°C); **(C,D)** GPI; **(E,F)** PI (m s^{-1}); **(G,H)** 500-hPa geopotential height (shaded; m) and 850–300 hPa vertically averaged wind (vectors; m s^{-1}); and **(I,J)** TC exposure (number of days of exposure per year per 2°×2° latitude–longitude grid box) and the positions of TC genesis (G), lifetime maximum intensity (M), and disappearance (D).

WNP TCs are usually steered by large-scale environmental flow, especially the flow in the main TC activity region (Chan & Gray, 1982; Sun et al., 2015), which modulates the geographical properties of TC track over the WNP. Therefore, the change of φ_{LMI} can always be attributed to changes in the GPI, PI and large-scale environmental flow.

Consistent with the previous studies (Burgman et al., 2008; Chen et al., 2008; Lee & McPhaden, 2008; Meehl & Arblaster, 2012; Henley et al., 2015), the IPO transferred from positive to negative phase in the late 1990s after the 1997–98 El Niño event. Thus, the period of 1980–1998 (1999–2015) can be considered as the positive (negative) IPO phase on interdecadal timescale (Figure 2B). Moreover, the time-averaged φ_{LMI} in the negative IPO phase (21.2°N) is notably higher than that in the positive IPO phase (20.4°N), which is significant above the 95% confidence level by the Two-sample *t*-test. The positive and negative phases of IPO are characterized by different regional patterns (Power et al., 1999; Folland et al., 2002; Henley et al., 2015), which are expected to play an important role in determining the GPI and PI spatial distributions and the large-scale environmental flow in the main TC activity region, and eventually affect φ_{LMI} of TCs over the WNP. However, based on what we understand, little is known about the impact of the regional pattern of IPO on the TC track migration. To further investigate the linkage between IPO and the WNP TC migration, we compare SST, GPI, PI, large-scale circulation, and TC exposure during the negative and positive IPO phases (Figure 5 and Figure 6). Note that, TC exposure is defined as the number of days per year per 2×2 latitude–longitude grid box when a TC center is located in that grid box.

During the transitional period from the positive IPO phase to negative IPO phase over the WNP, there are two main regions (Region 1 25°N-45°N, 130°E-180°E; Region 2 0°N-20°N, 135°E-155°E) where positive SST anomalies are significant at/above the 99% confidence level (Figure 5A). At first, the higher SST in Region 1 and Region 2 contribute to the significant increase of GPI in the three ocean areas (i.e., an ocean area to the south of Japan, an ocean area near the equator, and an ocean area near the central North Pacific). Compared with the first area that is to the north of the main WNP TC genesis area (see Figures 6C,D), the latter two areas are relatively farther from the main genesis region of WNP TC and thus contribute relatively smaller to the migration of TC genesis position (Figure 5B). Under the joint effects of GPI changes in the three areas, the time-averaged TC genesis position shifts poleward by 0.47 latitude (Figure 5E). Moreover, the higher SST in Region 1 leads to a relatively higher PI that favors further development of TCs at the high latitudes over the region (Figure 5C and Figures 6E,F), and eventually leads to the poleward shift of φ_{LMI}. More importantly, the higher SST in Region 2 induces positive geopotential height anomalies in this region as the ocean warming is favorable for the development of the deep warm high (i.e., WPSH) in the non-equatorial region (>5°N), which favors westward expansion of the WPSH over *Region 2* (Figure 5D and Figures 6G,H). The anticyclonic anomaly in the western boundary of the westward-expanded WPSH contributes to increases in the northward steering flow over the area of 10°N-22°N, 120°E-135°E, which tends to promote northward turning of westward moving TCs over the area (Figure 5D). In addition to the poleward shift of φ_{LMI}, the intensified northward steering flow also contributes to the increase in TC exposure over the regions of Taiwan, Ryukyu Islands, the southern coast of Japan, and the southeastern coast of China, but decreases TC exposure in the regions of Hainan, Vietnam, and Philippines (Figure 5E). Note that the response of equatorial circulations to higher SST is substantially different to that of mid- and low-latitude circulations. Over the equatorial area in Region 2, the prevailing easterly winds basically agree with the theory of Gill model (Gill, 2010), which indicates that an equatorial heating (e.g., SST warming) produces easterly flow over the eastern region of the heating (Figure 5D). Overall, due to the response of GPI, PI and large-scale flow to IPO, the WNP TCs tend to originate and intensify at high latitudes and turn poleward over certain regions, which contributes to the poleward shift of the location of LMI during the IPO transition period from positive to negative phase in the late 1990s.

4 Conclusion

This paper investigates that IPO impact on Migration of Tropical Cyclone Track over the Western North Pacific. We found that the location where TCs reach their lifetime maximum intensity (LMI) moved northward with a trend of 0.29 ± 0.38 latitude decade-1 from 1980 to 2020. But the trend was not significant, which is consistent across different datasets. The correlation analysis shows that the correlation coefficient between TC latitude at the time of LMI (φ_{LMI}) and JASON-mean TPI from 1980 to 2020 is as high as −0.70, and the PDO is −0.59, and the Niño3.4 index is −0.62. When applying a 13-years Chebyshev low-pass filter to TPI and φ_{LMI}, the correlation coefficient is −0.52, passed the 95% significance test. In order to study the effect of these natural variability on the motion of φ_{LMI}, we remove these three natural variability trends from φ_{LMI}. and the JASON-mean ENSO, PDO, IPO, and all these three indices together respectively explain 34.5%, 24.0%, 44.7%, and 44.7% of the φ_{LMI} variance. When the IPO variability is removed, the residual TC migration rate decreases significantly from 0.29 ± 0.38 latitude decade-1 to 0.03 ± 0.29 latitude decade-1. This phenomenon is inconsistent with the previous conclusion that human factors contribute to the polar movement of TC. Therefore, 14 CMIP5 models under the RCP4.5 and RCP8.5 Scenarios were used to investigate the anthropogenic contribution of TC to polar mobility. The results show that the poleward movement trend of TC is not as obvious as that during the observation period. In order to further explore why IPO affects TC poleward movement, genesis potential index (GPI),

potential intensity (PI), and large-scale environmental flow are analyzed respectively because of their contribution to TC genesis position, TC intensity evolution and TC track pattern. There are two main regions (Region 1 25°N-45°N, 130°E-180°E; Region 2 0°N-20°N, 135°E-155°E) where positive SST anomalies are significant at above the 99% confidence level, which contribute to the significant increase of GPI in the three ocean areas and induce a relatively higher PI that promotes further extension of TCs at the high latitudes over the region. The higher SST in Region 2 contributes to positive geopotential height anomalies that can lead to increases in the northward steering flow over the area of 10°N-22°N, 120°E-135°E, which helps TC's poleward shift.

In the following work, we will continue to study the contribution of various natural variability, including IPO, to the poleward movement of TC in future scenarios. We will also continue to use the latest numerical weather patterns on the impact of human activities on the TC for further explanation. We believe that human activity to a certain extent, also affect the change of the TC. However, further research is needed to determine whether this effect will affect TC as human activities affect natural variability, or directly affect TC itself.

Data availability statement

The original contributions presented in the study are included in the article/Supplementary Material, further inquiries can be directed to the corresponding author.

Author contributions

YS conceived the project. SL analyzed the results, produced the figures, and wrote the manuscript with contributions from ZZ, YUS and YIS wrote the codes on produced the TC data in CMIP5 models. ZZ advised on physical interpretation of IPO Modulation on TC track Migration.

Funding

This work is supported by the National Natural Science Foundation of China (No. 42075035 and 42075011).

Conflict of interest

The authors declare that the research was conducted in the absence of any commercial or financial relationships that could be construed as a potential conflict of interest.

Publisher's note

References

Allen, R. J. Norris, J. R. and Kovilakam, M. (2014). Influence of anthropogenic aerosols and the Pacific decadal oscillation on tropical belt width. *Nat. Geosci.* 7, 270–274. doi:10.1038/ngeo2091

Boo, K.-O. Booth, B. B. Byun, Y.-H. Lee, J. Cho, C. Shim, S., et al. (2015). Influence of aerosols in multidecadal SST variability simulations over the North Pacific. *J. Geophys. Res. Atmos.* 120, 517–531. doi:10.1002/2014jd021933

Burgman, R. J. Clement, A. C. Mitas, C. M. Chen, J. and Esslinger, K. (2008). Evidence for atmospheric variability over the Pacific on decadal timescales. *Geophys. Res. Lett.* 35, L01704. doi:10.1029/2007GL031830

Camargo, S. J. (2013). Global and regional aspects of tropical cyclone activity in the CMIP5 models. *J. Clim.* 26, 9880–9902. doi:10.1175/jcli-d-12-00549.1

Camargo, S. J. Kmanuel, K. A. and Sobel, A. H. (2007b). Use of a genesis index to diagnose ENSO effects on tropical cyclone genesis. *J. Clim.* 20, 4819–4834. doi:10.1175/JCLI4282.1

Camargo, S. J. Robertson, A. W. Gaffney, S. J. Smyth, P. and Ghil, M. (2007a). Cluster analysis of typhoon tracks. Part II: Large-scale circulation and ENSO. *J. Clim.* 20, 3654–3676. doi:10.1175/jcli4203.1

Cardon, O. D. Maarten, V. A. Joern, B. Maureen, F. Glenn, M. and Mechler, R. (2012). "Determinants of risk: Exposure and vulnerability." in *Managing the risks of extreme events and disasters to advance climate change adaptation*. Cambridge, United Kingdom: Cambridge University Press.

Chan, J. C. L. and Gray, W. M. (1982). Tropical cyclone movement and surrounding flow relationships. *Mon. Wea. Rev.* 110, 1354–1374. doi:10.1175/1520-0493(1982)110<1354:tcmasf>2.0.co;2

Chen, J. Del Genio, A. D. Carlson, B. E. and Bosilovich, M. G. (2008). The spatiotemporal structure of twentieth-century climate variations in observations and reanalyses. Part II: Pacific pan-decadal variability. *J. Clim.* 21, 2634–2650. doi:10.1175/2007jcli2012.1

Christensen, J. H. (2013). "Climate phenomena and their relevance for future regional climate change." in *Climate change 2013: The physical science basis. Contribution of working group I to the fifth assessment report of the intergovernmental panel on climate change*. Cambridge: Cambridge University Press.

Dee, D. P. Uppala, S. M. Simmons, A. J. Berrisford, P. Poli, P. Kobayashi, S., et al. (2011). The ERA-interim reanalysis: Configuration and performance of the data assimilation system. *Q. J. R. Meteorol. Soc.* 137, 553–597. doi:10.1002/qj.828

Emanuel, K. A. (1999). Thermodynamic control of hurricane intensity. *Nature* 401, 665–669. doi:10.1038/44326

Folland, C. K. Renwick, J. A. Salinger, M. J. and Mullan, A. B. (2002). Relative influences of the interdecadal pacific oscillation and ENSO on the south pacific convergence zone. *Geophys. Res. Lett.* 29, 21-1–21-4. doi:10.1029/2001gl014201

Gill, A. E. (2010). Some simple solutions for heat-induced tropical circulation. *Q. J. R. Meteorol. Soc.* 106, 447–462. doi:10.1002/qj.49710644905

Henley, B. J. Gergis, J. Karoly, D. J. Power, S. Kennedy, J. and Folland, C. K. (2015). A tripole index for the interdecadal pacific oscillation. *Clim. Dyn.* 45, 3077–3090. doi:10.1007/s00382-015-2525-1

Ho, C.-H. Baik, J.-J. Kim, J.-H. Gong, D.-Y. and Sui, C. H. (2004). Interdecadal changes in summertime typhoon tracks. *J. Clim.* 17, 1767–1776. doi:10.1175/1520-0442(2004)017<1767:icistt>2.0.co;2

Kalnay, E. Kanamitsu, M. Kistler, R. Collins, W. Deaven, D. Gandin, L., et al. (1996). The NCEP/NCAR 40-year reanalysis project. *Bull. Am. Meteorol. Soc.* 77, 437–471. doi:10.1175/1520-0477(1996)077<0437:tnyrp>2.0.co;2

Knapp, K. P. Kruk, M. C. Levinson, D. H. Diamond, H. J. and Neumann, C. J. (2010). The international best track archive for climate stewardship (IBTrACS): Unifying tropical cyclone data. *Bull. Am. Meteorol. Soc.* 91, 363–376. doi:10.1175/2009bams2755.1

Knapp, K. R. Diamond, H. J. Kossin, J. P. Kruk, M. C. and Schreck, C. J. (2018). International best track archive for climate stewardship (IBTrACS) project, version 4. *NOAA Natl. Centers Environ. Inf.* doi:10.25921/82ty-9e16

Knapp, K. R. and Kruk, M. C. (2010). Quantifying interagency differences in tropical cyclone best track wind speed estimates. *Mon. Weather Rev.* 138, 1459–1473. doi:10.1175/2009mwr3123.1

Knutson, T. R. McBride, J. L. Chan, J. Emanuel, K. Holland, G. Landsea, C., et al. (2010). Tropical cyclones and climate change. *Nat. Geosci.* 3, 157–163. doi:10.1038/ngeo779

Kossin, J. P. Camargo, S. J. and Sitkowski, M. (2010). Climate modulation of North Atlantic hurricane tracks. *J. Clim.* 23, 3057–3076. doi:10.1175/2010jcli3497.1

Kossin, J. P. Emanuel, K. A. and Camargo, S. J. (2016). Past and projected changes in western North Pacific tropical cyclone exposure. *J. Clim.* 29, 5725–5739. doi:10.1175/jcli-d-16-0076.1

Kossin, J. P. Emanuel, K. A. and Vecchi, G. A. (2014). The poleward migration of the location of tropical cyclone maximum intensity. *Nature* 509, 349–352. doi:10.1038/nature13278

Lee, T.-C. Knutson, T. R. Kamahori, H. and Ying, M. (2012). Impact of climate change on tropical cyclones in the Western North pacific basin. Part I: Past observations. *Trop. Cyclone Res. Rev.* 1, 213–230. doi:10.6057/2012TCRR02.09

Lee, T.-C. Knutson, T. R. Nakaegawa, T. Ying, M. and Cha, E. J. (2020). Third assessment on impacts of climate change on tropical cyclones in the Typhoon Committee Region – Part I: Observed changes, detection and attribution. *Trop. Cyclone Res. Rev.* 9, 1–22. doi:10.1016/j.tcrr.2020.03.001

Lee, T. and McPhaden, M. J. (2008). Decadal phase change in largescale sea level and winds in the Indo-Pacific region at the end of the 20th century. *Geophys. Res. Lett.* 35, L01605. doi:10.1029/2007GL032419

Liu, K. S. and Chan, J. C. L. (2013). Inactive period of western North Pacific tropical cyclone activity in 1998–2011. *J. Clim.* 26, 2614–2630. doi:10.1175/jcli-d-12-00053.1

Liu, K. S. and Chan, J. C. L. (2008). Interdecadal variability of western North Pacific tropical cyclone tracks. *J. Clim.* 21, 4464–4476. doi:10.1175/2008jcli2207.1

Lucas, C. Timbal, B. and Nguyen, H. (2014). The expanding tropics: A critical assessment of the observational and modeling studies. *WIREs Clim. Change* 5, 89–112. doi:10.1002/wcc.251

Mantua, N. J. Hare, S. R. Zhang, Y. Wallace, J. M. and Francis, R. C. (1997). A Pacific interdecadal climate oscillation with impacts on salmon production. *Bull. Amer. Meteor. Soc.* 78, 1069–1079. doi:10.1175/1520-0477(1997)078<1069:apicow>2.0.co;2

Meehl, G. A. and Arblaster, J. M. (2012). Relating the strength of the tropospheric biennial oscillation (TBO) to the phase of the Interdecadal Pacific Oscillation (IPO). *Geophys. Res. Lett.* 39, L20716. doi:10.1029/2012GL053386

Meehl, G. A. Hu, A. Arblaster, M. J. Fasullo, J. and Trenberth, K. E. (2013). Externally forced and internally generated decadal climate variability associated with the interdecadal pacific oscillation. *J. Clim.* 26, 7298–7310. doi:10.1175/jcli-d-12-00548.1

Mei, W. Xie, S.-P. Zhao, M. and Wang, Y. (2015). Forced and internal variability of tropical cyclone track density in the western North Pacific. *J. Clim.* 28, 143–167. doi:10.1175/JCLI-D-14-00164.1

Peduzzi, P. Chatenoux, B. Dao, H. De Bono, A. Herold, C. Kossin, J., et al. (2012). Tropical cyclones: Global trends in human exposure, vulnerability and risk. *Nat. Clim. Change* 2, 289–294. doi:10.1038/nclimate1410

Power, S. Casey, T. Folland, C. Colman, A. and Mehta, V. (1999). Inter-decadal modulation of the impact of ENSO on Australia. *Clim. Dyn.* 15, 319–324. doi:10.1007/s003820050284

Shen, Y. Sun, Y. Zhong, Z. Liu, K. and Shi, J. (2018). Sensitivity experiments on the poleward shift of tropical cyclones over the western North pacific under warming ocean conditions. *J. Meteorol. Res.* 32, 560–570. doi:10.1007/s13351-018-8047-0

Smith, T. M. and Reynolds, R. W. (2003). Extended reconstruction of global sea surface temperatures based on COADS data (1854–1997). *J. Clim.* 16, 1495–1510. doi:10.1175/1520-0442-16.10.1495

Sun, Y. Zhong, Z. Li, T. Yi, L. Shi, J. Shen, Y., et al. (2020). Superiority of mega ENSO index in the seasonal prediction of tropical cyclone activity over the western North pacific. *Earth Space Sci.* 7, e2019EA001009. doi:10.1029/2019ea001009

Sun, Y. Zhong, Z. Yi, L. Li, T. Chen, M. Wan, H., et al. (2015). Dependence of the relationship between the tropical cyclone track and western pacific subtropical high intensity on initial storm size: A numerical investigation. *J. Geophys. Res. Atmos.* 120, 11451–11467. doi:10.1002/2015jd023716

Wang, B. Liu, J. Kim, H. J. Webster, P. J. Yim, S. Y. and Xiang, B. (2013). Northern Hemisphere summer monsoon intensified by mega-El Niño/southern oscillation and Atlantic multidecadal oscillation. *Proc. Natl. Acad. Sci. U. S. A.* 110, 5347–5352. doi:10.1073/pnas.1219405110

Wang, C. and Wang, X. (2013). Classifying El Niño Modoki I and II by different impacts on rainfall in southern China and typhoon tracks. *J. Clim.* 26, 1322–1338. doi:10.1175/jcli-d-12-00107.1

Wang, R. Wu, L. and Wang, C. (2011). Typhoon track changes associated with global warming. *J. Clim.* 24, 3748–3752. doi:10.1175/jcli-d-11-00074.1

Zhang, W. Graf, H.-F. Leung, Y. and Herzog, M. (2012). Different El Niño types and tropical cyclone landfall in east asia. *J. Clim.* 25, 6510–6523. doi:10.1175/jcli-d-11-00488.1

frontiers | Frontiers in Earth Science

TYPE Original Research
PUBLISHED 09 September 2022
DOI 10.3389/feart.2022.986830

OPEN ACCESS

EDITED BY
Stephen Outten,
Nansen Environmental and Remote Sensing Center (NERSC), Norway

REVIEWED BY
Yaocun Zhang,
Nanjing University, China
Yong Zhao,
Chengdu University of Information Technology, China
Xueyuan Kuang,
Nanjing University, China

*CORRESPONDENCE
Suxiang Yao,
yaosx@nuist.edu.cn

SPECIALTY SECTION
This article was submitted to Atmospheric Science, a section of the journal Frontiers in Earth Science

RECEIVED 05 July 2022
ACCEPTED 15 August 2022
PUBLISHED 09 September 2022

CITATION
Sun T, Yao S and Huang Q (2022), The atmospheric quasi-biweekly oscillation during the Jiangnan Meiyu onset period. *Front. Earth Sci.* 10:986830. doi: 10.3389/feart.2022.986830

The atmospheric quasi-biweekly oscillation during the Jiangnan Meiyu onset period

Tianle Sun, Suxiang Yao* and Qian Huang

Key Laboratory of Meteorological Disaster, Ministry of Education (KLME)/Collaborative Innovation Center on Forecast and Evaluation of Meteorological Disasters (CIC-FEMD)/Joint International Research Laboratory of Climate and Environment Change (ILCEC), Nanjing University of Information Science and Technology, Nanjing, China

Meiyu is a typical rainy season during the East Asian Summer Monsoon whose early or late onset is closely related to an abnormal amount of rainfall. Based on the ERA-interim daily reanalysis data from 1979 to 2019 and the Meiyu index dataset provided by the CMA (the China Meteorological Administration), the characteristics of the intraseasonal oscillation (ISO) in different latitudes during the Jiangnan Meiyu onset period were examined. During the Meiyu onset period, the analysis of 500 hPa geopotential height shows that the key regions of circulation anomaly include the Ural Mountains in mid-high latitudes and the Northwest Pacific in low latitudes. Moreover, the geopotential height anomaly of the two regions shows significant quasi-biweekly scale (10–30 days) characteristics. The diagnosis of quasi-biweekly geopotential tendency shows that height variation in the mid-high latitude key region mainly depends on the influence of temperature advection, while the variation in the low-latitude key region relies on vorticity advection. Over the mid-high latitudes, the height anomaly of the Ural Mountains gradually increases before the day of Meiyu onset, and the contribution of quasi-biweekly oscillation (QBWO) to the total anomaly is approximately 55.9%. The fluctuations from Europe and the Aleutians spread toward the key region, and the abnormal warm advection lies over the key region, contributing to formation of the Ural-blocking pattern. Meanwhile, in the key region located over the Western Pacific, the contribution of the quasi-biweekly component reaches 51.2%. The oscillations over the Western Pacific propagate southwestward along the East Asian coast, while fluctuations over the East Asian continent migrate southward. Throughout this period, the negative vorticity advection occupies the key region, which is conducive to both the positive geopotential height variation and maintenance of the Western Pacific Subtropical High. Thus, the migration of QBWO in different latitudes could be an extended-range signal of the Jiangnan Meiyu prediction.

KEYWORDS

Jiangnan Meiyu, quasi-biweekly oscillation, geopotential height, different latitudes, power spectrum analysis (PSA)

1 Introduction

Meiyu, known as Baiu in Japan and Chang-ma in South Korea, refers to continuous rainy weather in June and July in the middle and lower reaches of the Yangtze River in China, central and southern Japan, and southern South Korea. During the Meiyu period, continuous high temperature and humidity enhance the occurrence of extreme weather events, such as heavy rainfall, causing massive loss to life and property. Additionally, the study of the Meiyu period is an important component of short-term climate prediction in various countries. Therefore, to ensure disaster prevention and mitigation strategies, it is urgent to conduct further research on the evolutionary characteristics of Meiyu and improve forecasting capabilities for the Meiyu season (Ninomiya and Muraki, 1986; Lee, 1989; Oh et al., 1997; Kawamura and Murakami, 1998; Krishnan and Sugi, 2001).

Due to inconsistency of the definition of the Meiyu onset, previous conclusions have often lacked consistency and comparability. Early efforts have often used indicators of the circulation situation (Yu, 1980; Zhou, 1980), precipitation process (Fu, 1981; Zhang and Zheng, 1981), or both (Chen and Qian, 2004; Xu, 2007; Liang et al., 2010; Liu et al., 2014) to determine the onset of Meiyu. Under different standards for the same observed fact, they have always led to inconsistent conclusions about the variability of atmospheric circulation, evolution of precipitation, and mutual feedback between weather systems. This confusion was not resolved until 2017 when the China National Climate Centre proposed the "New Monitoring Indices", which combines scientific zoning methods and detailed monitoring indicators.

Furthermore, multiple weather systems at different scales and their complex interactions in summer could be another challenge for Meiyu analyses. Major components of the East Asian Summer Monsoon (EASM) include the western Pacific subtropical high (WPSH), South Asian high (SAH), upper-level East Asian westerly jetstream, typhoons, and low-level southwesterly jets. All these components may affect EASM rainfall patterns and the evolution of Meiyu to varying degrees (Tao and Cheng, 1987; Ninomiya and Shibagaki, 2007; Sampe and Xie, 2010; Zhu et al., 2017; Liu et al., 2019; Ding et al., 2020). The location, dominant period, and intensity of the WPSH at low latitudes play an important role in setting the stage for the Meiyu season, providing plenty of water vapor for Meiyu precipitation (Tao et al., 1958; Wang, 1992; Huang and Tang, 1995; Yang et al., 2004; Mao and Wu, 2005; Liu et al., 2013b; Liu et al., 2013a). The formations of SAH and the East Asian subtropical westerly jet are considered to be the precursor signals of the Meiyu onset (Zhao et al., 2018). At mid-high latitudes, many studies have indicated that the variability of Meiyu circulation is closely related to the blocking pattern formation over the Urals, southward propagation of Rossby waves, cold southward airflow, and so on (Tao and Cheng, 1987; Wang, 1992; Chan et al., 2002; Wang and Gaoqiao, 2005).

As a part of the evolution of the EASM, the Meiyu onset implies that atmospheric circulation enters a short-term stable state. Numerous studies have pointed out that ISOs demonstrate great influence on the onset, maintenance, and extinction of the EASM and Meiyu (Chen et al., 2001; Wu and Wang, 2001; Li et al., 2003; Ju et al., 2005). The climatological intraseasonal oscillation (CISO) of the EASM is embodied in the oscillation characteristics of convection and wind fields at different time scales. The first mode of EASM CISO in the circulation shows that the jointly enhanced Mongolian cyclone, the western North Pacific subtropical high, and SAH correspond to a rainfall anomaly with strong Meiyu fronts over East Asia (Wang and Wu, 1997; Lian et al., 2016; Song et al., 2016). It has been found that Meiyu systems have typical ISO characteristics. For example, owing to the heat source of the Qinghai–Tibet Plateau and the southward transmission of low-frequency wave trains from Eurasia, the SAH has the characteristics of a 10–20-day oscillation, similar to the subtropical westerly jet. The aforementioned two factors have an important impact on precipitation in eastern China during Jianghuai Meiyu (Wang et al., 2016; Wang and Ge, 2016; Yang and Li, 2016; Amemiya and Sato, 2018; Ge, 2018). Meanwhile, as an important part of low-frequency waves at mid-high latitudes, the blocking high during the Meiyu period also has the characteristics of quasi-biweekly oscillation because of the atmospheric nonlinear interaction (Li et al., 2003). Moreover, the WPSH has both quasi-biweekly and 30–60-day oscillation characteristics (Su et al., 2017; Yang and Li, 2020). Some research studies have reported that remarkable ISO characteristics exist for meridional winds and water vapor transport in the lower troposphere (Zuo et al., 2009).

Previous study has been devoted to revealing the ISO feature and interactions between system members during the Meiyu season. However, few studies have been carried out on the mechanism of how ISO affects atmospheric circulation during the Meiyu onset. In addition, since the Jiangnan area defined in the new Meiyu monitoring indices is located at the southernmost end of the traditional Meiyu monitoring area, the determination of the Meiyu onset date in the Jiangnan area can provide advanced warning and indicative significance for the entire river basin during the Meiyu period. Consequently, this study aims to analyze the ISO characteristics at different latitudes during the Meiyu onset period (specified by the new indices) over the Jiangnan area to provide a theoretical reference for Meiyu forecasting. The rest of the study is organized as follows. Section 2 describes the data and methods used in this study. Section 3 illustrates the ISOs at different latitudes during the Jiangnan Meiyu onset. The main conclusions are summarized in Section 4, while the disscussion part is displayed in the last section.

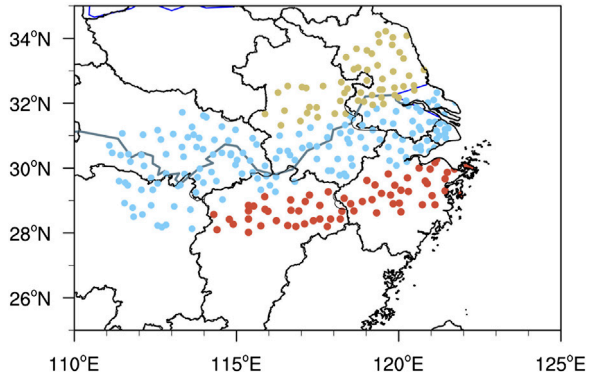

FIGURE 1
Distribution of CMA stations over the Meiyu region (red dots: Jiangnan area; blue dots: middle and lower reaches of the Yangtze River; yellow dots: Jianghuai area).

2 Data and methods

2.1 Data

Based on the "Meiyu Monitoring Indices" released by the China Meteorological Administration (CMA) in 2017 (Standardization administration, 2017), the variations in atmospheric circulation during the Meiyu onset period over the Jiangnan area were analyzed. The distribution of Meiyu monitoring stations is shown in Figure 1, which includes 277 CMA stations. According to the climatic characteristics, the Meiyu monitoring area is divided from south to north into the Jiangnan area (red), the middle and lower reaches of the Yangtze River (blue), and the Jianghuai area (yellow). As the southernmost monitoring region, the Jiangnan area tends to witness the earliest onset of the Meiyu period. Therefore, the study of this region can help predict the onset of the whole Meiyu region. In addition, the updated climatic dataset of the Meiyu season (including the onset/retreat date, intensity, and precipitation) was obtained from the National Climate Center (NCC) of China (https://www.ncc-cma.net). Since it contains the common influences of multiple factors, such as precipitation, air temperature, and circulation, the new indices can more accurately reflect the activity characteristics of Meiyu. For instance, the indices stipulate that the regional average daily temperature should be equal to or greater than 22°C during the Meiyu onset period over the Jiangnan area. Additionally, the ridge line of WPSH at 500 hPa should remain between 18°N and 25°N. Therefore, we also used the geopotential height data of ERA-interim (resolution: 1° × 1°) daily reanalysis (Dee et al., 2011) provided by the ECMWF (the European Centre for Medium-Range Weather Forecasts).

2.2 Methodology

In this study, power spectrum analysis was carried out to obtain the dominant period of the geopotential height anomaly during the Meiyu onset over the Jiangnan area. Furthermore, for multiscale quantitative analysis, the geopotential height anomaly was decomposed into four terms as follows (Hsu and Li, 2011; Yao et al., 2019):

$$\boldsymbol{H} = \bar{\boldsymbol{H}} + \boldsymbol{H}' + \boldsymbol{H}'' + \boldsymbol{H}^{*} \tag{1}$$

where $\bar{\boldsymbol{H}}$is the background condition with a time scale greater than 90 days and$\boldsymbol{H}'$ and $\boldsymbol{H}''$represent the perturbations on the 30–90-day and 10–30-day time scales, respectively. Both values were the results of the Butterworth bandpass filter. $\boldsymbol{H}^{*}$ represents synoptic disturbances with a time scale less than 10 days and was extracted by applying the Lanczos high-frequency (<10 days) filter.

Considering that a circulation field is an important object of Meiyu monitoring, we focused on the evolution and intraseasonal oscillation characteristics of the center and intensity of systems at 500 hPa altitude. In this study, the geopotential height anomaly (the differences between the preset day and its climatic state) was calculated to carry out quantitative analysis. In addition, the geopotential tendency equation (Lau and Holopainen 1984; Fang and Yang 2016; Ren et al., 2021) was used to examine the key physical processes, which can be simply written as follows:

$$\left(\nabla^2 + \frac{f^2}{\sigma}\frac{\partial^2}{\partial p^2}\right)\frac{\partial \phi}{\partial t} = -fV_g \cdot \nabla f - fV_g \cdot \nabla \zeta_g + \frac{f^2}{\sigma}\frac{\partial}{\partial p}\left(-V_g \cdot \nabla \frac{\partial \phi}{\partial p}\right) \tag{2}$$

where $(\frac{\partial \phi}{\partial t})$ represents the geopotential tendency at 500 hPa; the first term $((\nabla^2 + \frac{f^2}{\sigma}\frac{\partial^2}{\partial p^2})\frac{\partial \phi}{\partial t})$ is proportional to$-\frac{\partial \phi}{\partial t}$; the second term $(-fV_g \cdot \nabla f)$ represents the geostrophic vorticity advection; the third term $(-fV_g \cdot \nabla \zeta_g)$ represents the relative vorticity advection; and the last term $(\frac{f^2}{\sigma}\frac{\partial}{\partial p}(-V_g \cdot \nabla \frac{\partial \phi}{\partial p}))$ denotes the temperature advection with altitude variation.

3 Results

3.1 Climatic characteristics of the Meiyu onset period over the Jiangnan area

We first sorted out the time series of the Meiyu periods over the Jiangnan area from 1979 to 2019, as shown in Figure 2A. The values plotted on the vertical ordinate are the duration of the Meiyu periods and the climatic Meiyu onset date. The results reveal that the onset dates are mainly concentrated from May to June and show obvious interannual and interdecadal variabilities. The earliest Meiyu onset date is on the 25th of May 1995, 15 days

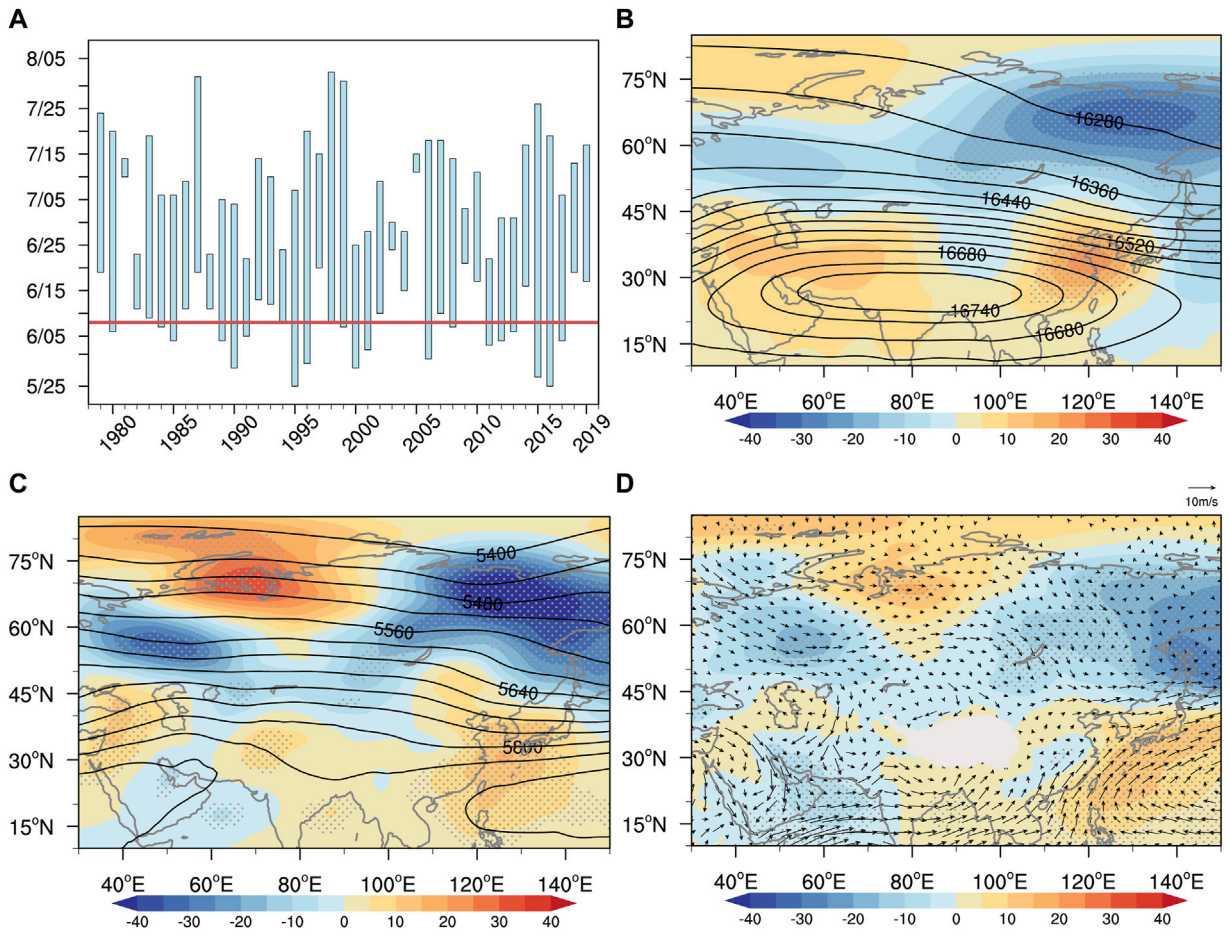

FIGURE 2
(A) Meiyu periods (blue bars) over the Jiangnan area and the climatic Meiyu onset day (red line) during 1979–2019. Geopotential height (contours, unit: gpm) and its anomaly (shading, unit: gpm) at 100 hPa **(B)** and 500 hPa **(C)** on the Meiyu onset day. Wind (vector, unit: m/s) and geopotential height anomaly (shading, unit: gpm) at 850 hPa **(D)** on the Meiyu onset day (dots are the areas with statistical significance exceeding the 95% level).

earlier than the climatological mean (8th of June). In contrast, in 2005, the Meiyu onset occurred on the 11th of July, 32 days later than normal.

On the Meiyu onset day, the climatic circulation and geopotential height anomaly at 100, 500, and 850 hPa are shown in Figures 2B–D. In the upper troposphere (Figure 2B), the latitudinal range of the South Asian high (SAH) extends from Africa eastward to the western Pacific, and the meridional range extends from the tropics to the mid-latitude westerly region, with the center located over the Tibetan Plateau. The Jianghuai area is controlled by a significant high anomaly, contributing to the eastward extension of the SAH. In the mid-troposphere (Figure 2C), it can be clearly seen at mid-high latitudes that the positive anomaly is mainly located over the Urals, while the negative centers dominate most of Europe and eastern Russia. The distribution of the anomalies not only contributes to the establishment of the blocking situation during the Meiyu onset period but also enhances the southward flow with cold and dry air. At lower latitudes, the western Pacific subtropical high (WPSH) is located in the South China Sea (SCS), with its ridge line remaining at approximately 20°N, while the ridge point extends to the west of 120°E. At the same time, the geopotential height from the Bay of Bengal to most of the Northwest Pacific shows a significant positive anomaly, with its center located to the northwest of the WPSH. The maintenance of the anomaly promotes the northwestward movement of the WPSH, thus providing abundant moisture to the Jiangnan area. The southward airflow in front of the Urals and the northward transportation of water vapor near the WPSH provide favorable conditions for the onset and maintenance of Meiyu over the Jiangnan area.

In the lower troposphere at 850 hPa (Figure 2D), parts of the Western Pacific at lower latitudes are similarly controlled by significant high-pressure anomalies, and pronounced low-pressure anomalies are situated in the mid-high latitudes east of Lake Baikal.

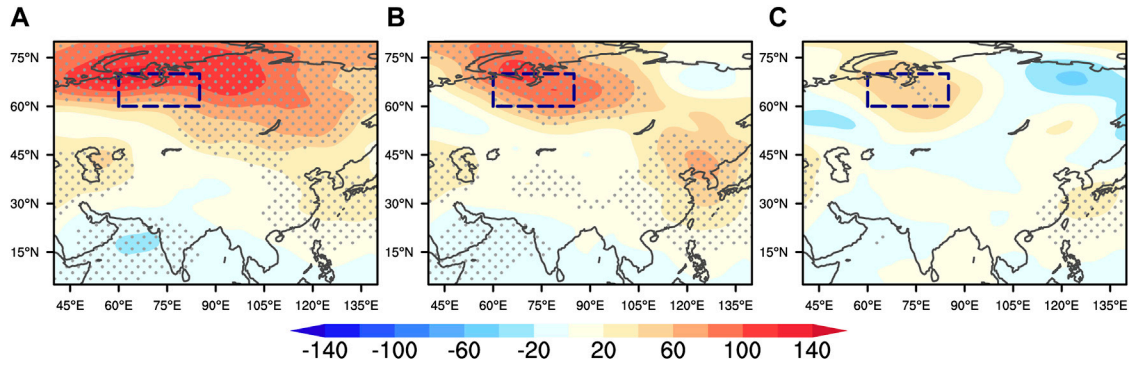

FIGURE 3
Differences of geopotential height between the onset day and the lead 15 d **(A)**, the lead 10 d **(B)**, the lead 5 d **(C)** (black box: the mid-high-latitude key region (60°N-70°N, 60°E-85°E); unit: gpm; dots are the areas with statistical significance exceeding the 95% level).

The strong southwesterly winds at the periphery of the anomalous high pressure confront the northwesterly winds at the back of the low pressure in the Jiangnan region, contributing to a favorable background of warm moisture for Meiyu precipitation. In addition, the distribution of the height anomalies from the upper to lower troposphere is relatively consistent in Figure 2. As a result, we chose 500 hPa as a representation for further analysis.

3.2 The intraseasonal oscillation characteristics of atmospheric circulation at mid-high latitudes

As a member of the East Asia Summer Monsoon (Zhang et al., 2018), the atmospheric circulation at mid-high latitudes exhibits an obvious transformation process before Meiyu onset. Therefore, to reveal the ISO characteristics at mid-high latitudes, the geopotential height differences between the onset day and the 15-day lead, 10-day lead, and 5-day lead are provided in Figures 3A–C. Apparently, during the 15-day lead and 10-day lead, the geopotential height gradually increases over most regions at mid-high latitudes. However, only the Ural Mountains area keeps growing until the 5-day lead. We accordingly selected the persistently significant area of difference (indicated by the black dashed frame: 60°N-70°N, 60°E-85°E) as the key region of the mid-high latitudes.

The power spectrum of the key region average geopotential height anomaly from May to July from 1979 to 2019 (Figure 4A) was analyzed to obtain the dominant periods of the atmospheric circulation variation over the Jiangnan area. The results show

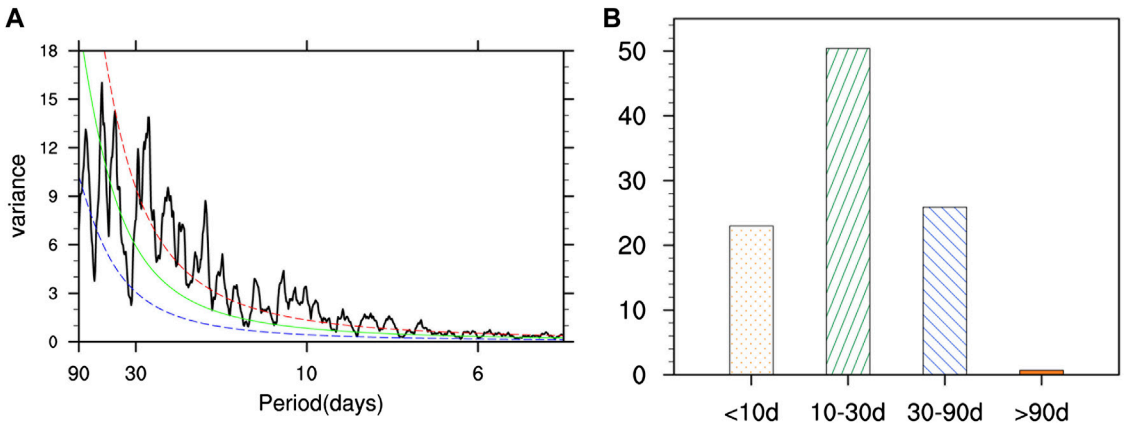

FIGURE 4
(A) Power spectrum analysis of geopotential height anomaly over the mid-high-latitude key region during May to July (unit: W^2 m^{-4}). The green dashed line is the red noise spectrum, and the red (blue) dashed line indicates values above the 95% (5%) confidence level. **(B)** Variation contributions of the perturbations at different time scales (unit: %).

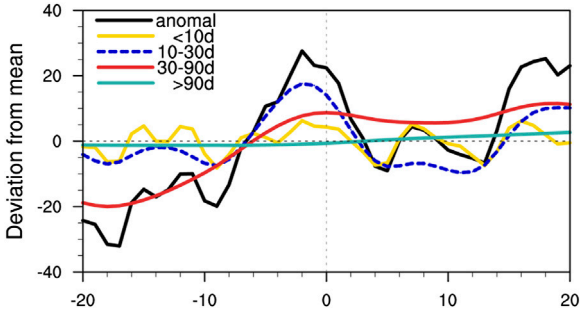

FIGURE 5
Variations of geopotential height anomaly over the mid-high-latitude key region at different time scales during Jiangnan Meiyu onset (unit: gpm; black, geopotential height anomaly; yellow, synoptic scale; blue, quasi-biweekly scale; red, intraseasonal scale; green, >90 d scale).

that the average height anomaly has remarkably high-frequency oscillations with periods of 10–30 days, while the rest of the periods (<10 days and 30–90 days) are also significant. By calculating the variation contributions of the perturbations at different scales, we found that the quasi-biweekly disturbances dominate most in the Meiyu periods. The variance contribution of the quasi-biweekly scale component is 50.4% (Figure 4B); this value is larger than that of the synoptic scale component (<10 days), intraseasonal (30–90 days) component, and background component. Then, to confirm the dominant period during the Meiyu onset period, the geopotential height anomaly of the key region was differentiated into four terms based on Eq. 1 for further analyses.

Figure 5 shows the evolution of the geopotential height anomaly at different time scales over the mid-high latitude key region. The regional average anomaly changes from negative to positive at the 6-day lead and continues to increase until it reaches a peak at the 2-day lead. This proves that enhancement of the positive anomaly of the key region with the Urals Mountains as the center is conducive to establishment of the blocking situation at mid-high latitudes. In addition, a quantitative diagnosis of the contribution of each component variation in the geopotential height anomaly 2 days ahead of Meiyu onset is provided in Table 1. The quasi-biweekly scale is the most important component of the oscillations, contributing approximately 55.9% of the total anomalies, indicating that the characteristics of the geopotential height anomaly variation in the key region are closely related to the quasi-biweekly (10–30 days) oscillations (QBWOs).

The propagation and evolution of the geopotential QBWO and its tendency were further analyzed (Figure 6). At the 10-day lead (Figure 6A), Eastern Europe is controlled by weak anomalous high pressure along with an obvious center of the positive tendency field. Meanwhile, the positive anomaly over Aleutian is relatively strong and extensive, and the tendency center is located west of the anomalous high. During the 10-day lead to 4-day lead (Figures 6A–D), the anomalous high over Europe gradually strengthens and is accompanied by a northeastward movement of the center. The high-pressure center over the Aleutian Islands continues to move westward. Then, these two centers merge at the 2-day lead (Figure 6E) and continue to increase southward. Eventually, the key region near the Urals Mountains, which was originally controlled by the abnormal low pressure, shifts to an anomalous high (Figure 6F). The propagation, evolution, and merging of two quasi-biweekly disturbances is an essential factor for the anomalous variation in geopotential height in the key region, and it is also one of the precursor signals of the Jiangnan Meiyu onset at mid-high latitudes.

Subsequently, to investigate the key physical process during the quasi-biweekly geopotential height variations in the mid-high latitude key region during the Jiangnan Meiyu onset, we calculated each term of the geopotential tendency equation by the given Eq. 2. It is obvious from Table 2 that the fourth component in the equation is −1.28, contributing most to the positive variation in the key region geopotential height. The quasi-biweekly geostrophic vorticity advection and relative vorticity advection are only 0.014 and −0.41, respectively, which indicates that the positive variation in the geopotential height in the key region mainly depends on the influence of quasi-biweekly temperature advection. The spatial distribution of the abnormal temperature advection is shown in Figure 7. In the mid-high latitudes, the regions over Europe and east of Lake Baikal are mainly controlled by anomalous cold advection, while the area to the north of Lake Balkhash shows significant warm advection anomalies. Over the key region, the quasi-biweekly warm advection anomaly promotes the increase in geopotential height in the key region before the Jiangnan Meiyu onset, which in turn encourages the establishment and maintenance of a blocking pattern in the Ural Mountains.

TABLE 1 Contribution of different time-scale anomalies in mid-high latitude key region.

Time scales	Anomaly (unit: gpm)	<10 d	10–30 d	30–90 d	>90 d
Total summation	45.6	7.29	25.47	14.07	−1.2
Proportion		16.0%	55.9%	30.9%	−2.6%

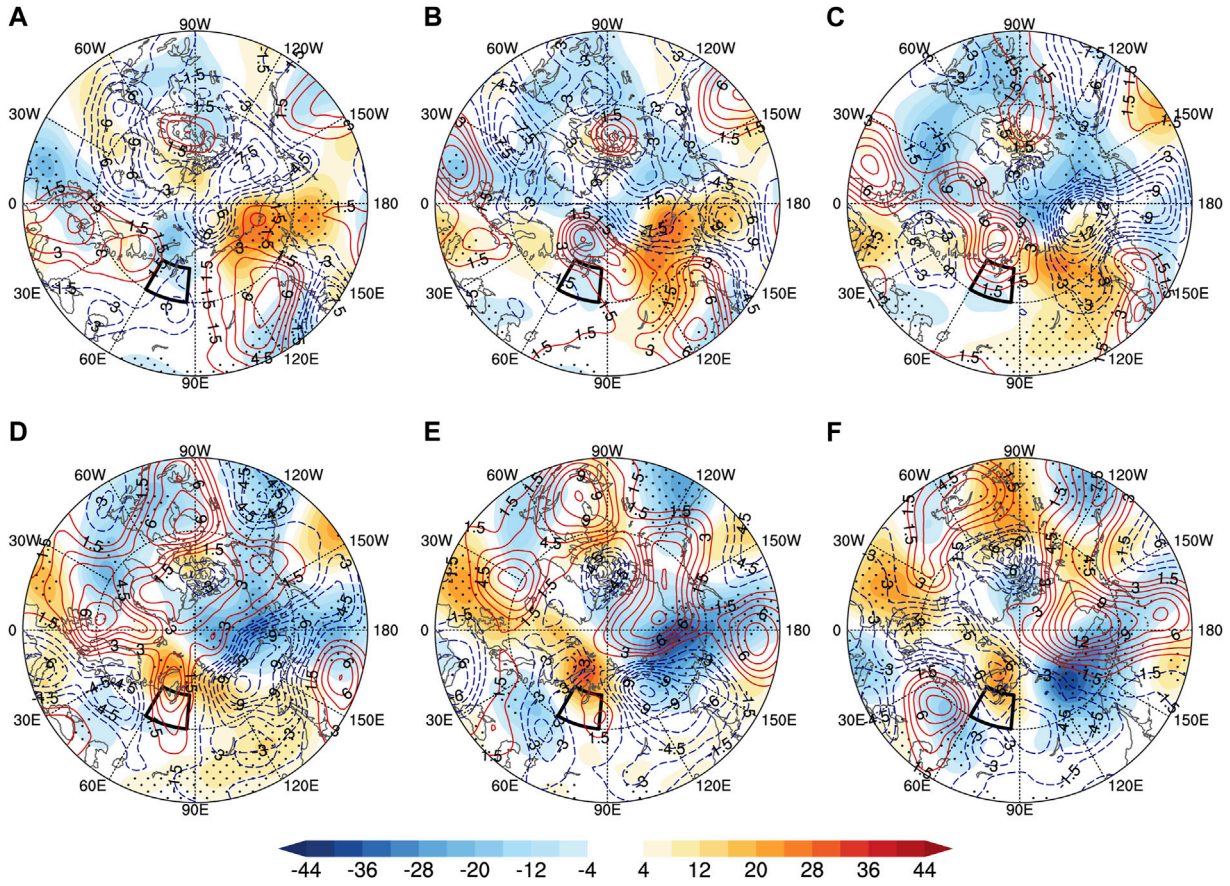

FIGURE 6
Quasi-biweekly-scale geopotential height anomaly (shading) and its tendency (contour) from day -10 to day 0 during the Meiyu onset period **(A–F)** (unit: gpm; black box: the mid-high latitude key region; the latitude of the outermost line is 40°N; dots are the areas with statistical significance exceeding the 95% level).

TABLE 2 Quasi-biweekly components of geopotential tendency equation over the mid-high latitude key region (unit: 10^{-10} s^{-2}).

	$-fV_g \cdot \nabla f$	$-fV_g \cdot \nabla \zeta_g$	$\frac{f^2}{\sigma}\frac{\partial}{\partial p}(-V_g \cdot \nabla \frac{\partial \phi}{\partial p})$
Mid-high latitude key region	0.014	−0.41	−1.28

3.3 The intraseasonal oscillation characteristics of atmospheric circulation at low latitudes

Intraseasonal oscillations of low-latitude atmospheric circulation play an important role in Meiyu onset (Li et al., 2015; Li and Zhou, 2015). The Meiyu rain belts often appear on the western and northern sides of the 588 dagpm isoline of the WPSH, and the precipitation amount is closely related to the distribution, migration, and variation in the WPSH (Qian and Guan, 2020). Therefore, we examined the ISO characteristics of the region closely related to the variation in the WPSH in this section. Figure 8 shows the distributions of the 588 dagpm isolines of the WPSH from the 15-day lead to the onset day, with an interval of 5 days. The composite analysis indicates that the WPSH gradually strengthens and extends westward before the Meiyu onset, finally expanding to the South China Sea. Consequently, the red box zone (15°N-23°N; 118°E-127°E) in Figure 8 is selected to be the key region at low latitudes.

Similar to the analysis method in the mid-high latitudes, we also analyzed the power spectrum of the geopotential height

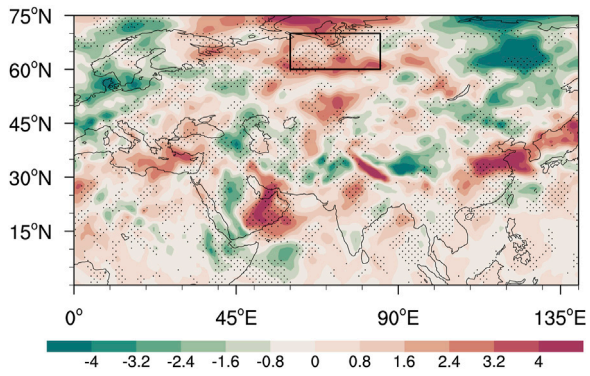

FIGURE 7
Quasi-biweekly temperature advection during the Meiyu onset period (unit: 10^{-5}K s^{-1}; dots are the areas with statistical significance exceeding the 95% level).

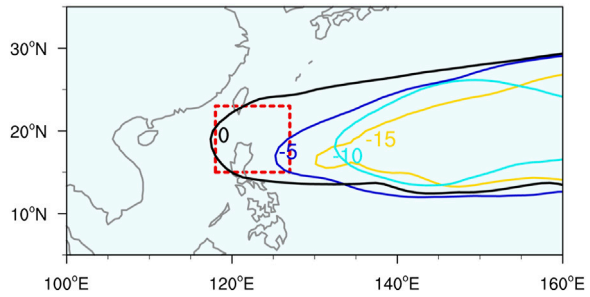

FIGURE 8
Distributions of 588 dagpm isograms from lead 15 d to the onset day (red box: the low-latitude key region (15°N-23°N,118°E-127°E); unit: dagpm; black counter, onset day; purple counter, lead 5 d; blue counter, lead 10 d; yellow counter, lead 15 d).

anomaly in the key region in the low latitudes. As indicated in Figure 9A, the red noise test shows that the cycle from 10 to 30 days is dominant, while the power spectrum peak at the synoptic scale (<10 days) partially passes the test. The quasi-biweekly disturbances contribute most to the low-latitude key region geopotential height anomalies, which is up to 47.9% (Figure 9B). Similar to the mid-latitude key region, this value is also larger than that of the other components. However, to explore the dominant period during the onset period, a more elaborate diagnosis still needs to be conducted.

Based on the scale separation method, the height anomaly in the key region of lower latitudes was examined. The anomaly remains constant in the negative phase until the 2-day lead (Figure 10), which suppresses the westward and northward extension of the WPSH. Then, with the increase in the 10–30-day anomaly, the geopotential height turns from a negative anomaly to a positive anomaly, promoting the intensification and westward extension of WPSH and transporting abundant water vapor to the Jiangnan area. During this process, the component of the 10–30-day scale contributes the most, reaching 51.2% of the total anomalies (Table 3). This indicates that during the Jiangnan Meiyu onset, the anomalous geopotential height variation in the low-latitude key region is mainly influenced by quasi-biweekly (10–30 days) scale oscillations.

To explore the source and propagation path of the low-latitude quasi-biweekly signal before the Meiyu onset, we analyzed the evolution of potential height anomalies and their tendency at the 10–30-day scale. At the 10-day lead (Figure 11A), most of the Asian continent is controlled by the abnormally low pressure in the zonal distribution. The two low-pressure centers are located in northern India and over northeastern China. Subsequently, an abnormally high-pressure center develops in the northeastern part of Balkhash Lake to separate the originally continuous low-pressure zone and weakens it continuously from the 10-day lead to the 2-day lead (Figures 11A–E). Meanwhile, the abnormal depression originating over northeastern China moves eastward into the sea and then propagates southwestward to take control of the key region. Moreover, at the 10-day lead (Figure 11A), over the eastern Japan Sea, there is a northeast-trending abnormal high-pressure zone, which weakens and splits at the 8-day lead (Figure 11B). Then, the anomalous center spreads southward along the east coast of Asia and gradually strengthens. At 2 days, leading to the onset day (Figures 11E,F), the disturbance from the western Pacific moves southward and meets the abnormally high pressure southeast of the continent. In this process, the positive geopotential tendency field controls Northeast Asia, with the center propagating southwestward. Eventually, the key region's potential height anomaly changes from a negative phase to a positive phase. Accordingly, the positive geopotential tendency takes control of the key region, which provides a conducive condition for the westward extension and maintenance of the WPSH in the precursor stage in regard to the Meiyu onset.

Similarly, we analyzed the key physical process during the variation in the geopotential height in the low-latitude key region, and the results are presented in Table 4. By calculation of each component of Eq. 2, it is known that the most contributing term is the quasi-biweekly relative vorticity advection, which is approximately −0.135 during the Meiyu onset period. The other terms of the equation are −0.006 and −0.019, which indicates that the positive anomaly of the geopotential height in the key region at low latitudes relies mostly on the relative vorticity advection. Figure 12 presents a detailed analysis of the spatial distribution of the quasi-biweekly relative vorticity advection during the Meiyu onset. The results show that quasi-biweekly positive vorticity advection dominates most of the low-latitude sea surface. Significant negative anomalies lie along the southeastern coast of China, as well as the region east of

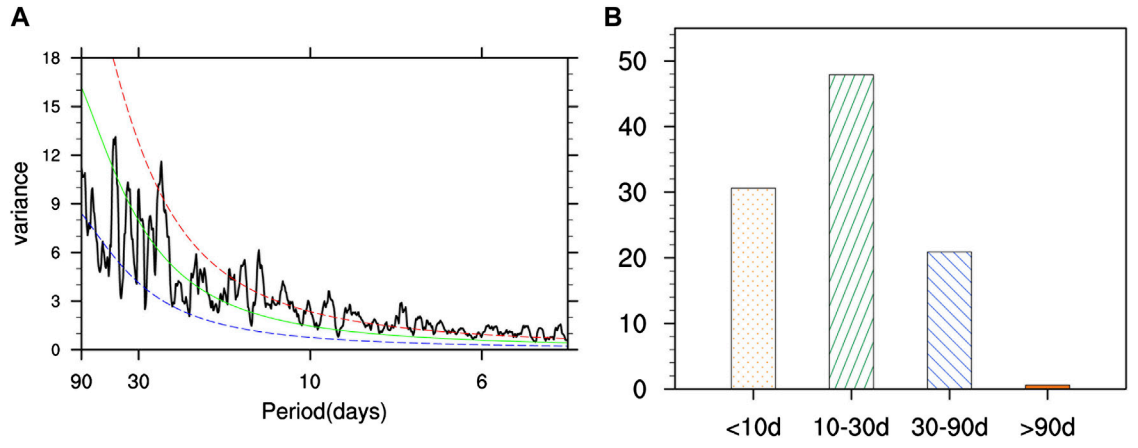

FIGURE 9
Same as Figure 4. **(A)** the power spectrum analysis and **(B)** variation contributions over the low-latitude key region.

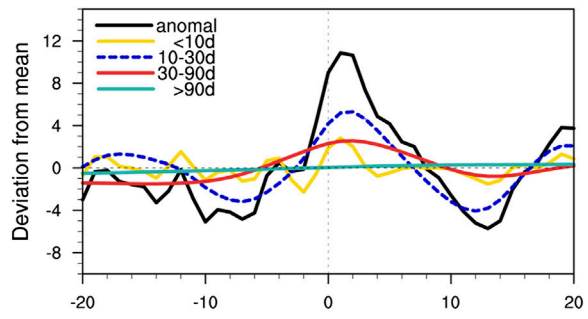

FIGURE 10
Same as Figure 5, but for the low-latitude key region.

Taiwan. Apparently, the significant quasi-biweekly negative vorticity advection in the key region favors the increasing potential height and induces the westward extension and northward shift of the Northwest Pacific Subtropical High.

4 Summary

Based on regional division and the Meiyu dataset defined by the Meiyu monitoring indicators, this study investigates the intraseasonal oscillation characteristics of the atmospheric circulation evolution during the Jiangnan Meiyu onset period from 1979 to 2019. The results reveal that there are significant interannual differences in the Meiyu onset in the Jiangnan area. On the onset day, the abnormal high over the Urals along with the anomalous low over Europe and eastern Russia promotes the formation of the blocking pattern in the mid-high latitudes. The positive height located to the northwest of the WPSH contributes to the advancing westward and northward shift of the WPSH at lower latitudes. As a result, abundant warm moisture accompanied by the peripheral flow of the WPSH meets with the cold air supplied by the blocking high, which provides favorable conditions for the occurrence and maintenance of precipitation during Jiangnan Meiyu periods.

During the Meiyu onset, intraseasonal oscillation characteristics of both mid-high latitudes and lower latitudes are studied by examining the filtered geopotential height anomaly. The results of the power spectrum analysis and the variation contributions of the perturbations at different time scales show that the circulation at different latitudes has significant quasi-biweekly scale (10–30 days) characteristics. The diagnostic analysis shows that the contribution of the quasi-biweekly scale oscillations accounts for 55.9% of the total height anomalies at mid-high latitudes and 51.2% at lower latitudes.

At mid-high latitudes, the abnormal high over the Aleutian Sea propagates westward, while the positive anomaly originating from

TABLE 3 Contribution of different time-scale anomalies in the lower-latitude key region.

Time scales	Anomaly (unit: gpm)	<10 d	10–30 d	30–90 d	>90 d
Total summation	13.2	1.30	6.76	4.26	0.07
Proportion		9.8%	51.2%	32.3%	0.5%

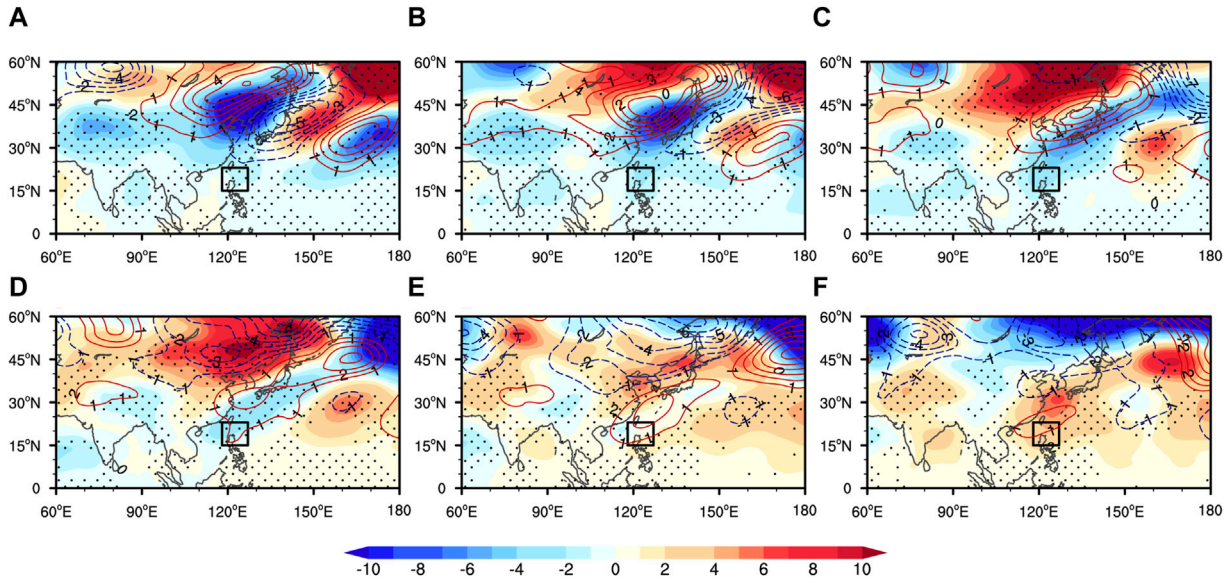

FIGURE 11
The quasi-biweekly-scale geopotential height anomaly (shading) and its tendency (contour) from day -10 to day 0 during the Meiyu onset period **(A-F)** (unit: gpm; black box: the low latitude key region; dots are the areas with statistical significance exceeding the 95% level).

TABLE 4 Quasi-biweekly components of geopotential tendency equation over the low-latitude key region (unit: 10^{-10} s^{-2}).

	$-fV_g \cdot \nabla f$	$-fV_g \cdot \nabla \zeta_g$	$\frac{f^2}{\sigma}\frac{\partial}{\partial p}(-V_g \cdot \nabla \frac{\partial \phi}{\partial p})$
Low-latitude key region	−0.006	−0.135	−0.019

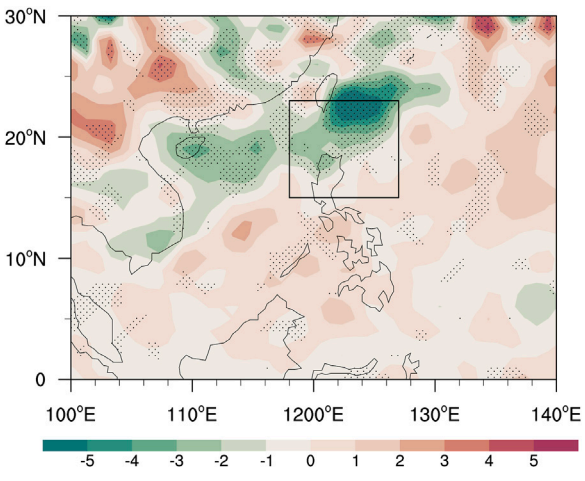

FIGURE 12
Quasi-biweekly relative vorticity during the Meiyu onset period (unit: 10^{-6} s^{-1}; dots are the areas with statistical significance exceeding the 95% level).

Eastern Europe gradually enhances and spreads to the northeast. Then, the two positive anomalies merge, continuously strengthen, and expand southward to take control of the key region in the Urals Mountains. The propagation, evolution, and merging of two quasi-biweekly disturbances facilitates the establishment of a mid-high-latitude blocking situation by influencing the height of geopotential anomalies in the key region, thus favoring the southward invasion of cold air at high latitudes. Subsequently, the diagnostic results of the quasi-biweekly scale geopotential tendency in this process show that the contribution of the temperature advection term is comparatively larger. During the onset period, the mid-high key region is mainly controlled by quasi-biweekly warm advection, while Europe and the region east of Lake Baikal are dominated by significant cold advection. Obviously, with such abnormal background circulation, the Ural Mountains blocking situation is more likely to be established and maintained.

In addition, the quasi-biweekly oscillations of the atmospheric circulation in the low-latitude key region are

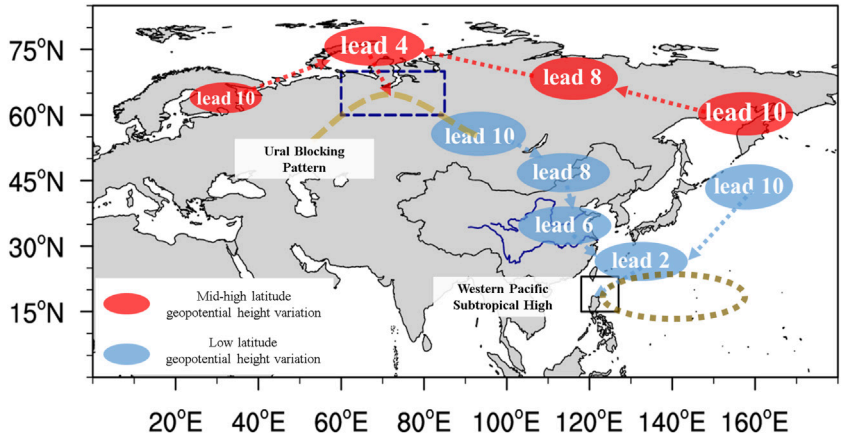

FIGURE 13
Schematic diagram of the evolution of atmospheric quasi-biweekly oscillations during Jiangnan Meiyu onset.

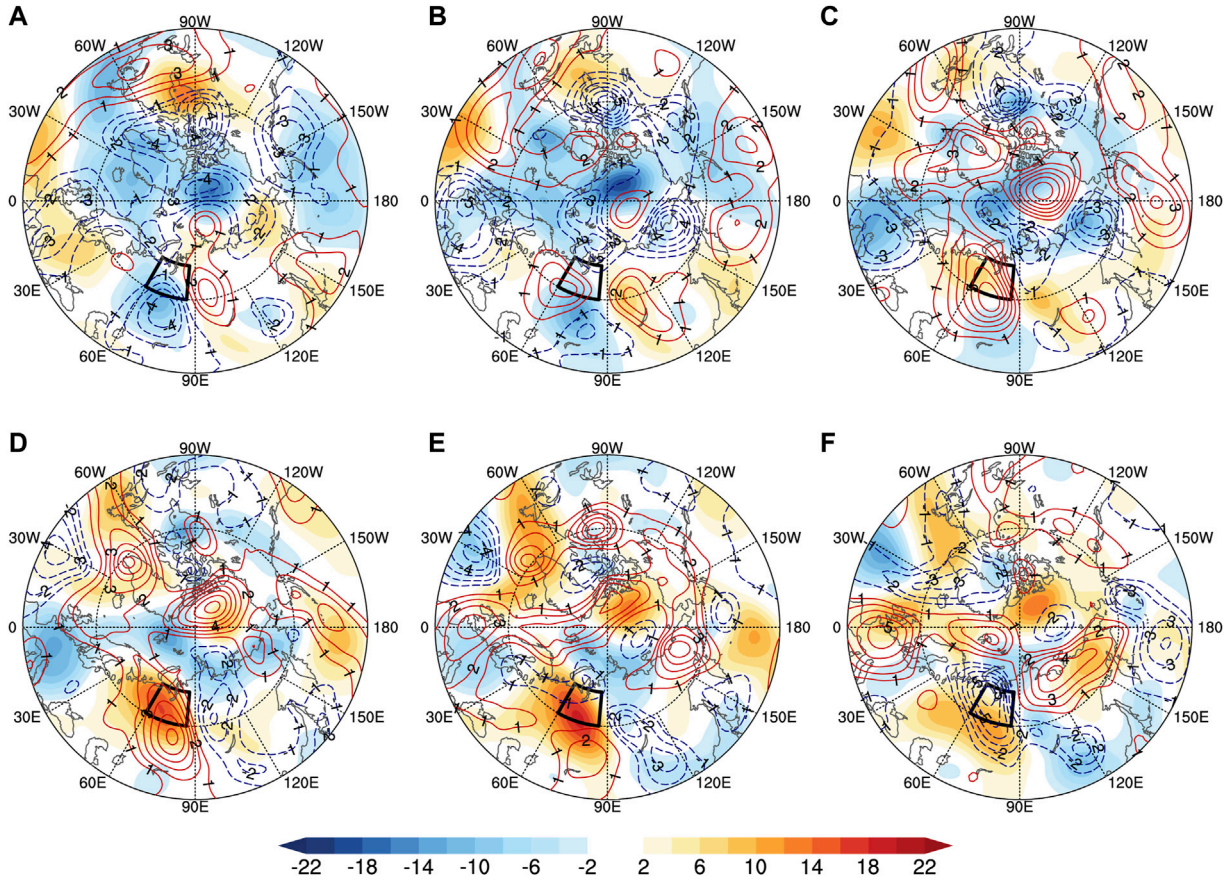

FIGURE 14
Quasi-biweekly-scale geopotential height anomaly (shading) and its tendency (contour) from day -10 to day 0 during the Meiyu onset period in 1998 **(A–F)** (unit: gpm; black box: the mid-high-latitude key region; the latitude of the outermost line is 40°N).

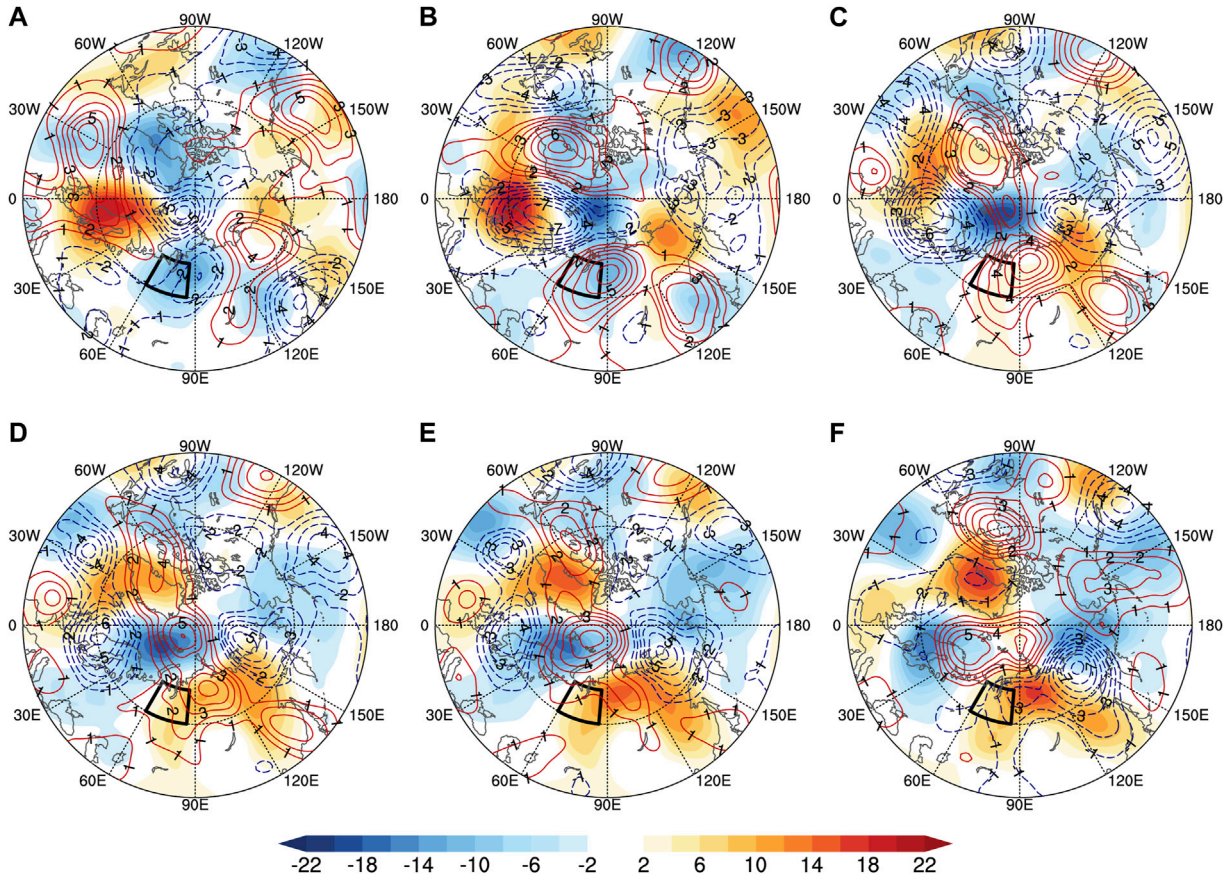

FIGURE 15
Quasi-biweekly-scale geopotential height anomaly (shading) and its tendency (contour) from day -10 to day 0 during the Meiyu onset period in 2011 **(A–F)** (unit: gpm; black box: the mid-high-latitude key region; the latitude of the outermost line is 40°N).

mainly influenced by the southward propagating 10–30 day-scale anomalous high over the Asian continent and the mid-latitude Pacific. During the Meiyu onset, the anomalous high over the mid-latitude Pacific intensifies and propagates southward along the east coast of Asia, while the positive anomalous center over the Asian continent travels eastward and expands southward, and the two finally merge over the key region. These two southward quasi-biweekly scale signals not only enhance the key region's geopotential height anomalies but also promote the westward extension of the WPSH. The warm and humid flow along the high ridge and the cold air transported from high latitudes standoff in the Jiangnan area, forming a favorable atmospheric circulation situation for Meiyu precipitation. Similarly, by diagnosing the quasi-biweekly geopotential height tendency in the low-latitude key region, it is found that the impact of relative vorticity advection is more significant. From the spatial distribution of the abnormal advection, the negative advection anomaly over the key region promotes the positive variation of geopotential height, which in turn influences the evolution of the position intensity of the western Pacific predominantly before Jiangnan Meiyu onset.

5 Discussion

This study mainly determined the characteristics of intraseasonal oscillations at different latitudes during the Jiangnan Meiyu onset under the new indices. It is worth highlighting that most studies have suggested that the north-transmitted ISOs at low latitudes are the main influencing factors on the position and intensity variations of the WPSH as well as the summer precipitation in China (Zhou and Johnny, 2005; Hsu et al., 2016; Su, et al., 2017). In this study, we found that the south-transmitted quasi-biweekly oscillation signals over the mid-latitude Pacific and Asian continents are also closely related to the westward extension

of the WPSH during Jiangnan Meiyu onset. A schematic diagram of the propagation of the oscillations is highlighted in Figure 13.

However, there are still some shortcomings that need to be studied in detail. For example, the Jiangnan Meiyu onset dates show a large interannual difference, but the relationship between the Meiyu onset date and the intensity and location of ISOs is still unclear. As indicated in Section 3.2, the origins of the quasi-biweekly disturbances with significant effects on the mid-high latitude key region are over Europe and the Aleutians. However, the annual analysis of individual cases shows that for some years, the geopotential height variation of the key region is mainly determined by the eastward disturbances over Europe, for example, in 1998 (Figure 14). At the 10-day lead (Figure 14A), the positive disturbance center lies in Europe, along with an obvious center of the positive tendency field in the northeastern area of Europe. However, over the Aleutians, the abnormal high is accompanied by a negative tendency field, which leads to a decrease in ISO intensity. Then, from the 8-day lead to the 0-day lead (Figures 14B–F), the positive anomaly over Europe continuously migrates eastward to the key region and then strengthens southward.

In contrast, for several years, the key region's geopotential height is dominated by westward-moving disturbances over the Aleutian area, such as in 2011 (Figure 15). At the 10-day lead (Figure 15A), both Europe and the Aleutian area are controlled by abnormal high centers. The positive tendency field is located in the westward region of both centers. Then, during the days before onset (Figures 15B–F), the anomalous high over the Aleutian Sea exhibits westward shift characteristics and eventually impacts the key region's geopotential height variation. In addition, the evolution of quasi-biweekly disturbances associated with the low-latitude key region also shows similar characteristics to that of mid-high latitudes. The examination of the causes of such interannual differences could be the focus of our future research study.

Data availability statement

The original contributions presented in the study are included in the article/Supplementary Material; further inquiries can be directed to the corresponding author.

Author contributions

SY and TS conceived the idea, conducted the data analysis, and prepared the figures. TS and QH discussed the results and wrote the manuscript.

Funding

This research was funded by the Key Program of the National Natural Science Foundation of China (41930969-3) and the National Natural Science Foundation of China (42088101).

Conflict of interest

The authors declare that the research was conducted in the absence of any commercial or financial relationships that could be construed as a potential conflict of interest.

Publisher's note

All claims expressed in this article are solely those of the authors and do not necessarily represent those of their affiliated organizations, or those of the publisher, the editors, and the reviewers. Any product that may be evaluated in this article, or claim that may be made by its manufacturer, is not guaranteed or endorsed by the publisher.

References

Amemiya, A., and Sato, K. (2018). A two-dimensional dynamical model for the subseasonal variability of the Asian monsoon anticyclone. *J. Atmos. Sci.* 75, 3597–3612. doi:10.1175/JAS-D-17-0208.1

Chan, J., Wang, Y., and Xu, X. (2002). Dynamic and thermodynamic characteristics associated with the onset of the 1998 South China Sea summer monsoon. *J. Meteorological Soc. Jpn.* 78, 367–380. doi:10.2151/jmsj1965.78.4_367

Chen, L., Zhu, C., Wang, W., and Zhang, P. (2001). Analysis of the characteristics of 30-60day low-frequency oscillation over Asia during 1998 SCSMEX. *Adv. Atmos. Sci.* 18, 623–638. doi:10.1007/s00376-001-0050-0

Chen, Y., and Qian, Y. (2004). Climatic characteristics of 116-year Mei-yu rainfall in the middle-lower reaches of Changjiang River. *J. Nanjing Inst. Meteor.* 01, 65–72. (in Chinese). doi:10.13878/j.cnki.dqkxxb.2004.01.009

Dee, D., Uppala, S., Simmons, A., Berrisford, P., Poli, P., Kobayashi, S., et al. (2011). The ERA-interim reanalysis: Configuration and performance of the data assimilation system. *Q. J. R. Meteorol. Soc.* 137, 553–597. doi:10.1002/qj.828

Ding, Y., Liang, P., Liu, Y., and Zhang, Y. (2020). Multiscale variability of meiyu and its prediction: A new review. *J. Geophys. Res. Atmos.* 125 (7), 31496. doi:10.1029/2019JD031496

Fang, J., and Yang, X. (2016). Structure and dynamics of decadal anomalies in the wintertime midlatitude North Pacific ocean–atmosphere system. *Clim. Dyn.* 47, 1989–2007. doi:10.1007/s00382-015-2946-x

Fu, Y. (1981). On the division of Meiyu period. *Meteor. Mon.* 05, 19–20. (in Chinese). doi:10.7519/j.issn.1000-0526.1981.5.006

Ge, J. (2018). *Distinct features of subseasonal zonal oscillation of South Asian High and its influence on precipitation over China during early and late summers*. Ph. D. dissertation. Nanjing, China: Dept. of Physics, Nanjing University, 101pp.

Hsu, B., Lee, J., and Ha, K. (2016). Influence of boreal summer intraseasonal oscillation on rainfall extremes in southern China. *Int. J. Climatol.* 36 (3), 1403–1412. doi:10.1002/joc.4433

Hsu, P., Li, T., and Tsou, C. H. (2011). Interactions between boreal summer intraseasonal oscillations and synoptic-scale disturbances over the western north

pacific. Part I: Energetics diagnosis*. *J. Clim.* 24, 927–941. doi:10.1175/2010JCLI3833.1

Huang, S., and Tang, M. (1995). The early summer flood periods of southern China and the summer monsoon circulation of East Asia. *J. Trop. Meteor.* 03, 203–213. (in Chinese). doi:10.16032/j.issn.1004-4965.1995.03.002

Ju, J., Qian, C., and Cao, J. (2005). The intraseasonal oscillation of east Asian summer monsoon. *Chin. J. Atmos. Sci.* 29, 187–194. (in Chinese). doi:10.3878/j.issn.1006-9895.2005.02.0

Kawamura, R., and Murakami, T. (1998). Baiu near Japan and its relation to summer monsoons over Southeast Asia and the Western North Pacific. *J. Meteorological Soc. Jpn.* 76, 619–639. doi:10.2151/jmsj1965.76.4_619

Krishnan, R., and Sugi, M. (2001). Baiu rainfall variability and associated monsoon teleconnections. *J. Meteorological Soc. Jpn.* 79, 851–860. doi:10.2151/jmsj.79.851

Lau, N., and Holopainen, E. (1984). Transient eddy forcing of the time-mean flow as identified by geopotential tendencies. *J. Atmos. Sci.* 41, 313–328. doi:10.1175/1520-0469(1984)041<0313:TEFOTT>2.0.CO;2

Lee, D. (1989). An observational study of the Northern Hemisphere summertime circulation associated with the wet summer and the dry summer in Korea. *Lkartidningen* 25, 205–220. doi:10.1007/978-3-642-03885-3_4

Li, C., and Zhou, W. (2015). Multiscale control of summertime persistent heavy precipitation events over South China in association with synoptic, intraseasonal, and low-frequency background. *Clim. Dyn.* 45, 1043–1057. doi:10.1007/s00382-014-2347-6

Li, C., Long, Z., and Mu, M. (2003). Atmospheric intraseasonal oscillation and its important effect. *Chin. J. Atmos. Sci.* 27, 518–535. (in Chinese). doi:10.3878/j.issn.1006-9895.2003.04.07

Li, J., Mao, J., and Wu, G. (2015). A case study of the impact of boreal summer intraseasonal oscillations on Yangtze rainfall. *Clim. Dyn.* 44, 2683–2702. doi:10.1007/s00382-014-2425-9

Lian, Y., Shen, B., Li, S., Liu, G., and Yang, Xu. (2016). Mechanisms for the formation of Northeast China cold vortex and its activities and impacts: An overview. *J. Meteorol. Res.* 30, 881–896. doi:10.1007/s13351-016-6003-4

Liang, P., Ding, Y., He, J., Chen, B., and Lei, X. (2010). A Study of determination index of regional Meiyu over the Yangze-Huaihe basin. *Chin. J. Atmos. Sci.* 34, 418–428. (in Chinese). doi:10.3724/SP.J.1037.2010.00186

Liu, M., Han, G., Zhang, B., and Jin, X. (2013a). Influence of subtropical high's variation period and structure on plum rain onset. *Sci. Meteor. Sin.* 33, 430–435. (in Chinese). doi:10.3969/2012jms.0166

Liu, Y., Hong, J., Liu, C., and Zhang, P. (2013b). Meiyu flooding of Huaihe River valley and anomaly of seasonal variation of subtropical anticyclone over the Western Pacific. *Chin. J. Atmos. Sci.* 37, 439–450. (in Chinese). doi:10.3878/j.issn.1006-9895.2012

Liu, M., Han, G., Zhang, B., Hu, L., and Sun, H. (2014). Variation features of meteorological factors about onset of Jianghuai Meiyu and its forecasting focus. *Sci. Meteor. Sin.* 34, 222–228. (in Chinese). doi:10.3969/2013jms.0002

Liu, Y., Liang, P., and Sun, Y. (2019). *The asian summer monsoon: Characteristics, variability, teleconnections and projection*. Amsterdam: Elsevier, 237.

Mao, J., and Wu, G. (2005). Intraseasonal variability in the Yangtze-Huaihe River rainfall and subtropical high during the 1991 meiyu period. *Acta Meteor. Sin.* 05, 762–770. (in Chinese). doi:10.3321/j.issn:0577-6619.2005.05.020

Ninomiya, K., and Muraki, H. (1986). Large-scale circulations over East Asia during Baiu period of 1979. *J. Meteorological Soc. Jpn.* 64, 409–429. doi:10.2151/jmsj1965.64.3_409

Ninomiya, K., and Shibagaki, Y. (2007). Multi-scale features of the Meiyu-Baiu front and associated precipitation systems. *J. Meteorological Soc. Jpn.* 85B, 103–122. doi:10.2151/jmsj.85B.103

Oh, T., Kwon, W., and Ryoo, S. (1997). Review of the researches on Changma and future observational study(KORMEX). *Adv. Atmos. Sci.* 14, 207–222. doi:10.1007/s00376-997-0020-2

Qian, D., and Guan, Z. (2020). Principal modes of the western pacific subtropical high anomaly and their possible impacts on precipitation in east Asia during meiyu season. *Sci. Meteor. Sin.* 40, 649–660. (in Chinese). doi:10.3969/2020jms.0078

Ren, Q., Jiang, X., Zhang, Y., Li, Z., and Yang, S. (2021). Effects of suppressed transient eddies by the Tibetan plateau on the east asian summer monsoon. *J. Clim.* 34, 8481–8501. doi:10.1175/jcli-d-20-0646.1

Sampe, T., and Xie, S. (2010). Large-scale dynamics of the Meiyu-Baiu rainband: Environmental forcing by the westerly jet. *J. Clim.* 23, 113–134. doi:10.1175/2009JCLI3128.1

Song, Z., Zhu, C., Su, J., and Liu, B. (2016). Coupling modes of climatological intraseasonal oscillation in the East Asian Summer monsoon. *J. Clim.* 29, 6363–6382. doi:10.1175/JCLI-D-15-0794.1

Standardization administration (2017). *Meiyu monitoring indices*. Beijing: China Standard Publishing House. GB/T 33671-2017Data Availability Statement.

Su, T., Xue, F., Chen, Y., and Dong, X. (2017). A mechanism study for the intraseasonal oscillation impact on the two northward jumps of the Western Pacific subtropical high. *Chin. J. Atmos. Sci.* 41, 437–460. (in Chinese). doi:10.3878/j.issn.1006-9895.1609.16125

Tao, S., and Cheng, L. (1987). *A review of recent research on the East Asian summer monsoon in China*. London: Oxford University Press.

Tao, S., Zhao, Y., and Chen, X. (1958). The relationship between MAY-YU in far east and the behavior of circulation over Asia. *Acta Meteorol. Sin.* 02, 119–134. (in Chinese). doi:10.11676/qxxb1958.014

Wang, B., and Xu, X. (1997). Northern Hemisphere summer monsoon singularities and climatological intraseasonal oscillation. *J. Clim.* 10, 1071–1085. doi:10.1175/1520-0442(1997)010<1071:NHSMSA>2.0.CO;2

Wang, L., and Ge, J. (2016). Relationship between low-frequency oscillations of atmospheric heat source over the Tibetan Plateau and longitudinal oscillations of the South Asia high in the summer. *Chin. J. Atmos. Sci.* 40, 853–863. (in Chinese). doi:10.3878/j.issn.1006-9895.1509.15164

Wang, W., Sun, C., Cai, X., and Xu, J. (2016). Relationship between South Asia high low frequency oscillation and the drought and flood in the middle and lower reaches of the Yangtze River. *Adv. Earth Sci.* 31, 529–541. (in Chinese). doi:10.11867/j.issn.1001-8166.2016.05.0529

Wang, Y. (1992). Effects of blocking anticyclones in Eurasia in the rainy season (Meiyu/Baiu season). *J. Meteorological Soc. Jpn.* 70, 929–1165. doi:10.2151/jmsj1965.70.5_929

Wang, Y., and Gaoqiao, Q. (2005). Decadal climate variability of rainfall around the middle and lower reaches of Yangtze River and atmospheric circulation. *J. Trop. Meteor.* 04, 351–358. (in Chinese). doi:10.16032/j.issn.1004-4965.2005.04.002

Wu, R., and Wang, B. (2001). Multi-stage onset of the summer monsoon over the western North pacific. *Clim. Dyn.* 17, 277–289. doi:10.1007/s003820000118

Xu, Q. (2007). Recent strong decadal change of Meiyu in 121 years. *Adv. water Sci.* 03, 327–335. (in Chinese). doi:10.3321/j.issn:1001-6791.2007.03.003

Yang, S., and Li, T. (2016). Zonal shift of the South Asian High on the subseasonal time-scale and its relation to the summer rainfall anomaly in China. *Q. J. R. Meteorol. Soc.* 142, 2324–2335. doi:10.1002/qj.2826

Yang, S., and Li, T. (2020). Cause for quasi-biweekly oscillation of zonal location of Western Pacific subtropical high during boreal summer. *Atmos. Res.* 245, 105079. doi:10.1016/j.atmosres.2020.105079

Yang, Y., Xu, L., and Gong, Z. (2004). A diagnostic analysis of moist potential vorticity for typhoon heavy rain in Shandong province. *Meteor. Mon.* 04, 20–25. (in Chinese). doi:10.1117/12.528072

Yao, S., Tong, Q., Li, T., and Gong, K. (2019). The 10-30-day oscillation of winter rainfall in southern China and its relationship with circulation patterns in different latitudes. *Int. J. Climatol.* 40 (1), 3268–3280. doi:10.1002/joc.6396

Yu, D. (1980). Regional rainy season and single station rainy period. *Meteor. Mon.* 10, 12–13. (in Chinese). doi:10.7519/j.issn.1000-0526.1980.10.005

Zhang, Y., and Zheng, Y. (1981). Meiyu season and Meiyu period. *Meteor. Mon.* 04, 19. (in Chinese). doi:10.7519/j.issn.1000-0526.1981.4.010

Zhang, Z., Sun, X., and Yang, X. (2018). Understanding the interdecadal variability of east Asian summer monsoon precipitation: Joint influence of three oceanic signals. *J. Clim.* 31, 5485–5506. doi:10.1175/JCLI-D-17-0657.1

Zhao, J., Chen, L., and Xiong, K. (2018). Climate characteristics and influential systems of Meiyu to the south of Yangze River based on the new monitoring rules. *Acta Meteor. Sin.* 76, 680–698. (in Chinese). doi:10.11676/qxxb2018.025

Zhou, W., and Johnny, C. (2005). Intraseasonal oscillations and the South China Sea summer monsoon onset. *Int. J. Climatol.* 25, 1585–1609. doi:10.1002/joc.1209

Zhou, Z. (1980). Delineation of the rainy season should be based on the seasonal adjustment of the circulation. *Meteor. Mon.* 09, 14–15. (in Chinese). doi:10.7519/j.issn.1000-0526.1980.9.006

Zhu, Z., Zhong, Z., and Ha, Y. (2017). Relationship between typhoon cyclone during Meiyu period over the northwest pacific and Jianghuai meiyu. *Sci. Meteor. Sin.* 37, 522–528. (in Chinese). doi:10.3969/2016jms.0060

Zuo, J., Ren, H., Li, W., Zhang, P., and Yang, M. (2009). Intraseasonal characteristics of the water vapor transport associated with the low-frequency rainfall regimes over Southern China in summer. *Chin. J. Geophys.* 52, 2210–2221. (in Chinese). doi:10.3969/j.issn.0001-5733.2009.09.004

frontiers | Frontiers in Earth Science

TYPE Original Research
PUBLISHED 21 September 2022
DOI 10.3389/feart.2022.1004612

OPEN ACCESS

EDITED BY
Shangfeng Chen,
Institute of Atmospheric Physics (CAS), China

REVIEWED BY
Ziqian Wang,
Sun Yat-Sen University, China
Shaobo Qiao,
Sun Yat-Sen University, China

*CORRESPONDENCE
Ma Qianrong,
maqianron_g@163.com
Zhi Rong,
z_rongphy@126.com

SPECIALTY SECTION
This article was submitted to Atmospheric Science, a section of the journal Frontiers in Earth Science

RECEIVED 27 July 2022
ACCEPTED 07 September 2022
PUBLISHED 21 September 2022

CITATION
Qianrong M, Fang J, Xiaoxue W, Youzhi C, Rong Z and Guoling F (2022), Characteristics and related mechanisms of the persistent extreme precipitation in August 2020 over Western China. *Front. Earth Sci.* 10:1004612. doi: 10.3389/feart.2022.1004612

Characteristics and related mechanisms of the persistent extreme precipitation in August 2020 over Western China

Ma Qianrong[1,2]*, Jia Fang[1,2], Wu Xiaoxue[3], Chang Youzhi[4], Zhi Rong[2]* and Feng Guoling[1,2]

[1]School of Physical Science and Technology, Yangzhou University, Yangzhou, China, [2]Laboratory for Climate Studies, National Climate Center, China Meteorological Administration, Beijing, China, [3]Hulunbuir Air Traffic Management Station, Hulunbuir, China, [4]Key Laboratory of Meteorological Disaster, Ministry of Education (KLME)/Joint International Research Laboratory of Climate and Environment Change (ILCEC)/Collaborative Innovation Center on Forecast and Evaluation of Meteorological Disasters (CIC-FEMD), Nanjing University of Information Science and Technology, Nanjing, China

The persistent heavy precipitation that occurred in most of West China (WC) during August 11–18, 2020, generated the highest rainfall record since recording began in 1961 and was selected as one of the top 10 worst national natural disasters of 2020 in China. Favorable circulation was sustained during August; WC was positioned between two anomalous high-pressure centers over the Tibetan Plateau and Sea of Japan and an anomalous low-pressure center over Mongolia located on its north side, which created a stable and long trough and formed a low-pressure center over WC. At 200 hPa, the subtropical westerly jet was much stronger than average and southward, and the South Asian High (SAH) was strong and extended eastward to 150°E. At 500 hPa, the western Pacific subtropical high (WPSH) was westward and exceptionally strong, which helped abundant water vapor reach the southeastern part of WC and provided favorable dynamic and thermodynamic conditions for precipitation in this region. In addition, the eastward extension of the SAH promotes the westward extension of WPSH, which collectively enhanced the precipitation in WC. At 850 hPa, the low-level jet corresponding to the west-extending subtropical high from the Sea of Japan to WC further enhanced and guided the water vapor transport to WC. In addition, the Mei-Yu front over the Yangtze River Basin in June and July strengthened the northwestward spread of diabatic heating, transient energy, and wave activity fluxes, which likely influenced the large-scale circulation factors and reinforced the precipitation in WC in August 2020.

KEYWORDS

extreme precipitation, characteristics, mechanisms, Western China, South Asian high (SAH)

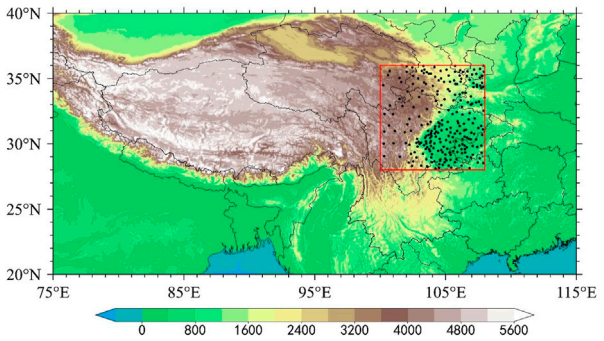

FIGURE1
Spatial distribution of the 250 meteorological stations (Dots) in western China and the geographical features (Unit: m).

1 Introduction

The WC mainly refers to the areas 28°N–36°N and 100°E–108°E and exhibits complex terrain, including plateaus, basins, plains, and hills (shown in Figure 1). Precipitation in WC has two predominant peaks, with the highest precipitation in summer and the second in autumn (Wei et al., 2018a; Zhou et al., 2021). The autumn precipitation in WC is regarded as the last rain belt associated with the retreat of the East Asian summer monsoon (Ding and Wang 2008; Han et al., 2018). Therefore, the variability in autumn precipitation in WC is a major concern for the scientific community (Gao and Guo 1958; Zhang et al., 2019; Zhou et al., 2021). However, under the combination of the Indian, East Asian, and Tibetan Plateau monsoons, abundant summer precipitation in WC (Zhu and Yu 2003; Wang et al., 2016; Xu et al., 2021) is prone to trigger various geological disasters, such as landslides and debris flows, which seriously affect human life and cause large economic losses (Nie and Sun 2022). A more in-depth understanding of precipitation during different seasons in WC has practical application value for improving the accuracy of climate predictions and disaster prevention.

Because of global warming since the second half of the 20th century, precipitation and precipitation extremes have exhibited significant changes and have been detected worldwide (Alexander et al., 2006; Stocker et al., 2014; Zhan et al., 2020). China has frequently experienced severe droughts and heavy floods. In particular, numerous studies on summer precipitation changes in China have detected interdecadal variations since the late 1970s (Wang et al., 2017, Ma et al., 2021). The annual precipitation has increased significantly in southeast, northeast, and western China and decreased from southwest China to northeast Inner Mongolia during the past decades (Shang et al., 2019). Autumn precipitation and rainy days in WC exhibited a significant reduction before the 1990s and increased after the 2000s (Yuan and Liu 2013; Wang et al., 2015; Wei et al., 2018), but the precipitation intensity has been enhanced (Wang et al., 2015; Zhang et al., 2019). Summer precipitation had decreased along a geographical band from the western Sichuan Basin to the southeastern part of Gansu Province, with an increasing trend found in the western Tibetan Plateau, eastern Sichuan Basin, and southwestern Shaanxi Province (Lu et al., 2014; Han et al., 2016; Wang et al., 2016; Jia et al., 2018; Shang et al., 2019). Lai et al. (2010) determined that summer precipitation intensity had increased and led to more floods and landslides. Because summer precipitation in WC has a substantial impact on agricultural production and disaster prevention, a better understanding of precipitation variability is critical for the development of the social economy.

Numerous studies have focused on the physical mechanism of precipitation variability in WC. Anomalous large-scale atmospheric circulation has also been emphasized. The variations in precipitation in WC were closely related to the western Pacific subtropical high (WPSH). When the WPSH extends westward and intensifies, warm and wet air from the south can be effectively delivered to WC, leading to increased precipitation (Zhu and Yu 2003; Wang et al., 2016; Zhou et al., 2019; Zhou and Wang 2019). Notably, the SAH also has a considerable impact on precipitation in WC. Chen et al. (2016) reported a significant positive correlation between summer water vapor content in southwest China and the SAH intensity index, area index, and eastward extension index. The abnormally strong SAH is conducive to water vapor transport from the South China Sea to the eastern Sichuan Basin; when accompanied by the upward movement from a low to a high level, precipitation is significantly enhanced (Chen et al., 2016). In addition, the position of the SAH has a significant influence on the regionality of precipitation in WC. When the SAH extended eastward and northward, more precipitation occurred in the western Sichuan Basin and reversed in the east (Wang et al., 2016). Numerous previous studies have shown that variations in precipitation in the WC are closely related to the East Asian jet stream (EAJS). The increase in sea surface temperature in the central equatorial Pacific had caused a southward shift of the EAJS, resulting in abnormal descending branches and less autumn precipitation in WC (Wei et al., 2018). In contrast, when the EAJS was strengthened and extended northward, precipitation increased in this region (Wang and Zhou 2019; Zhou et al., 2019; Zhou and Wang 2019). The strengthening of the WPSH and northward displacement of the EAJS have contributed to the enhancement of water vapor transport from the Bay of Bengal, South China Sea, and western Pacific, which enhances the precipitation in WC (Wei et al., 2018; Zhou et al., 2019).

In most areas of China, precipitation mainly occurs in the summer, among which the most typical is the Mei-Yu front in the Yangtze–Huai River Basin. An extreme Mei-Yu front in

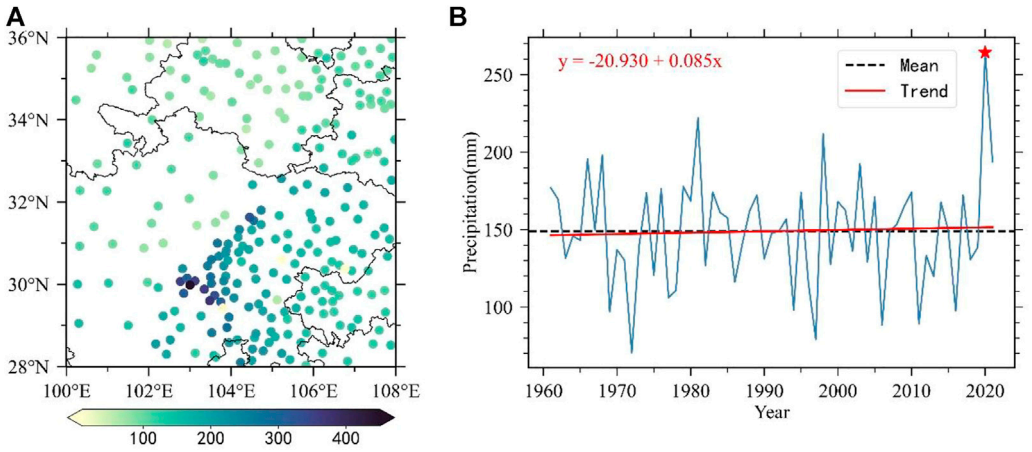

FIGURE 2
Spatial distribution of the climatology **(A)** precipitation distribution and **(B)** the station-averaged precipitation series in August during 1961–2021 in WC (Dashed black line and the red solid line represent the climatological mean and linear trend, respectively. Unit: mm).

2020 was sustained for approximately 62 days from June 1 to August 1. Precipitation anomalies have led to serious flooding in these areas (Zhao et al., 2021). During the Mei-Yu period, the periodic strengthening of the EAJS and SAH ridgeline moved northward and stabilized around 37°N–40°N and 26°N–28°N, which resulted in strong divergence in the upper troposphere, contributing to the upward movement and precipitation in most of southern China (Ding et al., 2021). The "two ridges and one trough" type existed in the middle and high latitudes of Eurasia at 500 hPa, and the WPSH was abnormally strong, westward, and continuous (Qiao et al., 2021). Meanwhile, the Northwest Pacific Anticyclone (WNPAC) at 850 hPa in the lower troposphere was also abnormally enhanced and directly affected the water vapor transport conditions in most of southern China (Zhao et al., 2021). Crucially, extremely heavy rainfall occurred in WC during August 2020, which has been regarded as one of the top 10 worst national natural disasters in China in 2020 (http://www.mem.gov.cn/xw/yjglbgzdt/202101/t20210102_376288.shtml). Waterlogging, landslides, and other disasters caused by heavy rain result in heavy losses and threats to human lives and property (Chen et al., 2022; Tang et al., 2022). Therefore, this study investigated the underlying relationship between the anomalous August precipitation in WC and the associated circulations in 2020.

The remainder of this paper is organized as follows. Section 2 introduces the data and methods used in this study. The spatiotemporal variations in the August 2020 precipitation over WC and the associated mechanisms are presented in Section 3. Finally, the conclusions and discussion are presented in Section 4.

2 Data and methods

2.1 Dataset

The daily observed precipitation data were obtained from the National Meteorological Information Center of the China Meteorological Administration, covering 2020 meteorological stations throughout China from 1961 to 2021. Because of the errors caused by missing data, only stations missing less than 5% of the total time series were retained, and the missing data from these retained stations were estimated using the inverse distance method (Eischeid et al., 2000). Finally, 250 stations in WC (shown in Figure 1) were chosen for this study.

The monthly and daily reanalysis data of ERA5 from 1961 to 2021 were provided by the European Center for Medium-Range Weather Forecasting (ECMWF), including potential height, temperature, zonal wind, meridional wind, vertical velocity, and specific humidity. The horizontal resolution was 1.0° × 1.0°, and the vertical layer was 1,000–1 hPa with 37 layers. In addition, the ERA5 dataset from July to August 2020 were used in this study.

2.2 Methods

The vertically integrated water vapor transport flux (WVT) was calculated from 1,000 to 300 hPa using the method proposed by Trenberth (1991). The wave activity flux (WAF) defined by Takaya and Nakamura (2001) was used to study the propagation of the Rossby wave train. The formula used is as follows:

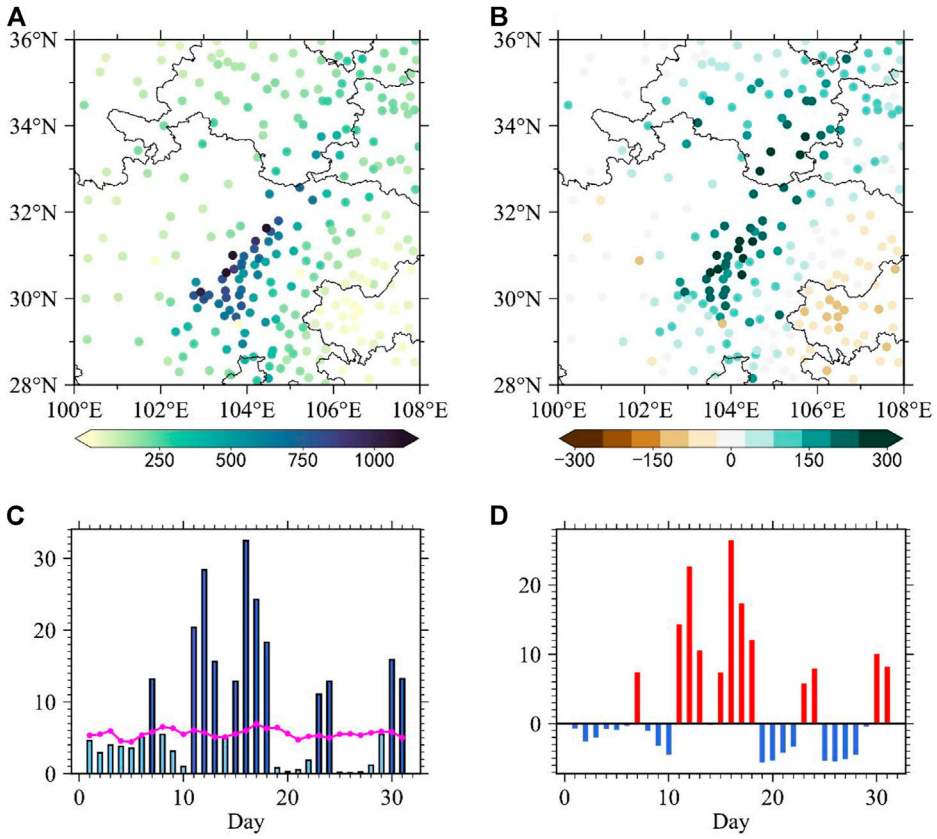

FIGURE 3
Spatial distribution of **(A)** precipitation (Unit: mm) and **(B)** precipitation anomaly percentage (Unit: %) in August 2020 in WC. **(C)** and **(D)** show the daily precipitation and precipitation anomalies (Unit: mm) in August 2020 in WC (Dark blue histogram and red line in **(C)** represent precipitation exceeding the August 2020 average and climatological daily mean precipitation in August during 1961–2021, respectively).

$$W = \frac{1}{2|\bar{U}|}\begin{pmatrix} \bar{u}\left(\psi_x'^2 - \psi'\psi_{xx}\right) + \bar{v}\left(\psi_x\psi_y' - \psi'\psi_{xy}\right) \\ \bar{u}\left(\psi_x'\psi_y' - \psi'\psi_x'\right) + \bar{v}\left(\psi_y'^2 - \psi'\psi_y'\right) \end{pmatrix}$$

where ψ and $U = (u, v)$ denote the stream function and horizontal wind, respectively, and W represents two-dimensional Rossby WAF. In addition, a barotropic Rossby wave source (RWS) is useful for inspecting the generation of Rossby waves. This was formulated by Sardeshmukh and Hoskins (1988) as follows:

$$RWS = -\nabla \cdot \left(V_\chi \xi_a\right) = -V_\chi \cdot \nabla \xi_a - \xi_a \nabla \cdot V_\chi$$

where V_χ is the divergence wind and ξ_a is the absolute vorticity.

The apparent heat source (Q) is used to characterize the diabatic heating (Zhang et al., 2009):

$$Q = c_p\left(\frac{\partial T}{\partial t} + \vec{V} \cdot \nabla T + \omega \cdot \left(\frac{p}{p_0}\right)^{\kappa}\frac{\partial \theta}{\partial p}\right)$$

where θ is the potential temperature, T is the temperature, ω is the vertical velocity, p_0= 1,000 hPa. $\kappa = R/c_p$ is generally 0.286 (R = 287 J·kg^{-1}·K^{-1}, c_p = 1,005 J·kg^{-1}·K^{-1}). The vertical integrated <Q> was calculated from the surface to 100 hPa according to

$$<Q> = \frac{1}{g}\int_{p_0}^{p} Q\,dp$$

To verify the synoptic-scale transient waves, u' and v' were obtained by the 2.5–6-day bandpass filtering technique at 200 hPa because of the transient wave activity major concentration in the upper troposphere (Chen et al., 2012). The transient disturbance kinetic energy k' is defined as:

$$k' = \frac{1}{2}\left(u'^2 + v'^2\right)$$

The Hybrid Single Particle Lagrange Integrated Trajectory (HYSPLIT) model was developed jointly by NOAA's Air Resources Laboratory and the Australian Bureau of Meteorology, and is widely used in tracking particles, moisture, or gas sources and transmission. In this study, HPSPLIT4.9 was used to capture the direction and proportion of water vapor.

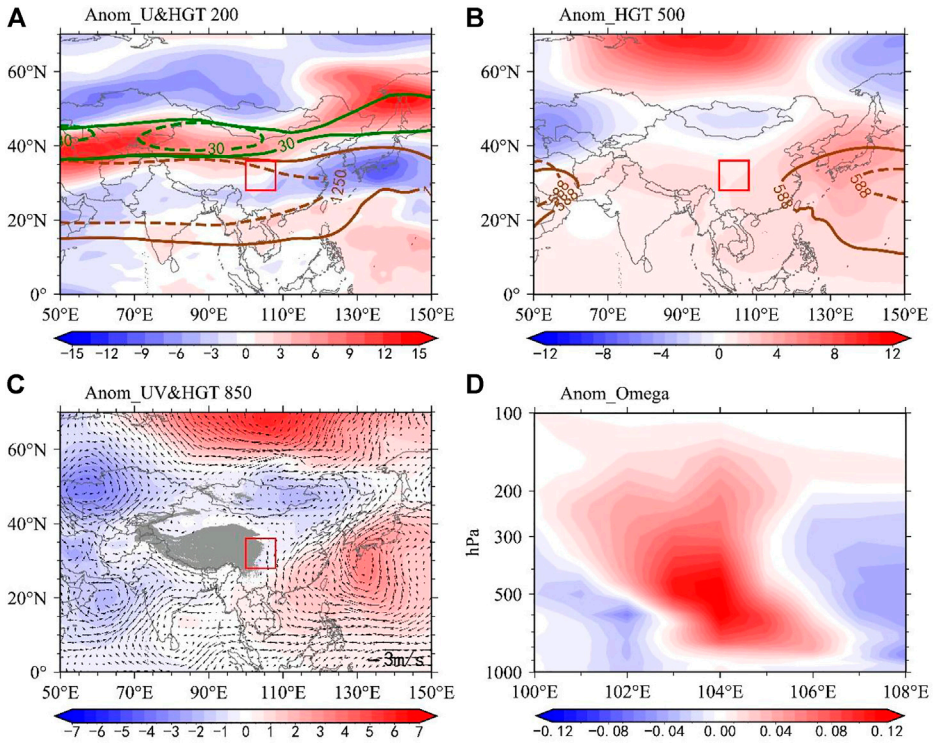

FIGURE 4
Characteristics of the anomalous atmospheric circulation in August 2020: **(A)** 200 hPa zonal wind anomaly (shading, Units: m·s^{-1}; the dashed and solid green lines represent the 30 m·s^{-1} isoline in the climatological mean and August 2020; the dashed and solid brown lines are the same as the green lines but for the 12,500 isolines at 200 hPa); **(B)** 500 hPa geopotential height anomaly (shading, Units: gpm; the dashed and solid brown lines are the 5,880 isolines in the climatological mean and August 2020); **(C)** 850 hPa geopotential height (shading, Units: gpm) and wind field anomalies (vectors, Units: m s^{-1}); **(D)** regional averaged vertical velocity anomalous height-longitude profile (Units: 10^{-1} Pa·s^{-1}). The red rectangular frame in **(A–C)** shows the location of WC, and the shaded gray areas in **(C)** exhibit the 850 hPa terrain.

2.3 Indices

To quantitatively depict the variability in the WPSH and SAH, the WPSH intensity index and SAH intensity index were calculated using traditional methods. Related methods were introduced by the National Climate Center of the China Meteorological Administration (http://cmdp.ncc-cma.net, in Chinese). The range of the 5,880-gpm contour at 500 hPa and the 12,500-gpm contour at 200 hPa were used to describe the WPSH and SAH, respectively.

3 Results

3.1 Characteristics of the extreme precipitation of August 2020 in West China

Figure 2 shows the spatial distribution and the corresponding station-averaged time series of August precipitation during 1961–2021 in WC to understand the characteristics and causes of the extraordinary precipitation. The spatial patterns of the precipitation increased from the northwest to the southeast (Figure 2A). High values were located in the Sichuan Basin, and low values occurred in high-elevation areas, which spanned 50–450 mm. The precipitation in WC exhibited an indistinctive increasing trend during 1961–2021 (Figure 2B). Notably, the precipitation in August 2020 was more than twice that of the previous record. After removing the value for 2020, precipitation in this region showed a slightly decreasing trend.

The spatial distribution of the precipitation in August 2020 (Figure 3A) varied from the climatology mean (Figure 2A), which exhibited a heavy precipitation belt in middle WC along 104°E–105°E and relatively lower precipitation in western and eastern WC. The precipitation anomaly percentage further confirmed that extraordinary precipitation occurred in middle WC (Figure 3B). The precipitation at 161 stations exceeded the historical average and were primarily scattered in the western Sichuan Basin, southeast Gansu, and southwest Shaanxi. The precipitation at 44 stations in Sichuan Province has been recorded since 1961. In addition, persistent heavy

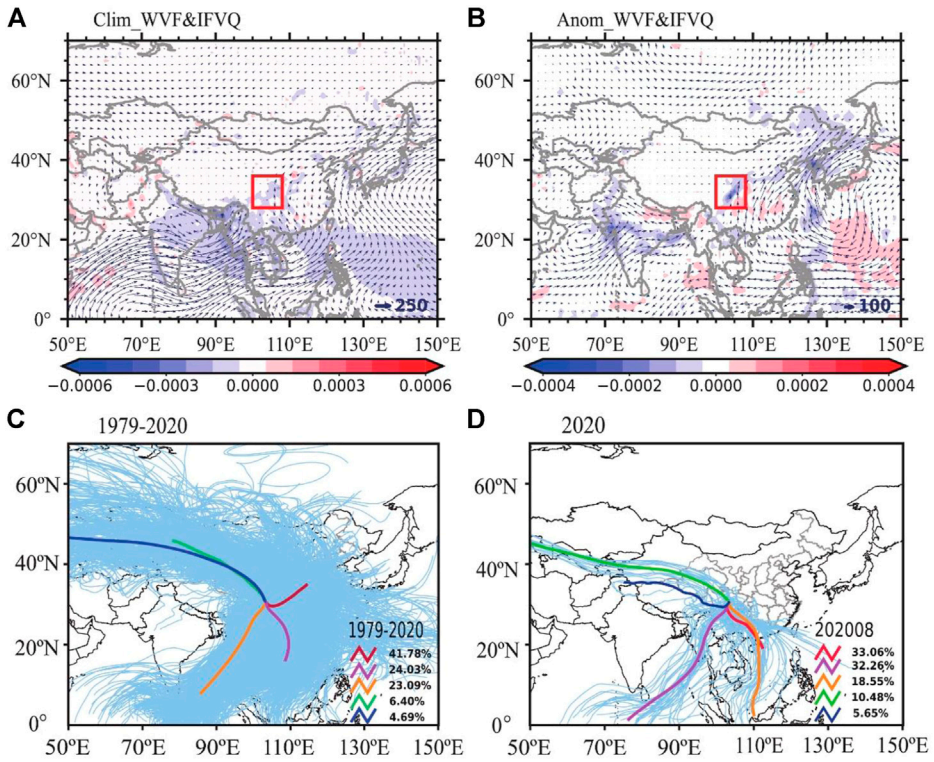

FIGURE 5
(A) August WVT (vectors, Units: kg·m^{-1} s^{-1}) and its divergence (shading, Units: kg·m^{-2} s^{-1}) during 1961–2020, **(B)** WVT (vectors, Units: kg·m^{-1} s^{-1}) and its divergence (shading, Units: kg·m^{-2} s^{-1}) in August 2020. The contribution rates of water vapor transport to WC **(C)** during 1979–2020 and **(D)** in August 2020.

precipitation occurred in WC during August 11–18, 2020 (Figures 3C,D), which was defined as one of China's top ten national natural disasters in 2020 (http://www.mem.gov.cn/xw/yjglbgzdt/202101/t20210102_376288.shtml). Chen et al. (2022) reported that this extraordinary precipitation caused waterlogging and mudslide disasters that affected 8.523 million people and caused 58 deaths. In addition, there were two consecutive heavy precipitation processes in late August 2020: from August 23 to 24 and from August 30 to 31. Therefore, it is of great significance to analyze the characteristics of the record-breaking precipitation that occurred in WC in August 2020.

3.2 Atmospheric circulation responsible for the extreme precipitation

Atmospheric circulation anomalies can directly cause precipitation anomalies. Thus, this section analyzes the circulation characteristics associated with the August 2020 precipitation anomaly in WC. The variable responses to the local anomalous atmospheric circulation for this extraordinary precipitation event are shown in Figure 4. The zonal wind at 200 hPa over East Asia to the Western Pacific (50°E–180°E, 30°N–40°N) was strong and southward, and the subtropical westerly upper-level jet was strong and southward. The maximum jet centers were located near (50°E–80°E, 30°N–40°N) and (150°E, 50°N). The WC was located south of the jet stream axis (50°E–80°E, 30°N–40°N). The jet stream and SAH were significantly stronger than normal in August 2020 (Figure 4A). In the middle troposphere, the WPSH was predominantly westward and stronger than usual (Figure 4B), which caused the southwest airflow on the southwest side of the WPSH northwestward, reaching the southern part of the WC and providing abundant water vapor for precipitation in this region. Meanwhile, in the middle latitudes of 500 hPa, anomalous low pressure and two high-pressure centers were observed over Mongolia, the Tibetan Plateau, and the Sea of Japan, respectively. WC was located in the middle of the two high-pressure centers and was affected by the low-pressure center. The abnormal low pressure over Mongolia was beneficial for the cold air transported southward, which finally mingled with warm and wet air in WC, forming substantial and persistent precipitation. At

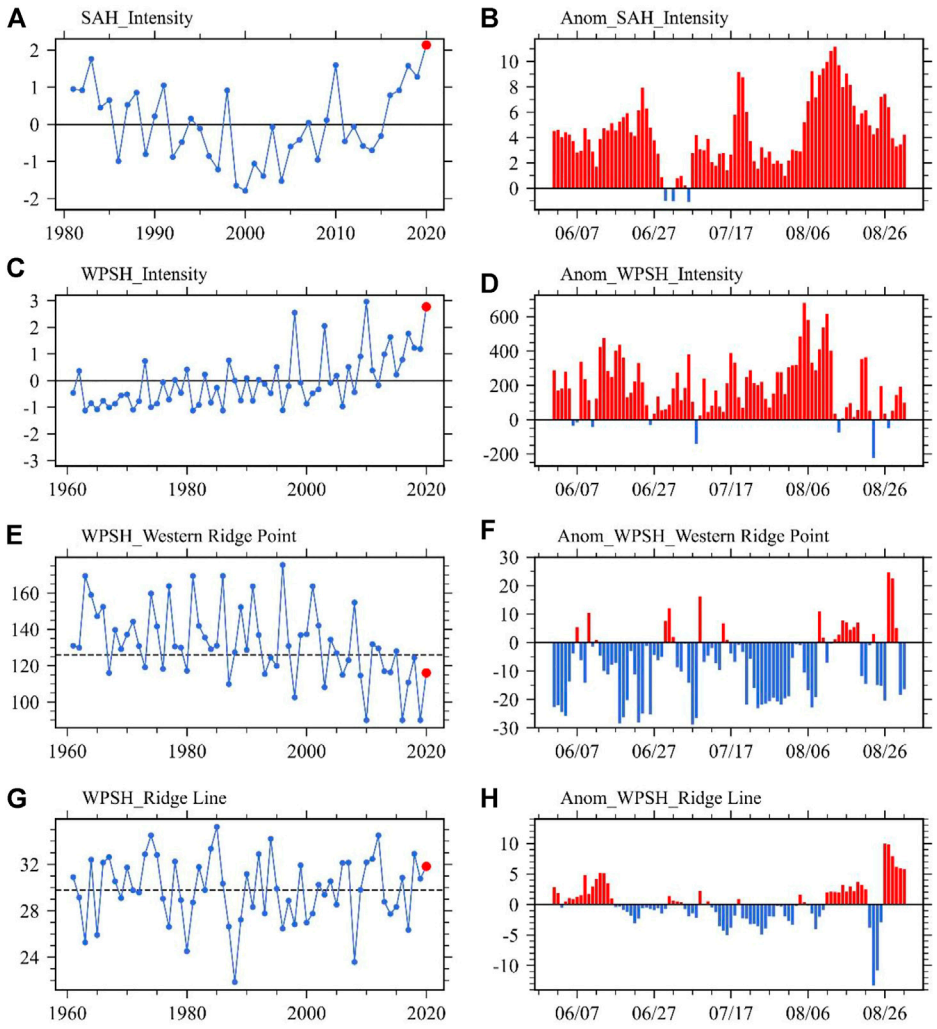

FIGURE 6
The WPSH intensity index, SAH intensity index, WPSH western ridge point index, and ridge line index in August during 1961–2020 **(A,C,E,G)** and anomalies in June–August 2020 **(B,D,F,H)** (The dotted lines in **(A,C,E,G)** represent the climatological average in August during 1961–2020).

TABLE 1 The correlations between the WPSH intensity index, SAH intensity index, WPSH western ridge point index, and ridge line index with precipitation anomaly in August 2020 over WC.

Index	The correlation coefficients
WASH Intensity	***r*= 0.32**
SAH Intensity	***r*=0.42**

Bold type indicates correlations are significant at the 95% confidence level.

850 hPa (Figure 4C), a south low-level jet corresponding to the west-extending subtropical high from the western Pacific Ocean to the eastern part of WC provided abundant water vapor conditions for precipitation. At the same time, strong divergence at the upper level and strong convergence at the lower level over WC combined with deep and strong vertical movement from the lower level to the upper level (Figure 4D) provided adequate dynamic conditions for precipitation.

In conclusion, the characteristics of the atmospheric circulation fields in August 2020 were favorable for sustained heavy precipitation in WC. At 200 hPa, the westerly jet stream was strong and was located just north of WC. The strong divergence at the upper level corresponded to a strengthened SAH and discernable convergence at the lower level. The above coupling effect further strengthened the south wind, convergence at the lower level, and vertical movement, which formed a positive feedback loop to maintain the precipitation process. Moreover, the WPSH was significantly westerly, so the warm and wet moisture from the southwest side of the WPSH could reach the WC.

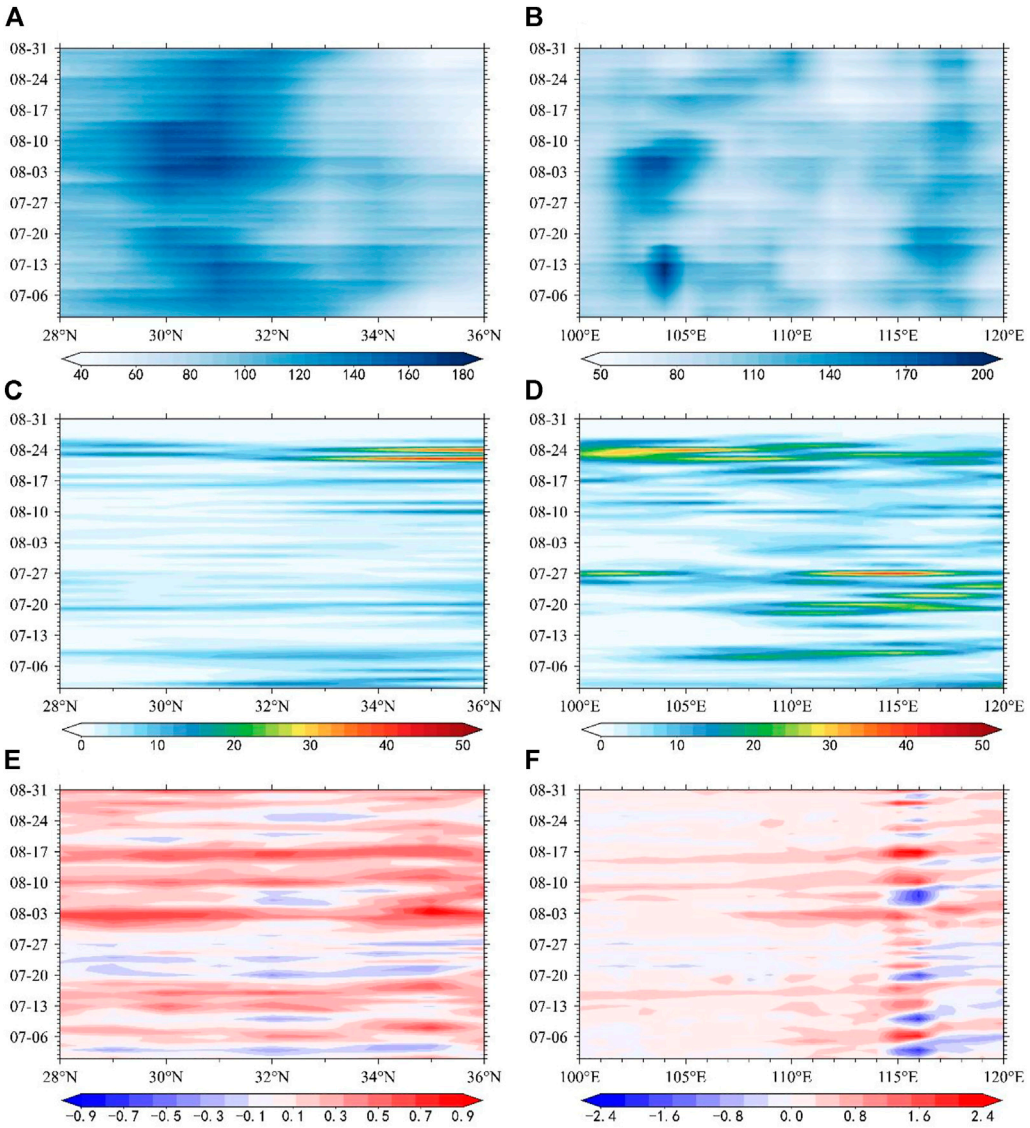

FIGURE 7
Latitude–time and longitude–time evolution of precipitation **(A)**, **(B)** (Units: mm); the transient disturbance kinetic energy k′ **(C)**, **(D)** (Units: $m^2 \cdot s^{-2}$) and diabatic heating **(E)**, **(F)** (Units: 10^{-4} K day^{-1}) within 28°N–36°N, 100°E–120°E in July to August 2020.

In addition to the dynamic conditions provided by favorable circulation, persistent precipitation also requires continuous water vapor transport. Figure 5 compares the climatological mean and August 2020 water vapor transport characteristics over WC. In Figure 5A, the westward water vapor from the western Pacific Ocean and the eastward water vapor transport from the Arabian Sea in the Indian Ocean and Bay of Bengal are the main moisture sources for August precipitation in WC. The water vapor converged predominantly in eastern and southern WC, which provided favorable conditions for precipitation in this region (Figure 2A). Obtained by the clustered daily backward track of water vapor in August from 1979 to 2020, Figure 5C shows the track 5 channels which were based on the increase in the growth rate of spatial variance. Water vapor primarily comes from the western Pacific Ocean, the Arabian Sea, and the Bay of Bengal in the Indian Ocean, and is partially transported by westerlies.

In August 2020, the water vapor from the western Pacific Ocean was significantly stronger as the strengthened WNPAC provided more moisture from the South China Sea (Figure 5B). Meanwhile, the water vapor formed a narrow convergence zone in WC, which corresponds to the characteristics of heavy precipitation in Figure 3A. The first five water vapor track channels for August 2020 (Figure 5D) demonstrate that the main water vapor transported by the WNPAC was

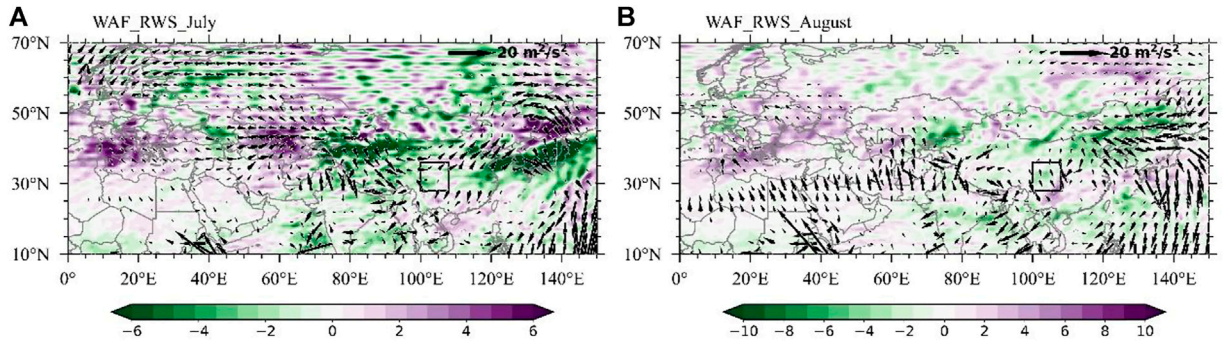

FIGURE 8
The WAF (vectors; unit: $m^2 \cdot s^{-2}$) and Rossby wave source (shading; units: 10^{-10} $m^2 \cdot s^{-1}$) at 200 hPa in July **(A)** and August **(B)** 2020.

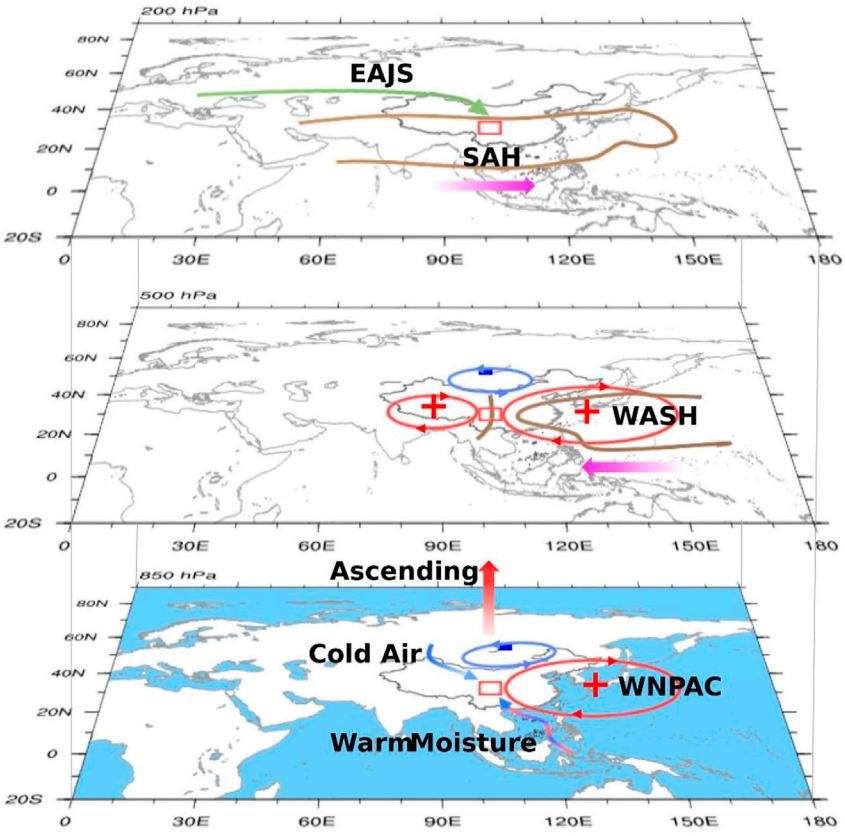

FIGURE 9
Schematic diagram describing what drives the anomalous strong precipitation over WC in August 2020.

southwesterly. The water vapor transport from the southern part of the WNPAC was more westerly than usual and turned northeast near Hainan Island, continuously conveying water vapor to southern WC and forming a distinct water vapor convergence zone. The above results demonstrate that the strengthened southern water vapor transport contributed to the specific humidity, which was slightly higher than the climatology mean. In addition, the strong convergence zone of water vapor and circulation provided favorable conditions for continuous heavy precipitation.

3.3 Related physical mechanisms underlying the extreme precipitation

During the rainfall period in WC, the intensity and position of key influential systems, such as the SAH and WPSH, have a significant impact on the rainfall intensity (Chen et al., 2022). In August 2020, the SAH significantly extended and strengthened eastward (Figure 4A). Thus, the standardized SAH intensity index is discussed first. As shown in Figures 6A,B, the SAH intensity in August reached a peak in 2020. The SAH intensity anomaly from July to August 2020 indicates that the SAH was the strongest in mid-August 2020, corresponding to the occurrence of heavy precipitation (Figure 3C). Moreover, the correlation coefficient between precipitation and the SAH intensity index in August 2020 reached 0.42 (significant at a confidence level of 0.05, Table 1). The results indicate that the anomalous SAH in August corresponds well with extreme precipitation in WC. As shown in Figure 6C, the intensity of the August WPSH exhibited a second peak in 2020. The WPSH intensity from June to August in 2020 was anomalously strong, especially in mid-August (Figure 6D). The correlation coefficient between precipitation and the WPSH intensity index in August 2020 reached 0.32 (significant at a 0.1 confidence level, Table 1). Moreover, the WPSH western ridge point extended westward, and the WPSH ridge line was more northerly than the climatological average (Figures 6E,G). In mid-August 2020, the WPSH anomalously moved westward and northward (Figures 6H). In addition, the intensification and abnormal eastward extension of the SAH influenced the precipitation accompanied with the strengthened and westward extended WPSH.

Therefore, the significant strengthening of the SAH and WPSH provided a stable circulation structure for this heavy precipitation. In the lower troposphere, the strong WPSH transported water vapor from the Pacific to the west, together with water vapor from the South China Sea, and then to WC along the western boundary of the WPSH. Combined with the topography of the Tibetan Plateau, abundant water vapor formed a narrow water vapor convergent belt over the WC.

Figure 7 shows the time-latitude and time-longitude profiles of the precipitation, disturbance kinetic energy, and diabatic heating. The daily distribution of precipitation in WC from July to August 2020 indicated that heavy precipitation occurred frequently and persistently in WC in mid-August (Figures 7A,B). The precipitation in July was significantly higher in the Yangtze River Basin than normal, which is related to the 2020 super Mei-Yu in June and July (Zhao et al., 2021). From July to August, the precipitation moved westward and northward from the Yangtze River Basin to WC. Relevantly, there are two significant disturbance kinetic energy paths: 110–120°E, which corresponded to the extreme Mei-Yu in the Yangtze River in July 2020, and 100–110°E, which was related to the heavy precipitation in WC in August 2020 (Figures 7C,D). Disturbance kinetic energy can strengthen the precipitation by influencing the intense convection (Para et al., 2019). In addition, the energy conversion from synoptic-scale disturbance to low-frequency fluctuation in the middle and lower troposphere has been significantly enhanced, which makes importation contributions to this heavy precipitation (Li 2007). From August 10 to 20, 2020, it can be clearly seen from Figures 7C,D that a large center of kinetic energy disturbance reached WC, which was beneficial for the transport of water vapor and the occurrence of this continuous extreme precipitation. In addition, the characteristics of diabatic heating were used to analyze the possible effects of atmospheric circulation on the continuous heavy precipitation process in WC in mid-August 2020 (Figures 7E,F). The evolution characteristics of diabatic heating differed from July to August, and stronger diabatic heating corresponded to continuous heavy precipitation in the Yangtze River Basin in July 2020 and in WC in mid-August 2020.

Abnormal circulation patterns control the intensity and location of persistent heavy precipitation and thus determine the evolution characteristics of the abnormal heating energy. Abnormal heating energy also has a feedback effect on atmospheric circulation (He and Zhai 2018). Figure 8 shows the WAF propagation during July and August 2020, which varied widely between the 2 months. There was a quasi-zonal " + - + -"wave train over the Eurasian continent over 30°N–50°N in July 2020 (Figure 8A). The wave flux propagated from west to east along the jet stream and affected the super Mei-Yu over the Yangtze River Basin. In August, quasi-stationary Rossby wave energy dispersed northward at 26°N–28°N and propagated from south to north. In conclusion, the continuous heavy precipitation in WC in mid-August 2020 was influenced by the maintenance of low-frequency atmospheric circulation and the diabatic heating caused by the precipitation. The abnormal atmospheric circulation, such as the abnormal SAH and WPSH, played a key role in the occurrence, maintenance, and extinction of this heavy precipitation. The released latent heat by the heavy precipitation process has positive feedbacks and partially strengthens the intensity and duration of precipitation (Hack et al., 1989; Rao and Srinivasan., 2016).

4 Conclusion and discussion

In summary, persistent heavy precipitation events have significant societal impacts. The persistent heavy precipitation event that occurred over WC in August 2020 broke the historical record since monitoring began in 1961. In addition, the widespread and devastating floods over most regions of WC are considered to be within the top 10 worst national natural disasters in China in 2020. In the present work, we aimed to understand extreme rainfall from large-scale circulation, and Figure 9 provides a schematic diagram of this heavy precipitation event.

The precipitation in WC in August 2020 set the historical record since monitoring began in 1961. The precipitation at 44 stations throughout WC, primarily distributed in Sichuan Province, set a historical record by reaching 34.99 mm. Persistent heavy precipitation occurred in WC, mostly concentrated during the period of August 10–20, 2020. Favorable circulation was sustained in August. At 200 hPa, the subtropical westerly jet was much stronger than normal and southward, and the maximum centers were located near 50°E–100°E and 130°E–150°E. The SAH was eastward and strong, and its intensity was significantly correlated with precipitation in WC. At 500 hPa, the WPSH was westward and strong, which helped abundant water vapor reach the southeastern part of the WC to provide favorable dynamic conditions for precipitation in this region. Chen et al. (2016) emphasized that the Mei-Yu rain band over the Yangtze–Huai River basin through its effect on water vapor transport, which indicates the anomalies precipitation in WC in August 2020 may influenced by the strong and persistent anomalous circulation of super Mei-Yu in 2020. At the same time, WC was positioned between two anomalous anticyclone centers over the Tibetan Plateau and Sea of Japan, with an anomalous cyclone over Mongolia located to the north that created a stable, long trough and formed a low-pressure center over WC. At 850 hPa, there was a low-level jet corresponding to the west-extending subtropical high from the Sea of Japan to WC. The anomalous low-level southerly jet enhanced and guided more water vapor transport to WC.

Studies show that the effect of tropical Indian Ocean SST plays a significant role in SAH and WPSH (Ding and Wang 2008; Huang et al., 2011). The standardized SAH intensity index and WPSH intensity index during the precipitation period ranked first in 1981 and second in 1961, respectively. The stronger SAH enhanced the upward movement over WC and strengthened the convergence of the water vapor. A strong WPSH strengthened the water vapor from the South China Sea and the Western Pacific into WC. Both provided sufficient dynamic and thermodynamic conditions for heavy precipitation. The occurrence and persistence of the super Mei-Yu in June and July 2020 are mainly due to the strengthening and westward expansion of the WPSH, a positive-phase Pacific–Japan (PJ) pattern and a mid-troposphere "two ridge–one trough" pattern over Asia (Qiao et al., 2021). In addition, the development of La Niña sustained the large-scale circulation, which leaded to the continuous development of the super Mei-Yu. The development and maintenance of large-scale circulation during Mei-Yu period played a positive role in the extreme precipitation in August over WC. The diabatic heating, transient energy, and wave activity fluxes generated by ultra-strong Mei-Yu may affect the precipitation of large-scale circulation factors and WC. Here is a possibility of the influence of Mei-Yu on the extreme precipitation in WC. The specific influencing mechanism needs to be further studied. In addition, the SST warming anomalies over the Tropical Indian Ocean enriched and extended the super Mei-Yu in the Yangtze river basin in 2020 (Qiao et al., 2021; Zhou et al., 2021). The warming of the Indian Ocean SST also plays an important role in the extreme precipitation in August 2020 over WC, which needs further study.

This study represents a persistent heavy precipitation event in WC that occurred in August 2020. Several avenues for future work exist to understand these extreme precipitation events. We remain unsure of the exact drivers of 10-day persistent heavy precipitation, such as MCSs and synoptic isotropic ascent (Schumacher and Johnson 2004). The occurrence probability of events with an intensity exceeding that of the event of August 10–20 and whether it will increase with global warming in the future requires further investigation.

Data availability statement

The original contributions presented in the study are included in the article/supplementary material, further inquiries can be directed to the corresponding authors.

Author contributions

QM and RZ conceived of the presented idea. QM and FJ developed the theory and performed the computations. XW and YC verified the analytical methods. GF encouraged to investigate and supervised the findings of this work.

Funding

This work was supported by the National Natural Science Foundation of China (Grant 41975088 and 42205023).

Acknowledgments

The station observed dataset is provided by the National Meteorological Information Center (NMIC), China. We sincerely thank reviewers for their insightful comments and useful suggestions.

Conflict of interest

The authors declare that the research was conducted in the absence of any commercial or financial relationships that could be construed as a potential conflict of interest.

Publisher's note

References

Alexander, L. V., Zhang, X., Peterson, T. C., Caesar, J., Gleason, B., Tank, A.., et al. (2006). Global observed changes in daily climate extremes of temperature and precipitation. *J. Geophys. Res.* 111, D05109. doi:10.1029/2005jd006290

Chen, D., Zhou, C., and Deng, M. (2016). Characteristics of water vapor content in southwest China and its association with the South Asian high in summer. *J. Appl. Meteorological Sci.* 27 (4), 473–479. doi:10.11898/1001-7313.20160410

Chen, H., Liu, L., and Zhu, Y. (2012). Possible linkage between winter extreme low temperature events over China and synoptic-scale transient wave activity. *Sci. China Earth Sci.* 56 (7), 1266–1280. doi:10.1007/s11430-012-4442-z

Chen, Q., Ye, Y., Zhang, W., and Zhou, T. (2022). Heavy rainfall event in mid-August 2020 in southwestern China: Contribution of anthropogenic forcings and atmospheric circulation. *Bull. Am. Meteorological Soc.* 103 (3), S111–S117. doi:10.1175/bams-d-21-0233.1

Ding, Y., Liu, Y., and Hu, Z. (2021). The record-breaking meiyu in 2020 and associated atmospheric circulation and tropical SST anomalies. *Adv. Atmos. Sci.* 38 (12), 1980–1993. doi:10.1007/s00376-021-0361-2

Ding, Y., and Wang, Z. (2008). A study of rainy seasons in China. *Meteorol. Atmos. Phys.* 100 (1), 121–138. doi:10.1007/s00703-008-0299-2

Eischeid, J. K., Pasteris, P. A., Diaz, H. F., Plantico, M. S., and Lott, N. J. (2000). Creating a serially complete, national daily time series of temperature and precipitation for the Western United States. *J. Appl. Meteor.* 39 (9), 1580–1591. doi:10.1175/1520-0450(2000)039<1580:cascnd>2.0.co;2

Gao, Y., and Guo, Q. (1958). On the autumn raining area in China. *Acta Meteor. Sin.* 29 (4), 264–273. (in Chinese).

Hack, J. J., Schubert, W. H., Stevens, D. E., and Kuo, H. C. (1989). Response of the hadley circulation to convective forcing in the ITCZ. *J. Atmos. Sci.* 46 (19), 2957–2973. doi:10.1175/1520-0469(1989)046<2957:rothct>2.0.co;2

Han, T., He, S., Wang, H., and Hao, X. (2018). Enhanced influence of early-spring tropical Indian Ocean SST on the following early-summer precipitation over Northeast China. *Clim. Dyn.* 51 (11), 4065–4076. doi:10.1007/s00382-017-3669-y

Han, X., Xue, H., Zhao, C., and Lu, D. (2016). The roles of convective and stratiform precipitation in the observed precipitation trends in Northwest China during 1961–2000. *Atmos. Res.* 169, 139–146. doi:10.1016/j.atmosres.2015.10.001

He, B., and Zhai, P. (2018). Changes in persistent and non-persistent extreme precipitation in China from 1961 to 2016. *Adv. Clim. Change Res.* 9 (3), 177–184. doi:10.1016/j.accre.2018.08.002

Huang, G., Qu, X., and Hu, K. (2011). The impact of the tropical Indian Ocean on South Asian High in boreal summer. *Adv. Atmos. Sci.* 28 (2), 421–432. doi:10.1007/s00376-010-9224-y

Jia, Y., Zhang, B., and Ma, B. (2018). Daily SPEI reveals long-term change in drought characteristics in southwest China. *Chin. Geogr. Sci.* 28 (4), 680–693. (in Chinese). doi:10.1007/s11769-018-0973-3

Lai, X., Fan, G., Dong, Y., Hua, W., Liu, Y., Yu, Z., et al. (2010). Analysis of summer daily precipitation variation characteristic in China during 19612007. *Resour. Environ. Yangtze Basin* 19 (11), 1277–1282. (in Chinese).

Li, Y. (2007). Conversion of kinetic energy from synoptic scale disturbance to low-frequency fluctuation over the Yangtze River valley in the summers of 1997 and 1999. *Adv. Atmos. Sci.* 24 (4), 591–598. doi:10.1007/s00376-007-0591-y

Lu, E., Zeng, Y., Luo, Y., Ding, Y., Zhao, W., Liu, S., et al. (2014). Changes of summer precipitation in China: The dominance of frequency and intensity and linkage with changes in moisture and air temperature. *J. Geophys. Res. Atmos.* 119 (2212), 575–612. doi:10.1002/2014jd022456

Ma, Q., Zhang, J., Ma, Y., Game, A., Chen, Z., Chang, Y., et al. (2021). How do multiscale interactions affect extreme precipitation in eastern central Asia?. *J. Clim.* 34 (18), 7475–7491. doi:10.1175/jcli-d-20-0763.1

Nie, Y., and Sun, J. (2022). Causes of interannual variability of summer precipitation intraseasonal oscillation intensity over southwest China. *J. Clim.* 35 (12), 3705–3723. doi:10.1175/jcli-d-21-0627.1

Para, J. A., Kesarkar, A., Bhate, J., Singh, V., Panchal, A., Munsi, A., et al. (2019). Large-scale dynamics of Western disturbances caused extreme precipitation on 24–27 January 2017 over Jammu and Kashmir, India. *Model. Earth Syst. Environ.* 6, 99–107. doi:10.1007/s40808-019-00661-4

Qiao, S., Chen, D., Wang, B., Cheung, H. N., Liu, F., Cheng, J., et al. (2021). The longest 2020 Meiyu season over the past 60 years: Subseasonal perspective and its predictions. *Geophys. Res. Lett.* 48 (9), e2021GL093596. doi:10.1029/2021gl093596

Rao, S., and Srinivasan, J. (2016). The impact of latent heating on the location and strength of the tropical easterly jet. *Meteorol. Atmos. Phys.* 128, 247–261. doi:10.1007/s00703-015-0407-z

Schumacher, R., and Johnson, R. (2004). Organization and environmental properties of extreme-rain-producing mesoscale convective systems. *Mon. Weather Rev.* 133 (4), 961–976. doi:10.1175/mwr2899.1

Shang, H., Xu, M., Zhao, F., and Tijjani, S. B. (2019). Spatial and temporal variations in precipitation amount, frequency, intensity, and persistence in China, 1973–2016. *J. Hydrometeorol.* 20 (11), 2215–2227. doi:10.1175/jhm-d-19-0032.1

Stocker, T. F., Qin, D., Plattner, G. K., Mmb, Tignor, Allen, S. K., Boschung, J., et al. (2014). *Climate change 2013: The physical science basis. Contribution of working group I to the fifth assessment report of IPCC the intergovernmental panel on climate change*. Cambridge university press: AGU Fall Meeting Abstracts.

Tang, S., Qiao, S., Feng, T., Fu, Z., Zhang, Z., and Feng, G. (2022). Predictability of the record-breaking rainfall over the Yangtze and Huaihe River valley in 2020 summer by the NCEP CFSv2. *Atmos. Res.* 266, 105956. doi:10.1016/j.atmosres.2021.105956

Trenberth, K. E. (1991). Climate diagnostics from global analyses: Conservation of mass in ECMWF analyses. *J. Clim.* 4 (4), 707–722. doi:10.1175/1520-0442(1991)004<0707:cdfgac>2.0.co;2

Wang, C., Ma, Z., Qin, N., Zhang, S., and Deng, B. (2016). Multi-scale variation of the summer rainfall over Sichuan-Chongqing Basin in recent 50 years. *Plateau Meteorol.* 35, 1191–1199. (in Chinese). doi:10.7522/j.issn.1000-0534.2015.00094

Wang, L., Chen, W., Zhou, W., and Huang, G. (2015). Teleconnected influence of tropical Northwest Pacific sea surface temperature on interannual variability of autumn precipitation in Southwest China. *Clim. Dyn.* 45 (9), 2527–2539. doi:10.1007/s00382-015-2490-8

Wang, Y., Zhou, B., Qin, D., Wu, J., Gao, R., and Song, L. (2017). Changes in mean and extreme temperature and precipitation over the arid region of northwestern China:observation and projection. *Adv. Atmos. Sci.* 34 (3), 289–305. doi:10.1007/s00376-016-6160-5

Wang, Z., and Zhou, B. (2019). Observed decadal transition in trend of autumn rainfall over central China in the late 1990s. *J. Clim.* 32 (5), 1395–1409. doi:10.1175/jcli-d-18-0112.1

Wei, T., He, S., Yan, Q., Dong, W., and Wen, X. (2018). Decadal shift in west China autumn precipitation and its association with sea surface temperature. *J. Geophys. Res. Atmos.* 123 (2), 835–847. doi:10.1002/2017jd027092

Wei, T., Song, W., Dong, W., Ke, Z., Sun, L., and Wen, X. (2018). A skilful prediction scheme for West China autumn precipitation. *Theor. Appl. Climatol.* 135 (1), 183–192. doi:10.1007/s00704-017-2363-7

Xu, H., Chen, H., and Wang, H. (2021). Interannual variation in summer extreme precipitation over Southwestern China and the possible associated mechanisms. *Int. J. Climatol.* 41 (6), 3425–3438. doi:10.1002/joc.7027

Yuan, X., and Liu, X. (2013). Onset-withdrawal dates of autumn persistent rains over Western China and associated autumn-to-winter evolution of atmospheric circulation. *Acta Meteorologpica Sin.* 71, 913–924. (in Chinese). doi:10.11676/qxxb2013.034

Zhan, W., He, X., Sheffield, J., and Wood, E. F. (2020). Projected seasonal changes in large-scale global precipitation and temperature extremes based on the CMIP5 ensemble. *J. Clim.* 33 (13), 5651–5671. doi:10.1175/jcli-d-19-0311.1

Zhang, B., Chen, L., He, J., Zhu, C., and Li, W. (2009). Characteristics of atmospheric heat sources over Asia in summer:comparison of results calculated using multiple reanalysis datasets. *J. Meteorological Res.* 23 (5), 585–597. doi:10.1029/2009JD012351

Zhang, C., Wang, Z., Zhou, B., Li, Y., Tang, H., and Xiang, B. (2019). Trends in autumn rain of West China from 1961 to 2014. *Theor. Appl. Climatol.* 135 (1), 533–544. doi:10.1007/s00704-017-2361-9

Zhao, J., Zuo, J., Zhang, H., Chen, L., Yang, J., Zhihai, Z., et al. (2021). The extreme precipitation over the yangtze–huaihe river basin in August 2021: Driven by the rapid tropical atlantic warming and the second developing La Niña. *Chin. J. Atmos. Sci.* 45 (6), 1433–1450. doi:10.21203/rs.3.rs-1364877/v1 (in Chinese).

Zhou, B., and Wang, Z. (2019). Enlightenment from heavy autumn rain of West China in 2017: Synergic role of atmospheric circulation at mid-high latitudes and oceanic background. *Theor. Appl. Climatol.* 138 (1), 263–274. doi:10.1007/s00704-019-02809-9

Zhou, B., Wu, J., Xu, Y., Han, Z., and Shi, Y. (2019). Projected changes in autumn rainfall over West China: Results from an ensemble of dynamical downscaling simulations. *Int. J. Climatol.* 39 (12), 4869–4882. doi:10.1002/joc.6115

Zhou, B., Xu, M., Sun, B., Han, T., and Cheng, Z. (2021). Possible role of Southern Hemispheric sea ice in the variability of West China autumn rain. *Atmos. Res.* 249, 105329. doi:10.1016/j.atmosres.2020.105329

Zhou, J., Zhao, J., and Zhi, R. (2019). Possible causes of the anomalous characteristics of autumn rain in Western China in 2017. *Theor. Appl. Climatol.* 138 (1), 1109–1123. doi:10.1007/s00704-019-02876-y

Zhou, Z., Xie, S., and Zhang, R. (2021). Historic Yangtze flooding of 2020 tied to extreme Indian Ocean conditions. *Proc. Natl. Acad. Sci. U. S. A.* 118 (12), e2022255118. doi:10.1073/pnas.2022255118

Zhu, Y., and Yu, R. (2003). Interannual variation of summer precipitation in the west of Sichuan basin and its relationship with large-scale circulation. *Chin. J. Atmos. Sci.* 27 (6), 1045–1056. (in Chinese). doi:10.3878/j.issn.1006-9895.2003.06.08

frontiers | Frontiers in Earth Science

TYPE Original Research
PUBLISHED 26 September 2022
DOI 10.3389/feart.2022.989073

OPEN ACCESS

EDITED BY
Wei Zhang,
Utah State University, United States

REVIEWED BY
Chujie Gao,
Hohai University, China
Yongli He,
Lanzhou University, China
Shaobo Qiao,
Sun Yat-sen University, China

*CORRESPONDENCE
Huixin Li,
lihuixin@nuist.edu.cn

SPECIALTY SECTION
This article was submitted to Atmospheric Science, a section of the journal Frontiers in Earth Science

RECEIVED 08 July 2022
ACCEPTED 05 September 2022
PUBLISHED 26 September 2022

CITATION
Zhu B, Li H, Sun B, Zhou B and Duan M (2022), Physical–empirical prediction model for the dominant mode of extreme high temperature events in eastern China during summer. *Front. Earth Sci.* 10:989073. doi: 10.3389/feart.2022.989073

Physical–empirical prediction model for the dominant mode of extreme high temperature events in eastern China during summer

Baoyan Zhu[1], Huixin Li[1,2]*, Bo Sun[1,2,3], Botao Zhou[1] and Mingkeng Duan[1]

[1]Collaborative Innovation Center on Forecast and Evaluation of Meteorological Disasters/Key Laboratory of Meteorological Disaster, Ministry of Education/Joint International Research Laboratory of Climate and Environment Change, Nanjing University of Information Science and Technology, Nanjing, China, [2]Southern Marine Science and Engineering Guangdong Laboratory (Zhuhai), Zhuhai, China, [3]Nansen-Zhu International Research Centre, Institute of Atmospheric Physics, Chinese Academy of Sciences, Beijing, China

The dominant mode of extreme high temperature events in eastern China during summer shows a dipole pattern with opposite anomalies over southern and northeastern China, which explains 25% of the variance. We document the limited prediction skill of the National Centers for Environmental Prediction Climate Forecast System, version 2 (CFSv2) for the dominant mode of these events. Based on the mechanisms related to the dominant mode, a physical–empirical model was established that improved the prediction of extreme high temperature events in eastern China, which will help in disaster prediction and mitigation. The physical connection between the dominant mode and the summer sea surface temperature (SST) over the western tropical and subtropical Pacific Ocean was predicted well by the CFSv2 hindcasts, and thus the areal mean CFSv2-hindcast SSTs over the western tropical and subtropical Pacific Ocean served as a predictor in the physical–empirical model. In the observations, the soil moisture over southern China in the preceding December (soil_Dec) combined the signal of the air–sea interactions over the tropical and northern extratropical Pacific Ocean, which induced anomalous SSTs in the Indian and western tropical Pacific oceans in the following summer and contributed to the dominant mode. Soil_Dec was therefore closely correlated with the dominant mode and was used as a predictor. The results of the one-year-leave cross-validation and independent hindcast showed that the time series of the dominant mode was better predicted by the physical–empirical model than by the CFSv2 hindcasts, with an improved correlation coefficient from insignificant to about 0.8, a root-mean-square error reduced by about 50% and an increased rate of same signs. The physical–empirical model showed advantages in the prediction of the dominant mode of summer extreme high temperature events over eastern China, which may be used in the prediction of other climate variables.

KEYWORDS

extreme high temperature events, interannual variability, dominant mode, eastern China, physical-empirical prediction model

Introduction

Extreme high temperature events (EHEs) are occurring with increasing frequency as a result of the global climate crisis, exerting a greater influence on human health, the social economy and the ecological environment (Chen et al., 2019; Borg et al., 2021; Igun et al., 2022). The number of deaths related to EHEs increased markedly in the decade from 2000 to 2010 compared with the decade from 1991 to 2000, accounting for a large proportion of the increased deaths caused by extreme climate events such as floods and droughts (WMO 2013). Model simulations indicate that EHEs will occur more frequently and with greater intensity in the future (Orlowsky and Seneviratne 2012; Chen and Sun 2018). It is therefore important for disaster prevention and reduction to investigate the variations in EHEs, to understand the associated mechanisms and to improve their prediction.

Eastern China is vulnerable to EHEs, which show a large variability in this region (Sun et al., 2014; Deng et al., 2019). Previous studies have shown that the frequency of EHEs (FEHEs) over China is characterized by variability on different timescales (You et al., 2017; Chen et al., 2018; Zhu et al., 2020b). You et al. (2017) showed that the FEHEs based on relative and absolute definitions has increased over the whole of China, particularly after 1990, reflecting rapid warming after this time. Superimposed on these long-term trends, there are also dominant interdecadal and interannual spatiotemporal variations in FEHEs over eastern China (Zhu et al., 2020b; Hong et al., 2020; Liu et al., 2021; Yang et al., 2021; Zhu et al., 2022). The interannual variability of FEHEs is relatively large over eastern China, which greatly contributes to the overall variability (Chen et al., 2018; Deng et al., 2019).

The prediction skill of current dynamic models for extreme climate events is limited (Pepler et al., 2015; Gao et al., 2018; Luo et al., 2020; Tang et al., 2021a; Tang et al., 2021b) and physical–empirical models have been used to improve predictions (Ji and Fan 2019; Yang et al., 2019; Tian and Fan 2020; Long et al., 2022). The crucial procedure in physical–empirical models is the detection of physically meaningful predictors (Gao et al., 2018; Han et al., 2020; Long et al., 2022). A combination of predictors from dynamic prediction systems and predictors in the observations includes the dynamic processes revealed in the dynamic models and the observations, improving the prediction skill (Zhang et al., 2019a; Zhang et al., 2019b; Chen and Sun 2020).

We need a better understanding of the mechanisms related to predictands to establish physical–empirical models. Many studies have analyzed the anomalous atmospheric circulation responsible for the occurrence of EHEs over China and the influence from the tropics and mid to high latitudes (Deng et al., 2019; Xu et al., 2019; Zhu et al., 2020a; Long et al., 2022; Zhou et al., 2022). The anomalous intensity or location of the western Pacific subtropical high could induce anomalous vertical motion and transport of water vapor over China, leading to anomalous adiabatic heating and surface heat fluxes, which could contribute to the occurrence of EHEs over China (Li et al., 2020; Ren et al., 2020). Several factors, such as the El Niño–Southern Oscillation (ENSO) and the sea surface temperature (SST) in the Indian Ocean, account for the variations in the western Pacific subtropical high (Zhang et al., 2019c; Sun et al., 2019; Tong et al., 2020) and could be considered as potential predictors for the FEHEs over eastern China. In addition, the mid- and high-latitude wave train propagating eastward to East Asia could also induce anomalous atmospheric circulation and contribute to the variations in the FEHEs over China, which may be associated with air–sea interactions over the North Atlantic, sea ice in the Arctic region and other factors (Li et al., 2018; Zhu et al., 2020a, 2022).

Most studies have focused on the simultaneous atmospheric circulation anomalies and influential factors related to EHEs. We therefore aimed to investigate the following two questions: 1) how are the dominant mode of the interannual variability of summer FEHEs over eastern China, the associated atmospheric circulation and SST anomalies predicted in the dynamic model; and 2) could a physical–empirical model be established to improve the prediction of the dominant mode of FEHEs over eastern China?

The rest of the paper is organized as follows. Section 2 introduces the data and methods. Section 3 investigates the prediction ability of the National Centers for Environmental Prediction (NCEP) Climate Forecast System, version 2 (CFSv2) for the dominant mode of the FEHEs over eastern China during summer. The predictors used in the physical–empirical model are detected and their physical connection to the dominant mode of the FEHEs are analyzed in Section 4. Section 5 presents the establishment and estimation of the physical–empirical model and conclusions are presented in Section 6.

Data and methods

Data

We calculated the FEHEs using the daily observed maximum temperature during summer (June–July–August) from the CN05.1 dataset, a gridded observational dataset with a resolution of (0.25°×0.25°) based on data from observational stations in China (Wu and Gao 2013). We obtained the

monthly mean 850 hPa horizontal wind, 500 hPa vertical velocity with a resolution of (2.5°×2.5°) and surface net shortwave radiation with a resolution of 92×192 grid points from the NCEP (Kalnay et al., 1996). We also used the Extended Reconstructed SST V5 with a resolution of (2°×2°) (Huang et al., 2017) and Climate Prediction Center (CPC) soil moisture with a resolution of 360×720 grid points (Huang et al., 1996) from the National Oceanic and Atmospheric Administration.

The hindcasts of the daily maximum temperature and monthly SSTs in summer were derived from the CFSv2, which is a state-of-the-art prediction system with interactions between the ocean, atmosphere and land on a global scale (Saha et al., 2014). The CFSv2 hindcasts were integrated for 9 months, with initial conditions every 5 days from 11 April to 6 Ma y, and we used the ensemble mean of the forecasts for summer. The CFSv2 data with a resolution of (1°×1°) cover the time period 1982–2018 and we selected the other observational and reanalysis data to be consistent with this time period. Both the observational and reanalysis data are referred to as observations to distinguish them from the prediction data in the CFSv2 hindcasts.

Methods

Taking into consideration the different climate states in different regions of China, we adopted the relative definition of EHEs—that is, we used the 95% percentile value of the daily maximum temperature during summer as the threshold (Zhu et al., 2020a; Long et al., 2022; Zhu et al., 2022). The threshold was different between grids and the number of days with maximum temperatures exceeding the threshold during summer was defined as the FEHEs. Because this study focused on the interannual variability, we applied Fourier analysis to all data before other calculations such as empirical orthogonal function decomposition, correlation analysis and so on, and the 9-year high-pass variability was reserved (Bloomfield 2004).

The linear signal of one variable (X) is removed from the other variable (Y) based on the following formula (Sun et al., 2019):

$$Y^* = Y - X \times \mathrm{cov}(X, Y)/\mathrm{var}(X),$$

where X and Y are the original time series, cov (X, Y) represents the temporal covariance between X and Y, var (X) represents the variance of X, and Y* represents the time series of Y with the linear signal of X removed.

We used the one-year-leave cross-validation and independent hindcast methods to estimate the prediction of the physical–empirical model. We used one-year-level cross-validation to predict the predictand in the specific year using the remaining years as the training period to build the physical–empirical model. The independent hindcast was similar to the real prediction and we chose the first training period—for example, the data for 1982–1999 were used to establish the first physical–empirical model and give the prediction in 2000 and then the data for 1982–2000 were used to build the second physical–empirical model and make the prediction in 2001, and so on. We used the prediction for 2000–2018 for verification. The prediction skill of the physical–empirical model was mainly reflected through the correlation coefficient, the root-mean-square error (RMSE) and the rate of same signs. The significance test of the correlation coefficient was based on Student's *t*-test.

Prediction skill of the CFSv2 hindcasts for the dominant mode of the FEHEs

To understand the skill of the CFSv2 hindcast data in predicting the FEHEs over eastern China, we analyzed the characteristics of FEHEs in the CFSv2 hindcasts and the observations. Figure 1A shows the standard deviation of FEHEs over eastern China in the observations, with two centers of relatively large values over southern and northeastern China. The center of relatively large standard deviations over northeastern China was captured in the CFSv2 hindcasts (Figure 1B), but the standard deviation was overestimated over northeastern and central China and underestimated over southern China (Figure 1A,B). Figure 1C shows that the RMSE between the FEHEs in the observations and the CFSv2 hindcasts was almost greater than one standard deviation over eastern China, with relatively large values over central China. The time correlation coefficients between the observed FEHEs and the CFSv2 hindcast FEHEs showed scattering positive correlation over northern and southern China (Figure 1D). The spatial discrepancies in the standard deviation (Figure 1A,B), the relatively large RMSE (Figure 1C) and the low time correlation coefficients (Figure 1D) indicate the limited prediction skill of the CFSv2 hindcasts for the FEHEs over eastern China.

To further investigate the prediction skill of the CFSv2 hindcasts for the temporal and spatial variations of the FEHEs, we calculated the first empirical orthogonal function modes of the FEHEs over eastern China in the CFSv2 hindcasts and the observations, which were separated from the remainder of EOF modes according to the criterion proposed by North et al. (1982). Figure 2A,B show that the dominant mode of the FEHEs over eastern China in the CFSv2 hindcasts was inconsistent with that in the observations, with a low spatial correlation coefficient of 0.23. The dominant mode of the FEHEs in the observations was characterized by a dipole pattern of negative (positive) anomalies over southern (northeastern) China (Figure 2A), with relatively large loadings over southern China. By contrast, the dominant mode of the FEHEs in the CFSv2 hindcasts showed relatively large positive anomalies over northeastern China and no uniform negative anomalies over southern China (Figure 2B). The

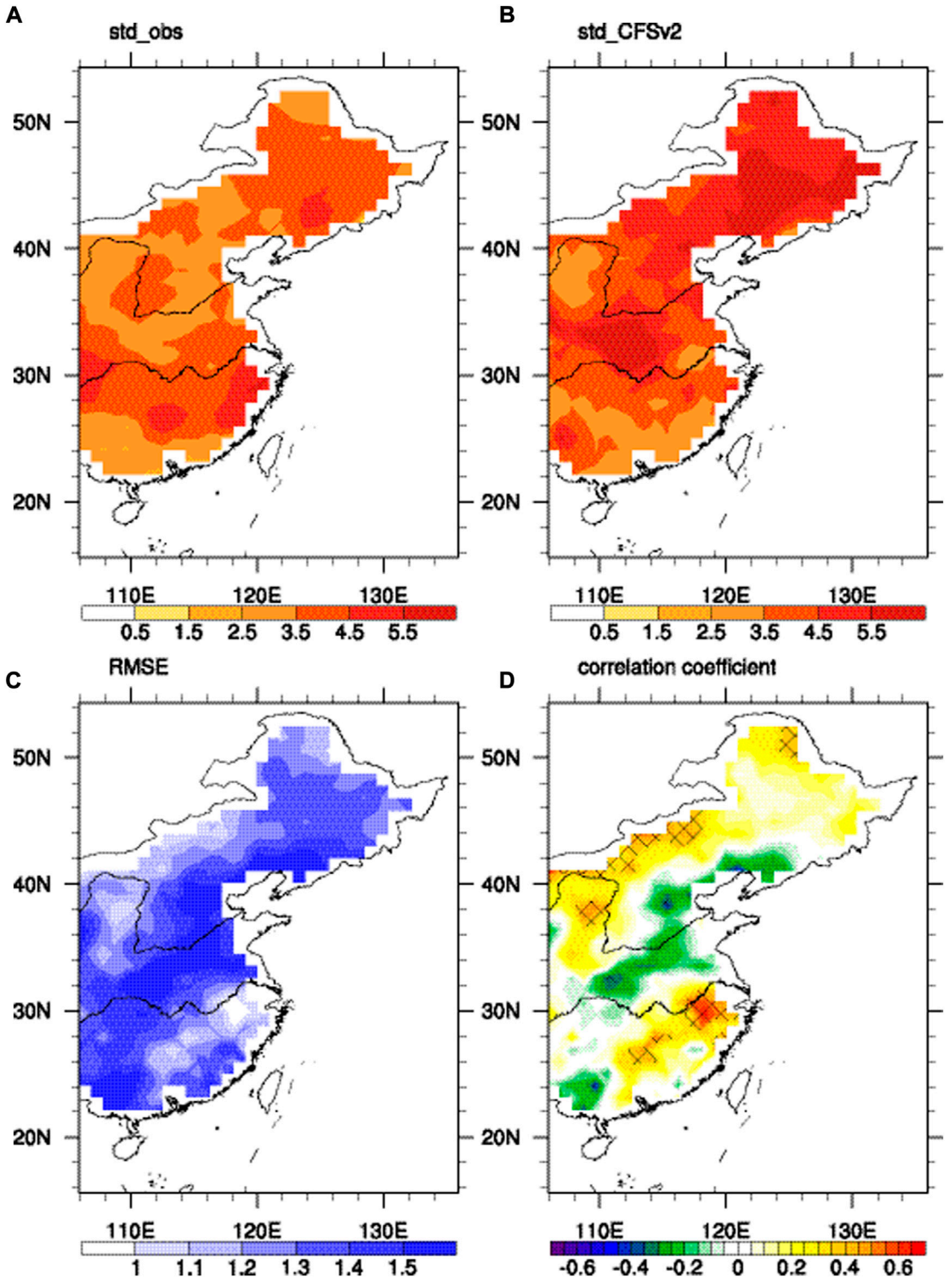

FIGURE 1
Standard deviation of FEHEs over eastern China during summer in **(A)** the observations and **(B)** the CFSv2 hindcasts. **(C)** The RMSE between the standardized time series of summer FEHEs in the observations and the CFSv2 hindcasts. **(D)** Time correlation coefficients between summer FEHEs in the observations and the CFSv2 hindcasts. The meshes in **(D)** denote the correlation coefficients significant at the 95% confidence level based on Student's *t*-test.

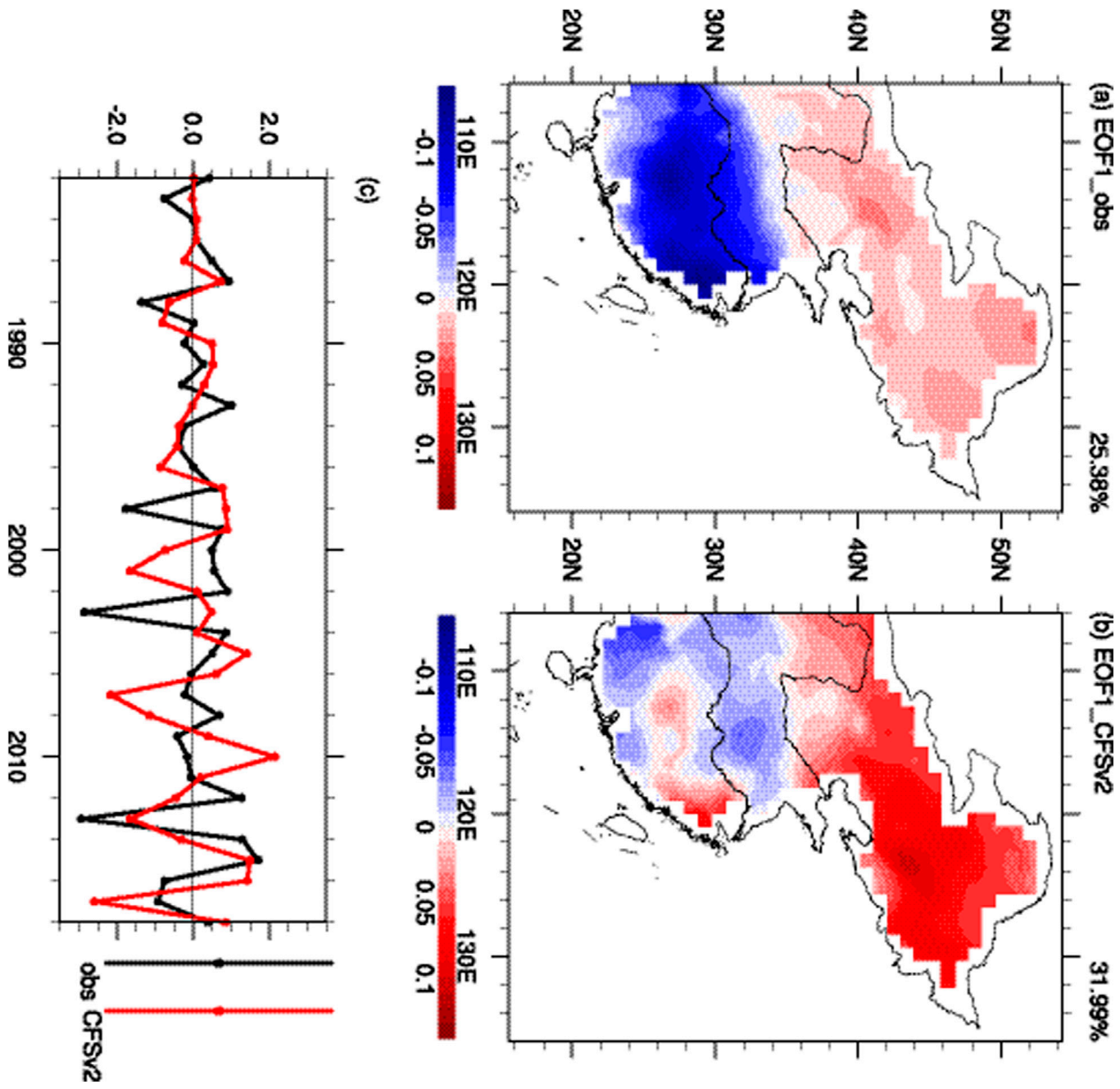

FIGURE 2
First empirical orthogonal function mode (EOF1) of summer FEHEs over eastern China in **(A)** the observations and **(B)** the CFSv2 hindcasts. **(C)** The standardized time series projected to the observed EOF1 of the FEHEs in the observations (black line) and the CFSv2 hindcasts (red line). The percentages in the top-right corner of **(A, B)** are the explained variance to the total variance.

relatively large anomalies over northeastern China in the dominant mode of the FEHEs in the CFSv2 hindcasts (Figure 2A,B) were related to the overestimation of the standard deviation of the FEHEs over northeastern China in the CFSv2 hindcasts (Figure 1A,B). The CFSv2 hindcasts therefore did not predict the spatial pattern of the dominant mode of the FEHEs over eastern China in the observations. To further investigate the prediction skill of the CFSv2 hindcasts for the time series of the dominant mode (PC1), we projected both the PC1s in the observations (PC1_obs) and the CFSv2 hindcasts (PC1_CFSv2) to the observed dominant mode (Figure 2A). Figure 2C shows that there was a large deviation between PC1_obs and PC1_CFSv2, with a RMSE of 1.28 and a correlation coefficient of 0.18 significant below the 90% confidence level. These results show the overall poor capability of the CFSv2 hindcasts for predicting the dominant mode of the summer FEHEs over eastern China.

10.3389/feart.2022.989073

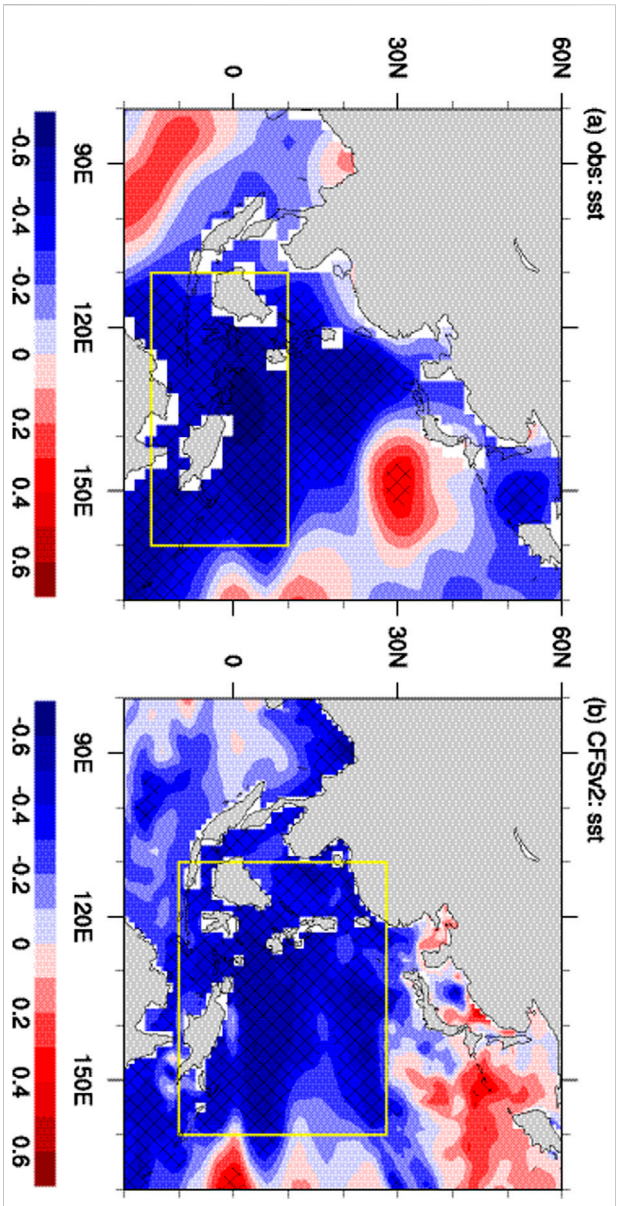

FIGURE 3
Correlation coefficients between PC1_obs and the summer SST in **(A)** the observations and **(B)** the CFSv2 hindcasts. The meshes denote the correlation coefficients significant at the 95% confidence level based on Student's *t*-test.

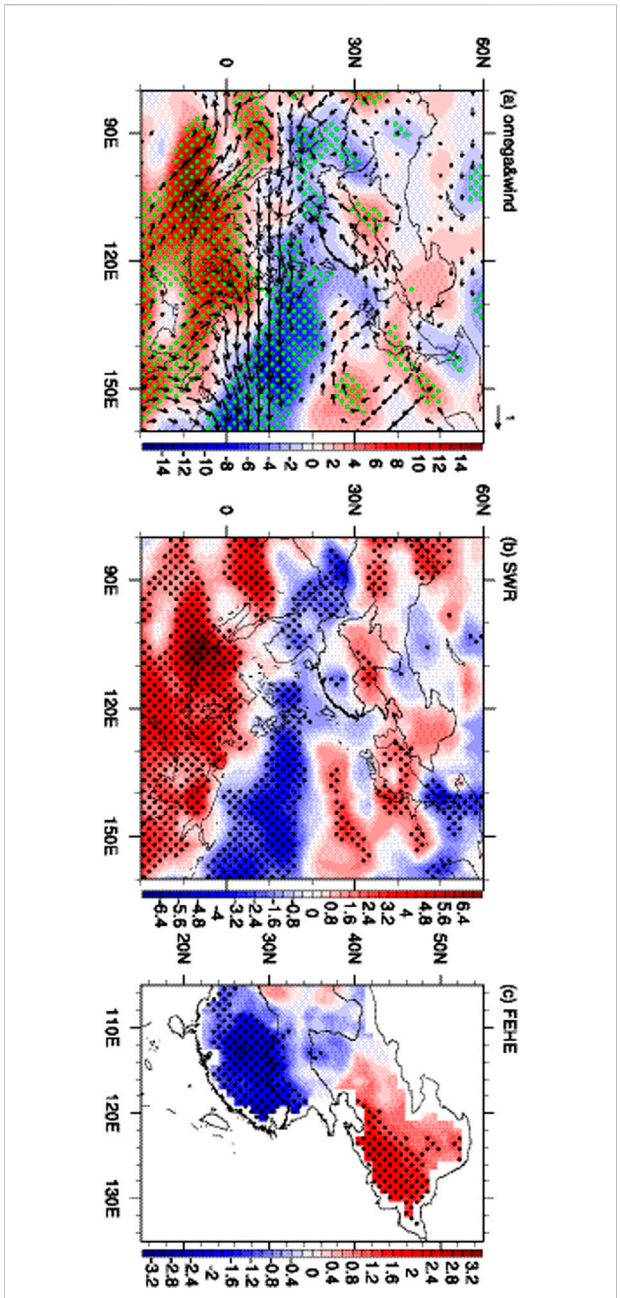

FIGURE 4
Anomalies of the summer **(A)** 500 hPa vertical velocity (shading; units: 10^{-3} Pa s^{-1}) and 850 hPa horizontal wind (vector; units: m s^{-1}), **(B)** surface net downward shortwave radiation (units: W m^{-2}) and **(C)** FEHEs in the observations regressed on the time series of the sign-reversed MCSST. The dots denote the anomalies significant at the 90% confidence level based on Student's *t*-test. Only the anomalies of the 850 hPa wind exceeding 0.1 m s^{-1} are shown.

Predictors used in the physical–empirical model for prediction of the dominant mode

Our previous studies have analyzed the mechanism associated with the dominant mode of the FEHEs over eastern China (Zhu et al., 2020a; Zhu et al., 2022). Based on these previous studies, we identified the predictors with a physical connection to the dominant mode, analyzed the corresponding mechanisms and used them to build the physical–empirical model.

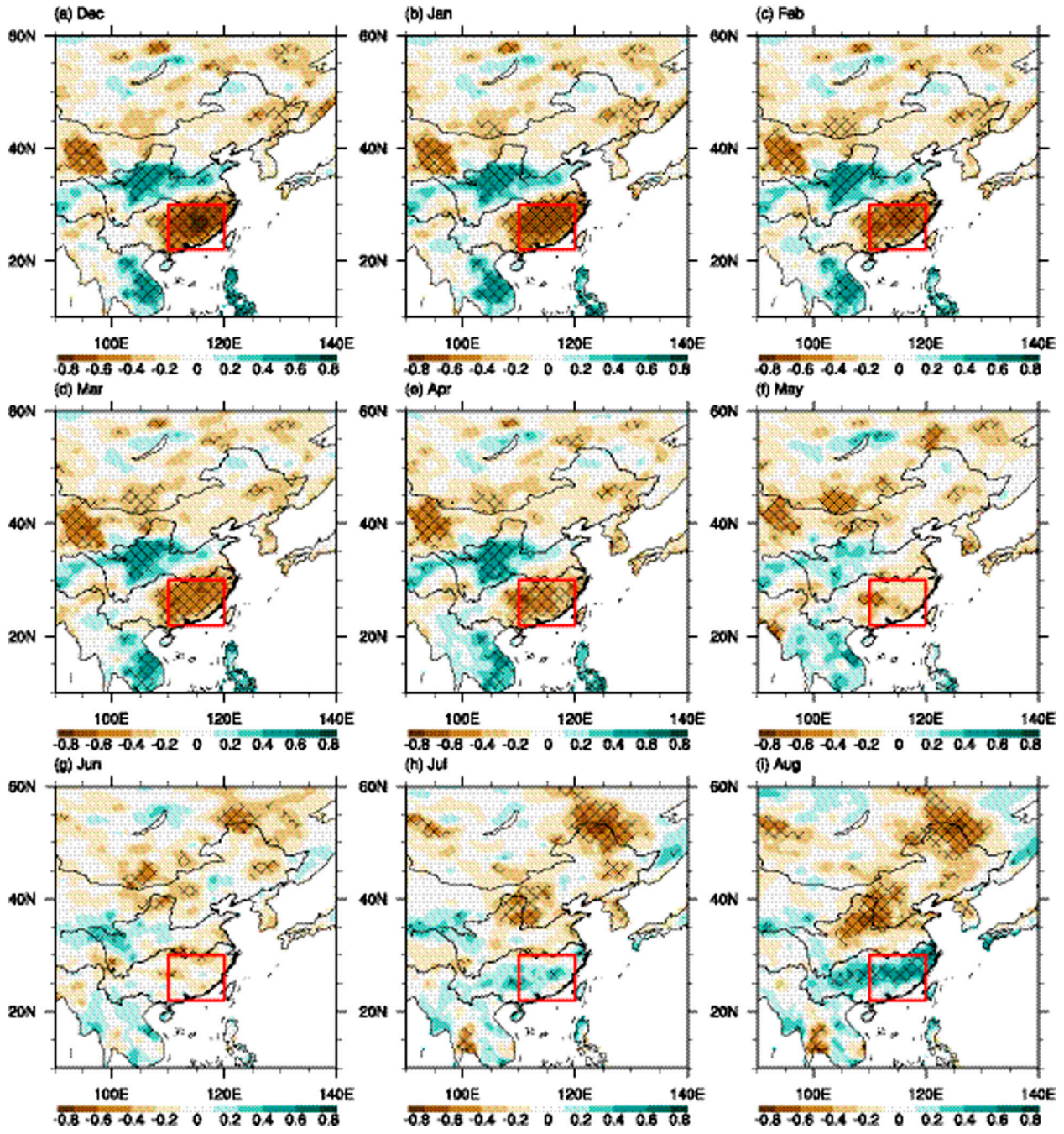

FIGURE 5
Correlation coefficients between PC1_obs and soil moisture in the preceding **(A)** December, **(B)** January, **(C)** February, **(D)** March, **(E)** April and **(F)** May and the simultaneous **(G)** June, **(H)** July and **(I)** August. The meshes denote the correlation coefficients significant at the 95% confidence level based on Student's *t*-test.

Predictor in the CFSv2 hindcasts

Previous studies have shown that the SSTs in the tropical Pacific Ocean have an important role in the variation of the summer climate over East Asia (Sun and Wang 2019; Zhu et al., 2020a; Hong et al., 2022). Figure 3A shows that there were significant negative correlation coefficients between the SSTs around the maritime continent and PC1_obs. To further explore the physical relationship between them, we investigated the climate anomalies associated with the SSTs

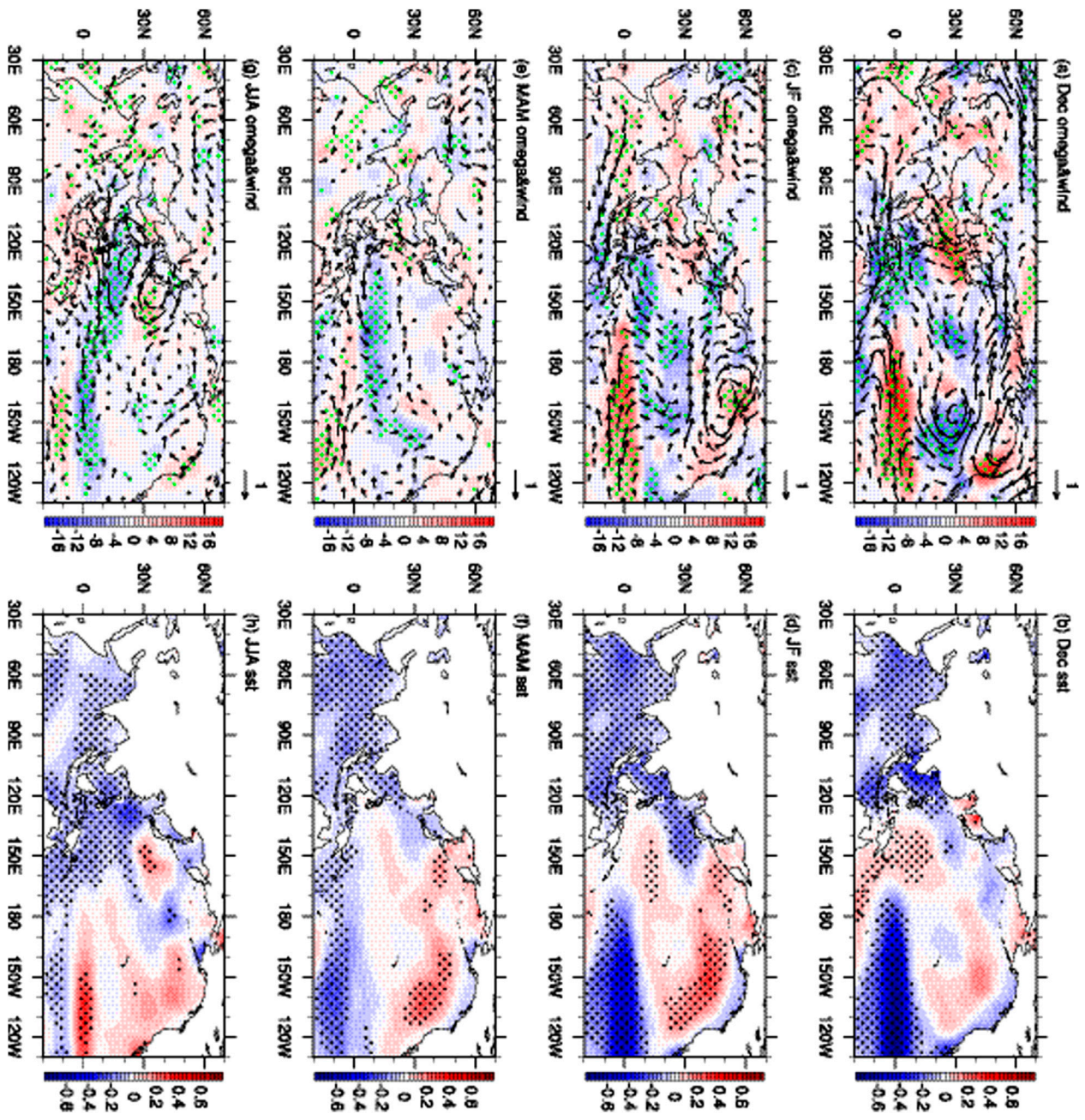

FIGURE 6
Anomalies of **(A,C,E,G)** the 500 hPa vertical velocity (shading; units: 10^{-3} Pa s^{-1}) and 850 hPa horizontal wind (vector; units: m s^{-1}) and **(B,D,F,H)** the SST (units: K) in the simultaneous **(A,B)** December, the following **(C,D)** January–February mean, **(E,F)** March–April–May mean and **(G,H)** summer regressed on the time series of the sign-reversed soil_Dec. The dots denote the anomalies significant at the 90% confidence level based on Student's *t*-test. Only the anomalies of 850 hPa wind exceeding 0.1 m s^{-1} are shown.

around the maritime continent and an SST index (MCSST) was defined as the areal mean SSTs within (15°S–10°N, 110–160°E) (Figure 3A). The anomalous cold SSTs around the maritime continent suppressed convection in the overlying troposphere (Figure 4A), which further led to an anomalous cyclone (anticyclone) and ascending (descending) motion over southern (northeastern) China via a meridional teleconnection similar to the Pacific–Japan/East Asia–Pacific (PJ/EAP) pattern (Nitta 1987; Huang 1992; Qiao et al., 2021). The anomalous atmospheric circulation related to the anomalous cold SSTs around the maritime continent could contribute to strengthened (weakened) convection over southern

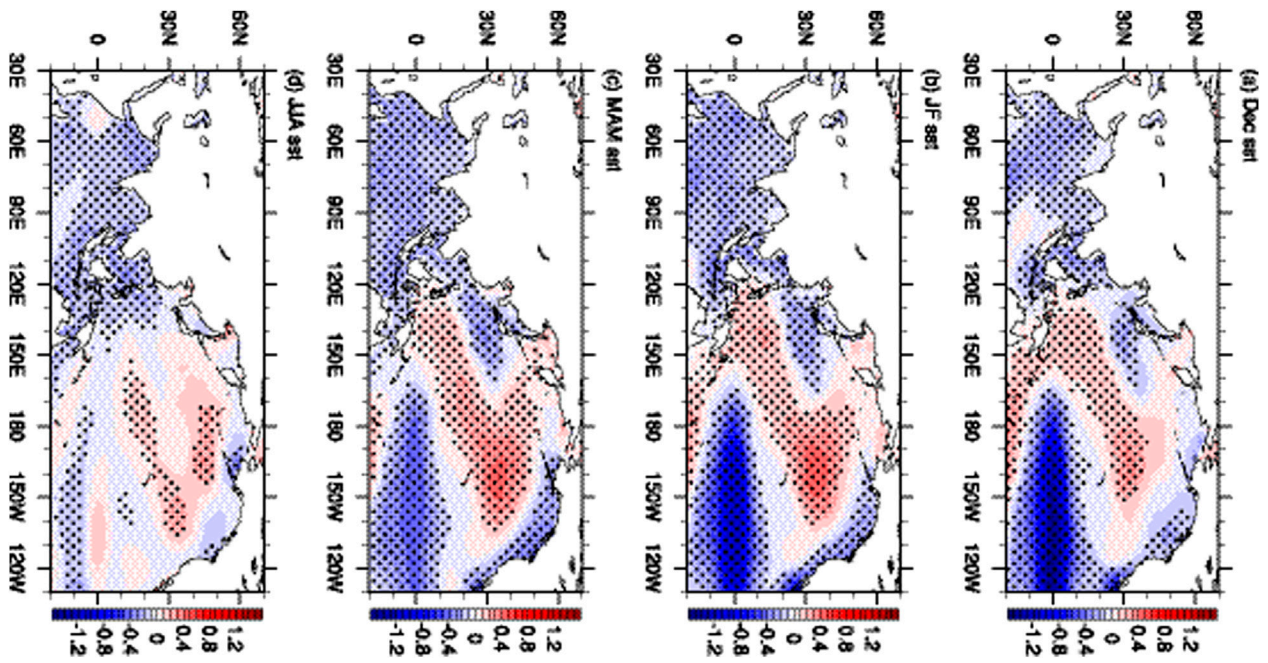

FIGURE 7
Anomalies of the SST (units: K) in the simultaneous **(A)** December, the following **(B)** January–February mean, **(C)** March–April–May mean and **(D)** summer regressed on the time series of the sign-reversed Nino3.4 in December. The dots denote the anomalies significant at the 90% confidence level based on Student's *t*-test.

(northeastern) China (Figure 4A), leading to less (more) downward shortwave radiation (Figure 4B), which could induce less (more) FEHEs over southern (northeastern) China (Figure 4C) and contribute to the dominant mode of FEHEs (Figure 2A).

The PJ/EAP index, defined as the first empirical orthogonal function mode of summer 850-hPa relative vorticity within (0°–60°N, 100–160°E) according to Kosaka and Nakamura (2010), was significantly correlated with PC1_obs and sign-reversed MCSST with correlation coefficients of 0.60 and 0.51 exceeding the 99% confidence level respectively. These results indicate that the PJ/EAP teleconnection was responsible for the linkage between the dominant mode of FEHEs and the SSTs around the maritime continent. The anomalous cyclonic surface wind over the western subtropical Pacific could induce the divergence of upper water and the upwelling of cold water (figures not shown; Price et al., 1987; Seager et al., 2001), and downward shortwave radiation was reduced (Figure 4B), which could lead to negative SSTs in the western subtropical Pacific (Figure 3A). As shown in Figure 3, the physical connection between PC1_obs and the anomalous cold SSTs in the western tropical and subtropical Pacific (Figure 3A) was well revealed in the CFSv2 hindcasts (Figure 3B). The areal mean CFSv2 hindcast SSTs within (10S°–28°N, 110–160°E; Figure 3B) was abbreviated as sst_CFSv2, which was physically connected to PC1_obs with a correlation coefficient of −0.58 significant at the 99% confidence level and could be used as a predictor in the physical–empirical model to predict the dominant mode of the FEHEs over eastern China.

Predictor in the observations

Soil moisture varies slowly and has a memory of climate anomalies. It has therefore been considered as a potential predictor of extreme climate events (Wu and Zhang 2015; Yang et al., 2019). We therefore examined the connection between the preceding soil moisture and PC1_obs. Figure 5 shows that there were significant negative correlation coefficients between the soil moisture over southern China in the preceding December and PC1_obs, which lasted from the preceding December to May. However, this negative relationship (Figure 5A–F) became positive in summer (Figure 5G–I), indicating that the persistence of soil moisture could not explain the relationship between the soil moisture over southern China in the preceding December and PC1_obs. To further study the physical connection between them, we defined a soil moisture index (soil_Dec) as the preceding December soil moisture averaged within (22–30°N, 110–120°E).

Figure 6B shows that the deficit of soil moisture over southern China in December was associated with La Nina-like SST anomalies over the tropical Pacific. These negative SST

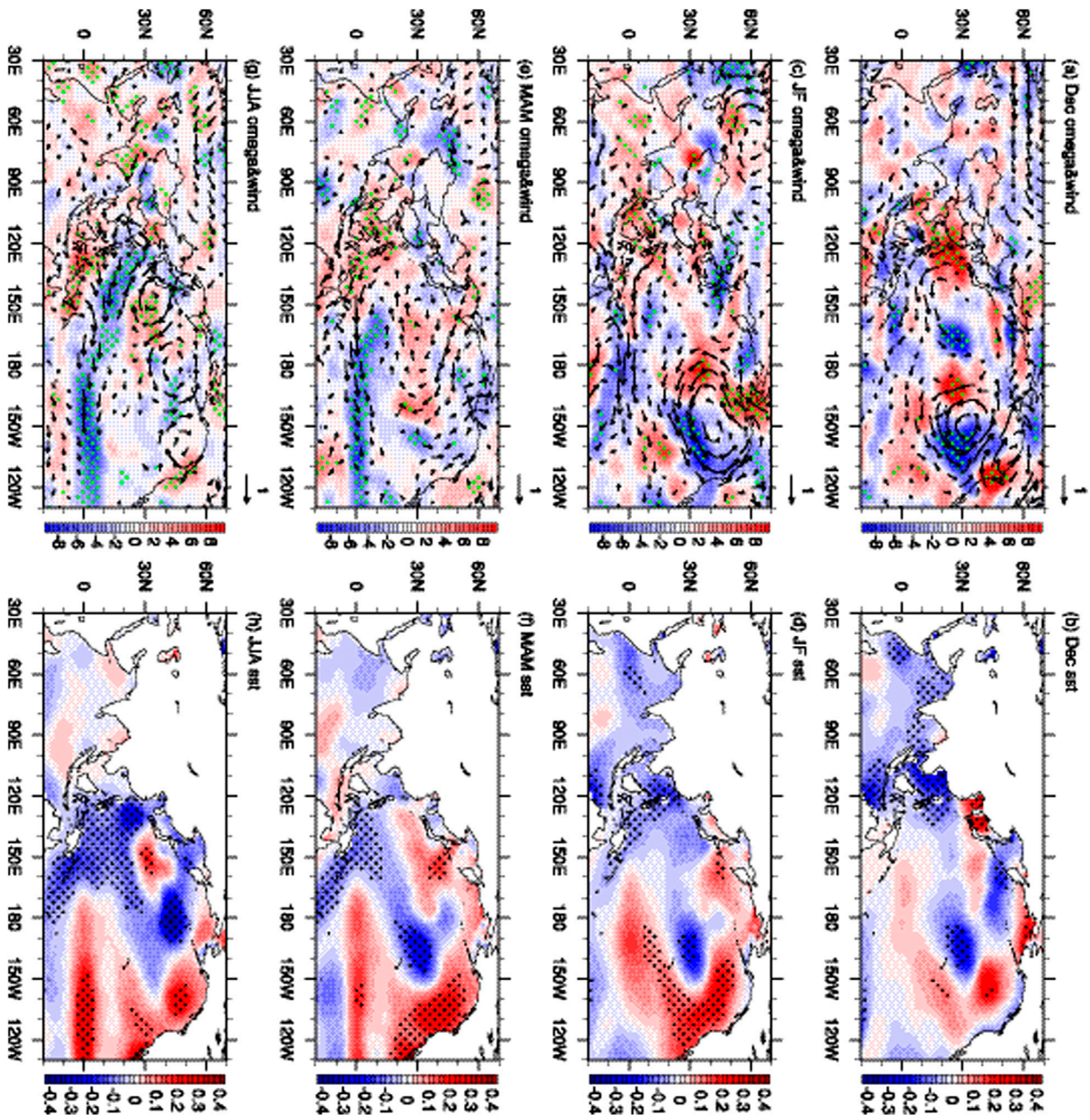

FIGURE 8
Anomalies of **(A,C,E,G)** the 500 hPa vertical velocity (shading; units: 10^{-3} Pa s^{-1}) and 850 hPa horizontal wind (vector; units: m s^{-1}) and **(B,D,F,H)** the SST (units: K) in the simultaneous **(A,B)** December, the following **(C,D)** January–February mean, **(E,F)** March–April–May mean and **(G,H)** summer regressed on the time series of the sign-reversed soil_Dec with the linear signal of Nino3.4 in December removed. The dots denote the anomalies significant at the 90% confidence level based on Student's *t*-test. Only the anomalies of the 850 hPa wind exceeding 0.1 m s^{-1} are shown.

anomalies over the eastern tropical Pacific Ocean can induce an anomalous cyclone over the western subtropical Pacific (Figure 6A) via the Pacific–East Asia teleconnection (Wang et al., 2000). The anomalous northerly wind to the west of the anomalous cyclone can suppress the transport of water vapor to southern China, inducing greater evaporation of the underlying sea surface and negative SST anomalies along the coast of southern China (Figure 6A,B). This can suppress convection and lead to the soil moisture deficit over southern China. From the preceding December to the following summer, the SST

TABLE 1 Definitions of the predictors and the correlation coefficients between PC1_obs and the predictors.

Predictor	Months	Definition	PC1_obs
sst_CFSv2	June–July–August	CFSv2-predicted SSTs averaged within (10°S–28°N, 110–160°E)	−0.58**
soil_Dec	December	Areal mean soil moisture within (22–30°N, and 110–120°E)	−0.78**

**Correlation coefficients significant at the 99% confidence level based on Student's *t*-test.

anomalies over the tropical Pacific Ocean were characterized by the decay of La Nina conditions (Figure 6B,D,F,H), with significant negative SST anomalies over the eastern tropical Pacific Ocean in December (Figure 6B) turning into positive anomalies in the following summer accompanied by negative anomalies over the western tropical Pacific Ocean (Figure 6H). The anomalous cold SSTs over the western tropical Pacific Ocean can induce anomalous descending motion over the maritime continent, which could lead to an anomalous cyclone (anticyclone) and ascending (descending) motion over southern (northeastern) China via the PJ/EAP teleconnection, contributing to the dominant mode of the FEHEs over eastern China (Figure 6G,H).

In addition, there were negative SST anomalies in the northern Indian Ocean in December, persisting to the following summer with the decay of La Nina conditions (Figure 6B,D,F,H). This is referred to as the Indian Ocean capacitor effect and extends the influence of the ENSO into the following summer (Xie et al., 2009). The anomalous cold SSTs over the Indian Ocean during the summer can suppress convection in the overlying troposphere (Figure 6G,H), which may contribute to an anomalous cyclone over the subtropical Pacific Ocean via a Kelvin wave-induced Ekman divergence mechanism, intensifying anomalous ascending motion over southern China and the western subtropical Pacific Ocean (Figure 6G; Sun et al., 2019). Moreover, the El Nino condition in December could contribute to positive soil moisture anomalies in southern China (figure not shown), which also decayed in the following seasons. This analysis shows that the connection between the soil moisture over southern China in December and the dominant mode of the summer FEHEs can be partly attributed to their responses to the ENSO. However, the correlation coefficient between PC1_obs and Nino3.4 in December (−0.39, significant at the 90% confidence level) was lower than that between PC1_obs and soil_Dec (−0.78), indicating that other physical processes were responsible for the relationship between PC1_obs and soil_Dec.

The SST anomalies associated with soil_Dec (Figure 6B,D,F,H) and Nino3.4 in December (Figure 7) showed similarity over the tropical Pacific Ocean. By contrast, there were discrepancies over the northern extratropical Pacific Ocean, with positive anomalies over the northeastern (northern central) Pacific Ocean related to soil_Dec (Nino3.4) (Figures 6, 7), indicating the influence of air–sea interactions over the northern extratropical Pacific Ocean on soil_Dec. After removing the linear signal of Nino3.4 in December from soil_Dec, the SST anomalies associated with soil_Dec showed positive (negative) anomalies over the northeastern (northern central) Pacific Ocean (Figure 8B), enhancing (weakening) convection in the overlying troposphere (Figure 8A). An anomalous cyclone was formed over the northeastern Pacific as a Rossby wave response to the enhanced convection (Figure 8A). The anomalous cyclone induced anomalous westerly wind over the tropical and subtropical Pacific Ocean, contributing to a weakened Walker circulation, anomalous cold SSTs over the South China Sea and descending anomalies over southern China (Figures 8A,B), which favored the deficit in soil moisture over southern China.

In late winter, the anomalous cyclone over the northeastern Pacific Ocean intensified and the anomalous westerly wind moved equatorward (Figure 8C), which provided favorable conditions for the developing El Niño, with negative (weak positive) SST anomalies over the western (eastern) tropical Pacific (Figure 8D). In spring, the air–sea interactions over the northeastern Pacific Ocean weakened and the anomalous cyclone disappeared (Figure 8E), but the anomalous westerly wind over the tropical Pacific Ocean lasted until summer and El Niño continued to develop via Bjerknes positive feedback (Bjerknes 1969). In summer, the anomalous cold SST over the western tropical Pacific Ocean induced anomalous descending motion over the maritime continent (Figure 8G,H), which further led to an anomalous cyclone and ascending motion over southern China and the western subtropical Pacific Ocean and exerted an influence on the dominant mode of the FEHEs over eastern China.

These results show that soil_Dec contained the signal of air–sea interactions over the tropical and northern extratropical Pacific Ocean in the preceding December, which can influence the atmospheric circulation and the dominant mode of the FEHEs over eastern China in the following summer by inducing anomalous SSTs in the Indian and tropical Pacific oceans (Figures 6-8). As a result of the combination of the signal of the air–sea interactions over the tropical and northern extratropical Pacific Ocean in the preceding December, the soil_Dec was closely correlated with PC1_obs with a correlation

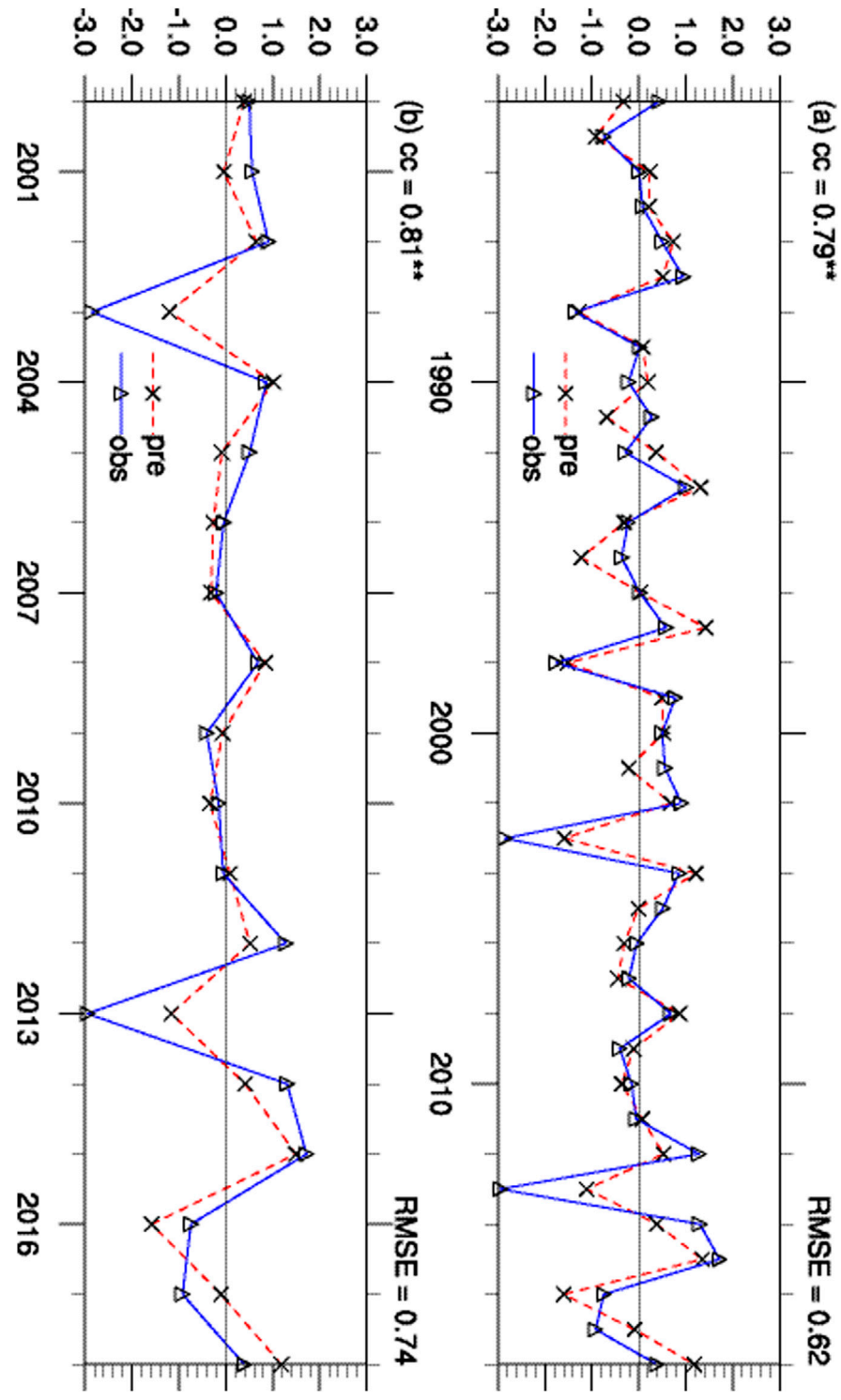

FIGURE 9
The physical–empirical model-predicted PC1 (PC1_PE, red dashed line) and PC1_obs (blue solid line) in **(A)** the one-year-leave cross-validation for 1982–2018 and **(B)** the independent hindcast for 2000–2018. The value in the top-left (top-right) corner of **(A–B)** is the correlation coefficient (RMSE) between PC1_PE and PC1_obs. ** denotes the correlation coefficients significant at the 99% confidence level based on Student's *t*-test.

TABLE 2 Correlation coefficient (CC), RMSE, the rate of same signs in all years (SS) and in extreme years (SS-extreme) between PC1_obs and PC1_CFSv2 during 1982–2018 (CC1, RMSE1, SS1 and SS1-extreme) and during 2000–2018 (CC2, RMSE2, SS2 and SS2-extreme). The correlation coefficient (CC), RMSE, the rate of same signs in all years (SS) and in extreme years (SS-extreme) between PC1_obs and PC1_PE in the one-year-leave cross validation (CC1, RMSE1, SS1 and SS1-extreme) and in the independent hindcast (CC2, RMSE2, SS2 and SS2-extreme). The bold value denotes that the correlation coefficients were significant at the 99% confidence level based on Student's *t*-test.

	CC1	CC2	RMSE1	RMSE2	SS1	SS2	SS1-extreme	SS2-extreme
PC1_CFSv2	**0.18**	0.19	1.28	1.59	19/37	8/19	3/8	2/5
PC1_PE	**0.79**	0.81	0.62	0.74	30/37	16/19	8/8	5/5

coefficient of −0.78 and served as a predictor in the physical–empirical model.

Establishment and estimation of the physical–empirical model

The physical–empirical model was established based on a multiple linear regression method using the sst_CFSv2 and soil_Dec predictors. Table 1 summarized the definitions of the predictors and their correlation coefficients with PC1_obs. Considering that the two predictors were not linear independent, the sst_CFSv2 with the linear signal of soil_Dec removed, was used in the physical–empirical model, which was still significantly correlated with PC1_obs at the 90% confidence level. The physical–empirical model is described as follows:

$$PC1_{obs} = a \times sst_{CFSv2} + b \times soil_{Dec} + c,$$

where a and b are the partial regression coefficients for the predictors sst_CFSv2 and soil_Dec, respectively, and c is the intercept of PC1_obs. The values of a, b and c will be different in the different training periods.

The prediction of the physical–empirical model for PC1_obs was evaluated by the methods of one-year-leave cross-validation for 1982–2018 and independent hindcast for 2000–2018. The results of the one-year-leave cross-validation showed that the physical–empirical model-predicted PC1 (PC1_PE) was highly consistent with PC1_obs (Figure 9A). Compared with the prediction of CFSv2 (Figure 2C), the correlation coefficient between the PC1_PE and PC1_obs increased to 0.79, significant at the 99% confidence level, and the RMSE was reduced by 52% (Table 2). Specifically, in some extreme years (e.g., 1998 and 2003), the anomalies of PC1_obs larger than one standardized deviation were captured better by the physical–empirical mode1 than by the CFSv2 prediction (Figure 9A). Accordingly, the rate of same signs was improved from 19/37 in the CFSv2 to 30/37 in the physical–empirical model and all the signs of PC1_obs in the extreme years (the absolute value of PC1_obs larger than one standard deviation) were correctly captured in the physical–empirical model (Table 2).

As for the independent hindcast results (Figure 9B), the physical–empirical model also showed an improved prediction of PC1_obs compared with the prediction of the CFSv2 hindcasts (Figure 2C). The interannual variability of PC1_obs was captured well by the physical–empirical model (Figure 9B), with a correlation coefficient of 0.81 and a reduced RMSE between PC1_obs and PC1_PE (Table 2). The signs of PC1_obs were better predicted in the physical–empirical model than in the CFSv2 hindcast (Table 2). The relationship between PC1_obs and predictors was robust (figures not shown), contributing to the stability of the prediction model. The prediction skill of the physical–empirical model based on sst_CFSv2 and soil_Dec, was better than that only based on soil_Dec (figure not shown). Therefore, the physical–empirical model has the ability to improve the prediction of the dominant mode of summer FEHEs over eastern China.

Conclusion

We have shown a limited prediction capability of CFSv2 hindcasts for summer FEHEs over eastern China. The CFSv2 hindcasts did not capture the dipole pattern of the dominant mode in the observations, which was characterized by negative (positive) anomalies over southern (northeastern) China and relatively large loadings over southern China. The time series in the CFSv2 hindcasts and in the observations projected to the observed dominant mode were also inconsistent, with a low time correlation coefficient of 0.18, significant below the 90% confidence level.

To improve the prediction of the dominant mode of the FEHEs, a physical–empirical model was established based on two predictors (sst_CFSv2 and soil_Dec). The SST anomalies in the western tropical Pacific Ocean influenced convection in the overlying troposphere, affecting the atmospheric circulation over eastern China via the PJ/EAP teleconnection and contributing to the dominant mode of the FEHEs. The physical connection between the dominant mode of FEHEs and the western tropical and subtropical Pacific Ocean was well revealed in the CFSv2 hindcasts and thus the CFSv2-predicted SSTs in the western tropical and subtropical Pacific Ocean was used as the predictor sst_CFSv2. The predictor in the observations was the soil

moisture over southern China in the preceding December (soil_Dec), which combined the signal of the air–sea interactions over the tropical and northern extratropical Pacific Ocean. The decaying La Nina was characterized by negative SST anomalies over the eastern tropical Pacific Ocean in December and negative SST anomalies over the western tropical Pacific and northern Indian oceans in the following summer, which contributed to the connection between the deficit in soil moisture over southern China in December and the dominant mode of the summer FEHEs over eastern China. The air–sea interactions over the northern extratropical Pacific Ocean associated with the deficit in soil moisture favored the developing El Niño and led to anomalous cold SSTs over the western tropical Pacific Ocean in the following summer, which contributed to the dominant mode of FEHEs over eastern China. The soil_Dec was physically connected to the dominant mode of FEHEs, with a significant correlation coefficient (−0.78, significant at the 99% confidence level) with PC1_obs.

The results of the one-year-leave cross-validation and independent hindcast showed that the interannual variability of PC1_obs was better captured by the physical–empirical model than by the CFSv2 hindcasts, with an improved correlation coefficient from insignificant to around 0.8 significant at the 99% confidence level, a reduction in the RMSE by about 50% and an increased rate of same signs. In extreme years (when the absolute value of PC1_obs was greater than one standard deviation), all the signs of PC1_obs were captured in the physical–empirical model. These results show that the physical–empirical model established on these two predictors significantly improved the prediction of the dominant mode of summer FEHEs over eastern China.

Data availability statement

Publicly available datasets were analyzed in this study. This data can be found here: https://data.cma.cn/data/cdcindex/cid/00f8a0e6c590ac15.html https://psl.noaa.gov/data/gridded/data.ncep.reanalysis.html https://psl.noaa.gov/data/gridded/data.noaa.ersst.v3.html https://www.ncei.noaa.gov/products/weather-climate-models/climate-forecast-system.

Author contributions

BS and HL contributed to the conception of the study. BaZ, BS, and HL contributed significantly to the analysis and preparation of the paper. BaZ performed the data analysis and wrote the paper. BS, HL, BoZ, and MD helped to edit the paper.

Funding

This study was funded by the Natural Science Foundation of China (Grants 41991283 and 42005015) and the Natural Science Foundation of Jiangsu Province of China (BK20200814).

Conflict of Interest

The authors declare that the research was conducted in the absence of any commercial or financial relationships that could be construed as a potential conflict of interest.

Publisher's note

References

Bjerknes, J. (1969). Atmospheric teleconnections from the equatorial Pacific. *Mon. Weather Rev.* 97, 163–172. doi:10.1175/1520-0493(1969)097<0163:atftep>2.3.co;2

Bloomfield, P. (2004). *Fourier analysis of time series: An introduction*. Hoboken, New Jersey, United States: John Wiley & Sons.

Borg, M. A., Xiang, J., Anikeeva, O., Pisaniello, D., Hansen, A., Zander, K., et al. (2021). Occupational heat stress and economic burden: A review of global evidence. *Environ. Res.* 195, 110781. doi:10.1016/j.envres.2021.110781

Chen, H. P., and Sun, J. Q. (2018). Projected changes in climate extremes in China in a 1.5 °C warmer world. *Int. J. Climatol.* 38, 3607–3617. doi:10.1002/joc.5521

Chen, P., and Sun, B. (2020). Improving the dynamical seasonal prediction of Western Pacific warm pool sea surface temperatures using a physical–empirical model. *Int. J. Climatol.* 40, 4657–4675. doi:10.1002/joc.6481

Chen, R., Wen, Z., and Lu, R. (2019). Influences of tropical circulation and sea surface temperature anomalies on extreme heat over Northeast Asia in the midsummer of 2018. *Atmos. Ocean. Sci. Lett.* 12, 238–245. doi:10.1080/16742834.2019.1611170

Chen, R., Wen, Z., and Lu, R. (2018). Interdecadal change on the relationship between the mid-summer temperature in South China and atmospheric circulation and sea surface temperature. *Clim. Dyn.* 51, 2113–2126. doi:10.1007/s00382-017-4002-5

Deng, K., Yang, S., Ting, M., Zhao, P., and Wang, Z. (2019). Dominant modes of China summer heat waves driven by global sea surface temperature and atmospheric internal variability. *J. Clim.* 32, 3761–3775. doi:10.1175/jcli-d-18-0256.1

Gao, M., Wang, B., Yang, J., and Dong, W. (2018). Are peak summer sultry heat wave days over the Yangtze–Huaihe River basin predictable? *J. Clim.* 31, 2185–2196. doi:10.1175/jcli-d-17-0342.1

Han, T., Li, S., Hao, X., and Guo, X. (2020). A statistical prediction model for summer extreme precipitation days over the northern central China. *Int. J. Climatol.* 40, 4189–4202. doi:10.1002/joc.6451

Hong, H., Sun, J., and Wang, H. (2020). Interdecadal variation in the frequency of extreme hot events in Northeast China and the possible mechanism. *Atmos. Res.* 244, 105065. doi:10.1016/j.atmosres.2020.105065

Hong, H., Sun, J., and Wang, H. (2022). Variations in summer extreme high-temperature events over northern Asia and the possible mechanisms. *J. Clim.* 35, 335–357. doi:10.1175/JCLI-D-21-0043.1

Huang, B., Thorne, P. W., Banzon, V. F., Boyer, T., Zhang, H. M., Lawrimore, J. H., et al. (2017). Extended reconstructed sea surface temperature, version 5 (ERSSTv5): Upgrades, validations, and intercomparisons. *J. Clim.* 30, 8179–8205. doi:10.1175/jcli-d-16-0836.1

Huang, J., van den Dool, H. M., and Georgakakos, K. G. (1996). Analysis of model-calculated soil moisture over the United States (1931–1993) and applications to long-range temperature forecasts. *J. Clim.* 9, 1350–1362. doi:10.1175/1520-0442(1996)009<1350:aomcsm>2.0.co;2

Huang, R. (1992). The East Asia/Pacific pattern teleconnection of summer circulation and climate anomaly in East Asia. *J. Meteorological Res.* 6, 25–37.

Igun, E., Xu, X., Hu, Y., and Jia, G. (2022). Strong heatwaves with widespread urban-related hotspots over Africa in 2019. *Atmos. Ocean. Sci. Lett.* 15, 100195. doi:10.1016/j.aosl.2022.100195

Ji, L., and Fan, K. (2019). Climate prediction of dust weather frequency over northern China based on sea-ice cover and vegetation variability. *Clim. Dyn.* 53, 687–705. doi:10.1007/s00382-018-04608-w

Kalnay, E., Kanamitsu, M., Kistler, R., Collins, W., Deaven, D., Gandin, L., et al. (1996). The NCEP/NCAR 40-year reanalysis project. *Bull. Am. Meteorol. Soc.* 77, 437–471. doi:10.1175/1520-0477(1996)077<0437:tnyrp>2.0.co;2

Kosaka, Y., and Nakamura, H. (2010). Mechanisms of meridional teleconnection observed between a summer monsoon system and a subtropical anticyclone. Part I: The Pacific–Japan pattern. *J. Clim.* 23, 5085–5108. doi:10.1175/2010jcli3413.1

Li, H., Chen, H., Wang, H., Sun, J., and Ma, J. (2018). Can Barents Sea ice decline in spring enhance summer hot drought events over northeastern China? *J. Clim.* 31, 4705–4725. doi:10.1175/jcli-d-17-0429.1

Li, M., Luo, D., Yao, Y., and Zhong, L. (2020). Large-scale atmospheric circulation control of summer extreme hot events over China. *Int. J. Climatol.* 40, 1456–1476. doi:10.1002/joc.6279

Liu, W., Chen, R., and Wen, Z. (2021). An interdecadal decrease in extreme heat days in August over Northeast China around the early 1990s. *Atmos. Ocean. Sci. Lett.* 14, 100001. doi:10.1016/j.aosl.2020.100001

Long, Y., Li, J., Zhu, Z., and Zhang, J. (2022). Predictability of the anomaly pattern of summer extreme high-temperature days over southern China. *Clim. Dyn.* 59, 1027–1041. doi:10.1007/s00382-022-06170-y

Luo, N., Guo, Y., Gao, Z., Chen, K., and Chou, J. (2020). Assessment of CMIP6 and CMIP5 model performance for extreme temperature in China. *Atmos. Ocean. Sci. Lett.* 13, 589–597. doi:10.1080/16742834.2020.1808430

Nitta, T. (1987). Convective activities in the tropical Western Pacific and their impact on the Northern Hemisphere summer circulation. *J. Meteorological Soc. Jpn.* 65, 373–390. doi:10.2151/jmsj1965.65.3_373

North, G. R., Bell, T. L., Cahalan, R. F., and Moeng, F. J. (1982). Sampling errors in the estimation of empirical orthogonal functions. *Mon. Weather Rev.* 110, 699–706. doi:10.1175/1520-0493(1982)110<0699:seiteo>2.0.co;2

Orlowsky, B., and Seneviratne, S. I. (2012). Global changes in extreme events: Regional and seasonal dimension. *Clim. Change* 110, 669–696. doi:10.1007/s10584-011-0122-9

Pepler, A. S., Díaz, L. B., Prodhomme, C., Doblas-Reyes, F. J., and Kumar, A. (2015). The ability of a multi-model seasonal forecasting ensemble to forecast the frequency of warm, cold and wet extremes. *Weather Clim. Extrem.* 9, 68–77. doi:10.1016/j.wace.2015.06.005

Price, J. F., Weller, R. A., and Schudlich, R. R. (1987). Winddriven ocean currents and Ekman transport. *Science* 238, 1534–1538. doi:10.1126/science.238.4833.1534

Qiao, S., Chen, D., Wang, B., Cheung, H., Liu, F., Cheng, J., et al. (2021). The longest 2020 Meiyu season over the past 60 years: Subseasonal perspective and its predictions. *Geophys. Res. Lett.* 48, e2021GL093596. doi:10.1029/2021gl093596

Ren, L., Zhou, T., and Zhang, W. (2020). Attribution of the record-breaking heat event over northeast Asia in summer 2018: The role of circulation. *Environ. Res. Lett.* 15, 054018. doi:10.1088/1748-9326/ab8032

Saha, S., Moorthi, S., Wu, X., Wang, J., Becker, E., Tripp, P., et al. (2014). The NCEP climate forecast system version 2. *J. Clim.* 27, 2185–2208. doi:10.1175/jcli-d-12-00823.1

Seager, R., Kushnir, Y., Naik, N. H., Cane, M. A., and Miller, J. (2001). Wind-driven shifts in the latitude of the Kuroshio–Oyashio Extension and generation of SST anomalies on decadal timescales. *J. Clim.* 14, 4249–4265. doi:10.1175/1520-0442(2001)014<4249:wdsitl>2.0.co;2

Sun, B., Li, H., and Zhou, B. (2019). Interdecadal variation of Indian Ocean basin mode and the impact on Asian summer climate. *Geophys. Res. Lett.* 46, 12388–12397. doi:10.1029/2019gl085019

Sun, B., and Wang, H. (2019). Enhanced connections between summer precipitation over the Three-River-Source region of China and the global climate system. *Clim. Dyn.* 52, 3471–3488. doi:10.1007/s00382-018-4326-9

Sun, Y., Zhang, X. B., Zwiers, F. W., Song, L. C., Wan, H., Hu, T., et al. (2014). Rapid increase in the risk of extreme summer heat in Eastern China. *Nat. Clim. Chang.* 4, 1082–1085. doi:10.1038/nclimate2410

Tang, S., Qiao, S., Feng, T., Jia, Z., Zang, N., and Feng, G. (2021a). Predictability of the mid-summer surface air temperature over the yangtze river valley in the national centers for environmental prediction climate forecast system. *Int. J. Climatol.* 41, 811–829. doi:10.1002/joc.6670

Tang, S., Qiao, S., Feng, T., Wang, Y., Yang, Y., Zhang, Z., et al. (2021b). Asymmetry of probabilistic prediction skills of the midsummer surface air temperature over the middle and lower reach of the Yangtze River valley. *Clim. Dyn.* 57, 3285–3302. doi:10.1007/s00382-021-05866-x

Tian, B., and Fan, K. (2020). Climate prediction of summer extreme precipitation frequency in the Yangtze River valley based on sea surface temperature in the southern Indian Ocean and ice concentration in the Beaufort Sea. *Int. J. Climatol.* 40, 4117–4130. doi:10.1002/joc.6446

Tong, Q., Huang, Y., Duan, M., and Zhao, Q. (2020). Possible contribution of the PDO to the eastward retreat of the Western Pacific subtropical high. *Atmos. Ocean. Sci. Lett.* 14, 100005. doi:10.1016/j.aosl.2020.100005

Wang, B., Wu, R., and Fu, X. (2000). Pacific–East asian teleconnection: How does ENSO affect East asian climate? *J. Clim.* 13, 1517–1536. doi:10.1175/1520-0442(2000)013<1517:peathd>2.0.co;2

WMO (2013). *The global climate 2001–2010: A decade of climate extremes.* Geneva, Switzerland: World Meteorological Organization Rep. WMO-1103, 110.

Wu, J., and Gao, X. J. (2013). A gridded daily observation dataset over China region and comparison with the other datasets. *Chin. J. Geophys.* 56, 1102–1111. in Chinese. doi:10.6038/cjg20130406

Wu, L., and Zhang, J. (2015). The relationship between spring soil moisture and summer hot extremes over North China. *Adv. Atmos. Sci.* 32, 1660–1668. doi:10.1007/s00376-015-5003-0

Xie, S., Hu, K., Hafner, J., Tokinaga, H., Du, Y., Huang, G., et al. (2009). Indian Ocean capacitor effect on Indo–Western Pacific climate during the summer following El Niño. *J. Clim.* 22, 730–747. doi:10.1175/2008jcli2544.1

Xu, K., Lu, R., Mao, J., and Chen, R. (2019). Circulation anomalies in the mid–high latitudes responsible for the extremely hot summer of 2018 over northeast Asia. *Atmos. Ocean. Sci. Lett.* 12, 231–237. doi:10.1080/16742834.2019.1617626

Yang, K., Zhang, J., Wu, L., and Wei, J. (2019). Prediction of summer hot extremes over the middle and lower reaches of the Yangtze River valley. *Clim. Dyn.* 52, 2943–2957. doi:10.1007/s00382-018-4302-4

Yang, Y., Lin, Z., Luo, L., Zhang, Y., and Li, Z. (2021). Inhomogeneous trends in the onset date of extreme hot days in China over the last five decades. *Atmos. Ocean. Sci. Lett.* 14, 100080. doi:10.1016/j.aosl.2021.100080

You, Q. L., Jiang, Z. H., Kong, L., Wu, Z. W., Bao, Y. T., Kang, S. C., et al. (2017). A comparison of heat wave climatologies and trends in China based on multiple definitions. *Clim. Dyn.* 48, 3975–3989. doi:10.1007/s00382-016-3315-0

Zhang, D., Huang, Y., Sun, B., Li, F., and Wang, H. (2019b). Verification and improvement of the ability of CFSv2 to predict the Antarctic Oscillation in boreal spring. *Adv. Atmos. Sci.* 36, 292–302. doi:10.1007/s00376-018-8106-6

Zhang, D., Huang, Y., and Sun, B. (2019a). Verification and improvement of the capability of ensembles to predict the winter arctic oscillation. *Earth Space Sci.* 6, 1887–1899. doi:10.1029/2019ea000771

Zhang, Y., Zhou, W., and Leung, M. (2019c). Phase relationship between summer and winter monsoons over the South China sea: Indian Ocean and ENSO forcing. *Clim. Dyn.* 52, 5229–5248. doi:10.1007/s00382-018-4440-8

Zhou, Y., Yuan, J., Wen, Z., Huang, S., Chen, X., Guo, Y., et al. (2022). The impacts of the East Asian subtropical westerly jet on weather extremes over China in early and late summer. *Atmos. Ocean. Sci. Lett.* 15, 100212. doi:10.1016/j.aosl.2022.100212

Zhu, B., Sun, B., Li, H., and Wang, H. (2020b). Interdecadal variations in extreme high-temperature events over southern China in the early 2000s and the influence of the Pacific Decadal Oscillation. *Atmosphere* 11, 829. doi:10.3390/atmos11080829

Zhu, B., Sun, B., and Wang, H. (2020a). Dominant modes of interannual variability of extreme high-temperature events in eastern China during summer and associated mechanisms. *Int. J. Climatol.* 40, 841–857. doi:10.1002/joc.6242

Zhu, B., Sun, B., and Wang, H. (2022). Increased interannual variability in the dipole mode of extreme high-temperature events over east China during summer after the early 1990s and associated mechanisms. *J. Clim.* 35, 1347–1364. doi:10.1175/jcli-d-21-0431.1

frontiers | Frontiers in Earth Science

TYPE Original Research
PUBLISHED 09 January 2023
DOI 10.3389/feart.2022.1076396

OPEN ACCESS

EDITED BY
Shangfeng Chen,
Institute of Atmospheric Physics (CAS), China

REVIEWED BY
Shuoyi Ding,
Fudan University, China
Jing Ma,
Nanjing University of Information Science and Technology, China
Jinling Piao,
Chinese Academy of Sciences (CAS), China

*CORRESPONDENCE
Botao Zhou,
zhoubt@nuist.edu.cn

SPECIALTY SECTION
This article was submitted to Atmospheric Science, a section of the journal Frontiers in Earth Science

RECEIVED 21 October 2022
ACCEPTED 08 December 2022
PUBLISHED 09 January 2023

CITATION
Fan Y, Yao X, Zhou B, Li H and Liu M (2023), Decadal variation of the summer extreme high temperature days in northern Eurasia during 1960–2018. *Front. Earth Sci.* 10:1076396. doi: 10.3389/feart.2022.1076396

Decadal variation of the summer extreme high temperature days in northern Eurasia during 1960–2018

Yi Fan[1,2], Xiaona Yao[3], Botao Zhou[1]*, Huixin Li[1,2] and Mei Liu[4]

[1]Collaborative Innovation Center on Forecast and Evaluation of Meteorological Disasters, Key Laboratory of Meteorological Disaster, Ministry of Education, Joint International Research Laboratory of Climate and Environment Change, School of Atmospheric Sciences, Nanjing University of Information Science and Technology, Nanjing, China, [2]Nansen-Zhu International Research Centre, Institute of Atmospheric Physics, Chinese Academy of Sciences, Beijing, China, [3]School of Earth Sciences, Yunnan University, Kunming, China, [4]Jiangsu Meteorological Observatory, Nanjing, China

Unprecedented heat waves have been demonstrated sweeping across much of the Northern Hemisphere in recent summers. However, this study reveals that for northern Eurasia (30°–70°N, 10°–130°E), significant increases in summer extreme high temperature days (EHTDs) have already commenced since the mid-1990s, with the peaks centered on the surrounding areas of the Caspian Sea and Lake Baikal. Results indicate that compared with the period of 1960–1994 (P1), during 1995–2018 (P2) high-pressure and anticyclonic anomalies occupy the areas around the Caspian Sea and Lake Baikal, thus suppressing local cloud cover and precipitation, enhancing the solar radiation and high-temperature anomalies. The anticyclonic anomaly over Lake Baikal shows a close relationship with the increasing trend of global temperature, and the anomalous anticyclone over the Caspian Sea is under the influence of the warm North Atlantic and anomalous upper-troposphere jet stream during P2. The warmer than normal North Atlantic leads to the high-pressure anomaly over the Caspian Sea by modulating the Rossby wave activity. In addition, during P2, the temperatures in the middle North Atlantic and Western Europe show greater increments than those over higher latitudes, and thus the temperature gradient enhances the westerly thermal wind, which therefore leads to an anomalous upper-level jet stream to the North of the Caspian Sea. Under this circumstance, the Caspian Sea is located to the right side of the anomalous jet exit, inducing the suppressed upward motion over there and favoring the occurrence of more EHTDs after the mid-1990s.

KEYWORDS

northern Eurasia, extreme high temperature, decadal variation, North Atlantic, jet stream

1 Introduction

The northern part of the Eurasian continent is located deep inland to the east of the Atlantic and south of the Arctic with a temperate continental climate over most of the area. Due to the year-round control of continental air masses, this area is characterized by large annual temperature differences, being fragile and sensitive to background climate variations (e.g., Li et al., 2016; Ji and Fan, 2019). Moreover, the northern part of the Eurasian continent constitutes the "heartland" of the world and has become a necessary place for cultural and economic exchanges between Asia and western countries. Therefore, it is important to study the characteristics of extreme temperature variations in this region.

Extreme high temperature day (EHTD) is usually defined as a day with the maximum temperature exceeds a threshold indicator, which is generally considered to be the 90th percentile (Tx90p) if a cumulative distribution function is used to represent the daily maximum temperature (e.g., Zhang et al., 2005; Cornes and Jones, 2013). As global warming intensifies in recent decades, EHTDs occur more frequently in many regions of the world, with serious impacts on electricity, water supply, and public health, constraining the stable development of society (e.g., Greenough et al., 2001; Meehl and Tebaldi, 2004; Alexander et al., 2006; Coumou and Rahmstorf, 2012; Lesk et al., 2016; Ge et al., 2019; Allan et al., 2021).

For many years, studies have indicated that the frequency and intensity of various extreme events are exhibiting significant decadal changes, which could often be attributed to the influences from external forcing caused by increasing greenhouse gas concentrations due to anthropogenic emissions (e.g., Wang et al., 2012; Fischer and Knutti, 2015; Dong et al., 2017; Chen and Dong, 2019; Vautard et al., 2019; Hu et al., 2020; Ge et al., 2021). However, changes in oceanic and atmospheric circulation from internal variability of the climate system and their teleconnections are also important in determining the occurrence of regional climate extremes, especially EHTDs (e.g., Fan and Wang, 2004; Zhou and Wu, 2016; Hong et al., 2017; Sun et al., 2019; Jiang et al., 2020; Zhang et al., 2020; Fan et al., 2022; Li et al., 2022). It is indicated that under the modulation of teleconnections such as the Eurasian teleconnection pattern, Silk Road pattern, and East Asia–Pacific pattern, the frequency of EHTDs in Northeast China increased after the mid-1990s (Liu et al., 2021). Li et al. (2018) pointed out that the anomalous wave activity caused by the warming tropical Atlantic is the main reason for the increased variability of high-temperature extremes in Mongolia. Besides, the heat wave events in the Korean Peninsula and China have been strongly affected by the Scandinavian and the circumglobal teleconnection patterns and show decadal changes in the interannual variability (Choi et al., 2020).

Previous studies have shown that due to the polar amplification effect, the climate architecture in polar areas undergoes a more dramatic change than in lower latitudes, leading to changes in jet and North Atlantic sea surface temperature (SST) (e.g., Screen and Simmonds, 2010; Francis and Vavrus, 2015; Ma et al., 2021). The anomalous summer jet and the teleconnection patterns are significant in modulating the atmospheric background, which in turn affect Eurasian surface temperatures through cloud-radiation feedback and temperature advection processes (e.g., Smith et al., 2010; Zhu et al., 2011; Hanlon et al., 2013; Chen and Wu, 2017). Considering the above factors, characteristics of the interdecadal variability of local climate extremes in northern Eurasia and possible reasons caused by the background changes in circulation and SSTs are to be investigated in this study.

The main contents of this paper are as follows: Data and methods are introduced in Section 2. Spatial and temporal characteristics of the EHTD in northern Eurasia, decadal variability, and the corresponding changes in the climatic background, as well as the possible reasons, are analyzed in Section 3. A summary and discussion of this study are provided in Section 4.

2 Data and methods

The Tx90p index is calculated as the percentage of days when the maximum daily temperature exceeds the 90th percentile during a certain time interval to present the EHTD (Zhang et al., 2005). The extreme indices are provided by the Met Office Hadley Centre observations datasets: HadEX3 (Dunn et al., 2020), on a 1.25° × 1.875° grid from 1960 to 2018 (https://www.metoffice.gov.uk/hadobs/hadex3/index.html). The number of EHTDs is calculated as the sum of the Tx90p indices in summer: June, July, and August. The monthly reanalysis datasets for circulation, sea level pressure, geopotential height, total cloud cover, rate of precipitation, downward solar radiation flux, and air temperature with resolutions of 2.5° × 2.5° are derived from the National Centers for Environmental Prediction-National Center for Atmospheric Research (NCEP-NCAR) Reanalysis 1 (http://www.psl.noaa.gov/data/gridded/data.ncep.reanalysis.derived.html) from 1960 to 2018. The SST is obtained from the National Oceanic and Atmospheric Administration (NOAA) Extended Reconstructed SST V5 (https://www.ncei.noaa.gov). The Atlantic Multidecadal Oscillation (AMO) index is calculated as the detrended area-weighted average summer SST over the North Atlantic from the website of https://psl.noaa.gov/data/timeseries/AMO/.

In this paper, the climate mean is calculated using the average values during 1960–2018. The empirical orthogonal function (EOF) method is used to decompose the number of EHTDs in northern Eurasia into spatial and temporal components to reflect the main spatial characteristics. North-test is employed to verify that the EOFs are reasonably distinct from each other (North et al., 1982). The

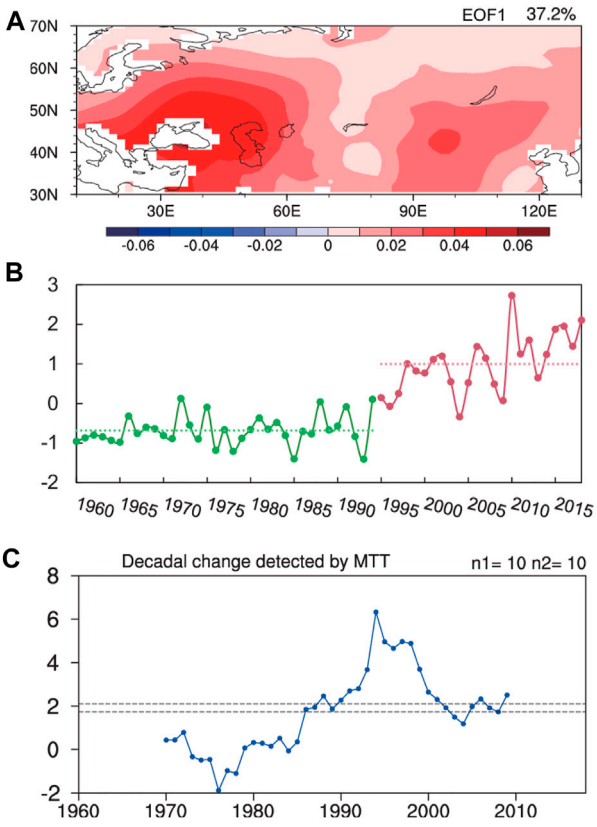

FIGURE 1
(A) The first eigenvector of the EOF analysis on the EHTDs. **(B)** Year-by-year series (scatter) of the summer EHTD indices in northern Eurasia (10°–130°E, 30°–70°N) from 1960 to 2018, and the averaged values (dashed lines) of the index on time for 1960–1994 (P1) and 1995–2018 (P2), respectively. **(C)** Decadal change of EHTDs in northern Eurasia according to the sliding *t*-test (blue: sliding *t*-test statistic, two dotted lines for low and high indicate significance at 90% and 95% confidence levels, respectively).

sliding *t*-test is used to test the significance of interdecadal changes in the time series of the number of EHTDs. Simple linear regression and Pearson's correlation are used to investigate the relationship between different fields (Wilks, 2011).

To investigate the wave-activity flux for large-scale stationary waves during different periods, the horizontal component at pressure level p of wave-activity flux (Takaya and Nakamura, 2001) is:

$$W = \frac{p}{2|\bar{u}|}\begin{Bmatrix} \bar{u}\left(\psi_x'^2 - \psi'\psi_{xx}'\right) + \bar{v}\left(\psi_x'\psi_y' - \psi'\psi_{xy}'\right) \\ \bar{u}\left(\psi_x'\psi_y' - \psi'\psi_{xy}'\right) + \bar{v}\left(\psi_y'^2 - \psi'\psi_{yy}'\right) \end{Bmatrix}$$

where the overbars and primes denote mean states and deviations from the mean states, respectively; the subscripts x and y represent zonal and meridional gradients; $u = (u, v)$ denotes horizontal wind velocity; and ψ' represents eddy stream functions.

3 Results

3.1 Decadal variation of the EHTD

EOF analysis on the EHTDs in summer northern Eurasia (30°–70°N, 10°–130°E) during 1960–2018 shows that the first eigenvector explains 37.2% of the total variance (Figure 1A). The first eigenvector is well separated from the second according to the criterion developed by North et al. (1982), with consistent values across the region. Therefore, a regional average of the EHTDs in summer in this region could be carried out to obtain the EHTD index. As shown in Figure 1B, during 1960–1994, the EHTD index fluctuates slightly and the average value is relatively small, while the mean EHTD index increased during 1995–2018 with a relatively large mean value. Moreover, statistical analysis of the decadal variation characteristic of the EHTD index with sliding *t*-test (Figure 1C) reveals that the average value of the index changes significantly around 1994/1995. According to the variation in the number of EHTDs in summer in northern Eurasia, the total period is divided into two phases, i.e., fewer EHTDs during the period of 1960–1994 (P1), and more EHTDs during the period of 1995–2018 (P2).

Figures 2A, B show the anomalies of EHTDs during P1 and P2, respectively. Negative anomalies are mainly distributed over most areas in northern Eurasia during P1 (Figure 2A), while positive anomalies of EHTD occupy almost all the regions with the large values located around the Caspian Sea and Lake Baikal during P2 (Figure 2B). The difference in the EHTDs between P2 and P1 shows a similar pattern as that between P2 and the climatology, showing more EHTDs during P2 than P1 (Figure 2C). Concerning the significant decadal increase in the EHTDs, how the associated atmospheric circulation and sea surface temperature background change during the two periods and the possible causes responsible for these anomalies are to be investigated in the next subsection.

3.2 Decadal variations of associated atmospheric circulations

The lower-troposphere circulation anomalies for P1 and P2 show generally contrary characteristics (Figures 2D–F). During the P1 period, low pressure and cyclonic circulation anomalies are observed over Greenland, eastern Europe, and Mongolia, whereas high pressure and anticyclonic circulation anomalies occupy the North Atlantic (Figure 2D). The cyclonic circulation over northern Eurasia is favorable for the formation of clouds and precipitation (Figures 3A, D), which suppresses the solar radiation reaching the surface (Figure 3G) and the formation of anomalous EHTDs during P1 (Figure 2A). In contrast, during the P2 period, high pressure and anticyclonic circulation anomalies are detected over the northern Eurasia region (Figure 2E), leading to a clearer sky with less cloud cover

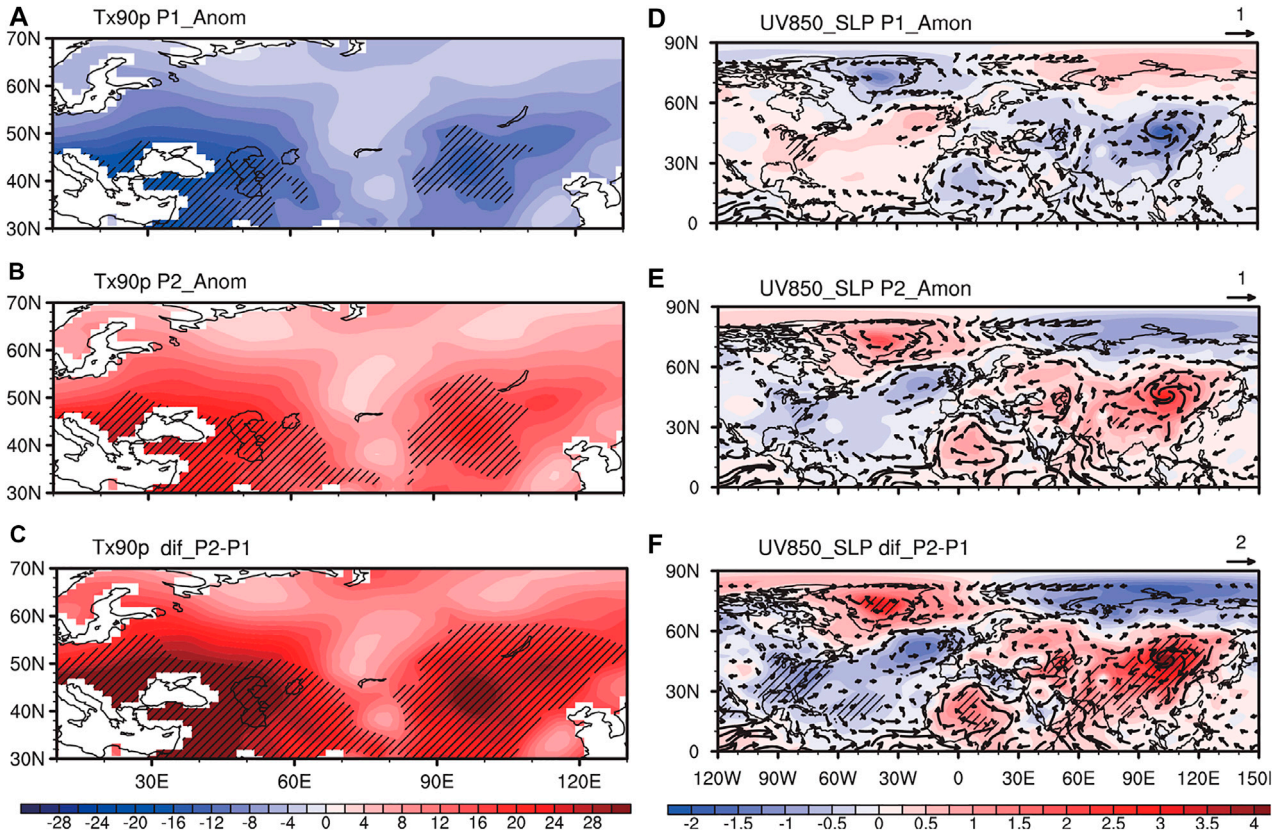

FIGURE 2
Differences in terms of the EHTDs between **(A)** P1 and the climatology, **(B)** P2 and the climatology, and **(C)** P2 and P1 (unit: %); the second column [**(D–F)**] for the sea level pressure (shading, unit: hPa) and wind field at 850 hPa (vector, unit: m/s). Dashed areas indicate significance at 99% confidence level according to the Student's *t*-test.

(Figure 3B), less precipitation (Figure 3E), more solar radiation (Figure 3H), and finally benefiting the occurrence of EHTDs (Figure 2B). As shown in Figures 3C, F, I, the differences in terms of cloud cover, precipitation and solar radiation between P2 and P1 exert similar patterns as shown in Figures 3B, E, H: Less cloud cover and precipitation are accompanied by more solar radiation reaching the surface as well as more EHTDs during P2 than P1.

3.3 Possible physical mechanisms

The ocean and atmosphere compose a complex coupled system. Ocean provides heat, water vapor, and energy to the atmosphere, influencing the temperature, humidity, and atmospheric circulations (e.g., Gill and Adrian, 1982; Webster, 1994; Trenberth et al., 2001; Si and Ding, 2016; Chen and Wu, 2017; Fan et al., 2019). To further investigate the causes of the circulation anomalies, the following parts focus on the relationship between the circulation anomaly over northern Eurasia and the surrounding SST.

A composite analysis of SST at different periods reveals that the key areas with significant decadal changes in SST are mainly located in the North Atlantic. The North Atlantic SST is colder than normal during P1 (Figure 4A) while warmer than normal during P2 (Figures 4B, C), playing important roles in the decadal variation of EHTDs in northern Eurasia. In addition, the correlation coefficient between the AMO indices and the EHTD index is 0.69, which is significant at the 99% confidence level according to the Student's *t*-test, indicating the influence of AMO on the interdecadal timescale. That is, the positive correlation between the changes in North Atlantic SST and the EHTDs in northern Eurasia indicates that the warmer (colder) than normal North Atlantic is consistent with more (less) EHTDs in northern Eurasia. Furthermore, the AMO index is standardized for P1 and P2, respectively (Supplementary Figure S1), to obtain the warm cases with AMO indices greater than 1.5 standard deviation (1960 and 1989 for P1, and 2010 for P2). The anomalous wave activity flux and geopotential height at 200 hPa for warm cases during P1 and P2 are shown in Figure 5. A propagation route of the anomalous

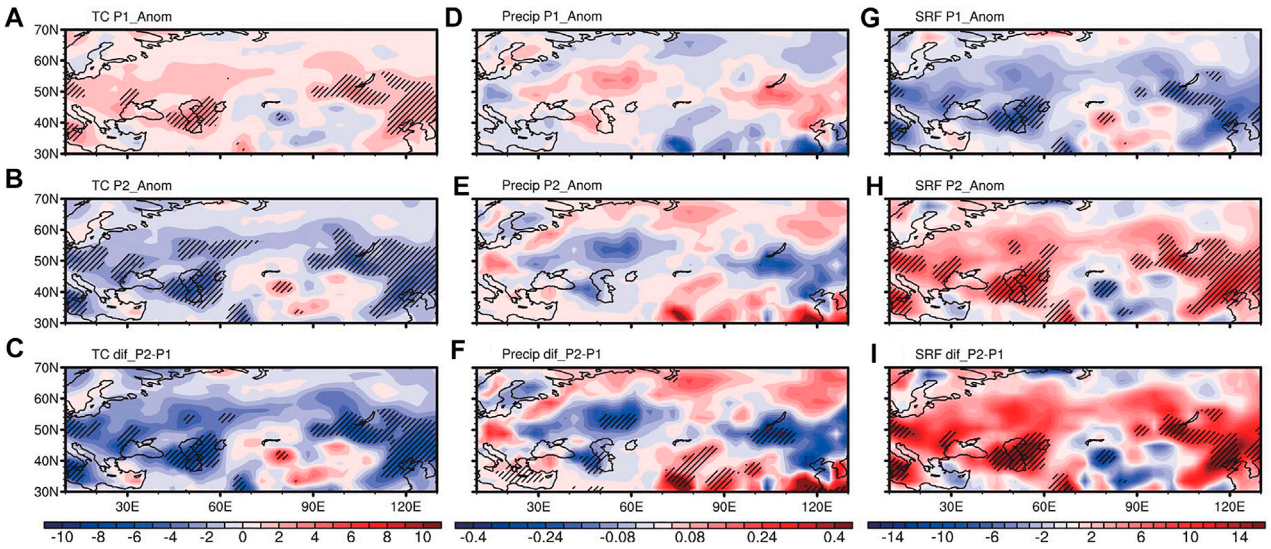

FIGURE 3
Differences in terms of the total cloud cover between **(A)** P1 and the climatology, **(B)** P2 and the climatology, and **(C)** P2 and P1 (unit: %); the second column [**(D–F)**] for the rate of precipitation (unit: mm/day); the third column [**(G–I)**] for the downward solar radiation flux at surface (unit: W/m^2). Dashed areas indicate significance at 95% confidence level according to the Student's *t*-test.

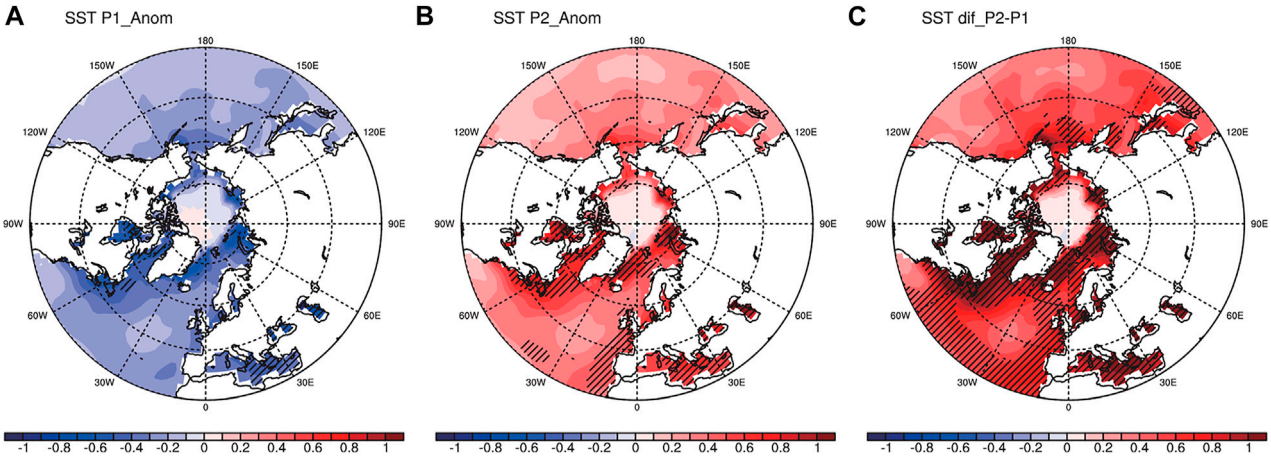

FIGURE 4
Differences in terms of the SST between **(A)** P1 and the climatology, **(B)** P2 and the climatology, and **(C)** P2 and P1 (unit: K). Dashed areas indicate significance at 95% confidence level according to the Student's *t*-test.

wave activity flux with alternating high- and low-pressure anomalies from the northern Atlantic to the Caspian Sea could be figured out for both P1 and P2 (Figure 5), indicating that a warmer than normal North Atlantic favors the high-pressure anomaly over the Caspian Sea. During P2, the North Atlantic is warmer than P1 (Figure 4), and the wave activity flux and pressure anomalies over the Caspian Sea are stronger (Figure 5). Meanwhile, the sinking motion accompanied by high pressure would bring more clear sky and solar radiation (Figures 3C, F, I), increasing EHTDs in northern Eurasia (Figure 2C).

Another important factor affecting the summer climate in northern Eurasia is the position of the upper-level jet stream (e.g., Smith et al., 2019; Ma et al., 2021; Streffing et al., 2021). As shown in Figure 6, during P2 (P1), the temperatures in the middle North Atlantic and Europe show significant increments (decreases) than those over higher latitudes, and thus the temperature gradient is larger

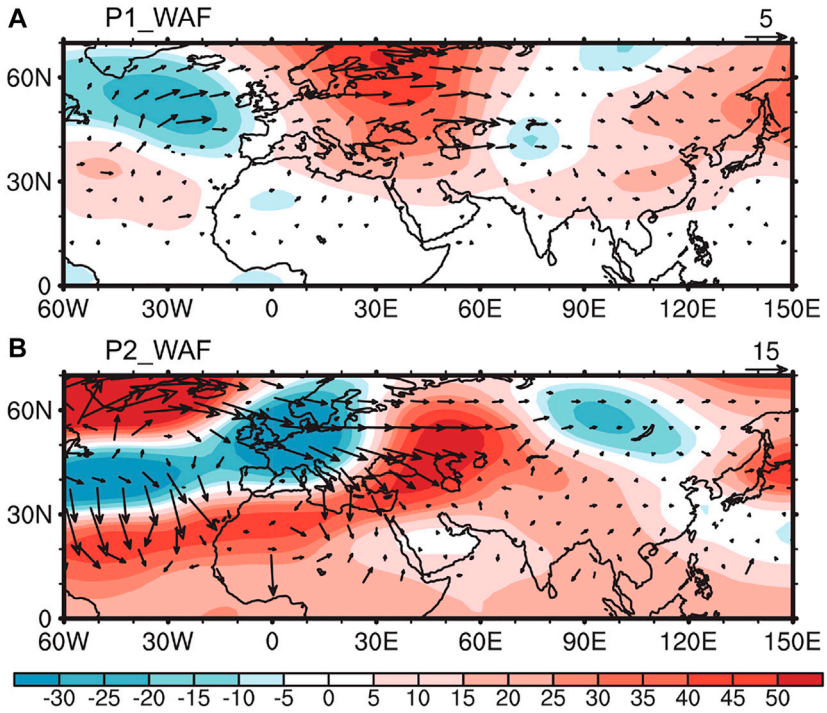

FIGURE 5
The 200 hPa geopotential height (unit: gpm) and wave activity flux (vector, unit: $m^2\ s^{-2}$) anomalies for warm North Atlantic years during **(A)** P1 and **(B)** P2.

(smaller) than normal along these areas along 50°N. Moreover, according to the thermal wind principle, the westerly jet stream over there would be accelerated. As shown in Figure 7, the climatology of the 200 hPa horizontal wind speed over Europe shows that the average position of the jet stream is located at around 45°N, while the anomalous westerly jet stream is southward (northward) at around 30°N (50°N) during P1 (P2). Therefore, during P2, the Caspian Sea is located on the right side of the anomalous upper-level jet stream exit. Due to that the wind speed decreases rapidly in the jet exit area and the wind speed along the jet axis is larger than that on both sides, there is a negative vorticity advection resulting in the anticyclonic anomaly on the right side of the jet exit area at 200 hPa. Furthermore, under the Coriolis forcing effect, convergence anomaly exits at the upper-level troposphere, leading to high pressure and divergence anomalies at the lower troposphere as well as the abnormal sinking motion between the two layers. With the joint impacts of the northwards-than-normal jet stream, negative vorticity advection, and strengthening sinking movement, the summer EHTDs are inclined to increase in the Caspian Sea during P2.

The AMO phase changes twice during 1960–2018, which appear around 1965 and 1995, respectively. The decadal change in EHTDs is consistent with the phase of the AMO from the cold phase to the warm phase. During the positive AMO phase, more frequent occurrences of negative NAO may contribute to the increased EHTDS over the Caspian Sea and Lake Baikal by modulating the eastward propagated wave trains such as the Silk Road pattern and inducing the high-pressure anomalies (Hong et al., 2022). Besides, regression analysis shows that the global warming trend shows a significant influence on the positive pressure anomalies over the areas to the South of Lake Baikal (Supplementary Figure S2). It indicates the contribution of global warming on the increasing EHTDs over areas around Lake Baikal.

4 Summary and discussion

In recent decades, the summer extreme high temperature days (EHTDs) in the Northern Hemisphere has been frequently detected, posing a serious threat to the safety of human life, agricultural production, and the ecological environment of many countries. This study investigates the decadal variation of summer EHTDs in northern Eurasia during 1960–2018, using the EHTD index provided by Hadley Center and the atmospheric circulation and sea surface temperature (SST) data provided by NOAA. The corresponding climate factors are also analyzed with statistical and dynamic diagnosis methods. The obtained conclusion are summarized as follows.

The number of summer EHTDs in northern Eurasia undergoes a significant decadal variation around the mid-1990s, especially over the areas around Lake Baikal and the Caspian Sea, with fewer

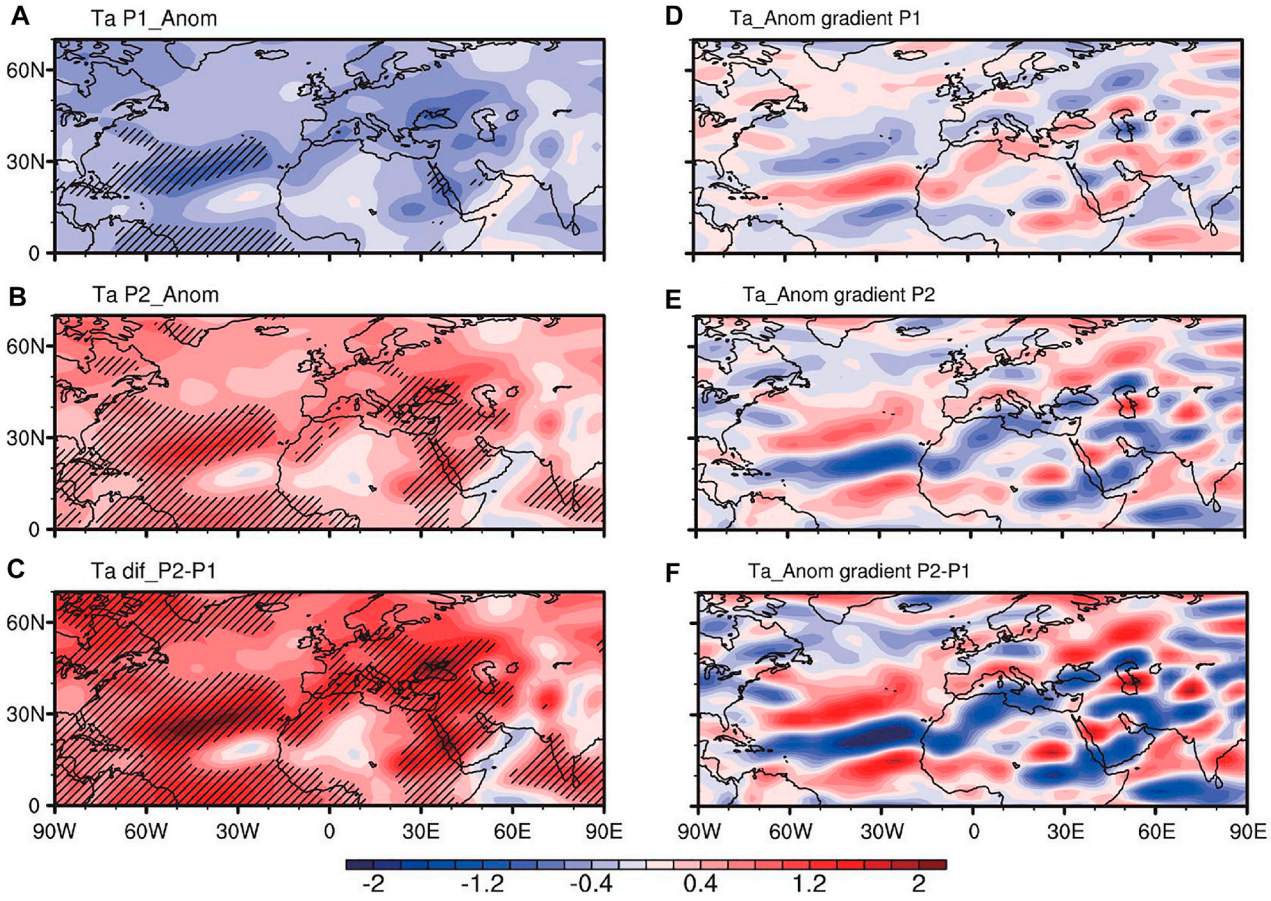

FIGURE 6
Differences in terms of the 850 hPa air temperature between **(A)** P1 and the climatology, **(B)** P2 and the climatology, and **(C)** P2 and P1 (unit: K). Dashed areas indicate significance at 99% confidence level according to the Student's *t*-test. [**(D–F)**] The meridional gradient of air temperature in [**(A–C)**], respectively (unit: K kkm^{-1}).

EHTDs during 1960–1994 and more EHTDs during 1995–2018. The circulation background also shows a corresponding decadal variation at that time. During 1960–1994 (1995–2018), low pressure and cyclonic (high pressure and anticyclonic) anomalies control Lake Baikal and the Caspian Sea, favoring more (less) cloud cover and precipitation, absent (sufficient) solar radiation and decreased (increased) EHTDs over there.

During 1995–2018, the anomalous Rossby wave activities induced by warmer than normal North Atlantic leads to high-pressure anomalies over the Caspian Sea, resulting in the significant anticyclonic anomaly over the area, which favors the more frequent occurrence of EHTDs than those during 1960–1994. Meanwhile, the Atlantic jet is located northward. The area around the Caspian Sea is to the right side of the jet stream exit. On such a background, the negative vorticity advection at the upper-level troposphere would lead to the divergence anomaly and strengthen the sinking motion between lower- and higher-levels. Thus, the summer EHTD tends to be maintained over the Caspian Sea. As for the increasing EHTD over areas around Lake Baikal, the influence of global warming and the modulation of AMO on the NAO-Silk Road teleconnection relationship might play important roles, and corresponding mechanisms still need further exploration. Besides, previous study has also pointed out that the variations in summer Arctic contribute to the heatwaves in Eurasia (Wu and Francis, 2019). Therefore, the impacts of the sea surface temperature and sea ice cover in Arctic on decadal change in EHTDs over Northern Eurasia are also to be further investigated.

In this paper, the causes of decadal variation of the summer EHTD in northern Eurasia are investigated primarily from the perspective of changes in circulation backgrounds. However, it is also important to further detect whether the contributions are mainly attributed to the internal variability of the climate system or the external forcing signals such as human-induced greenhouse gas emissions and anthropogenic aerosols. Therefore, future studies will make further investigations with numerical model experiments and state-of-the-art methods of attribution analysis.

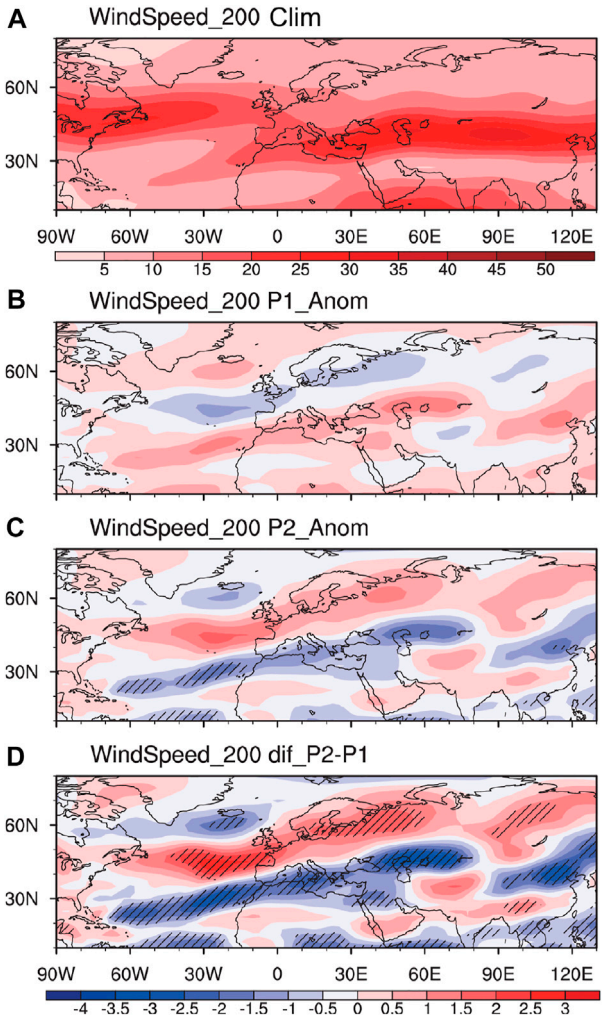

FIGURE 7
Horizontal wind speed at 200 hPa for **(A)** climatology, **(B)** difference between P1 and climatology, **(C)** difference between P2 and climatology, and **(D)** difference between P2 and P1 (unit: m/s, shading indicates significance at 90% confidence level according to the Student's *t*-test).

Data availability statement

The datasets presented in this study can be found in online repositories. The names of the repository/repositories and accession number(s) can be found below: http://www.psl.noaa.gov/data/gridded/data.ncep.reanalysis.derived.html.

Author contributions

All authors equally collaborated in the research presented in this publication by making the following contributions. Conceptualization, YF and BZ; data curation, BZ; formal analysis, YF and XY; investigation, YF, XY, and ML; methodology, YF, BZ, and HL; writing—original draft, YF; Writing—review and editing, YF, BZ, HL, XY, and ML.

Funding

This work is jointly supported by Grants from the National Natural Science Foundation of China (Grants 41991285; 42105030; 42005015), the Natural Science Foundation of the Jiangsu Higher Education Institutions of China (21KJB170005), and the Natural Science Foundation of Jiangsu Province (BK20200814).

Acknowledgments

We thank the editor and reviewers, who helped a lot in improving the manuscript. We also thank the support from the Startup Foundation for Introducing Talent of NUIST.

Conflict of interest

The authors declare that the research was conducted in the absence of any commercial or financial relationships that could be construed as a potential conflict of interest.

The reviewer JM declared a shared affiliation with the authors YF, BZ, and HL to the handling editor at time of review.

Publisher's note

Supplementary material

The Supplementary Material for this article can be found online at: https://www.frontiersin.org/articles/10.3389/feart.2022.1076396/full#supplementary-material

SUPPLEMENTARY FIGURE S1
Standardized AMO index during **(A)** P1 and **(B)** P2, respectively.

SUPPLEMENTARY FIGURE S2
Regression coefficients of global temperature (index derived from https://climate.nasa.gov/vital-signs/global-temperature/) onto sea level pressure (shading, dots indicate significance at 90% confidence level according to the Student's *t*-test).

References

Alexander, L. V., Zhang, X., Peterson, T. C., Caesar, J., Gleason, B., Klein Tank, A. M. G., et al. (2006). Global observed changes in daily climate extremes of temperature and precipitation. *J. Geophys. Res. Atmos.* 111 (D5), D05109. doi:10.1029/2005jd006290

Allan, R. P., Hawkins, E., Bellouin, N., and Collins, B. (2021). "IPCC, 2021: Summary for policymakers," in *Climate change 2021: The physical science basis. Contribution of working group I to the sixth assessment report of the intergovernmental panel on climate change*. Editors V. Masson-Delmotte, P. Zhai, and A. Pirani, Cambridge, UK: Cambridge University Press.

Chen, S., and Wu, R. (2017). Interdecadal changes in the relationship between interannual variations of spring North Atlantic SST and eurasian surface air temperature. *J. Clim.* 30, 3771–3787. doi:10.1175/jcli-d-16-0477.1

Chen, W., and Dong, B. (2019). Anthropogenic impacts on recent decadal change in temperature extremes over China: Relative roles of greenhouse gases and anthropogenic aerosols. *Clim. Dyn.* 52, 3643–3660. doi:10.1007/s00382-018-4342-9

Choi, N., Lee, M., Cha, D., Lim, Y. K., and Kim, K. M. (2020). Decadal changes in the interannual variability of heat waves in East Asia caused by atmospheric teleconnection changes. *J. Clim.* 33, 1505–1522. doi:10.1175/jcli-d-19-0222.1

Cornes, R. C., and Jones, P. D. (2013). How well does the ERA-Interim reanalysis replicate trends in extremes of surface temperature across Europe? *J. Geophys. Res. Atmos.* 118, 10262–10276. doi:10.1002/jgrd.50799

Coumou, D., and Rahmstorf, S. (2012). A decade of weather extremes. *Nat. Clim. Change* 2, 491–496. doi:10.1038/nclimate1452

Dong, B., Sutton, R. T., and Shaffrey, L. (2017). Understanding the rapid summer warming and changes in temperature extremes since the mid-1990s over Western Europe. *Clim. Dyn.* 48, 1537–1554. doi:10.1007/s00382-016-3158-8

Dunn, R. J. H., Alexander, L. V., Donat, M. G., Zhang, X., Bador, M., Herold, N., et al. (2020). Development of an updated global land in situ-based data set of temperature and precipitation extremes: HadEX3. *J. Geophys. Res. Atmos.* 125, e2019JD032263. doi:10.1029/2019jd032263

Fan, K., and Wang, H. J. (2004). Antarctic oscillation and the dust weather frequency in North China. *Geophys. Res. Lett.* 31, L10201. doi:10.1029/2004gl019465

Fan, Y., Fan, K., Zhu, X., and Fraedrich, K. (2019). El niño–related summer precipitation anomalies in southeast asia modulated by the atlantic multidecadal oscillation. *J. Clim.* 32, 7971–7987. doi:10.1175/jcli-d-19-0049.1

Fan, Y., Li, J., Zhu, S., Li, H., and Zhou, B. (2022). Trends and variabilities of precipitation and temperature extremes over Southeast Asia during 1981–2017. *Meteorology Atmos. Phys.* 134, 78. doi:10.1007/s00703-022-00913-6

Fischer, E. M., and Knutti, R. (2015). Anthropogenic contribution to global occurrence of heavy-precipitation and high-temperature extremes. *Nat. Clim. Change* 5, 560–564. doi:10.1038/nclimate2617

Francis, J. A., and Vavrus, S. J. (2015). Evidence for a wavier jet stream in response to rapid Arctic warming. *Environ. Res. Lett.* 10, 014005. doi:10.1088/1748-9326/10/1/014005

Ge, F., Zhu, S., Luo, H., Zhi, X., and Wang, H. (2021). Future changes in precipitation extremes over southeast asia: Insights from CMIP6 multi-model ensemble. *Environ. Res. Lett.* 16, 024013. doi:10.1088/1748-9326/abd7ad

Ge, F., Zhu, S., Peng, T., Zhao, Y., Sielmann, F., Fraedrich, K., et al. (2019). Risks of precipitation extremes over southeast asia: Does 1.5° C or 2° C global warming make a difference?[J]. *Environ. Res. Lett.* 14, 044015. doi:10.1088/1748-9326/aaff7e

Gill, A. E., and Adrian, E. (1982). *Atmosphere-ocean dynamics*. Cambridge, MA, USA: Academic Press.

Greenough, G., McGeehin, M., Bernard, S. M., Trtanj, J., Riad, J., and Engelberg, D. (2001). The potential impacts of climate variability and change on health impacts of extreme weather events in the United States. *Environ. Health Perspect.* 109, 191–198. doi:10.2307/3435009

Hanlon, H. M., Hegerl, G. C., Tett, S. F. B., and Smith, D. M. (2013). Can a decadal forecasting system predict temperature extreme indices?[J]. *J. Clim.* 26, 3728–3744. doi:10.1175/jcli-d-12-00512.1

Hong, X., Lu, R., Chen, S., and Li, S. (2022). The relationship between the North atlantic oscillation and the Silk Road pattern in summer. *J. Clim.* 35 (20), 3091–3102. doi:10.1175/jcli-d-21-0833.1

Hong, X., Lu, R., and Li, S. (2017). Amplified summer warming in europe–west asia and Northeast asia after the mid-1990s. *Environ. Res. Lett.* 12, 094007. doi:10.1088/1748-9326/aa7909

Hu, T., Sun, Y., Zhang, X., Min, S. K., and Kim, Y. H. (2020). Human influence on frequency of temperature extremes. *Environ. Res. Lett.* 15 (6), 064014. doi:10.1088/1748-9326/ab8497

Ji, L., and Fan, K. (2019). Climate prediction of satellite-based spring eurasian vegetation index (NDVI) using coupled singular value decomposition (SVD) patterns. *Remote Sens.* 11, 2123. doi:10.3390/rs11182123

Jiang, D., Si, D., and Lang, X. (2020). Evaluation of east asian summer climate prediction from the CESM large-ensemble initialized decadal prediction project. *J. Meteorological Res.* 34, 252–263. doi:10.1007/s13351-020-9151-5

Lesk, C., Rowhani, P., and Ramankutty, N. (2016). Influence of extreme weather disasters on global crop production. *Nature* 529, 84–87. doi:10.1038/nature16467

Li, D., Zhou, T., Zou, L., Zhang, W., and Zhang, L. (2018). Extreme high-temperature events over East Asia in 1.5°c and 2°c warmer futures: Analysis of ncar cesm low-warming experiments. *Geophys. Res. Lett.* 45, 1541–1550. doi:10.1002/2017gl076753

Li, J., Fan, K., and Xu, Z. (2016). Links between the late wintertime North Atlantic Oscillation and springtime vegetation growth over Eurasia. *Clim. Dyn.* 46, 987–1000. doi:10.1007/s00382-015-2627-9

Li, J., Hao, X., Liao, H., Wang, Y., Cai, W., Li, K., et al. (2022). Winter particulate pollution severity in North China driven by atmospheric teleconnections. *Nat. Geosci.* 15, 349–355. doi:10.1038/s41561-022-00933-2

Liu, W., Chen, R., and Wen, Z. (2021). An interdecadal decrease in extreme heat days in August over Northeast China around the early 1990s. *Atmos. Ocean. Sci. Lett.* 14, 100001. doi:10.1016/j.aosl.2020.100001

Ma, W., Chen, G., Peings, Y., and Alviz, N. (2021). Atmospheric River response to arctic sea ice loss in the polar amplification model intercomparison project. *Geophys. Res. Lett.* 48, e2021GL094883. doi:10.1029/2021gl094883

Meehl, G. A., and Tebaldi, C. (2004). More intense, more frequent, and longer lasting heat waves in the 21st century. *Science* 305, 994–997. doi:10.1126/science.1098704

North, G. R., Bell, T. L., Cahalan, R. F., and Moeng, F. J. (1982). Sampling errors in the estimation of empirical orthogonal functions. *Mon. Weather Rev.* 110, 699–706. doi:10.1175/1520-0493(1982)110<0699:seiteo>2.0.co;2

Screen, J. A., and Simmonds, I. (2010). The central role of diminishing sea ice in recent Arctic temperature amplification. *Nature* 464, 1334–1337. doi:10.1038/nature09051

Si, D., and Ding, Y. (2016). Oceanic forcings of the interdecadal variability in east asian summer rainfall. *J. Clim.* 29, 7633–7649. doi:10.1175/jcli-d-15-0792.1

Smith, D. M., Screen, J. A., Deser, C., Cohen, J., Fyfe, J. C., Garcia-Serrano, J., et al. (2019). The polar amplification model intercomparison project (PAMIP) contribution to CMIP6: Investigating the causes and consequences of polar amplification. *Geosci. Model. Dev.* 12, 1139–1164. doi:10.5194/gmd-12-1139-2019

Smith, D. R., Eade, N. J., Dunstone, D., Fereday, D., Murphy, J. M., Pohlmann, H., et al. (2010). Skilful multi-year predictions of Atlantic hurricane frequency. *Nat. Geosci.* 3, 846–849. doi:10.1038/ngeo1004

Streffing, J., Semmler, T., Zampieri, L., and Jung, T. (2021). Response of northern Hemisphere weather and climate to arctic sea ice decline: Resolution independence in polar amplification model intercomparison project (PAMIP) simulations. *J. Clim.* 34, 8445–8457.

Sun, X., Li, S., Hong, X., and Lu, R. (2019). Simulated influence of the atlantic multidecadal oscillation on summer eurasian nonuniform warming since the mid-1990s. *Adv. Atmos. Sci.* 36, 811–822. doi:10.1007/s00376-019-8169-z

Takaya, K., and Nakamura, H. (2001). A formulation of a phase-independent wave-activity flux for stationary and migratory quasigeostrophic eddies on a zonally varying basic flow. *J. Atmos. Sci.* 58, 608–627. doi:10.1175/1520-0469(2001)058<0608:afoapi>2.0.co;2

Trenberth, K. E., Caron, J. M., and Stepaniak, D. P. (2001). The atmospheric energy budget and implications for surface fluxes and ocean heat transports. *Clim. Dyn.* 17, 259–276. doi:10.1007/pl00007927

Vautard, R., Christidis, N., Ciavarella, A., Alvarez-Castro, C., Bellprat, O., Christiansen, B., et al. (2019). Evaluation of the HadGEM3-A simulations in view of detection and attribution of human influence on extreme events in Europe. *Clim. Dyn.* 52, 1187–1210. doi:10.1007/s00382-018-4183-6

Wang, H. J., Sun, J. Q., Chen, H. P., Zhu, Y. L., Zhang, Y., Jiang, D. B., et al. (2012). Extreme climate in China: Facts, simulation and projection. *Meteorol. Z.* 21, 279–304. doi:10.1127/0941-2948/2012/0330

Webster, P. J. (1994). The role of hydrological processes in ocean-atmosphere interactions. *Rev. Geophys.* 32, 427–476. doi:10.1029/94rg01873

Wilks, D. S. (2011). *Statistical methods in the atmospheric sciences*. Cambridge, MA, USA: Academic Press.

Wu, B., and Francis, J. A. (2019). Summer arctic cold anomaly dynamically linked to east asian heat waves. *J. Clim.* 32 (4), 1137–1150. doi:10.1175/jcli-d-18-0370.1

Zhang, G., Zeng, G., Li, C., and Yang, X. (2020). Impact of PDO and AMO on interdecadal variability in extreme high temperatures in North China over the most recent 40-year period. *Clim. Dyn.* 54, 3003–3020. doi:10.1007/s00382-020-05155-z

Zhang, X., Hegerl, G., Zwiers, F. W., and Kenyon, J. (2005). Avoiding inhomogeneity in percentile-based indices of temperature extremes. *J. Clim.* 18, 1641–1651. doi:10.1175/jcli3366.1

Zhou, Y., and Wu, Z. (2016). Possible impacts of mega-el niño/southern oscillation and atlantic multidecadal oscillation on eurasian heatwave frequency variability. *Q. J. R. Meteorological Soc.* 142, 1647–1661. doi:10.1002/qj.2759

Zhu, X., Bothe, O., and Fraedrich, K. (2011). Summer atmospheric bridging between Europe and East Asia: Influences on drought and wetness on the Tibetan plateau. *Quat. Int.* 236, 151–157. doi:10.1016/j.quaint.2010.06.015

frontiers | Frontiers in Earth Science

TYPE Original Research
PUBLISHED 09 January 2023
DOI 10.3389/feart.2022.1032313

OPEN ACCESS

EDITED BY
Bo Sun,
Nanjing University of Information Science and Technology, China

REVIEWED BY
Zixuan Han,
Hohai University, China
Shaobo Qiao,
Sun Yat-sen University, China
Qin Wen,
Nanjing Normal University, China

*CORRESPONDENCE
Guolin Feng,
fenggl@cma.gov.cn

SPECIALTY SECTION
This article was submitted to Atmospheric Science, a section of the journal Frontiers in Earth Science

RECEIVED 30 August 2022
ACCEPTED 21 September 2022
PUBLISHED 09 January 2023

CITATION
Cheng J, Zhao Y, Zhi R and Feng G (2023), Meridional circulation dominates the record-breaking "Dragon Boat Water" rainfall over south China in 2022.
Front. Earth Sci. 10:1032313.
doi: 10.3389/feart.2022.1032313

Meridional circulation dominates the record-breaking "Dragon Boat Water" rainfall over south China in 2022

Jianbo Cheng[1], Yuheng Zhao[2], Rong Zhi[2] and Guolin Feng[3,4]*

[1]School of Environmental Science and Engineering, Yancheng Institute of Technology, Yancheng, China, [2]Laboratory for Climate Studies, National Climate Center, China Meteorological Administration, Beijing, China, [3]College of Physical Science and Technology, Yangzhou University, Yangzhou, China, [4]Southern Marine Science and Engineering Guangdong Laboratory (Zhuhai), Zhuhai, China

During the "Dragon Boat Water" season in 2022, record-breaking anomalous rainfall occurred over South China (SC). In this study, the causes of anomalous rainfall are investigated by using the novel moisture budget equation of three-pattern circulations. The results show that the anomalous rainfall over SC caused by the horizontal, meridional, and zonal circulations was −10 mm, 168 mm, and 45.3 mm, which contribute −5%, 86%, and 23% of the actual rainfall anomaly (195.1 mm), respectively, suggesting that the meridional circulation contributes most to anomalous rainfall, followed by zonal circulation, and horizontal circulation contributes negatively. Further analysis based on the three-pattern decomposition of the global atmospheric circulation shows that the spatial configuration of the anomalous horizontal circulation and vertical vorticity provides the background for generating the anomalous divergence and convergence of meridional and zonal circulations and further anomalous vertical velocity of the meridional and zonal circulations, ultimately resulting in anomalous rainfall.

KEYWORDS

record-breaking rainfall, "dragon boat water" season, south China, novel moisture budget equation, meridional circulation

1 Introduction

South China (SC) is located in the southernmost region of China, which comprises the southern region of the Yangtze River basin and the eastern region of the Tibetan Plateau; it includes the Guangdong, Guangxi, Hainan, and Fujian Provinces and their surrounding areas. SC has abundant rainfall that is characterized by a large annual mean value, high frequency of rainstorms, and long duration (Zhai and Eskridge, 1997; Yuan et al., 2010; Chu et al., 2018; Miao et al., 2019; Chu et al., 2020). According to the differences in influencing factors and time periods, the flood season of SC can be divided into two periods (Ramage, 1952; Yang and Sun, 2005; Yuan et al., 2019). The first flood season is generally called the "first rainy season" or "early rainy season" of China, which occurs from April to June. The second flood

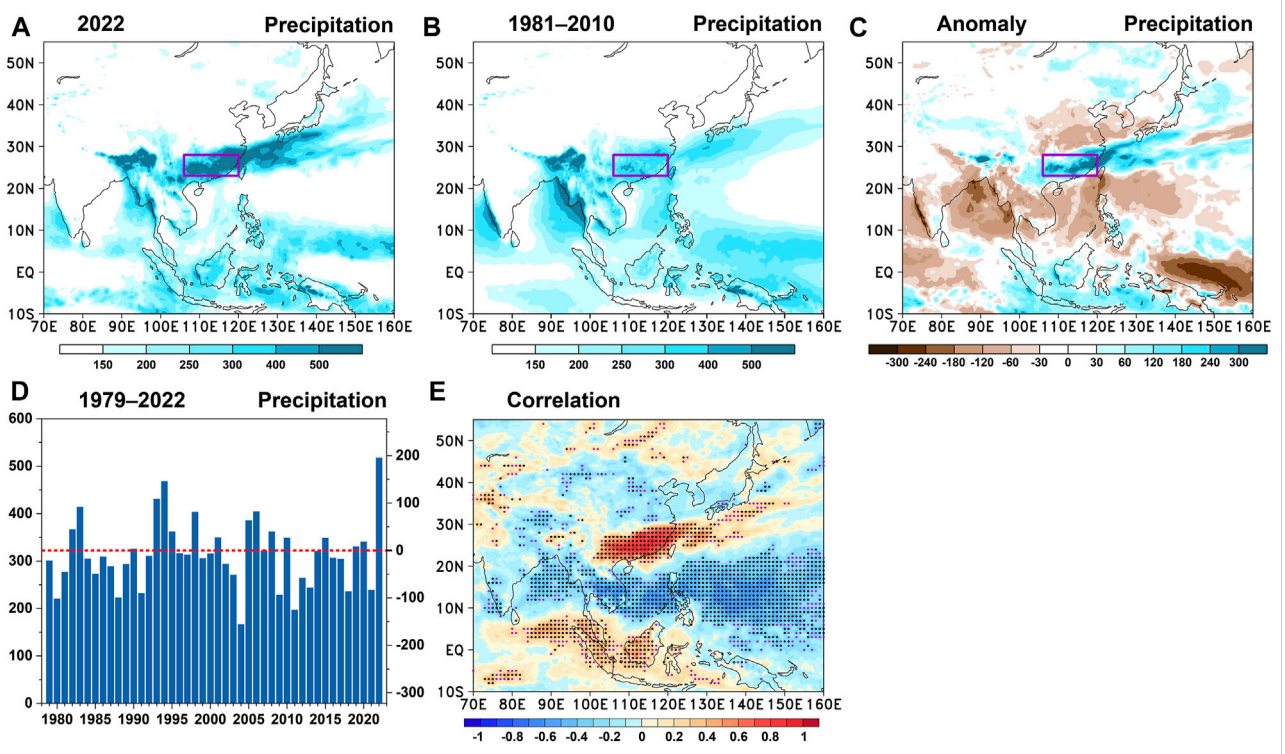

FIGURE 1
(A) Distribution of the accumulated rainfall during the "Dragon Boat Water" season (21 May to 20 June) in 2022; **(B)** and **(C)** are the same as **(A)** but for the climatological rainfall during 1981–2010 and the rainfall anomaly in 2022, respectively. The rainfall anomaly is calculated by subtracting the climatological rainfall during 1981–2010. The purple box in **(A–C)** represents the region of South China (SC; 106°E–120°E, 23°N–28°N). **(D)** Time series of the regionally averaged rainfall over SC during 1979–2022. The Y-axis on the left (right) represents the rainfall (rainfall anomaly). The red dashed line represents the climatological rainfall (zero line of rainfall anomaly) for the Y-axis on the left (right). **(E)** Correlation between the regionally averaged rainfall anomaly over SC and the rainfall anomaly during 1979–2022. Black (purple) dots over the shading represent that those correlation coefficients are significant above the 95% (90%) confidence level based on Student's t test. Units of the rainfall and rainfall anomaly are mm.

season is generally called the "second rainy season" or "late rainy season" of China, which occurs from July to September. In the first rainy season, the rainfall in SC is mainly influenced by monsoon circulations, including the subtropical jet, western Pacific subtropical high, South Asia high, and low-level southwest jet in the subtropics and the East Asian trough and northeastern cold vortex in the mid–high latitudes (Yuan et al., 2012; Li et al., 2018; Miao et al., 2019; Liu et al., 2022). In the second rainy season, the rainfall in SC is mainly influenced by typhoons or tropical depressions (Lee et al., 2010; Yuan et al., 2019).

During the first rainy season, there is a special time period called the "Dragon Boat Water" rainfall season. The name "Dragon Boat Water" rainfall season originates from 21 May to 20 June, which includes the Chinese Dragon Boat Festival (Lin et al., 2009; Gu and Zhang, 2012; Qian et al., 2020). During the "Dragon Boat Water" rainfall season, the rainfall is concentrated and generally accompanied by thunderstorms over SC. Climatically, the regionally averaged rainfall during the "Dragon Boat Water" season over SC (106°E–120°E, 23°N–28°N) is 322.3 mm (Figures 1B,D). In 2022, an extreme "Dragon Boat Water" rainfall occurred, with the regionally averaged rainfall reaching 517.5 mm, which is 1.6 times the climatological mean value and represents the highest record since 1979 (Figures 1A–D). Since extreme rainfall can lead to great socioeconomic losses, crop destruction, and casualties (Qiao et al., 2021), thus, the primary causes of the extreme rainfall during the "Dragon Boat Water" season should be studied. In addition to the record-breaking "Dragon Boat Water" rainfall, the zonal negative rainfall anomaly belt in the north and south of SC, the zonal positive rainfall anomaly belt in the Southern Hemisphere, and the negative rainfall anomaly in the east of the Malay Archipelago can be observed (Figure 1C). Further correlation analysis (Figure 1E) suggests that the anomalous "Dragon Boat Water" rainfall over SC is generally accompanied by the anomalous rainfall shown in Figure 1C, implying that the same anomalous atmospheric circulation system caused the anomalous rainfall in 2022 shown in Figure 1C.

According to previous studies (Seager et al., 2010; Han et al., 2021), the moisture budget equation can be used to investigate the relative contributions of anomalous atmospheric circulation (dynamic term) and anomalous moisture (thermodynamic term) to anomalous rainfall. Additionally, a novel decomposition of atmospheric circulation, which is called the three-pattern decomposition of global atmospheric circulation (3P-DGAC), can be used to explore anomalous atmospheric circulation (Liu et al., 2008; Hu et al., 2017; Hu et al., 2018a; Hu et al., 2018b; Hu et al., 2020). However, the quantitative contribution of the three-pattern circulations (i.e., horizontal, meridional, and zonal circulations) to anomalous rainfall cannot be obtained using the 3P-DGAC method. To solve this issue, Han et al. (2021) and Cheng et al. (2022) developed a novel moisture budget equation of the three-pattern circulations by incorporating the 3P-DGAC method into the moisture budget equation. Namely, the rainfall anomaly can be linked up with three-pattern circulations by using the novel moisture budget equation. By using the novel moisture budget equation, Cheng et al. (2022) studied the extreme rainfall in Henan Province in July 2021 and found that zonal circulation played the dominant role in causing this anomalous rainfall. In this study, the novel moisture budget equation of three-pattern circulations is adopted to investigate the relative contribution of the three-pattern circulations to the record-breaking "Dragon Boat Water" rainfall over SC in 2022.

This study is organized as follows. The study area, datasets, and methods used are described in Section 2. The quantitative contribution of the three-pattern circulations to anomalous rainfall is investigated using the novel moisture budget equation in Section 3. The anomalous three-pattern circulations and underlying mechanism are studied in Section 4. Finally, the summary and conclusion are given in Section 5.

2 Materials and methods

2.1 Study area

According to the spatial pattern of the anomalous rainfall during the "Dragon Boat Water" season in 2022 (Figure 1C), the study area of the SC in the present study is defined as (106°E–120°E, 23°N–28°N), which is shown as a purple box in Figure 1.

2.2 Source of data

The hourly rainfall, specific humidity, surface pressure, zonal wind, meridional wind, and vertical velocity from the European Center for Medium Range Weather Forecasts Reanalysis 5 (ERA5) (Hersbach et al., 2020) are used for the investigation in this study. The original horizontal resolution of these datasets is 0.25° × 0.25°, and we interpolate these datasets into the 0.5° × 0.5° horizontal resolution for this study. In the vertical direction, we adopt the commonly used 17 pressure levels, i.e., 1000, 925, 850, 700, 600, 500, 400, 300, 250, 200, 150, 100, 70, 50, 30, 20, and 10 hPa. We use the datasets during the "Dragon Boat Water" rainfall season (i.e., 21 May to 20 June) from 1979 to 2022.

2.3 Novel moisture budget equation of three-pattern circulations

Based on the moisture budget equation (Seager et al., 2010; Han et al., 2021) and the 3P-DGAC method (Liu et al., 2008; Hu et al., 2017; Hu et al., 2018a; Hu et al., 2018b; Cheng et al., 2018; Hu et al., 2020), Han et al. (2021) and Cheng et al. (2022) developed a novel moisture budget equation of three-pattern circulations as follows:

$$\delta P = \delta P\_H + \delta P\_M + \delta P\_Z + \delta R, \tag{1}$$

where δP represents the anomalous rainfall. δP_H, δP_M, and δP_Z represent the anomalous rainfall caused by the horizontal, meridional, and zonal circulations. δR represents the anomalous rainfall caused by the residual term. δ represents the difference during the "Dragon Boat Water" season between 2022 and the climatological mean of 1981–2010 in this study.

Since the novel moisture budget equation can be written as $\delta P = \delta MCDA + \delta MCDD + \delta THA + \delta THD + \delta R$, therefore, δP_H, δP_M, and δP_Z can be further decomposed as follows:

$$\begin{cases} \delta P\_H = \delta MCDA\_H + \delta MCDD\_H + \delta THA\_H + \delta THD\_H, \\ \delta P\_M = \delta MCDA\_M + \delta MCDD\_M + \delta THA\_M + \delta THD\_M, \\ \delta P\_Z = \delta MCDA\_Z + \delta MCDD\_Z + \delta THA\_Z + \delta THD\_Z, \end{cases} \tag{2}$$

where δMCDA and δMCDD represent anomalous rainfall caused by the change in advection and divergence to the dynamic term. δTHA and δTHD represent advection and divergence to the thermodynamic term. H, M, and Z on the right of each term represent that those terms are induced by the horizontal, meridional, and zonal circulations, respectively. δMCDA, δMCDD, δTHA, and δTHD can be represented as follows:

$$\begin{cases} \delta MCDA = -\frac{1}{\rho_w g}\int_{P_s}^{0}\left(\delta\vec{V}\cdot\nabla q_0\right)dp, \\ \delta MCDD = -\frac{1}{\rho_w g}\int_{P_s}^{0}\left(q_0\nabla\cdot\delta\vec{V}\right)dp,\Big)dp, \\ \delta THD = -\frac{1}{\rho_w g}\int_{P_s}^{0}\left(\overrightarrow{V_0}\cdot\nabla\delta q\right) \\ \delta THA = -\frac{1}{\rho_w g}\int_{P_s}^{0}\left(\overrightarrow{V_0}\cdot\nabla\delta q\right)dp, \end{cases} \tag{3}$$

where ρ_w, g, $\vec{V}$, and q represent the density of water, gravitational acceleration, horizontal wind, and specific humidity, respectively. Subscript 0 represents that the variables are the climatological

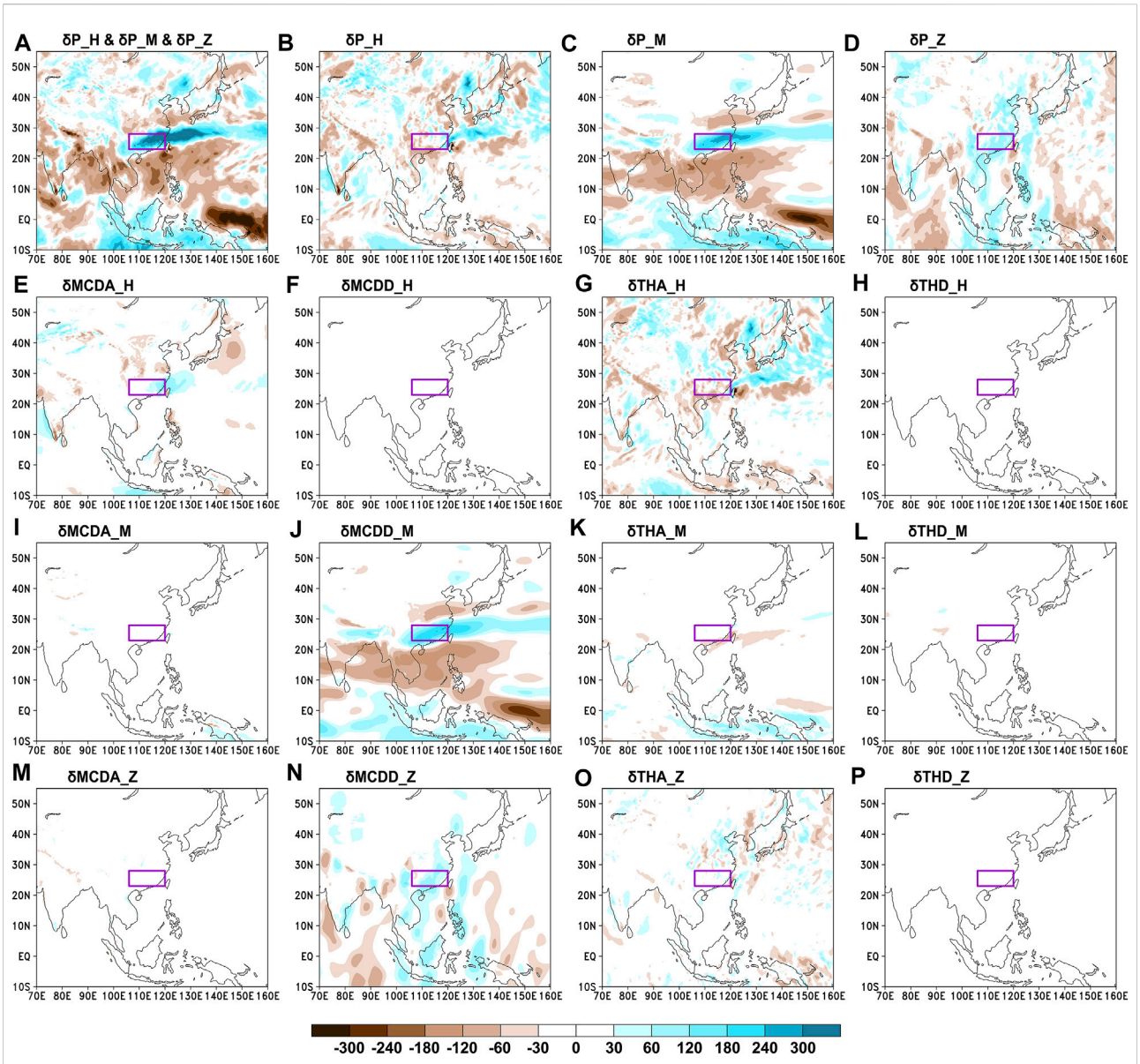

FIGURE 2
(A) Anomalous rainfall caused by the combined effects of horizontal (δP_H), meridional (δP_M), and zonal (δP_Z) circulations (i.e., δP_H + δP_M + δP_Z) during the "Dragon Boat Water" season in 2022 based on the novel moisture budget equation; **(B–D)** are the same as **(A)** but for the anomalous rainfall caused by the **(B)** horizontal, **(C)** meridional, and **(D)** zonal circulations. **(E–H)** Anomalous rainfall caused by the change in **(E)** advection (δMCDA_H) and **(F)** divergence (δMCDD_H) to the dynamic term and **(G)** advection (δTHA_H) and **(H)** divergence (δTHD_H) to the thermodynamic term induced by the horizontal circulation; **(I–L)** and **(M–P)** are the same as **(E–H)** but for those induced by the meridional and zonal circulations, respectively. **(I–L)** are δMCDA_M, δMCDD_M, δTHA_M, and δTHD_M, and **(M–P)** areδMCDA_Z, δMCDD_Z, δTHA_Z, and δTHD_Z. Units of the anomalous rainfall caused by changes in the moisture budget components are mm.

mean of 1981–2010. δMCDA, δMCDD, δTHA, and δTHD of the three-pattern circulations can be obtained using the corresponding anomalous horizontal wind in Eq. 3, i.e., $\delta\vec{V}_{\mathrm{H}}$ and $\vec{V}_{\mathrm{H0}}$ for the horizontal circulation, $\delta\vec{V}_{\mathrm{M}}$ and $\vec{V}_{\mathrm{M0}}$ for the meridional circulation, and $\delta\vec{V}_{\mathrm{Z}}$ and $\vec{V}_{\mathrm{Z0}}$ for the zonal circulation, respectively. The novel moisture budget equation of three-pattern circulations can be used to investigate the relative contribution of the three-pattern circulations to the record-breaking "Dragon Boat Water" rainfall over SC in 2022, which cannot be obtained by using the moisture budget equation or the 3P-DGAC method independently.

In the process of calculation, the δMCDA, δMCDD, δTHA, and δTHD of the three-pattern circulations are first calculated by using Eq. 3. Second, the anomalous rainfall caused by the horizontal,

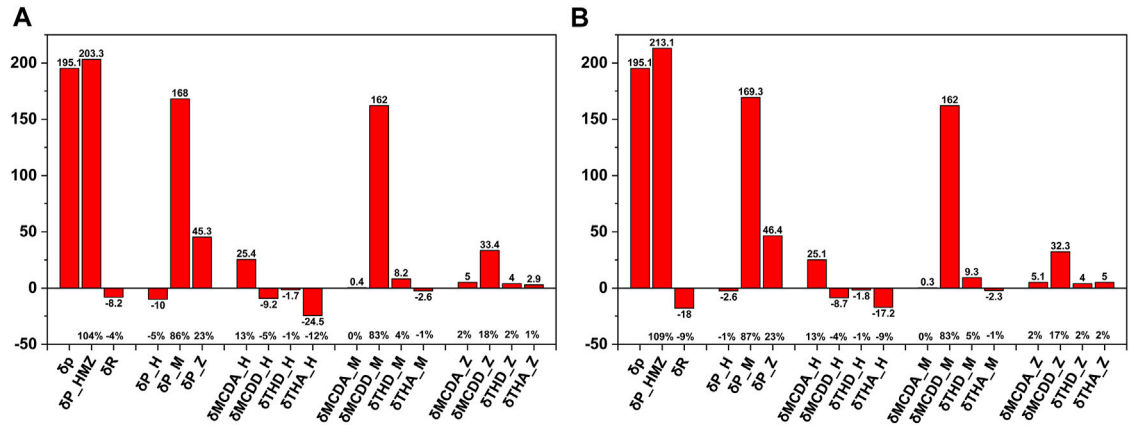

FIGURE 3
(A) Regionally averaged rainfall anomaly (δP) and the regionally averaged anomalous rainfall caused by changes in the moisture budget components over SC during the "Dragon Boat Water" season in 2022. δP_HMZ represents anomalous rainfall caused by the combined effects of horizontal, meridional, and zonal circulations (i.e., δP_H + δP_M + δP_Z). δR represents anomalous rainfall caused by the residual term. The physical meanings of the other terms are the same as those in Figure 2 but for the regionally averaged values. The percentages on the bottom represent the contributions of changes in the moisture budget components to δP. **(B)** is the same as **(A)** but for the results where the upper limit of vertical integration of Eq. 3 changes to 500 hPa. Units of the rainfall anomaly and anomalous rainfall caused by changes in the moisture budget components are mm.

meridional, and zonal circulations is calculated by using Eq. 2. Third, the residual term δR is calculated by using Eq. 1. More details of the 3P-DGAC method can be obtained in (Hu et al., 2017; Hu et al., 2018a; Hu et al., 2018b), and a detailed deduction of the novel moisture budget equation can be obtained in (Han et al., 2021; Cheng et al., 2022).

3 Quantitative contribution of the three-pattern circulations to anomalous rainfall

Figure 2A displays the spatial distribution of the anomalous rainfall caused by the combined effects of horizontal, meridional, and zonal circulations (i.e., δP_H + δP_M + δP_Z) during the "Dragon Boat Water" season in 2022. The spatial distribution of the anomalous rainfall caused by the three-pattern circulations is similar to the actual rainfall anomaly, with the spatial similarity coefficient reaching 0.74 (Figure 1C, Figure 2A). The anomalous rainfall over SC caused by the three-pattern circulations is 203.3 mm, which is equal to 104% of the actual rainfall anomaly (195.1 mm), while the anomalous rainfall caused by the residual term is −8.2 mm, which contributes −4% (Figure 3A), implying that the total rainfall change in 2022 can be largely explained by the sum of three-pattern circulations.

Figures 2B–D show the anomalous rainfall caused by the horizontal, meridional, and zonal circulations, respectively. By comparing Figures 2A,C, it can be observed that the anomalous rainfall caused by the meridional circulation is similar to that caused by the three-pattern circulations, and the spatial similarity coefficient between Figures 2A,C is 0.82. Additionally, by comparing Figures 2B–D, it can be observed that the meridional circulation contributes most to the anomalous rainfall, followed by zonal circulation, and the contribution of the horizontal circulation is the least, implying that the meridional circulation plays the dominant role in the anomalous rainfall. The quantitative anomalous rainfall over SC caused by the horizontal, meridional, and zonal circulations is −10 mm, 168 mm, and 45.3 mm, which contribute −5%, 86%, and 23% of the actual rainfall anomaly, respectively (Figure 3A).

Figures 2E–H show the anomalous rainfall caused by the change in advection (δMCDA_H) and divergence (δMCDD_H) to the dynamic term and changes in advection (δTHA_H) and divergence (δTHD_H) to the thermodynamic term induced by the horizontal circulation. By comparing Figures 2B,G, it can be observed that the anomalous rainfall caused by δTHA_H is similar to that caused by δP_H, and the spatial similarity coefficient between Figures 2B,G is 0.89, implying that δTHA_H contributes most to δP_H.

Figure 2I–L show the anomalous rainfall caused by δMCDA_M, δMCDD_M, δTHA_M, and δTHD_M. By comparing Figures 2C,J, it can be observed that the anomalous rainfall caused by δMCDD_M is similar to that caused by δP_M, and the spatial similarity coefficient between Figures 2C,J is 0.95, implying that δMCDD_M contributes most to δP_M. The quantitative anomalous rainfall over SC caused by δMCDA_M, δMCDD_M, δTHA_M, and δTHD_M is 0.4 mm, 162 mm, −2.6 mm, and 8.2 mm, which contributes 0%, 83%, −1%, and 4% of the actual rainfall anomaly, respectively (Figure 3A).

Figures 2M–P show the anomalous rainfall caused by δMCDA_Z, δMCDD_Z, δTHA_Z, and δTHD_Z. By comparing Figures 2D,N, it can be observed that the anomalous rainfall caused

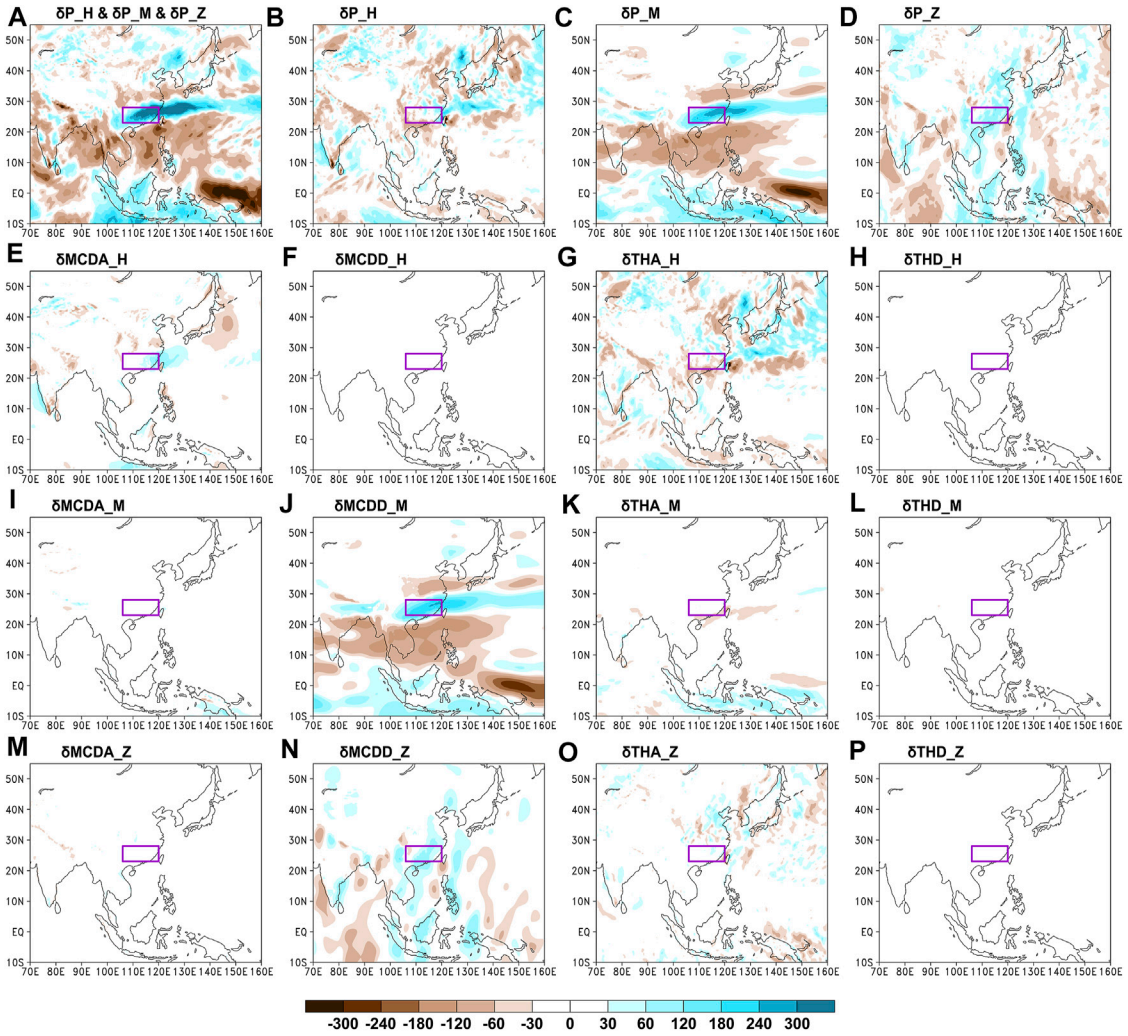

FIGURE 4
Figures 4A–P are the same as Figure 2A–P, except for that the results where the upper limit of vertical integration of Eq. 3 changes to 500 hPa.

by δMCDD_Z is similar to that caused by δP_Z, and the spatial similarity coefficient between Figures 2D,N is 0.79, implying that δMCDD_Z contributes most to δP_Z. The quantitative anomalous rainfall over SC caused by δMCDA_Z, δMCDD_Z, δTHA_Z, and δTHD_Z is 5 mm, 33.4 mm, 2.9 mm, and 4 mm, which contributes 2%, 18%, 1%, and 2% of the actual rainfall anomaly, respectively (Figure 3A).

Since the moisture mainly exists below 500 hPa (Supplementary Figure S1), the results where the upper limit of vertical integration of Eq. 3 changes to 500 hPa are similar to those obtained from Eq. 3 (comparing Figure 2, Figure 4). Additionally, the main conclusions of the quantitative contribution of the three-pattern circulations to the anomalous rainfall do not change (comparing Figures 3A,B).

Generally, δP_M (meridional circulation) contributes most to anomalous rainfall over SC, δP_Z (zonal circulation) follows, and δP_H (horizontal circulation) contributes negatively. Additionally, the main contributors to δP_H, δP_M, and δP_Z are δTHA_H, δMCDD_M, and δMCDD_Z, respectively.

4 Anomalous three-pattern circulations and underlying mechanism

4.1 Anomalous meridional and zonal circulations

Figures 5A–C display the total vertical velocity anomaly and the vertical velocity anomaly of meridional and zonal circulations, respectively, during the "Dragon Boat Water" season in 2022. Figure 5A shows that there exists a zonal negative velocity anomaly belt over SC, implying that there is

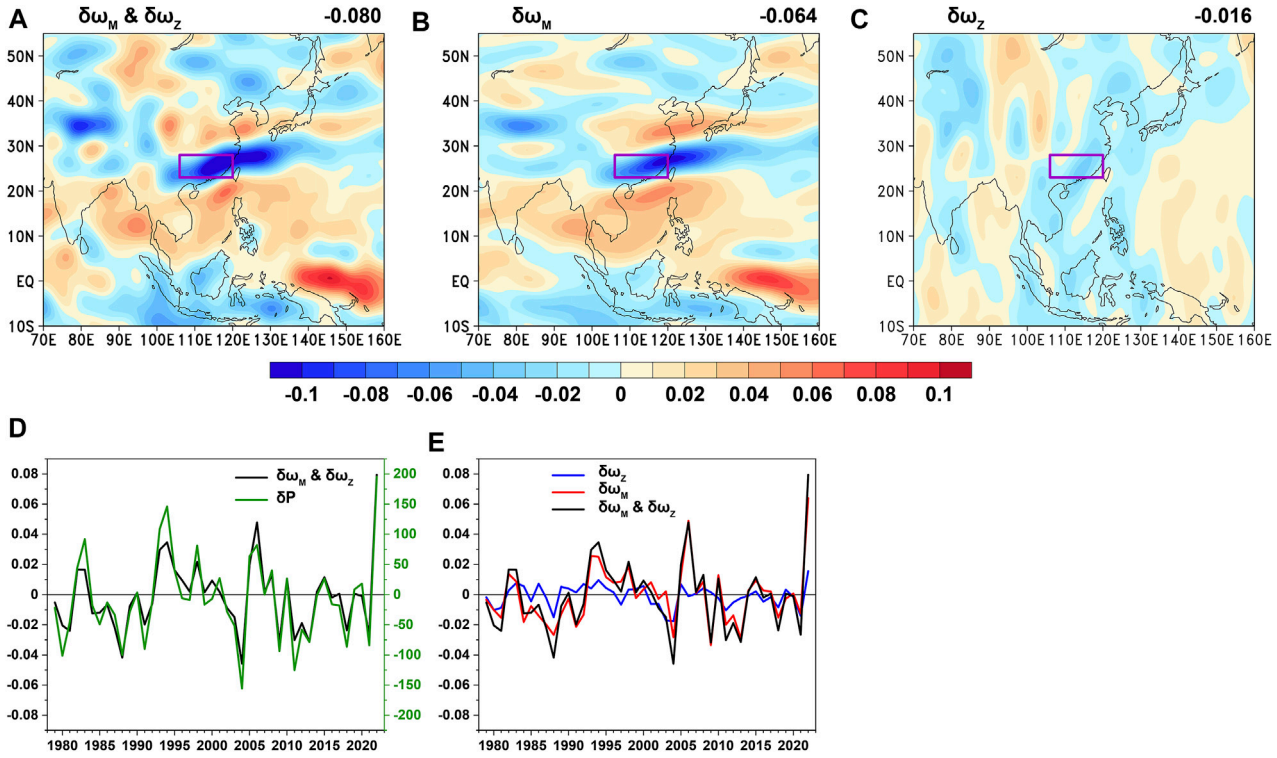

FIGURE 5
(A) Distribution of the vertical velocity anomaly during the "Dragon Boat Water" season in 2022; **(B)** and **(C)** are the same as **(A)** but for the vertical velocity anomaly of **(B)** meridional and **(C)** zonal circulations, respectively. Positive (negative) values in **(A–C)** represent sinking (rising) motion. The values in the upper right corners of **(A–C)** represent the regionally-averaged vertical velocity anomalies over SC. **(D)** Time series of the regionally-averaged vertical velocity anomaly (black line) and rainfall anomaly (green line) over SC during 1979–2022. The Y-axis on the left (right) represents the vertical velocity (rainfall) anomaly. **(E)** Time series of the regionally-averaged vertical velocity anomaly (black line) and vertical velocity anomaly of meridional (red line) and zonal (blue line) circulations over SC during 1979–2022. Vertical velocity anomalies in **(D)** and **(E)** are multiplied by −1 for convenience. Units of the vertical velocity anomaly and rainfall anomaly are Pa s^{-1} and mm, respectively.

anomalous rising motion over SC. Additionally, the zonal positive velocity anomaly belt in the north and south of SC, the zonal negative velocity anomaly belt in the Southern Hemisphere, and the positive velocity anomaly in the east of the Malay Archipelago can be observed. Comparing Figure 1C, Figure 5A, the spatial patterns of the vertical velocity anomaly and rainfall anomaly are similar, and the spatial similarity coefficient is −0.76, implying that the anomalous rainfall is caused by the anomalous vertical velocity of meridional and zonal circulations. This result is also supported by Figure 5D since the correlation between the time series of the regionally averaged vertical velocity anomaly (multiplied by −1) and rainfall anomaly over SC during 1979–2022 reaches 0.95. Therefore, the extremely anomalous vertical velocity over SC leads to record-breaking "Dragon Boat Water" rainfall in 2022 (Figure 5D).

Figures 5A,B show that the spatial patterns of the total vertical velocity anomaly and vertical velocity anomaly of meridional circulation are similar. Additionally, the regionally-averaged vertical velocity anomaly of the meridional circulation over SC is −0.064 Pa s^{-1}, which contributes 80% of the total vertical velocity anomaly (−0.08 Pa s^{-1}), while the regionally-averaged vertical velocity anomaly of the zonal circulation is −0.016 Pa s^{-1}, which contributes 20% of the total vertical velocity anomaly (Figure 5E). The results proposed above are similar to those obtained from the novel moisture equations. This is because the vertical velocity anomalies of meridional and zonal circulations are closely related to δMCDD_M and δMCDD_Z, which are the main contributors to the anomalous rainfall, as shown in Figure 2, Figure 4. This proposal can be proven by the following deduction. According to Eq. 3, δMCDD_M and δMCDD_Z can be written as follows:

$$\begin{cases} \delta\text{MCDD\_M} = -\dfrac{1}{\rho_w g}\displaystyle\int_{P_s}^{0}(q_0\nabla\cdot\delta\vec{V}_{\text{M}})dp, \\ \delta\text{MCDD\_Z} = -\dfrac{1}{\rho_w g}\displaystyle\int_{P_s}^{0}(q_0\nabla\cdot\delta\vec{V}_{\text{Z}})dp. \end{cases} \tag{4}$$

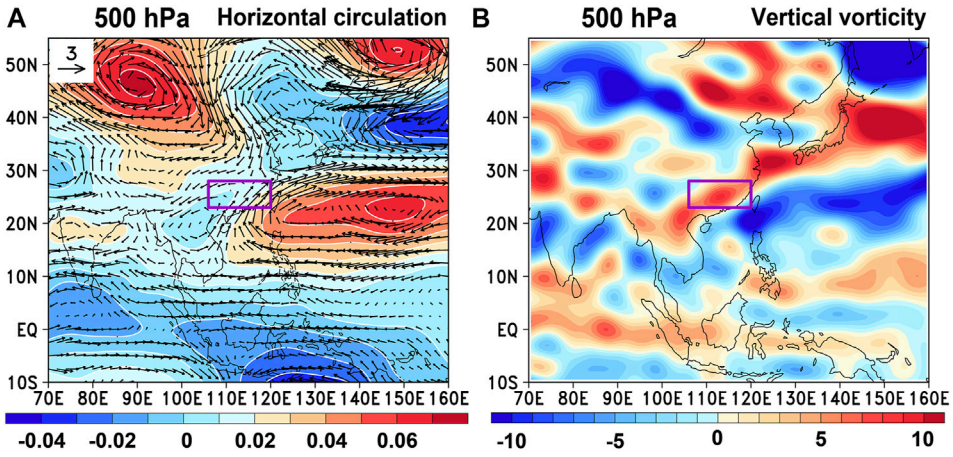

FIGURE 6
(A) Distribution of the horizontal circulation anomaly at 500 hPa during the "Dragon Boat Water" season in 2022. Shading and vector represent the stream function anomaly and wind anomaly of the horizontal circulation; **(B)** is the same as **(A)** but for the distribution of the vertical vorticity anomaly of horizontal circulation at 500 hPa. Units of the stream function, wind, and vorticity anomalies are 10^{-6} s^{-1}, m s^{-1}, and 10^{-6} s^{-1}, respectively.

Since the specific humidity mainly exists below 500 hPa, Eq. 4 can be rewritten as follows:

$$\begin{cases} \delta\text{MCDD\_M} \approx -\dfrac{1}{\rho_w g}\displaystyle\int_{P_s}^{500hPa}(q_0\nabla\cdot\delta\vec{V}_{\text{M}})dp, \\ \delta\text{MCDD\_Z} \approx -\dfrac{1}{\rho_w g}\displaystyle\int_{P_s}^{500hPa}(q_0\nabla\cdot\delta\vec{V}_{\text{Z}})dp. \end{cases} \tag{5}$$

The deduction from Eq. 4, to Eq. 5 can be confirmed by Figure 2, Figure 4. Since q_0 represents the climatological specific humidity during 1981–2010, δMCDD_M and δMCDD_Z are mainly controlled by $-\int_{P_s}^{500hPa}\nabla\cdot\delta\vec{V}_{\text{M}}\text{dp}$ and $-\int_{P_s}^{500hPa}\nabla\cdot\delta\vec{V}_{\text{Z}}\text{dp}$. According to the 3P-DGAC method, the meridional circulation $\vec{V}_{\text{M}}=\vec{j}v_{\text{M}}+\vec{k}\omega_{\text{M}}$ and zonal circulation $\vec{V}_{\text{Z}}=\vec{i}u_{\text{Z}}+\vec{k}\omega_{\text{Z}}$ satisfy the two continuity equations as follows:

$$\begin{cases} \dfrac{1}{a\cos\varphi}\dfrac{\partial v_{\text{M}}}{\partial\lambda}+\dfrac{\partial\omega_{\text{M}}}{\partial p}=0, \\ \dfrac{1}{a}\dfrac{\partial u_{\text{Z}}}{\partial\varphi}+\dfrac{\partial\omega_{\text{Z}}}{\partial p}=0. \end{cases} \tag{6}$$

The continuity equations can be rewritten as follows:

$$\begin{cases} \dfrac{\partial\omega_{\text{M}}}{\partial p}=-\dfrac{1}{a\cos\varphi}\dfrac{\partial v_{\text{M}}}{\partial\lambda}, \\ \dfrac{\partial\omega_{\text{Z}}}{\partial p}=-\dfrac{1}{a}\dfrac{\partial u_{\text{Z}}}{\partial\varphi}. \end{cases} \tag{7}$$

Therefore, the vertical velocity of the meridional and zonal circulations at 500 hPa can be calculated as follows:

$$\begin{cases} \omega_{\text{M}}=-\displaystyle\int_{P_s}^{500hPa}\frac{1}{a\cos\varphi}\frac{\partial v_{\text{M}}}{\partial\lambda}dp=-\int_{P_s}^{500hPa}\nabla\cdot\vec{V}_{\text{M}}dp, \\ \omega_{\text{Z}}=-\displaystyle\int_{P_s}^{500hPa}\frac{1}{a}\frac{\partial u_{\text{Z}}}{\partial\varphi}dp=-\int_{P_s}^{500hPa}\nabla\cdot\vec{V}_{\text{Z}}dp. \end{cases} \tag{8}$$

Thus, the vertical velocity anomaly of the meridional and zonal circulations at 500 hPa can be obtained by using the following equations:

$$\begin{cases} \delta\omega_{\text{M}}=-\displaystyle\int_{P_s}^{500hPa}\nabla\cdot\delta\vec{V}_{\text{M}}dp, \\ \delta\omega_{\text{Z}}=-\displaystyle\int_{P_s}^{500hPa}\nabla\cdot\delta\vec{V}_{\text{Z}}dp. \end{cases} \tag{9}$$

Since δMCDD_M and δMCDD_Z are the main contributors to anomalous rainfall (Figure 2, Figure 4) and δMCDD_M and δMCDD_Z are mainly controlled by $-\int_{P_s}^{500hPa}\nabla\cdot\delta\vec{V}_{\text{M}}\text{dp}$ and $-\int_{P_s}^{500hPa}\nabla\cdot\delta\vec{V}_{\text{Z}}\text{dp}$ (i.e., $\delta\omega_{\text{M}}$ and $\delta\omega_{\text{Z}}$ at 500 hPa), the spatial patterns of the vertical velocity anomaly and the rainfall anomaly are similar. Additionally, the similarity between the quantitative contributions of the meridional and zonal circulations to the vertical velocity anomaly and those to the anomalous rainfall can also be explained.

4.2 Anomalous horizontal circulation

As proposed in the previous section, anomalous rainfall is caused by the anomalous vertical velocity of meridional and zonal

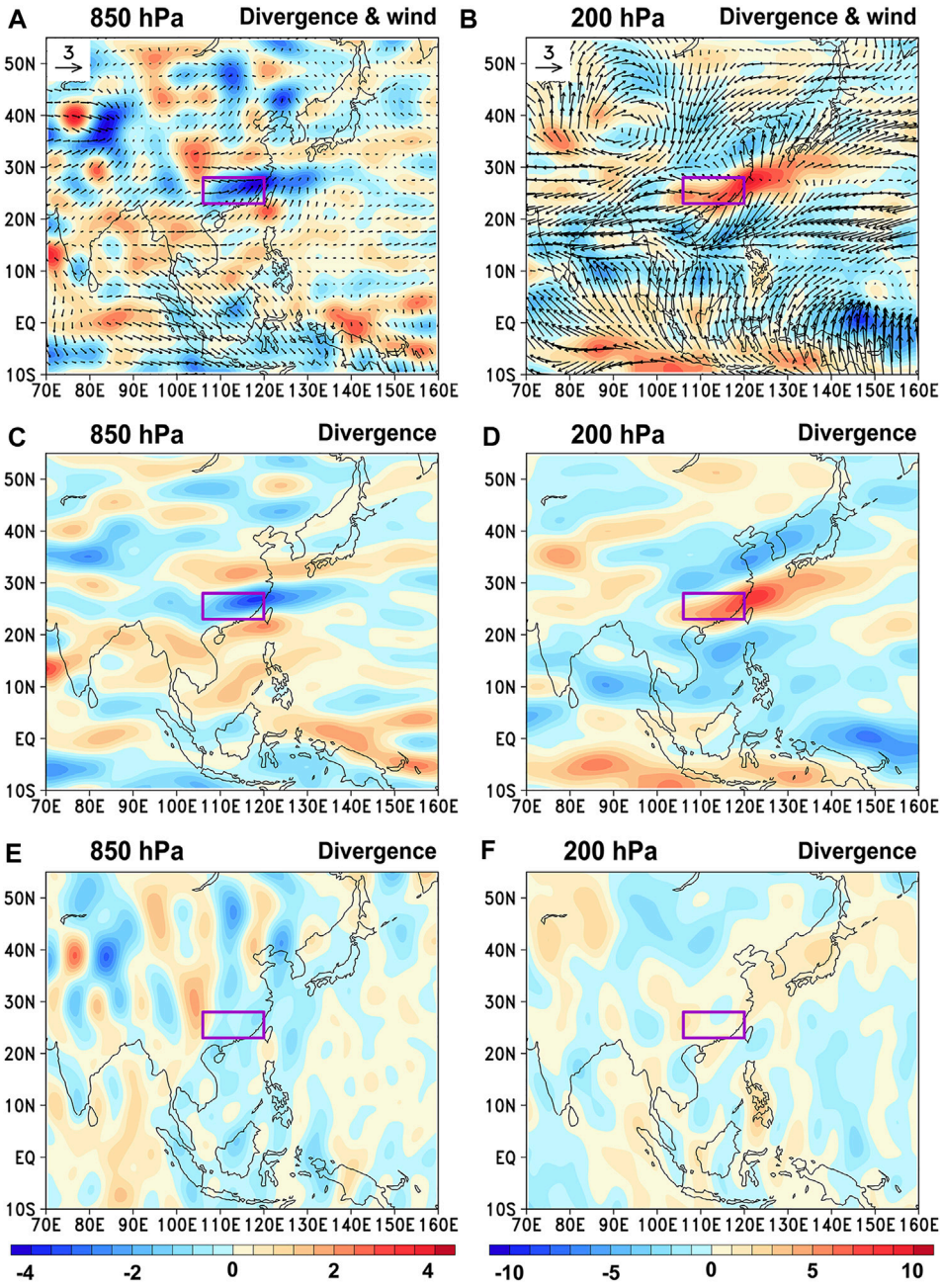

FIGURE 7
(A),(B) Distribution of the divergence anomaly (shading) and wind anomaly (vector) of the vertical circulation (i.e., the meridional and zonal circulations) at **(A)** 850 hPa and **(B)** 200 hPa during the "Dragon Boat Water" season in 2022; **(C),(D)** and **(E),(F)** are the same as **(A),(B)** but for the distribution of the divergence anomaly of the meridional and zonal circulations, respectively. Units of the divergence and wind anomalies are 10^{-6} s^{-1} and m s^{-1}, respectively.

circulations; thus, the cause of the anomalous vertical velocity is investigated in this section. Figure 6 displays the horizontal circulation anomaly and vorticity anomaly at 500 hPa during the "Dragon Boat Water" season in 2022. Figure 6 shows that affected by the continental high, anomalous anticyclonic circulation and negative vorticity exist over the region north of SC, which can result in anomalous divergence (convergence) in the lower (higher) troposphere (Figures 7A,B) and further anomalous sinking motion (Figure 5A). Over SC, affected by the anomalous continental high, anticyclonic circulation in the western Pacific,

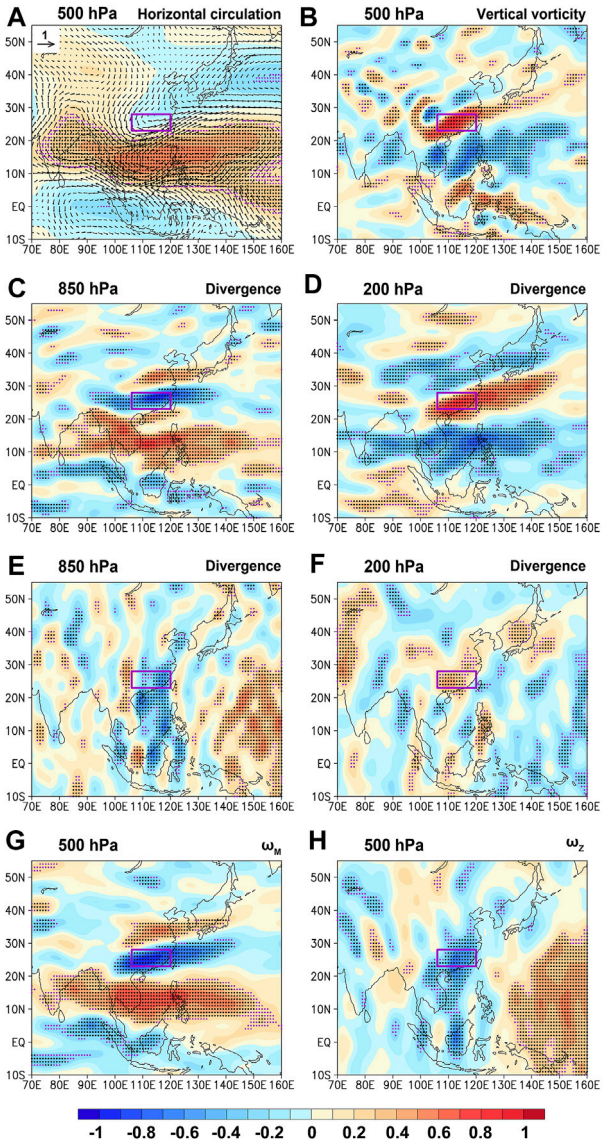

FIGURE 8
Correlation between the regionally averaged rainfall anomaly over SC and different variables during 1979–2022. **(A)** Horizontal circulation anomaly at 500 hPa. Shading and vector are for the stream function anomaly and wind anomaly of the horizontal circulation. **(B)** Vertical vorticity anomaly of horizontal circulation at 500 hPa. **(C),(D)** Divergence anomaly of meridional circulation at **(C)** 850 hPa and **(D)** 200 hPa. **(E),(F)** are the same as **(C),(D)** but for the zonal circulation. **(G),(H)** Vertical velocity anomaly of the **(G)** meridional and **(H)** zonal circulations at 500 hPa. Black (purple) dots over the shading represent that those correlation coefficients are significant above the 95% (90%) confidence level based on Student's t test.

and the trough north of the western Pacific anticyclone, anomalous cyclonic circulation and positive vorticity exist, which can result in anomalous convergence (divergence) in the lower (higher) troposphere and further anomalous rising motion. In the western Pacific and the area southeast of southern India, anomalous anticyclonic circulation and negative vorticity exist, which can result in anomalous divergence (convergence) in the lower (higher) troposphere and further anomalous sinking motion. Between 5°S and 5°N, except for the region east of the Malay Archipelago, anomalous cyclonic circulation and positive vorticity exist, which can result in anomalous convergence (divergence) in the lower (higher) troposphere and further anomalous rising motion. Generally, the spatial configuration of the anomalous horizontal circulation provides the background for the generation of the anomalous vertical velocity.

Additionally, the anomalous divergence of the meridional circulation is similar to that of the vertical circulation (i.e., meridional and zonal circulations) and is larger than that of the zonal circulation (Figures 7A–F), which corresponds to the dominant role of meridional circulation in influencing anomalous rainfall during the "Dragon Boat Water" season in 2022.

4.3 Correlation analysis

To verify the mechanism proposed above, correlation analysis is conducted. Figure 8 displays the correlation maps between the regionally averaged rainfall anomaly over SC and different variables during 1979–2022. By comparing Figure 8A, Figure 6A, the main characteristics of the spatial configuration are found to be similar, i.e., the anomalous continental high and the trough north of the western Pacific anticyclone in the mid–high latitudes, the anomalous anticyclonic circulation over the western Pacific and the area southeast of southern India in the subtropics, and the anomalous cyclonic circulation south of 5°N. The similarity of the spatial configurations of the anomalous horizontal circulation also leads to the similar spatial configuration of the vertical vorticity (Figure 8B, Figure 6B). Furthermore, the spatial configuration of the anomalous horizontal circulation and vertical vorticity leads to the anomalous divergence of meridional and zonal circulations (Figures 8C–F and Figures 7C–F) and further anomalous vertical velocity of the meridional and zonal circulations (Figures 8G,H and Figures 5B,C), which finally results in anomalous rainfall (Figure 1E). Additionally, the similarity between Figure 1E, Figure 8G corresponds to the findings that the meridional circulation dominates the anomalous rainfall during the "Dragon Boat Water" season in 2022.

5 Summary and conclusion

During the "Dragon Boat Water" season in 2022, record-breaking anomalous rainfall existed over SC and was accompanied by the zonal negative rainfall anomaly belt in the north and south of SC, the zonal positive rainfall anomaly belt in the Southern Hemisphere, and the negative rainfall anomaly in the east of the Malay Archipelago. In this study,

the causes of anomalous rainfall are investigated by using the novel moisture budget equation of three-pattern circulations, and the following conclusions are obtained.

(1) The anomalous rainfall over the SC caused by the horizontal (δP_H), meridional (δP_M), and zonal (δP_Z) circulations are −10 mm, 168 mm, and 45.3 mm, which contribute −5%, 86%, and 23% of the actual rainfall anomaly (195.1 mm), respectively, suggesting that δP_M contributes most to anomalous rainfall, δP_Z follows, and δP_H contributes negatively.
(2) The dynamic terms caused by the anomalous divergence of meridional (δMCDD_M) and zonal (δMCDD_Z) circulations are the main contributors to δP_M and δP_Z, while the thermodynamic term caused by the anomalous vapor advection of horizontal circulation (δTHA_H) is the main contributor to δP_H.
(3) Since δMCDD_M and δMCDD_Z are largely determined by the anomalous vertical velocity of the meridional and zonal circulations according to the novel moisture budget equation and continuity equation, and δMCDD_M and δMCDD_Z are the main contributors to anomalous rainfall, the anomalous vertical velocity leads to anomalous rainfall.
(4) The spatial configuration of the anomalous horizontal circulation and vertical vorticity provides the background for the generation of the anomalous divergence of meridional and zonal circulations and further the anomalous vertical velocity of the meridional and zonal circulations, ultimately resulting in anomalous rainfall.

It should be noted that the external forcings that cause anomalous horizontal, meridional, and zonal circulations are not investigated in this study and should be explored in the future.

Data availability statement

The original contributions presented in the study are included in the article/Supplementary Material, further inquiries can be directed to the corresponding author.

Author contributions

YZ and JC: methodology. YZ, JC, RZ, and GF: writing original draft preparation. YZ and JC: visualization. All authors contributed to the article and approved the submitted version.

Funding

This work was funded by National Natural Science Foundation of China (42130610, 42005012, 41975088), Natural Science Foundation of Jiangsu Province (BK20201058), and School-level research projects of Yancheng Institute of Technology (xjr2020022).

Conflict of interest

The authors declare that the research was conducted in the absence of any commercial or financial relationships that could be construed as a potential conflict of interest.

Publisher's note

All claims expressed in this article are solely those of the authors and do not necessarily represent those of their affiliated organizations, or those of the publisher, the editors and the reviewers. Any product that may be evaluated in this article, or claim that may be made by its manufacturer, is not guaranteed or endorsed by the publisher.

Supplementary material

The Supplementary Material for this article can be found online at: https://www.frontiersin.org/articles/10.3389/feart.2022.1032313/full#supplementary-material

References

Cheng, J., Gao, C., Hu, S., and Feng, G. (2018). High-stability algorithm for the three-pattern decomposition of global atmospheric circulation. *Theor. Appl. Climatol.* 133, 851–866. doi:10.1007/s00704-017-2226-2

Cheng, J., Zhao, Y., Zhi, R., and Feng, G. (2022). Analysis of the July 2021 extreme precipitation in Henan using the novel moisture budget equation. *Theor. Appl. Climatol.* 149, 15–24. doi:10.1007/s00704-022-04022-7

Chu, Q., Wang, Q., and Feng, G. (2020). The roles of moisture transports in intraseasonal precipitation during the preflood season over South China. *Int. J. Climatol.* 40, 2239–2252. doi:10.1002/joc.6329

Chu, Q., Wang, Q., Qiao, S., and Feng, G. (2018). Feature analysis and primary causes of pre-flood season "Cumulative Effect" of torrential rain over South China. *Theor. Appl. Climatol.* 131, 91–100. doi:10.1007/s00704-016-1947-y

Gu, D., and Zhang, W. (2012). The strong dragon-boat race precipitation of Guangdong in 2008 and qusi-10-day oscillation. *J. Trop. Meteorology* 3, 349. (in Chinese)

Han, Z., Zhang, Q., Li, Q., Feng, R., Haywood, A. M., Tindall, J. C., et al. (2021). Evaluating the large-scale hydrological cycle response within the pliocene model intercomparison project phase 2 (PlioMIP2) ensemble. *Clim. Past.* 17, 2537–2558. doi:10.5194/cp-17-2537-2021

Hersbach, H., Bell, B., Berrisford, P., Hirahara, S., Horányi, A., MuñozSabater, J., et al. (2020). The ERA5 global reanalysis. *Q. J. R. Meteorol. Soc.* 146, 1999–2049. doi:10.1002/qj.3803

Hu, S., Cheng, J., and Chou, J. (2017). Novel three-pattern decomposition of global atmospheric circulation: Generalization of traditional two dimensional decomposition. *Clim. Dyn.* 49, 3573–3586. doi:10.1007/s00382-017-3530-3

Hu, S., Cheng, J., Xu, M., and Chou, J. (2018). Three-pattern decomposition of global atmospheric circulation: Part II—dynamical equations of horizontal, meridional and zonal circulations. *Clim. Dyn.* 50, 2673–2686. doi:10.1007/s00382-017-3763-1

Hu, S., Chou, J., and Cheng, J. (2018). Three-pattern decomposition of global atmospheric circulation: Part I—decomposition model and theorems. *Clim. Dyn.* 50, 2355–2368. doi:10.1007/s00382-015-2818-4

Hu, S., Zhou, B., Gao, C., Xu, Z., Wang, Q., and Chou, J. (2020). Theory of three-pattern decomposition of global atmospheric circulation. *Sci. China Earth Sci.* 63, 1248–1267. doi:10.1007/s11430-019-9614-y

Lee, M. H., Ho, C. H., and Kim, J. H. (2010). Influence of tropical cyclone landfalls on spatiotemporal variations in typhoon season rainfall over South China. *Adv. Atmos. Sci.* 27, 443–454. doi:10.1007/s00376-009-9106-3

Li, G., Chen, J., Wang, X., Luo, X., Yang, D., Zhou, W., et al. (2018). Remote impact of North Atlantic sea surface temperature on rainfall in southwestern China during boreal spring. *Clim. Dyn.* 50, 541–553. doi:10.1007/s00382-017-3625-x

Lin, L., Wu, N., Huang, Z., and Cai, A. (2009). Causality analysis of the infrequent dragon-boat precipitation in Guangdong province in 2008. *Meteorol. Mon.* 35, 43. (in Chinese)

Liu, F., Wang, B., Ouyang, Y., Wang, H., Qiao, S., Chen, G., et al. (2022). Intraseasonal variability of global land monsoon precipitation and its recent trend. *npj Clim. Atmos. Sci.* 5, 30. doi:10.1038/s41612-022-00253-7

Liu, H., Hu, S., Xu, M., and Chou, J. (2008). Three-dimensional decomposition method of global atmospheric circulation. *Sci. China Ser. D-Earth. Sci.* 51, 386–402. doi:10.1007/s11430-008-0020-9

Miao, R., Wen, M., Zhang, R., and Li, L. (2019). The influence of wave trains in mid-high latitudes on persistent heavy rain during the first rainy season over South China. *Clim. Dyn.* 53, 2949–2968. doi:10.1007/s00382-019-04670-y

Qian, W., Ai, Y., Chen, L., and Li, H. (2020). Anomalous synoptic pattern of typical dragon boat precipitation process in Guangdong province. *J. Trop. Meteorology* 36, 433. (in Chinese)

Qiao, S., Chen, D., Wang, W., Cheung, H. N., Liu, F., Cheng, J., et al. (2021). The longest 2020 Meiyu season over the past 60 years: Subseasonal perspective and its predictions. *Geophys. Res. Lett.* 48, e2021GL093596. doi:10.1029/2021GL093596

Ramage, C. S. (1952). Variation of rainfall over South China through the wet season. *Bull. Am. Meteorol. Soc.* 33, 308–311. doi:10.1175/1520-0477-33.7.308

Seager, R., Naik, N., and Vecchi, G. A. (2010). Thermodynamic and dynamic mechanisms for large-scale changes in the hydrological cycle in response to global warming. *J. Clim.* 23, 4651–4668. doi:10.1175/2010JCLI3655.1

Yang, H., and Sun, S. (2005). The characteristics of longitudinal movement of the subtropical high in the Western Pacific in the pre-rainy season in South China. *Adv. Atmos. Sci.* 22, 392–400. doi:10.1007/BF02918752

Yuan, C., Liu, J., Luo, J. J., and Guan, Z. (2019). Influences of tropical Indian and Pacific oceans on the interannual variations of precipitation in the early and late rainy seasons in South China. *J. Clim.* 32, 3681–3694. doi:10.1175/JCLI-D-18-0588.1

Yuan, F., Wei, K., Chen, W., Fong, S., and Leong, K. (2010). Temporal variations of the frontal and monsoon storm rainfall during the first rainy season in South China. *Atmos. Ocean. Sci. Lett.* 3, 243–247. doi:10.1080/16742834.2010.11446876

Yuan, Y., Ren, F., Wang, Y., Sun, L., and Guo, Y. (2012). Analysis of the precipitation feature and general circulation anomaly during the pre-flood season in South China in 2012. *Meteorol. Mon.* 38, 1247. (in Chinese)

Zhai, P., and Eskridge, R. E. (1997). Atmospheric water vapor over China. *J. Clim* 10, 26432–32652. doi:10.1175/1520-0442(1997)010<2643:AWVOC>2.0

frontiers | Frontiers in Earth Science

TYPE Original Research
PUBLISHED 11 January 2023
DOI 10.3389/feart.2022.1064940

OPEN ACCESS

EDITED BY
Bo Sun,
Nanjing University of Information Science and Technology, China

REVIEWED BY
Anning Huang,
Nanjing University, China
Gang Zeng,
Nanjing University of Information Science and Technology, China

*CORRESPONDENCE
Zhaohui Lin,
lzh@mail.iap.ac.cn

SPECIALTY SECTION
This article was submitted to Atmospheric Science, a section of the journal Frontiers in Earth Science

RECEIVED 08 October 2022
ACCEPTED 25 November 2022
PUBLISHED 11 January 2023

CITATION
Omondi OA and Lin Z (2023), Trend and spatial-temporal variation of drought characteristics over equatorial East Africa during the last 120 years. *Front. Earth Sci.* 10:1064940. doi: 10.3389/feart.2022.1064940

Trend and spatial-temporal variation of drought characteristics over equatorial East Africa during the last 120 years

Onyango Augustine Omondi[1,2] and Zhaohui Lin[1,2,3]*

[1]International Center for Climate and Environment Sciences (ICCES), Institute of Atmospheric Physics, Chinese Academy of Sciences, Beijing, China, [2]College of Earth and Planetary Science, University of Chinese Academy of Sciences, Beijing, China, [3]Collaborative Innovation Center on Forecast and Evaluation of Meteorological Disasters (CIC-FEMD), Nanjing University of Information Science and Technology, Nanjing, China

Centennial drought characteristics in Equatorial East Africa (EEA) is investigated using the Standardized Precipitation Evapotranspiration Index (SPEI) derived from the Climatic Research Unit (CRU) dataset. The spatial pattern of drought distribution, as well as drought duration, intensity and frequency, are analyzed for SPEI at a 3-month timescale for March-April-May (MAM) season. Rotated Empirical Orthogonal Function (REOF), Mann-Kendall method (MK), and wavelet analyses are used to study drought's spatial pattern, trend, and periodicity. The result of the principal component analysis returned six homogenous drought sub-regions. A low drought frequency characterizes EEA (<20%). The drought in the MAM season lasts between 2.2 and 2.8 months. Overall, the result showed a weak long-term drying trend for most parts of EEA that were significant in some sub-regions and insignificant in others. An increase in drought areal extent after the 1980s could be ascribed to the increase in potential evapotranspiration (PET) and is consistent with the negative trend in SPEI value over the six sub-regions. The apparent increase is mainly attributed to the increase in moderate and severe droughts area rather than extreme drought areas. The spectral analysis further reveals that inter-annual drought variability with periodicities less than 8 years dominates in all sub-regions of Equatorial East Africa, which is associated with the critical role of El-Niño in driving the drought variations in EEA.

KEYWORDS

drought trend, drought variability, SPEI, equatorial East Africa, rotated empirical orthogonal function (REOF)

1 Introduction

Drought is an extreme event characterized by a protracted period of insufficient water supply emanating from erratic and irregular rainfall distribution, high evapotranspiration and higher demand for water than supply (Bhuiyan, 2009). Unlike other meteorological disasters, drought developed slowly and is only recognized once its effect on the environment and population is felt. It places an immense burden on agricultural production, water resource, energy production and causes damage to the ecological environment (Iglesius et al., 2001; Winslow et al., 2011). Droughts may emanate from a combination of drivers of climate variability and anthropogenic forcing and, as such, cannot be blamed on one driver alone. Beyond the drought itself, the extent of the impact depends on the vulnerability and exposure of societies. Poor land management practices can also worsen the drought and lead to soil degradation (Cook et al., 2009). Dai (2013) suggested that the warming trend since the 1980s has led to the expansion of global drought areas by about 8%. Many studies reported more frequent and severe droughts in different regions in the 21st century as the global mean surface temperature continues to rise (Sheffield et al., 2012; Cook et al., 2015; Schwalm et al., 2017; Trenberth et al., 2013).

Equatorial East Africa (hereafter, EEA) is among the drought-sensitive regions owing to the large interannual rainfall variability. The observed variability has been characterized by the region's increased frequency and intensity of extreme events (Nicholson, 2014). In addition, as much as 69% of East Africa may be classified as arid and semi-arid, with annual rainfall less than 50% of the mean annual potential evapotranspiration (UNDP/UNSO, 1997). The demand for water resources is increasingly under pressure owing to population growth and the region's larger interannual rainfall variability. Severe drought has occurred in East Africa in recent decades, and the events have direly impacted socio-economic activities in the region. Funk et al. (2014) reported that East Africa experienced drought for 8 years between the 1990s and 2000s. The economic impact of drought has been significant. For instance, Mogaka et al. (2006) estimated the 1998–2000 drought episode over East Africa caused agricultural losses estimated to be worth USD 370M. On the other hand, the 2008–2011 dry conditions affected over 13 million people in the region and led to a severe shortage of water, food and pasture, leading to loss of life and livelihood (AghaKouchak, 2015; Uhe et al., 2017). These losses and the impact of earlier severe droughts, such as 1983/84, highlight the region's susceptibility to drought.

East Africa has shown a neutral to slight decline in rainfall (Lyon and Dewitt, 2012; Yang et al., 2014; Tierney et al., 2015). Nicholson (2014) reported that the first decade of the 21st century experienced an increased frequency of below-average rainfall that lasted over a longer time in the Greater Horn of Africa (GHA) region. The reduction in rainfall, coupled with the increase in regional temperature, has increased the frequency and intensity of drought over the region. For example, Mpelasoka et al. (2018) linked the region's drought-like crises to rainfall reduction. Several studies have attempted to explain the causal mechanisms of these droughts and the observed rainfall variability. For instance, it is a well-established fact that La-Niña suppresses rainfall over East Africa (Ogallo, 1989). Lyon (2014) reported that the post-1998 decline in rainfall is strongly driven by natural multi-decadal variability in the tropical Pacific Ocean rather than anthropogenic climate change. Hastenrath et al. (2005, 2010) reported that the surface equatorial westerlies were fast during the 2005 and 2008 droughts. Consequently, they linked the 2005 and 2008 droughts to the fast-moving westerlies, often accompanied by anomalously cold waters in the northwestern and warm anomalies in the southeastern Indian Ocean. Lyon (2014) further found that sea surface temperature (SST) anomalies in the tropical Pacific and Indian Oceans shows a strong association with October-November-December (OND) season drought, especially in locations that have a bimodal rainfall pattern. The study also reported that this influence depended on the ability of ENSO to affect SSTs outside the Pacific. Wainright et al. (2019) reported that the decrease in rainfall results from the late onset and early withdrawal of rainbands over East Africa. Williams and Funk (2011) link the reduction in rainfall to the enhanced warming of Indian Ocean sea surface temperature (SST), which they argue is driven by anthropogenic emissions.

Defining drought is complicated due to its complex nature. Among the indices developed to monitor and characterize drought, the Standard Precipitation Index (SPI; McKee et al., 1993), the Standardized Precipitation Evapotranspiration Index (SPEI; Vicente-Serrano et al., 2010) and the Palmer drought severity index (PDSI; Palmer, 1965) are the popular and the commonly used. However, PDSI has limitations such as having a fixed time scale, limited spatial comparability, and dependent on data calibration (Wells et al., 2004; Andreadis et al., 2005). On the other hand, SPI boasts simple calculations but is solely based on rainfall. Indeed, Ntale and Gan (2003) recommended using SPI over East Africa owing to its ability to produce more consistent spectral patterns, modest data requirements and adaptability to the local climate. However, while changes in rainfall patterns broadly define drought, processes such as temperature and wind speed determine water availability by controlling the evapotranspiration rate, thus affecting the drought. Given this, the SPEI drought index is adopted in the current study, which incorporates a water balance making it suited to quantify drought much better (Beguería et al., 2013).

Studies that give spatial and temporal variability of drought in the region are limited. Most studies focus on explaining the drivers responsible for a drought event or declining rainfall in the region. In addition, most of the earlier studies are confined to watersheds scale or larger areas (e.g. GHA) but with different climate zones. Despite the increasing drought risk, the intrinsic

characteristics of East Africa climate zones have been given little or no attention in past drought studies. For instance, Mpelasoka et al. (2018) found regional differences in the probability of occurrence of drought year over the GHA region, while Gebremeskel et al. (2020) reported differences in drought trends for individual East Africa countries. This shows that while a large-scale forcing may drive the regional drought, the local response may lead to variation in drought intensity. However, studies on the entire region or country level led to a loss of information on the uniqueness of climate regime-specific responses. Consequently, to address this, the current study classifies East Africa into homogenous sub-regions using principal component analysis and varimax rotation and proposes the drought characteristics for each zone.

In addition, studies show that successive seasons are uncorrelated over East Africa; thus, drought development in one season does not guarantee its persistence to the next season (Nicholson et al., 2014; Lyon, 2014). Given this, the current study focuses on the spring season (March-April-May, MAM) drought characteristics over East Africa using the centennial drought dataset since 1901. The season locally referred to as *Masika,* corresponds to the primary planting season for major food crops across East Africa when moisture availability is critical for the plant's growth (Supplementary Figure S1).

Specifically, the study aims to analyze the spatio-temporal characteristics of drought events over EEA-during 1901–2020 using the SPEI index at regional and sub-regional scales and further delineate the possible relationship between SPEI and key regional climatic indices. The paper is organized as follows. Section 2 describes the data and analysis methods, while Section 3 discusses the region's characteristics and dynamics of droughts. Finally, Section 4 gives a summary and concludes the research findings.

2 Study area, data and methodology

2.1 Study domain

The current study defines Equatorial East Africa (EEA) as the area bounded by Kenya, Uganda, Tanzania, Rwanda, and Burundi (28.5°E-42°E, 12°S-5.5°N) as shown in Figure 1. Rainfall in most of EEA shows a bimodal seasonal distribution pattern influenced by the seasonal movement of the Inter-Tropical Convergence Zone (ITCZ; Mutai and Ward 2000; Camberlin and Philippon 2002). This movement of ITCZ is accompanied by a change in wind direction that brings in moisture from the adjacent Indian Ocean. The rainfall peaks occur in March-May and October-December seasons and are separated by short dry periods in June and July and January and February. The mean annual precipitation varies from about 400 mm in the eastern and northern parts of Kenya to more than 2800 mm over the Lake Victoria basin. The region is dotted with lakes, key among them L. Victoria which drives a local land/lake breeze that controls the convective activities around the lake basin (Anyah et al., 2006; Onyango et al., 2020). On the other hand, the Kenyan highland deflects the cross-equatorial flow strengthening it during boreal summer (Peagle and Geisler, 1986; Chakraborty et al., 2009).

2.2 Data

While *in situ* rainfall data remains the most accurate, the gauge network density in EA is sparse, thus inadequate to describe drought's spatial distribution accurately. In addition, the limited length and inconsistency in the observational data (Schreck and Semazzi, 2004; Shilenje and Ongoma, 2016) limit our ability to assess the long-time observed drought changes over the region. In this study, the monthly rainfall and potential evapotranspiration data from CRU TS 4.05 (Harris et al., 2014) were used to calculate the drought index.

One of the reasons for using CRU data is because it includes all the climate variables that allow for the SPEI index computation. Secondly, all grid points have complete data over a 120-year long period during 1900–2020 with relatively higher resolution of 0.5° x 0.5°. Meanwhile, the PET data from CRU uses the FAO-recommended Penman-Monteith method that incorporates daily temperature, radiation, humidity and wind speed. Moreover, the CRU dataset performs relatively well in hydrometeorological studies over East Africa. Ongoma and Chen (2017) found that CRU data outperforms the GPCC dataset in reproducing the East Africa rainfall cycle. The CRU dataset has also been widely used for climate variability studies over East Africa, including the rainfall decadal variation and the model performance evaluation (e.g., Yang et al., 2014; Ayugi et al.,2020; Mbigi et al., 2022). It is noted that, the spring season in this study refers to March, April and May (MAM). Monthly Nino3.4 and PDO indices data were obtained from the NOAA Climate Prediction Center (https://psl.noaa.gov/gcos_wgsp/Timeseries/).

2.3 Method

2.3.1 Definition of drought index

The study used SPEI to define drought during the MAM season. The index was estimated using the monthly rainfall and the potential evapotranspiration (PET) for 1901–2020. SPEI is based on a water balance approach and uses the difference between rainfall and potential evapotranspiration (PET) to analyze the dry and wet spells over multiple timescales (Vicente-Serrano et al., 2010). The index is computed by

TABLE 1 SPEI classification.

SPEI value	Drought classification
SPEI ≤ −2.00	Extremely dry
−1.99 ≤SPEI≤-1.5	Severely dry
−1.49 ≤SPEI≤-1.0	Moderately dry
−0.99 ≤SPEI≤ 0.99	Near normal
1.0 ≤SPEI≤ 1.49	Moderately wet
1.5≤SPEI≤ 1.99	Severely wet
SPEI ≥ 2.00	Extremely wet

subtracting potential evapotranspiration from corresponding rainfall and summing up the result with a moving window of width equivalent to the user-specified timescale known as the accumulation period. The accumulated monthly values are then fitted to a parametric statistical distribution where non-exceedance probabilities are transformed into a standard normal distribution (McKee et al., 1993; Guttmann, 1998). The parameter of the Log-logistic distribution function is adopted here to fit cumulative probability distribution aggregated over 3-month rainfall time series. SPEI values were computed using the R package developed by Vicente-Serrano et al. (2010).

To obtain the drought classification, the SPEI drought index was firstly calculated from CRU hydrometeorological observations, then the drought category was further classified based on the predefined threshold on the SPEI index value as defined by Vicente-Serrano et al. (2010), and was shown in Table 1. We adopted the run model (Yevjevich, 1967) to define the drought-related characteristics for our study period. Here, drought is considered anytime the SPEI value equals or less than −1 and ends when the value is above this threshold. Once a drought event is detected, it is assigned drought characteristics. These are drought duration, the number of consecutive months in which the SPEI value remains below the threshold value. At the same time, the area under the curve represents the magnitude of drought severity. The ratio of drought severity to its duration gives the drought intensity. SPEI3 values from May 1901–2020 were used to analyze drought in this study.

2.3.2 Rotated empirical orthogonal function analysis

Due to the high dimensionality and non-linearity of hydrometeorological data (Hannachi et al., 2007), the Empirical Orthogonal Function (EOF) is commonly used to systematically decompose data into a smaller set of variables that explain most of the original variance. However, EOF often exhibits subdomain instability, domain shape dependence, and sampling problems that may hamper their utility in isolating individual modes of variation (Richman, 1986). Consequently, the Rotated Empirical Orthogonal Function (REOF) methodology has been applied to the SPEI dataset in this study to identify the regions with similar drought features. REOF is computed by the rotation of eigenvectors obtained in the EOF analysis to achieve a more stable localized pattern that retains its orthogonality. The number of EOF retained for rotation is decided based on the rule of thumb (North et al., 1982) and the cumulative proportion of variance explained by the principal components.

2.3.3 Wavelet analysis

In general, the variation of SPEI can be analyzed using Fourier transform. However, owing to the intricacy of factors from which the drought arises, its time series may exhibit non-stationary properties (Abdourahamane, 2018). The time series of REOF is analyzed in a time-frequency domain using continuous wavelet transform (CWT) to identify the periodicity. CWT transforms the temporal drought variability pattern onto a time-frequency plane where their duration and dominant periodicities can be easily identified.

Further, the study investigated the relationship between the Niño3.4 index, a leading mode of regional interannual variability, and SPEI using wavelet coherence (WCO; Torrence and Compo, 1998; Grinsted et al., 2004). WCO measures the time and scale of interaction between two processes as a function of frequency and may be taken as a decomposition of the correlation coefficient across multiple timescales (Casagrande et al., 2015). We adopt the Morlet wavelet function due to its ability to balance time and frequency. The analysis was tested for significance using Monte Carlo techniques at a 95% confidence level. The WCO values range from zero to one, and a closer value to one shows a higher correlation.

2.3.4 Trend analysis

The long-term wetting and drying trend were estimated at each grid point over EEA for the study period 1901–2020 using the non-parametric Mann-Kendall test (MK; Mann 1945; Kendall 1975). The MK test is a non-parametric test that applies to all types of distribution. Due to its low sensitivity, MK does not require samples to conform to any particular distribution. It is also less sensitive to the missing values making it appropriate for studying hydrometeorological variables. The mathematical description of the MK method can be found in Gao et al. (2020).

3 Results

3.1 Regionalization of spring drought characteristics over EA

In order to clarify the sub-regional difference in drought characteristics over EEA, this study adopted the maximum

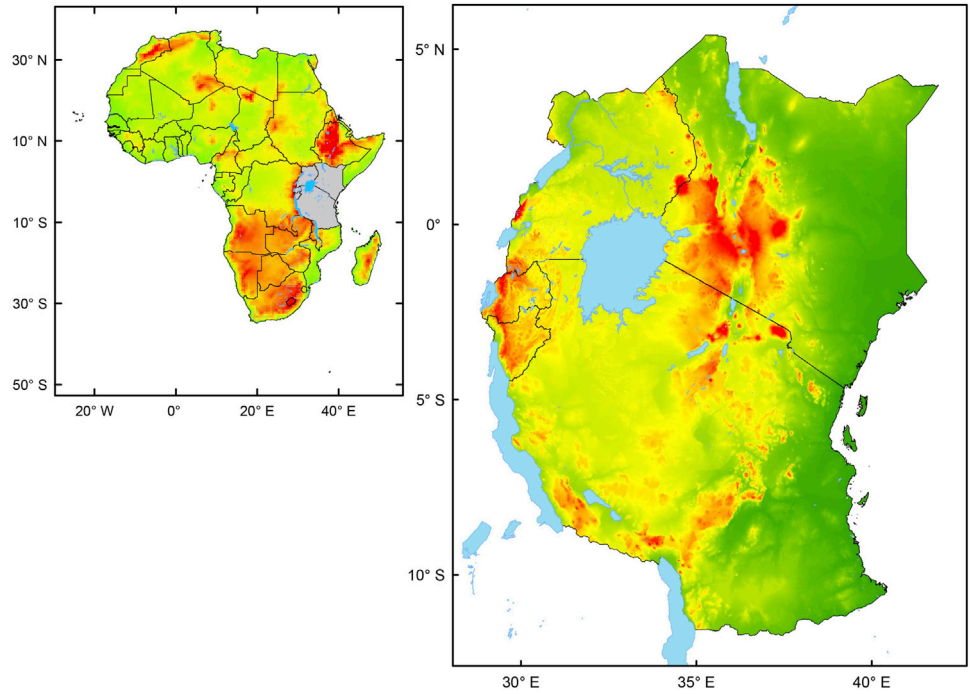

FIGURE 1
Geographical location and elevation map for East Africa and Equatorial East Africa.

loading rule (Vincent Serrano, 2006) to identify the sub-regional boundaries for drought analysis. Figure 2 presents the spatial pattern of the top six dominant REOF modes that were well-demarcated and shows clear spatially disjunctive patterns that did not overlap when a loading threshold of ±0.05 was applied. The six modes explained approximately 77.9% of the total variance in the original SPEI series. The leading mode of variability explains 18.5% of the total variance and has a maximum magnitude in northeastern Kenya. The second mode represents the south of Lake Victoria basin, central and western Tanzania and explains 18.3% of the total variance. The third mode represents Kenya and Tanzania's coastal strip and explains 12.9% of the total variance. The fourth mode explains 10.1% of the total variance and has its center in western Kenya, Central and northern Uganda. The fifth mode has its maximum magnitude in southern Tanzania and explains 9.9% of the total variance. Lastly, the sixth mode has the largest magnitude in south Uganda, Rwanda and Burundi.

For brevity, the zones were named as follows; Northern Kenya (NK; REOF1), Central Region (CR; REOF2), Coastal Strip (CS; REOF3), Northern Uganda (NU; REOF4), Southern Tanzania (ST; REOF5) and Western Sector (WS; REOF6). We further performed a Spearman correlation between the rotated principal component (RPC) for each dominant REOF mode and the averaged SPEI values corresponding to each region. The correlation coefficients were generally higher than 0.70, except for the NU Region, with a coefficient value of 0.46. The high correlation coefficients between any two corresponding regions imply that the demarcation is appropriate for studying regionally homogeneous drought characteristics.

3.2 Spatial pattern of drought characteristics

The estimated SPEI values were used to characterize drought based on frequency, intensity and duration for the analysis period. The spatial distribution of drought characteristics over EA is shown in Figure 3, with lower drought frequency (<20%) found over the region. More specifically, the frequency is relatively lower in the WS sub-region, with a value below 14%. Conversely, CR, NU, ST, and NK sub-regions have a relatively higher frequency (15–20%) of drought occurrence (Figure 3A). The frequency has a maximum magnitude of ~20% in the CR region at the border of Kenya and Tanzania. On the other hand, Figure 3B reveals that drought in the MAM season lasts between 2.2 and 2.8 months. Drought rarely occurs in all months of the season as it coincides with the long rainfall season when the region receives its maximum rainfall. Higher drought duration occurs mostly in NU, with a large portion of the sub-region having an average duration of 2.7 months. Parts of the western CR and southern WS sub-regions also experience a high

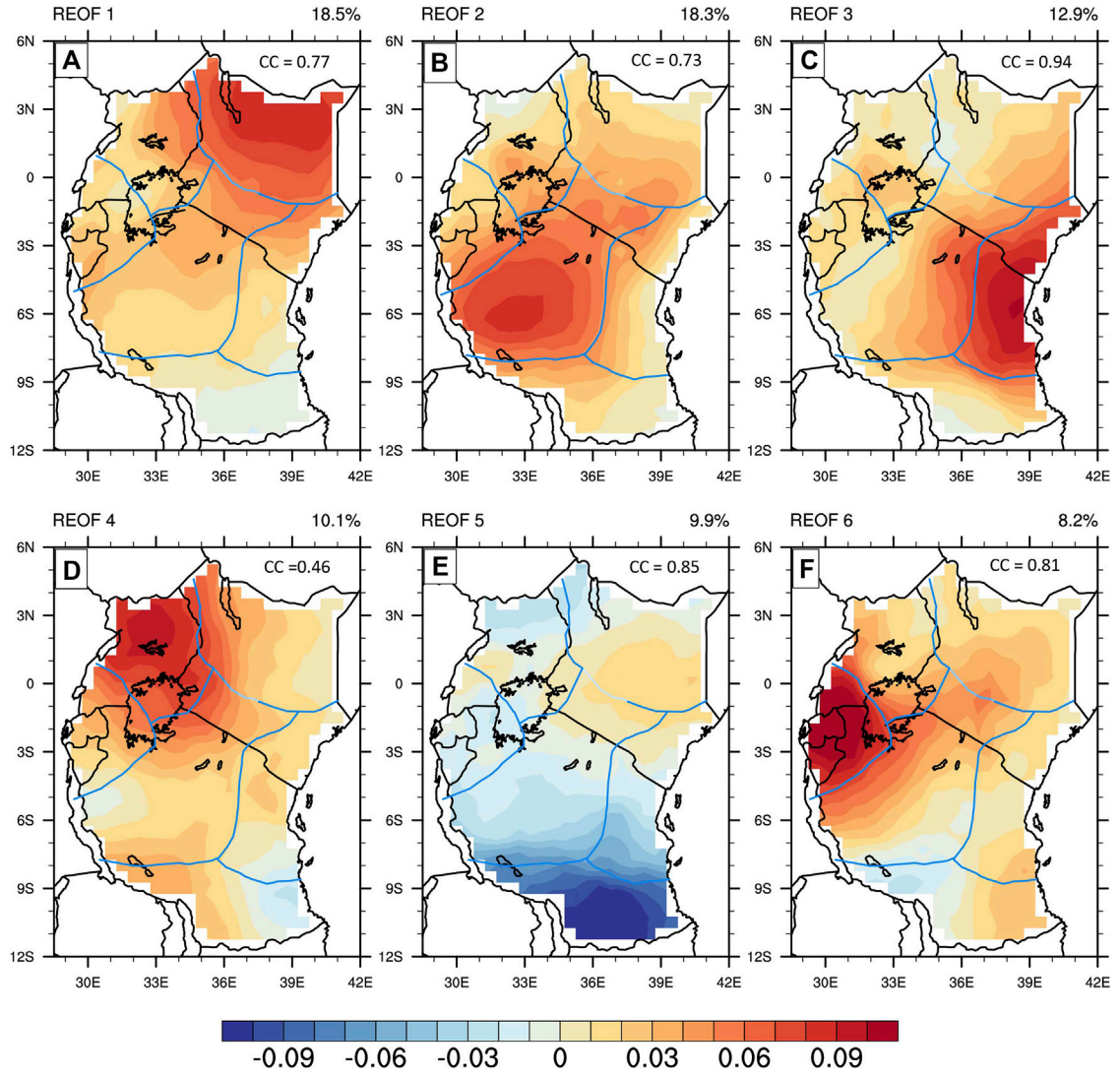

FIGURE 2
Spatial patterns of the six leading Rotated Empirical Orthogonal Function (REOF) modes of SPEI3 over equatorial East Africa. **(A)** is the leading mode representing NK, **(B)** the second mode representing CR, **(C)** the third mode representing CS, **(D)** the fourth mode representing NU, **(E)** the fifth mode representing ST and **(F)** the sixth mode representing WS. The solid blue line indicates the boundary of sub-regions based on the spatial pattern of the leading REOFs. CC gives the temporal correlation coefficients between the rotated principal component and the corresponding averaged SPEI values over the sub-region.

average drought duration of 2.6 months. The CS region shows the lowest drought frequency relative to the other sub-region, with the highest duration of approximately 2.2 months. Figure 3C shows that CR and NK sub-regions exhibit relatively lower drought intensity (~1.44/month) than the rest of EEA, while the WS shows the largest intensity (1.6/month). Generally, the higher frequency and lower intensity of drought in the CR and NK sub-regions indicates that the zones experience more droughts that are less intense, probably due to the reduced rainfall received in the season. In contrast, the NU sub-region showed higher frequency that lasted a relatively longer duration hence the large drought intensity over the region during the MAM season.

3.3 Spatial distribution of drought trends

The spatial distributions of the drought trend for the entire study period are mapped in Figure 4. The linear trend of MAM SPEI3 majorly returned drying over EA. The trend is insignificant at a 95% confidence level in most parts of EA except southwestern Tanzania, northern Tanzania and parts

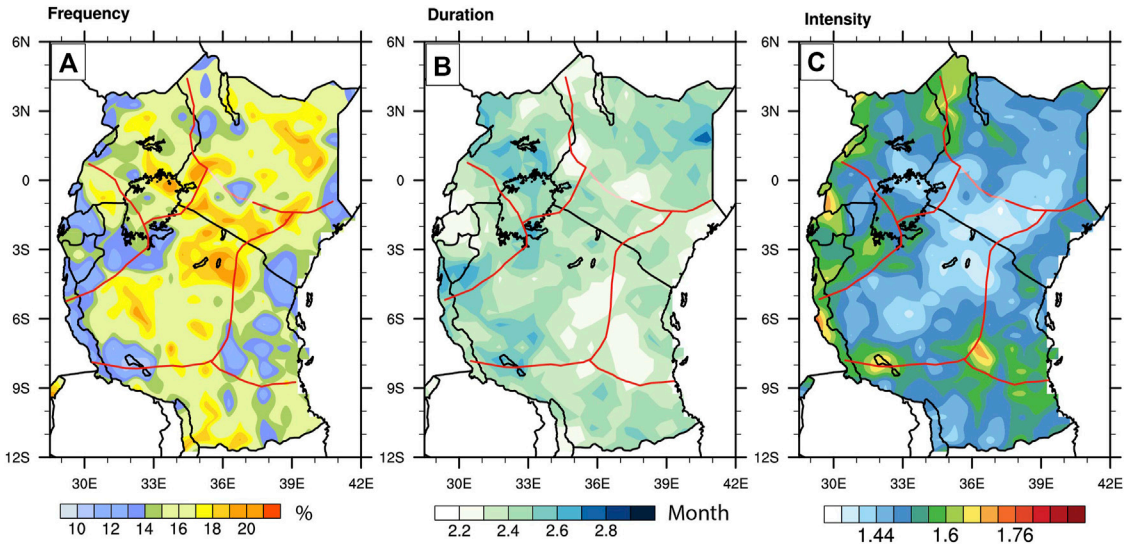

FIGURE 3
Spatial patterns of MAM seasonal mean **(A)** drought frequency **(B)** Drought duration and **(C)** drought intensity over Equatorial East Africa during the 1901–2020 period. The solid red line indicates the boundary for various sub-region.

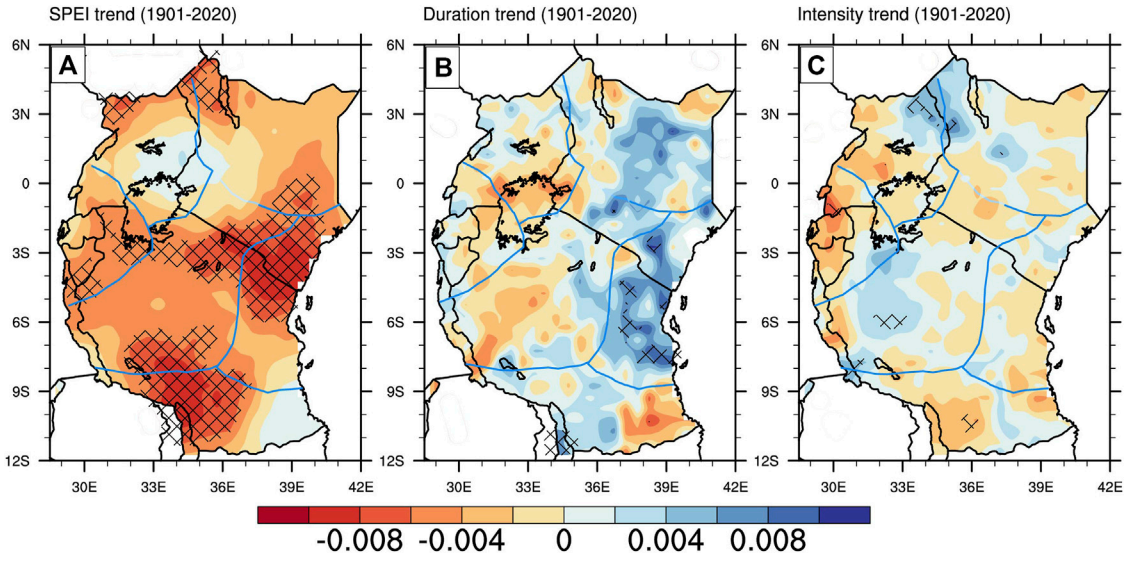

FIGURE 4
Spatial pattern of Mann-Kendall (MK) trend for **(A)** SPEI, **(B)** Drought duration and **(C)** Drought Intensity over equatorial East Africa during the 1901–2020 period. Cross-hatching shows regions where trends are significant at a 95% confidence level.

of northern Kenya and Uganda, where the magnitude is about −0.008/yr (Figure 4B). The result shows that most regions had a mild to moderate increase in drought. Conversely, a small region north of Lake Victoria Basin and southeastern Tanzania shows a weak wetting trend of about 0.002 years^{-1}. Lake Victoria is known to control the diurnal variation of rainfall in the surrounding area, making the basin wetter than the surrounding. Skliris et al. (2016) found that the Lake makes its basin wetter relative to other regions through the "amplification of the water cycle" that occurs at a slower rate due to global warming. Figure 4B reveals a mixture of an increasing and a decreasing trend in drought duration that is largely insignificant over EA. CS sub-region mainly shows an increase in drought duration with an annual trend reaching 0.008/yr for

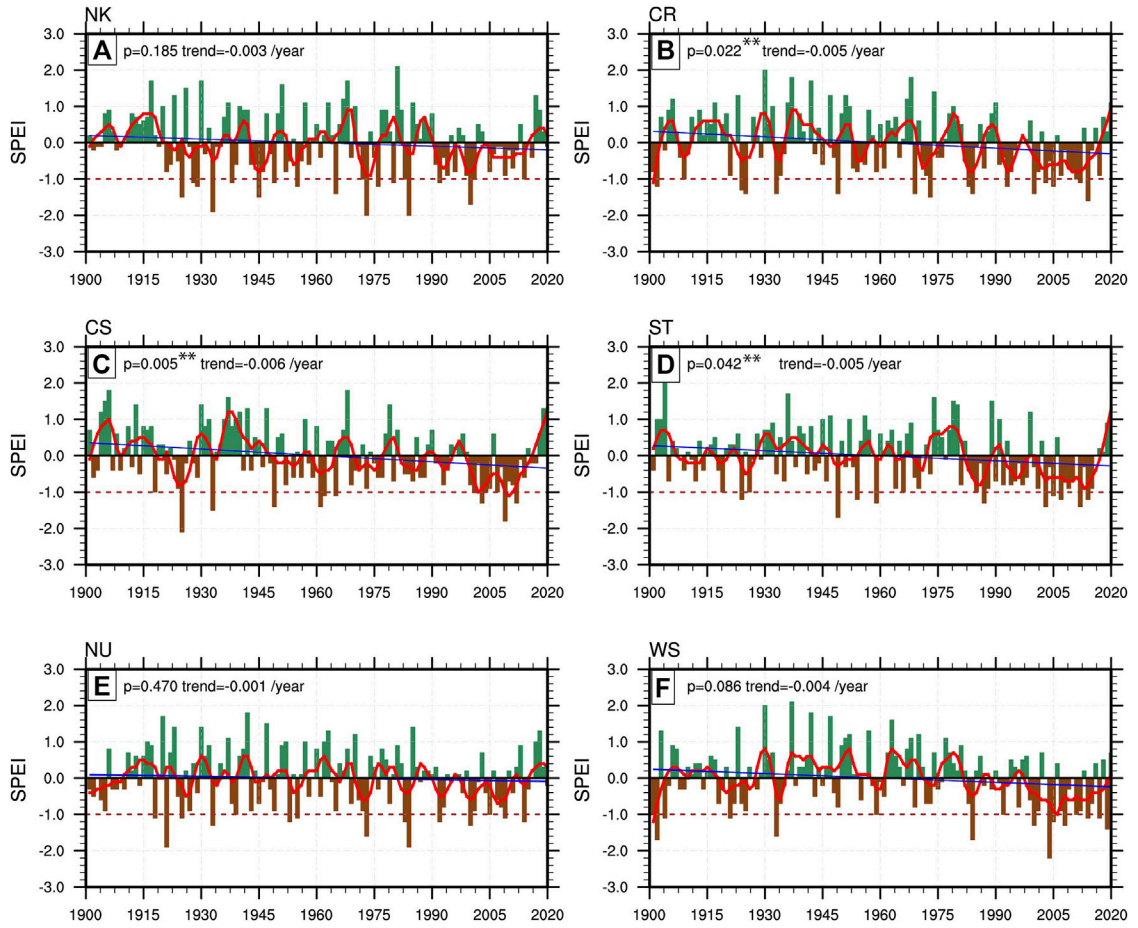

FIGURE 5
Temporal evolution of SPEI3 over six sub-regions of equatorial East Africa **(A)** NK, **(B)** CR, **(C)** CS, **(D)** ST, **(E)** NU and **(F)** WS. The red line shows an 11-year smoothed LOESS line, and the trend (blue) shows the rate of change of SPEI based on the Mann-Kendall trend test. *p* values with an asterisk (**) show statistically significant trends at a 95% confidence level.

some areas that exhibit a significant trend. Similarly, the NK sub-region shows a positive trend in most parts but appears insignificant, with an annual trend value of about 0.004/yr. Figure 4C shows that drought intensity also shows a combination of both downward and upward trends. The reduction in intensity is mainly located in northwestern Kenya (~0.006/yr) and parts of western CR sub-regions (~0.003/yr), where the trend is significant. The decreasing trend is mainly located in WS and western parts of NU sub-regions, where the trend is as high as 0.007/yr.

3.4 Temporal variation of drought indices over EA

The time series of SPEI in different sub-regions may help understand the temporal evolution of drought indices at a sub-domain scale and their regional differences. Figure 5 gives the temporal evolution of SPEI over the six sub-regions. The linear trend line and the local regression (LOESS) curves with 11 years are fitted to the SPEI time series to represent the linear and non-linear patterns of SPEI. From Figure 5, we can find that the SPEI3 drought index shows considerable inter-annual variation between wet and dry years. Meanwhile, the 11-year loess curve reveals that negative SPEI3 values have dominated the SPEI evolution since the 1980s in all sub-regions. This indicates that a large portion of EEA is gradually becoming drier in recent decades. The evolution of the SPEI drought index reveals the widespread drought events over EA in 1902, 1921, 1924/25, 1933, 1943, 1949, 1953, 1955, 1961, 1969, 1971/73, 1976, 1983/84, 1992/93, 2000/01, 2004/05, 2007/09, 2011/2012, 2014, and 2017. The drought events identified in the second half of the 20th century correspond well with the findings of previous studies (e.g., Nicholson, 2014; Agutu et al., 2017).

Regarding the regional differences, even more, drought years were identified in different years. For instance, the NK

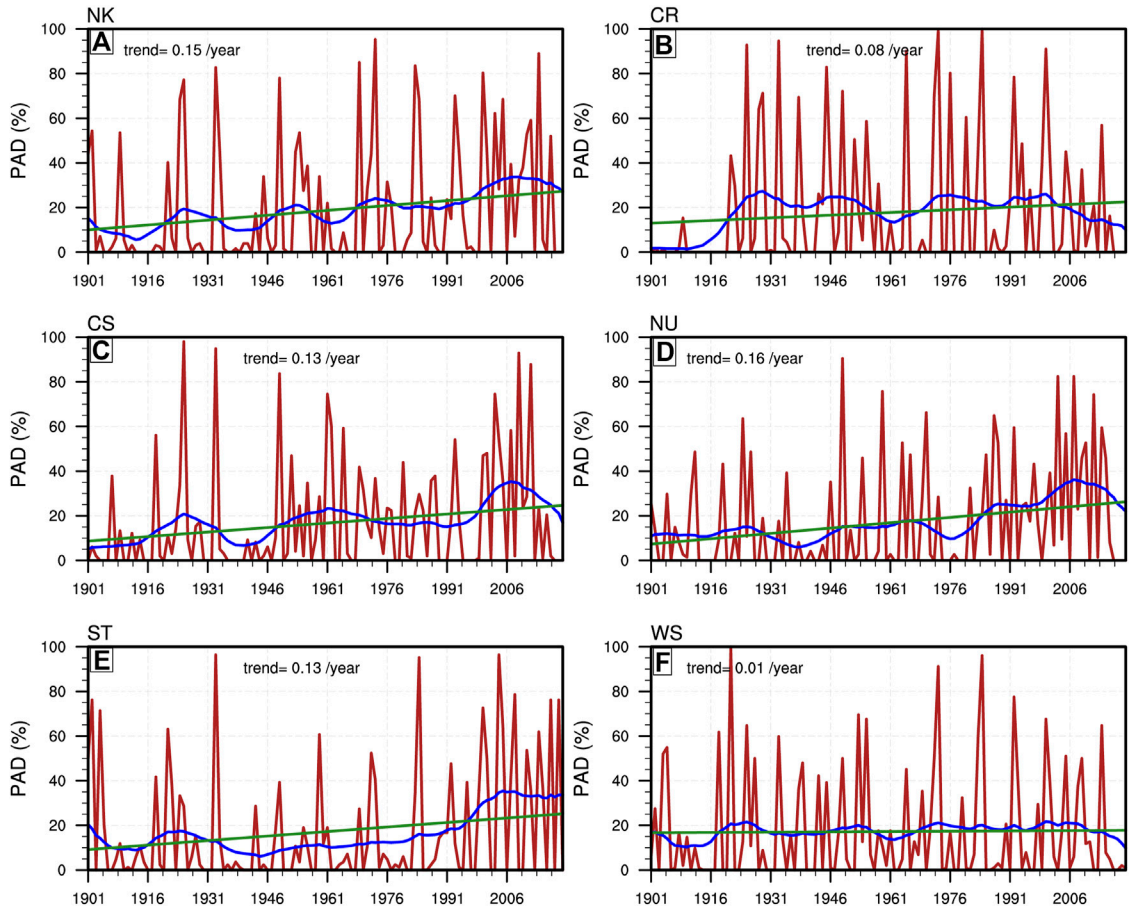

FIGURE 6
Temporal Evolution of percentage area under drought (PAD) for **(A)** NK, **(B)** CR, **(C)** CS, **(D)** ST, **(E)** NU and **(F)** WS sub-regions of the equatorial East Africa. The blue line denotes the reconstructed area under drought using the leading SSA principal component, while the black curve is the trend in the percentage drought area.

sub-region had drought events in 1928/29, 1938,1945,1976,1980, and 1999 (Figure 5A); CR had droughts in 1909 and 1993 (Figure 5B); CS had droughts in 1961 and 1962 (Figure 5C). For ST, more drought can be found in 1919, 1954, 1957, 1964, 1970, and 1988 (Figure 5D); for NU in 1905, 1939, 1943, and 1953 (Figure 5E) and WS in 1901, 1904, and 2020 (Figure 5F). Generally, many years identified as having sub-regional droughts had negative SPEI values in some of the sub-regions that did not satisfy our drought threshold. This indicates that while there would be a large-scale driver of drought in a particular year, each zone's distinct interaction with the local physical mechanism may suppress or enhance the dry condition. The time evolution of SPEI shows a weak negative trend in all the sub-regions. The trend is significant in CR (0.005/yr.), CS (0.006/yr.), and ST (0.005/yr.) and insignificant in NK (0.003/yr.), NU (0.001/yr.) and WS (0.004/yr.).

3.5 Temporal variation of the drought area

The areal drought extent was computed as a ratio of grid points with SPEI values less than −1 to the total number of all the grid points in that sub-region. Figure 6 shows the time series of percentage drought areas for the six sub-regions of EEA, we can find that the area affected by drought fluctuated significantly year by year, with magnitude ranging between 0% and 95% for the six sub-regions during the study period. Meanwhile, increasing trend of drought affected areas can also be found for all six sub-regions.

The variability of the drought area suggests that the positive linear trend observed may not be monotonous during the entire study period. Moreover, the high percentages of drought areas experienced in the later stages of the study period are likely to affect changes in the slope of the linear fitting. Consequently, we performed a non-linear trend analysis using singular value decomposition (SSA) for each sub-region separately. We chose

a window frame of 11 years and reconstructed the time series using the dominant mode to represent the time evolution of the series better. Figure 6 reveals a gradual rise in the area under drought for NK, CS, ST, and NU sub-regions, while the CR and WS show a flat curve, with relatively smaller increasing trends.

The percentage drought areas can further be categorized into four classes, i.e., moderate, severe and extreme drought area. For each category, the percentage area is obtained by comparing the total number of grids under that specific category to the total number of grids in each year. The result revealed that the total increase of percentage drought area is dominated by an increase in the area under moderate and severe droughts, rather than that under extreme drought (Supplementary Figure S2).

In most regions with larger increasing trend of percentage drought area extent, large spatial extension of drought can be also found after the 1980s. Previous study suggested that the decadal variation of rainfall anomalies in East Africa could be linked to the Pacific decadal oscillation (PDO; Bahaga et al., 2018). To understand the potential linkage between drought variation in EEA and PDO, the time series of the PDO index and 11-year running mean SPEI3 drought index over EEA region during 1900–2020 is presented (Supplementary Figure S3). It is found that the correlation between PDO index and SPEI drought index is weak during the whole study period, with temporal correlation coefficient of only 0.17. However, the correlation increase to around 0.88 after 1980. These suggest that the PDO signal can enhance the drought extension after 1980s, but this relationship is not significant over the whole time period.

3.6 Contribution of PET and rainfall to the drought

Based on the SPEI definition, the driving factors considered were rainfall and PET and, thus, their contribution to the total drought area. However, the influence of PET and rainfall on SPEI depend on their independence from one another (Cook et al., 2014). To quantify the contribution of rainfall and PET on SPEI-based drought changes, we adopted the detrending method described by Hamlet and Lettenmaier (2007), which references the SPEI by incorporating changes in either variable. To isolate the impact of rainfall, we calculated the SPEI index using the original data that retained the transient changes in rainfall and detrended PET and named it SPEI-PRE. Similarly, to isolate the impact of PET, SPEI was calculated using detrended rainfall and the original values of PET and referred result as SPEI-PET.

As shown in Figure 9, the combined effects of rainfall and PET on drought either reinforced the area under drought (mid-20th century) or acted in opposition (beginning and end of the 20th century) to mitigate the effect of each other for most regions in EEA. Additionally. Figure 7 also reveals that in the first half of the 20th century, the percentage of drought area computed using detrended rainfall (PET) was higher (lower) than the observed conditions in all six regions. Consequently, the findings suggest that lower PET values reduced drought intensity. However, the result reverses in the post-1975 period, where the increase in PET had a positive effect on drought, indicated by the rise in drought area calculated using varPre. Therefore, the apparent increase in areal drought extent in the post-1980s may be attributed to the high evaporative demands that exert greater stress on an already declining rainfall, thus exacerbating the drought severity. The impact of PET was pronounced in CR, NK, WS, and NU regions (Figure 7).

To explore the impact of PET on areal drought extent further, we compared the area under drought computed using SPEI to that SPI index (Supplementary Figure S4). The result shows divergent evolution of the percentage of land area affected by drought defined by the two indices. Furthermore, the result indicates that since the 1950s, the SPEI index has progressively identified more drought extent, thus pointing to the role of PET in the increase of drought coverage in all the sub-regions. Therefore, the apparent growth in drought areal extent in the post-1980s may be attributed to the high evaporative demands that exerted significant stress on an already declining rainfall, thus exacerbating the drought severity.

3.7 Variability of spring drought and its relationship with climate indices

REOF helps identify drought variability patterns but fails to provide information on the periodicities of the observed variabilities. Consequently, we apply the wavelet analysis to isolate dominant periodicity in the drought records and identify the coherence between drought and teleconnection indices. Figure 8 shows the result of the wavelet power spectrum of spatially averaged SPEI3 over the six sub-regions. The thick black line encloses values that have passed the red noise test at a 95% confidence level as determined by the Monte Carlo process (Jevrejeva et al., 2003). However, the Cone of Influence (COI) gives the region potentially influenced by the edge effect of data during wavelet transformation, and the area inside it provides an accurate time-frequency representation of the data. In contrast, the area outside it suffers from edge effects, thus unreliable.

For the NK sub-region (Figure 8A), a significant power region exists in the 3 years band in the 1920s, increasing to a periodicity of 6 years in the 1940s before decreasing and decaying by 1955. In addition, there is a strong amplitude between the 1970s and 1985 in the 4 years band and a weak amplitude in the 8 years band between 1940 and 2000s. Figure 8B shows that for the CR sub-region, significant power regions are distributed in the 3–6 years band between 1920 and 1950 and a 9–14 years band between the 1960s and 1990s. Figure 8C shows intermittent wave spectra between 1901 and 1980 in the CS sub-region. A weak 8–12 years band exists between 1960 and 2010, as well as a strong band outside the cone of influence in the 30–48 years band.

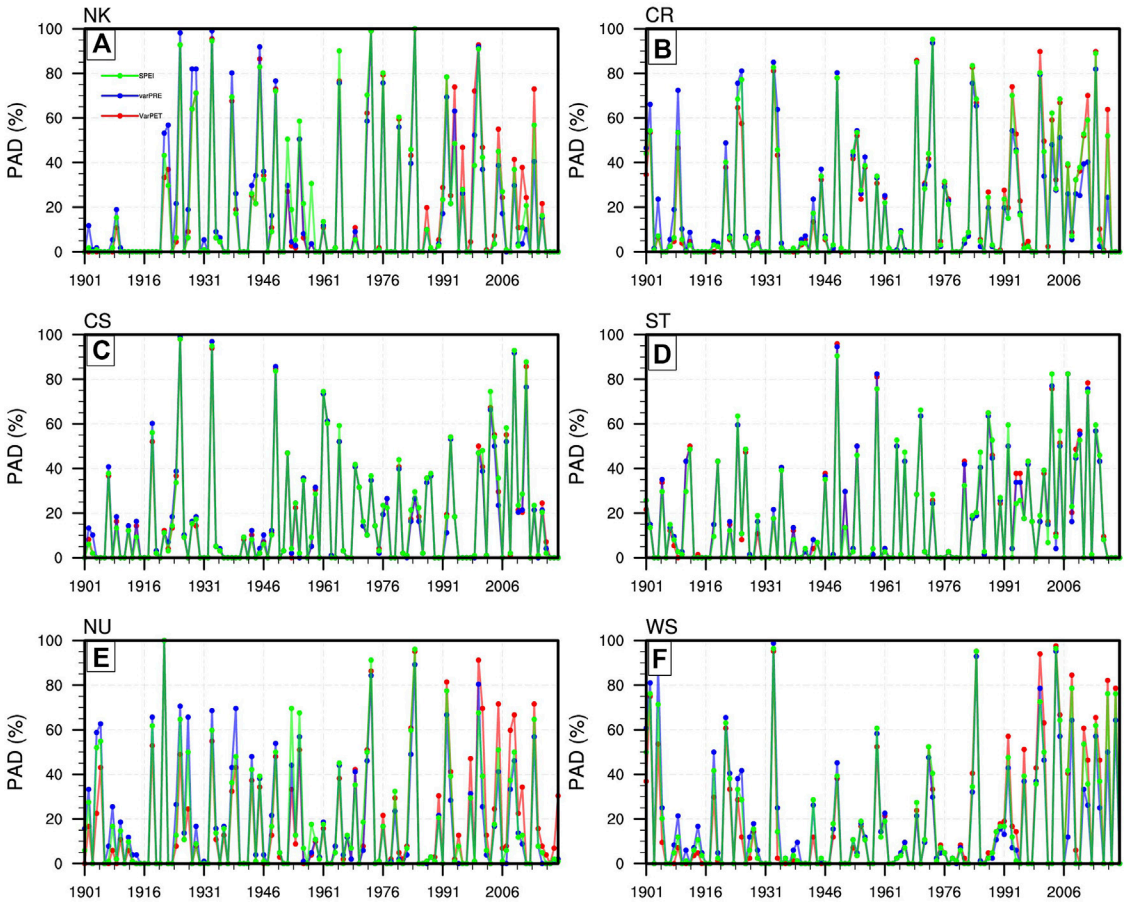

FIGURE 7
Temporal evolution of the percentage area under drought conditions computed for **(A)** NK, **(B)** CR, **(C)** CS, **(D)** ST, **(E)** NU and **(F)** WS sub-regions of Equatorial East Africa. The green time series represent the original SPEI, blue computed by varying rainfall and red computed by varying PET.

Figure 8D shows the local wavelet spectra in the 2–7 years band for the NU sub-region. The result appears weak throughout the study period except in 1920, 1930–1950, and 1980–1985. For the ST sub-region, the local wavelet spectra are in the 2–6 years band and 8–30 years band between 1950 and 2000 (Figure 8E). The inter-annual periodicity decreases from the 6 years to 2 years band from the 1980s. The sub-region also has a significant wavelet power in the 30–48 years band outside the cone of influence. In contrast, Figure 8F shows that WS has the weakest periodicity of all the sub-regions throughout the study period, with a reduced level of activities in pre-1920 and post-2000. In general, the regular periodicity is relatively stable at 2–6 years, indicating a large inter-annual variability within the period 1920–1980, while a decadal (8–16 years) variability also exists in some sub-regions. This suggests that inter-annual periodicities (<6years) dominate drought variability across EA. Overall, CR, CS, and ST sub-regions revealed the strongest interannual variations with maximum yellow regions.

Over EEA region, the dominant inter-annual (2–6 years) oscillations observed in the periodicity are mainly modulated by the El-Niño southern oscillation (ENSO; Ogallo, 1989; Kiladis and Diaz, 1989; Nicholson and Kim, 1997; Indeje et al., 2000). Consequently, we explore the interdependency between SPEI3 and the Niño3.4 index using cross-wavelet transformations. In case of any association between the two indices, a slowly varying phase lag is expected, and the phenomenon would be phase-locked, i.e., the phase arrows point only in one direction for a given wavelength (Grinsted et al., 2004). The use of arrows expresses the relationship between the two factors. The arrows pointing east reflect the in-phase relationship, whereas the arrow pointing west indicates an out-of-phase relationship. Conversely, arrows pointing upward (downward) indicate drought lag (lead) the index by a quarter cycle and reveals a non-linear relationship. Higher wavelength transforms coefficients correspond to a stronger correlation between drought and the Niño3.4 index.

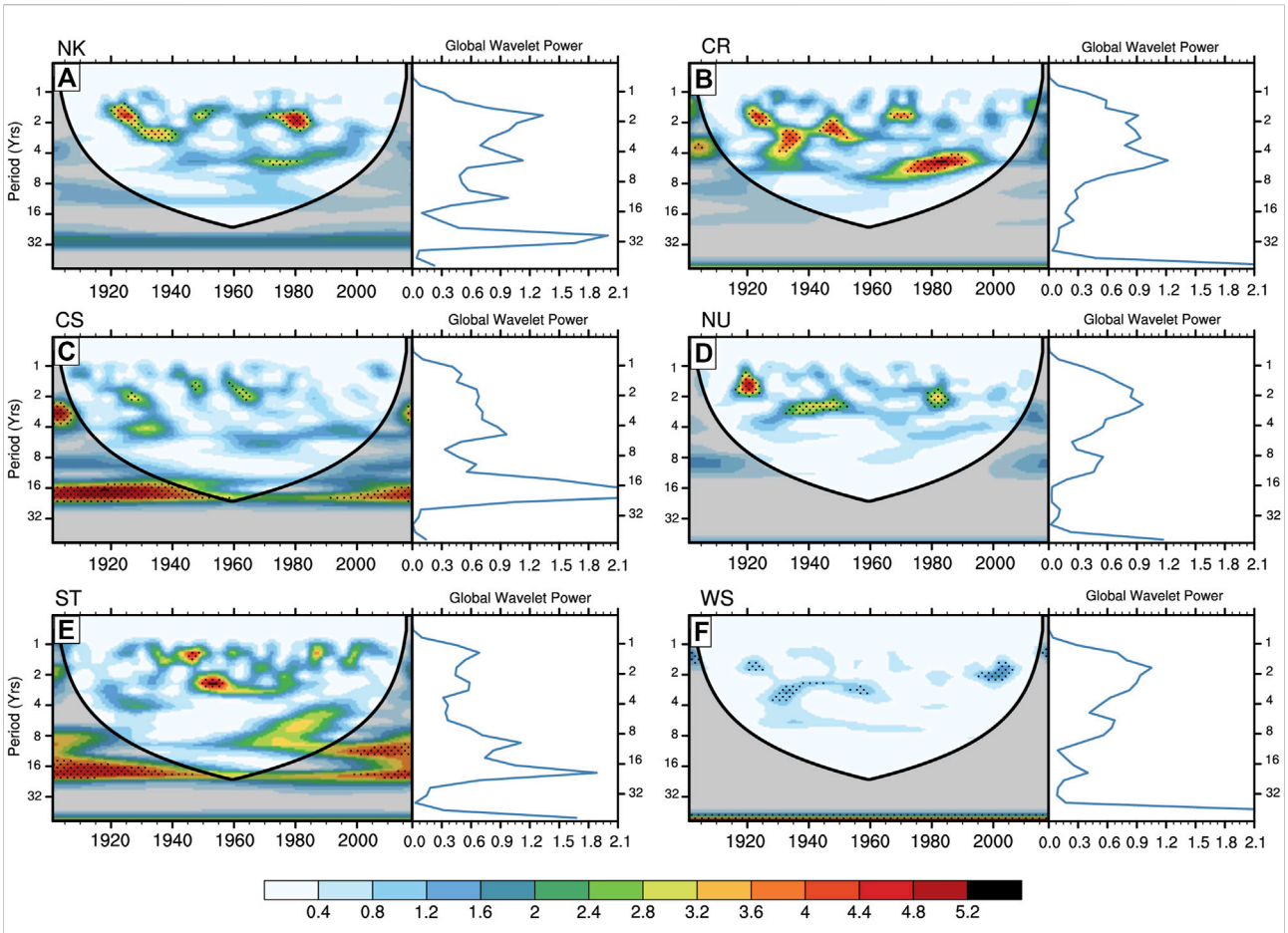

FIGURE 8
Wavelet power spectra of averaged SPEI time series over **(A)** NK, **(B)** CR, **(C)** CS, **(D)** ST, **(E)** NU and **(F)** WS sub-regions of equatorial East Africa. The solid dark contour denotes the 95% confidence level against the red noise. The cone of influence (COI) is shown as a semi-circle with a dark shade.

Figure 9 shows the result of cross wavelet transformation between Niño3.4 and SPEI with high wavelet coherence larger than 0.6 shown with arrows. As shown in Figure 9A, NK showed high energies between SPEI and Niño3.4 in the 8–12 years frequency band in 1920–1960 years; and 4–6 years in the 1930s. The observed coherence between Niño3.4 and SPEI was in-phase during the periods as arrows points to the east. However, from 1970 to 1990, the two indices were out of phase within the 3–5 years period band. Nevertheless, the coherence in the later period failed the significance test. In the CR sub-region, a significant correlation between the indices appeared intermittently from the 1920s to 1990s in the 2–6 years band (Figure 9B). In the beginning, the two indices were in-phase, followed by Niño3.4 leading SPEI and later an antiphase relationship. Figure 9C shows that the CS sub-region exhibited a statistically significant relationship between SPEI and Niño3.4 between 1940 and 1970; however, the former index led the latter by about 3–4 months. The anti-phase association infers no or weak influence on drought by the ENSO. Another high power appears in the 16–24 years band where the relationship is in-phase. NU sub-region shows a scattered high coherence between the two indices within a 2–6 years band with in-phase coherence between 1920–1940 and Niño3.4 leading SPEI by 3–4 months in the 1950s and 1980s (Figure 9D). Figure 9E reveals that SPEI were out of phase with Niño3.4 in the 1920s over the ST sub-region with high energies lasting 2–6 years. Another statistically significant high power is evident in the 1970s and 1980s, where SPEI lags Niño3.4 by 3–4 months lasting between 9 and 15 years. Over the WS sub-region, significant high power was concentrated in the 2–6 years band and was in-phase between 1920–1940, while the variability of SPEI lagged that of Niño3.4 in 1960 (Figure 9F).

In general, the 2–6 years oscillation is more robust, suggesting a strong inter-annual coherence between drought and ENSO, and this is consistent with findings by previous studies (Rodhe and Virji, 1976; Nicholson and Entekhabi, 1986). It is suggested that ENSO can produce anomalous diabatic heating/cooling over the western

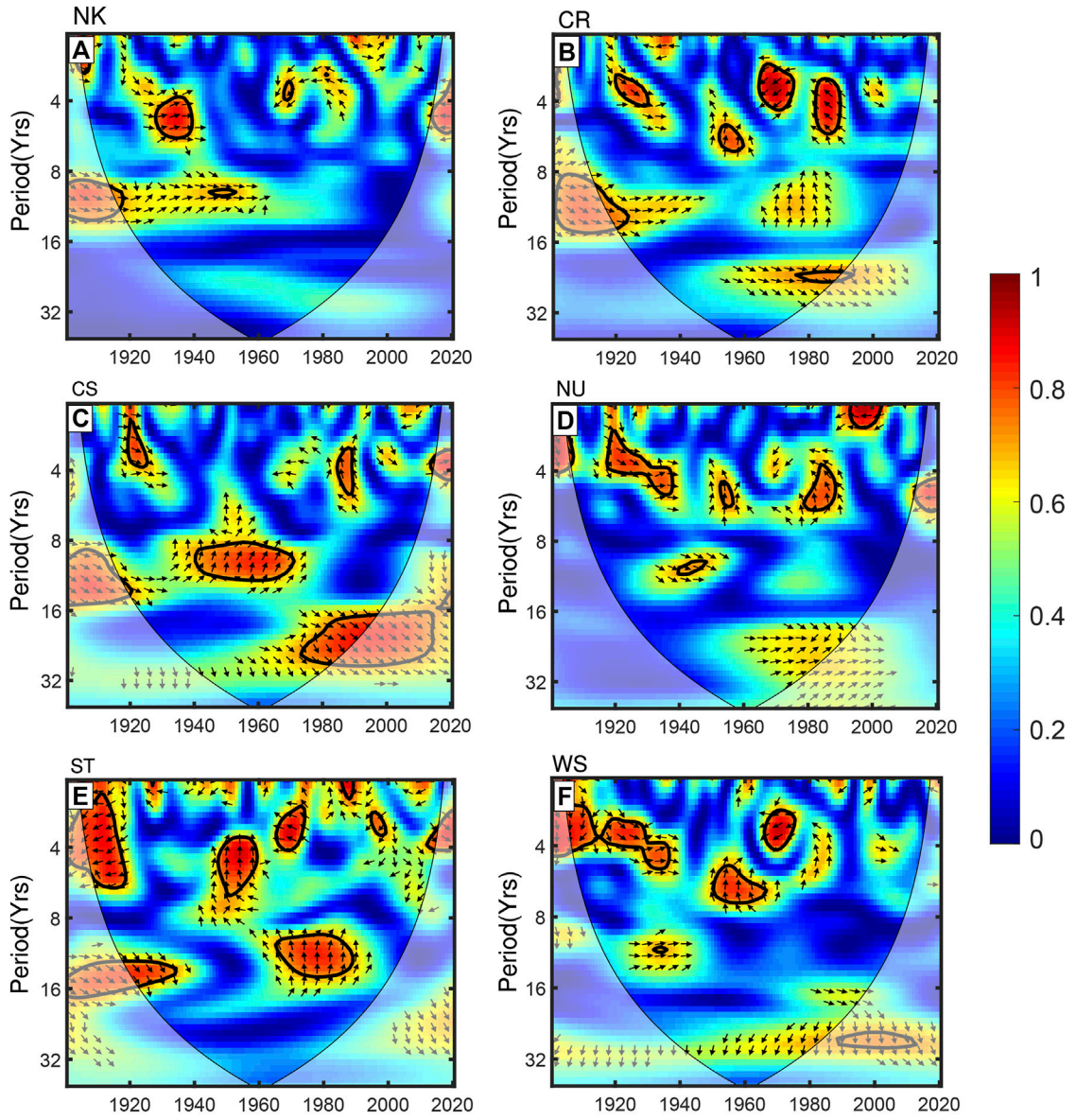

FIGURE 9
Squared wavelet coherence between the spatially averaged SPEI for **(A)** NK, **(B)** CR, **(C)** CS, **(D)** ST, **(E)** NU and **(F)** WS sub-regions and MAM Niño3.4. The colour increment from blue to red denotes the increasing coherency between the two indices. Phase arrows pointing right indicate signals are in phase, whereas left-pointing arrows indicate an antiphase relationship. Arrows pointing upward (downward) shows lead (lag) relationships between the two signals. The black contour designates the 95% confidence level against red noise, and the cone of influence (COI) is shown as a black semi-circle with a lighter shade.

Pacific Ocean, creating a dynamically forced anomalous ascent/descent in the region, thus modifying the walker-type zonal circulation in the equatorial Indian Ocean (Goddard and Graham 1999; Mutai and Ward, 2000). Pohl and Camberlin (2011) also reported that the interannual variability of rainfall in all season except the boreal summer over EEA are strongly controlled by zonal wind shear between 850 mb and 150 mb level over the equatorial Indian Ocean, which was closely correlated to ENSO in all seasons.

4 Discussion and conclusion

The current study gives a simple but complete picture of meteorological drought characteristics over EEA during the MAM season based on SPEI3 using a long-term CRU dataset. MAM was chosen because it corresponds to the primary planting season for major food and because the season is the best candidate for investigating the observed rainfall decline's impact on drought characteristics. SPEI index is relatively easier to characterize but

provides subtle information on drought behavior vital to drought mitigation and water resource management. The Meteorological drought discussed herein is the precursor for other types of drought. Therefore, the knowledge of its temporal variability may reveal the susceptibility of an area to different drought types. The evolution of SPEI during the period of study points toward an increase in spatial coverage of drought areal extent. Most of this increase was observed in moderate and severe drought, while extreme drought remained stable during the observation period. The result of REOF identified six distinct spatial patterns that partly resemble the MAM daily rainfall homogeneous sub-regions identified by Indeje et al. (2000). The observed variation may be attributed to the SPEI calculation, which uses PET that is influenced by other climatic factors. The sub-regions identified may be helpful in regional drought risk assessment and management. SPEI3 used was able to capture the major drought events documented over EEA. For the study period, the notable droughts occurred in 1902, 1921, 1924/25, 1933, 1943, 1949, 1953, 1955, 1961, 1969, 1971/73, 1976, 1983/84, 1992/93, 2000/01, 2004/05, 2007/09, 2011/2012, 2014, and 2017.

Although there is no apparent pattern in the occurrence of these events, the first 2 decades at the beginning of the 20th century are marked by a persistent period of positive SPEI values. The opposite has been true from the late 20th century to recent decades, signaling the increase in drought events in the region. The recent increase in drought has been linked to warming in the western Pacific Ocean that is associated with the cold PDO phase (Williams and Funk, 2011; Funk et al., 2014).

The warming extends the warm pool into the eastern Indian Ocean, creating an anticyclonic flow that disrupts the moisture flow to EA by enhancing subsidence over EEA. A similar decline in rainfall has also been reported in Africa's monsoon region (Han et al., 2019). Non-etheless, Bahaga et al. (2018) found that the Greater Horn of Africa (a larger part of eastern Africa) receives above (below) normal rain during warm (cold) PDO phases. However, the correlation coefficient between PDO and drought variation is pretty weak, when only Equatorial East Africa region is considered. Consequently, this points to a complicated relationship between decadal pacific variability and drought over Equatorial East Africa in MAM season, and care should be taken when analyzing such a relationship.

EEA region generally experienced increased drought frequency between 1981 and 2020, with the drought-afflicted area remaining at an average above 30% for most of the sub-regions. Such an increase in areal extent increases the community's vulnerability through reduced portable water and food production. Additionally, the strength and direction of the SPEI trend seemed to change depending on the period chosen. However, the trend magnitude weakened considerably when the entire study period was considered. We further analyzed how changes in rainfall and PET influence SPEI. The contribution of rainfall was dominant over the contribution of PET on SPEI variation; however, the latter has contributed positively to the increase in drought areas in the post-1980 era. The implicit assumption from the above result is that factors that drive droughts, such as temperature, have changed over the decades. Indeed, the comparison between the percentage of land affected by drought using SPI and SPEI indices showed a progressive divergent evolution. The difference between the two indices shows the percentage of land area affected by drought should the phenomenon be defined using the water balance rather than rainfall alone. The result suggests that before the 1970s, changes in drought were primarily related to the rainfall variability over the region. Besides the decline in rainfall during the MAM season, evapotranspiration has exacerbated the spread of drought. These findings are coherent with rainfall and temperature evolution over EEA, where studies have reported general temperature increases and reductions in rainfall (Ongoma and Chen, 2017). While the SPEI value shows a decreasing trend, it lacks clear evidence of substantial significant changes. This result agrees with the findings of Mpelasoka et al. (2018), who reported a lack of significant changes in the long-term probability of the annual occurrence of drought over the larger greater horn of Africa.

The result of spectral analysis of the cyclic behavior of MAM drought reveals that 2–6 years cycles are frequent in almost all sub-regions suggesting that inter-annual periodicities (<6 years) dominate drought variability across EA. The periodicity nature of drought signifies good news for policymakers as this implies ease of predicting the drought phenomenon. Analyses of drought using wavelets show a significant relationship with Niño3.4 at a periodicity of 2–6 years that occurs intermittently throughout the study period. The strength of influence of Niño3.4 varies from one period to another and from one sub-region to another. Onyutha and Willems (2017) reported that although the large-scale mechanism responsible for drought may be the same, its characteristics may be influenced by the local land-atmosphere feedback response determined by topography and the presence of water bodies (Funk et al., 2015; Wainwright et al., 2019).

Data availability statement

All the CRU TS 4.05 data used in this study are available at https://crudata.uea.ac.uk/cru/data/hrg/index.htm#current. Nino 3.4 and PDO indices are available in NOAA Climate Prediction Center website at https://psl.noaa.gov/gcos_wgsp/Timeseries/

Author contributions

ZL: conceptualized, supervised, reviewed and edited the manuscript while the AO curated the data, did formal analysis

and drafted the original manuscript. Both authors have read and agreed to the published version of the manuscript.

Funding

This study is jointly supported by the Chinese Academy of Sciences Strategic Priority Research Program (Grant No. XDA19030403), the National Natural Science Foundation of China (Grant Nos. 42075166 and 41975119), and NSFC Research Fund for International Young Scientists (Grant No. 42150410394).

Acknowledgments

The authors are grateful to the University of East Anglia Climate Research Program for the CRU dataset and NOAA Climate Prediction Center for the Nino3.4 and PDO data used. OA acknowledges the support of the CAS-TWAS President Fellowship and the CAS-TWAS Center of Excellence for Climate and Environment Sciences for the infrastructure to conduct the study. We also thank the anonymous reviewers for their helpful comments and suggestions.

Conflict of interest

The authors declare that the research was conducted in the absence of any commercial or financial relationships that could be construed as a potential conflict of interest.

Publisher's note

Supplementary material

The Supplementary Material for this article can be found online at: https://www.frontiersin.org/articles/10.3389/feart.2022.1064940/full#supplementary-material

SUPPLEMENTARY FIGURE S1
Major planting season for various food crops in EA. Adopted from FAO GIEWS - Global Information and Early Warning System (Accessed 28 March 2022).

SUPPLEMENTARY FIGURE S2
Evolution of percentage area under drought for NK **(A–D)**, different sub-regions for moderate drought (left column), severe drought (mid column) and extreme (right column). Figures CR **(E–H)**, CS **(I–L)**, ST **(M–P)**, NU **(Q–T)** and WS **(U–X)** The blue denotes the reconstructed area under drought using the leading SSA principal component, while the black curve is the trend in the percentage drought area.

SUPPLEMENTARY FIGURE S3
Time series of PDO (red) and Equatorial East Africa spatially averaged SPEI (green) for MAM. An 11-year moving average has was applied to both series. R denotes the correlation coefficient between the PDO and SPEI time series.

SUPPLEMENTARY FIGURE S4
Difference in percent area under drought calculated as the difference between MAM SPEI and SPI for **(A)** NK, **(B)** CR, **(C)** CS, **(D)** ST, **(E)** NU and **(F)** WS sub-regions of the equatorial East Africa.

References

Abdourahaman, E. Z. S., and Acar, R. (2018). Analysis of meteorological drought variability in Niger and its connections with climate indices. *Hydrol. Sci. J.*, v. 63, n. 8, p. 1203–1218, doi:10.1080/02626667.2018.1489542

AghaKouchak, A. (2015). A multivariate approach for persistence-based drought prediction: Application to the 2010–2011 East Africa drought. *J. Hydrol. X.* 526, 127–135. doi:10.1016/j.jhydrol.2014.09.063

Agutu, N., Awange, J., Zerihun, A., Ndehedehe, C., Kuhn, M., and Fukuda, Y. (2017). Assessing multi-satellite remote sensing, reanalysis, and land surface models' products in characterizing agricultural drought in East Africa. *Remote Sens. Environ.* 194 (0), 287–302. doi:10.1016/j.rse.2017.03.041

Andreadis, K. M., Clark, E. A., Wood, A. W., Hamlet, A. F., and Lettenmaier, D. P. (2005). Twentieth-century drought in the conterminous United States. *J. Hydrometeorol.* 6 (6), 985–1001. doi:10.1175/jhm450.1

Anyah, R. O., Semazzi, F. H., and Xie, L. (2006). Simulated physical mechanisms associated with climate variability over Lake Victoria basin in East Africa. *Mon. Weather Rev.* 134 (12), 3588–3609. doi:10.1175/mwr3266.1

Ayugi, B., Tan, G., Gnitou, G. T., Ojara, M., and Ongoma, V. (2020). Historical evaluations and simulations of precipitation over East Africa from Rossby centre regional climate model. *Atmos. Res.* 232, 104705. doi:10.1016/j.atmosres.2019.104705

Bahaga, T. K., Fink, A. H., and Knippertz, P. (2018). Revisiting inter-annual to decadal teleconnections influencing seasonal rainfall in the Greater Horn of Africa during the 20th century. *Int. J. Climatol.* 39, 2765–2785. doi:10.1002/joc.5986

Beguería, S., Vicente-Serrano, S. M., Reig, F., and Latorre, B. (2013). Standardized precipitation evapotranspiration index (SPEI) revisited: Parameter fitting, evapotranspiration models, tools, datasets and drought monitoring. *Int. J. Climatol.* 34 (10), 3001–3023. doi:10.1002/joc.3887

Bhuiyan, C., Flügel, W. A., and Singh, R. P. (2009). Modelling of ground water recharge-potential in the hard-rock aravalli terrain, India: A GIS approach. *Environ. Earth Sci.* 59 (4), 929–938. doi:10.1007/s12665-009-0087-4

Camberlin, P., and Philippon, N. (2002). The East african march–may rainy season: Associated atmospheric dynamics and predictability over the 1968–97 period. *J. Clim.* 15, 1002–1019. doi:10.1175/1520-0442(2002)015<1002:teammr>2.0.co;2

Casagrande, E., Mueller, B., Miralles, G., Entekhab, i. D., and Molini, A. (2015). Wavelet correlations to reveal multiscale coupling in geophysical systems. *J. Geophys. Res. Atmos.* 120, 7555–7572. doi:10.1002/2015jd023265

Chakraborty, A., Nanjundiah, R. S., and Srinivasan, J. (2009). Impact of African orography and the Indian summer monsoon on the low-level Somali jet. *Int. J. Climatol.* 29 (7), 983–992. doi:10.1002/joc.1720

Cook, B. I., Miller, R. L., and Seager, R. (2009). "Amplification of the North American Dust Bowl drought through human-induced land degradation," in Proceedings of the National Academy of Sciences. doi_10.1073.pnas.0810200106.New York, NY.

Cook, B. I., Seager, R., and Smerdon, J. E. (2014). The worst north American drought year of the last millennium: 1934. *Geophys. Res. Lett.* 41 (20), 7298–7305. doi:10.1002/2014GL061661

Cook, B. I., Smerdon, J. E., Seager, R., and Coats, S. (2015). Global warming and 21st century drying. *Clim. Dyn.* 43, 2607–2627. doi:10.1007/s00382-014-2075-y

Dai, A. (2013). Increasing drought under global warming in observations and models. *Nat. Clim. Chang.* 3, 52–58. doi:10.1038/nclimate1633

Funk, C., Hoell, A., Shukla, S., Bladé, I., Liebmann, B., Roberts, J. B., et al. (2014). Predicting East African spring droughts using Pacific and Indian Ocean sea surface temperature indices. *Hydrol. Earth Syst. Sci.* 18 (12), 4965–4978. doi:10.5194/hess-18-4965-2014

Funk, C., Nicholson, S. E., Landsfeld, M., Klotter, D., Peterson, P., and Harrison, L. (2015). The centennial trends Greater Horn of Africa precipitation dataset. *Sci. Data* 2, 150050. doi:10.1038/sdata.2015.50

Gao, F., Wang, Y., Chen, X., and Yang, W. (2020). Trend analysis of rainfall time series in Shanxi Province, Northern China (1957–2019). *Water* 12 (9), 2335. doi:10.3390/w12092335

Gebremeskel Haile, G., Tang, Q., Leng, G., Jia, G., Wang, J., Cai, D., et al. (2020). Long-term spatiotemporal variation of drought patterns over the Greater Horn of Africa. *Sci. Total Environ.* 704, 135299. doi:10.1016/J.SCITOTENV.2019.135299

Goddard, L., and Graham, N. E. (1999). Importance of the Indian Ocean for simulating rainfall anomalies over eastern and southern Africa. *J. Geophys. Res.* 104, 19099–19116. doi:10.1029/1999jd900326

Grinsted, A., Moore, J. C., and Jevrejeva, S. (2004). Application of the cross wavelet transform and wavelet coherence to geophysical time series. *Nonlinear process. geophys.* 11, 561–566. doi:10.5194/npg-11-561-2004

Guttman, N. (1998). Comparing the palmer drought index and the standardized precipitation index. *J. Am. Water Resour. Assoc.* 34, 113–121. doi:10.1111/j.1752-1688.1998.tb05964.x

Hamlet, A. F., and Lettenmaier, D. P. (2007). Effects of 20th century warming and climate variability on flood risk in the Western US. *Water Resour. Res.* 43, W06427. doi:10.1029/2006WR005099

Han, Z., Su, T., Huang, B., Feng, T., Qu, S., and Feng, G. (2019). Changes in global monsoon precipitation and the related dynamic and thermodynamic mechanisms in recent decades. *Int. J. Climatol.* 39 (3), 1490–1503. doi:10.1002/joc.5896

Hannachi, A. (2007). Pattern hunting in climate: A new method for finding trends in gridded climate data. *Int. J. Climatol.* 27, 1–15. doi:10.1002/joc.1375

Harris, I., Jones, P. D., Osborn, T. J., and Lister, D. H. (2014). Updated high-resolution grids of monthly climatic observations –the CRU TS3.10 Dataset. *Int. J. Climatol.* 34, 623–642. doi:10.1002/joc.3711

Hastenrath, S., Polzin, D., and Mutai, C. (2005). Diagnosing the 2005 drought in Equatorial East Africa. *J. Clim.* 20, 4628–4637. doi:10.1175/jcli4238.1

Hastenrath, S., Polzin, D., and Mutai, C. (2010). Diagnosing the droughts and floods in Equatorial East Africa during boreal autumn 2005-08. *J. Clim.* 23, 813–817. doi:10.1175/2009JCLI3094.1

Iglesius, A., Yang, X. B., Epstein, P., Chivian, E., and Rosenzweig, C. (2001). Climate change and extreme weather events-implications for food production, plant diseases, and pests. *Glob. Chang. Hum. Heal.* 2, 90–104. doi:10.1023/A:1015086831467

Indeje, M., Semazzi, F. H. M., and Ogallo, L. J. (2000). ENSO signals in East African rainfall seasons. *Int. J. Climatol.* 20 (1), 19–46. doi:10.1002/(sici)1097-0088(200001)20:1<19::aid-joc449>3.0.co;2-0

Jevrejeva, S., Moore, J. C., and Grinsted, A. (2003). Influence of the Arctic oscillation and El Niño-Southern oscillation (ENSO) on ice conditions in the Baltic Sea: The wavelet approach. *J. Geophys. Res.* 108 (D21), 4677. doi:10.1029/2003JD003417

Kendall, M. G. (1975). *Rank correlation methods*. London, UK: Charles Griffin.

Lyon, B., and Dewitt, D. G. (2012). A recent and abrupt decline in the East African long rains. *Geophys. Res. Lett.* 39 (2), L02702. doi:10.1029/2011GL050337

Lyon, B. (2014). Seasonal drought in the greater horn of Africa and its recent increase during the march–may long rains. *J. Clim.* 27, 7953–7975. doi:10.1175/jcli-d-13-00459.1

Mann, H. B., Mbigi, D., Onyango, A. O., Mtewele, Z. F., Kiprotich, P., and Xiao, Z. (1945). Non-parametric tests against trend. *Econometrica* 13Coupled model intercomparison project phase 6 simulations of the spatial structure of rainfall variability over East Africa: Evaluation and projection. *Int. J. Climatol.* 1, 245–259. – 21. doi:10.1002/joc.7868

McKee, T. B., Doeskin, N. J., and Kleist, J. (1993). "The relationship of drought frequency and duration to time scales," in Proceedings of the 8th Conference on Applied Climatology(Boston, MA: American Meteorological Society), 179–184.

Mogaka, H., Gichere, S., Davis, R., and Hirji, R. (2006). *World Bank Working Paper No. 69*. Washington, DC: World Bank (Accessed July 11, 2019).Climate variability and water resources degradation in Kenya: Improving water resources development and management

Mpelasoka, F., Awange, J. L., and Zerihun, A. (2018). Influence of coupled ocean–atmosphere phenomena on the Greater Horn of Africa droughts and their implications. *Sci. Total Environ.* 610–611, 691–702. doi:10.1016/j.scitotenv.2017.08.109

Mutai, C. C., and Ward, M. N. (2000). East African rainfall and the tropical circulation/convection on intraseasonal to interannual timescales. *J. Clim.* 13, 3915–3939. doi:10.1175/1520-0442(2000)013<3915:earatt>2.0.co;2

Nicholson, S. E. (2014). A detailed look at the recent drought situation in the Greater Horn of Africa. *J. Arid. Environ.* 103, 71–79. doi:10.1016/j.jaridenv.2013.12.003

Nicholson, S. E., and Entekhabi, D. (1986). The quasi-periodic behavior of rainfall variability in Africa and its relationship to the Southern Oscillation. *Arch. Mater. Geoph. Biocl. A* 34, 311–348. doi:10.1007/bf02257765

Nicholson, S. E., and Kim, J. (1997). The relationship of the el-niño-southern oscillation to african rainfall. *Int. J. Climatol.*, 17, 117–135. doi:10.1002/(SICI)1097-0088

North, G., Bell, T., Cahalan, R., and Moeng, F. (1982). Sampling errors in the estimation of empirical orthogonal functions. *Mon. Wea. Rev.* 110, 699–706. doi:10.1175/1520-0493(1982)110<0699:seiteo>2.0.co;2

Ntale, H. K., and Gan, T. Y. (2003). Drought indices and their application to East Africa. *Int. J. Climatol.* 3, 1335–1357. doi:10.1002/joc.931

Ogallo, L. J. (1989). The spatial and temporal patterns of the East African seasonal rainfall derived from principal component analysis. *Int. J. Climatol.* 9, 145–167. doi:10.1002/joc.3370090204

Ongoma, V., and Chen, H. (2017). Temporal and spatial variability of temperature and precipitation over East Africa from 1951 to 2010. *Meteorol. Atmos. Phys.* 129 (2), 131–144. doi:10.1007/s00703-016-0462-0

Onyango, A. O., Xu, H. M., and Lin, Z. H. (2020). Diurnal cycle of rainfall over Lake Victoria Basin during the long-rain season based on TRMM satellite estimate. *Int. J. Climatol.*, 40, 4622–4637, doi:10.1002/joc.6479

Onyutha, C., and Willems, P. (2017). Influence of spatial and temporal scales on statistical analyses of rainfall variability in the River Nile basin. *Dyn. Atmos. Oceans* 77, 26–42. doi:10.1016/j.dynatmoce.2016.10.008

Palmer, W. C. (1965)., 45. US weather bureau research paper, 58.*Meteorol. drought*

Peagle, J., and Geisler, J. E. (1986). The effect of East African topography on flow driven by zonally symmetric forcing. *J. Atmos. Sci.* 43 (17), 1862–1872. doi:10.1175/1520-0469(1986)043<1862:teoeat>2.0.co;2

Pohl, B., and Camberlin, P. (2011). Intraseasonal and interannual zonal circulations over the equatorial Indian Ocean. *Theor. Appl. Climatol.* 104, 175–191. doi:10.1007/s00704-010-0336-1

Richman, M. B. (1986). Rotation of principal components. *J. Climatol.* 6, 293–335. doi:10.1002/joc.3370060305

Rodhe, H., and Virji, H. (1976). Trends and periodicities in East African rainfall data. *Mon. Weather Rev.* 104, 307–315. doi:10.1175/1520-0493

Schreck, C. J., and Semazzi, F. H. M. (2004). Variability of the recent climate of eastern Africa. *Int. J. Climatol.* 24, 681–701. doi:10.1002/joc.1019

Schwalm, C., Anderegg, W., Michalak, A., Fisher, J. B., Biondi, F., Koch, G., et al. (2017). Global patterns of drought recovery. *Nature* 548, 202–205. doi:10.1038/nature23021

Sheffield, J., Wood, E. F., and Roderick, M. L. (2012). Little change in global drought over the past 60 years. *Nature* 491, 435–438. doi:10.1038/nature11575

Shilenje, Z., and Ongoma, V. (2016). The effectiveness of agrometeorological information in the realization of Kenya's vision 2030; lessons learned from China. *Ital. J. Agrometeorol.* 21 (1), 67–72.

Skliris, N., Zika, J. D., Nurser, G., Josey, S. A., and Marsh, R. (2016). Global water cycle amplifying at less than the Clausius-Clapeyron rate. *Sci. Rep.* 6, 38752. doi:10.1038/srep38752

Tierney, J. E., Ummenhofer, C. C., and De-Menocal, P. B. (2015). Past and future rainfall in the horn of Africa. *Sci. Adv.* 1 (9), e1500682. doi:10.1126/sciadv.1500682

Torrence, C., and Compo, G. P. (1998). A practical guide to wavelet analysis. *Bull. Am. Meteorol. Soc.* 79, 61–78. doi:10.1175/1520-0477(1998)079<0061:apgtwa>2.0.co;2

Uhe, P., Philip, S., Kew, S., Shah, K., Kimutai, J., Mwangi, E., et al. (2017). Attributing drivers of the 2016 Kenyan drought. *Int. J. Climatol.* 38 (51), e554–e568. doi:10.1002/joc.5389

Undp/, U. N. S. O. (1997). New York: UNDP Office to Combat Desertification and Drought UNSO.*Aridity zones and dryland populations: An assessment of population levels in the world's drylands with particular reference to Africa*

Vicente-Serrano, S. M., Beguería, S., and López-Moreno, J. I. (2010). A multiscalar drought index sensitive to global warming: The standardized

precipitation evapotranspiration index. *J. Clim.* 23 (7), 1696–1718. doi:10.1175/2009jcli2909.1

Wainwright, C. M., Marsham, J. H., Keane, R. J., Rowell, D. P., Finney, D. L., Black, E., et al. (2019). Eastern African Paradox' rainfall decline due to shorter not less intense Long Rains. *npj Clim. Atmos. Sci.* 2, 34. doi:10.1038/s41612-019-0091-7

Wells, N., Goddard, S., and Hayes, M. J. (2004). A self-calibrating palmer drought severity index. *J. Clim.* 17, 2335–2351. doi:10.1175/1520-0442(2004)017<2335:aspdsi>2.0.co;2

Winslow, M. D., Vogt, J. V., Thomas, R. J., Sommer, S., Martius, C., and Akhtar-Schuster, M. (2011). Science for improving the monitoring and assessment of dryland degradation. *Land Degrad. Dev.* 22 (2), 145–149. doi:10.1002/ldr.1044

Yang, W., Seager, R., Cane, M. A., and Lyon, B. (2014). The East African long rains in observations and models. *J. Clim.* 27, 7185–7202. doi:10.1175/JCLI-D-13-00447.1

Yevjevich, V. (1967). *Hydrology paper 23*. Fort Collins,CO: Colorado State University, 18.An objective approach to definitions and investigations of continental hydrologic droughts

frontiers | Frontiers in Earth Science

TYPE Original Research
PUBLISHED 12 January 2023
DOI 10.3389/feart.2022.1063372

OPEN ACCESS

EDITED BY
Stephen Outten,
Nansen Environmental and Remote Sensing Center (NERSC), Norway

REVIEWED BY
Chujie Gao,
Hohai University, China
Minggang Li,
Chengdu University of Information Technology, China

*CORRESPONDENCE
Zhaoyong Guan,
guanzy@nuist.edu.cn

SPECIALTY SECTION
This article was submitted to Atmospheric Science, a section of the journal Frontiers in Earth Science

RECEIVED 07 October 2022
ACCEPTED 31 October 2022
PUBLISHED 12 January 2023

CITATION
Huo L, Guan Z, Zhang M, Jin D, Wang J, Shi Y, Wang Y, Liu Y and Liu C (2023), An unusual Northwest–Southeast oriented Meiyu rain belt in 2021.
Front. Earth Sci. 10:1063372.
doi: 10.3389/feart.2022.1063372

An unusual Northwest–Southeast oriented Meiyu rain belt in 2021

Liwei Huo[1], Zhaoyong Guan[1]*, Mengke Zhang[1,2], Dachao Jin[1], Ji Wang[3], Yinglong Shi[4], Yi Wang[5], Yin Liu[6,7] and Chun Liu[8]

[1]Key Laboratory of Meteorological Disaster, Joint International Research Laboratory of Climate and Environment Change (ILCEC), Collaborative Innovation Center on Forecast and Evaluation of Meteorological Disasters (CIC-FEMD), Ministry of Education (KLME), Nanjing University of Information Science and Technology, Nanjing, China, [2]Chinese Academy of Meteorological Sciences, Beijing, China, [3]Beijing Regional Climate Center, Beijing, China, [4]College of Meteorology and Oceanography, National University of Defense Technology, Changsha, China, [5]Jiangsu Meteorological Observatory, Nanjing, China, [6]Jiangsu Meteorological Observation Center, Nanjing, China, [7]Key Laboratory of Atmosphere Sounding, China Meteorological Administration, Chengdu, China, [8]Anhui Meteorological Observatory, Hefei, China

Affected by the East Asian summer monsoon, summer floods occur frequently in eastern China, causing huge economic losses and social impacts. In 2021, the precipitation anomaly during the Meiyu period in Yangtze-Huaihe River Valley (YHRV) was abnormally high, with a value of 188.0 mm, about 1.7 standard deviations above normal. However, it did not cause serious flood disasters. This was mainly due to the existence of two precipitation anomaly centers in YHRV, which shared the impact of the excessive precipitation. These two centers were located at the junction of Anhui Province and Henan Province and the junction of Jiangsu Province, Anhui Province and Jiangxi Province, respectively. And more notably, the 2021 Meiyu precipitation anomalies were distributed in a Northwest-Southeast oriented band that is very rare. During the 2021 Meiyu period, the western Pacific subtropical high (WPSH) weakened and extended westward. An anticyclonic circulation anomaly in the lower troposphere was observed over eastern China, which was found to be related to the quasi-stationary wave trains propagating eastward from Hainan Island to the northwestern Pacific by vorticity budget analysis. And the Rossby wave source term played a critical role. In addition, the tropical Atlantic anomalous warming produced convergence anomaly over the eastern Mediterranean and excited quasi-stationary wave trains propagating downstream at the mid-latitudes in upper layers through a monsoon-desert-like teleconnection. It raised the geopotential height over eastern China and thus favored the westward extension of WPSH. These large-scale circulation anomalies generated the anomalous easterly winds along the eastern coast of China and the anomalous southwesterly winds from Guangxi Province to the middle and lower reaches of the Yangtze River. Similar features can be found in the anomalous water vapor transport and the water vapor converged in the YHRV. The above-mentioned reasons jointly caused the abnormally high precipitation anomaly and its unusual pattern in the 2021 Meiyu season. This study might provide a scientific basis and clues for understanding Meiyu precipitation anomalies and disaster prevention and mitigation.

KEYWORDS

2021 Meiyu season, Northwest-Southeast oriented rain belt, precipitation anomaly, western Pacific subtropical high, tropical Atlantic, atmospheric circulation anomalies

1 Introduction

Eastern China, the densely populated and the most developed region in China, is also one of the major crop production areas. Influenced by the East Asian summer monsoon (EASM), floods occur frequently in eastern China. In the summer of 1998, a devastating flood occurred on the Yangtze River, which caused over 3,000 deaths and disappearances, and resulted in 260 billion RMB in direct economic losses (Huang et al., 1998). During the summer of 2020, the middle and lower reaches of the Yangtze River suffered a persistent extremely heavy precipitation event (Liu et al., 2020; Takaya et al., 2020; Wang et al., 2021; Zhou et al., 2021) that resulted in more than 140 deaths or missing persons, and 76 billion RMB in direct economic losses (Ding et al., 2021). The summer flooding events in the Yangtze River Basin seriously affect the local people's life and socio-economic development.

The precipitation during the flood season of the Yangtze River Basin is closely tied to the Meiyu period from mid-June to mid-July (Ding et al., 2021). During the Meiyu period, the rain belt in eastern China is mainly located in the middle and lower reaches of the Yangtze River. The high values of average precipitation are situated in the southern Anhui Province and the junction of Anhui Province, Fujian Province, and Zhejiang

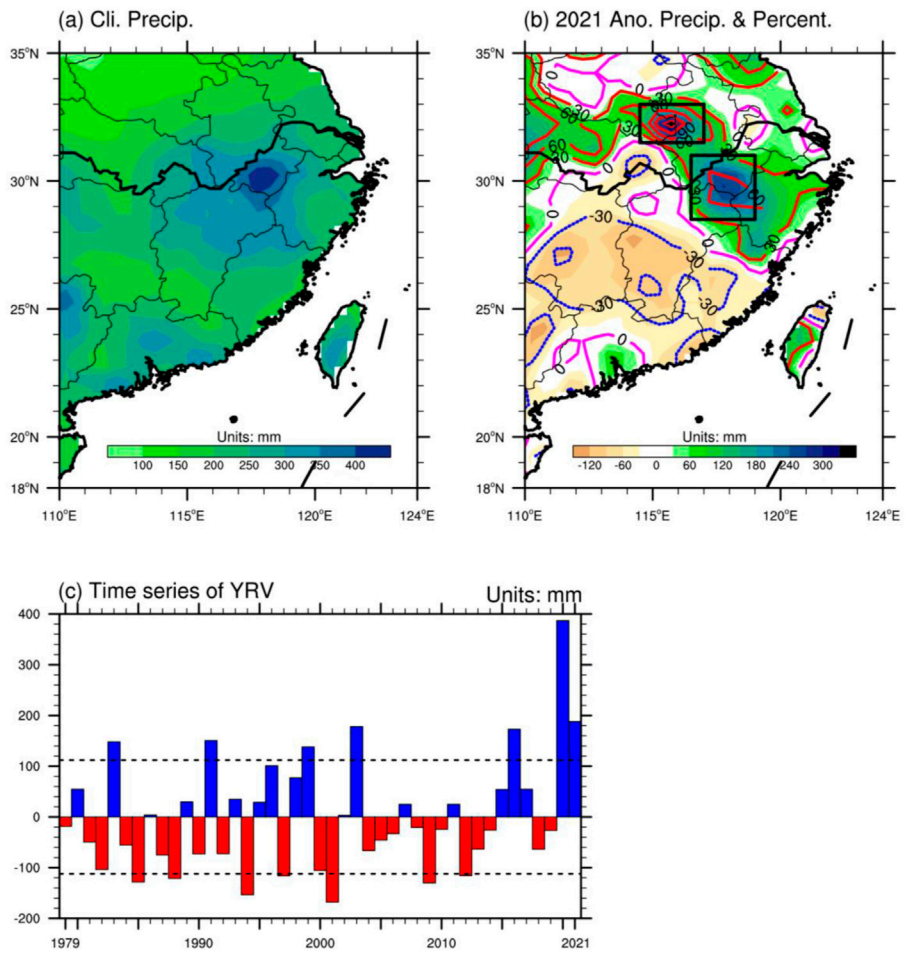

FIGURE 1
(A) 1979–2021 climatological mean precipitation (shading, units: mm) during Meiyu period (from 10 June to 11 July); **(B)** Anomalous precipitation (shading, units: mm) and percentage of precipitation anomaly (contours, units: %). The red solid (blue dotted) line represents a positive (negative) percentage, and the magenta solid line denotes zero values; **(C)** Time series of the regional mean [two rectangular regions showed in **(B)**] precipitation anomaly (units: mm) over Yangtze-Huaihe River Valley (YHRV) during Meiyu period.

Province, with an extreme value exceeding 400 mm (Figure 1A). The Meiyu precipitation over the Yangtze River Basin is usually distributed in a Southeast-Northwest or East-West oriented narrow belt. For instance, the Yangtze River basin suffered from persistent extreme heavy precipitation events in the 2020 Meiyu season, with an almost West-East oriented rain belt along the Middle and Lower of the Yangtze River (Liu et al., 2020; Takaya et al., 2020; Wang et al., 2021; Zhou et al., 2021). In 2021, the Meiyu season started on 10 June and ended on 11 July, lasting for 31 days. However, the spatial distribution of the precipitation anomaly in the 2021 Meiyu period exhibited an unusual Northwest-Southeast tilted feature, which was different from the typical Meiyu rain belt. There were two dominant precipitation anomaly centers. One was located at the junction of Anhui Province and Henan Province, and the extreme value of precipitation anomaly exceeded 300 mm and the corresponding precipitation anomaly percentage exceeded 150%. The other large value center was situated at the junction of Jiangsu Province, Anhui Province, and Jiangxi Province, with an anomalous precipitation extreme value greater than 240 mm and a precipitation anomaly percentage extreme value exceeding 60%. In the eastern Hubei Province, there were negative precipitation anomalies, with a minimal value of less than -90 mm and a precipitation anomaly percentage of less than −30% (Figure 1B).

The time series of regional-averaged precipitation (two rectangular areas shown in Figure 1B) during the Meiyu period in Yangtze-Huaihe River Valley (YHRV) for 1979–2021 show that there are not only significant interannual and interdecadal variations but also obvious long-term trends in Meiyu precipitation of YHRV (Figure 1C). The mean Meiyu precipitation in the YHRV is 289.3 mm for 1979–2021, with a standard deviation of 112.1 mm. The highest Meiyu total precipitation occurred in 2020 (Ding et al., 2021), with a precipitation anomaly of 386.9 mm. During the 2021 Meiyu period, the total precipitation in the YHRV is the second most in the past four decades. And the precipitation anomaly was 188.0 mm, about 1.7 standard deviations. It can be seen that during the 2021 Meiyu season, the precipitation anomaly in YHRV was positive. In addition, different from the zonal distribution of precipitation in typical Meiyu years, the precipitation anomaly was distributed in a southeast-northwest trending narrow area.

There are numerous factors influencing the Meiyu precipitation in YHRV. The EASM system and the Meiyu precipitation anomaly are closely linked (Ding, 2004; Zhang, 2015). El Niño-Southern Oscillation (ENSO) is an important air-sea coupling phenomenon in the tropics. It is found that ESNO can regulate the anomalies of the EASM system (Wang et al., 2000; Xie et al., 2009), and thus exerts important effects on Meiyu precipitation anomalies (Zhang et al., 1996; Xie et al., 2010; Jin et al., 2016). Northern Atlantic Oscillation (NAO; Walker and Bliss, 1932; Hurrell, 1995) can modulate the summer precipitation anomaly in East Asia by affecting the atmospheric teleconnection in the upper troposphere at mid-high latitudes (Wu et al., 2009; Jin and Guan, 2017; Liu et al., 2020). The tropical Atlantic sea surface temperature (SST) anomaly regulates the western Pacific subtropical high (WPSH) and then influences the Meiyu precipitation anomaly in YHRV (Jin and Huo, 2018). Furthermore, the soil moisture of the Indo-China Peninsula in early spring (Gao et al., 2020), the Arctic Oscillation (Gong et al., 2002), and the Antarctic Oscillation (Nan and Li, 2003) can also affect the precipitation during the flood season of YHRV.

To investigate the causes of the abnormal precipitation and its atypical pattern in 2021 Meiyu season, this study focuses on the atmospheric circulation anomalies associated with the WPSH and the tropical Atlantic SST. The remainder of this paper is organized as follows: Section 2 describes the data and methods used in this paper. The causes of precipitation anomaly and its spatial distribution in the 2021 Meiyu season are presented in Section 3. The conclusion and discussion are provided in Section 4.

2 Data and methods

The NCEP/NCAR daily reanalysis data with a horizontal resolution of 2.5°×2.5° (Kalnay et al., 1996) and daily precipitation data of Climate Prediction Center (CPC) with a horizontal resolution of 0.5°×0.5° for 1979–2021 are utilized (Chen et al., 2008). The Meiyu season in 2021 started on 10 June and ended on 11 July. Therefore, this period is taken as the Meiyu period to obtain the average value of each variable in this study. The COBE monthly SST data with a horizontal resolution of 1° × 1° are also obtained (Ishii et al., 2005). The long-term trends are deducted from all data except that the raw data are used in Figure 2B to show the contour line of 588 dagpm. The anomaly in this paper is defined as the deviation of the Meiyu period from the climatological mean for 1979–2021.

Linear vorticity equation (Kosaka and Nakamura, 2006) is utilized in Section 3.2 to analyze the vorticity budget:

$$S\underbrace{-\bar{u}_{\psi}\frac{\partial\zeta'}{\partial x}}_{ZA}\underbrace{-\bar{v}_{\psi}\frac{\partial\zeta'}{\partial y}}_{MA}\underbrace{-u_{\psi}'\frac{\partial\bar{\zeta}}{\partial x}-v_{\psi}'\frac{\partial\left(f+\bar{\zeta}\right)}{\partial y}}_{\beta}-R_{res}=0$$

where S denotes the linearized Rossby wave source (RWS) (Sardeshmukh and Hoskins, 1988):

$$S=-\nabla_{\mathrm{H}}\cdot\left\{\mathbf{u}_{\chi}'\left(f+\bar{\zeta}\right)\right\}-\nabla_{\mathrm{H}}\cdot\left(\bar{\mathbf{u}}_{\chi}\zeta'\right)$$

ZA and MA are mean zonal and meridional advection of anomalous vorticity, respectively. β term represents the horizontal advection of the mean absolute vorticity by anomalous winds. R_{res} denotes the residual term.

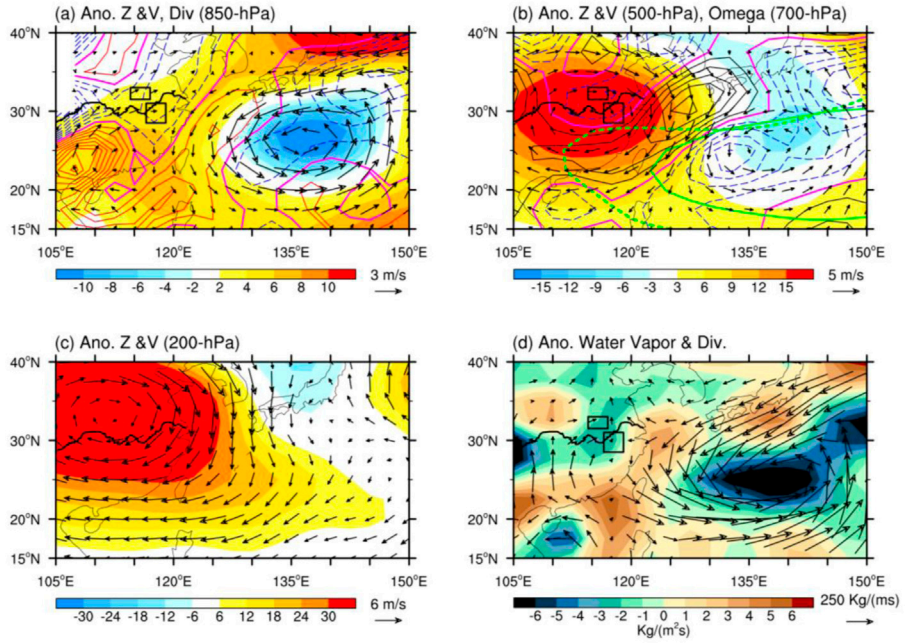

FIGURE 2
(A) Anomalous geopotential height (shading, units: gpm), divergence (contours, units: 10^{-6} s^{-1}) and winds (vectors, units: m/s) at 850-hPa during 2021 Meiyu period; **(B)** Anomalous geopotential height (shading) and winds (vectors) at 500-hPa, and anomalous vertical velocity (units: Pascal/s) at 700-hPa during 2021 Meiyu period; **(C)** Anomalous geopotential height (shading) and winds (vectors) at 200-hPa during 2021 Meiyu period; **(D)** Anomalous water vapor flux (vectors, units: kg/ms) integrated from surface to 300-hPa and its divergence (shading, units: kg/m^2s) during 2021 Meiyu period. The red solid/blue dashed line represents divergence/convergence anomaly, and the magenta solid line denotes zero values in **(A)**. The black solid line, magenta solid line, and blue dashed line in **(B)** represent positive, zero, and negative values, respectively. The green solid and dashed lines in **(B)** are the 588-dagpm contours for climate mean and for the 2021 Meiyu period, respectively.

3 Results

The precipitation anomaly during the Meiyu season in East Asia is closely related to the WPSH (e.g., Wang et al., 2000; Jin and Huo, 2018; Qian and Guan, 2020; Zhou et al., 2021). Therefore, from the perspective of local atmospheric circulation anomaly and SST anomaly, the following paper aims to explore the causes of the abnormal total precipitation over YHRV in 2021 Meiyu and the atypical pattern of precipitation anomaly.

3.1 Local atmospheric circulation anomaly

During the 2021 Meiyu season, a cyclonic anomaly and a negative geopotential height anomaly center appeared in the lower troposphere over the northwestern Pacific. And an anticyclonic anomaly and a positive geopotential height anomaly center can be seen from the South China Sea to the middle and lower reaches of the Yangtze River. Abnormal easterly winds prevailed from the Kuroshio extension area to the coastal region of eastern China. And the region from Guangxi Province to the middle and lower reaches of the Yangtze River was controlled by the anomalous southwesterly winds. These two branches of anomalous airflows converged in YHRV (Figure 2A). The convergence anomaly was observed in the middle and lower troposphere over YHRV (Figures 2A,B). Above circulation anomalies were conducive to the anomalous upward motion in the middle and lower troposphere (Figure 2B), and thus increased precipitation over YHRV.

Note that the negative geopotential height anomaly and cyclonic anomaly in the middle and lower troposphere were maintained over the northwestern Pacific (Figures 2A,B) during the 2021 Meiyu period. The regional average geopotential height anomaly within [20–30°N, 130–150°E] at 850-hPa was calculated as the WPSH index according to the scope of the area with the large absolute value of the negative geopotential height anomaly in the lower troposphere (Figure 2A). It is found that the WPSH index during the 2021 Meiyu period was −0.35 standard deviation, indicating that the intensity of WPSH during the 2021 Meiyu period was weaker than the climate mean. However, the location of WPSH showed by 588 dagpm isoline was approximately 10 longitudes west compared with its climate mean position. And it approximately extended to 112°E (Figure 2B) in the 2021 Meiyu period, which signs that the WPSH during this period was characterized by a relatively large range and a westward extension.

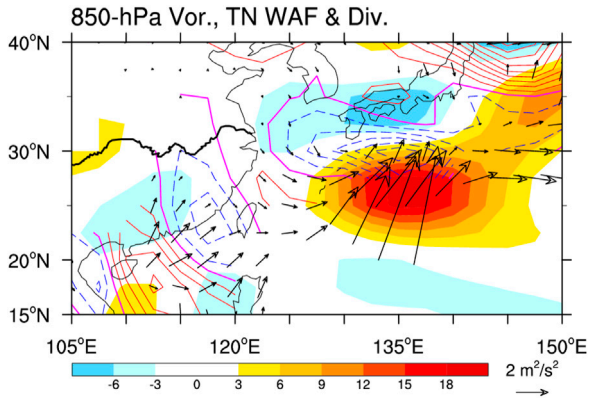

FIGURE 3
Anomalous vorticity (shading, units: 10^{-6}/s), wave activity flux (vectors, units: m^2/s^2) and its divergence (contours, units: 10^{-5} m/s^2) at 850-hPa during the 2021 Meiyu period. The red solid (blue dashed) line represents divergence (convergence), and the magenta solid line denotes zero values.

As shown in Figure 2C, a positive anomaly center of geopotential height anomaly and an anticyclonic anomaly appeared over eastern China and the adjacent ocean. Meanwhile, a positive geopotential height anomaly and an anticyclonic anomaly in the middle (500-hPa) and lower (850-hPa) troposphere were located over eastern China (Figures 2A,B), denoting that the anticyclonic circulation anomaly in eastern China showed an equivalent barotropic structure. However, in the middle and upper troposphere, the area to the north of YHRV was controlled by anomalous westerly winds (Figures 2B,C), suggesting that the positive precipitation anomaly and its unusual pattern over YHRV in the 2021 Meiyu season may also be related to the circulation anomaly in the upper troposphere at mid-latitudes. This will be further analyzed in the following.

The integrated water vapor flux anomaly and its divergence during the 2021 Meiyu period in Figure 2D show that there was anomalous anticyclonic (cyclonic) transport of water vapor over the south of the Yangtze River (northwestern Pacific). Due to the weakened WPSH, the abnormal water vapor was transported from the Kuroshio extension area to the middle and lower reaches of the Yangtze River along the northern side of WPSH (Figures 2A,B). The other branch of abnormal water vapor was transported from the South China Sea to the JHRV along the western side of WPSH, which was due to the expanded range of WPSH and the westward extension of the ridge point (Figure 2B). These two branches of anomalous water vapor converged in JHRV, and the convergence center was located over JHRV (the two rectangular boxes as shown in Figure 2D), which was primarily responsible for the excessive precipitation and the atypical spatial distribution of precipitation anomaly in JHRV.

3.2 Influence of quasi-stationary wave trains

To explore the mechanism of WPSH affecting the atypical precipitation anomaly pattern during the 2021 Meiyu period, we analyzed the Rossby wave energy dispersion in the lower troposphere over the western Pacific, followed by Takaya and Nakamura (2001).

The wave activity fluxes dispersed northeastward from the east of Hainan Island to the Kuroshio extension area (Figure 3), showing a typical great circle path (Hoskins and Karoly, 1981). The Rossby wave energy diverged over the east of Hainan Island, while converged over the south of the Yangtze River and the northwestern Pacific. The disturbances of Rossby wave energy in the above two regions enhanced the anticyclonic anomaly over eastern China and the cyclonic anomaly over the northwestern Pacific, respectively (Figure 2A). The anomalous positive vorticity (Figure 3) and convergence (Figure 2A) were observed over the east of Hainan Island, which manifests the airflow converged here and the quasi-stationary wave trains were excited and propagated northeastward.

To further study the structure of wave trains propagating from the east of Hainan Island to the northwestern Pacific, we diagnosed the vorticity budget using the linear vorticity equation according to Kosaka and Nakamura (2006).

Figure 4 shows the contributions of 850-hPa RWS, ZA, MA, and β terms to the East Asian circulation anomalies during the 2021 Meiyu period. It can be seen that the RWS term played a critical role in maintaining the low-level anticyclonic anomaly in the south of the Yangtze River (Figure 4A), and the MA term had a positive/negative contribution to the North/South of anticyclonic circulation anomaly (Figure 4C). The β term negatively contributed to the southeast of the anomalous anticyclone circulation (Figure 4D), while the ZA term slightly promoted to the anticyclonic anomaly (Figure 4B).

For the cyclonic anomaly in the northwestern Pacific, the RWS and ZA terms were positive anomalies (Figures 4A,B), facilitating the generation of low-level cyclonic vorticity anomaly in the northwestern Pacific. However, the MA and β terms showed negative anomalies in most of the northwestern Pacific (Figures 4C,D), which thus partially offset the contributions of RWS and ZA terms to the cyclonic vorticity anomaly in the lower troposphere of this region.

3.3 Influence of tropical Atlantic SST anomaly

Although the above analysis denotes that precipitation anomaly during the 2021 Meiyu period was closely related to the anomalous WPSH. However, previous studies indicated that the tropical Atlantic SST anomaly also exerts a dominant influence on East Asian climate anomalies (e.g., Rong et al.,

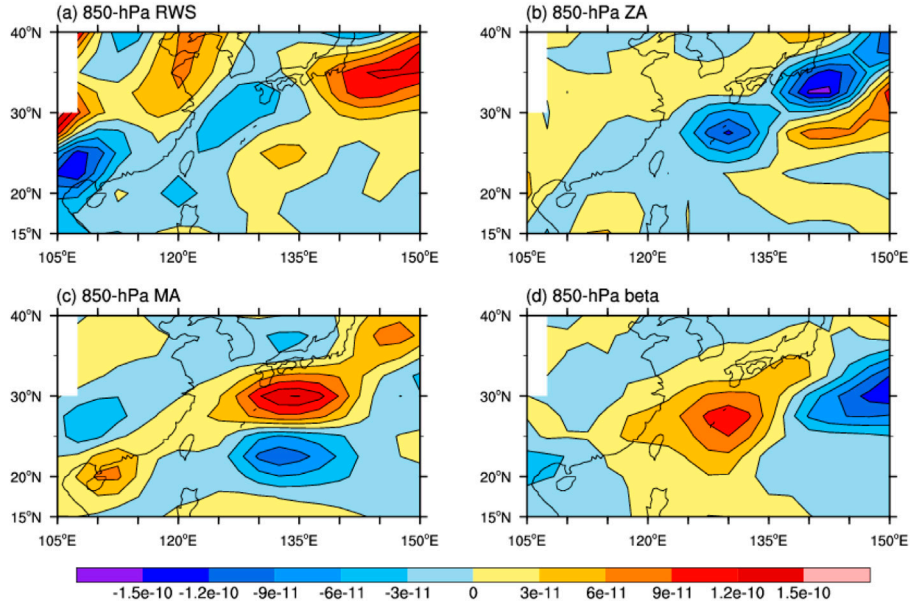

FIGURE 4
Anomalous **(A)** Rossby wave source (RWS), **(B)** mean zonal advection of anomalous vorticity (ZA), **(C)** mean meridional advection of anomalous vorticity (MA), and **(D)** β terms at 850-hPa during the 2021 Meiyu period (units: $10^{-12}/s^2$).

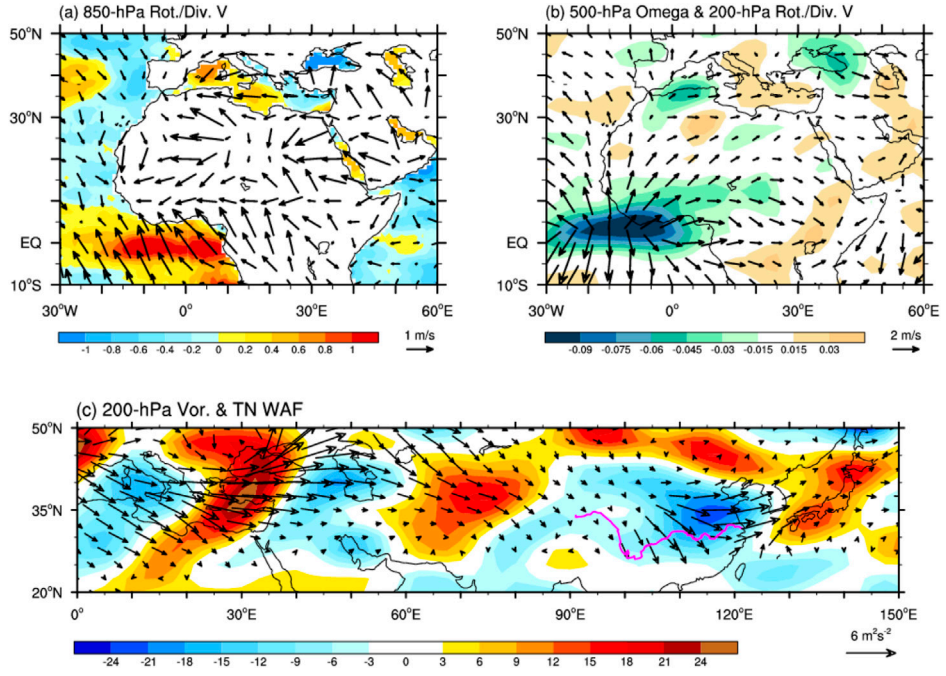

FIGURE 5
(A) Anomalous SST (shading, units: °C) and divergent wind (vectors, units: m/s) at 850-hPa; **(B)** Anomalous vertical velocity at 500-hPa (shading, units: Pascal/s) and divergent wind at 200-hPa (vectors, units: m/s); **(C)** Anomalous vorticity (shading, units: $10^{-6}/s$) and wave activity flux at 200-hPa (vectors, units: m^2/s^2) during the 2021 Meiyu period.

2010; Huo et al., 2015; Jin and Huo, 2018; Li et al., 2022). To elucidate whether the precipitation anomaly and atypical pattern of Meiyu rain in 2021 are associated with the tropical Atlantic SST anomaly, we also analyzed the tropical Atlantic SST anomaly and the related circulation anomaly in the 2021 Meiyu season (Figure 5).

During the 2021 Meiyu period, the SST anomaly in the tropical Atlantic [5°S–5°N, 20°W–10°E] was positive with the amplitude exceeding 1°C in most areas (Figure 5A). Such warm SST in the tropical Atlantic led to anomalous convergence in the lower troposphere (Figure 5A), and resulted in upward movement through Ekman pumping and anomalous divergence in the upper troposphere over this region (Figure 5B). The above circulation anomaly caused the anomalous convergence in the upper troposphere and anomalous downdraft over the eastern Mediterranean (Figure 5B), accompanied by the anomalous divergence at low levels (Figure 5A), which is similar to the monsoon-desert-like teleconnection (Rodwell and Hoskins, 1996). The quasi-stationary wave trains propagating downstream along the mid-latitudes were stimulated by the positive vorticity anomaly (Figure 5C) and the RWS term (Figure is not shown) in the upper troposphere over the eastern Mediterranean, which may be correlated to the "Silk Road pattern" (Lu et al., 2002; Enomoto et al., 2003; Guan and Yamagata, 2003; Ding and Wang, 2005). Note that the wave trains accumulated energy over the South of the Yangtze River (Figure 5C), which enhanced the energy disturbance in the upper troposphere, thus reinforced the geopotential height anomaly over this area (Figure 2C). These results imply that there was an equivalent barotropic feature in the anomalous anticyclone over eastern China, and the intensified geopotential height in upper troposphere was conducive to uplifting the low-level geopotential height and enhancing anticyclonic circulation anomaly (Figure 2A). Therefore, the WPSH significantly extended westward (Figure 2B) comparing to its climate mean location, which was beneficial to the positive precipitation anomaly and the atypical rain belt orientation during the 2021 Meiyu period.

4 Conclusion and discussion

This study analyzed the abnormally high total precipitation over YHRV during the 2021 Meiyu period, and the causes of the unusual Northwest–Southeast oriented Meiyu rain belt by utilizing NCEP/NCAR daily reanalysis, CPC daily precipitation and COBE monthly SST data from 1979 to 2021. The conclusion are summarized as follows:

(1) The 2021 Meiyu period lasted from 10 June to 11 July, a total of 31 days. The precipitation in YHRV was above abnormal with the regional average total precipitation of 477.3 mm. The precipitation anomaly reached 188.0 mm, which was approximately 1.7 standard deviation. In 2021, there were two precipitation centers in YHRV, which were located at the junction of Anhui Province and Henan Province and the junction of Jiangsu Province, Anhui Province, and Jiangxi Province, respectively. Different from the zonal distribution of typical Meiyu precipitation anomaly, the Meiyu rain belt in 2021 was oriented from Northwest to Southeast.

(2) During the 2021 Meiyu period, the intensity of WPSH was weaker and extended further westward, causing a low-level cyclonic anomaly in the northwestern Pacific and an anomalous anticyclone in eastern China. In the east of Hainan Island, a positive vorticity anomaly was located in the lower troposphere, which stimulated the quasi-stationary wave trains propagating from this area to the northwestern Pacific through eastern China. The energy disturbance in eastern China and the northwestern Pacific generated low-level anticyclonic and cyclonic circulation anomalies in the above two areas, respectively. To some extent, the ZA, MA, and β terms contributed to the vorticity anomaly in the above two regions, but the contribution of the RWS term was the most prominent.

(3) The westward extension of WPSH was also associated with anomalous warming in the tropical Atlantic. During the 2021 Meiyu period, the positive SST anomaly in the tropical Atlantic led to anomalous convergence in the lower troposphere and anomalous divergence in the upper troposphere. The convergence anomaly in the upper troposphere over the eastern Mediterranean was caused by the monsoon-desert mechanism, which excited the quasi-stationary wave trains propagating downward along the mid-latitudes. Thus, the geopotential height in eastern China was intensified, which was favorable for the westward extension of WPSH.

(4) The WPSH weakened and extended further westward in the 2021 Meiyu season, which caused the anomalous easterly winds prevailed over the coastal areas of eastern China and southwesterly winds prevailed from Guangxi to the middle and lower reaches of the Yangtze River. And the airflows converged in YHRV. Similar transport and convergence anomalies existed in water vapor anomalies. The above-mentioned local circulation anomalies were jointly conducive to the positive anomaly of total precipitation in YHRV and the atypical spatial distribution of the Meiyu rain belt in 2021.

In addition to the weaker intensity and westward extension of WPSH during the 2021 Meiyu period, did the WPSH show similar characteristics in other years? If so, was the precipitation anomaly and its pattern in YHRV similar to those in the 2021 Meiyu period? The tropical Atlantic SST anomaly can stimulate the wave trains propagating downstream along the mid-latitudes in the Mediterranean through a monsoon-desert-like teleconnection, and thus affect the downstream climate anomaly. To further verify this mechanism, we plan to conduct several sets of sensitivity experiments related to the tropical Atlantic SST anomaly by using the atmospheric general

circulation model in future studies. What are responsible for the weaker but westward extension of the WPSH in 2021? It is also worthy of further study.

Data availability statement

The original contributions presented in the study are included in the article, further inquiries can be directed to the corresponding author.

Author contributions

HL and GZ conceived and designed the study. HL, GZ, and ZM wrote the main manuscript text. All authors contributed to the discussion of the results and reviewed the manuscript.

Funding

This research is jointly supported by the National Key R&D Program of China (2019YFC1510201), the National Natural Science Foundation of China (Grants 42005016, 41905061), the Key Scientific Research Projects of Jiangsu Provincial Meteorological Bureau (KZ202203), the fund of "Key Laboratory of Atmosphere Sounding, CMA" (2021KLAS01M), and the Youth Project of Natural Science Foundation of Anhui Province (2008085QD190).

Conflict of interest

The authors declare that the research was conducted in the absence of any commercial or financial relationships that could be construed as a potential conflict of interest.

Publisher's note

All claims expressed in this article are solely those of the authors and do not necessarily represent those of their affiliated organizations, or those of the publisher, the editors and the reviewers. Any product that may be evaluated in this article, or claim that may be made by its manufacturer, is not guaranteed or endorsed by the publisher.

References

Chen, M., Shi, W., Xie, P., Silva, V. B. S., Kousky, V. E., Wayne Higgins, R., et al. (2008). Assessing objective techniques for gauge-based analyses of global daily precipitation. *J. Geophys. Res.* 113, D04110. doi:10.1029/2007JD009132

Ding, Q., and Wang, B. (2005). Circumglobal teleconnection in the northern hemisphere summer. *J. Clim.* 18, 3483–3505. doi:10.1175/JCLI3473.1

Ding, Y. H., Liu, Y. Y., and Hu, Z.-Z. (2021). The record-breaking mei-yu in 2020 and associated atmospheric circulation and tropical SST anomalies. *Adv. Atmos. Sci.* 38 (12), 1980–1993. doi:10.1007/s00376-021-0361-2

Ding, Y. H. (2004). "Seasonal march of the east Asian summer monsoon," in *East Asian monsoon*. Editor C.-P. Chang (Singapore: World Sci.), 3–53.

Enomoto, T., Hoskins, B. J., and Matsuda, Y. (2003). The formation mechanism of the Bonin high in August. *Q. J. R. Meteorol. Soc.* 129, 157–178. doi:10.1256/qj.01.211

Gao, C., Li, G., and Xu, B. (2020). Weakening influence of spring soil moisture over the Indo-China Peninsula on the following summer mei-yu front and precipitation extremes over the Yangtze River basin. *J. Clim.* 33 (23), 10055–10072. doi:10.1175/jcli-d-20-0117.1

Gong, D., Zhu, J., and Wang, S. (2002). Significant relationship between spring AO and the summer rainfall along the Yangtze River. *Chin. Sci. Bull.* 47, 948–952. doi:10.1360/02tb9212

Guan, Z., and Yamagata, T. (2003). The unusual summer of 1994 in east Asia: IOD teleconnections. *Geophys. Res. Lett.* 30, 1544. doi:10.1029/2002GL016831

Hoskins, B. J., and Karoly, D. J. (1981).The steady linear response of a spherical atmosphere to thermal and orographic forcing, *J. Atmos. Sci.*, 38, 1179–1196. doi:10.1175/1520-0469(1981)038<1179:TSLROA>2.0

Huang, Ronghui, Xu, Yuhong, Wang, Pengfei, and Zhou, Liantong (1998). The features of the catastrophic flood over the changjiang River basin during the summer of 1998 and cause exploration. *Clim. Environ. Res. (in Chinese)* 3 (4), 300–313.

Huo, L., Guo, P., Hameed, S. N., and Jin, D. (2015). The role of tropical Atlantic SST anomalies in modulating western North Pacific tropical cyclone genesis. *Geophys. Res. Lett.* 42, 2378–2384. doi:10.1002/2015GL063184

Hurrell, J. W. (1995). Decadal trends in the north atlantic oscillation: Regional temperatures and precipitation. *Science* 269, 676–679. doi:10.1126/science.269.5224.676

Ishii, M., Shouji, A., Sugimoto, S., and Matsumoto, T. (2005). Objective analyses of sea-surface temperature and marine meteorological variables for the 20th century using ICOADS and the kobe collection. *Int. J. Climatol.* 25, 865–879. doi:10.1002/joc.1169

Jin, D., and Guan, Z. (2017). Summer rainfall seesaw between Hetao and the middle and lower reaches of the Yangtze River and its relationship with the North Atlantic Oscillation. *J. Climate* 30, 6629–6643. doi:10.1175/JCLI-D-16-0760.1

Jin, D., and Huo, L. (2018). Influence of tropical Atlantic sea surface temperature anomalies on the East Asian summer monsoon. *Q. J. R. Meteorol. Soc.* 144, 1490–1500. doi:10.1002/qj.3296

Kalnay, E., Kanamitsu, M., Kistler, R., Collins, W., Deaven, D., Gandin, L., et al. (1996). The NCEP/NCAR 40-year reanalysis project. *Bull. Amer. Meteor. Soc.* 77, 437–471. doi:10.1175/1520-0477(1996)077<0437:tnyrp>2.0.co;2

Kosaka, Y., and Nakamura, H. (2006). Structure and dynamics of the summertime Pacific-Japan teleconnection pattern. *Q. J. R. Meteorol. Soc.* 132, 2009–2030. doi:10.1256/qj.05.204

Li, H., Sun, B., Wang, H., and Yuan, X. (2022). Joint effects of three oceans on the 2020 super mei-yu. *Atmospheric and Oceanic Science Letters* 15, 100127. doi:10.1016/j.aosl.2021.100127

Liu, B., Yan, Y., Zhu, C., Ma, S., and Li, J. (2020). Record-breaking Meiyu rainfall around the Yangtze River in 2020 regulated by the subseasonal phase transition of the North Atlantic Oscillation. *Geophysical Research Letters* 47, e2020GL090342. doi:10.1029/2020GL090342

Lu, R.-Y., Oh, J.-H., and Kim, B.-J. (2002). A teleconnection pattern in upper-level meridional wind over the North African and Eurasian continent in summer. *Tellus* 54A, 44–55. doi:10.3402/tellusa.v54i1.12122

Nan, S., and Li, J. (2003). The relationship between the summer precipitation in the Yangtze River valley and the boreal spring Southern Hemisphere annular mode. *Geophys. Res. Lett.* 30, 2266. doi:10.1029/2003GL018381

Qian, Daili, and Guan, Zhaoyong (2020). Principal modes of the western pacific subtropical high anomaly and their possible impacts on precipitation in east Asia during meiyu season (in Chinese). *Journal of the Meteorological Sciences* 40 (5), 649–660.

Rodwell, M. J., and Hoskins, B. J. (1996). Monsoons and the dynamics of deserts. *Q. J. R. Meteorol. Soc.* 122, 1385–1404. doi:10.1002/qj.49712253408

Rong, X., Zhang, R., and Li, T. (2010). Impacts of Atlantic sea surface temperature anomalies on Indo-East Asian summer monsoon–ENSO relationship. *Chin. Sci. Bull.* 55, 2458–2468. doi:10.1007/s11434-010-3098-3

Sardeshmukh, P. D., and Hoskins, B. J. (1988).The generation of global rotational flow by steady idealized tropical divergence, *J. Atmos. Sci.*, 45, 1228–1251. doi:10.1175/1520-0469(1988)045<1228:TGOGRF>2.0

Takaya, K., and Nakamura, H. (2001).A formulation of a phaseindependent wave-activity flux of stationary and migratory quasigeostrophic eddies on a zonally varying basic flow, *J.Atmos. Sci.*, 58, 6082–6627. doi:10.1175/1520-0469(2001)058,0608:AFOAPI.2.0

Takaya, Y., Ishikawa, I., Kobayashi, C., Endo, H., Ose, T., Walker, G. T., et al. (2020). Enhanced meiyu–baiu rainfall in early summer 2020: Aftermath of the 2019 super IOD event. Geophys. Res. Lett., 47. *World weather V. Mem. Roy. Meteor. Soc.*, 4, 53–84.

Walker, G. T., and Bliss, E. W. (1932). World weather V. *Mem. R. Meteorol. Soc.* 4 (36), 53–84.

Wang, B., Wu, R., and Fu, X. (2000).Pacific–East Asian teleconnection: How does ENSO affect East Asian climate? *J. Climate*, 13, 1517–1536. doi:10.1175/1520-0442(2000)013<1517:PEATHD>2.0

Wang, X., Guan, Z., Jin, D., and Zhu, J. (2021). East Asian summer monsoon rainfall anomalies in 2020 and the role of Northwest Pacific anticyclone on the intraseasonal-to-interannual timescales. *JGR. Atmospheres* 126, e2021JD034607. doi:10.1029/2021JD034607

Wu, Z. W., Wang, B., Li, J. P., and Jin, F. F. (2009). An empirical seasonal prediction model of the East Asian summer monsoon using ENSO and NAO. *J. Geophys. Res.* 114, D18120. doi:10.1029/2009JD011733

Xie, S.-P., Hu, K., Hafner, J., Tokinaga, H., Du, Y., Huang, G., et al. (2009). Indian Ocean capacitor effect on Indo–western Pacific climate during the summer following El Niño. *J. Clim.* 22, 730–747. doi:10.1175/2008JCLI2544.1

Xie, S. P., Du, Y., Huang, G., Zheng, X. T., Tokinaga, H., Hu, K., et al. (2010). Decadal shift in el niño influences on indo–western pacific and East Asian climate in the 1970s. *J. Clim.* 23, 3352–3368. doi:10.1175/2010jcli3429.1

Zhang, R. (2015). Changes in East Asian summer monsoon and summer rainfall over eastern China during recent decades. *Sci. Bull. (Beijing).* 60, 1222–1224. doi:10.1007/s11434-015-0824-x

Zhang, R., Sumi, A., and Kimoto, M. (1996). Impact of el niño on the east asian monsoon: A diagnostic study of the '86/87 and '91/92 events. *Journal of the Meteorological Society of Japan.* 74, 49–62. doi:10.2151/jmsj1965.74.1_49

Zhou, Z.-Q., Xie, S.-P., and Zhang, R. (2021). Historic Yangtze flooding of 2020 tied to extreme Indian Ocean conditions. *Proc. Natl. Acad. Sci. U. S. A.* 118, e2022255118. doi:10.1073/pnas.2022255118

frontiers | Frontiers in Earth Science

TYPE Original Research
PUBLISHED 08 February 2023
DOI 10.3389/feart.2023.1037826

OPEN ACCESS

EDITED BY
Hans Von Storch,
Helmholtz Zentrum Hereon, Germany

REVIEWED BY
Qianrong Ma,
Yangzhou University, China
Lidia Gaslikova,
Helmholtz Centre for Materials and Coastal Research (HZG), Germany

*CORRESPONDENCE
Stephen Outten,
stephen.outten@nersc.no

SPECIALTY SECTION
This article was submitted to Atmospheric Science,
a section of the journal
Frontiers in Earth Science

RECEIVED 06 September 2022
ACCEPTED 23 January 2023
PUBLISHED 08 February 2023

CITATION
Wolf T, Outten S, Mangini F, Chen L and Nilsen JEØ (2023), Analysis of storm surge events along the Norwegian coast.
Front. Earth Sci. 11:1037826.
doi: 10.3389/feart.2023.1037826

Analysis of storm surge events along the Norwegian coast

Tobias Wolf[1], Stephen Outten[1]*, Fabio Mangini[1], Linling Chen[2] and Jan Even Øie Nilsen[3]

[1]Nansen Environmental and Remote Sensing Center and Bjerknes Centre for Climate Research, Bergen, Norway, [2]Department of Earth Science, University of Bergen, Bergen, Norway, [3]Institute of Marine Research and Bjerknes Centre for Climate Research, Bergen, Norway

Observed extreme sea levels are caused by a combination of extreme astronomical tide and extreme storm surge, or by an extreme value in one of these variables and a moderate value in the other. We analyzed measurements from the Norwegian tide gauge network together with storm track data to assess cases of extreme sea level and storm surges. At most stations the highest storm surges only coincided with moderate astronomical tides and *vice versa*. Simultaneously the extreme storm surges often only coincided with moderate storm intensities. This opens for the possibility of flooding events, where extreme tides and storm surges co-occur, and which could exceed existing sea level records and national building standards. This study also raises the possibility to assess extreme sea level return values as a three-variable system, treating separately the astronomical tide, storm location and storm intensity, instead of the one- or two-variable approach currently used.

KEYWORDS

sea level, storm surge, tide gauge, flooding, compound extreme event

1 Introduction

Because of the potential for flooding of highly urbanized coastal areas with both dense, expensive infrastructure and high population density, storm-surges (StSs) are considered an economic and safety hazard (Munich RE, 2019). This risk is projected to increase dramatically due to future sea-level rise and socio-economic developments (Hallegatte et al., 2013). For necessary climate adaptation planning by decision makers, an in-depth knowledge of the mechanisms steering the heights of StSs is thus relevant. This study assesses the interplay between astronomical tides (ATs) and StSs based on local sea level (SL) measurements from tide gauges (TGs) along the Norwegian coastline, together with storm track data over the North Atlantic region.

Typically, extreme water levels are estimated in terms of return levels. Return levels are the water levels that will be exceeded with a specific very low probability in a given year, approximately corresponding the occurrence of the event once in a set number of years. 100 years return event, for instance, would be a water level occurring in a single year with the probability corresponding to it occurring once in 100 years. These are calculated with different methods applying extreme value statistics (Haigh et al., 2010). So-called direct methods use extreme value analysis of SL observations of between a few decades to 100 years length in order to calculate the return levels (e.g., Simpson et al., 2017). In Norway, a slightly unusual direct method, the average conditional exceedance rate (ACER) statistical method (Næss and Gaidai, 2009) is found to be the most suitable for estimating extreme sea level return periods (Haug, 2012; Skjong et al., 2013). The method has also been successfully adopted for calculating sea level allowances together with projections of future sea level rise (Simpson et al., 2015; 2017).

The problem with direct approaches is that the interaction between ATs and StSs is not considered in the calculation of the return levels. In the comparatively short measurement

records extreme SL measurements could be biased by the fact that StSs may have occurred during comparatively low ATs, while combinations of high ATs and StSs are possible over longer time spans. The so-called indirect methods are specifically designed to mitigate this shortcoming by using separate statistics for ATs and StSs and considering the overlap of both phenomena. It is thus argued that shorter SL records can be used for a more precise estimation of return values since all so far occurred StS heights are considered and ATs can be predicted through harmonic functions (Haigh et al., 2010). In Norway, as in many countries around the world, return levels based on direct measurements are the basis of the national building standards, regulating at what height infrastructure can be built.

Recent studies using TG observations have focused on the relevance of the so-called "near misses" (Dangendorf et al., 2016; Haigh et al., 2016). These are situations where an extreme StS coincides with an AT that is below the highest astronomical tide, i.e. the elevation of the highest predicted astronomical tide expected to occur at a specific tide station based on any combination of astronomical conditions. While the occurrence of a moderate AT in combination with an extreme StS can lead to record-breaking sea levels, the co-occurrence with the highest astronomical tide could have made the flooding far more devastating. This can also lead to a significant shift in the expected return levels, highlighting the instability of SL extreme value statistics (Dangendorf et al., 2016). Moreover, dynamical modeling based studies also showed (potential) effects of various constellations of storms and tidal phases on historical (Horsburgh et al., 2021) and on future water level extreme events (Grabemann I., et al., 2020). In this work, with a special focus on the Norwegian coastline, we address the question of whether or not there is a need to assess the components that give rise to extreme sea level events independently? We also address the question of how storm tracks and the passage of storms shape the observed extreme sea level events?

Because of their limitations, statistical techniques can be conveniently complemented by deterministic approaches. Deterministic approaches are designed to identify the drivers of extreme sea-level events in coastal areas (Ganske et al., 2018), and they are useful from a coastal adaptation perspective because they quantify the impact of possible, though highly unlikely, extreme sea-level events in coastal areas (Ganske et al., 2018; Wei et al., 2019; Horsburgh et al., 2021). A notable example is presented in Horsburgh et al., (2021). They showed that variations in the intensity and position of storm Xavier, which hit northern Europe in December 2013, could have led the sea level to exceed the observed values by up to 1.5 m at some locations.

In this paper, we adopt a deterministic approach by focusing on the overlap between ATs and StSs for the generation of SL extremes. In addition, we attempt to understand the relevance of single storms on the extremes caused. Our findings suggest that the two-parameter system treated with the indirect measurements may still underestimate the maximum possible combination of ATs and StSs. The StS itself is dependent both on the location and the strength of the passing storm systems. Thus, it may be useful to treat the two-parameter system of ATs and StSs rather as a three-parameter system of ATs, storm location, and strength.

The manuscript is structured as follows: Section 2 describes the data and methods, while the results are presented in Section 3. Section 4 presents the discussion and conclusions, setting the results into the perspective of the existing literature.

2 Data and methods

2.1 Tide gauge measurements

For the analysis of the SL height along the Norwegian coast we used data from 21 of the 23 permanent Norwegian TGs operated by the Norwegian Mapping Authority (http://api.sehavniva.no/tideapi_no.html). We use the entire available record for each of the TGs with a 10 min measurement interval (Figure 1). This dataset contains observed SLs and the predicted ATs. Two permanent TGs are not included in this study: Oslo (too short high-frequency data record) and Mausund (large gap in the record). For each TG we detrended the SL and AT by removing the respective linear trend of the entire record length. The maximum difference between the original and the processed SL was small (6.2 cm at Narvik and below 4.3 cm elsewhere). The maximum difference for AT was less than 1 cm at any station. In Norway the mean SL rise has so far been much smaller than for other countries, largely due to the glacial isostatic adjustment after the melting of the Fennoscandinavian ice sheet. For some of the stations the mean SL trend is negative, while the maximum was around 1 mm/yr for the 1960–2010 period (Richter et al., 2012). We detrended AT (no mean trend since calculated from harmonic analysis) in order to make it fully comparable to the SL. The AT could be in a different phase at the beginning and end of the datasets, creating a small apparent trend in both datasets.

2.2 Skew surges

Apart from land motion, the observed SL consists of three contributions: mean sea-level, astronomical tide, and weather effects (e.g. Haigh et al., 2016). To quantify the weather effect on the SL we use the frequently applied concept of skew surges (SkS) (e.g. de Vries et al., 1995). The SkS is the difference between the maximum observed SL and the maximum predicted AT during each tidal cycle irrespective of their temporal offset. The concept of SkS is commonly preferred over that of non-tidal residual, which is the difference between the observed SL and the predicted AT each instant in time, because it helps better assess the impact of storms in coastal areas. Coastal dwellers are indeed concerned by the residual relative to the maximum in sea level that would be experienced in the absence of a meteorological forcing (e.g., Horsburgh et al., 2010; Pugh and Woodworth, 2014) a high non-tidal residual would have a little flooding effect if the corresponding observed SL exceeded the maximum high tide by only a few centimeters.

The mean SL is influenced by two factors, the mean SL over a longer averaging period, e.g. monthly means, and of a possible long-term trend (see Section 2.1). For simplicity we will not discuss separately the longer-term trend, as it can have multiple causes, such as long-term ocean variability or changes in the inflow into ocean basins from large-scale weather modes (e.g., Richter et al., 2009, 2012). These possible contributions are thus part of the diagnosed SkS heights.

In our analysis of the TG data we reduced the 10 min datasets to full tidal cycles (approximately 12 h). We used the full 10-min dataset for the identification of the SkS values. For this we first identified the AT cycles searching for all n AT maxima at points in time $\{T_1, \ldots, T_n\}$

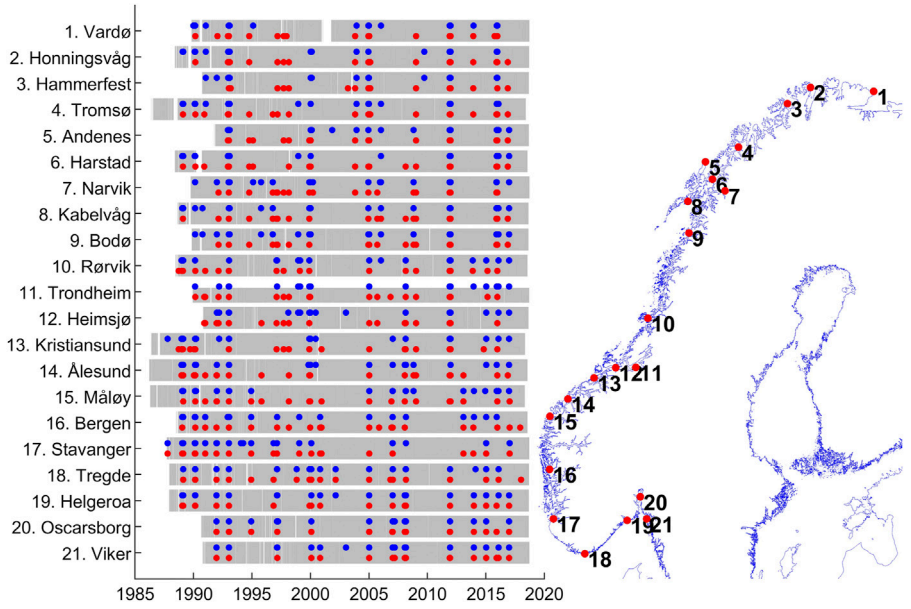

FIGURE 1
Overview over the 21 permanent tide gauges. Left: Data availability for each TG in grey. Cases of extreme sea level and extreme skew surge are marked with red and blue dots, respectively. Right: Location of the TGs along the Norwegian coastline (from EEA, 2018).

for each dataset. To be identified as a maximum a peak's prominence must be at least 5 cm. We calculated the SkSs for each tidal cycle defined as lasting from time $(T_{k-1}+T_k)/2$ until $(T_{k+1}+T_k)/2$, with $k \in \{2, \ldots, n-1\}$. Tidal cycles are therefore not defined as equally spaced 12 hourly time intervals but as the time intervals between tidal minima. The remaining analysis is done on this dataset with reduced frequency. Each time step is now defined at the maximum of the respective tidal cycle. For the identification of extreme cases of SLs and SkSs we used a 99.9th percentile threshold, high enough to give a manageable number of cases. Finally, we applied a criterion that any two distinct extremes must be separated by at least four tidal cycles (≈48 h).

2.3 Storm tracks

For the analysis of the effect of cyclones on the SL, we used the storm track dataset described in Chen et al., (2016) for the period between 1979 and 2013. This dataset is based on the relative vorticity at 850 hPa in the ERA-Interim reanalysis (Dee et al., 2011). A storm track here refers to the path of a single storm described by the location of the storm center points and its intensity described by the 850 hPa relative vorticity at the storm's center point with a 6 hourly temporal resolution using the TRACK algorithm developed by Hodges (1999). To be more comparable to the higher temporal resolution TG dataset, we increased the temporal resolution of the identified storm tracks to 1.5 h using linear interpolation of the 6-h latitude-longitude positions. This was necessary since the storm center points should be related to specific SL extremes in the approximately 12 hourly dataset (reduced from 10 min data as described in Section 2.2 above). The storm centers and SL extremes would have been mismatched if the storm track dataset were used in its original 6 hourly format.

3 Results

3.1 Interplay between the different components creating high sea levels and skew surges

We would like to better understand the relative contribution of SkS and AT to the generation of SL extremes along the Norwegian coast. Figure 1 marks the cases exceeding the 99.9th percentile of the SLs and SkSs. A clustering appears to exist for some cases affecting the entire Norwegian coast with both extremes in SL and SkS. However, closer inspection revealed that these were often cases that occurred within a few weeks of each other and not at the same time. Only the case during January 1993 affected the entire Norwegian coast with extreme SL. Only the TGs south of Heimsjø were affected by an extreme SkS simultaneously, and no single case exists where all TGs were affected by extreme SkSs simultaneously. Investigating the January 1993 case revealed, at the Bergen TG for example, that the AT exceeded the 97.0 percentile of all AT maxima and reached 87.6% of the highest astronomical tide, while the SkS exceeded the 99.9 percentile but only reached 68.9% of the highest observed SkS. In short, a rare and high AT coincided with a very rare but only moderately high SkS at the Bergen TG. Further north the storm's relative influence weakened compared to other StSs at the respective TGs. One possible explanation of this is the propagation of the storm along the entire Norwegian coast, causing extreme SLs together with the very high AT. Other cases only affected parts of the TG network, suggesting that the storms' influences in those cases were more confined to only parts of the Norwegian coast.

Different combinations of AT and SkSs are assessed in more detail in Figure 2. In this figure, we have isolated the 99.9th percentile of SL events (left column for each TG, black), and the 99.9th percentile of extreme SkS events (right column for each TG, red). Each event is

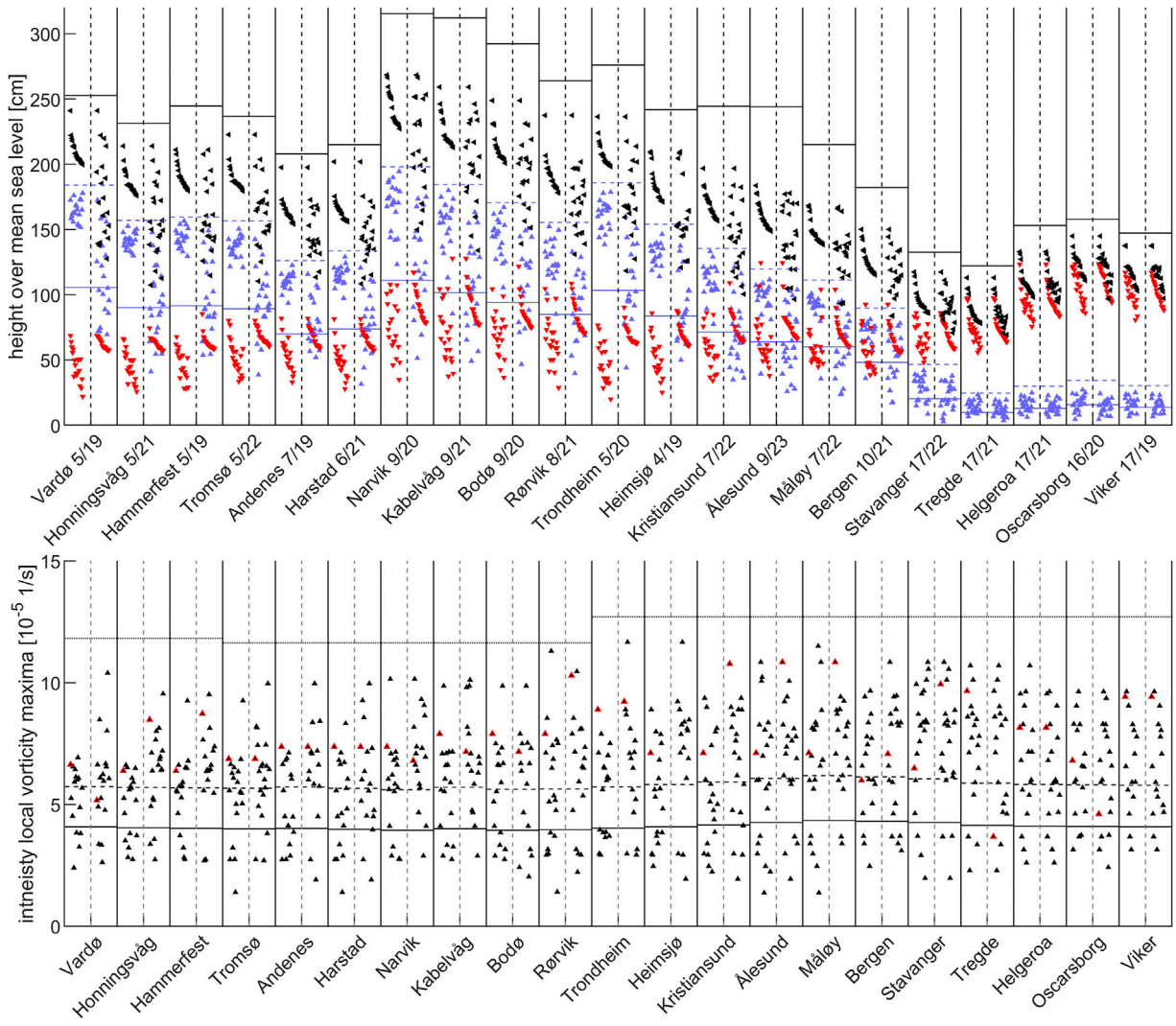

FIGURE 2
Upper panel: Observed SL maxima (black), SkS maxima (red) and AT maxima (blue) during each tidal cycle. Left and right columns for each TG show the 99.9th percentile of the SL maxima and SkSs, respectively. Numbers after the station names state the number of cases, where the 99.9th percentile is exceeded for both SkSs and the observed SL during a period ± 48 h from each other/the total number of cases, where the 99.9th percentile is exceeded for SkSs only. Blue lines mark the mean (solid) and maximum observed (dashed) AT for each TG. Black lines mark the maximum combination of AT and SkS irrespective of temporal overlap. Lower panel: Storm intensities of the nearest center point for the same cases as above. The cases with the highest observed SL (left column) and SkS (right column) are marked in red. The black lines mark the mean (solid), mean + 1 standard deviation (dashed), and maximum (dotted) storm track intensity within 500 km from each TG.

shown with its SL (black), AT (blue), and SkS (red), thus any single SL event is shown with AT and SkS which sum up to produce that SL. Along the coast the extreme SLs follow high ATs. One exception is in the area near the amphidromic point in Southern Norway (Gjevik, 2009; Simpson et al., 2015), where there are hardly any tides, as seen in the last five stations on the right side of Figure 2. Northward from Stavanger, ATs and extreme SLs generally increase, with a slight reversal between Narvik and Harstad (across the Lofoten islands) only to increase again further northward. A division into approximately the same regions is also seen for SkSs, which are strong in the southeast, increasing in the west (after a slight decrease), and rather similar levels among the stations north of Narvik and the Lofoten archipelago. The distinct change in the tidal regime across the Lofoten islands is caused by the local bathymetry and described in more detail in Moe et al., [2002].

For all TGs with maximum ATs as high as or higher than the maximum SkSs, less than half of the extreme SkSs coincide with extreme SLs, indicating that most of the extreme SL came from the AT. ATs and SkSs only overlapped in magnitude consistently for the stations in Southern Norway (c.f. Kristiansund to Bergen). As an example, the maximum AT Narvik is the highest of all TGs and so is the maximum observed sea level. During cases with extreme SL, the AT reached a maximum of 175 cm (highest blue point, left column). The maximum AT in the entire dataset reached 180 cm (where the highest astronomical tide is 180 cm). Simultaneously, the maximum SkS was 122 cm (highest red point, right column) but the highest SkS during any of the cases of extreme SL was 111 cm (highest red point, left column), which is more than 10 cm lower than the highest SkS. In fact, the case with the highest SkS had a maximum AT of only 81 cm, leading the SL to be only 203 cm or 64 cm lower than the highest SL.

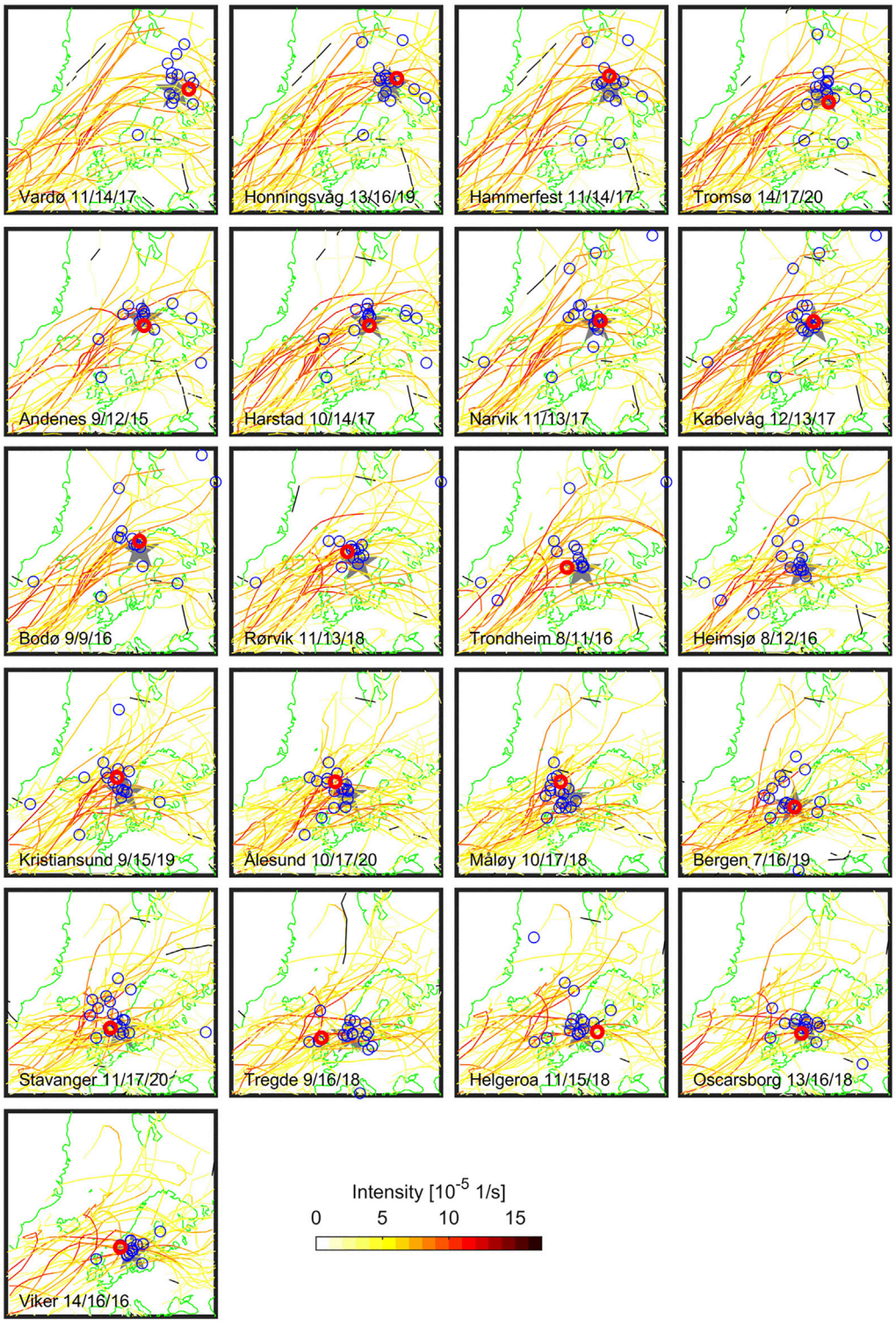

FIGURE 3
Storm tracks for the 99.9th percentile SkS for each TG. Blue rings mark the nearest storm center point at the time of each SkS maximum (occurred ± 6 h of the maximum AT). Red rings mark the center points for the highest SkSs in the dataset. Storm track colors indicate their intensity. The location of TGs is marked with a grey star. The numbers next to the station name give the number of SkSs with storm center points closer than 500 km/1,000 km/all cases.

This illustrates the situation that is found at most of the stations, that the cases with the highest SkSs typically coincided with moderately high ATs, while the cases with the highest SLs only coincided with moderately high SkSs. The numbers after the TG names in Figure 2 reinforce this conclusion by showing how many of the cases of extreme SL occurred with extreme SkSs. For example, at the first station at

Vardø, 19 cases were identified as having SL at the 99.9th percentile, but only 5 of these events had SkSs which were also at the 99.9th percentile, meaning 14 extreme SL cases occurred without an extreme in SkS.

Often, this mismatch between AT and SkS is considered expected due to the inverse relationship between the water depth and the SkS height for shallow shelves. However, under these assumptions a consistent time-lag should exist between the maxima of AT and SL, and along the Norwegian coast, no such time-lag exists (see Supplementary Material). It is therefore plausible for any AT to occur with any SkS, as was shown by Williams et al., (2016) for the UK coast, thus opening the possibility for far more extreme SL events to occur given the right combination of AT and SkS.

Assuming the highest observed SkS at Narvik would have coincided with the highest astronomical tide, this would have led to a sea level of 320 cm or 53 cm higher than the maximum observed SL (Figure 2, black solid line). A similar picture is visible for most TGs with the highest astronomical tide as high as or higher than the maximum observed SkSs. Thus, the solid black lines for each TG in Figure 2 indicate the SL that would have been reached if the highest SkS had occurred with the highest astronomical tide, and their height above the highest black mark for each TG indicates how much more the extreme SL could have been if the two had co-occurred. This is based purely on the observations of the past 30–35 years. Exceptions are Andenes, Harstad, Tromsø and Vardø, where the maximum SL nearly reached the maximum possible combination of ATs and SkSs. A different picture is also visible for the stations in Southern Norway, e.g., Stavanger onwards. Here AT is very low and thus, the combination with the highest SkSs and the highest astronomical tides is not far above the maximum observed SL.

So far, we only treated the maximum possible SL as a system with two factors, AT and SkS. However, the SkS itself is influenced by numerous effects, primarily the effect of storm systems near the TG. Storms exert a direct effect on the sea level through both the inverse barometric effect and the wind forcing, and upon meeting the coastline as a barrier for the water they form storm surges. Other factors that we neglect in this work include for example waves from storm systems far away from TGs (e.g. Benoit Cushman-Roisin & Beckers, 2011; Dangendorf et al., 2016). Based on the inverse barometric effect, a storm's impact on the SkSs can be described by the strength of a storm system and the location of the storm itself. The lower panel of Figure 2 shows the strength of the storms that were closest to each TG during extreme SLs or SkSs. Intensity does not seem to vary much along the coastline, but there is a clear difference north and south of Trondheim/Rørvik with slightly higher maxima occurring near the TGs in the southern half of the Norwegian coast. Extreme (exceeding the 99.9th percentile) SLs or SkSs rarely coincided with the maximum nearby observed storm intensity and in many cases even coincided with storms of below average intensity. Even the single cases with the highest SL or SkS did not coincide with particularly high storm intensities.

Again, using Narvik as an example, the storm with the highest intensity near to Narvik in the entire dataset had an intensity that is around 42% stronger than the nearest storm during the case with the highest SkS. While the effect of the storm intensity on SkS may not be linear, it is safe to say that a such strong increase in intensity may lead to a stronger SkS assuming all other factors (e.g., location) unchanged.

3.2 Storm track locations

Figure 3 shows the storm tracks during extreme SkSs. From this, TGs may be separated into two categories, all TGs north of and including Trondheim and those south of and including Heimsjø. The storm tracks temporally coinciding with extreme SkSs at the northern Norwegian TGs mostly pass northeastward through the North Atlantic Ocean at some distance along the Norwegian coast. Eventually they 'glance' the coast, impacting the respective TGs before the storms pass on into the Barents Sea. The storm tracks coinciding with extreme SkSs at the southern Norwegian TGs more often cross Norway at the latitude of the respective TGs. One exception to this is the northernmost TG, at Vardø. Storms connected to extreme SkSs there must intersect Norway since Vardø is sheltered from the North Atlantic and thus the typical storm tracks by Northern Norway.

For most TGs, the nearest storm track centers temporally coinciding with extreme SkSs are less than 500–1,000 km away from each TG. The centers for the northern TGs are either located to the north or west of the stations in accordance with a storm traveling along the Norwegian coastline, meaning these storms are mostly glancing the coast at the respective stations. For the southern Norwegian TGs, the center points are often distributed around the stations or directly atop of them. Most of the storm tracks show weak to moderate intensities, consistent with the analysis of the intensity of the center points closest to the observed extreme SkSs in Figure 2.

The center point positions during the highest SkSs for each TG are marked with red circles in Figure 3. They are mostly located close to the TGs, suggesting that both the barometric effect and the wind forcing played a role for the height of the related StSs. For Heimsjø no storm track could be found, since the highest SkS occurred later than the extent of the storm track record. For Narvik the closest center point during the highest SkS was located over Svalbard. This storm likely did not directly trigger an extreme SL at Narvik due to the large distance of its center from the TG. We do not know why this SkS reached such a high level. Possibly a cyclone or a polar low could have been missed by the TRACK algorithm or SkS could have been caused purely by other phenomena.

4 Discussion and conclusion

The proposed independence of StSs from ATs motivating our study is in agreement with the study by Williams et al., (2016). They propose such independence for most of the TGs along the U.K. coast. This would enable a simple convolution of the return frequencies for extreme StSs and extreme ATs for assessment of the return frequencies for plausible extreme SL events outside of the SL statistics observed. Furthermore, the TGs at Andenes, Harstad, Tromsø and Vardø confirm this hypothesis, since very high ATs coincided with very high StSs.

As an example of what this implies, at the Bergen TG the same distribution of SkS events but a re-sampling of the single incidences leads to a maximum possible SL extreme of 182 cm (Figure 2, horizontal solid black line in Bergen column). Such a SL exceeds the currently highest observed SL in Bergen that occurred on 27 February 1990 by 32 cm. Furthermore, under the RCP8.5 scenario future mean SL rise around Bergen is projected to be 53 cm by 2,100 (Norwegian Mapping and Cadastre Authority,

2019; Simpson et al., 2015), on top of which our possible maximum SL extreme event would reach 235 cm, which is 15 cm above the Norwegian national building code standard for critical infrastructure of 220 cm (National Office of Building Technology and Administration, 2019). It should be restated that the possible extreme event of 182 cm would only be produced by the coincidence of the highest astronomical tide and the largest SkS seen in the last 35 years. Such an event may be rarer than the 1000 year return frequency that the national building code level for Bergen is defined at. The probabilities of such an event occurring could be assessed for Bergen and for each tide gauge in Norway individually using joint probabilities, though this is not covered here and will be the focus of future work.

Similar approaches for the definition of extreme floods due to coinciding high ATs and SkSs have been adapted to the U.K. (Haigh et al., 2010; Tawn, 1992), and referred to as indirect methods for the inference of return values. An important part of the correct statistical treatment is a reduction of the likelihood of the highest possible overlaps due to mismatches in the occurrences of extreme ATs (mostly around the solstice points) and extreme SkSs (mostly in winter). Without performing a thorough examination of the return periods for Norway by different methods (which is beyond the scope of this paper), we can instead highlight specific situations during the 30 year database that would have exceeded the 1000 year return level for Bergen. This return level was calculated using direct extreme value statistics to be 148 cm (Simpson et al., 2015). The highest ever observed SL in Bergen was 150 cm on 27 February 1990. The SkS and AT the time of this event were 77.0 cm and 73.0 cm, respectively. During the last 30 year record this AT was exceeded 154, 111, and 66 times during December, January and February or on average around 5, 4, and 2 times per month during the last 30 year record, and the SkS level was exceeded once during each December, January and February. This suggests that an overlap of ATs and SkSs exceeding the current estimate of the 1000 year return level for Bergen is very possible and that we already here can identify so-called "near misses" (Dangendorf et al., 2016; Haigh et al., 2016).

Such near misses are of course much more likely considering the rather short datasets available for the analysis of extreme sea level events. Due to the desire to use high frequency - high quality automated measurements for this work, the length of the available dataset is severely limited. Simultaneously, the datasets on which the Norwegian building code is based are not much longer. The return levels for the Norwegian TGs in Simpson et al., (2015) were calculated from record lengths typically less than 79 years and maximum 100 years, equal or less than 10% of the target 1000-year return period. A repetition of the analysis presented in this publication with datasets spanning up to 100 years would be desirable, if suitable data were available. A longer dataset would allow the conclusions on the coincidence between ATs and SkSs to be tested since it should show a wider variety of possible combinations Ats and SkSs. However, the possibility for such super-flooding may be better assessed using paleo reconstructions which have far longer records. Some historic records might exist of extreme events for the last several hundred years, for example from the Hanseatic activity in Bergen. Possible weaknesses in the return-level calculations based on an only 100 years-long data series was highlighted during a StS event on 11 February 2020, where the maximum SL of 149 cm was reached in Bergen. The 1000 years return level has thus been exceeded twice in 30 years. Even though much of this increase in occurrences can be attributed to long term SL rise, it does suggest that indirect methods may be more desirable.

There is a need to mention the large spatial variability of possible exceedances of return levels and national building code thresholds. The strongest recorded SkS for Oscarsborg nearby Oslo (123 cm, record length of 29 years) together with the projected mean SL rise in the RCP8.5 scenario (28 cm) and highest AT in the record (28 cm) would be 186 cm, 47 cm below the national building code threshold of 233 cm relative to the mean sea level from 1996 to 2014. The national building code threshold would not be exceeded, even using the 95% confidence interval for the mean sea level rise of 61 cm. The relevance of the coincidence between AT and SkS is strongly reduced since the Oslo area shows one of the strongest isostatic adjustments and the AT amplitude is low due to its proximity to the amphidromic point.

It is clear that future studies are needed to uncover what independence between AT and SkS means for extreme SL events along the Norwegian coastline. The role of storms and their paths and strength is also important to discuss. There appears to be a separation of storm tracks, as seen by two typical main paths of single storms relative to the Norwegian coastline, affecting extreme SkSs at stations north of Trondheim and south of Heimsjø. This can be linked to the analysis of Chafik et al., (2017) despite a focus on different time scales. They found monthly mean extreme SL (detrended, seasonalized and the inverse barometric effect removed) in Bergen to coincide with a mean sea level pressure pattern with a maximum over central Germany and a minimum southwest of Iceland. For SL extremes in Tromsø the maximum was located over Denmark and the minimum over Southeast Greenland. This resulted in monthly mean winds crossing Norway over Bergen or propagating further along the Norwegian coast, similar to the storm tracks in our analysis. The observed 'glancing' of the Norwegian coast at the location of the TGs is therefore a result of the shape of the Norwegian coastline with a meridional orientation in Southern Norway and a more zonal orientation in Northern Norway. A northward or southward shift in the pressure pattern causes the isolines either to follow the Norwegian coast or cross it, respectively. Chafik et al., (2017) attributed the extreme monthly mean SLs in Bergen to a positive North Atlantic Oscillation (NAO) modulated by a positive East Atlantic Pattern and neutral Scandinavian Pattern. The extreme monthly mean SLs at Tromsø they attributed also to a positive NAO, modulated by a light positive East Atlantic Pattern and a negative Scandinavian Pattern. The positive NAO is consistent with the typical mean storm track location over Norway, compared to the more southern mean storm tracks for a negative NAO phase (Bader et al., 2011; Trigo, 2006).

In order to better understand extreme sea-level events in a region with such a complex geometry such as the Norwegian coast, it is important to make the connection between SL events and the specific properties of extratropical cyclones rather than connecting them with storm tracks or large scale pressure patterns. We know from the literature that storm intensity, location, size, and speed of propagation can greatly affect the risk and impact of flooding in coastal areas (e.g., Jelenianski, 1972; Azam et al., 2004; Benavente et al., 2006; Haigh et al., 2016; Wei et al., 2019). However, to the authors' knowledge, the combination of different storms' properties along the coast of Norway has not been addressed by the literature. For example, the intensity of storms is associated with the strength of wind stress over the ocean and could be related to anomalously high sea-level events. However, the intensities of storms have to be considered in relationship with their paths. The path followed by a storm affects the wind pattern in coastal areas and, therefore, can determine whether water piles up or not

along certain portions of the coast (Andrée et al., 2022). A future study could follow Dangendorf et al. (2016) and propose an analysis of storm surges that takes into consideration ATs, storms' location, and the storms' strengths. Or, it could exploit other deterministic approaches, such as those in Ganske et al. (2018) and Horsburgh et al. (2021), for example, using a high-resolution numerical model to reproduce the impact of a storm from the past, and understand how it changes as some of the cyclone's characteristics are modified.

Data availability statement

Publicly available datasets were analyzed in this study. This data can be found here: Coastline dataset from the European Environment Agency (©EEA). Tide gauge data and predicted tides are provided by the Norwegian Mapping Authority licensed under Creative Commons Attribution 4.0 international (CC BY 4.0). The tide gauge data can be accessed from the Norwegian Mapping Authority's website using their API at https://www.kartverket.no/en/api-and-data/tidal-and-water-level-data.

Author contributions

Scientific concept, analysis, and writing by TW Scientific concept and writing by SO Data and scientific discussions by LC and JN Scientific discussions with FM.

Funding

This research has been supported by the Utdannings- og forskningsdepartementet (Basic funding to Bjerknes Centre for Climate Research) through the Climate Hazards and Extremes (CHEX) strategic project of the Bjerknes Centre for Climate Research.

Acknowledgments

The authors thank the European Environment Agency for the coastline dataset (©EEA). Tide gauge data and predicted tides are provided by the Norwegian Mapping Authority licensed under Creative Commons Attribution 4.0 international (CC BY 4.0).

Conflict of interest

The authors declare that the research was conducted in the absence of any commercial or financial relationships that could be construed as a potential conflict of interest.

Publisher's note

Supplementary material

The Supplementary Material for this article can be found online at: https://www.frontiersin.org/articles/10.3389/feart.2023.1037826/full#supplementary-material

References

Andrée, E., Drews, M., Su, J., Larsen, M. A. D., Drønen, N., and Madsen, K. S. (2022). Simulating wind-driven extreme sea levels: Sensitivity to wind speed and direction. *Weather Clim. Extrem.* 36, 100422. doi:10.1016/j.wace.2022.100422

Azam, M.H., Samad, M.A., and Mahboob-Ul-Kabir (2004). Effect of cyclone track and landfall angle on the magnitude of storm surges along the coast of Bangladesh in the northern Bay of Bengal. *Coastal engineering journal* 46 (03), pp.269–290. doi:10.1016/j.atmosres.2011.04.007

Bader, J., Mesquita, M. D. S., Hodges, K. I., Keenlyside, N., Østerhus, S., and Miles, M. (2011). A review on northern hemisphere sea-ice, storminess and the North atlantic oscillation: Observations and projected changes. *Atmos. Res.* 101 (4), 809–834. doi:10.1016/j.atmosres.2011.04.007

Chafik, L., Nilsen, J., and Dangendorf, S. (2017). Impact of North Atlantic teleconnection patterns on northern European sea level. *J. Mar. Sci. Eng.* 5 (3), 43. doi:10.3390/jmse5030043

Chen, L., Fettweis, X., Knudsen, M., and Johannessen, O. M. (2016). Impact of cyclonic and anticyclonic activity on Greenland ice sheet surface mass balance variation during 1980. *Int. J. Climatol.* 36, 3423–3433. doi:10.1002/joc.45652013December 2015

Cushman-Roisin, Benoit, and Beckers, J.-M. (2011). *Introduction to geophysical fluid dynamics, physical and numerical aspects*. 2nd ed. Cambridge, MA, USA: Academic Press. https://www.elsevier.com/books/introduction-to-geophysical-fluid-dynamics/cushman-roisin/978-0-12-088759-0.Retrieved from

Dangendorf, S., Arns, A., Pinto, J. G., Ludwig, P., and Jensen, J. (2016). The exceptional influence of storm 'Xaver' on design water levels in the German Bight. *Environ. Res. Lett.* 11 (5), 054001. doi:10.1088/1748-9326/11/5/054001

de Vries, H., Breton, M., de Mulder, T., Krestenitis, Y., Ozer, J., and Proctor, R., (1995). A comparison of 2D storm surge models applied to three shallow European seas. *Environ. Softw.* 10 (1), 23–42. doi:10.1016/0266-9838(95)00003-4

Dee, D. P., Uppala, S. M., Simmons, a. J., Berrisford, P., Poli, P., and Kobayashi, S., (2011). The ERA-interim reanalysis: Configuration and performance of the data assimilation system. *Q. J. R. Meteorological Soc.* 137 (656), 553–597. doi:10.1002/qj.828

Eea (2018). EEA coastline for analysis. Retrieved from https://www.eea.europa.eu/data-and-maps/data/eea-coastline-for-analysis-2#tab-metadata July 4, 2019).

Ganske, A., Fery, N., Gaslikova, L., Grabemann, I., Weisse, R., and Tinz, B. (2018). Identification of extreme storm surges with high-impact potential along the German North Sea coastline. *Ocean. Dyn.* 68, 1371–1382. doi:10.1007/s10236-018-1190-4

Gjevik, B. (2009). *Flo og fjære - langs kysten av Norge og Svalbard*. Oslo: Farleia Forlag.

Grabemann, I., L. Gaslikova, T. Brodhagen, and E. Rudolph (2020). Extreme storm tides in the German Bight (North Sea) and their potential for amplification. Natural Hazards and Earth System Sciences, 20(7), 1985–2000. doi:10.3390/jmse5030043

Haigh, I. D., Nicholls, R., and Wells, N. (2010). A comparison of the main methods for estimating probabilities of extreme still water levels. *Coast. Eng.* 57 (9), 838–849. doi:10.1016/j.coastaleng.2010.04.002

Haigh, I. D., Wadey, M. P., Wahl, T., Ozsoy, O., Nicholls, R. J., and Brown, J. M., (2016). Spatial and temporal analysis of extreme sea level and storm surge events around the coastline of the UK. *Sci. Data* 3 (1), 160107. doi:10.1038/sdata.2016.107

Hallegatte, S., Green, C., Nicholls, R. J., and Corfee-Morlot, J. (2013). Future flood losses in major coastal cities. *Nat. Clim. Change* 3 (9), 802–806. doi:10.1038/nclimate1979

Haug, E. (2012). "Extreme value analysis of sea level observations,". Technical Report DAF 12-1 (Stavanger, Norway: Norwegian Mapping Authority, Hydrographic Service), 180.January

Hodges, K. I. (1999). Adaptive constraints for feature tracking. *Mon. Weather Rev.* 127 (6), 1362–1373. doi:10.1175/1520-0493(1999)127<1362:ACFFT>2.0.CO;2

Horsburgh, K., Haigh, I. D., Williams, J., De Dominicis, M., Wolf, J., and Inayatillah, A., (2021). "Grey swan" storm surges pose a greater coastal flood hazard than climate change. *Ocean. Dyn.* 71 (6), 715–730. doi:10.1007/s10236-021-01453-0

Horsburgh, K., T. Ball, B. Donovan, and G. Westbrook, (2010). Coastal flooding, MCCIP Annual Report Card 2010-11. Lowestoft, Marine Climate Change Impacts Partnership. (MCCIP Summary Report 2010).

Jelesnianski, C.P. (1972). SPLASH I: Landfall Storms. NOAA Technical Memorandum NWS-TDL 46. Silver Spring, Maryland, NWS Systems Development Office.

J. Benavente, L. Del Río, F.J. Gracia, and J.A. Martínez-del-Pozo (2006). Coastal flooding hazard related to storms and coastal evolution in Valdelagrana spit (Cadiz Bay Natural Park, SW Spain), Continental Shelf Research. *Coastal engineering journal* 26 (09), pp.1061–1076. doi:10.1016/j.csr.2005.12.015

Moe, H., Ommundsen, A., and Gjevik, B. (2002). A high resolution tidal model for the area around the Lofoten Islands, northern Norway. *Cont. Shelf Res.* 22, 485–504. doi:10.1016/s0278-4343(01)00078-4

Munich, R. E. (2019). Storm surges. Retrievedfrom https://www.munichre.com/touch/naturalhazards/en/naturalhazards/hydrological-hazards/flood/storm-surges/index.html August 28, 2019).

Næss, A., and Gaidai, O. (2009). Estimation of extreme values from sampled time series. *Struct. Saf.* 31, 325–334. doi:10.1016/j.strusafe.2008.06.021

National Office of Building Technology and Administration (2019). Byggteknisk forskrift (TEK17). Retrievedfrom https://dibk.no/byggereglene/byggteknisk-forskrift-tek17/7/7-2/July 10, 2019).

Norwegian Mapping and Cadastre Authority (2019). Se havnivå. Retrievedfrom https://www.kartverket.no/en/sehavniva/Lokasjonsside/?cityid=9000002&city=Bergen#tab2 July 10, 2019).

Pugh, D., and Woodworth, P. (2014). *sea-level science. Sea-level science - understanding tides, surges, tsunamis and mean seasea-level changes*. Cambridge, MA, USA: Cambridge University Press. doi:10.1017/CBO9781139235778

Richter, K., Furevik, T., and Orvik, K. A. (2009). Effect of wintertime low-pressure systems on the Atlantic inflow to the Nordic seas. *J. Geophys. Res.* 114 (C9), C09006. doi:10.1029/2009JC005392

Richter, K., Nilsen, J. E. Ø., and Drange, H. (2012). Contributions to sea level variability along the Norwegian coast for 1960-2010. *J. Geophys. Res. Oceans* 117 (C5). doi:10.1029/2011JC007826

Simpson, M. J. R., Nilsen, J. E. Ø., Ravndal, O. R., Breili, K., Sande, H., and Kierulf, H. P., (2015). sea level change for Norway - past and present observations and projections to 2100. Retrieved from https://www.miljodirektoratet.no/globalassets/publikasjoner/M405/M405.pdf.

Simpson, M. J. R., Ravndal, O., Sande, H., Nilsen, J., Kierulf, H., and Vestøl, O., (2017). Projected 21st century sea-level changes, observed sea level extremes, and sea level allowances for Norway. *J. Mar. Sci. Eng.* 5 (3), 36. doi:10.3390/jmse5030036

Skjong, M., Næss, A., and Næss, O. E. B. (2013). Statistics of extreme sea levels for locations along the Norwegian coast. *J. Coast. Res.* 29, 1029–1048. doi:10.2112/jcoastres-d-12-00208.1

Tawn, J. (1992). Estimating probabilities of extreme sea-levels. *J. R. Stat. Soc. Ser. C Appl. Statistics)* 41 (1), 77–93. doi:10.2307/2347619

Trigo, I. F. (2006). Climatology and interannual variability of storm-tracks in the euro-atlantic sector: A comparison between ERA-40 and NCEP/NCAR reanalyses. *Clim. Dyn.* 26 (2–3), 127–143. doi:10.1007/s00382-005-0065-9

Wei, X., Brown, J. M., Williams, J., Thorne, P. D., Williams, M. E., and Amoudry, L. O. (2019). Impact of storm propagation speed on coastal flood hazard induced by offshore storms in the North Sea. *Ocean. Model.* 14, 101472. doi:10.1016/j.ocemod.2019.101472

Williams, J., Horsburgh, K. J., Williams, J. A., and Proctor, R. N. F. (2016). Tide and skew surge independence: New insights for flood risk. *Geophys. Res. Lett.* 43 (12), 6410–6417. doi:10.1002/2016GL069522

frontiers | Frontiers in Earth Science

TYPE Original Research
PUBLISHED 17 February 2023
DOI 10.3389/feart.2022.1021953

OPEN ACCESS

EDITED BY
Shangfeng Chen,
Institute of Atmospheric Physics (CAS), China

REVIEWED BY
Ping Liang,
Shanghai Meteorological Bureau, China
Lei Song,
Institute of Atmospheric Physics (CAS), China

*CORRESPONDENCE
Xiong Chen,
chenxmails@163.com

SPECIALTY SECTION
This article was submitted to Atmospheric Science, a section of the journal Frontiers in Earth Science

RECEIVED 18 August 2022
ACCEPTED 19 December 2022
PUBLISHED 17 February 2023

CITATION
Li L, Chen X, Li C, Li X and Yang M (2023), Comparison of Madden-Julian oscillation in three super El Niño events.
Front. Earth Sci. 10:1021953.
doi: 10.3389/feart.2022.1021953

Comparison of Madden-Julian oscillation in three super El Niño events

Lifeng Li[1], Xiong Chen[2]*, Chongyin Li[2,3], Xin Li[2] and Minghao Yang[2]

[1]Institute of Aerospace Information, Space Engineering University, Beijing, China, [2]College of Meteorology and Oceanography, National University of Defense Technology, Changsha, China, [3]State Key Laboratory of Numerical Modeling for Atmospheric Sciences and Geophysical Fluid Dynamics (LASG), Institute of Atmospheric Physics, Chinese Academy of Sciences, Beijing, China

This paper investigated the characteristics of Madden-Julian Oscillation (MJO) in three super El Niño events (i.e., 1982/83, 1997/98 and 2015/16 El Niño events) based on reanalysis data. MJO with apparent eastward propagation can be observed during the developing stages of these three super El Niño events. Enhanced MJO zonal wind was observed over the western Pacific, especially in 1997/98 and 2015/16 El Niño events, which is mainly attributed to the effects of tropical background circulation and extratropical anomalous circulation. During the mature stages of 1982/83 and 1997/98 El Niño events, MJO with noticeable eastward propagation cannot be observed, and the MJO zonal wind amplitude at 850 hPa was weakened (enhanced) over the Indian Ocean and western Pacific (central and eastern Pacific). However, MJO zonal wind amplitude over the central and eastern Pacific was enhanced and the prominent eastward propagation was also found in the mature stage of 2015/16 El Niño. The eastward propagation of MJO was also observed during the decaying stages of the three super El Niño events, but its intensity was weaker compared with the developing and mature stages. The abnormal activity of MJO during the mature and decaying stages may be closely related to the characteristics in circulation and moisture anomalies caused by El Niño and the seasonal cycle of circulation and moisture. In addition, this study found that the RMM index and MJO zonal wind amplitude may lead to contradictory results in identifying the characteristics of MJO activity, especially during the developing and decaying stages.

KEYWORDS

Madden-Julian Oscillation (MJO), super El Niño, comparative study, extratropical anomalous circulation, RMM index

1 Introduction

Madden-Julian Oscillation (MJO) is the most important component of tropical atmospheric intraseasonal oscillation (Madden and Julian, 1971; Madden and Julian, 1972), and is also the bridge between weather and climate, which means that MJO plays a critical role in the anomalous weather and climate in many regions (Zhang, 2013; Li et al., 2014; Li et al., 2020). El Niño–Southern Oscillation (ENSO), as the strongest signal of large-scale sea-air interaction, shows significant variability on interannual timescales in the tropical ocean and atmosphere. ENSO and MJO are two of the vital systems in the tropic. Although the time scales of ENSO and MJO are very different, they are closely related. The MJO plays an important role in the initiation and termination of ENSO (Lau and Chan, 1988; Takayabu et al., 1999; Bergman et al., 2001; Miyakawa et al., 2017). On the one hand, the strengthened MJO could induce a stronger stochastic forcing like westerly wind burst, which trigger the El Niño (Lau and Chan

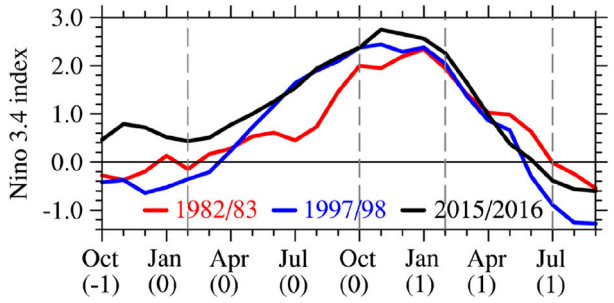

FIGURE 1
Evolution of monthly Niño 3.4 index during the three super El Niño events. The –1, 0 and 1 represent super El Niño event previous, onset and next year, respectively.

1988; Bergman et al., 2001). On the other hand, the robust MJO activities and its eastward propagation in May 1998 strengthened the easterly anomalies over the eastern Pacific, which caused the abrupt decaying of El Niño (Takayabu et al., 1999; Miyakawa et al., 2017). The MJO activity could be modulated by the ENSO (Lau and Chan, 1986; Moon et al., 2011; Lee et al., 2019; Wei and Ren, 2019). The El Niño might reduce the frequency of the MJO *via* the air–sea interactions (Lau and Chan, 1986). Wei and Ren (2019) indicated that ENSO can regulate the propagation of MJO. The equatorially symmetric eastward propagation of MJO is fast from the Indian Ocean to the equatorial western Pacific during El Niño, whereas the MJO during La Niña is very slow *via* the southern Maritime Continent. In addition, the teleconnection from the MJO could be modulated by the ENSO (Moon et al., 2011; Lee et al., 2019).

Accompany the evolution of El Niño, anomalous MJO activity can be observed in many regions (Li and Zhou, 1994; Hendon et al., 2007; Chen et al., 2015; Chen et al., 2016). MJO activity is enhanced over the western Pacific before the occurrence of El Niño, while it is weakened rapidly after El Niño (Li and Zhou, 1994; Li and Li, 1995). During the developing stages of El Niño, anomalous MJO activity will lead to westerly wind bursts in the western Pacific (Vecchi and Harrison, 2000; Hendon et al., 2007), causing sinking Kelvin wave in the ocean (Kessler et al., 1995; Seo and Xue, 2005), thus affecting the sea surface temperature in the equatorial Pacific and providing advantageous environment for the developing stages of El Niño (Zhang and Gottschalck, 2002; McPhaden et al., 2006). The combination of the atmospheric barotropic instable mode mainly excited by El Niño and the MJO circulation results in the MJO tending to a barotropic structure in the vertical direction during El Niño (Li and Li, 1995; Li and Smith, 1995; Chen et al., 2015). During the El Niño event, due to the increase of moisture and moist static energy over the central and eastern Pacific, MJO zonal winds in the lower tropospheric are enhanced over the central Pacific while it weakened over the western Pacific. Meanwhile, the location of the maximum growth rate of MJO moves eastward and the eastward propagation speed of the MJO slow down (Fink and Speth, 1997; Tam and Lau, 2005). In addition, the convective activity strengthens in the central and eastern Pacific during El Niño, changing the position of atmospheric adiabatic heating, so that the eastward propagation of the MJO is not obvious, and some regions have westward propagation, especially in the Pacific (Li, 1995; Li and Smith, 1995; Chen et al., 2015).

In recent years, many researchers have paid more attention to the relationship between the MJO and two types of El Niño, especially the relationship between the MJO and the central Pacific El Niño (Feng et al., 2015; Yuan et al., 2015). In the eastern Pacific El Niño, the MJO activity over the western Pacific are enhanced during spring and summer, while they are significantly weakened during the four to 5 months the after eastern Pacific El Niño matures (Gushchina and Dewitte, 2012; Chen et al., 2016). However, the enhancement of the MJO in the central Pacific El Niño mainly occur in the mature and decaying stages of El Niño (Gushchina and Dewitte, 2012; Chen et al., 2016). During the central Pacific El Niño, the anomalous circulation and moisture over the maritime continent and western Pacific are conductive to the increase of moist static energy and the conversion from barotropic and baroclinic energy from the low-frequency background field to MJO scale, thus strengthening the MJO activity in these regions (Hsu et al., 2018; Wang et al., 2018). The horizontal and vertical moisture advection over the central Pacific is stronger during the central Pacific El Niño compared with during the eastern Pacific El Niño, resulting in the stronger intensity and the furtherer eastward propagation of the MJO during the central Pacific El Niño (Chen et al., 2016). Dasgupta et al. (2021) indicated that the first and second MJO frequency pattern is most prominent during the negative central Pacific and positive eastern Pacific ENSO phases, respectively, which is caused by the horizontal convergence of mean background moisture through intraseasonal winds during the two types of ENSO phases.

This study selected three El Niño events (1982/83, 1997/98 and 2015/16 El Niño) with the strongest SST anomalies in recent decades, which are usually called super El Niño (Chen et al., 2016; Yuan et al., 2016; Mu and Ren, 2017; Abellán et al., 2018). The evolution characteristics of SST during the super El Niño and their effects on global weather and climate are significantly distinct compared with those during the ordinary El Niño (Li and Min, 2016; Bi et al., 2017; Liu et al., 2018; Qian and Guan, 2018). Affected by the 2015/16 El Niño event the precipitation significantly increased in the southern China during the autumn and winter in 2015, especially in the South China in winter, with the precipitation reaching the strongest value in history record (Yuan et al., 2016; Zhai et al., 2016). At the same time, there are many similarities and differences between the three super El Niño events (Shao and Zhou, 2016; Paek et al., 2017; Rao and Ren, 2017; Abellán et al., 2018). The center of positive SST anomaly during the 2015/16 El Niño was apparently westward compared with the previous two El Niño (Ren et al., 2017), which is the mixed characteristics of the central Pacific El Niño and eastern Pacific El Niño (Paek et al., 2017). The intraseasonal zonal westerly in the 2015/16 El Niño was weaker than that in the 1997/98 El Niño, which lead to weaker intraseasonal SST (Lyu et al., 2018). The thermocline feedback in the 2015/16 El Niño was weaker than the other two super El Niño, while the advection feedback was significantly enhanced (Zheng et al., 2019).

The super El Niño events have gradually received more attention due to the characteristics in the evolution and their enormous influence on the global weather and climate, which bring the new challenges to our research and forecasting. MJO and ENSO are the two systems with the most significant variation in the tropical atmosphere and ocean, and their interaction has always been a hot topic. The MJO activity appear significantly abnormal along with the evolution of El Niño. So what are the characteristics of MJO activity during super El Niño? What are the differences in MJO activities between the three super El Niño? In view of these problem, this paper will attempt to compare and analyze the abnormal characteristics of MJO from the

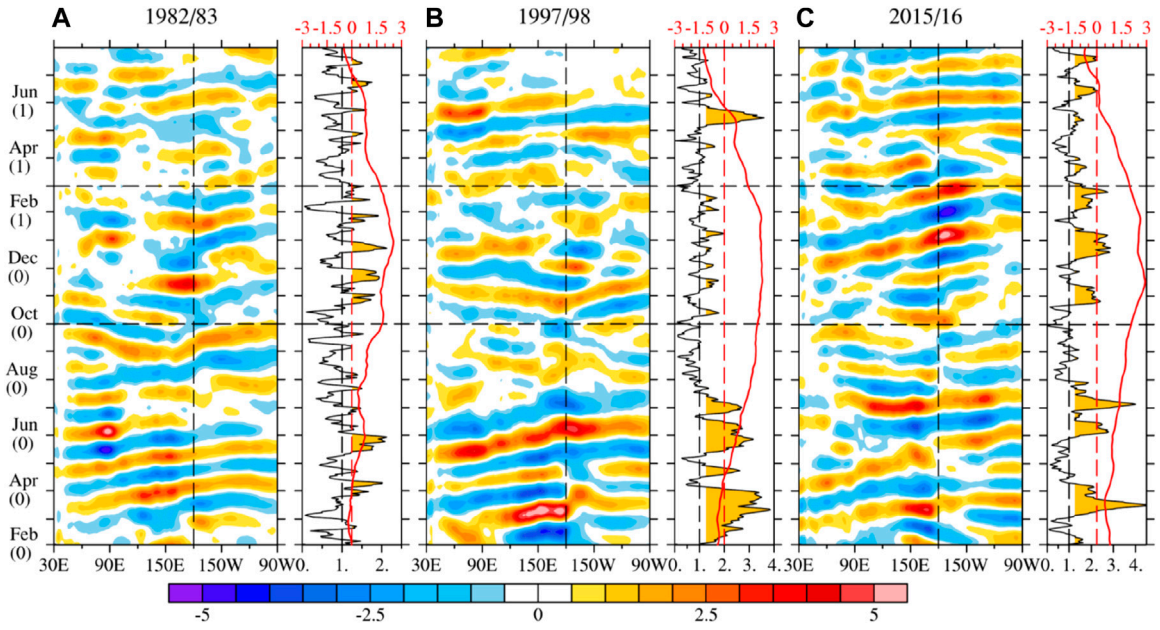

FIGURE 2
Evolution of MJO zonal wind at 850 hPa averaged over 10°S-10°N (colors shading, m s^{-1}), RMM index (black lines, RMM index exceeding 1.2 are marked with orange), and Niño 3.4 index (red lines) during three super El Niño events. The 0 and 1 represent super El Niño event onset and next year, respectively. **(A–C)** represent 1982/83,1997/98 and 2015/16, respectively.

developing, mature and decaying stages of the super El Nino events, and explore the relationship between MJO and super ENSO, so as to provide important support for the prediction of MJO. The paper is organized as follows. Section 2 describes the data and analysis techniques. The evolution characteristics of MJO and possible causes of anomalous MJO activity are presented in section 3 and section 4, respectively. We present concluding remarks with discussions in section 5.

2 Materials and methods

Daily mean atmospheric data at a horizontal resolution of 1.5 × 1.5, including horizontal winds and specific humidity, were from the European Center for Medium-Range Weather Forecasts Interim Re-Analysis (ERA-Interim; Dee et al., 2011). SST data were obtained from the National Oceanic and Atmospheric Administration (NOAA) for both temporal resolutions of daily (Optimum Interpolation SST V2; Reynolds et al., 2007) and monthly (Extended Reconstructed SST V5 (Huang et al., 2017), at a horizontal resolution of .25 × .25 and 2.0 × 2.0, respectively. Furthermore, daily real-time multivariate MJO indexes (RMM; Wheeler and Hendon, 2004) were obtained from the Australian Bureau of Meteorology, which is the multivariate combined EOF of 850 h Pa zonal wind, 200 h Pa zonal wind and outgoing longwave radiation. RMM can reflect the real-time variation of intensity and position for the MJO. The record length of all data compiled in this study is 39 years from 1 January 1979 to 31 December 2017.

Anomalies were obtained by removing the seasonal cycle and linear trend. The MJO signal was obtained by the Lanczos band-pass filter with 201 days of smoothing (Duchon, 1979). The time-space spectrum analysis is used to analyze the distribution of vibration energy with wave number and frequency (Hayashi, 1982). The evolution of the three super El Niño was represented by the Niño 3.4 index (SST anomaly average over the 5°S-5°N,170°-120°W). Figure 1 shows the evolution of the Niño 3.4 index during the three super El Niño. The maximum of Niño 3.4 index is higher than 2.0°C in super El Niño, while there are prominent differences in the evolution of Niño 3.4 index among the three events. According to the evolution of Niño 3.4 index, the super El Niño events can be divided into three stages: developing stages (from February to September) that is a stable growth period before Niño 3.4 index reaches 2.0°C, mature stages (from October to February of the following year) that is a period when Niño 3.4 index remains around 2.0°C, and decaying stages (from March of the following year to July) that is a period when Niño 3.4 index is below 2.0°C and turn into a negative value. The Niño 3.4 index turn from a negative anomaly to a positive anomaly except for the 2015/16 El Niño, which is mainly attributed to the warming events of the Pacific in 2014 (Zhai et al., 2016; Chen et al., 2017). In the decaying stages, the evolution of the Niño 3.4 index in the three super El Niño shows a similar pattern. However, the Niño 3.4 indices during developing stages are distinct, and it is prominent that the intensity of the Niño 3.4 index for the 1982/83 El Niño is significantly weaker compared with those for the other two El Niño events.

3 Activity and evolution of MJO

Figure 2 exhibits the evolution of MJO zonal wind at 850 hPa averaged over the 10°S-10°N, RMM index and Niño 3.4 index during the three super El Niño. It is evident that there are significant

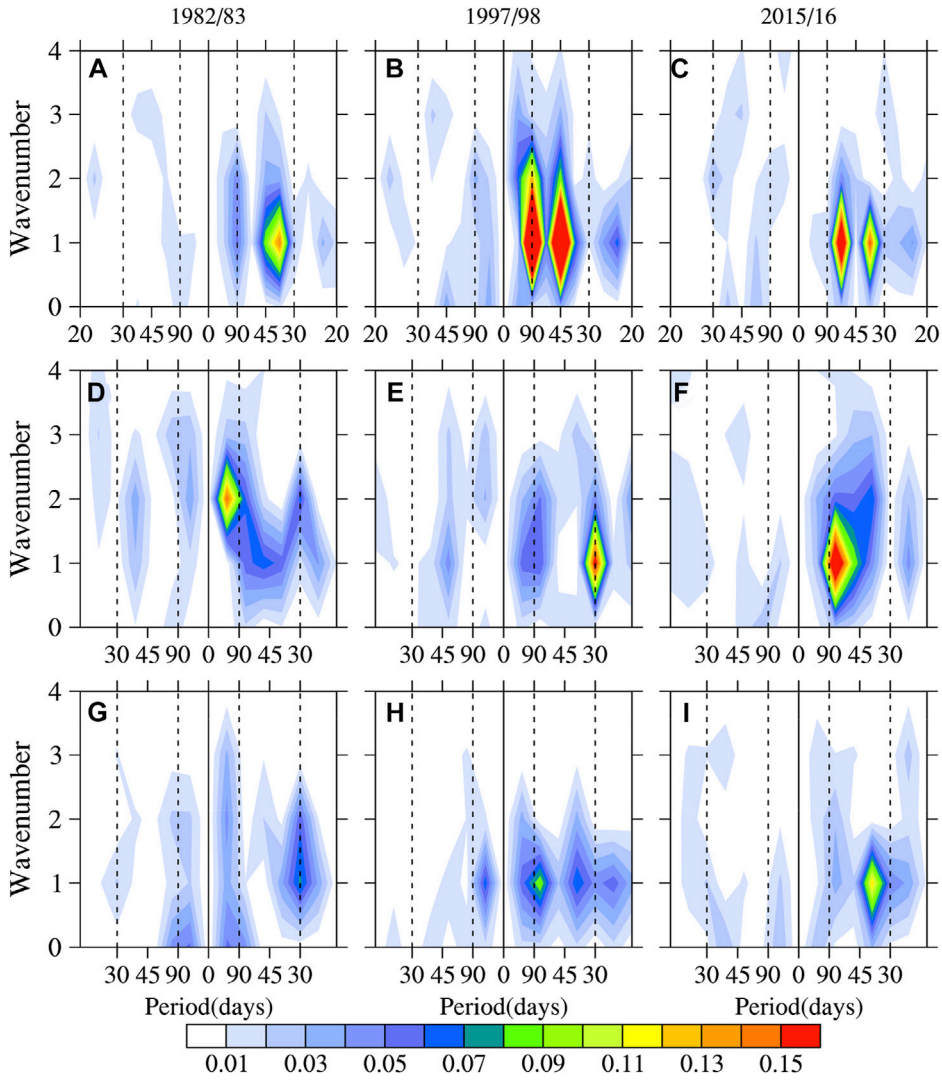

FIGURE 3
Time-space spectra of zonal wind at 850 hPa averaged over 10°S-10°N for 1982/83 (left), 1997/98 (middle), and 2015/16 (right) super El Niño during developing stages **(A–C)**, mature stages **(D–F)**, and decaying stages **(G–I)**.

discrepancies in the characteristics of MJO activity during the different stages in the three super El Niño.

3.1 Developing stage

In the developing stage, especially from February to July, the enhanced MJO significantly propagated eastward from the Indian Ocean to the Pacific during the three super El Niño (Figure 2). However, there were prominent differences in intensity, speed and distance of propagation. The spatiotemporal spectrum analysis (Figure 3) illustrated that the strongest power spectrum of eastward propagation occurs in the developing stages of 1997/98 El Niño with the main periods of 45 days and 90 days. During the 2015/16 El Niño, the power spectrum of eastward propagation was relatively weak with a major period of 40 days and 60 days. During the 1982/83 El Niño, the power spectrum of eastward propagation was the weakest with a main period of about 40 days. The eastward propagation of the MJO was primarily dominated by zonal 1 wave, and the eastward propagation of zonal 2 wave was also strong during the 1997/98 El Niño. In addition, eastward propagation of strong high-frequency waves with a period of about 25 days occurred during the developing stage, especially for 1997/98 El Niño.

The evolution of RMM index (Figure 2) illustrated that the strongest RMM index appeared in March 2015, and this robust MJO activity directly promoted the development of 2015/16 El Niño (Chen et al., 2017; Hong et al., 2017). The average value of RMM index is about 1.2 in winter. Thus, the strong MJO event is defined, when the RMM index is equal or greater than 1.2. The strong MJO event occurred with the longest duration in the developing stages of the 1997/1998 El Niño, while the relatively weak RMM index in the developing stages of the 1982/83 El Niño. Figure 4 depicts the evolution characteristics of MJO phase and intensity. Two strong MJO events occurred in the 1997/98 and 2015/16 El Niño events. Furthermore, the abnormal enhanced MJO activity primarily appeared in phase 5–8. However, the strengthened MJO activity mainly appeared in phase 1–3 during the

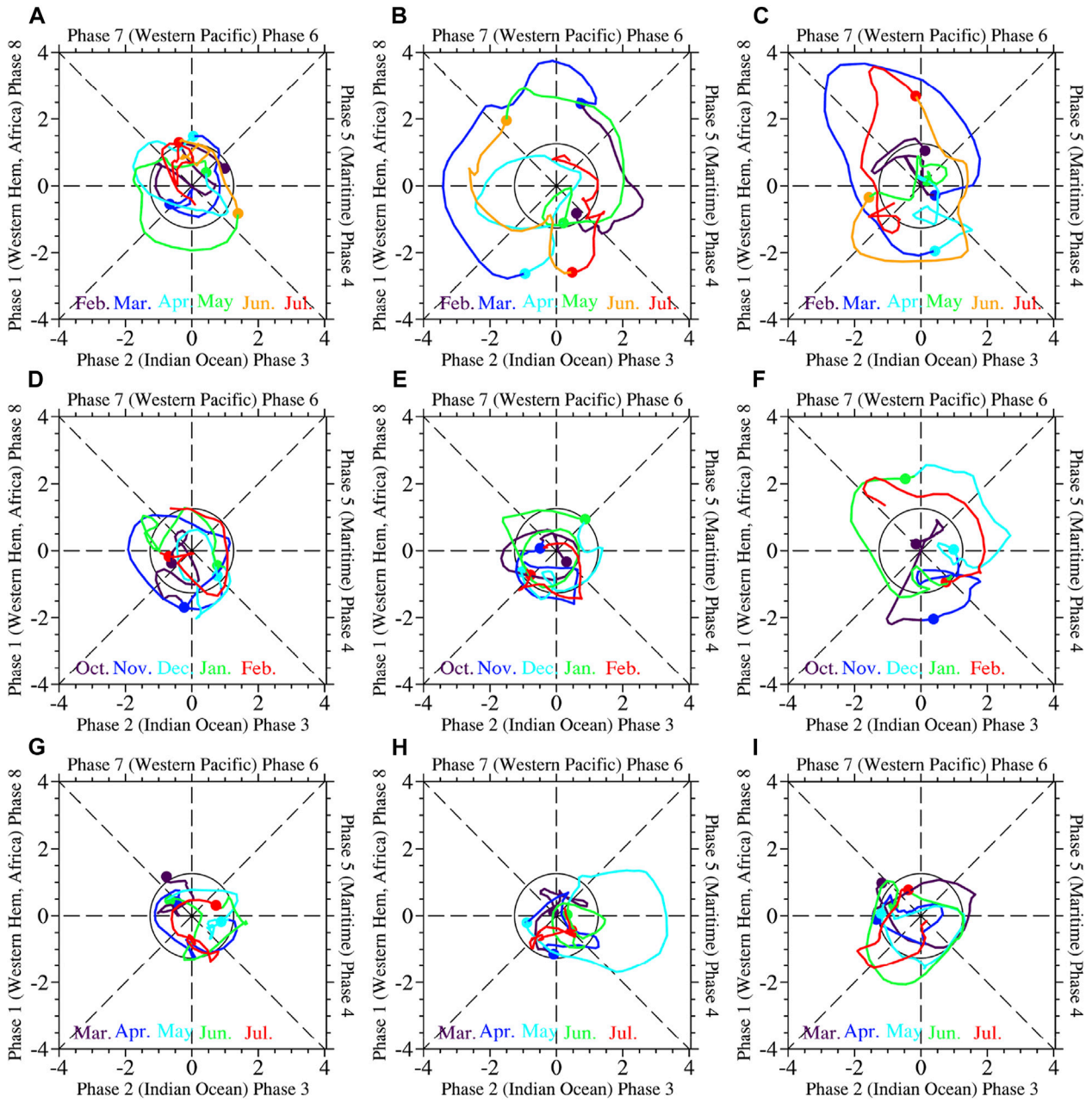

FIGURE 4
RMM index for 1982/83 (left), 1997/98 (middle), and 2015/16 (right) super El Niño during developing stages **(A–C)**, mature stages **(D–F)**, and decaying stages **(G–I)**.

developing stages of the 1982/83 El Niño. Many studies have shown that eastward propagation of the MJO zonal westerly during the 1997/98 El Niño and 2015/16 El Niño directly leads to the variation of ocean thermocline, thus promoting the development of El Niño (McPhaden, 1999; L'Heureux et al., 2017). As shown in Figure 2, two prominent eastward propagation of MJO zonal westerly appeared during the developing stages of the 1982/83 El Niño, and the MJO activity over the western Pacific were strengthened to a certain extent. However, the role of the MJO in the development of this El Niño event had not been deeply examined due to the lack of data. At the same time, weak MJO activities were detected during the developing stages of three super El Niño, particularly in the 1982/83 El Niño. The composite RMM index of each phase during the developing stages of three super El Niño showed that, on average, MJO activities in each phase weakened during the developing stages of the 1982/83 El Niño while enhanced in each phase during the 1997/98 El Niño, especially phase 1 and phase5-8. However, the MJO activities weakened in phase4-6 of the 2015/16 El Niño while strengthened in the other phases.

Some studies (Li and Li, 1995; Chen et al., 2015) suggest that MJO activities are significantly enhanced during the developing stages of the 1982/83 El Niño, whereas the composite RMM index shows that MJO activities are weakened during the developing stages of the 1982/83 El Niño, which may be related to the method used. Figure 6 exhibits the MJO zonal wind amplitude anomalies during the three super El Niño

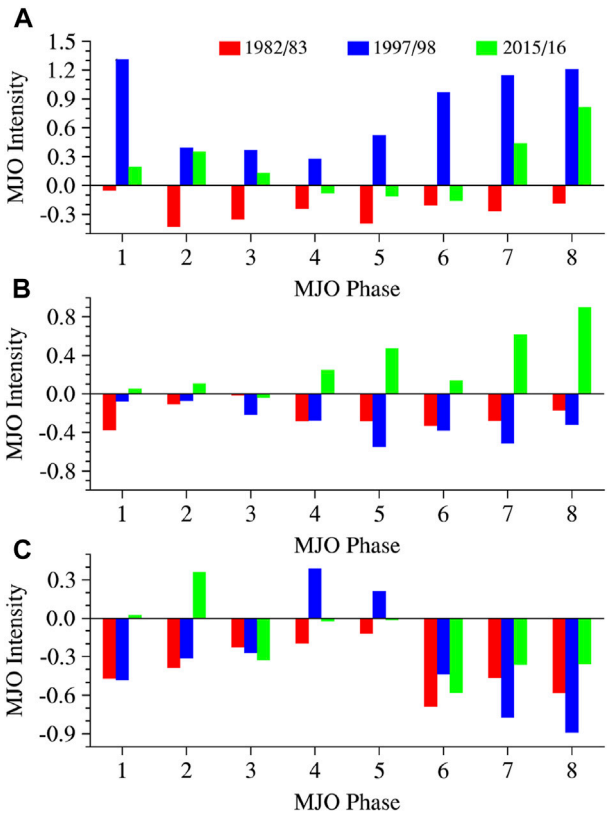

FIGURE 5
Composite RMM index at different MJO phases during the **(A)** developing stages, **(B)** mature stages, and **(C)** decaying stages for the three super El Niño events.

events. The MJO zonal wind amplitude refers to the 3-month sliding standard deviation of MJO zonal wind at 850 hPa (Chen et al., 2016). It was clear that MJO zonal wind amplitude in the developing stages of the three El Niño events were strengthened, but there were also obvious differences. The positive MJO amplitude anomalies were the weakest and primarily concentrated in the western Pacific during the developing stages of the 1982/83 El Niño. The MJO over the Indian Ocean near 90°E was also enhanced from April to July. For the 1997/98 El Niño, the MJO amplitude anomalies were the strongest, and they are significantly strengthened throughout the Indian Ocean and Pacific in the spring and early summer. The abnormal intensity of MJO amplitude in the 2015/16 El Niño was between the previous El Niño events, and the enhanced MJO amplitude mainly occurred in the Pacific, while there were negative MJO amplitude anomalies in the Indian Ocean. These results indicate that there are certain differences between the anomalous MJO zonal amplitude and anomalous RMM index. The discrepancies may be attributed to the differences in the analysis methods and emphases that evaluate the MJO intensity, which leads to contradictory results in different studies.

3.2 Mature stages

During the mature stages of the 2015/16 El Niño, the robust MJO was detected along with significant eastward propagation over the Indian Ocean and Pacific. In contrast, the MJO activities were weakened during the other two super El Niño, and their eastward propagation were not prominent, and even westward propagation existed in some regions (Figure 2). The spatiotemporal spectral analysis as shown in Figure 3 illustrated that the power spectrum of eastward propagation in the intraseasonal scale was the strongest during the mature stages of the 2015/16 El Niño, with a central period of about 75 days, whereas they were significantly weakened during the 1982/83 El Niño and 1997/98 El Niño, especially in the 1997/98 El Niño. The intraseasonal wave of eastward propagation was primarily zonal wave 1, while the zonal wave 2 was also robust during the 2015/16 El Niño. The prominently enhanced eastward propagation of zonal wave 2 of more than 90 days appeared in the mature stages of the 1982/83 El Niño, which may be caused by the conversion of the MJO energy to low-frequency energy of more than 90 days (Li and Zhou, 1994; Li and Li, 1995). In addition, the power spectrum of westward propagation at the intraseasonal and low-frequency (>90 days) scales were also significantly enhanced during the 1982/83 and 1997/98 El Niño events.

MJO intensity weakened during the mature stages compared with that during the developing stages, especially in the 1997/98 El Niño (Figure 4), which is consistent with previous studies that the MJO activity is enhanced during the developing stages of El Niño, while weakened during the mature stages (Li and Zhou, 1994; Li and Li, 1995). During the mature stages of the 1982/83 El Niño, RMM indexes of some days were stronger than the climate mean. The prominent MJO activity were not observed during the mature stages of the 1997/98 El Niño. However, two significant eastward propagation appeared in the 2015/16 El Niño, and the enhanced MJO activities were primarily located in phase 5–8. The composite RMM index of different phase (Figure 5) showed that MJO activities were weakened during the mature stages of the 1982/83 and 1997/98 El Niño events, especially at phase 4–8. However, the MJO activities were enhanced except for phase 3 during the mature stages of the 2015/16 El Niño, especially in phase 4-5 and phase 7-8. It was clear that the RMM index was incapable of capturing the phenomenon that the MJO activity was weakened over the western Pacific and enhanced in the central and eastern Pacific during the mature phase of El Niño. However, this phenomenon could be reflected by the MJO amplitude (Figure 6). During the early mature stages of the 1982/83 and 1997/98 El Niño events, negative MJO amplitude anomalies mainly occurred in the Indian Ocean and western Pacific. With the evolution of time, the negative anomaly gradually expanded eastward, then extended to the central Pacific in the late mature stages and continued to the decaying stages (Figures 6A, B). The enhanced MJO amplitude primarily occurred in the central Pacific during the 1982/83 El Niño before December, while they were mainly appeared in the eastern Pacific after December (Figure 6A). In the 1997/98 El Niño, the MJO amplitude strengthened over the central and eastern Pacific before December, while prominent anomalies were not detected anymore over the central and eastern Pacific after December (Figure 6B). During the mature stages of the 2015/16 El Niño, negative MJO amplitude anomalies in the Indian Ocean and western Pacific were not obvious, but positive anomalies were significantly enhanced over the central and eastern Pacific, especially after November (Figure 6C).

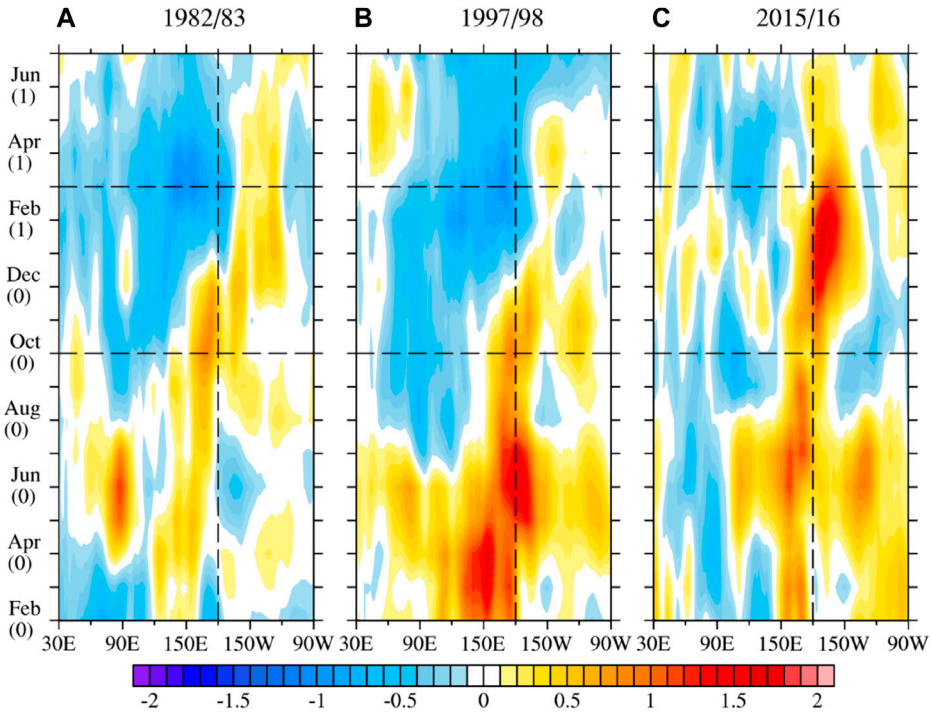

FIGURE 6
Anomalous MJO amplitude of zonal wind at 850 hPa averaged over 10°S—10°N during the three super El Niño events (m s^{-1}). The 0 and 1 represent super El Niño event onset and next year, respectively. **(A–C)** represent 1982/83,1997/98 and 2015/16, respectively.

3.3 Decaying stages

The eastward propagation of the MJO could be observed during the decaying stages of the three super El Niño, but their intensity, duration and propagation distance were significantly weakened compared with those in the developing and mature stages (Figure 2). The spatiotemporal spectral analysis in Figure 3 also showed that power spectrum of intraseasonal eastward propagation during the decaying stages of the 1997/98 and 2015/16 El Niño events were relatively stronger than those during the 1982/83 El Niño. The central periods of the eastward propagation for the MJO were mainly 40 days and 75 days during the decaying stages of 1997/98 El Niño, and it was primarily 40 days for the 2015/16 El Niño. However, there is no center of intraseasonal eastward propagation during the 1982/83 El Niño. The strong wave of eastward and westward propagation of lager than 90 days appeared in the decaying stages of the 1982/83 and 1997/98 El Niño events, which may be induced by the conversion of the MJO energy to low-frequency energy of above 90 days (Li and Zhou, 1994; Li and Li, 1995). At the same time, the high-frequency wave activities of the eastward propagation were prominent at 20–30 days during the decaying stages of the 1997/98 El Niño. In addition, the eastward propagation center of zonal wave 2 was detected during the decaying stages of the 1982/83 El Niño.

The evolution and composite results of the RMM index during decaying stages of three super El Niño illustrated that the MJO activity in the decaying stages is significantly weaker than that in the developing and mature stages. The MJO intensity in the decaying stages was the weakest, especially for the 1982/83 and 1997/98 El Niño events (Figure 2; Figure 4; Figure 5). The RMM indexes of phase 4–8 during the decaying stages of the 1997/98 and 2015/16 El Niño changed from positive anomaly in the mature stages to negative anomalies, particularly in phase 6–8 (Figure 5C). The strong MJO activity led to the increase in the average RMM index of phase 4-5 in May 1998. The two robust MJO activities in June and July 2016 also enhanced the average RMM index of phase 1-2 during the decaying stages of the 2015/16 El Niño. Many studies had indicated that the robust MJO activity in May 1998 triggered the easterly anomalies, resulting in the termination of El Niño. After the MJO event, the Niño 3.4 index rapidly decayed from positive anomaly to negative anomaly (Takayabu et al., 1999; Miyakawa et al., 2017). Figure 2 showed that during the decaying stages of three super El Niño, when Niño 3.4 index turned from positive to negative, the MJO easterly existed in the eastern Pacific, which demonstrated that the MJO easterlies may accelerate the extinction of strong El Niño. Meanwhile, the MJO westerlies in April 1998 and June 2016 existed in the eastern Pacific, while the decaying rate of the Niño 3.4 index was prominently reduced. The anomalous MJO zonal wind amplitudes in the Indian Ocean and Pacific were weakened in the decaying stages, especially in the 1982/83 and 1997/98 El Niño, while they were enhanced in the central and eastern Pacific, particularly in the 2015/16 (Figure 6). The MJO zonal wind amplitudes strengthened over the eastern Pacific, which may lead to the stronger 2015/16 El Niño. These results indicate that the MJO plays a critical role in the decaying stages of El Niño while it is

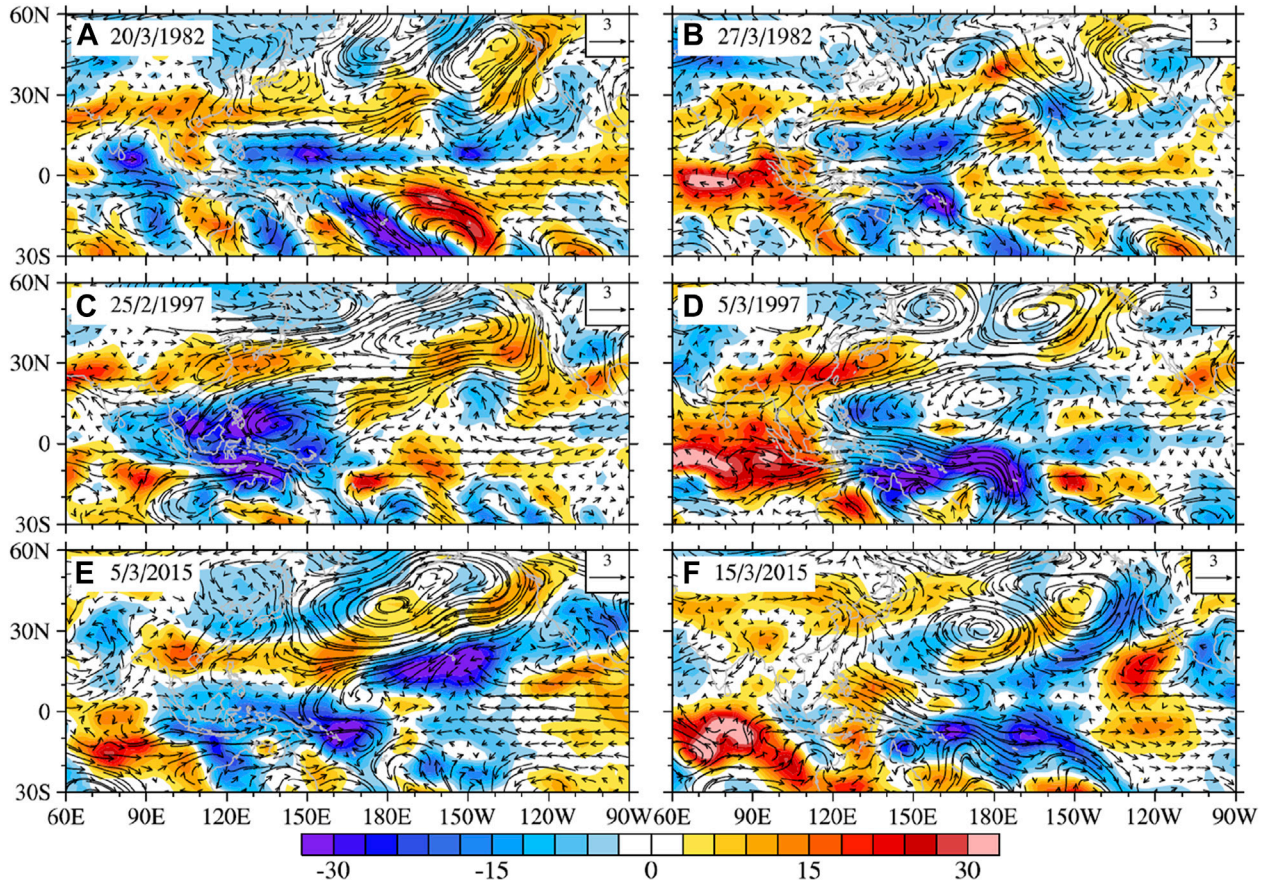

FIGURE 7
MJO wind at 850 hPa (vectors, m s^{-1}) and MJO OLR (colors, W m^{-2}) during the developing stages of the three super El Niño events. The 0 and 1 represent super El Niño event onset and next year, respectively. **(A–C)** represent 1982/83, 1997/98 and 2015/16, respectively.

necessary to further study the interaction between the MJO and the decaying stages of El Niño.

4 Possible cause of anomalous MJO activity

Figure 2 showed that the zonal westerlies of several MJO events were enhanced around 150°E during the early developing stages of three super El Niño, and the maximum center of MJO zonal wind occurred also around 150°E. Chen et al. (2017) indicated that the enhanced MJO zonal westerlies near 150°E are largely affected by the extratropical atmosphere. For the several MJO events during the developing stage of three super El Niño, our study discovered that the enhanced MJO zonal wind near 150°E is induced by extratropical circulation. Figure 7 shows the MJO circulation at 850 hPa and MJO OLR during the developing stage of the three super El Niño. The results clearly demonstrated that the MJO active near 150°E was closely related to the long-lasting extratropical circulations that reach the equator, which strengthened the activities of MJO zonal wind and OLR. The extratropical circulations originated from the northeastern Pacific (Figures 7A, C–E) as well as Siberia (Figures 7B, F). At the same time, due to the change of background field circulation (low-frequency circulation of more than 90 days) during the developing stages of El Niño, the MJO zonal westerly wind activity will strengthen around 150°E. From the anomalous 850 hPa zonal wind and specific humidity, it was clear that zonal westerly anomalies were appear in the western Pacific during the developing stages, and the strongest in the 1997/98 El Niño. The zonal winds of climate states over the central and eastern Pacific are robust easterlies and gradually weaken to the west. Thus, the anomalous westerly over the western Pacific amplify the zonal gradient of background zonal wind. Hsu et al. (2018) indicate that the conversion of low-frequency kinetic energy of more than 90 days to MJO kinetic energy is proportionate to the zonal gradient of background zonal wind ($-u'^2\frac{\partial \bar{u}}{\partial x}$, "′" and "–" are MJO scale and background wind). Therefore, the occurrence of background westerly anomaly over the western Pacific may lead to reinforcing the barotropic energy conversion from the low-frequency background field to the MJO scale, resulting in enhancing the activities of MJO zonal westerly.

In the mature stages of El Niño, the easterly anomaly from the Indian Ocean to the western Pacific Ocean, and the abnormal subsidence movement and negative moisture anomaly in the maritime continent and the western Pacific Ocean are not conducive to the MJO activities in these areas (Chen et al., 2016). The circulation and moisture anomaly in the western Pacific were relatively weak during the 2015/16 El Niño, so the weakening degree of MJO is relatively weak (Figure 8).

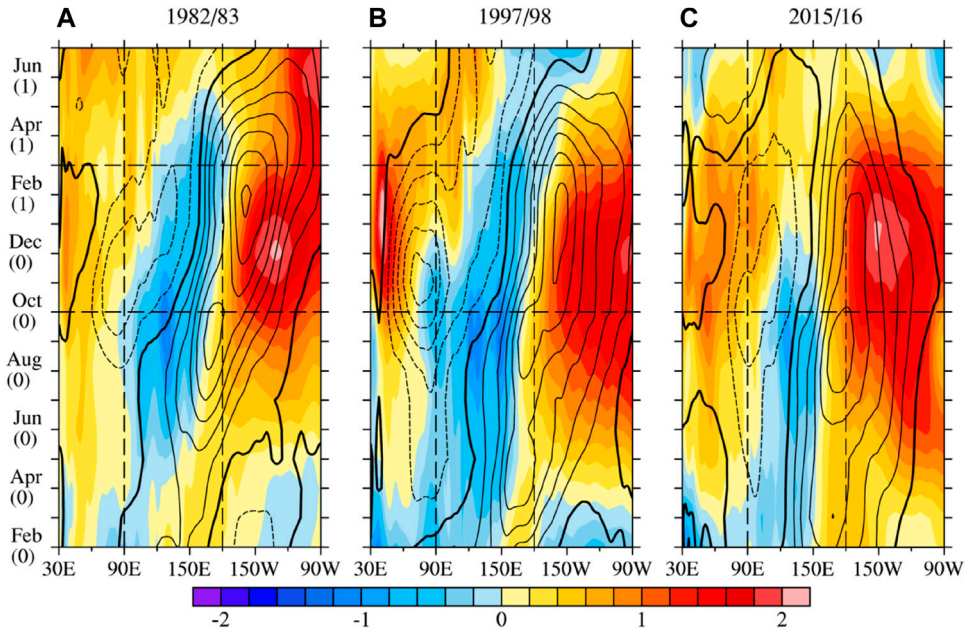

FIGURE 8
Anomalous zonal wind (contours, negative values are represented by dashed with the interval of 1 m s^{-1} and bold lines represent zero isolines) and specify humidity (colors, g kg^{-1}) at 850 hPa averaged over 10°S—10°N during the three super El Niño events. The 0 and 1 represent super El Niño event onset and next year, respectively. **(A–C)** represent 1982/83, 1997/98 and 2015/16, respectively.

Meanwhile, positive moisture anomaly and anomalous ascending motion appeared in the central and eastern Pacific during the mature stages of El Niño, which provide a favorable background field for the MJO activity, resulting in a stronger MJO amplitude over the central and eastern Pacific (Figure 6). It is noteworthy that the zonal westerly and positive moisture anomaly over the central and eastern Pacific was significantly westward during the mature stages of the 2015/16 El Niño, comparing with the other two El Niño events, which is consistent with the location of positive anomaly of MJO zonal wind amplitude to the west as shown in Figure 6. The circulation and moisture anomalies from the Indian Ocean to the western Pacific impeded the propagation of MJO during the mature stages of 1982/83 and 1997/1998 El Niño events, which caused the discontinuous eastward propagation. The 2015/16 El Niño showed some characteristics similar to the central Pacific El Niño (Paek et al., 2017). Although a certain easterly anomaly appeared over the western Pacific, the moisture was not prominent and positive moisture anomalies appeared in the later. Furthermore, the center of positive moisture anomaly over the central and eastern Pacific was westward. Consequently, the combination of anomalous moisture background and MJO circulation strengthens the moisture convergence in the lower troposphere on the eastern side of MJO convection ($-u'\frac{\partial \bar{q}}{\partial x}$), which promotes the activity and eastward propagation of MJO over the central and eastern Pacific (Chen et al., 2016).

In the decaying stages, the easterly anomaly and negative moisture anomaly over the western Pacific and maritime continent were also not conductive to the MJO activity in these areas. As the zonal westerly and positive moisture anomaly over the central and eastern Pacific rapidly weakened, resulting in weakening their strengthened role on the MJO. At the same time, the MJO activity weaken seasonally, due to the seasonal change of the background field (Dong et al., 2004). Therefore, the combination of anomalous circulation and moisture induced by El Niño with the seasonal variation of background field greatly weakened the MJO activity, which led to make the decaying stages the weakest period of MJO activity. However, the related physical process and mechanism of the abnormal MJO activity during the decaying stages of El Niño still need to be further researched.

5 Conclusion and discussion

The relationship between MJO and El Niño has always been a hot topic. Based on the reanalysis data, this paper deeply compared and analyzed the characteristics of MJO intensity and propagation during the developing, mature, and decaying stages of three super El Niño. Furthermore, this study identified the essential processes that induce abnormal MJO activities. The main conclusions are as follows:

There were three MJO events with obvious eastward propagation during the developing stages of the three super El Niño. The RMM index illustrated that MJO intensity decreased (or increased) in all phase during the developing stages of the 1982/83 (1997/98) El Niño event. The MJO activities weakened in phase 4–6 during the developing stages of the 2015/16 El Niño while significantly strengthened in other phases. In addition, the MJO zonal wind amplitude over the western Pacific strengthened during the developing stages of three super El Niño, especially during the 1997/98 El Niño.

The eastward propagation of MJO were not prominent during the mature stages of the 1982/83 and 1997/98 El Niño events, and there were even westward propagation. On the contrary, the prominent eastward propagation of MJO still appeared in the 2015/16 El Niño.

The RMM index showed that MJO intensities in all phase obviously decreased during the mature stages of the 1982/83 and 1997/98 El Niño events, while prominently increased in phase 4–8 during the 2015/16 El Niño. The MJO zonal wind amplitude weakened over the Indian Ocean and western Pacific during the mature stages of the 1982/83 and 1997/98 El Niño, while slightly strengthened over the central and eastern Pacific. However, MJO zonal wind prominently strengthened over the central and eastern Pacific during the mature stages of 2015/16 El Niño.

Although the eastward propagation of the MJO appeared during the decaying stages of three super El Niño, the intensity were weaker compared with the developing and mature stages, and decaying stages was the weakest stages of MJO activity. The RMM index indicated that the MJO primarily decreased in phase 1–3 and phase 6–8, while the MJO zonal wind amplitude mainly decreased over the Indian Ocean and western Pacific.

This study found that the activity and evolution characteristics of the MJO were mainly dominated by the low-frequency atmospheric circulation and anomalous moisture induced by El Niño, and they also were regulated by the extratropical circulation. In addition, the anomalous MJO activities played an obvious role in the developing and decaying stages of El Niño. This study also quantified the abnormal characteristics of MJO activities by the RMM index and MJO amplitude during the super El Niño, and there were contradictory results from the two method. Thus, we should pay more attention to they in the scientific research and practice applications to avoid misunderstanding the MJO characteristics. At present, many studies have focused on the interaction between MJO and El Niño during the developing and mature stages of El Niño. However, it is still necessary to further study the interaction between the MJO and El Niño during the decaying stages of El Niño and the corresponding cooperative effect on climate.

Data availability statement

The raw data supporting the conclusion of this article will be made available by the authors, without undue reservation.

Author contributions

XC provided the original idea and discuss with LL and CL. LL and XC plotted the figures and wrote the initial manuscript. XL and MY provided valuable advice for the research and presentation. All the authors contributed to the writing, editing, presentation, and reviewing of the manuscript.

Funding

This work was supported by the National Natural Science Foundation of China (Grant 42205045), the Hunan Natural Sciences Foundation (Grant 2022JJ30660), the National Key Research and Development Program of China (Grant 2018YFC1505901).

Acknowledgments

The ERA-Interim reanalysis dataset was obtained online (https://www.ecmwf.int/en/forecasts/datasets/reanalysis-datasets/era-interim). The Optimum Interpolation SST V2 (https://psl.noaa.gov/data/gridded/data.noaa.oisst.v2.html) and Extended Reconstructed SST V5 (https://psl.noaa.gov/data/gridded/) were provided by the NOAA. The MJO index was obtained from the Australian Bureau of Meteorology (http://www.bom.gov.au/climate/mjo/graphics/rmm.74toRealtime.txt).

Conflict of interest

The authors declare that the research was conducted in the absence of any commercial or financial relationships that could be construed as a potential conflict of interest.

Publisher's note

References

Abellán, E., Mcgregor, S., England, M. H., and Santoso, A. (2018). Distinctive role of ocean advection anomalies in the development of the extreme 2015–16 El Niño. *Clim. Dyn.* 51, 2191–2208. doi:10.1007/s00382-017-4007-0

Bergman, J. W., Hendon, H. H., and Weickmann, K. M. (2001). Intraseasonal air–sea interactions at the onset of El Niño. *J. Clim.* 14, 1702–1719. doi:10.1175/1520-0442(2001)014<1702:iasiat>2.0.co;2

Bi, B., Zhang, X., and Dai, K. (2017). Characteristics of 2016 severe convective weather and extreme rainfalls under the background of super El Niño. *Chin. Sci. Bull.* 62, 928–937. doi:10.1360/n972016-01136

Chen, L., Li, T., Wang, B., and Wang, L. (2017). Formation mechanism for 2015/16 super El Niño. *Sci. Rep.* 7, 2975–3010. doi:10.1038/s41598-017-02926-3

Chen, X., Li, C., and Tan, Y. (2015). The influence of El Niño on MJO over the equatorial Pacific. *J. Ocean Univ. China* 14, 1–8. doi:10.1007/s11802-015-2381-y

Chen, X., Ling, J., and Li, C. (2016). Evolution of the madden–julian oscillation in two types of El Niño. *J. Clim.* 29, 1919–1934. doi:10.1175/jcli-d-15-0486.1

Dasgupta, P., Roxy, M., Chattopadhyay, R., Naidu, C., and Metya, A. (2021). Interannual variability of the frequency of MJO phases and its association with two types of ENSO. *Sci. Rep.* 11, 11541–11616. doi:10.1038/s41598-021-91060-2

Dee, D. P., Uppala, S. M., Simmons, A. J., Berrisford, P., Poli, P., Kobayashi, S., et al. (2011). The ERA-Interim reanalysis: Configuration and performance of the data assimilation system. *Q. J. R. meteorological Soc.* 137, 553–597. doi:10.1002/qj.828

Dong, M., Zhang, X., and He, J. (2004). A diagnostic study on the temporal and spatial characteristics of the tropical intraseasonal osicllation. *Acta Meteor Sin.* 62, 821–830. (in Chinese). doi:10.11676/qxxb2004.078

Duchon, C. E. (1979). Lanczos filtering in one and two dimensions. *J. Appl. Meteorology Climatol.* 18, 1016–1022. doi:10.1175/1520-0450(1979)018<1016:lfioat>2.0.co;2

Feng, J., Liu, P., Chen, W., and Wang, X. (2015). Contrasting madden–julian oscillation activity during various stages of EP and CP El niños. *Atmos. Sci. Lett.* 16, 32–37. doi:10.1002/asl2.516

Fink, A., and Speth, P. (1997). Some potential forcing mechanisms of the year-to-year variability of the tropical convection and its intraseasonal (25–70-day) variability. *Int.*

J. Climatol. A J. R. Meteorological Soc. 17, 1513–1534. doi:10.1002/(sici)1097-0088(19971130)17:14<1513::aid-joc210>3.0.co;2-u

Gushchina, D., and Dewitte, B. (2012). Intraseasonal tropical atmospheric variability associated with the two flavors of El Niño. *Mon. Weather Rev.* 140, 3669–3681. doi:10.1175/mwr-d-11-00267.1

Hayashi, Y. (1982). Space-time spectral analysis and its applications to atmospheric waves. *J. Meteorological Soc. Jpn. Ser. II* 60, 156–171. doi:10.2151/jmsj1965.60.1_156

Hendon, H. H., Wheeler, M. C., and Zhang, C. (2007). Seasonal dependence of the MJO–ENSO relationship. *J. Clim.* 20, 531–543. doi:10.1175/jcli4003.1

Hong, C.-C., Hsu, H.-H., Tseng, W.-L., Lee, M.-Y., Chow, C.-H., and Jiang, L.-C. (2017). Extratropical forcing triggered the 2015 madden–julian oscillation–el Niño event. *Sci. Rep.* 7, 46692–46698. doi:10.1038/srep46692

Hsu, P.-C., Fu, Z., and Xiao, T. (2018). Energetic processes regulating the strength of MJO circulation over the Maritime Continent during two types of El Niño. *Atmos. Ocean. Sci. Lett.* 11, 112–119. doi:10.1080/16742834.2018.1399049

Huang, B., Thorne, P. W., Banzon, V. F., Boyer, T., Chepurin, G., Lawrimore, J. H., et al. (2017). Extended reconstructed sea surface temperature, version 5 (ERSSTv5): Upgrades, validations, and intercomparisons. *J. Clim.* 30, 8179–8205. doi:10.1175/jcli-d-16-0836.1

Kessler, W. S., McPhaden, M. J., and Weickmann, K. M. (1995). Forcing of intraseasonal Kelvin waves in the equatorial Pacific *J. Geophys Res.* 100, 10613–10631.

Lau, K.-M., and Chan, P. H. (1988). Intraseasonal and interannual variations of tropical convection: A possible link between the 40–50 day oscillation and ENSO? *J. Atmos. Sci.* 45, 506–521. doi:10.1175/1520-0469(1988)045<0506:iaivot>2.0.co;2

Lau, K., and Chan, P. (1986). The 40–50 day oscillation and the El niño/southern oscillation: A new perspective. *Bull. Am. Meteorological Soc.* 67, 533–534. doi:10.1175/1520-0477(1986)067<0533:tdoate>2.0.co;2

Lee, R. W., Woolnough, S. J., Charlton-Perez, A. J., and Vitart, F. (2019). ENSO modulation of MJO teleconnections to the north atlantic and europe. *Geophys. Res. Lett.* 46, 13535–13545. doi:10.1029/2019gl084683

L'heureux, M. L., Takahashi, K., Watkins, A. B., Barnston, A. G., Becker, E. J., Di Liberto, T. E., et al. (2017). Observing and predicting the 2015/16 El Niño. *Bull. Am. Meteorological Soc.* 98, 1363–1382. doi:10.1175/bams-d-16-0009.1

Li, C., and Li, G. (1995). Kinetic energy changes in the tropical atmospheric system associated with El Niño. *Chin. Sci. Bull.* 40, 1866–1869. doi:10.1360/csb1995-40-20-1866

Li, C., Ling, J., Song, J., Pan, J., Tian, H., and Chen, X. (2014). Research progress in China on the tropical atmospheric intraseasonal oscillation. *J. Meteorological Res.* 28, 671–692. doi:10.1007/s13351-014-4015-5

Li, C., and Smith, I. (1995). Numerical simulation of the tropical intraseasonal oscillation and the effect of warm SST. *Acta Meteor. Sin.* 9, 1–12.

Li, C. (1995). Some fundamental problems of intraseasonal oscillation in the tropical atmosphere. *J. Trop. Meteorology* 11, 276–288. (in Chinese).

Li, C., and Zhou, Y. (1994). Relationship between intraseasonal oscillation in the tropical atmosphere and ENSO. *Chin. J. Geophys.* 37, 17–26. (in Chinese).

Li, Q., and Min, Q. (2016). A dialogue with Renhe Zhang: The heavy rainfall over southern China in the first half year of 2016 and its relation to the 2015/2016 super El Niño. *Chin. Sci. Bull.* 61, 2659–2662. doi:10.1360/zk2016-61-24-2659

Li, T., Ling, J., and Hsu, P.-C. (2020). Madden-Julian oscillation: Its discovery, dynamics, and impact on East Asia. *J. Meteorological Res.* 34, 20–42. doi:10.1360/zk2016-61-24-2659

Liu, M., Ren, H., Zhang, W., Ren, P., and Liu, X. (2018). An echo state network algorithm based on recursive least square for electrocardiogram denoising. *Acta Meteorol. Sin.* 76, 539–549. doi:10.7507/1001-5515.201710072

Lyu, Y., Li, Y., Tang, X., Wang, F., and Wang, J. (2018). Contrasting intraseasonal variations of the equatorial Pacific Ocean between the 1997–1998 and 2015–2016 El Niño events. *Geophys. Res. Lett.* 45, 9748–9756. doi:10.1029/2018gl078915

Madden, R. A., and Julian, P. R. (1972). Description of global-scale circulation cells in the tropics with a 40–50 day period. *J. Atmos. Sci.* 29, 1109–1123. doi:10.1175/1520-0469(1972)029<1109:dogscc>2.0.co;2

Madden, R. A., and Julian, P. R. (1971). Detection of a 40–50 day oscillation in the zonal wind in the tropical Pacific. *J. Atmos. Sci.* 28, 702–708. doi:10.1175/1520-0469(1971)028<0702:doadoi>2.0.co;2

Mcphaden, M. J. (1999). Genesis and evolution of the 1997-98 El Niño. *Science* 283, 950–954. doi:10.1126/science.283.5404.950

Mcphaden, M. J., Zhang, X., Hendon, H. H., and Wheeler, M. C. (2006). Large scale dynamics and MJO forcing of ENSO variability. *Geophys. Res. Lett.* 33, L16702. doi:10.1029/2006gl026786

Miyakawa, T., Yashiro, H., Suzuki, T., Tatebe, H., and Satoh, M. (2017). A Madden-Julian Oscillation event remotely accelerates ocean upwelling to abruptly terminate the 1997/1998 super El Niño. *Geophys. Res. Lett.* 44, 9489–9495. doi:10.1002/2017gl074683

Moon, J.-Y., Wang, B., and Ha, K.-J. (2011). ENSO regulation of MJO teleconnection. *Clim. Dyn.* 37, 1133–1149. doi:10.1007/s00382-010-0902-3

Mu, M., and Ren, H.-L. (2017). Enlightenments from researches and predictions of 2014-2016 super El Niño event. *Sci. China. Earth Sci.* 60, 1569–1571. doi:10.1007/s11430-017-9094-5

Paek, H., Yu, J. Y., and Qian, C. (2017). Why were the 2015/2016 and 1997/1998 extreme El Niños different? *Geophys. Res. Lett.* 44, 1848–1856. doi:10.1002/2016gl071515

Qian, D., and Guan, Z. (2018). Different features of super and regular El Niño events and their impacts on the variation of the West Pacific subtropical high. *Acta Meteorol. Sin.*, 394–407. doi:10.11676/qxxb2018.011

Rao, J., and Ren, R. (2017). Parallel comparison of the 1982/83, 1997/98 and 2015/16 super El Niños and their effects on the extratropical stratosphere. *Adv. Atmos. Sci.* 34, 1121–1133. doi:10.1007/s00376-017-6260-x

Ren, H.-L., Wang, R., Zhai, P., Ding, Y., and Lu, B. (2017). Upper-ocean dynamical features and prediction of the super El Niño in 2015/16: A comparison with the cases in 1982/83 and 1997/98. *J. Meteorological Res.* 31, 278–294. doi:10.1007/s13351-017-6194-3

Reynolds, R. W., Smith, T. M., Liu, C., Chelton, D. B., Casey, K. S., and Schlax, M. G. (2007). Daily high-resolution-blended analyses for sea surface temperature. *J. Clim.* 20, 5473–5496. doi:10.1175/2007jcli1824.1

Seo, K. H., and Xue, Y. (2005). MJO-related oceanic Kelvin waves and the ENSO cycle: A study with the NCEP Global Ocean Data Assimilation System. *Geophys. Res. Lett.* 32, L07712. doi:10.1029/2005GL022511

Shao, X., and Zhou, B. (2016). Monitoring and diagnosis of the 2015/2016 super El Niño event. *Meteorol. Mon.* 42, 540–547. (in Chinese). doi:10.7519/j.issn.1000-0526.2016.05.003

Takayabu, Y., Iguchi, T., Kachi, M., Shibata, A., and Kanzawa, H. (1999). Abrupt termination of the 1997–98 El Niño in response to a madden–julian oscillation. *Nature* 402, 279–282. doi:10.1038/46254

Tam, C.-Y., and Lau, N.-C. (2005). Modulation of the madden-julian oscillation by ENSO: Inferences from observations and GCM simulations. *J. Meteorological Soc. Jpn. Ser. II* 83, 727–743. doi:10.2151/jmsj.83.727

Vecchi, G., and Harrison, D. E. (2000). Tropical Pacific sea surface temperature anomalies, El Niño and equatorial westerly wind events. *J. Clim.* 13, 1814–1830. doi:10.1175/1520-0442(2000)013<1814:TPSSTA>2.0.CO;2

Wang, L., Li, T., Chen, L., Behera, S. K., and Nasuno, T. (2018). Modulation of the MJO intensity over the equatorial Western Pacific by two types of El Niño. *Clim. Dyn.* 51, 687–700. doi:10.1007/s00382-017-3949-6

Wei, Y., and Ren, H.-L. (2019). Modulation of ENSO on fast and slow MJO modes during boreal winter. *J. Clim.* 32, 7483–7506. doi:10.1175/jcli-d-19-0013.1

Wheeler, M. C., and Hendon, H. H. (2004). An all-season real-time multivariate MJO index: Development of an index for monitoring and prediction. *Mon. weather Rev.* 132, 1917–1932. doi:10.1175/1520-0493(2004)132<1917:aarmmi>2.0.co;2

Yuan, Y., Gao, H., Jia, X., and Wan, J. (2016). Influences of the 2014-2016 super El Niño event on climate. *Meteorol. Mon.* 42, 532–539. (in Chinese). doi:10.7519/j.issn.1000-0526.2016.05.002

Yuan, Y., Li, C., and Ling, J. (2015). Different MJO activities between EP El Niño and CP El Niño. *Sci. China Earth Sci.* 45, 318–334. (in Chinese). doi:10.1360/zd-2015-45-3-318

Zhai, P., Yu, R., Guo, Y., Li, Q., Ren, X., Wang, Y., et al. (2016). The strong El Niño in 2015/2016 and its dominant impacts on global and China's climate. *Acta Meteor Sin.* 74, 309–321. (in Chinese). doi:10.11676/qxxb2016.049

Zhang, C., and Gottschalck, J. (2002). SST anomalies of ENSO and the Madden–Julian oscillation in the equatorial Pacific. *J. Clim.* 15, 2429–2445. doi:10.1175/1520-0442(2002)015

Zhang, C. (2013). Madden–Julian oscillation: Bridging weather and climate. *Bull. Am. Meteorological Soc.* 94, 1849–1870. doi:10.1175/bams-d-12-00026.1

Zheng, Y., Chen, Z., Wang, H., and Du, Y. (2019). Features of 2015/2016 extreme El Niño event and its evolution mechanisms. *J. Trop. Oceanogr.* 38, 10–19. (in Chinese). doi:10.11978/2018114

Frontiers in Earth Science

Investigates the processes operating within the major spheres of our planet

Advances our understanding across the earth sciences, providing a theoretical background for better use of our planet's resources and equipping us to face major environmental challenges.

Discover the latest Research Topics

See more →

Frontiers

Avenue du Tribunal-Fédéral 34
1005 Lausanne, Switzerland
frontiersin.org

Contact us

+41 (0)21 510 17 00
frontiersin.org/about/contact